Debris Flows:

Interior Velocity Profiles

A thesis submitted in partial fulfilment of the requirements for the Degree of

Masters of Engineering in Civil Engineering

University of Canterbury

Author: Joshua J Bird

2013

Academic Supervisor: Elisabeth Bowman

Associate Academic Supervisor: Roger Nokes

Department of Civil and Natural Resources

College of Engineering

University of Canterbury

Abstract

Debris flows are an increasingly potential hazard in steep mountain valleys. Obtaining understanding of this phenomena is made difficult by the highly complex interaction between fluid and solid particles of a wide range of sizes. Debris flows are an interaction of both fluid and geotechnical engineering disciplines. They have a highly mobile, unsaturated coarse front, a highly dynamic body and a fluidised tail. The major defining features are the segregation of the flow and the ability to move the largest fraction along the free surface in a conveyer like system, creating damming and surging phenomena. The majority of historical research has been done on highly concentrated fluid flows and the flow rheologies reflect this. Field and laboratory investigation is limited by the opaque nature of the material.

The main aim was to identify the influence of boundary effects, moisture content and slope on the micro-mechanical behaviour of debris flows. This was conducted by an innovative combination of planar laser-induced fluorescence (PLIF) and particle imaging velocimetry (PIV). The laser plane was used to illuminate an interior plane for recording a series of high speed images from both the interior and exterior of laboratory debris flow experiments. By substituting real opaque materials for transparent solids and fluids that are optically matched, the laser light was able to be captured from the interior of the flow. The resulting images were of black particles in a white illuminated fluid. This combination of pattern was ideal for particle imaging velocimetry (PIV) which was able to calculate the velocity and displacement of sections of the flow. This methodology was used to look directly within the flow while giving non-invasive data on the behaviour of the solid particles and fluid. The resulting outputs were able to give velocity with depth and time to help analyse the spatial and temporal behaviour.

Measures of run-out, deposit shape, deposit particle size distributions, spot-heights and height-over-time plots demonstrated the PLIF material behaved in a manner consistent with field observations of debris flows. There was a high level of variability that is intrinsic to the complex nature making debris flows difficult to statistical analyse. Instantaneous velocity plots at various locations in the flow demonstrated evolving behaviour that was more significant than the changes in slope and moisture content. A slip velocity in the front of the flow was the most observable difference between exterior and interior images. Another difference identified was the slowing of the flow at the boundary wall. Large particles were

seen to accumulate smaller particles, creating damming structures and in some cases small surges.

The methodology was well tested and provided quality insights into the interior mechanics of the flows in a mainly qualitative fashion that supported many theories that had not been observed directly. The findings of this research shows how complex and dynamic debris flows are and how hazardous and unpredictable the velocity and surging behaviour can be. The observations obtained through PLIF and PIV are a step toward applying more effective rheologies and theories to these unique flows.

Acknowledgements

I would like to acknowledge all those talented people that have helped me prepare my thesis;

- Dr Elisabeth Bowman
- Dr Rodger Nokes
- Dr Nicolleta Sanvitale for the pioneering work she did on the experimental procedure.
- Martin Single, Rose Harding and Deborah McFarlane for the editing and assistance with grammar and formatting
- The Technical staff in the University of Canterbury, Civil and Natural Resources Engineering Department
- Marsden Fund for the financial support.

Table of Contents

Table of Tables

Table of Figures

Table of Symbols

i. Lower case Latin

Character	Definition
c	Volume concentration
c^*_0	Most densely packed volume concentration
du	Change in slope-normal velocity
du/dz	Shear strain rate
d_r	Camera pixel size
dz	Change in height
e	Void ratio
g	Gravity
h,	Flow depth
h_{max}	Maximum depth.
i	Mesh row (depth)
j	Pair of images used in the calculation
k	Permeability
l_{oil}	Modified length scale in oil
l_{water}	Length scale of natural particles in water
t	Time
u	Slope-normal velocity
v	Slope-parallel velocity
v_s	Solid phase velocity
w	Moisture content
w	Width of the flume

ii. Upper Case Latin

Character	Definition
A_1	Empirical constant from Rickenmann (1999)
B	Batch size
C	Number of columns of patches
$C_{k\text{-}c}$	Kozeny-Carman empirical coefficient
C_u	Coefficient of uniformity
C_Z	Coefficient of curvature
D_{10}	10^{th} percentile particle diameter
D_{50}	50^{th} percentile particle diameter
D_B	Bead diameter
F_d	Drag force
G_s	Specific gravity
I_{test}	Test patch
I_{search}	Search patch
L_{Fan}	Run-out along the fan
$L_{optical}$	Optical axis length
Lp	Length of patch
M	Image magnification
N	Number of grains above slip surface
N_{Bag}	Bagnold number
N_{mass}	Ratio of solid mass to fluid mass.
N_{Sav}	Savage number
$p_{Base\ flume}$	Height at the base of the flume taken from the image
P_{lower}	Number of patches removed from mesh lower bounds
$p_{Mesh\ lower}$	Height at the bottom of the mesh
$p_{Mesh\ upper}$	Height at the top of the mesh
$p_{Sat\ surface}$	Height at saturation surface for all images in a batch
P_{Size}	Patch size
P_{Total}	Total number of rows of patches in the mesh
P_{upper}	Number of patches removed from mesh upper bound
Q	Flow rate

R_i	Refractive index
S_{max}	Max search length
S	Search patch
SF	Shape factor
S_0	Specific surface area per unit volume of particles
T	Temperature
U	Displacement of patch
Y_{Step}	Slope-normal pixel step between patches.

iii. Greek

Character	**Definition**
γ	Unit weight
δ	Typical grain diameter
δ_{eff}	Effective particle diameter
ΔR_i	Difference in refractive index
εPD	Imaged position error
λ	Linear concentration
μ	Dynamic viscosity
ν	Kinematic viscosity
ν_{oil}	Kinematic viscosity of the oil
ν_{water}	Kinematic viscosity of water
ν_s	Solid volume fraction
π	Pi
σ_i	Standard deviation of patch i
ρ_f	Fluid density
ρ_s	Solid density
τ	Shear stress
ϕ	Bulk friction angle

iv. Units

Character	Name	Use
°	Degrees	angle
°C	Degrees Celsius	unit of temperature
cm	Centimetres	unit of length
cSt		unit of kinematic viscosity
fps	Frames per second	unit of images over time of recording
g	Grams	unit of mass
g/cm^3	Grams per cubic centimetre	unit of density
Hz	Hertz	unit of frequency
kg	Kilogram	unit of weight
mJ	Milli-Joules	unit of energy
mg/L	Milligram per litre	unit of concentration
min	Minutes	unit of time
mm	Millimetres	unit of length
mW	Milli-Watt	unit of power
nm	Nanometre	unit of length
s	Second	unit of time
µm	micrometre	unit of length

Glossary

i. Abbreviations

Characters	Definition
ADV	Acoustic Doppler Velocimetry
EX	Exterior location of view
ICV	Image Correlation Velocimetry
IN	Interior location of view
LDA	Laser Doppler Anemometry
LDV	Laser Doppler Velocimetry
LIF	Laser-Induced Fluorescence
LSV	Laser Speckle Velocimetry
LOV	Location of View
MRI	Magnetic Resonance Imaging
NMR	Nuclear Magnetic Resonance
PIV	Particle Imaging Velocimetry
PLIF	Planner Laser-Induced Fluorescence
PSD	Particle Size Distribution
PSV	Particle Streak Velocimetry
PTV	Particle Tracking Velocimetry
QI	Quantitative Imaging
RIM	Refractive Index Matching
S##	Slope of angle (°) of ##
USGS	United States Geological Survey
W##	Moisture Content (%) of ##

ii. Terminology

Batch	The number of images used in a single comparison of an instantaneous location within the flow
Body	The saturated section of a debris flow that starts from the maximum saturation height and represents the bulk of the mass moving at a relatively high velocity
Exterior	The slice of the flow directly against the window of the flume
Floating	When a particle appears to move to the free surface and stay there above the other particles
Front	Is both the unsaturated snout and saturated body section up to the maximum saturation height
Geo-PIV	The Matlab code used for PIV analysis.
Image	One frame from the series of frames taken from the high speed camera used for analysis.
Interior	The slice of the flow sitting inside the debris flow that is derived from the laser plane used in internal imaging.
Jumping	When a particle is fully ejected vertical from the flow
Moisture Content	The amount of fluid compared to total mass
Slope	The angle of inclination of the flume to the horizontal
Snout	The unsaturated section of the debris flow that is continuous contact with the debris flow mass.
Tail	The saturated section of a debris flow after the body that represents the highly fluid slow shallow end of the debris flow
Patch	The square area of an image that is used for comparison in PIV.

Chapter 1. Introduction

1.1. Overview

Somewhere on the natural continuum between pure water floods and a rock avalanche there is an area where the fluid and solid particle mechanics are equally active. These behaviours combine to form a particular type of mass transport called debris flows. Debris flows are characterised as being composed of saturated eroded materials that are fast moving and are generally confined to a channel.

This thesis investigates the interior mechanics, particularly the interior velocity profiles of debris flows. It will do this through non-intrusive measurement of small-scale laboratory experiments.

Debris flows are one of New Zealand's least understood and potentially destructive slope hazards. Protection from these events has largely been provided by unintentional avoidance. A current example of concern for debris flows is around the Central North Island's volcanic zones, particularly following some eruptions at Mt Tongariro (Watson, 2012). This is typical of the class of debris flows known as lahars. In the Tongariro case it is mainly transport infrastructure that is at risk. However, if damage was to correspond with peak tourist times or a large eruption then there is potential loss of life. There are some attempts being made to design structural protection measures in the case of Matata, Bay of Plenty (Bowman, pers comm.) and Thames (McSaveney & Beetham, 2006) (McSaveney, Beetham, & Leonard, 2005).

Debris flows occur ubiquitously in areas with steep slopes and at least occasional rainfall (Jakob & Hungr, 2005). New Zealand's topography and climate presents many areas that are susceptible due to steep slopes, high rainfall and erodible soils. Interaction between soil, water and gravity creates high flow velocities, high impact forces and long run-out in debris flows. As land development increases, more pressure is being placed to develop the land around debris flow deposits, as they often are ideal scenic locations for building homes. A better understanding of the potential risks and behaviours will help with intentional avoidance and protection measures.

Previous studies have used empirical field or externally measured lab results for validation of models of debris flows. These do not adequately investigate the interior mechanisms away from boundary conditions.

Traditional mechanical theories of debris flow split the flow into a solid and liquid phase which are characterized by momentum and energy transfer (Iverson, 1997). Debris flows represent a complex behaviour caused by inertial grain collisions, grain contact friction, viscous shear and solid-fluid interactions. Highly complex models relating the stress and strain dynamically are often difficult to use in practice (Chen, 1988). Iverson, Logan, LaHusen & Berti (2010) states that it is not a new rheology that we are looking for to predict behaviour but the way in which these rheologies evolve dynamically. As a result, instead of using a mechanical theory of behaviour, these processes are often modelled based on empirical or assumed equations. These equations relate the concentration of solids, the rate of strain, the stress and the energy of the mixture to assume the micro-mechanical aspects of particle motion and material interactions of the particles and fluid (Iverson, 1997).

Unfortunately the verification of such models against in-situ observations is rendered extremely difficult because of the remoteness and unpredictable occurrence of events. Therefore laboratory-scale physical model tests have become critical to understanding. There is concern over the accuracy of laboratory behaviour compared to the actual natural process where scale may change the interior behaviour (Iverson, 1997). However, it has recently been shown that if particle and fluid properties are selected carefully for laboratory tests, debris flow type behaviour may be reproduced in small scale experiments (Bowman & Sanvitale, 2009). It is expected that laboratory experiments in which parameter values and boundary conditions are well-defined and well-controlled will give accurate and translatable observations upon which to base physical rules and the validation of mechanistic models.

1.2.Conceptual context

This thesis is a companion work developing the technique originally developed by Sanvitale (2010). Her work investigated debris flows using small-scale flumes to first use natural well-graded material, focusing on changing the particle size distribution of the material. Secondly, she developed a novel Planar Laser-Induced Fluorescence technique that used Refractive Index Matching to investigate the interior behaviour of concentrated debris flows. She

verified the feasibility of the method through comparison with the natural material experiments.

However, Sanvitale (2010) did not investigate if the interior and exterior images gave a substantially different result or the effect of slope and moisture content on the interior mechanics of the concentrated flow. Therefore this thesis will add to the previous work by comparing the interior with an exterior behaviour in order to appreciate the similarity or difference from using a non-intrusive method and the reasons for the differences. Conducting experiments with different slope and moisture contents will allow a relatively comprehensive depiction of the influences on interior debris flow behaviour.

1.3.Research Objectives

This thesis aims to add some complexity to simplified laboratory models in order to move from older models that assume uniform perfect spheres in 2D space to a more realistic scenario. This is balanced with the need to keep the factors simple enough so as to produce data which can be used to generate better theories of the material behaviour of debris flows.

These aims will be achieved through small scale laboratory experiments with reduced boundary conditions using a non-intrusive technique. This will require an extension of a technique developed by Sanvitale (2010) in order to determine the relationship between the interior, exterior and boundary conditions, as well as slope and moisture content. It is intended that the findings of this study will enable better validation of data to calibrate rheological models.

The objectives of this research will, therefore, be to:

- Refine the experimental technique and setup to obtain an increase in image quality for computational programme analysis, of the relationship between horizontal velocities and depth;
- Carry out tests using a non-intrusive technique and more common exterior recording technique to observe and describe the interior velocities and particle interaction of a laboratory simulated debris flow, with respects to existing flow rheologies for various parts of a moving debris flow;

- Show velocity profiles within both interior and exterior sections to see boundary impacts, segregation, distribution of particle and how they are affected by changes in material and flow properties, particularly the impact of small change in slope and moisture content.

1.4.Thesis Outline

Chapter 1 of this thesis will introduce the motivation, within New Zealand, that has led to the importance of studying debris flows. It will also outline the context that determines the aims that are sought to be addressed and the structure of the thesis.

Chapter 2 is a large chapter that will investigate and review the conceptual, theoretical and background to investigating behaviour of debris flows, paying attention to contemporary literature. The chapter will begin with a general description of the behaviour and flow phenomena particular to debris flows. It will then will look at the most common theoretical descriptions of 'rheology' or response of material to applied stress. This chapter needs to cover rheologies and phenomena to an in-depth level in order to give context to the observations of velocities presented in Chapter 4. Finally, the background of physical modelling and the relatively innovatively applied, non-intrusive physical modelling is summarised.

Chapter 3 will outline the physical and computational methodology procedures, apparatus and methods that will be undertaken to investigate small laboratory-scale debris flows. The material properties form an integral part of the visualisation techniques. The techniques are explained in detail with factors that may impact the image quality. The computation methodology is defined and explained using preliminary results with additional sensitivity studies in the Appendices referred to.

Chapter 4 will start with the deposition results, broken into camera location, moisture content and slope. These will be compiled to show behaviour consistent with stony debris flows and to identify any potential discrepancies in testing that may affect the velocity profiles. The results will include deposition outlines, PSDs of various locations in the deposit, height over time, velocity over time velocity profiles at specific locations within the flow and an approximation of the flow rates over time. Velocity profiles will be compared based on the location of the camera, moisture content and slope.

Chapter 5 is a discussion of results and implications in context to other research and modelling. The results in Chapter 4 are compared with previous work by Sanvitale (2010) and the differences are accounted for. The observations taken from the experiments will be used to create and compare the flow anatomy. This will then be used to evaluate how the velocity profiles link to each part of the anatomy. This chapter will then investigate the particular finds obtained by comparing exterior to interior tests and the impacts of individual phenomena and behaviours identified during testing. The discussion then links the behaviour of the anatomy regions to rheologies for modelling. Finally evaluations of the technique are presented followed by recommendation for improving the methodology and adapting new techniques to the current method.

The Chapter 6 concludes the findings of this thesis and emphasises the nature of debris flows and their hazard potential. Chapter 7 is the list of references contained within this thesis. Chapter 8 is a series of Appendices used to give additional information on a range of sections within the thesis,

- Appendix A: The material preparation required to reuse material.
- Appendix B: A study on the effects of altering the image quality and issues relating to the conversion of recordings into a format for PIV analysis.
- Appendix C: Sensitivity studies of the PIV parameters relating to patch size, location and setup of mesh.
- Appendix D: A summary and comparison of each set of variables used to identify trends and abnormalities within each test.
- Appendix E: The deposit data recorded for all tests including deposit shapes outlined over actual images of deposit, spot height diagrams and PSDs.
- Appendix F: Height-over-time graphs including saturation and absolute heights over the entire image recording with notation of particular structures in the images. Separate saturation levels and absolute heights have been plotted with moving averages for the snout and initial body of all flows.
- Appendix G: The PIV velocity profiles for each flow including the PIV height-over-time, flow-over-time and velocity-over-time. The profiles have also been normalised and presented for all test.

Chapter 2. Conceptual, Theoretical and Experimental Background

This chapter reviews the conceptual phenomena, theoretical behaviours, physical modelling and the non-intrusive measuring methods that can be applied to physical models of debris flows. Each of these sections is required to understand a natural process that is a highly variable 'black box.'

The conceptual section (Section 2.1) defines the behaviour and apparent mechanism of debris flows, paying attention to the visible signs and measurements that can be used to define debris flow behaviour. This is required to show how debris flows are unique, highly chaotic, and at the intersection of a number of material behaviours.

The theoretical section (Section 2.2) presents a number of rheologies and material theories the most common are summarised in order to show the historical approach to modelling the behaviour of the material. These rheologies are all valid attempts to describe debris flows and can apply to a single flow as it varies spatially and temporally.

The physical modelling section (Section 2.3), looks at the field, empirical large and small scale laboratory results. This section is an overview of experimental work that has been conducted to show the unique behaviour and effect of various parameters on flow behaviour.

The non-intrusive section (Section 2.4), introduces a number of physical recording methods particularly Refractive Index Matching and Laser-Induced Fluorescence. The section will also outline a number of quantitative imaging techniques, expanding on Particle Imaging Velocimetry and how it can be combined with LIF to assist analysis of granular geotechnical flows. Non-intrusive methods are a relatively innovative technique that has only been applied in a limited way to complex debris flows.

The combination and depth of each these sections allows the results of this thesis (Chapter 4) to be discussed in terms of the methodology and observed behaviour that can identify, reinforce, or validate the way in which velocity profiles are measured and numerical modelled.

2.1. General Description and Concepts

2.1.1. Definition of Debris Flow

Debris flows are eroded materials and water that combine to become a rapid flow moving down slope under the influence of gravity often in a constrained channel (Jakob & Hungr, 2005).

Debris flows are highly kinetic and chaotic water-saturated masses of natural material. They are mountain slope, mass movements, which are generally channelized and originate from unstable sediment deposits. In debris flows there is a high percentage of solids compared with fluids and are a type of granular flow. Debris flows are still able to attain high speeds and are recognised as the most hazardous type of granular flow due to their high mobility and destructive power (Jakob & Hungr, 2005). Debris flows have the potential to damage structures, alter stream flows and occasionally cause loss of human life. A notable debris flow disaster occurred in central Virginia in 1969 which resulted in 150 deaths and hundreds of millions of dollars' worth of property damage. In California between 1978 and 1982 a debris flow resulted in tens of deaths. Near the Nevado del Ruiz volcano, Colombia in 1985 a debris flow took the lives of more than 23,000 people (Iverson, Costa, & LaHusen, 1992). Figure 2-1 and Figure 2-2 shows examples of the scale and destruction documented in Austria, Washington State, USA and Switzerland.

Figure 2-1: Debris flow deposit in Austria (left) (Spaaks, 2010). Bridge and culvert destruction (right) Washington State (USA) (Sarikhan, 2007).

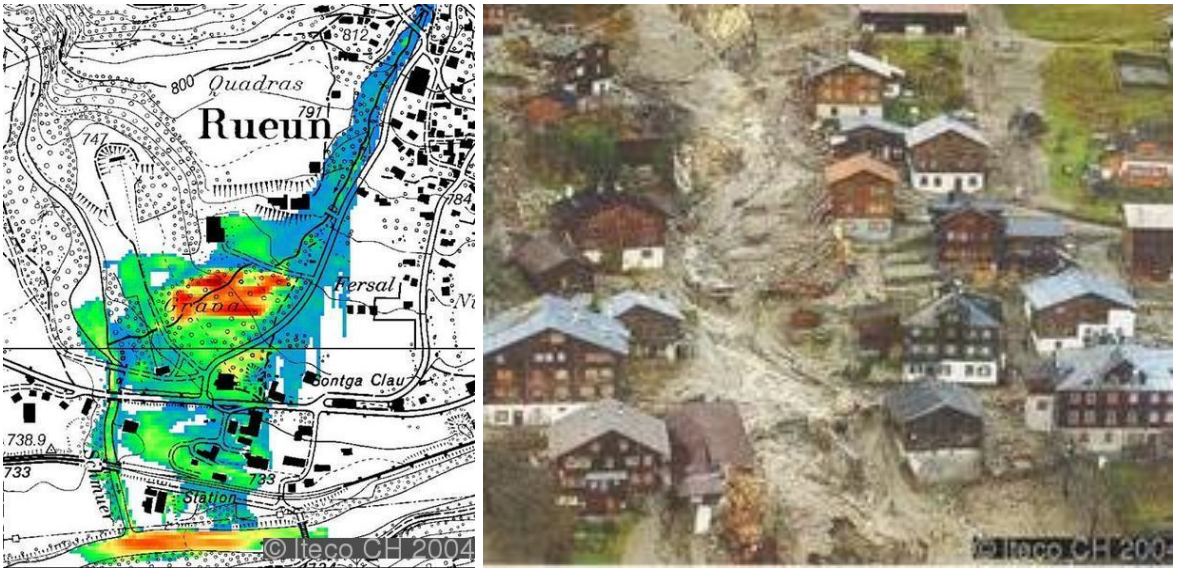

Figure 2-2: Simulation (left) and photo (right) of Rueun, Switzerland, debris flow in 2002 (Iverson, 1997).

Traditionally debris flows are seen as existing on a continuum. A simple development of the continuum from fluid-dominated process to granular-dominated process can be expressed in the following general order: Pure Newtonian flows like rivers, sediment rich slurries, hyper-concentrated flows, debris flows, slip planes, dry sliding and collision-driven forms of mass wasting like rock avalanches (Lorenzini & Mazza, 2004). As seen in Lorenzini and Mazza (2004) debris flow mechanics exist between those of concentrated flood flows and rock avalanches. Interactions between soil, water, and gravity create high-flow velocities, destructive impact forces and long run-out. In Figure 2-3, debris flows are shown in context with other flows based on sediment concentration and mean velocity. It shows that debris flows exist between hyper-concentrated stream flow (mud flow) and viscous granular flows (earth flows).

Defining whether a particular mass movement of material down a slope is a debris flow is difficult but is commonly based on the idea of two phase interactions (Iverson & Vallance, 2001). In a debris flow there are both fluid and granular particle effects, and when both the soil and fluid process are dominant then the flow can be called a debris flow. In fluid-dominated flow, sediment is transported as bed load. In granular-dominated flows, the particle collisions and transfer of momentum controls motion, and there are typically insignificant fluid or pore pressure effects.

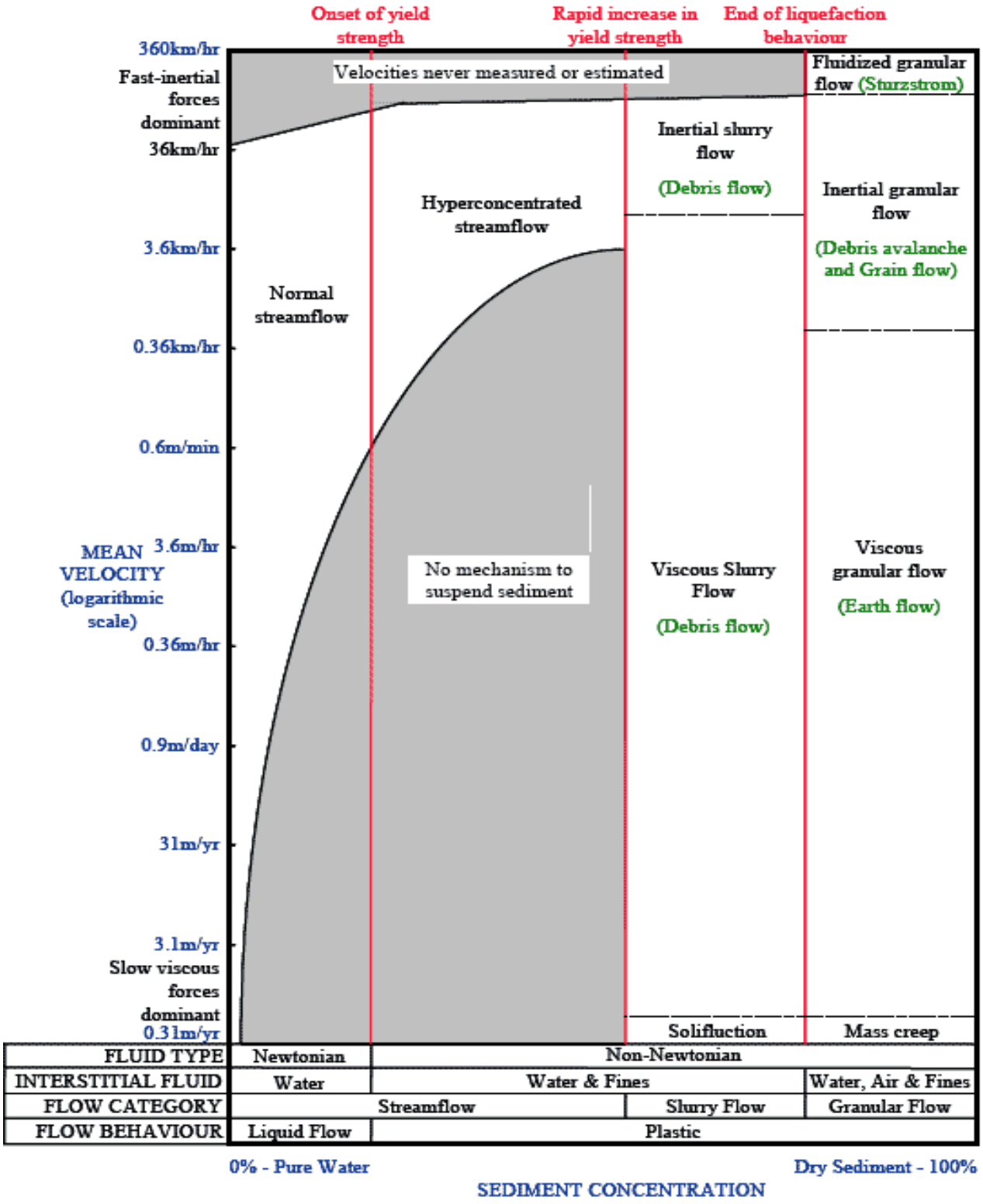

Figure 2-3: Pierson, Costa & Vancouver (1987) classification of sediment flows.

2.1.2. Life Cycle of Debris Flows

Field investigation of debris flows are separated into zones of initiation, transport, and deposition. As this thesis focuses on laboratory modelling, a brief summary of these stages in the field follows.

2.1.2.1. Initiation

The triggering factors for debris flow are similar to most rapid mass movements and include: increased loading from water or other material, reduced friction or cohesion and tectonic activity. These gravity and water effects are often a result of violent rainfall, human activity leading to increased erosion, earthquakes or volcanic eruptions (Lorenzini & Mazza, 2004). Most other forms of mass movements that mobilize into debris flows are usually the result of a large reduction of shear strength, due to liquefaction or semi-liquefaction (Wang, Sassa & Fukuoka, 2003).

Due to the channelized nature of debris flows the most common trigger for initiation is rapid saturation of material leading to slope failure of a head wall or the side slope of gully or stream. Initiation can also be the result of unstable bed load in steep channels entraining and accumulating to the point where granular forces are equally dominate in flow behaviour. Initiation of flow occurs mainly on steep slopes of 20 - 45˚. This is because debris flows need high levels of energy to overcome resistance in the static material and to distribute and sustain particles throughout the depth of flow. Therefore, initiation requires at least a slope of 10%, even with the optimum material and fluid combinations (Hungr, 1995).

2.1.2.2. Flow Transport

There are three modes of particle motion: (1) rolling and or sliding motion; (2) saltation motion; and (3) suspended particle motion (Van Rijn, 1984). After yield stress is achieved the particles roll or slide then, as shear increases, the particles start to make regular jumps into the flow or saltation. When the turbulent or dissipative stresses are higher than the fall velocity the particles are suspended within the fluid.

Debris flows will start off as either a highly fluid or highly granular flow, depending on where and how it was initialised. Channelized, the flow will entrain or deposit on the slope

depending on the channel morphology and velocity. These factors affect the ability to support debris in the flow.

Flows can be roughly assumed to be blocks or material sliding on a thin shear region, partially fluidised or fully fluidised (Figure 2-4). All of these models assume a no-slip boundary which is accurate for the fluid within a debris flow but may not be accurate for the solid particles. Other descriptions combine the multiple regions with depth (Jan & Shen, 1997).

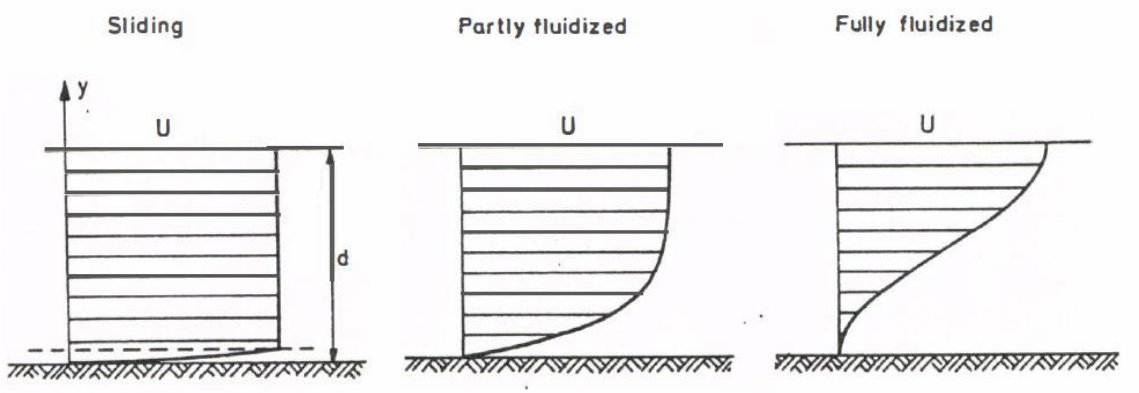

Figure 2-4: Measurement and analysis of the motion of dense flow avalanches (Salm & Gubler, 1985).

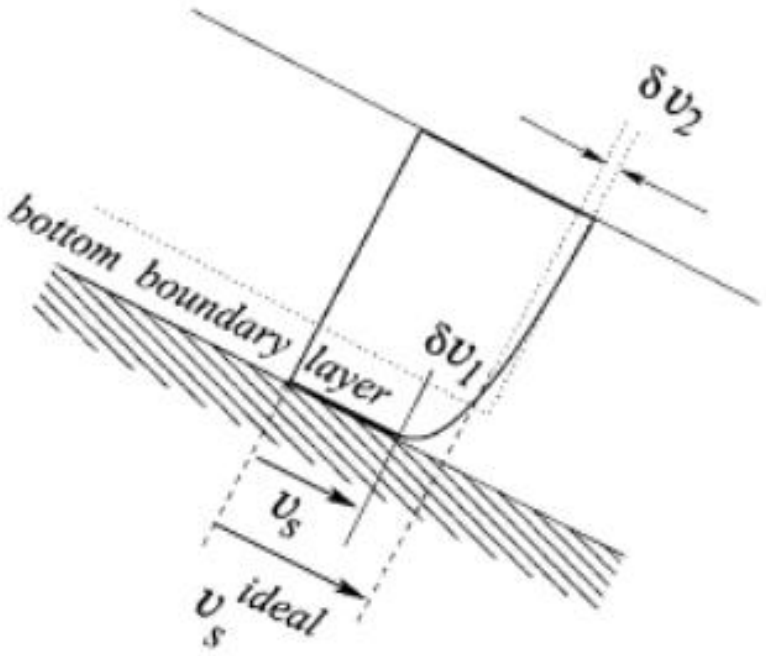

Figure 2-5: Velocity profile of a gravity driven shear flow (avalanche). Where v_s is sliding contribution, δv_1 is the boundary layer shear contribution, $v_{s\ ideal}$ is from the limited shear layer contribution and δv_2 very small shearing contribution (Adrian, 2005).

Figure 2-5 shows an avalanche model (granular dominated) that allows for a slip condition at the base and shows a plug-like flow with a relatively thick bottom shear layer and a relatively uniform velocity upper block. It is similar to a sliding mechanism, but allows for the bottom boundary layer to have a thickness rather than being a thin sliding surface. There is also an allowance for shearing in the upper block layer. This conceptual model allows for shear forces to be translated to various degrees throughout the flow.

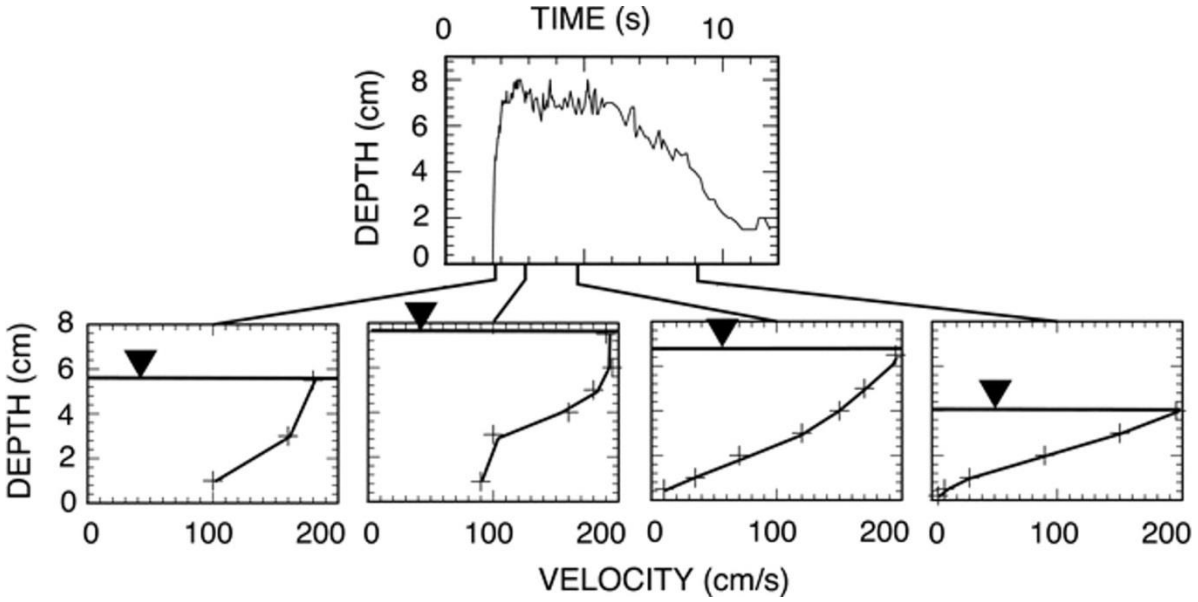

Figure 2-6: Variation in flow depth and vertical velocity profiles in small scale experimental debris flow (Iverson & Vallance, 2001).

The flow depth and velocity changes over time and so does the velocity profile. Figure 2-6 shows a small scale experiment that indicates initially, a sliding or partly fluidised flow which turns into a more fluid flow. The number of measurements of depth with respect to velocity is low making it difficult to see effects caused by particular particles within the flow. However, the depth with time shows a good resolution and spikes in height indicate the presence of large particles.

2.1.2.3. Deposition

Debris flows often form an apron at the foot of the slope as a result of slope reduction and reduction in confinement. When the flow stops the material being carried in the flow collapses, the front material pushes forward and as the front slows it steepens and expels material to the margins. This material creates levees of coarse material along the sides of the deposit. The fluid following the flow can overtake the coarse boulder train and as it does it reworks the deposit.

Major (1997) outlines the deposits of a series of tests using the USGS large-scale flume (described further in section 2.3.3). The deposits form through horizontal and vertical accretion, with shouldering aside by successive waves. The morphological features include "Lobate" (in reference to the lobe shape) platforms, steep blunt margins, marginal levees and acute surface ridges.

The deposition process is strongly influenced by the water content. Unsaturated deposits with relatively deep lobes have a high aspect ratio of width to length. Saturated deposits are longer and shallower with a lower aspect ratio. Saturated deposits also have a more variable margin with less developed levees. Figure 2-7 shows the shape of various deposits from (Major, 1997) with source and deposit attribute values presented in Table 2-1. The non-uniform nature of deposit shape is evident; there is a tendency for the front of the deposition to occasionally occur biased to one side, with peaks within the deposit and generally steep edges.

Table 2-1: Attributes of Experimental Debris-Flow Deposits (Major, 1997)

Number (a)	Approximate degree of saturation	Source volume	Depositional area (unconfined)	Length beyond flume mouth	Length beyond confined channel	Mean width	Aspect ratio	Maximum thickness	Source debris dry bulk density (b)	Deposit dry bulk density (b)
Unit	(percent)		(m2)	(m)	(m)	(m)		(m)	(kg/m3)	(kg/m3)
1c	<<100	~ 13	39.6	8.8	8.8	4.5	0.51	0.35	-	-
3	<<100	7.4	23.4	6.3	6.3	3.7	0.6	0.36	1630	1720
4	100	6.6	52.9	14.1	14.1	3.7	0.26	0.28	-	-
5	100	6.2	38.8	11.9	11.9	3.2	0.27	0.24	2000	-
6	100	6.5	46.4	10	10	4.6	0.46	0.2	-	-
7	90	12.1	60.2	14.7	14.7	4	0.27	0.23	1820–2000	2520–2620
13	100	8.4	69	15.2	15.2	4.5	0.3	0.32	1630–1810	1870–1930
15	100	9	80.6	14.9	14.9	5.4	0.36	0.22	1400–1700	1630–2470
17 (d)	70	9	50.9	21.4	12.8	4	0.31	0.14	1340–1410	1680–2050

(a) Tests 1-14 are sand and gravel mixture; Tests 15-16 are silt, sand and gravel mixture.
(b) Collected at source debris and deposit surfaces (Iverson in press).
(c) From J. E. Costa (unpublished data).
(d) Channel confines 8.5m across concrete run-out pad.

In terms of the run-out length Rickenmann (1999) proposed that the run-out length empirically shows some linear dependence on the volume of material, but is also affected by PSD and water content. Figure 2-7 supports this but also shows the large effect of material composition and saturation level on the deposit. The lowest saturation of test three had a very steep deposit with a small area and the tests with the added fines had more spread out deposits.

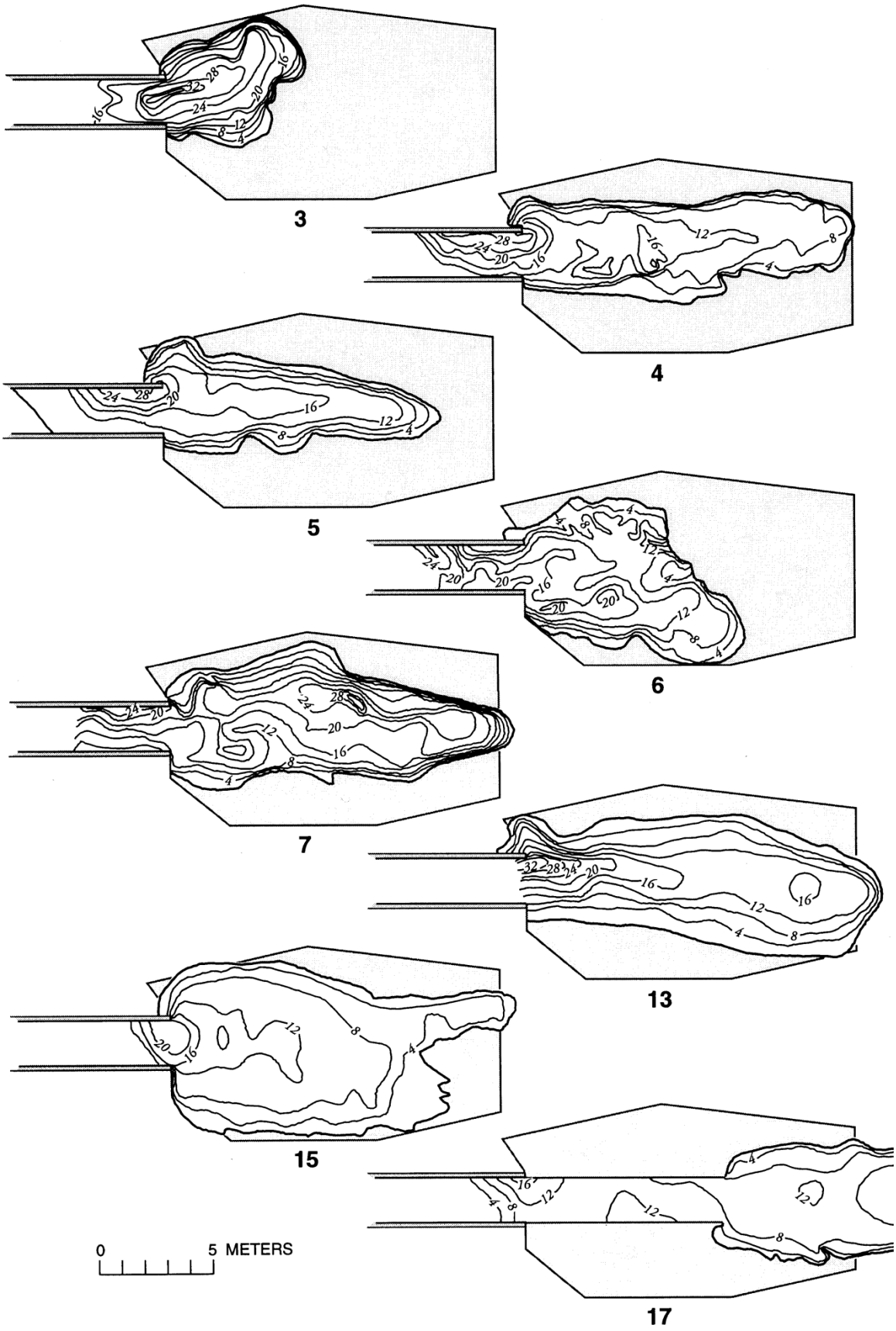

Figure 2-7: Isopach maps of experimental deposits contours at 4 cm intervals (Major, 1997).

2.1.3. Anatomy of a Debris flow

Takahashi (1991) describes the anatomy of a debris flow as having a front and a tail. The front is a bore with little preceding material. It is short and contains the largest particles. The tail follows the front and behaves like a mud flow. Other descriptions (Ancey, 2001; Iverson, 1997; Lorenzini & Mazza, 2004), include a body of flow which separates the front into a snout and body, as seen in Figure 2-8. Figure 2-9 graphical, depicts the parts of a debris flow including the 'lateral levee,' which as a coarsening of the front sides of the flow or deposit. The snout is locally very coarse and has reduced water content. The coarse front is commonly friction dominated and causes resistance at the surge front. The body is the majority of the high front and generally tapers from the snout, with decreasing depth of flow and is composed of interacting fluid and solid phases. The body section has high interior viscous stresses and grain collisions (Iverson & Vallance, 2001). The last section is the slender dilute tail and is typically more dilute with high suspended fines rather than collisional particles (Lorenzini & Mazza, 2004).

The flow velocity, height profiles, and material composition of a typical debris flow is both variable over time and length. Over time, the flow will move through various flow regimes and is not always strictly a debris flow. During most initiation phases the flow density is similar to water, or a hyper-concentrated flow. There is rapid saturation of fine particles taking place, which are suspended or carried as bed load. The next stage is a fully developed flow where there is increasing fluid density and granular interaction as more material is entrained. As the flow decelerates, the debris flow disintegrates and deposition occurs on slopes at low angles. The finer body may push through the coarse snout as it slows; forming coarse deposit ridges at the outer extent of the deposition. The deposits are generally described as having a rigid outer skeleton of coarse particles in a roughly pear shape with highly fluidised fines in the middle. The fluid is able to filter out of the deposit as it consolidates (Lorenzini & Mazza, 2004).

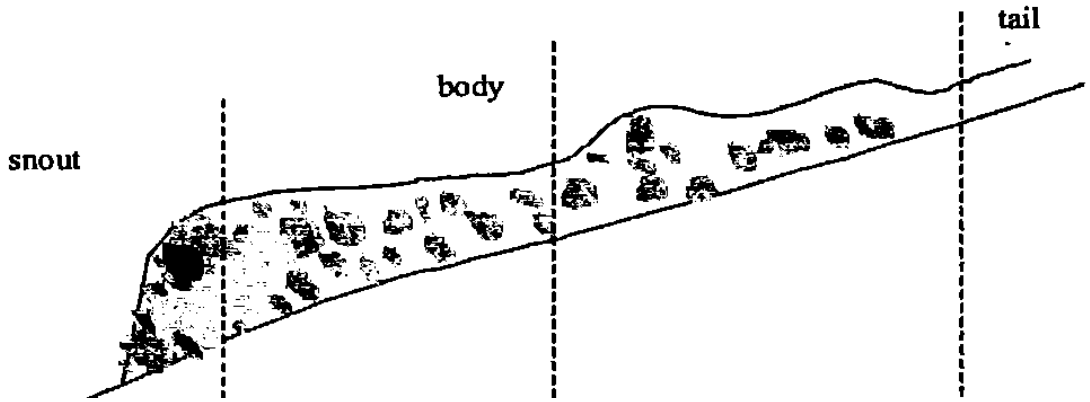

Figure 2-8: Idealised representation of debris flow in longitudinal profile (Ancey, 2001).

Levees, like those in Figure 2-9, are another part of the deposit and flow anatomy of a debris flow. These are coarse material deposits that form along the sides of the debris flow. The coarse-grained snouts are displaced laterally by subsequent finer material (Johnson, Kokelaar, Iverson, Logan, LaHusen & Gray, 2012). Early work assumed a Bingham rheology model where the levee forms independent of interior flow dynamics. However, reproduction of large scale experiments (Iverson, 1997; Major, 1997) showed that coarse grains levee formation appeared to involve the same process as the size segregation that produced the coarse front.

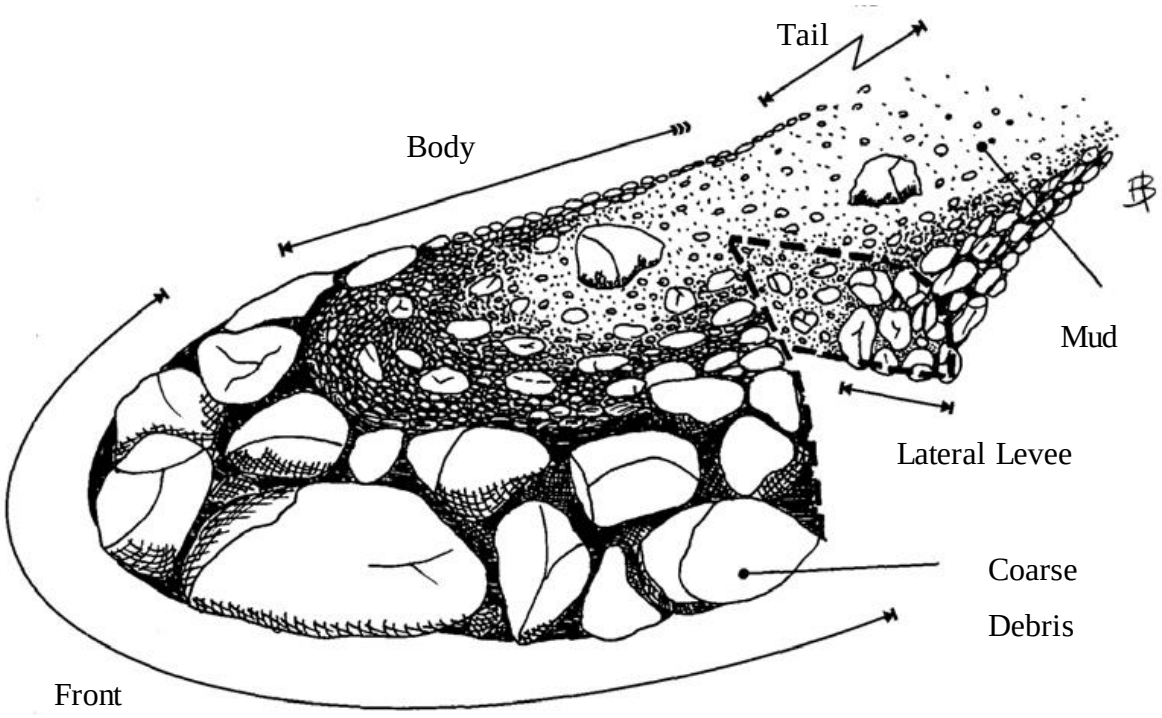

Figure 2-9: Idealised representation of a debris flow as a flow and deposit. Figure reproduced from Bardou (2002)

2.1.4. Classification

Debris flows are a type of mass movement flow. Debris flows typically flow at rates of 16 ms^{-1} on slopes as low as 4° (Innes, 1983; Sassa, Kaibori & Kitera, 1985).

Hungr, Evans, Bovis, & Hutchinson, (2001) describes debris material as generally unsorted, gap-graded, low plasticity material with less than 5% plasticity in its finer fractions. Debris can contain everything from boulders to clay. When the debris flow involves volcanic materials they are called lahars or pyroclastic flows and have an added effect from gases and high temperatures (Lorenzini & Mazza, 2004). Debris flows have large peak discharge as much as 50 times a major flood (Jakob & Jordan, 2001) this gives them huge destruction potential.

2.1.4.1. Flow Regime Defining

The flow regime may be defined using the Bagnold number (Iverson, 1997; Pierson, 1981; Takahashi, 1981)

$$N_{Bag} = \frac{v_s}{1-v_s}\frac{\rho_s \delta^2}{\mu}\frac{du}{dz} \quad (2\text{-}1)$$

where; N_{Bag} = Dimensionless Bagnold number, v_s is solid phase velocity, ρ_s is solid density, δ is characteristic grain diameter, μ is dynamic viscosity of fluid and du/dz is shear strain rate. The Bagnold number is a non-dimensional number relating the inertia stress to the viscous stress behaviour. The transition in dominant stress is either approached as a continuum with balance laws and general constitutive relationships, or as particular theories based on grain collisions using statistical averaging (Chou, 2000).

Iverson (1997) and Iverson and Vallance (2001) consider Bagnold's number not to be a solely effective way of relating shear and normal stresses to shear rate, as it removes the existence of normal stresses as Bagnold's original experiments camouflaged gravity effects (Bagnold, 1954). Iverson advocates the use of the Savage number to relate grain stresses to normal gravitational stresses.

$$N_{Sav} = \frac{\rho_s \delta}{N(\rho_s - \rho_f)g\tan\phi}\left(\frac{du}{dz}\right)^2 \quad (2\text{-}2)$$

where; N_{Sav} is the dimensionless Savage number, ρ_f is the fluid density, ϕ is the bulk friction angle, N is the number of grains above slip surface and g is gravity.

Rheology relationships are only fixed when there is no change of state (Iverson & Vallance, 2001). It can be assumed that the grain fluid mixtures exist in different states throughout flow development. Hence, rheology actually varies with time, position and feedbacks occurring within the debris flow.

Table 2-2 shows the relative sizes of dimensional and dimensionless parameters of some well-studied mass movements including small scale laboratory experiment, large scale physical experiments and some field examples. Because N_{mass} (the ratio of solid to fluid mass) is greater than unity, Table 2-2 implies that momentum transport by solid grains is dominant particularly for pyroclastic and avalanche flows (Iverson & Vallance, 2001). Typical values of N_{Bag} for granular-dominated debris flows are above 450 with more fluid behaviour present between 40 and 450. Values for N_{Sav} are typically less than one.

Table 2-2: Values of key parameters estimated for some well documented granular mass flows recreated from Iverson and Vallance (2001) and Iverson (1997)

Parameter	**Flow location and type (with data source where available)**						
	Small Flume Debris Flow	USGS flume Debris Flow (Iverson, 1997)	Kamikamihorizawa Debris Flow (Takahashi, 1991)	Oddstad Debris Flow	Osceola Mudflow	Mt St. Helens Pyroclastic Flows (Lipman & Mullineaux, 1981)	Elm Rock Avalanche (Hsü, 1975, 1978)
h (m)	0.04	0.2	2	1	20	1	5
ρ_s(kg/m^3)	2700	2700	2700	2700	2700	2600	2400
ρ_f (kg/m^3)	1000	1000	1000	1100	1200	2	2
ν_s(none)	0.5	0.6	0.6	0.6	0.6	0.3	0.5
δ (m)	0.006	0.01	0.2	0.001	0.001	0.02	0.5
du/dz (s^{-1})	30	50	3	10	1	10	5
μ (Pa-s)	0.001	0.01	0.1	-	0.01	2×10^{-5}	2×10^{-5}
N_{mass}	3	4	4	4	4	600	1000
N_{Sav}	0.1	0.2	0.03	2×10^{-4}	1×10^{-7}	0.004	0.1
N_{Bag}	8000	6000	10,000	4	0.4	9×10^{5}	4×10^{8}

Definitions and methods of estimation of physical parameters:
h, typical flow depth, estimated from observations and measurements of flow and deposit thicknesses
ρ_s solid grain mass density estimated from densities of grain in deposits
ρ_f pore fluid mass density estimated from typical densities of liquid water or dusty air, as appropriate
ν_s solid volume fraction, estimated from real-time measurements or deposit bulk densities
δ typical grain diameter, estimated from sampled deposits and descriptive accounts
du/dz typical shear rate, estimated by dividing observed flow speeds by typical flow thicknesses
μ pore-fluid viscosity, estimated from typical values for water, muddy water, and dusty air, as appropriate
N_{mass} Ratio of solid mass to fluid mass.

2.1.4.2. Types of Debris flows

Classification the general type of debris flows has been based on relative velocity, type of movement (Sharpe, 1938), grain support mechanism, (Takahashi, 1981), fine fraction and morphological properties (Coussot & Meunier, 1996). The amount of fines (less than 40 µm (Coussot & Meunier, 1996) or less 50 µm (Takahashi, 1997), is a defining parameter. It has been shown that increasing fine particle content, increases the apparent density and viscosity of fluid, making the fluid exert higher viscous shear stresses within the flow.

Takahashi (1991), looked at classifying debris flows based on the level of saturation or concentration of solids, which gave rise to the terminology of "mature" and "immature" debris flows. The debris flow is deemed to be mature at the concentration where all the particles are dispersed within the entire flow depth. The concentration at which flow is typically classed as mature is approximately 50% solid to fluid (Larcher, Fraccarollo, Armanini, & Capart, 2007). The mature flow demonstrates the phenomenon of segregation and coarse blocks floating and moving to the front, which will be discussed later in section 2.1.5.

Muddy or viscous debris flows have a fines content more than 10% total by weight (Coussot & Meunier, 1996). These types are generally modelled as Bingham fluids. Viscous debris flows are also referred to as immature debris, where the sediment size and distribution means that there is a more dominant particle interaction regime. However the sediment concentration is still not large enough to disperse particles throughout the flow. Low concentrations means the solids are contained in the lower fraction, allowing a fluid layer on top that may suspend some particles.

Once the fines are less than 10%, total sediment by weight (Coussot & Meunier, 1996), the debris flows enter in to more granular dominated flows. Dilatant fluid model particle collisions dominate and interstitial fluid is negligible if the flow has fines. Then the density of interstitial fluid increases and allows larger particle carrying. The velocity profile has an inflection point near the bottom. Takahashi defines these flows as 'Stony' and splits them into three regimes (Figure 2-10), which are dependent on Bagnold's number shown against a representative stress term G^2. These three regimes are quasi-static, macro-viscous and fully inertial.

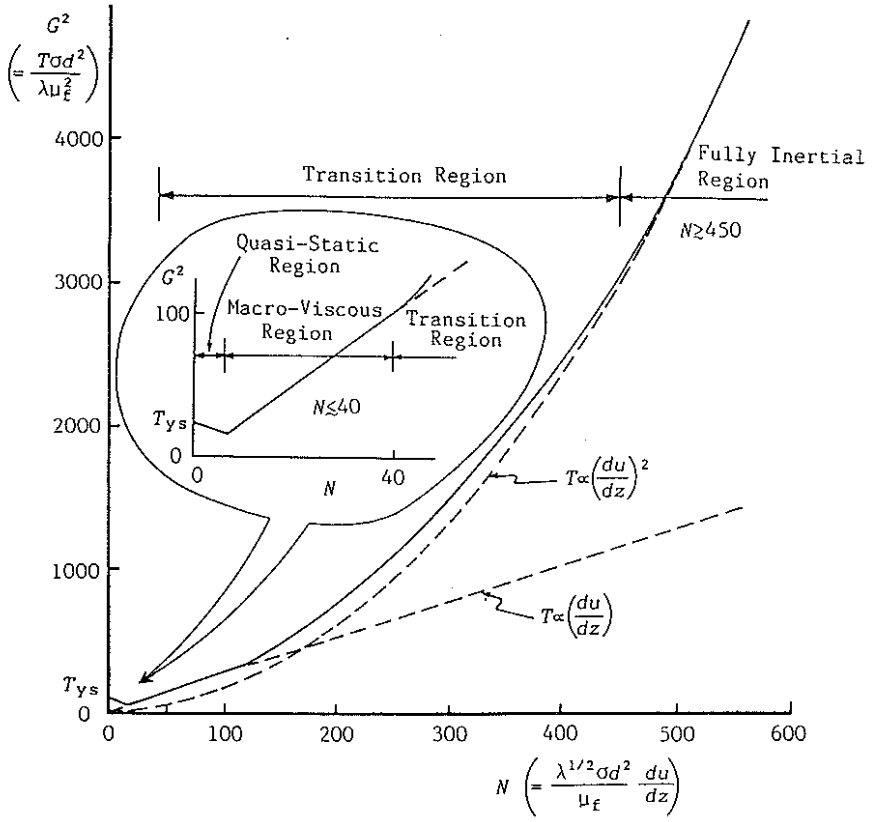

Figure 2-10: The stress and rate of deformation relationship for debris flows (Takahashi, 1991) where N is the Bagnold number, T_{ys} is the yield stress and G^2 is a representative term.

In the quasi-static regime the velocity is small so dispersive pressure from particle collision and other dynamics are small. The Bagnold number is very small. The particles are in close contact and sliding over each other. This means dry friction and prolonged contact is important and inertial contributions from collisions are negligible. Therefore, quasi-static debris flows can only occur on very steep slopes greater than 20˚. This is often during the initial phase of a debris flow (Takahashi, 1997).

The Macro-viscous regime is where viscous effects in the fluid and solid interactions start to cause stresses within the flow. The Bagnold number less than 40. This regime is similar to a slurry in that there is a large volume concentration but the particles are not in consistent contact. This means the dispersive pressures are a result of the dynamic structure and the displacement of fluid rather than particle collision. As a result of this dispersive pressure the particles are more mobile within the fluid and the macro-viscous regime can exist on flatter slopes than quasi-static regime.

The Inertial granular regime is dominated by the granular inertia associated with each particle. As the particles “dilate” (the particles move over each other causing an increase in void volume) the momentum transfer between particles, provides the dispersive pressures that

keep the particles uniformly distributed throughout the flow. The fluid has limited impact as the dispersive pressures are reduced by the smaller spacing between particles and higher magnitude dilative stresses. This regime requires a large Bagnold number of greater than 450. This regime is characterised by large flow velocities in a highly energetic flow.

Turbulent flows are a form of hybrid between viscous and granular flows, where the stresses due to collision and turbulent mixing, are both dominant (Takahashi, 1997). If the particles are suspended mainly by turbulence it tends toward a viscous flow. However, as the concentration increases there is a complex interaction between both types of flow. A uniform velocity appears in the upper section and particles are turbulently suspended with dilatant flow below.

2.1.5. Flow Phenomena

2.1.5.1. Suspension of Particles

If a particle is suspended longer than the length of the debris flow then can be assumed to be part of the interstitial fluid. Lorenzini and Mazza (2004) use the approximation

$$t = h/2v \qquad (2\text{-}3)$$

where t is time, h is height of flow and v is the horizontal velocity of the flow. This is an average approximation that uses the relative time scales in a very basic sense to determine if the particle will settle to the base of flow over the length of the flow.

Typically the solid concentration will determine the size of a shear layer within the flow. There is typically high shear rate occurring for low solid volume concentration; the basal shearing layer can be around five to fifteen grain sizes diameters thick and is characterised by sediment rolling, sliding or bouncing along the flow bed as it tries to gain energy and escape the high shearing (Wang & Hutter, 1999). For flows with higher, more dominant solid volume fractions, particles can interlock causing a more plug like flow.

Takahashi (1997) proposes the use of the linear concentration λ, defined by Bagnold (1954), to link how particles are suspended and which forces are causing suspension. The linear concentration is the ratio of particle diameter to the mean free distance between particles given by

$$\lambda = \{(c^*_0/v_s)^{1/3}-1\}^{-1} \quad (2\text{-}4)$$

where v_s is volume concentration and c^*_0 is the most densely packed volume concentration. Table 2-3 gives the forces responsible for particle suspension if for perfect spheres $\lambda \cong 8$ is the most spare square packing, $\lambda \cong 14$ is the most spare cannon ball spacing and $\lambda \cong 17$ is the value at which particles not dislocate each other.

Table 2-3: Suspension forces based on notes by Takahashi (1997)

Regime	Particle suspension	Forces Neutral buoyant
$\lambda < 8$	Any particle is free from any other particle.	Viscous fluid stresses and any fluid yield strength dominate.
$8 < \lambda < 14$	Sparse square to Cannon ball packing.	General shearing of particles with viscous fluid stresses incorporated. Grains have collisions of various frequencies.
$14 < \lambda < 17$	Particles are always in contact.	Shear must overcome the resisting stress due to the internal friction and yield strength of the interstitial fluid and so dilate.
$\lambda > 17$	Particles cannot dislocate from each other.	Dilation must occur before motion can occur between particles, flow may still occur as plug like section of flow but the particles locked in place within the moving block.

However, under gravity the particles need additional forces to support them. This is assumed to be mainly from frequent collisions. This requires a high-energy regime. If the interstitial fluid is dense and viscous then pore pressure may develop sufficiently to suspend the particles through the squeezing and expulsion of fluid from voids between approaching particles. Small particles moving between larger particles may affect the relative density and viscosity of the fluid increasing the pore pressure forces. This leads to the statement by Takahashi (1997) "very fine materials (smaller than 0.05 mm) seems important to determine the mechanism of debris flow."

2.1.5.2. Effect of Well Grading

In the natural world debris flows are mostly well graded, with particles sizes from boulders to clays. The largest particle may be many orders of magnitude larger (10^5 - 10^6 times) than the smallest (Sparks, 1976). Most models and rheologies developed for debris flow allow for a change in characteristic particle size but assume uniform grading. However, many examples show that the grading has a large impact on mobility, permeability and behaviour of particles

within the flow (Bowman & Sanvitale, 2009; Pierson, 1981). Very fine particles suspended in the fluid are generally incorporated into the fluid property, but at a micro-mechanical scale are linked to the yield strength of some fluids. Kinetic mass flows are very effective at sorting particles by size, this leads to segregation and inverse grading, which will be further explained in the following section.

2.1.5.3. Segregation

Segregation and inverse grading (upward coarsening) (Bagnold, 1954) occurs within debris flows, particularly granular ones. This is caused by differential kinetic sieving and squeeze expulsion. Kinetic sieving is where fine particles percolate downward within the flow, as they are more likely to drop into voids produced as grains move apart. This is only able to happen as the flow dilates slightly. Coarse particles are displaced upward as the fine particles drop beside, then beneath, the coarse particles. This prevents coarse particles from moving down once they have moved upward. The resulting inverse grading shows large grains in the top of flows and deposits and small grains toward the base of the flow or deposit, in much the same way as small grains settle on a shake table. Once underneath, the small particles gradually lever the larger particles upwards to equilibrate the solids volume fraction and pressure (Gray & Kokelaar, 2010). Gray and Kokelaar (2010) developed a "large particle transportation equation" that takes into account the difference in particles sizes and predict the preferential movement of the large particles.

Segregation has a measurable impact on the material behaviour of a debris flow (Pouliquen, Forterre, & Euml, 2002). Segregation is most prominent where the gravity stress is much greater than grain stresses. Still, there needs to be some grain stresses in order to facilitate segregation (Iverson & Vallance, 2001). This is required to allow the flow to shear and dilate (Johnson et al., 2012). Segregation in debris flows can be affected by other mechanisms. Solids, like pumice (Sparks, 1976) in lahars or other organic material that have a low density, have positive buoyancy which promotes segregation. Segregation can also be hindered by wide distribution of grain size, particularly increased fines. The fines combine with the interstitial fluid reducing density difference between fluid and solid phase and increasing viscosity (Thornton, Gray, & Hogg, 2006; Vallance & Savage, 2000).

Johnson et al, (2012) showed that transport of coarse particles to the flow front is balanced by the deposition of coarse particles in static lateral levees. These static levees are limited in a

laboratory flume experimental setup, as the channel has high walls that prevent material moving into low velocity zones for deposition on the flume. Once the flow moves to a run-out zone (commonly a flat deck at the end of the flume), the material can move outward.

As a result of the slope normal process of segregation, the coarse material at the top obtains the highest velocity, due to a non-linear velocity profile driven by viscous stresses at the base of flow. With higher velocity it can migrate to the front of the flow. This conveyor phenomena pushes coarse particles over the body to the snout which can consolidate, causing the snout to slow and dam, forming an obstacle to the rest of the material (Lorenzini & Mazza, 2004). Surges are observed as the front is enveloped by the building pore pressure behind it and the coarse particles are recycled back into the flow. The buried coarse particles are then able to recirculate and segregate upward again. This can cause a short recirculation cycle in the front of the body and snout (Davies, 1990; Pouliquen, Delour, & Savage, 1997) and the result is a resistive boulder flow front. Gray and Ancey (2009) observed that as additional coarse material was incorporated into the front, the front did not necessarily change in size but deposited coarse material in the substrate.

The movement of the particles at the front is dependent on the type of flow. Figure 2-11 shows how a plug-like flow with uniform velocity will push particles out to the sides whereas a simple shear flow with roll over the material in a slope normal direction only. If there is both shear and basal slip then the material will spiral down and out to the sides (Figure 2-12).

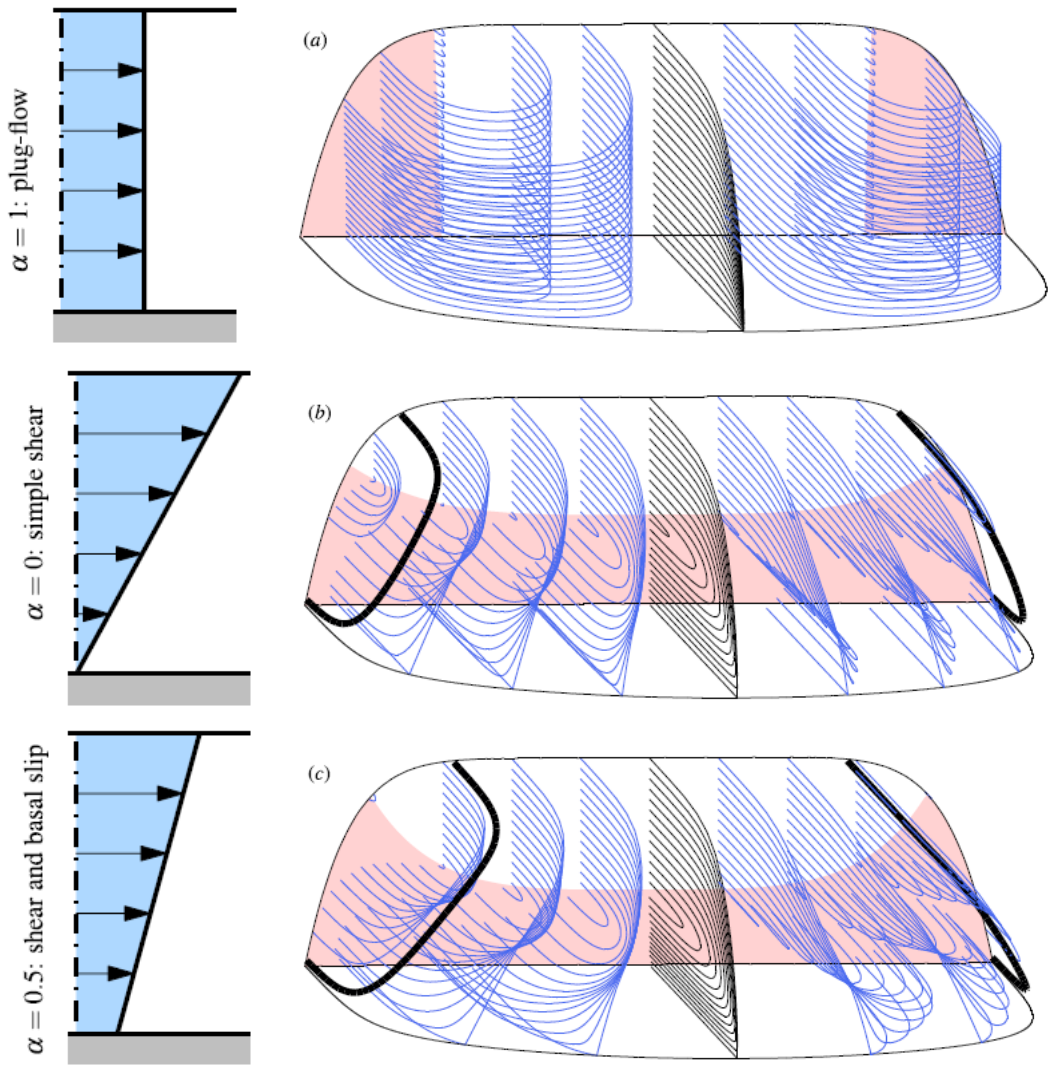

Figure 2-11: Computed three-dimensional particle paths within a flow head. Pink zones are relatively slower (retreating material). (a) In plug flow the material moves laterally and recedes at the outer edges of flow. (b) Simple shear material at the top half folds over the bottom half very little transvers motion. (c) Intermediate velocity flow is transported laterally and vertically (Johnson et al., 2012).

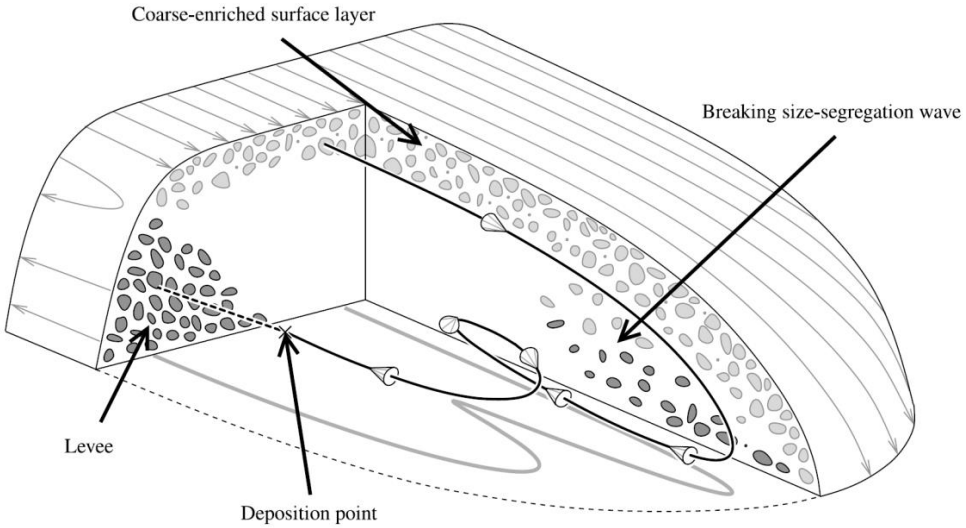

Figure 2-12: Typical spiral flow path of individual particles in the front and snot (Johnson et al., 2012)

2.1.5.4. Surging

Debris flows can move in surges or slugs of boulder fronts with finer mass watery flow in between. The development of multiple high and fast boulder fronts means the average flow is not the parameter that gives the potential damage forces for prediction and hazard design. Pierson (1980) and Davies (1990) described highly intermittent pulsing flow when the bulk density was above a threshold of about 1.8 T/m^3. These flows have high density and coarse particles distributed through the slope normal depth of flow. Takahashi (1981) described flows of similar bulk density with single surges occurring with lower, or no, fines content. The reasons for surges are flow instability, non-simultaneous triggering, periodic stalling of sluggish flow followed by boulder dam breach and re-mobilisation. Surges may be the same or different volumes (Lorenzini & Mazza, 2004). Davies (1990) did moving bed flow experiments that showed that spontaneous roll waves appeared with the wave fronts, showing particle segregation and recirculation. This required a critical length of flume and slope given a certain mixture of particle size concentrations. Major (1997) stated that, in addition to explanations of episodic release of material from a channel, single or multiple source areas, "surge waves can develop as a result of mechanical instability within a single mass … in the absence of any constrictions and blockages within a channel."

2.1.5.5. Entrainment of Bed

Where a channel is erodible, the bed and banks can be incorporated into the flow, increasing the mass, and has been observed to increase the destructive potential of the flow. Coe et al (2011) conducted field measurements at the Chalk Cliffs, Colorado, USA. These measurements showed an erosion of depth and entrainment rate of 0.5 cm/s. Local high pore pressures were seen to weaken the sediment and aided entrainment of the near surface layer.

Entrainment of static material in a debris flow should retard the motion of flow by conservation of momentum, where friction remains unchanged. However, this is not always the case. Iverson, Reid, et al. (2010) found that entrainment can be accompanied by increased flow momentum and speed. This occurred when the overriding debris flow created large positive pore pressures within wet sediments. Conversely, dry sediment had the opposite effect of creating negative pore pressures and reduced the momentum.

2.1.6. Conceptual Summary

This section has defined and classified what a debris flow is in terms of material and flow behaviour as related to other mass movements. An outline of the initiation transportation and deposition has briefly shown the life cycle of a debris flow. The anatomy has shown that the debris flow has a snout, body and tail; each of different composition and saturation. The most particular behaviours of debris flow are the segregation and surging nature of the flow which are a function of the well graded nature of the debris flow material.

2.2. Historical Theoretical Research

The theoretical research into debris flow has historically been championed from a fluids perspective and so relies on progression from mudflow and debris torrent theories. More recent work has incorporated more geotechnical and granular physics concepts such as Coulomb friction angle and granular collisions (Iverson, 2003). Due to the complexity of the phenomenon theoretical understanding has required simplification. The traditional state of research in debris flows is either highly simplified theoretical models or more empirically extrapolated from geological observations.

Research into deformation and flow of matter aims to produce a relationship between the forces applied or stress and the spatial effect or strain induced by the by the forces on a particular material. This is the rheology and if expressed mathematically forms a constitutive equation. A constitutive equation for material behaviour is the keystone for analytical modelling.

2.2.1. Newtonian or Non-Newtonian

In order to determine a rheological relationship the basic form of the material needs to be assumed. The first assumption is if the material is a classic simple Newtonian fluid or more complex non-Newtonian fluid. A Newtonian fluid has a constant viscosity and the stress is linearly dependent on the rate of strain. For an incompressible and isotropic Newtonian fluid the viscous stress is related to the strain rate

$$\tau = \mu \frac{du}{dz} \qquad (2\text{-}5)$$

where; τ is shear stress, μ is viscosity, du is the velocity, dz is the height above datum and du/dz is the shear rate. If a normal stress is applied to a Newtonian fluid it is transferred

throughout the material via transfer to a shear stress resulting in a proportional increases in the volumetric flow rate.

A non-Newtonian fluid exhibits a yield point and can have a variable viscosity. Newtonian flows require the particles to be dilute and have no significant particle interaction. Debris flows are non-Newtonian because of the high level of particle interaction. However, modelling of hyper concentrated flows or a fluid in a multiphase has assumed Newtonian fluid stresses (Hunt, 1994; Pierson, 1980; Yu, Hsieh, & Rutledge, 2010).

2.2.1.1. Viscosity

Regardless of how the material is defined in terms of Newtonian or non-Newtonian the interstitial fluid acts to resists motion due to its own viscosity. All fluids have a viscosity that describes their internal resistance to flow and may be thought of as a measure of fluid friction. The fluid's viscosity arises from the shear stress between the fluid layers that ultimately oppose any applied force. This interaction between fluid layers results in the velocity profile of the flow assuming a no-slip boundary condition. Figure 2-13 shows the velocity profile created from a laminar Newtonian fluid under shear flow.

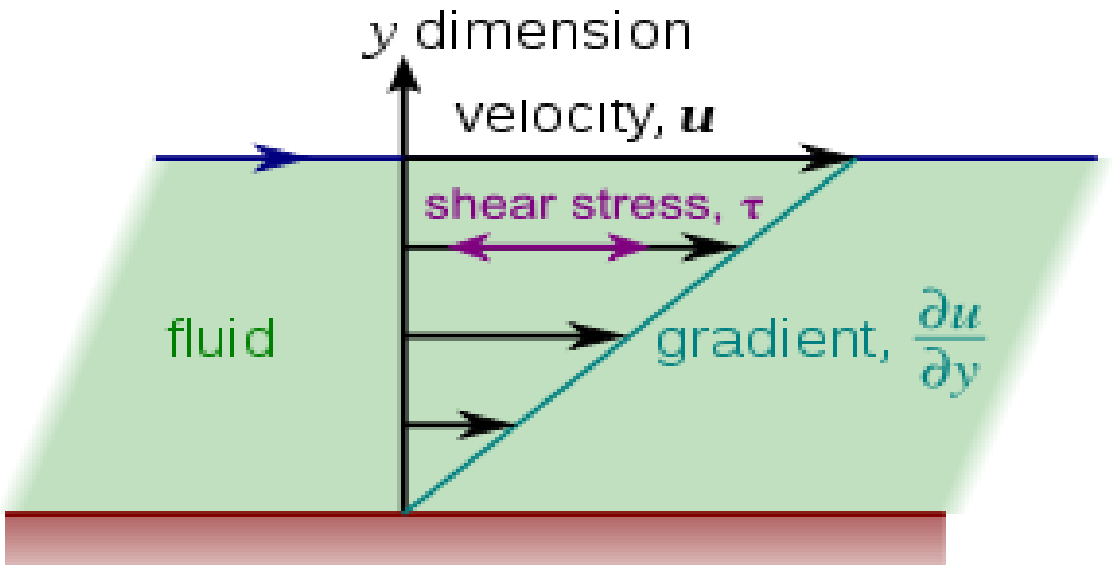

Figure 2-13: Laminar shear in a fluid (Duk, 2005).

2.2.2. Types of Rheologies

There are various simple relationships for how the viscosity changes with shear rate in a Non-Newtonian fluid. These include:

- **Shear thickening (dilatant)**: viscosity *increases* with the rate of shear. E.g. sand in water
- **Shear thinning (Pseudo-plastic)**: viscosity *decreases* with the rate of shear. E.g., some silicone oils, ice or blood.
- **Thixotropic**: materials which become *less* viscous over time when shaken, agitated, or otherwise stressed. E.g., yogurt, some clays and most paints.
- **Rheopectic**: materials which become *more* viscous over time when shaken, agitated, or otherwise stressed. E.g., gypsum pastes and some printer inks.
- A **Bingham plastic** is a material that behaves as a solid at low stresses but flows as a viscous fluid at high stresses. E.g., toothpaste.

Figure 2-14 shows graphically the difference between the Newtonian and non-Newtonian relationships. The Newtonian is a linear relationship through the origin whereas the non-Newtonian variants are either non-linear or have a yield stress shown as the non-zero y-axis intersection.

Rheological relationships for debris flows draw heavily from multi-phase mixture research (Iverson, 2003). They require equations that deal with viscous fluid-fluid, solid-fluid and solid-solid interactions. The most common rheologies used to model debris flows are: Bingham or visco-plastic (mud flow), Hershey-Bulkley a pseudo plastic model (mud flow), Bagnold dilative fluid (neutral buoyant granular flow), inertial dilative (granular flow), frictional (plug flow), coulomb frictional (granular flow) and Vollemy (snow avalanche).

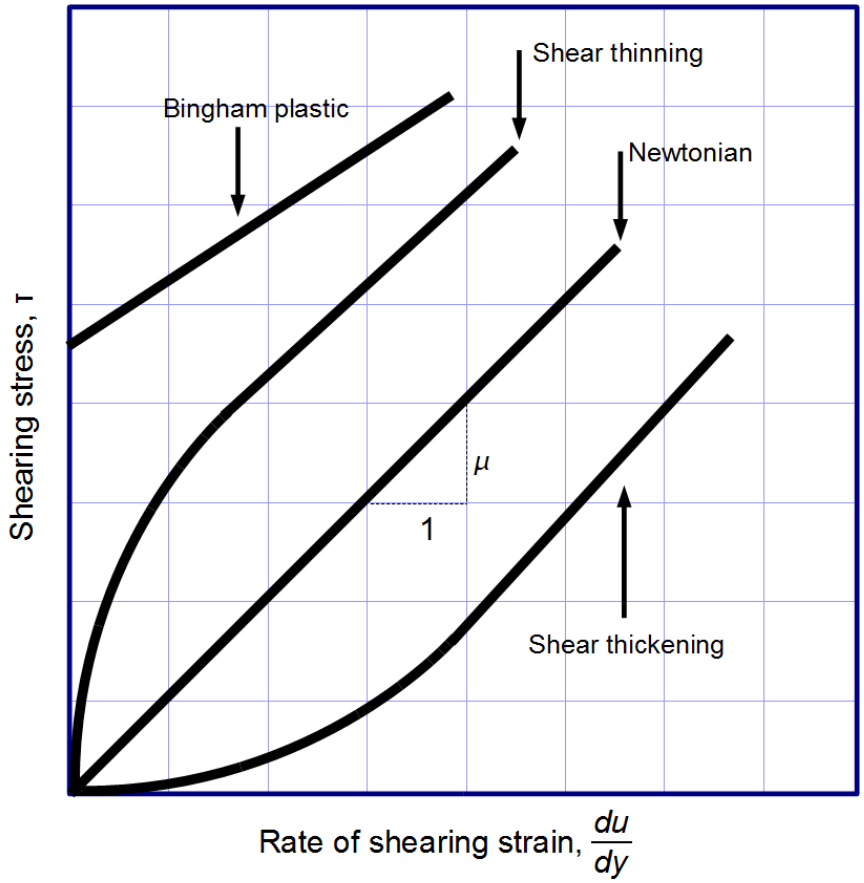

Figure 2-14: Representation of flow behaviour for varies types of rheologies (Image sourced from http://en.wikipedia.org/wiki/Viscosity).

2.2.2.1. Bingham – Visco-Plastic

A visco-plastic material behaves as a rigid body at low stress but flows as a viscous fluid at high stress. The most common visco-plastic model for use in modelling the rheology of debris flows is the Bingham flow model (Coussot, Laigle, Arattano, Deganutti, & Marchi, 1998). A visco-plastic material has both Newtonian and plastic attributes. Figure 2-15 shows the behaviour of an ordinary viscous (or Newtonian) fluid, a plastic material and a visco-plastic material.

A plastic material acts as a rigid body until a large enough stress to yield the material. Once this yield pressure is met the material moves plastically. Plastic flow has a constant shear rate or maximum allowable shear stress as seen in the right graph of Figure 2-15. This can occur in situations like glacier movement. In a debris flow plastic flow is used to model the solid phase, however, in a debris flow there are too many transient structures forming to be simplified to this sort of model. Within a debris flow the snout and particularly the body are considered to be plastic bodies. However, the tail is more Newtonian.

A Bingham fluid is a combination of the two, an initial level of stress can be applied but it will not cause flow until a yield stress is reached. Beyond this point the flow rate increases steadily with increasing shear stress (Steffe, 1996). In a debris flow, the yield stress increases exponentially with solid concentration (Coussot et al., 1998). The physical reason for this behaviour is that the Bingham material particles have a form of structural interaction or interlock. In creating a solid body, a certain amount of stress is required to mobilise the solid by reducing the particle interaction. Once the structure has been mobilised, the material is free to move under viscous forces. When the stress is removed, the particles stop their motion and reform their interlock or interaction (Phillips, 2008).

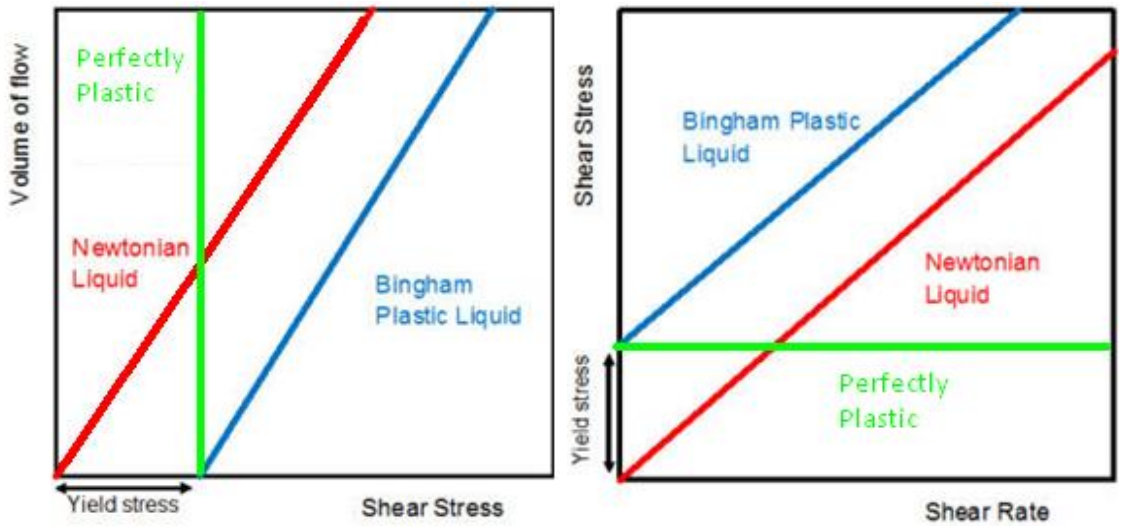

Figure 2-15: Bingham Plastic flow; left is volume relationship to shear stress, right is the shear stress to shear rate (Modified from public images sourced from http://en.wikipedia.org/wiki/Bingham_fluid).

Simple Bingham flow assumes that the resistance force is a function of depth and velocity, constant yield strength and a (constant) viscosity. The Bingham model has been experimentally proven to approximate mud-rich sandy slurries which are at the more fluidised end of the debris flow continuum (Whipple, 1997). The Bingham model also does not account for shear thinning which violates the constant plastic yield stress. Models such as the Herschel-Bulkley rheology can be substituted to account for this.

2.2.2.2. Herschel-Bulkley – Pseudo-Plastic

The Herschel-Bulkley is a common pseudo-plastic model which has been consistently advocated for mudflows by (Coussot et al., 1998; Coussot & Meunier, 1996). Mudflows are a more fluidised and fine clayey version of a debris flow and come close in behaviour as the debris flow moisture and fines content increases. This is determined to be where the fine

fraction (<40 μm) is equal to or larger than ~ 10% (Coussot et al., 1998). Muds with high solid concentrations generally experience more severe shear thinning than those with low solid concentrations (Whipple, 1997).

Figure 2-16 shows how the Herschel-Bulkley model has a distinct curvature to it. The Herschel-Bulkley in this diagram has a yield stress but it can vary. For mud flows there are researchers (Coussot & Meunier, 1996) (Wang & Hutter, 1999) who argue that in some circumstances yield may be neglected as being insignificant, giving the shear thinning only curve.

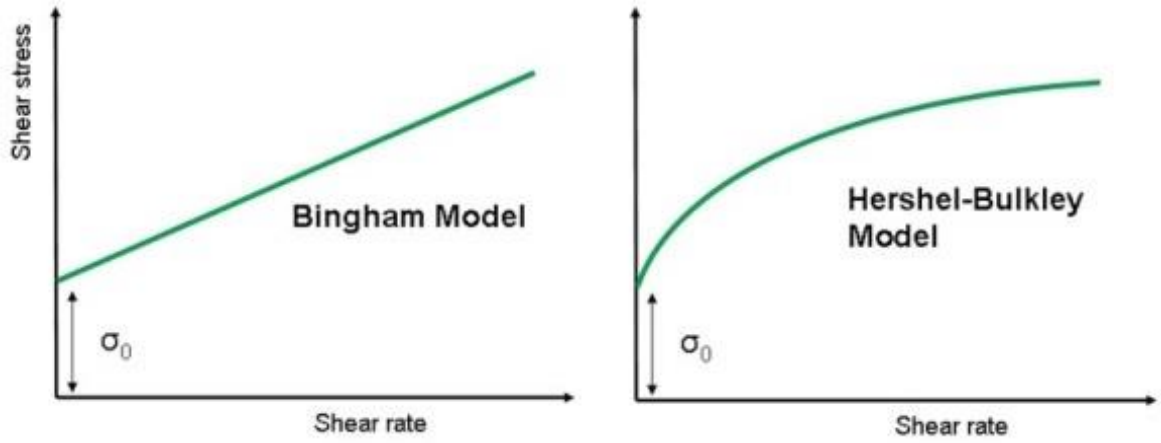

Figure 2-16: Comparison of Bingham and Herschel-Bulkley models where σ_0 is yield stress (Image sourced from http://www.azom.com/article.aspx?ArticleID=9929).

2.2.2.3. Bagnold – Original Dilative

Bagnold (1954) proposed a dilatant fluid model whose theory states that there is an additional stress caused by grain collisions in excess of the normal stress from the fluid. Bagnold's experiments (Bagnold, 1954) annularly sheared a dispersion of neutrally buoyant wax particles in a Newtonian fluid. The shearing caused the solid particles to ride over one another resulting in the material dilating. This change in volume exerted pressure on the walls, or the annulus, perpendicular to the main flow. Bagnold concluded that this dispersive pressure is caused by grain encounters which act to transfer momentum between particles in all directions. The dispersive pressure was found to be proportional to the shear stress as this was the force which acts in the same way viscosity transfers turbulence in a fluid flow.

Iverson and Vallance (2001) consider Bagnold's work on particle interaction in a gravity-free environment to not be a solely effective way of relating shear and normal stresses to shear rate, as it removes the existence of normal stresses as the original experiments camouflaged

gravity effects. Bagnold's work is the basis of many other models but has been altered significantly from the original model to try and include the inertial grain flows in the model (Hungr, Morgan, & Kellerhals, 1984; Takahashi, 1991; Takahashi & Yoshida, 1979).

2.2.2.4. Dilative Inertial

Takahashi (1991) suggest the shear stress is a function of a viscosity times the shear rate. The sediment concentration and Bagnold number is used to distinguish between dominant flow regimes. Figure 2-10 shows the way in which the Bagnold number is used to classify debris flow in section 2.1.4. Each of these regimes (Stony, Immature or Muddy) can have a different dispersive pressure equation under the Bagnold theory of flow. If the Bagnold number is less than 40 then it is deemed to be viscous and a different rheology is needed.

A dilatant inertial relationship is based on the Bagnold model of dilation (Iverson, 1997). Used when grain shearing processes dominate the flow behaviour and the flow is fully in the inertial range. This holds particularly for coarse-grained or granular debris flows where grain collisions dominate the flow behaviour. The dilatant-inertial grain-shearing relation proposed by (Naef, Rickenmann, Rutschmann, & Mcardell, 2006) indicates the dispersive pressure is a function of mainly granular parameters such as grain size, solid concentration, particle density, and angle of internal friction.

2.2.2.5. Friction Based Flow

Frictional flow is where the material slides along the flow bed with minimal deformation of the assumed rigid block of material. Friction flow assumes that the flow resistance is a function of the normal stress only at the base of the flow. It is therefore a function of the material strength and how it is loaded on the base. The normal stress is a function of the depth, the unit weight and pore pressures at the base level (Hungr, 1995).

Simpler models of friction flow use the St Venant shallow water approach which have been successfully applied to debris flow models (Naef et al., 2006). St Venant's equations use a shallow flow assumption stating that variations in the flow occur over lengths much greater than the thickness of the flow which allows depth averaging along the flow. St Venant's approach simplifies the rheology to a single basal frictional stress that develops between the interface of the flow and the bed surface (Pouliquen et al., 2002). In a steady flow, such as

that upon a plane inclined at a moderate angle, the velocity is controlled by a balance between friction and gravity.

This approach does not fully cover the material behaviour because of spatial variations that break the assumption of single thickness over extended lengths. Also this does not account for segregation where in flows with high particle size distribution the large particles rise to the free surface.

2.2.2.6. Coulomb Viscous Flow

In the most simplistic way, Coulomb-viscous flow is an expansion of the Bingham model where the yield strength is rewritten to take into account of normal stress. This model therefore incorporates the viscous nature of the fluid with the frictional component and is an attempt to incorporate many of the differing rheologies occurring in the multi-phase mixture. The Coulomb-viscous flow is an example of an attempt to develop a two-phase rheological model. The case of saturated granular flows is less studied and so limited rheology on which to draw (Pailha & Pouliquen, 2009). Often the dry constitutive relationship is used (Iverson, 1985) and it is assumed that the single-phase behaviour is the same in the presence of an interstitial fluid.

More recent research has incorporated geotechnical concepts to model the granular contact within the flow. Iverson (2003) has hypothesised that grain contact and Coulomb friction generates the most shear resistance in granular mass flows. The Coulomb friction equation is deemed sufficient to describe the shear resistance of the granular material. However, the Coulomb friction changes as fine grained soils liquefy. This is due to the pore pressure being a flow property and obeying a forced diffusion equation. The discrepancy between the frictional and fluidised shear portions means there is limited success with a set rheological representation.

2.2.2.7. Voellmy Fluid

The Voellmy fluid model was originally developed for snow avalanches and contains both a sliding friction coefficient and a turbulent friction coefficient (Hungr, 1995). This allows the model to account for both the solid-to-solid and the fluid-like shear stresses. A Voellmy fluid is similar to a Friction fluid except that the pore pressure coefficient has been removed and a turbulent viscosity relationship has been added.

The turbulence coefficient is an empirical factor that is fitted to data from back calculations incorporating the thickness of the basal layer (Hungr, 1995). The basal layer can, in isolation, be described as a thin, un-drained, layer of semi-liquefied material. When granular material is rapidly sheared under constant volume the strength increases with the square of the strain rate (Bagnold, 1954). The frictional-turbulent Voellmy fluid flow rheology has been applied to granular debris flows both in continuum models (Hungr, 1995) and in the mass point model (Rickenmann, 1990). Hürlimann, et al., 2008) used the Voellmy fluid rheology for modelling debris flows as it was felt that the resistance law was the best fit with the field observations.

2.2.3. Determining the Rheology

The models presented in section 2.2.2 are either granular friction or fluid viscosity based rheologies or a combination of both. Because the fluid models are based on fluid mechanics, they perform better in high moisture content mud or hyper concentrated flows but do not capture the full behaviour of more granular events.

Most models are single phase due to the difficulty and lack of knowledge of solid-fluid interactions. In many cases the more complex models rely heavily on flow properties like velocity and flow depth rather than state variables. This highlights the huge issue with dynamic modelling of debris flows as many flow parameters vary greatly both temporally and spatially. In the simplified case where velocity-dependent terms are negligible the models calculate a relatively rigid plug (Hungr, 1995) with a uniform velocity above a thin basal layer. This generally means that the shear stress is not being dispersed upward into the material and friction flow is dominant. The simplification does not hold for most debris flows due to the complex collision regime between various sized particles.

2.2.3.1. Rheological Parameters

Determining the natural rheological parameters is difficult for debris flows as they are dependent on many heterogeneous attributes of the material and topology. Field measurements can be made from debris flow deposits or observations during flow. The thickness, channel dimensions, size of particles and super elevation of flow around bends can all be used to help estimate rheological parameters (Phillips & Davies, 1991). These can give some indication of the volumes, geometry, velocities and heights at various locations that are required for each rheology. Material properties can be gathered in the field after an event but

they will not be able to tell the initial condition of the insitu material. Material samples can be taken to labs for testing but have issues associated with disturbing the material that field testing does not have.

Determining the important parameter of yield strength, required for Bingham and Hershey-Bulkley rheologies, has been tried using a variety of penetrometers, vane test and viscometers. However, these are generally deemed unsuitable due to the often coarse granular nature of deposits. Their accuracy is often reduced by a maximum testable grain size and the empirical nature of the test. The range in particles size from clays to boulders means that any technique needs to be capable of containing an extremely large range of particle sizes.

Phillips & Davies (1991) efforts at measuring rheological parameters showed that

- Apparent viscosity is extremely sensitive to water content. A change of 1% results in twice the change in shear stress and apparent viscosity measurements.
- It is important to conduct laboratory measurements at low shear rates to keep close to natural state of debris flow. It is generally impractical to test at high shear rates
- Debris flows with uniform, low coarse or high fine contents had a plastic or visco-plastic rheology
- Debris flows with more well graded grain size had dilatant plastic rheologies
- Instantaneous shear stresses vary greatly and are considered to be affected by the grain-grain collisions.

2.2.3.2. Studies Applying Rheologies to Field Data

The majority of rheology validation and calibration studies (Arattano & Franzi, 2003; Koch, 1998; Rickenmann, 1999) have been conducted on muddy debris flows. Koch (1998) used a 1-D version of a Lagrangian central finite difference shallow water model to test various rheologies. The rheologies covered included the Newtonian laminar, dilatant inertial, Newtonian turbulent and Voellmy fluid models. The parameters where calibrated to fit debris flow events in: Saas Valley in Switzerland, lahars in Pine Creek and Muddy River at Mount St Helens in the USA and Kamikamihori Valley in Japan.

Koch (1998) found that the Newtonian turbulent and the Voellmy rheologies gave the best agreement between simulations and field observations for the front velocity at steep sections

of flow. The dilatant, Bingham and the Newtonian laminar models gave less accurate solutions suggesting that the shear stress was proportional to the velocity squared. The Bingham and Newtonian laminar models showed similar poor performance. The dilatant inertial, Newtonian laminar and Newtonian turbulent models do not simulate the stoppage of the flow as they continued to move out as a fluid. However, it was suggested that connecting the models with a yield strength would allow the material to form a solid deposit.

Arattano and Franzi (2003) empirical fitted seven rheological models to a torrent event in Moscardo, in the Eastern Italian Alps. The event had a fines content of 20-25% on a rigid straight channel with no erosion or deposition. Arattano and Franzi (2003) caution that the use of assumptions derived from field analysis could be misleading. They found that the dilatant model and particularly the Herschel-Bulkley model would overestimate impact force based on assumed rheological parameters. The parameters best fitted to the event were similar to those proposed by Rickenmann (1999) indicating a muddy flow.

Studies on more granular dominated stony flows are less common, particularly those that model the rheologies of these flows. Arattano et al. (2006), is an example of a stony debris flow occurring in the same location as Arattano and Franzi (2003). The flows in the later examples were coarser with relatively little fines content compared to earlier muddy flows. These events were better represented by a dilatant model such as that proposed by Takahashi (1979, 1980, 1991). Shieh et al., (1996) is another stony debris flow that used laboratory and field data to calibrate and validate the methods proposed by Takahashi (1979, 1980, 1991). The dilatant rheology-based numerical model showed good fit with both the field and laboratory data for flow discharge, deposition and run-out.

2.2.1. Theoretical Summary

This theoretical section has given some of the more historic theories on the behaviour and rheologies involved in debris flow modelling. Particularly the need for a non-Newtonian rheology like the seven present in Section 2.2.2. These rheologies have been shown to be difficult to apply as the flow exhibits various types of rheology both spatial and temporally during an event. Measure and derivation of each rheology's parameters can be hard to obtain in the field or from theoretical understanding, producing potential for significant variation in predictions.

2.3.Physical Modelling

2.3.1. Introduction on Physical Modelling

Current debris flow models tend to be empirical or highly idealised analytical models. Mechanical behaviour is characterized by many phenomena including inertial grain collisions, grain contact friction, viscous shear and solid-fluid interactions. These processes are often modelled on assumed constitutive laws. Unfortunately the verification of models is extremely difficult as hazardous field conditions and the opaque nature of debris flows makes visualising and measuring flows in the laboratory problematic.

Assumptions are generally necessary in order to create usable models that do not require significant computation; however, they are not generally realistic in terms of natural debris flows. Examples of common simplifications are:

- Rounded particles
- Uniform particle size distributions
- Two-dimensional flows
- Side wall observations are valid throughout flow
- Depth averaging of mass and velocities
- Steady flow
- Uniform with depth or length
- Straight rectangular channel geometry
- Smooth channel sides
- Material and fluid is not entrained during flow
- Fixed rheologies in time and space.

Issues relating to the suitability of these assumptions are not covered in detail here however; Myles and Parkin (2008) found that more angular particles give shorter run-out than rounded particles. Iverson and Vallance (2001) shows that the velocity is reduced at the side wall compared to the centre of the flow, and that rheology is not fixed for properties like viscosity in time and space.

Many constitutive (Iverson 1997, Takahashi 2007) equations used in a wide variety of academic papers have been proposed based on the interaction of particles. The main processes that are common to theories of particle motion are particle to particle displacement, inelastic collision of particles and pore pressure build up. Micro-behaviour of particle

collision remains one of the less understood processes within a debris flow and simplifications made for modelling include inelastic collisions and only two particles can collide at once.

Finding and investigating an occurring debris flow is often an impractical and dangerous exercise. By nature, there is very little control over initiating, repeating or controlling a field event. Numerical methods currently suffer from uncertainties around the driving mechanisms occurring internally and many models are empirically rather than analytically based.

Empirically based observations have been made on geological forensic investigations of debris flow deposits where velocities are calculated from super elevations on banking bends and eyewitness accounts (Hungr, Morgan, & Kellerhals, 1984). For length of run-out, some techniques rely on creating empirical constants for certain soils, specific location, and topography relating the run-out length to the velocity squared. Rickenmann (1999) proposes a variety of flow variables can be calculated based on the volume of flow. The resulting simple linked equations do not account significantly for the material composition and so give significant scatter rather than detailed trends. For example, Rickenmann (1999) proposed the following relationship for run-out length of

$$L_{Fan} = A_1 V^{0.333} \qquad \textbf{(2-6)}$$

Where L_{Fan} is the run-out along the fan A_1 is an empirical constant (A_1 is quoted at 15 in Rickenmann (1999)) and V is the volume. While the run-out on the fan is linked only to volume, the channel geometry and material properties were seen as important factors. In comparison the full travel distance relates the volume and the height of the flow.

Field-based empirical methods are typically statistical extrapolations and are only valid for similar circumstances, therefore generally limited in extrapolation to other sites. Even within a site these methods are also based on the assumption that future events will have consistent parameters as past measured ones. However, Arattano, et al. (2006) shows that depending on material composition the same sites can have significantly different flow compositions and behaviours. The process of collecting from field work has limitations on the ability to represent the transient forms of the flow development and may not capture the entire process. Physical modelling allows controlled replication of complex field phenomena in a safe and flexible environment that allows targeting of theories and behaviour.

2.3.2. Small Scale Flume Testing

Laboratory flume testing allows concentration on a particular behaviour and tighter control over variables, than field or large scale testing. Flume tests are simple downsized representations of flow on a natural slope. The reduced scale means that the construction and inputs required are cheaper and easier to manufacture than large scale or complex physical experiments. Flumes are easy to conceptually align with real flows unlike some of the other techniques like continuous conveyor belts (Davies, für Wasserbau, & und Glaziologie, 1988), centrifuges (Bowman, Laue, Imre, & Springman, 2010) and rotating drums (Liu & Chang, 2010; Longo & Lamberti, 2002). The observations of micro-scale interactions cannot be made in the field due to the specialised equipment required, but the micro-scale behaviour can be recorded and analysed in detail within a small laboratory setup.

Laboratory experiments, in which parameter values and boundary conditions are well-defined and well-controlled, give accurate and translatable observations upon which to base physical rules and the validation of mechanistic models. Laboratory flumes allow easy parametric studies (Fannin & Bowman, 2007), giving systematic and consistent change in variables that explains the significance of each variable and identifies limits where material performance drastically changes.

2.3.2.1. Typical Laboratory Setups

A laboratory flume is typically made up of three sections corresponding to initiation, flow, and deposition (Weber & Rickenmann, 1999). Figure 2-17 shows a simplified diagram of the basic flume set up used for debris flows. The first section is a hopper or dam inside this structure. The material is made up and readied before initiation of flow. A hopper like that described in (Sanvitale, 2010) is a simple open-ended aluminium trapezoid box with a pneumatic gate at the short end. The gate is sealed to prevent loss of moisture and can be remotely triggered. Alternatively a dam may be used in a dam setup material is stored behind a barrier gate in the channel which is removed for initiation.

The second section of a laboratory flume is the chute itself. The chute can range in shape but is generally rectangular and can have a fixed or variable slope. Traditionally the channel walls are glass to allow observations at the sides during flow. The base can be smooth metal, rubber matting or other materials glued on to it to provide various degrees of roughness. The chute can be subdivided into two sections depending on the experiment being conducted. The

first reach is an acceleration and establishment section that allows the material to increase in speed and possibly guided from free fall on to the slope using a curved shape. The next reach is the experimental reach where it is assumed the flow has fully developed and observations and changes to variables can be made.

The final section is a horizontal tray for deposition. The connection from the main chute may be gently expanded with a curved end of chute or wings expanding out to the horizontal deck itself. It is, however, more common for the chute to simply end at a discontinuity in slope and widen out straight away. In some cases the run-out zone is the same width as the sloped channel but this is not often the case.

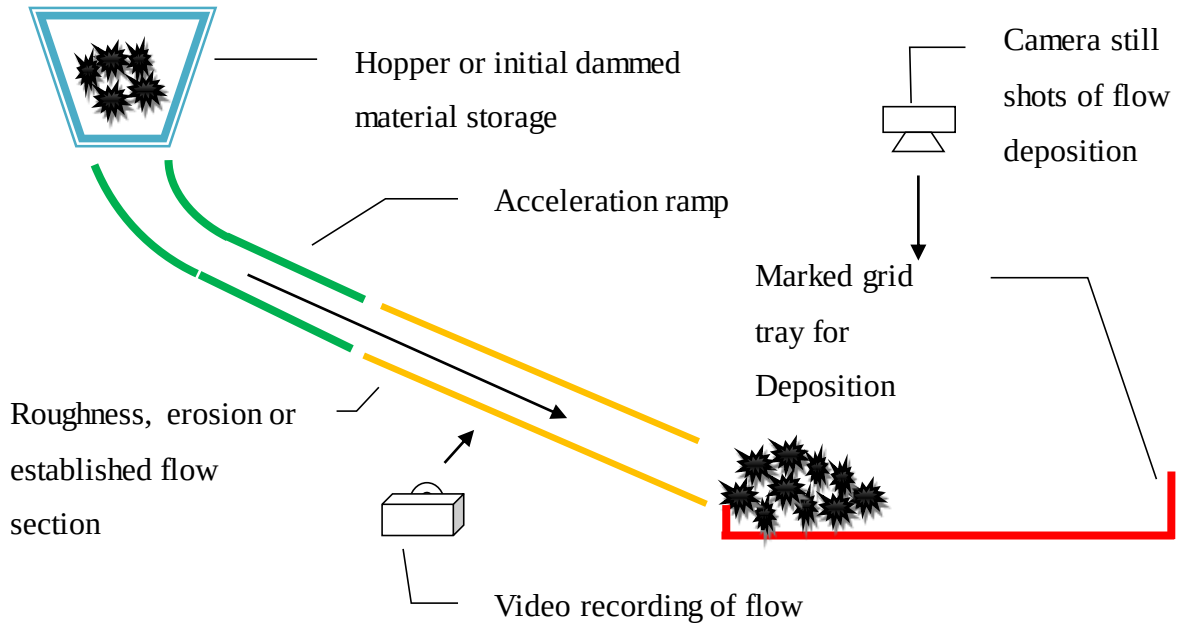

Figure 2-17: Basic flume setup for debris flows

Video and camera imaging is common for flume testing in the laboratory. Videos are taken perpendicular to the material as it flows down the chute through glass windows built into the side of the flume. The video camera is often linked to the flow trigger because the flow is very fast and it is impractical when using high-speed cameras to take images over a long period of time prior to a run. The deposition is often imaged using a still-shot camera positioned directly above the tray. This gets a less distorted view of the marked grid for distance referencing of the deposition shape.

There are a limited number of systematically varied experiments that have explored the changes in conditions and behaviour of debris flows. The most comprehensive source of this research is T. Takahashi (Takahashi, 1991; Takahashi & Yoshida, 1979) who has looked at

variations in velocity and solid concentrations in debris flow front with channel slope as well as the impact of denser liquids which could be analogous to an increase in very fine particles, during laboratory-scale work. Takahashi has also made an effort to track individual particles shown in Figure 2-18.

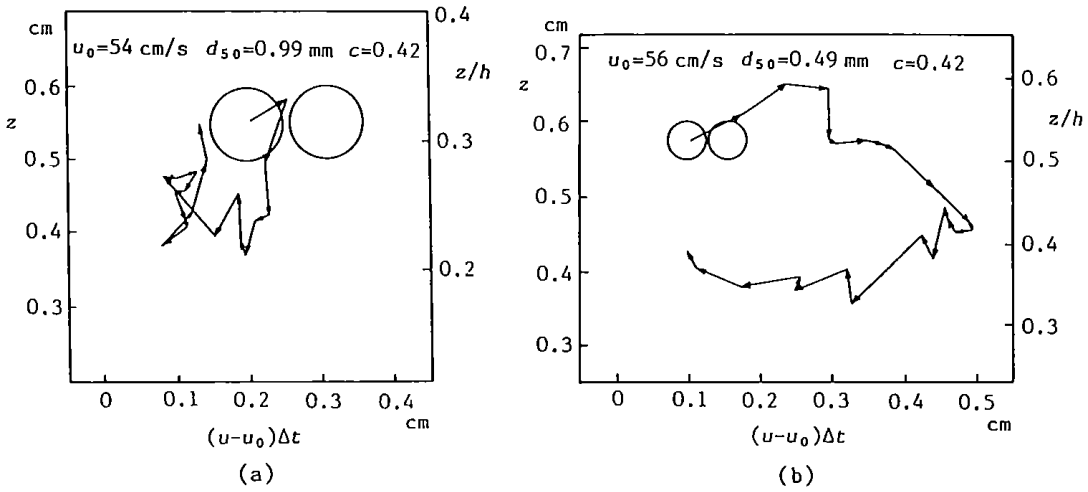

Figure 2-18: Tracked particle paths where large circles represent the size of particle and second circle give picture of the average distance from other particles (Takahashi, 1991).

2.3.3. Large Scale Flume Testing

In 1991 the U.S. Geological Survey (USGS), in cooperation with the U.S. Forest Service, constructed a large scale flume to conduct controlled experiments on debris flows. Large-scale modelling allows better representation of the physical scales eliminating the major limitation of small-scale modelling. The USGS facility in Washington State (USA) provides research opportunities available nowhere else at this kind of scale.

A considerable amount of large-scale research has been conducted on the USGS debris-flow flume and has focused on global behaviour more than specific mechanisms. Numerous papers have been produced that evaluate the use of laboratory experiments and theories developed to model behaviour (Iverson, 1997, 2009; Iverson et al., 1992; Iverson & Denlinger, 2001; Iverson, Logan, et al., 2010; Iverson & Vallance, 2001).

Large flumes like the USGS flume give detailed real-time measurements from near-scale debris flows. Larger flumes have allowed broader exploration of various rheologies, sedimentology and morphology of debris-flows and their deposits. The debris-flow flume allows measurements at a near-field scale and has two main objectives; testing of debris flow

mitigation techniques and providing data from experimental runs that can be used to develop, calibrate and validate existing numerical models.

2.3.3.1. USGS Flume Description

The USGS flume is made from a reinforced concrete channel which is 95 metres long, 2 metres wide, and 1.2 metres deep as seen in Figure 2-20. It has a fixed slope of 31° which is an angle typical of natural debris flows terrain**.** There are 18 data-collection ports in the floor of the flume. These permit measurement of shear forces from sliding and colliding particles along the base of the flume (Iverson et al., 1992). The flume operates with up to 20 cubic meters of saturated sediment. A reasonably flat run-out surface exists at the base of the flume for the ensuing debris flow to form a deposit after exiting the flume itself. The run-out area has a one-metre grid to provide scale as seen in Figure 2-19. The flume is designed to allow experimentation and measurement, for research, at all stages of initiation, flow and deposition. The wide range of material mixtures range from clean uniform gravels and sands to well graded heterogeneous natural debris flow material.

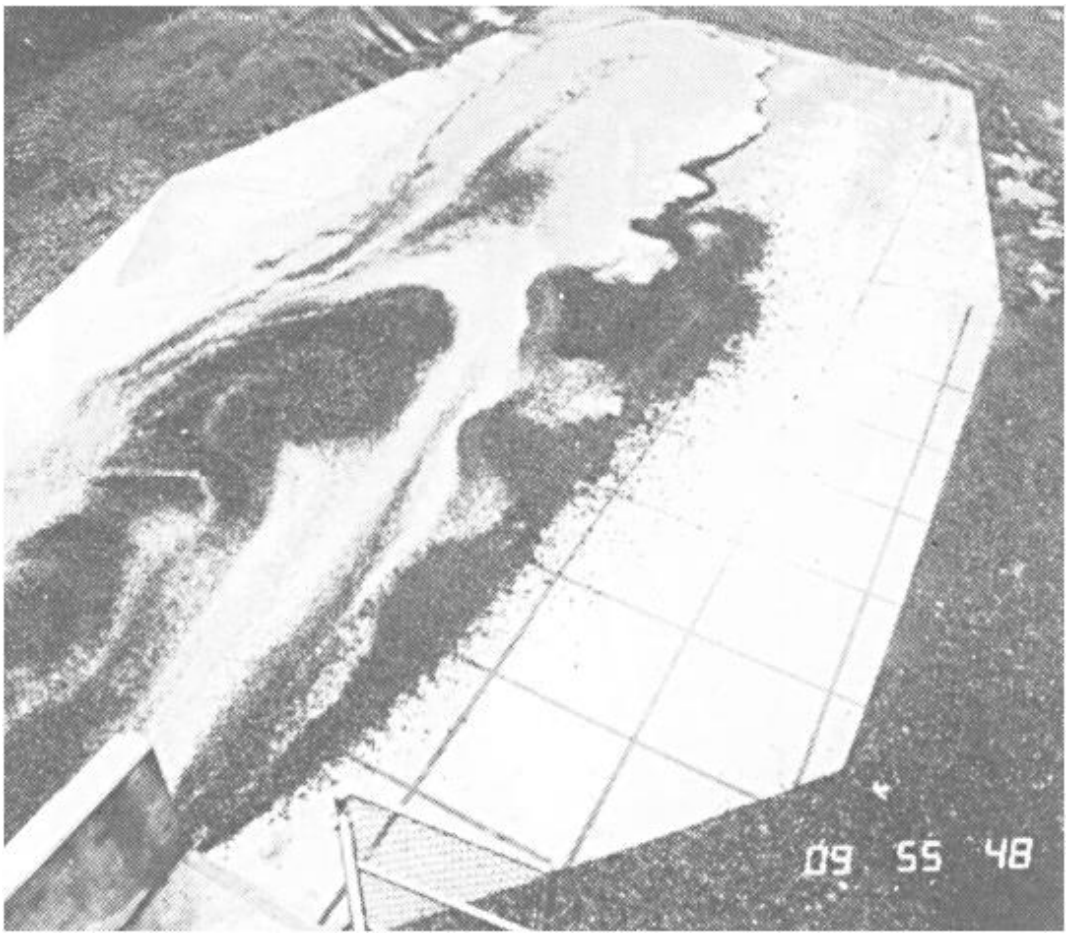

Figure 2-19: Flat gridded deposition area for debris flows on the USGS flume (Iverson et al., 1992).

Figure 2-20: The large USGS flume at H.J. Andrews Experimental Forest (Iverson et al., 1992).

2.3.3.2. Measurement in the Large USGS Flume

The current USGS set up gives a wide range of measurements from flow-front velocities, flow-surface velocities, flow depths, vertical velocity profiles, to shear and normal forces at the channel bed. More innovative techniques include using ultrasonic imaging to inspect the interior of flows as well as adding "smart rocks" to the flow. The smart rocks are miniature sensors that can measure accelerations during the flow down slope. Figure 2-21 shows an example of ultrasonic measurements results showing the flow depth and force for a small section of the flow. The results show the distinct surges seen in real debris flows. These types of sensors allow temporal and magnitude analysis of the surge phenomena that is difficult to produce in the field or at smaller scales.

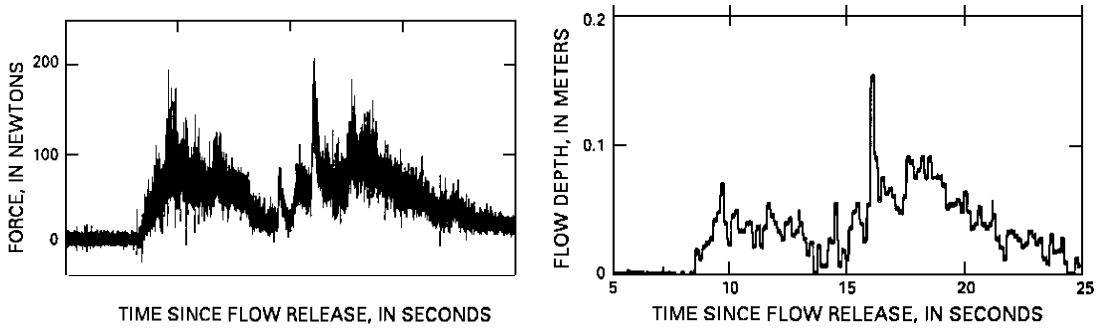

Figure 2-21: Records of flow depth, measured ultrasonically, and normal force on a 0.05 square meter (0.5 square foot) plate on the flume bed as two debris flow surges passed (Iverson et al., 1992).

2.3.3.3. Limitations

Large flume testing is mainly limited by its high cost. Building a large flume is considerably more expensive than a laboratory flume as they need to be made of strong robust materials and take many workers to build. The land requirement of a reasonably large sloping section means that it cannot be built anywhere and is often outside away from the academic institutes that run them. Travel times and poor weather conditions means that it is harder to schedule test and the sizes means longer to set up experiments. The operating costs are also much higher as more material and robust sensor equipment is needed and far more personnel than small flumes. Material can no longer be easily moved but requires heavy machinery.

The large concrete flumes are often built with fixed geometries. This means that it is nearly impossible to alter the slope and channel geometry. The slope is one of the key geometric parameters and could majorly impact the form that the flow takes and the level of deposition in the channel and run-out. Bends and humps are hard to model without building inside the

existing flume which compromises the benefit from the large size of the flume. At this size the control of boundary conditions are much more difficult to control. Triggering and regulating flow parameters like velocity are limited due to the bulk mass of material needed. In a small flume there are multiple ways to alter the initiation method or the roughness of the channel bed and slope.

2.3.4. Particle Size Distributions

The particle size distribution has a significant impact on the behaviour of debris flows. However, the dynamic and segregative nature means that there is non-homogenous behaviour. Few studies look directly at the effect of changes in the particle size distribution (PSD).

2.3.4.1. Average Particle Size

In a systematic study on particle size distributions by Bowman and Sanvitale (2009) the values of D_{50} and coefficient of uniformity (C_u) were varied and the run-out length and front velocities measured. These samples can be classified as stony debris flows which are relatively uniform and coarse with a high average particle size (D_{50}) (Takahashi, 1991). According to Takahashi the coarse material means that the permeability of the material is relatively high and so pore pressure is able to dissipate quickly. This increases the inertial and viscous interactions, and the grain collision and frictional stresses between particles. In geotechnical terms, the Coulomb friction increases. Results have shown that the pore pressure that builds up behind the stony front has the ability to remobilise and drive the front of the deposit.

Figure 2-22 shows that as in Bowman and Sanvitale (2009) as the material becomes stonier, the run-out length reduces, supporting Takahashi's definition of stony flows. In terms of the less concentrated flows there seems to be a maximum run-out that can be obtained by reducing D_{50} as the values become relatively constant. This is suggested as being more fluid-dominated as the finer particles are fully suspended in the flow. This means viscous effects determine run-out for flows with very small grain size, rather than the pressure developed to drive the impermeable front.

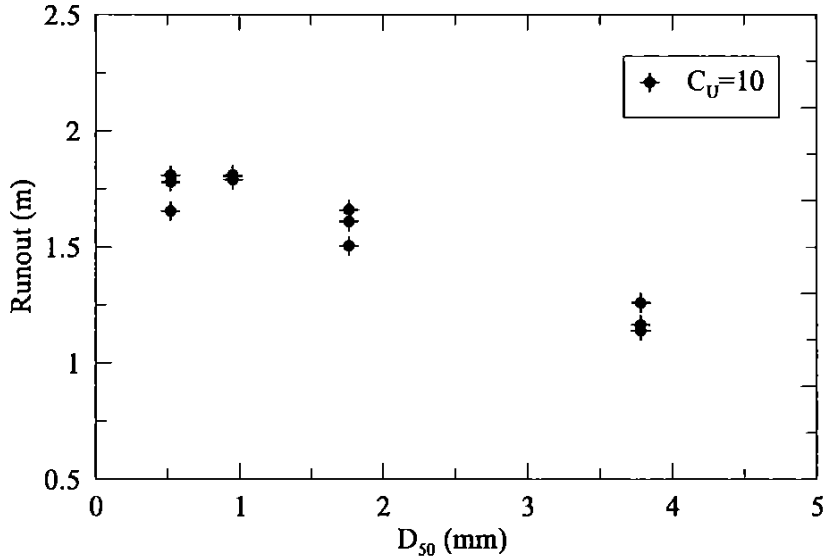

Figure 2-22: Run-out against D_{50} for test with constant C_u (Bowman & Sanvitale, 2009).

The simple empirical relationship between run-out length and the square of velocity for a given geology and geometry (Hungr et al., 1984) has been proved to perform well in the lab Figure 2-23 (Bowman and Sanvitale, 2009). The faster the material the greater the run-out so finer material gives the faster flows up to a limit as viscous forces take over. Bowman and Sanvitale (2009) suggest that even though most PSDs are quoted at the average value, a smaller percentile may reflect the behaviour more accurately. For example, D_{10} (diameter at which 10% of particles are smaller than) might represent behaviour better as it is the fine particles that determine permeability and so pore pressure build up and the Coulomb friction acting between particles.

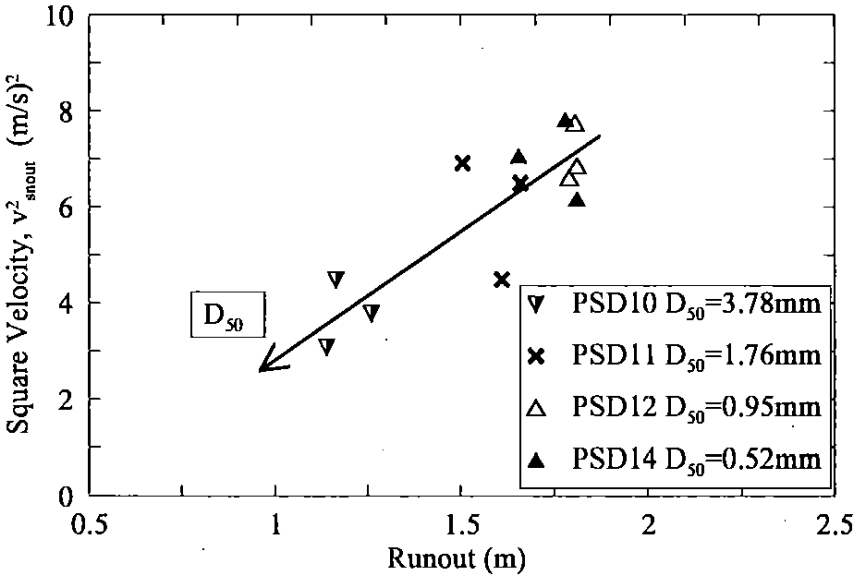

Figure 2-23: Relationship between velocity and run-out for constant uniformity Cu =10. (Bowman & Sanvitale, 2009).

2.3.4.2. Uniformity

(Bowman & Sanvitale, 2009) found that as uniformity decreased, the run-out length increased, showing that a range of particle size is a key part of producing realistic debris flow behaviour. The relationship between run-out and uniformity is not linear, determining that debris flows gain considerable run-out for initially small decreases in uniformity. Also, this change is likely to be negligible with very uniform materials. It could be that with decreased uniformity there is, in the most simplistic sense, a reduced permeability.

Bowman & Sanvitale (2009) found that changes in uniformity with run-out shown in Figure 2-24, did not follow the empirical relationship in (O. Hungr et al., 1984) . This means the factor used to describe changes in uniformity for an empirical setting would not change linearly. Segregation of the particles could change the frictional resistance by building up pore pressure and reducing the effective stress for the middle of the flow by pushing the segregated front forward. This means momentum is lost less rapidly as opposed to the uniform case where there is a steady frictional resistance and more evenly distributed fluid.

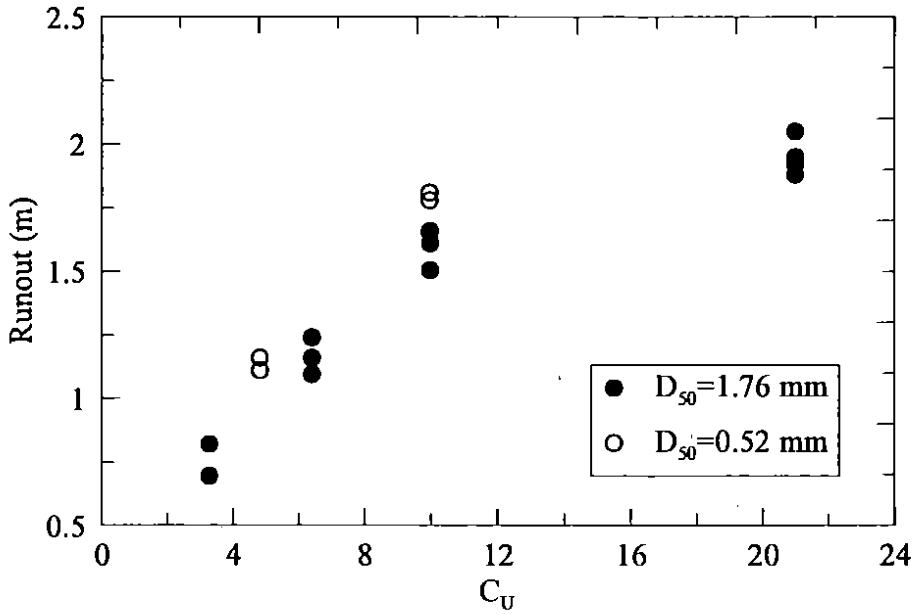

Figure 2-24: Run-out against C_u for test with constant D_{50} (Bowman & Sanvitale, 2009).

2.3.5. Role of Fluid

For the fluid the main influence is drag or flow resistance between the constituents which is often a function of the viscosity parameter. With high drag coefficient the material will flow as a combination of fluid and solid. However, with low drag coefficient the flow will decouple and segregate causing the fluid to move separately to the solid constituents. During

a flow the solid particles will try to accumulate in low shear areas (Iverson, 2003) giving rise to segregation. This could be because the particles are able to rest in the less turbulent low shear sections without being re-entrained in the flow.

2.3.5.1. Moisture Content

The gravimetric moisture content is generally referred to in terms of the concentration of solid particles. The concentration of solids and the moisture content can be given by:

$$v_s = \frac{G_s w}{1+G_s w} \tag{2-7}$$

where v_s is solid concentration, w is moisture content and G_s is the specific gravity, typically 2.65 for quartz sand.

Moisture content is a driving factor in the behaviour of debris flows and is one of the more developed experimental variables. During a debris flow the concentration has been found to be variable with time, depth and length. However, the initial concentration of the mixed material does help determine the location of the flow on the continuum between floods and rock avalanches. The initial moisture content available does have an effect of the interior inter-particle collisions, velocities and run-out.

At smaller concentrations, the particles are located in the lower depth of the flow with a fluid layer above. An immature debris flow is more of a sediment transport problem, and bed load models can predict the movement of both solid and fluids. A third classification of flow regime is called “plug flow”. This occurs when the concentration is high enough that the fluid level drops below the top of the flow. The larger grains push to the top tends to lock up and 'float' as a plug block on the liquidised fluid below (Larcher et al., 2007).

2.3.5.2. Pore pressure

In many mass movement rheological behaviours the pore-water pressure is assumed to be insignificantly affected by deformation which in turn implies that the relative motion still allows drainage on the pore fluid within the mass movement (Iverson, 1985). This is not the case for a rapid mass movement like a debris flow.

In a debris flow the pore-pressure can build up thanks to the relatively impermeable nature of the material. The excess pore-fluid pressure in debris flow can be linked to the downward flux of buoyant sediment rather than from external surface loading. Liquefaction pore-fluid

pressure develops and persists during the brief lifetime of a typical 10 m^3 sized experimental debris flows (Major 2000) indicating that pore-fluid pressures do not dissipate or decay substantially over the lifetime of a typical debris flow. This complicates the rheology with additional pressures that are not intrinsically identified in traditional rheologies.

Friction and Coulomb viscous rheologies discussed earlier in this chapter both contain a pore-water pressure term. The pore pressure can occur from simple hydrostatic conditions as well as additional excess pore pressures. Excess pore pressure is created from rapidly applied loads acting on pore fluid that is incompressible. As particles try to rearrange to a stable configuration there is a temporary resistance and fluid pressure equals the change in total stress. The dissipation of this pressure is linked to permeability as flow of fluid is required to allow inter-granular contacts to take over load (Major, 2000).

The fluid in debris flows reduces the effective coefficient of friction (reduce the normal effective stress) (Legros, 2002). Under high pore pressure and low permeability sections of a debris flow can become liquefied when solid material is totally supported by fluid and inter-particle friction reduces to negligible values. Debris flows are more mobile as water content increases because there is less particle interlocking. This does not mean, however, that there are not further interactions that affect a drier, less uniform, coarse flow. There are various combinations of particle distributions and water content that give the same run-outs.

Chau, et al. (2000) found that the moisture content had a significant impact on the run-out using similar slope and moisture contents. The minimum particle size was 0.6 mm and the maximum was 5 mm. The experiments presented in Chau et al. (2000) were compared to empirical models and was found to fit a Vollemy rheology but not dilatant or conservation of momentum methods. The sensitivity of the test to moisture content may have been a result of the uniformity of the material.

2.3.6. Influence of Slope

(Takahashi, 1991) is one of the only researchers contributing to the small amount of work on variation in slope angle, some results are shown in Figure 2-25 and Figure 2-26.

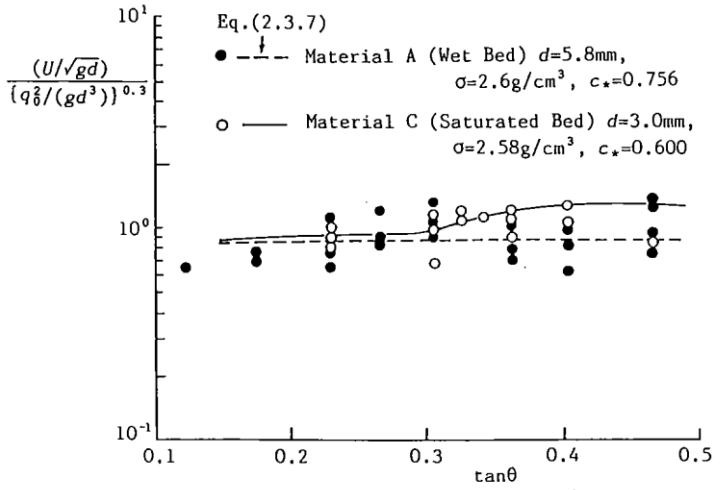

Figure 2-25: Non-dimensional translation velocity versus channel slope (Takahashi, 1991).

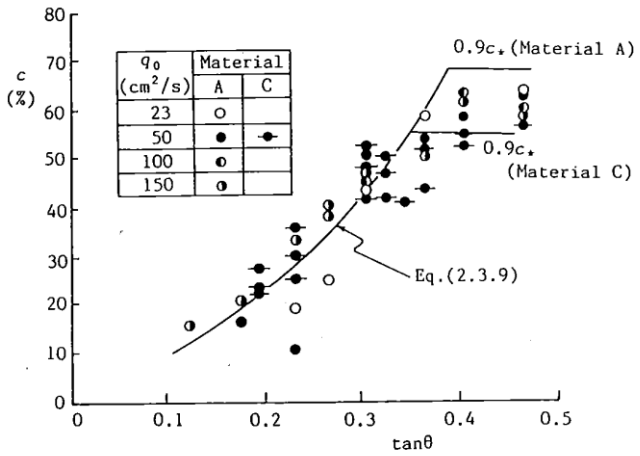

Figure 2-26: Solid concentration in the snout of debris flow with the slope (Takahashi, 1991).

Figure 2-25 shows that the non-dimensional mean velocity is related to channel slope but still includes a reasonable level of variability. The concentration of the debris flow front against slope angle shows that as the concentration of the front increases to a value of approximately 22° at which point it remains constant. This could be explained by considering low slope angles (less than 22°) have a developing flow behaviour that is not dominate or present in higher slopes. Hungr, Morgan et al. (1984) have showed that at a slope of less than approximately 12°, flows start to deposit solid particles rather than transport them and may represent a lower bound on the ability of debris flows to form. No research was found on the effect of change in PSD or moisture when related to the slope.

2.3.7. Boundary Conditions

Natural channelized flow has a transverse variation in flow velocity due to friction and interactions with the side walls of the channels. Figure 2-27 shows various transverse velocity profiles, in some cases there is a very small boundary layer with a flat profile through the middle of the flow. In other cases the shear is distributed throughout the flow giving a more parabolic transverse velocity profile. The profiles in Figure 2-27 assume a no slip boundary condition but within stony debris flow there is potential for the grains at the front to exhibit a slip velocity.

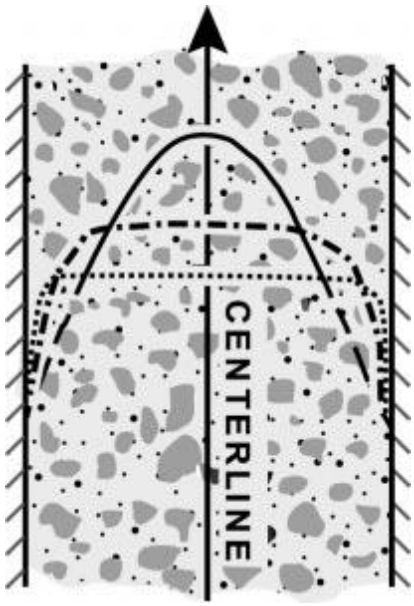

Figure 2-27: Iverson and Vallance (2001) various velocity profiles transvers to flow direction.

Breien, et al. (2007) studied sub-aerial and sub-aqueous debris flows at the wall of a flume. They found there was a wall effect for sub-aerial debris flows. The effect was evident as the front and averaged velocities of the near wall differed. They did however assume that the near wall velocities were representative of the interior of the flow. Video visualisation of the interior has been difficult due to the opaque nature of the material, there has been some evidence of a difference in velocity caused by the walls through the use of basal sensors.

The studies by Davies (1990) on moving bed channels showed that the main effect of the walls on the flow was most prominent at the base. Figure 2-28 shows, the effect of the side wall in an erodible bed situation, increasing the velocity gradient at the base of the flow and reducing the gradient further away from the bed. It is noted that the wall component in a flume test is often much smaller than in a natural channel as the wall is flat and smooth.

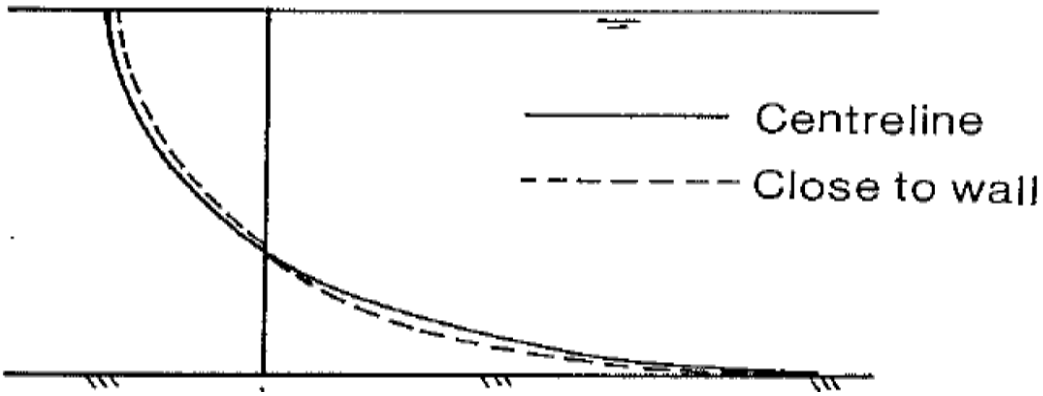

Figure 2-28: Effect of sidewall on velocity profile of a erodible bed channel (Davies, 1990).

In terms of the base of the flow the boundary condition is erodible or non-erodible. If the base of flow is not erodible then the roughness of the bed creates the most significant effect on debris flow behaviour. The roughness can be measured using Manning's coefficient but is often assumed as part of a friction coefficient. In most flume experiments the base is assumed flat with relatively low friction unless a synthetic surface is added to the base of the flow

Suzuki and Hotta (2006) considered the addition of roughness to the bed of a debris flow experiment. The concept was to make the roughness comparable to the particles mobilised in the flow. This was done using a series of strips of rectangular wooden slats attached to the bed of the flume at a set scale to get a roughness. A modified resistance term was used to measure the impact of the increased roughness.

When the height of the flow was relatively close to the height of the roughness, then there was a large increase in resistance which reduced with increasing height of flow. The resistance values became constant once height flow was about five times the roughness height. The concentration of the flow did not change considerably or affect the resistance at the base of the flow.

2.3.8. Physical Modelling Summary

The physical models described in this section include the generic empirical field-based studies, small flume studies and the large flume studies with how they work and some limitations. The impact of the PSD in terms of uniformity, average size and fine content is evident. Other factors like fluid slope and boundary conditions have been shown to have significant impacts on the behaviour of debris flows.

2.4.Non-Intrusive Laboratory Methods

2.4.1. Physical Imaging Techniques

Methods of laboratory testing for debris flows before the 1980s were based on macroscopic measurements using rheometers and viscometer theory to link bulk flow measurements to a velocity flow profile. Current trends focus on direct measurement of the flow profile. However, when focusing on sensitive flows classic flow instruments introduced their own effects and non-intrusive methods needed to be developed. New methods, for example Refractive Index Matching (RIM), are non-intrusive and so do not affect the flow itself. RIM is an optical method of making two substances optical transparent.

Some of the non-intrusive methods used in granular measurements and experiments are:

- Nuclear Magnetic Resonance (NMR) – widely used in clinical medicine. Uses distortions in the magnetic field produced by atomic nucleus. Has the advantages of not needing an opaque flow, quick 3D measurements of velocity and can measure many parameters, particularly porosity and pore networks (Fukushima, 1999). Drawbacks are the spatial and temporal resolutions with complex response as well as the equipment being bulky and expensive (Wiederseiner, et al., 2011)
    - Magnetic Resonance Imaging (MRI) – is a sub field of NMR which works deep within a sample and does not assume a preferential orientation of movement (Nakagawa, et al, 1993)
- Acoustic Doppler Velocimetry (ADV) – is still in early stages of development for granular flow. A three-pronged probe emits and records high-frequency sound and measures the Doppler shift to determine motion. This method has trigonometry, noise, signal aliasing, and other disturbances (McLelland & Nicholas, 2000)
- Laser Doppler Velocimetry or Anemometry (LDV or LDA) – the use of light reflection rather than sound waves and requires RIM. LDV is a measure reflected light fluctuations caused by particles passing through two laser beams. A Doppler shift in frequency between the incident and reflections can measure velocities.
- Laser Induced Fluorescence (LIF) – a RIM technique using laser illumination. LIF will be expanded in the next section.

2.4.2. LIF Experimental Technique

Laser Induced Fluorescents (LIF) or Planer Laser Induced Fluorescence (PLIF) is the use of laser light to illuminate a plane or targeted medium inside an otherwise transparent experiment. The illuminated medium or tracers give a framework for tracking both the path of individual particles (Eulerian) and flows within a controlled region (Lagrangian). This can be done in terms of both velocity and strain throughout the laser sheet's two-dimensional plane (the laser sheet is spread for PLIF).

PLIF for geotechnical research gives non-invasive data that is easily visualised and can be recorded on cameras. It does, however, rely heavily on RIM. RIM is very sensitive to changes in temperature and the presence of other substances that cause refraction and reflection. LIF has been used in a range of granular suspension studies in the last ten years. According to Wiederseiner et al. (2011) most previous work has been done with illuminated particles or at a transparent boundary wall, whereas, in Andreini (2012), Sanvitale (2010) and Hunter (2012) the PLIF technique used was unique because the fluorescent illumination was provided by the fluid. The solid particles were therefore the seeds because of their absence of illumination rather than being illuminated.

A comparison of three PLIF methods is present below in Table 2-4. Andreini (2012) and Sanvitale (2010) used small-scale granular flows using flumes with the fluorescent dye contained in the fluid phase. Hunter (2012) used the same LIF equipment as Sanvitale (2010) in a much lower speed erosion application. The following table is a summary of the methodology and results produced with corresponding images.

Table 2-4: LIF experiment comparisons

Setup Parameter	Andreini (2012)	Sanvitale (2010)	Hunter (2012)
Setup Images	Figure 2-30	Figure 2-33	Figure 2-37
Solid	The solid was spherical PMMA (polymethacrylate) beads, mean particle size of approximately 100 – 200 µm	Borosilicate glass (Schott Duran)	Borosilicate glass (Schott Duran)
Fluid	Triton X1000, 1, 6-Dibromohexane and UCON oil 75-H450. Three fluids were needed as both density and refractive index were matched	Cargille Immersion Liquid (code 5095)	Cargille Immersion Liquid (code 5095)
Flume length	2960 mm	2000 mm	Permeameter 100 mm square base
Flume width	100 mm	150 mm	150 mm
Flume Slope		24.5°	
Laser Fan angle	30°	60°	60°
Laser Sheet Thickness	150 µm	2000 µm	2000 µm
Laser Power		800 mW	800mW
Laser Wavelength	527 nm	514 nm	514 nm
Camera Frame Rate	200-1000 Hz	600 - 1000 Hz	10 Hz
Camera Sensor Size	12 x 12 µm	10 x 10 µm	13.68 x 13.68 µm
Laser Plane Location	Exact middle of flume	45 mm from the side of the flume	45 mm from the front of the tank

2.4.2.1. Andreini (2012) Methodology

In Andreini (2012) and (Ancey, Andreini, & Epely-Chauvin, 2013), LIF is used to model neutrally buoyant suspensions of non-Brownian particles in a viscous fluid. The solid and fluid were mixed and de-aired to ensure RIM within 0.0006.

Figure 2-29 and Figure 2-30 shows the camera setup, via the base of the flume using the Scheimpflug principle, to allow direct access to the centre of the flume. This was able to keep the top of the image in focus for a thin flow. This approach has a limitation on the depth of flow but not the location of the laser plane or the width of the flume. A wider flume would allow larger particles to be tested without jamming. The thickness of the laser is close to the average particle size used and is relatively very narrow with laser pulse (f = 1 kHz) energy of 20 mJ. This gave clear images in Figure 2-30 (bottom) where most particles are individually distinct, particularly at the base of the flow.

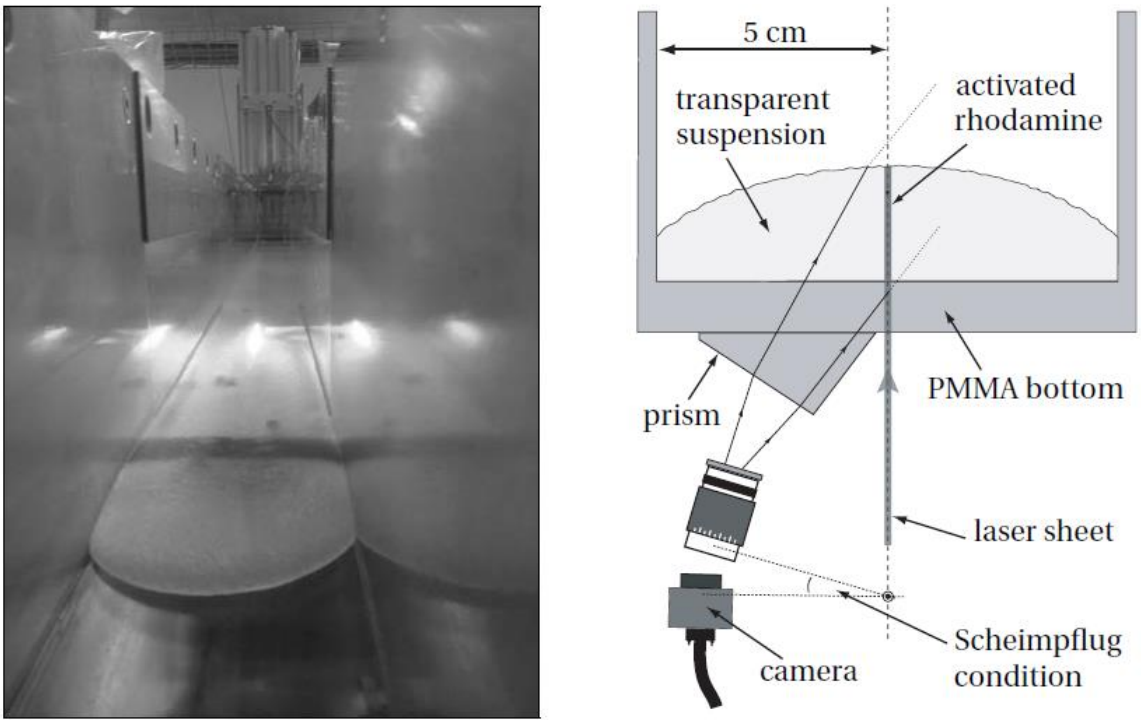

Figure 2-29: (Left) Photo of flow looking up the flume. (Right) diagram of camera and laser setup during flow. (Andreini, 2012).

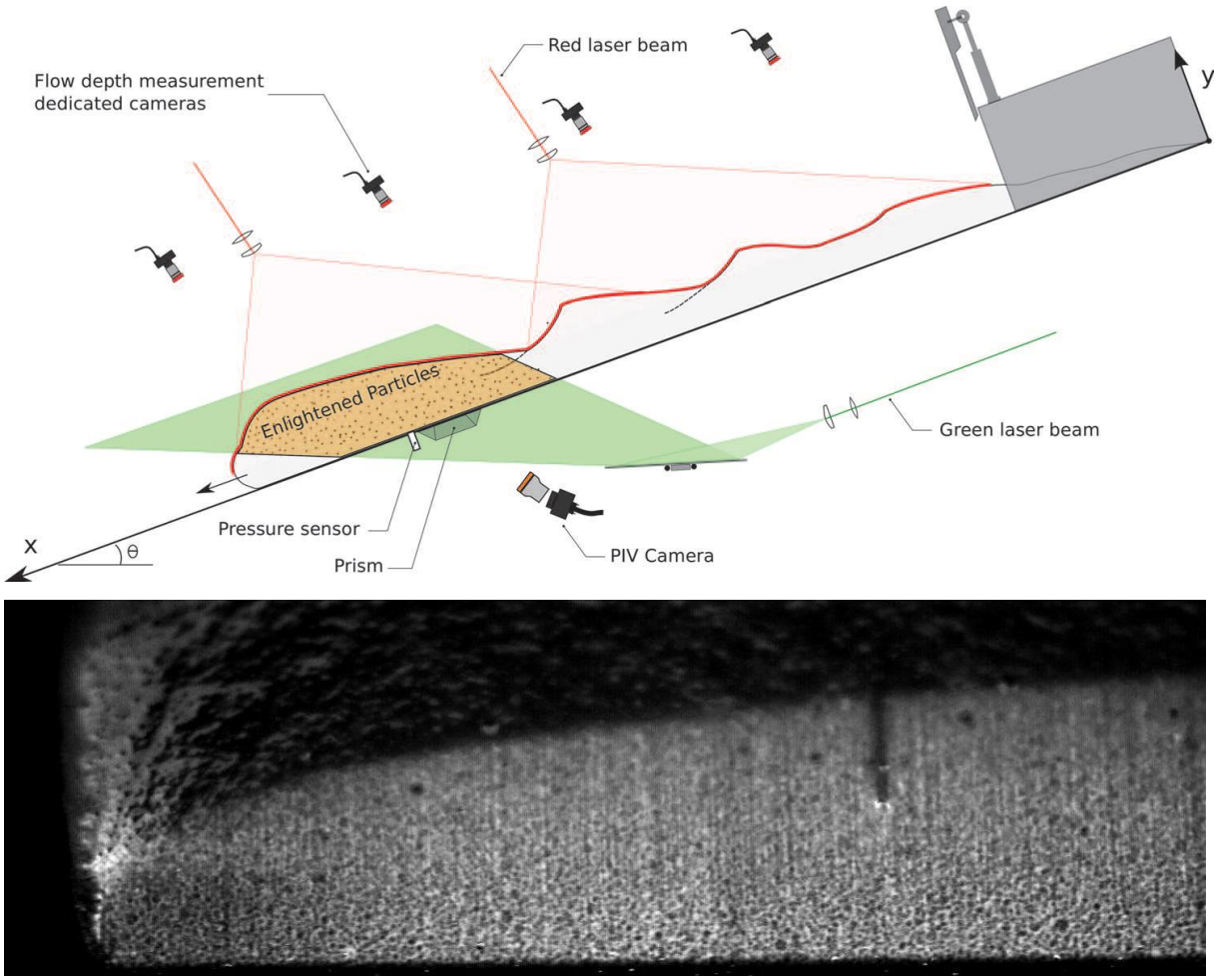

Figure 2-30: (Top) side view of LIF set up with additional cameras. (Bottom) typical raw image with black particles and white fluid the depth was 15 mm (Andreini, 2012).

2.4.2.2. Andreini (2012) Results

For low solid fractions less than 45%, the flow behaved like a homogenous viscous fluid, no migration or sedimentation was observed. The velocity profiles appeared to be perfectly Newtonian. For tests with an intermediate solid faction 45-55%, the bulk behaviour was viscous. However, local migration of particles toward the free surface occurred causing a blunting of the velocity profile with maximum flow velocities less than 150 mm/s. The normalised profiles agreed with a normalised Mills and Snabre (2009) model but the actual velocities were overestimated for the model. At high solid concentrations, the flow behaviour was dependent on the mass of the flow. For small masses the flow separated and the solid halted, whereas larger masses produced first inertial then pseudo-viscous flow before developing slower fronts and stick slip regimes before separating.

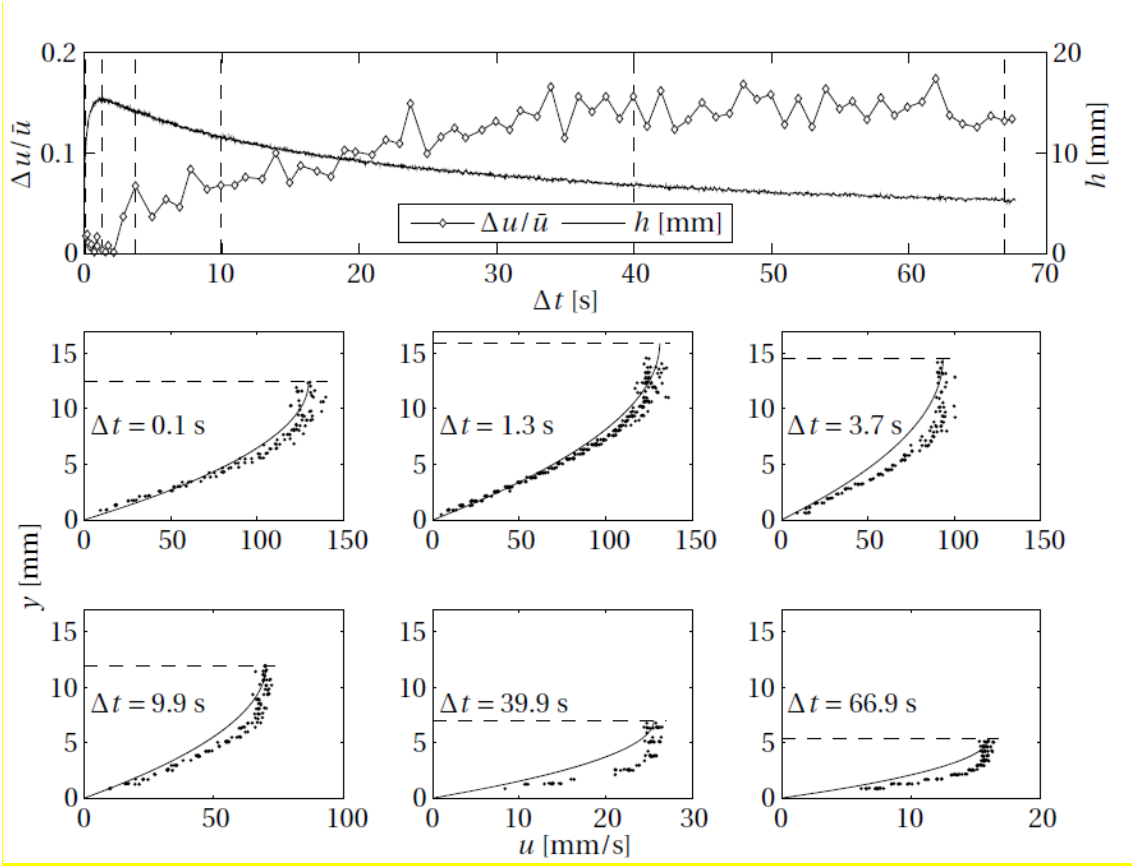

Figure 2-31: (Top) the left axis shows the height over time of flow at a set point on solid line. The right axis is a normalised deviation from Newtonian shape. The bottom six panels are velocity profiles at each time interval noted in the top panel, solid line is the theoretical Newtonian profile. The spots are the actual experimental result. Dashed line is the free surface. Plots from Andreini (2012).

2.4.2.3. Sanvitale (2010) Methodology

Sanvitale (2010) conducted experiments with real debris flow material using the PSDs shown in Figure 2-32. These PSDs where the bases for the substitute material used after scaling the in PLIF experiments. Sanvitale (2010) used a single moisture content of 27.8% and a single slope value of 24.5˚. The scaling for change in viscosity between the oil and natural fluid was based on permeability using the Kozney-Carmen equations (Barr, 2001). Sanvitale (2010) originally started with the laser applied from the top but this was shifted to the bottom to reduce light scattering (Sanvitale, Bowman, & Genevois, 2010).

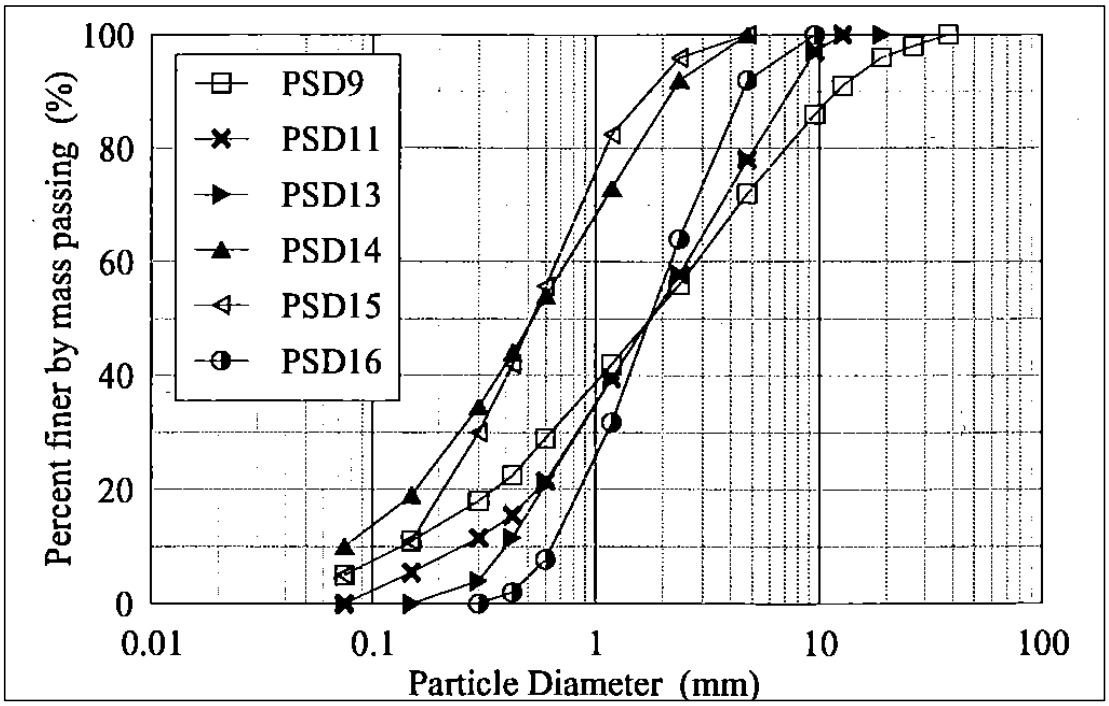

Figure 2-32: Various particle size distributions with varying Cu used for PLIF experiments (Bowman & Sanvitale, 2009; Sanvitale et al., 2010).

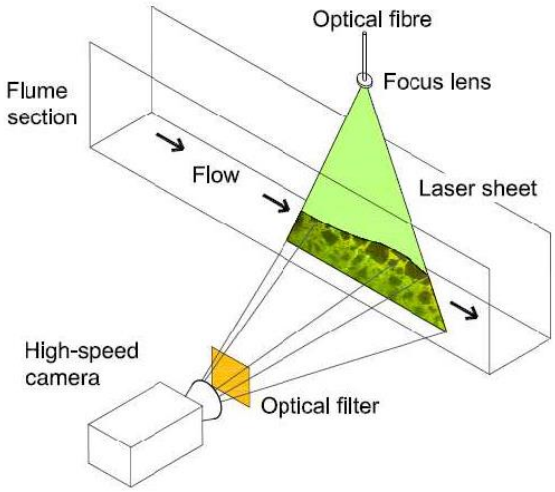

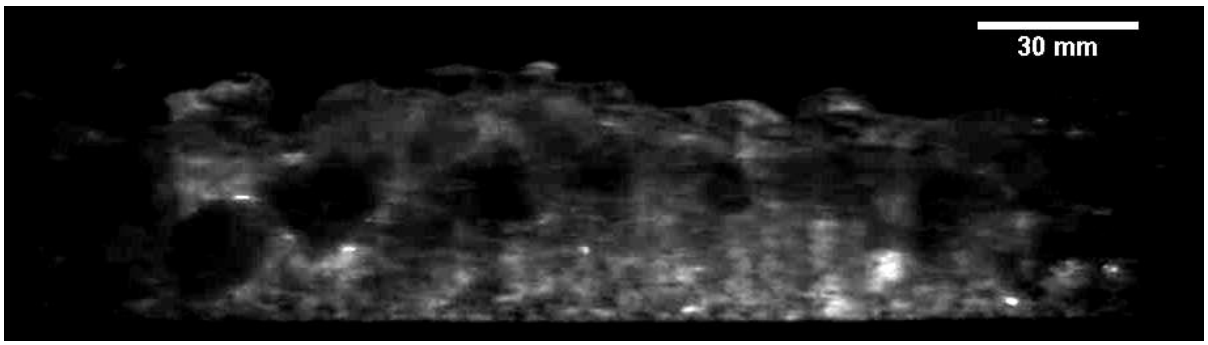

Figure 2-33: (Left) Photo of deposit looking up the flume, note the green laser plane seen at the end of the flume. (Right) diagram of camera and laser setup during flow. (Bottom) typical raw image with black particles and white fluid the depth was 35 mm (Sanvitale, 2010).

2.4.2.4. Sanvitale (2010) Results

Sanvitale (2010) produced velocity profiles with depth in the slope normal and parallel direction (Figure 2-34) for various sections of flow (Figure 2-35) and used these to produce a mean flow velocity with time (Figure 2-36). Calculation and imaging of the front was limited due to poor saturation of this section of the flow. However, the front and body sections showed a slip velocity at the base which is less apparent in other externally measured debris flow experiments.

The body showed features such as segregation along the length and depth, with coarse particles concentrated at the front. Collisions between large particles were evident and could be tracked visibly. In the tail the image quality improved with increased saturation. The behaviour was less collisional and the material was homogenously distributed with depth.

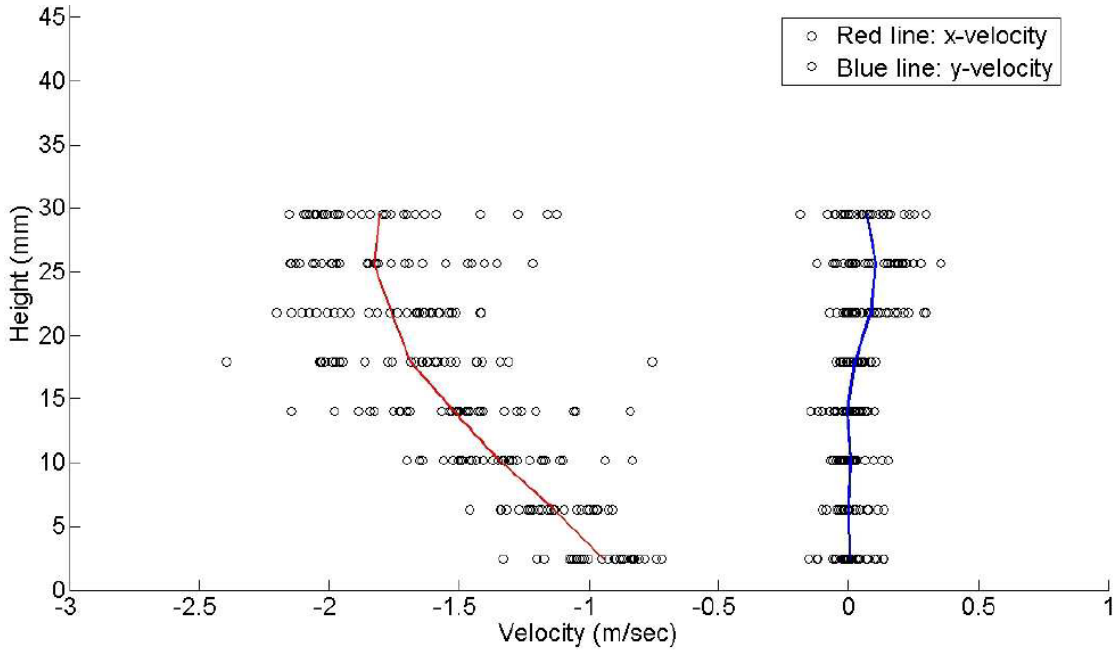

Figure 2-34: Velocity estimate output from Geo-PIV mesh a particular location for both slope normal (y) and parallel (x) velocities (Sanvitale 2010).

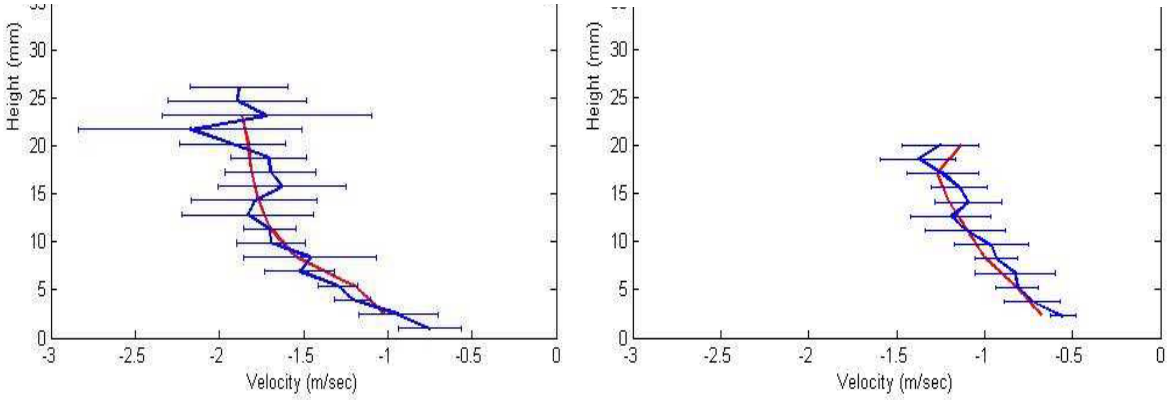

Figure 2-35: Velocity profiles derived from PIV analysis. (Top) front at time = 0.136 s and start of tail at time = 0.554 s. The blue line is the velocity using small patches and the red line uses larger patches error bars are at one standard deviation (Sanvitale, 2010).

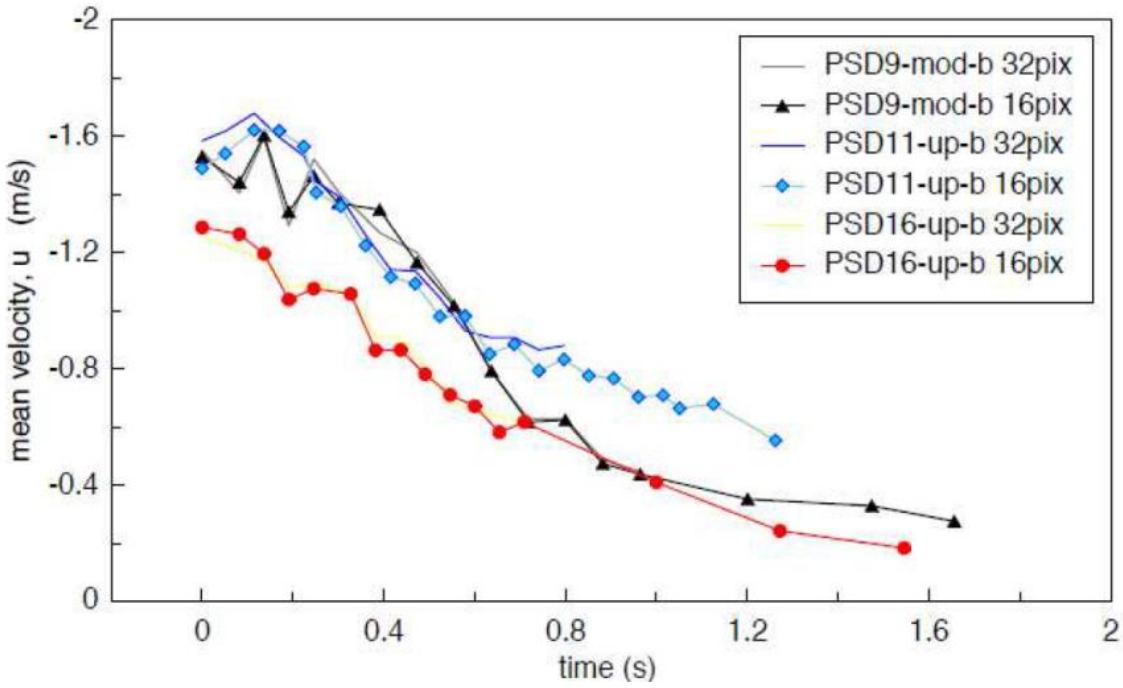

Figure 2-36: Mean velocity with time (Sanvitale 2010).

2.4.2.5. Hunter (2012) Methodology

Hunter's work (Hunter, 2012) used the same imaging equipment and material as Sanvitale, applied to much slower phenomena in a different apparatus. This meant that the exposure did not limit the image quality. While this frame rate cannot be used for high speed debris flows it does show some of the LIF issues and trends.

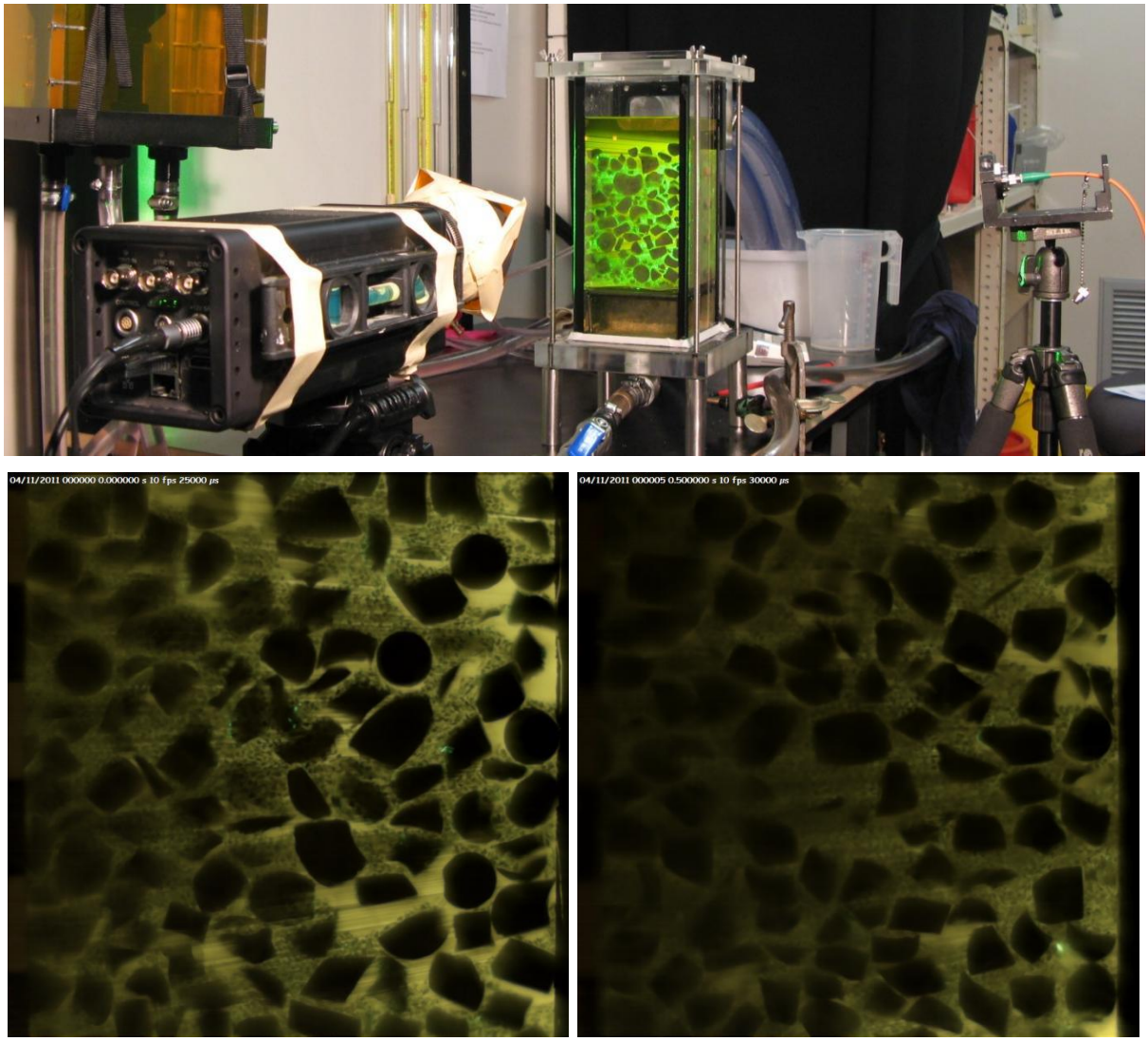

Figure 2-37: 1cm and 4cm from front base scale 100mm Hunter (2012).

2.4.2.6. Limitations Identified in LIF Methods

Hunter's (2012) method allowed a number of the limitations in the LIF technique to become apparent. Figure 2-37 shows the effect of moving the laser from 10 mm to 40 mm into the material. This change in Location Of View (LOV) shows how that individual particles of less than 1 mm can be seen but not as the LOV increases inward from the front. Also the attenuation of the laser from one side of the sample to the other shows that as the laser moves through the particles, it is less able to distinguish particles. Areas with fewer particles (bottom right corner of images) allow the fluorescent light to better penetrate the sample.

A summary of the limitations in the PLIF techniques used is presented below:

- As individual particles become smaller they are more difficult to detect, with a limit of around 0.425 mm
- Small particles reduce the overall image clarity giving a cloudy appearance. This is due to significantly more particle-fluid interfaces which magnifies the RIM errors
- Scaling and size of apparatus may limit the range of large scale particles resulting in issues in mimicking PSD of natural samples
- Air bubbles are present even with sample placed in a vacuum desiccator as used by Hunter (2012). The filter was successful at eliminating reflections caused by the bubbles but the bubbles themselves were visible and would have been incorporated into the PIV analysis.
- There was light attenuation with depth with about 50 mm deep clear before the image deteriorated.
- There are issues with the thickness of the laser, so particles that are smaller than the beam width and the irregular edges of large partials are blurred (Figure 2-38).

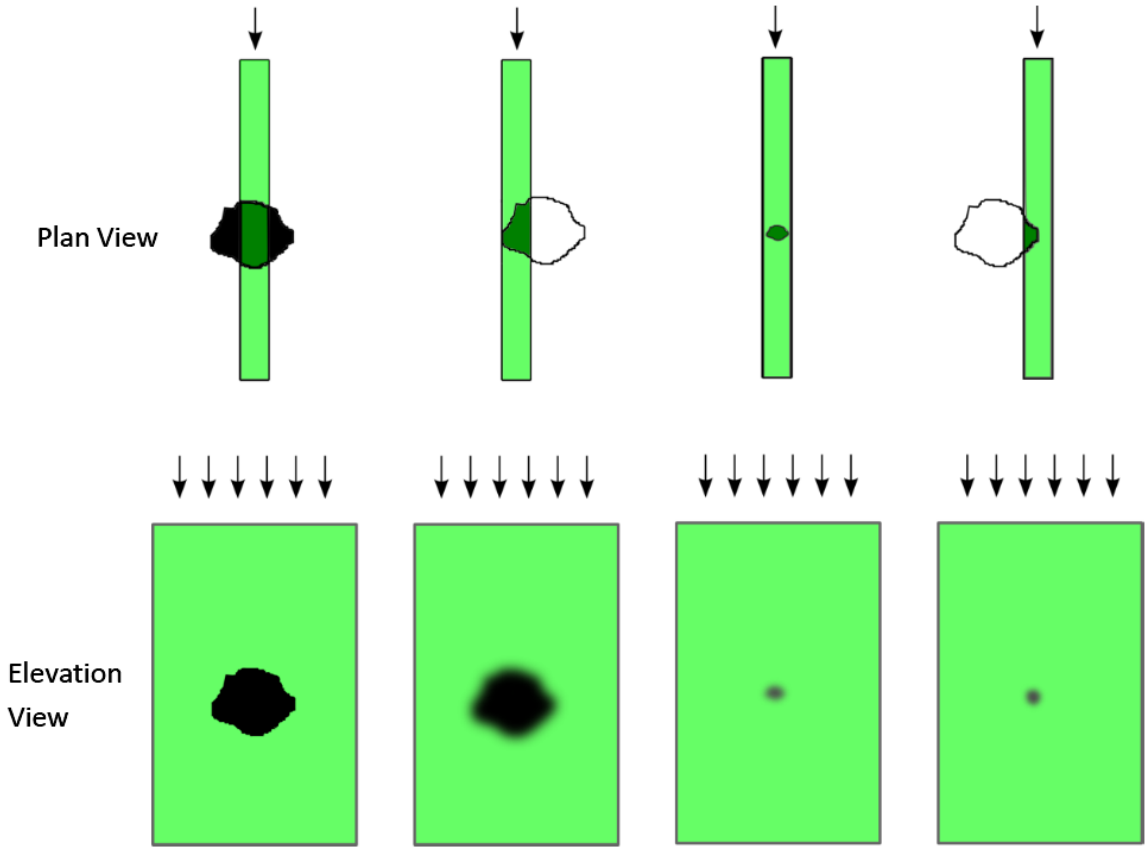

Figure 2-38: Light-particle interaction between laser sheet and glass particles of varying sizes, Hunter (2012).

2.4.2.7. Comparisons of LIF Methods

The main imaging difference between Andreini (2012) and Sanvitale (2010) is the use by Andreini (2012) of the Scheimpflug principle to position the camera, allowing visualisation in the exact centre of the flow. The significant difference in behaviour of the flow is that the material in Andreini (2012) is much finer and viscous. The type material resulted in a slower flow than Sanvitale (2010). This difference in velocity allows the exposure to be longer, allowing more light to the camera (both cameras have similar sensor sizes so generally receive the same amount of light rays). Sanvitale's laser would have given (at 1 kHz frame rate) 0.8 mJ in a thicker beam which is considerably less than Andreini resulting in less illumination of the particles.

The PLIF setup for this thesis is based on Sanvitale (2010). The exact set up is explained further in Chapter 3. Sanvitale's method is better suited to this thesis as it less expensive and allows variable flow depth to be tested. The distortion caused by impurities and poor RIM is consistent with depth and Sanvitale's method can be brought up to the same clarity level with more powerful laser or camera. The following comparisons where made of the PLIF techniques utilising illuminated fluids:

- While Andreini (2012) does not investigate a debris flow (having none of the coarse fraction) it does represent the closest application found to Sanvitale's LIF technique. It has less variation in the scatter of data points that make up the velocity profiles – which may be due to the particle size being more uniform as much as the PLIF technique.
- The Andreini (2012) camera setup allows a wider flume and more freedom to locate the LIF plane in the transverse flow direct.
- Hunter (2012) shows that slow-moving (higher exposure rate) phenomena give much clearer images of particles. This was also found in Sanvitale's (2010) static images of material.
- Hunter (2012) shows the illumination provided by the laser and LIF attenuated through the sample. This is a major limitation to calculating concentration of particles from light intensity
- Hunter (2012) showed that a relatively thick laser beam gave issues with blurring large and small (diameter less than laser beam thickness) particles

- Andreini (2012) had a thinner laser beam than Sanvitale (2010). Sanvitale (2010) could not achieve this due to the power of laser apparatus requiring more light while operating at a higher frame rate. This thinner beam and slower flow rate appears to have illuminated much finer particles in Andreini (2012) than Sanvitale (2010).

2.4.3. Quantitative Imaging

Quantitative imaging (QI) is a general class of optical-based laboratory measurement techniques originally developed in the field of fluid mechanics. These techniques have only been developed within the last 15 years for application in granular materials. This application has developed with powerful computers which have increased the effectiveness of tracking algorithms on large detailed flows. QI techniques can be fundamentally grouped by what is used to represent motion or 'seed' the flow. This can be discrete particles both as additional to the flow and as part of the flow, continuous tracers (florescent dye) or flows without seeds. Discrete particles are often used for velocity measurement and there are a number of common ways of converting the seed's motion into velocities. The most common are:

- Laser Speckle Velocimetry (LSV) – High seeding density. High numbers of seeds scatters light to form an interference pattern of 'speckles' that can be matched using a autocorrelation function
- Particle Streak Velocimetry (PSV) – Medium/high seeding density. Long exposure times result in the blurring of particle motion into streaks along direction of motion
- Particle Image Velocimetry (PIV) – Medium seeding density. Takes sections of an image and matches the texture using an autocorrelation function
- Particle Tracking Velocimetry (PTV) – Low seeding density. Many non-overlapping particles are individually recognised and tracked between frames
- Image Correlation Velocimetry (ICV) – No seeding density. Motion is measured without discrete particles. For example using shadows or colour intensities within a flow.

The two typical setups for digital imaging are a rotating drum or particle release from a hopper down a static pile. (Jesuthasan, Baliga, & Savage, 2006) experiments used the hopper

setup as it was able to produce a free surface flow down a slope with a thickness independent of distance of flow. A focus has been made on slope flow for this thesis literature review.

All particle-based QI attempts to measure instantaneous velocities by measuring the displacement of the particles suspended in a fluid at known time steps. This displacement can therefore be converted into a velocity. Use of QI in a laboratory granular flow setting is more limited due to scaling issues which, in cases of granular flows like debris flows, do not exist in complete forms scaled for all parameters. Use of QI in a LIF or transparent medium is even more limited.

2.4.3.1. PIV

PIV is a rapidly increasingly popular laboratory technique advanced by the demand for actual data to validate numerical codes (Raffel, Willert, & Kompenhans, 1998). The removal of limitations due to computational power has also contributed to the increase in popularity of PIV in a wide range of engineering applications. This includes: human airways, heart valves, turbulence, combustion, flow-in industrial appliances and engines, wind tunnels, granular flows and air or liquid flows around many different shaped objects (Schroeder, 2008).

PIV evolved along with LSV and they differ mainly on how the particle seeding density is handled. Both are based on the most probable statistical value and results are presented in a uniformly spaced grid. "Correlation of either particle images or speckles can be done using identical techniques and result in the local displacement of the fluid." (Paul, Atiemo-Obeng, & Kresta, 2004). Hence, LSV and PIV are essentially the same technique differentiated by different seeding density of particles or the "source density" (Adrian, 2005; Paul et al., 2004). PIV has been used intensively for turbulent analysis of fluids. This is due to PIV being able to measure over a wide dynamic range of scales in length and velocity.

PIV traditionally takes double exposure images or more recently pairs of frames from high speed recording and divides the image up into a grid (usually overlapping) of patches for interrogation (Westerweel, 1993; Willert & Gharib, 1991). Then a Fourier transform is used to identify the mean displacement of the patch in the secondary image (Figure 2-39). Originally Young's fringes (Adrian RJ, 1984; Sutton, Chao, & Taylor, 1983) were used for matching but more modern methods use auto-correlation. Correlation covers a number of methods including: auto-correlation, cross-correlation, hierarchical correlation (Hart, 2000) and grid less correlation (Okamoto, Hassan, & Schmidl, 1995).

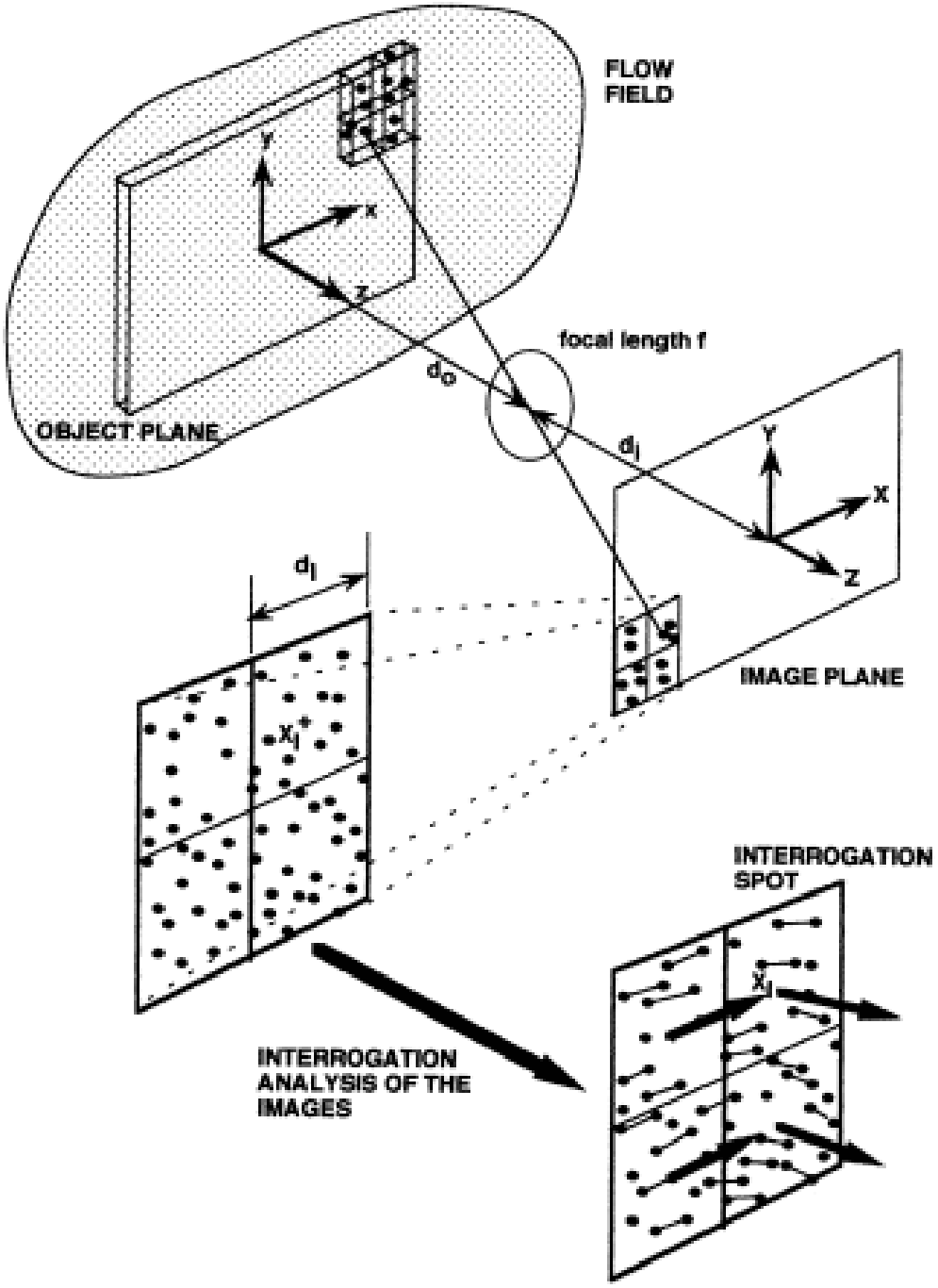

Figure 2-39: Analysis of a grid of interrogation spots (Adrian, 2005).

The output after correlation of two images is shown in Figure 2-40 (front panel). The PIV programme is based on a small patch being matched to a larger search zone (back two panels of Figure 2-40). This gives the map of 'degree of match', the map is used to identify peaks in correlation. The displacement of the patch from one image to the other is represented by the largest peak. The main challenge to correlation is whether the signal peak is distinguishable from the random noise in the correlation plane. If the peak is smaller than the random noise then analysis will indicate the wrong displacement.

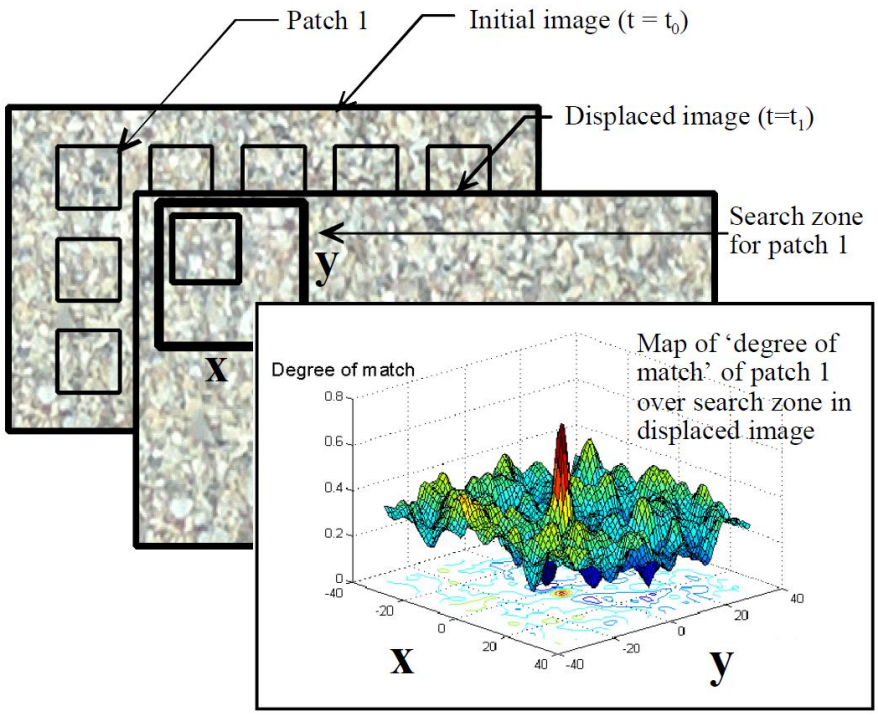

Figure 2-40: PIV analysis with auto-correlation (White, Take, & Bolton, 2001)

The most modern and complex form of PIV is stereoscopic or three dimensional PIV. This form is becoming more reliable but is currently less accurate in the third dimension. Stereoscopic PIV is not covered further in this review because of its complex nature.

2.4.3.2. PIV in Granular Flows

PIV has been modified from fluid-based scenarios for implementation in geotechnical and granular modelling. The main change is while fluid experiments require seeding with particles to give texture for image processing; granular materials have their own texture. The texture comes from the light and shadows formed between particles and the case of most natural materials the colour of the grains themselves. For synthetic and uniform materials texture can be added by the addition of coloured 'flock' materials or dyed grains (White et al., 2003).

PIV applied to granular flows such as debris flows is relatively recent, particularly the use of non-uniform particle sizes. Typically PIV has been used in dry granular or opaque debris flows. Pudasaini et al (2010) used granular PIV based on cross-correlation on an avalanche of quartz sand filmed from the front relying on the granular shadows rather than seed particles. Keane and Adrian (1992) performed PIV analysis on a recording of a debris flow conducted at a transparent wall.

A combination of a RIM technique like PLIF with a QI approach like PIV is still relatively innovative and unique in granular flows. Its main advantage is that it is able to look directly within the flow, reducing the need to consider boundary conditions in laboratory work, while giving non-invasive data on the behaviour of the solid particles and fluid (Nokes, 2008; Paul et al., 2004; Wiederseiner et al., 2011).

Wiederseiner et al. (2011) discussed the use of RIM materials with PIV and PTV for use in suspended particle concentrations. PIV and PTV were seen to work well in combination with RIM. These flows were quoted as having similar solid concentrations but much smaller particle sizes to typical debris flows. This often led to fewer particle dominated flows and less energetic collisions. Also the flows were typically a more uniform seed size and were typically analysed through PTV.

White et al. (2003) developed a PIV deformation system, Geo-PIV, for geotechnical testing. Geo-PIV is particularly designed for the analysis of displacement in soils, for example the installation of a pile or the failure or an earthen embankment. Their method showed their PIV system gave an order of magnitude increase in accuracy and precision of the displacement of patches compared to previous PIV correlation methods. This system was developed further to form the basis of the Sanvitale (2010) PIV analysis programme termed Static Mesh Geo-PIV. The method of this programme is presented in Chapter 3

2.4.3.3. PIV vs. PTV

The most promising QI method for analysis of granular flows is PTV due to its ability to track the path of a particle and to give particle rotational displacements. PTV is also better suited to steep velocity gradients than PIV (Jesuthasan et al., 2006). However, PTV requires small seeding density or distinct seeds in order to be able to track individual particles from frame to frame. This low density results in information being located in more random locations and greater potential errors. By not requiring distinct seeds PIV has an advantage over PTV by being able to track highly concentrated particles that move in intermittent contact.

2.4.4. Non-intrusive Summary

Non-intrusive methods of measuring flow parameters tend to combine a physical imaging technique with a computer analysis package. RIM and LIF are particularly effective non-

intrusive ways of illuminating the fluid and solids within a granular flow. Quantitative methods like PIV can use the output of the RIM and LIF techniques to identify displacements and velocities within a flow to a small temporal and spatial resolution. Of the examples of the combined techniques summarised in this section, Sanvitale's (2010) method is the least complex and least expensive application suited to stony debris analysis.

2.5.Chapter Summary

The purpose of this chapter has been to investigate four areas of literature and knowledge in order to form the context for this thesis. The first section was on defining what a debris flow is and the phenomena particular to debris flows. This was done in order to show the unique nature of these flows both spatially and temporally, how potentially dangerous they can be, and how complex they are to research.

The second section summarises some of the rheological theories that govern the micromechanical behaviour of debris flows. The main focus was on non-Newtonian fluids where a wide range of behaviours were outlined. Each of the rheologies used appear to hold for different types of debris flows and even locations within the flow. The main criteria for choosing between rheologies is was found to be the amount of solids compared to fluid and the fine content of the solid fraction.

The third section covers the general physical modelling approaches that have been conducted into debris flows, focusing on flume studies. This show there is a dominance of small flume testing with a great deal of research contributed from the large USGS flume. The literature shows the impact of various alterations in variables like PSD, moisture content, slope and boundary conditions found from flume testing.

The final section introduces the relatively innovative and non-intrusive physical modelling techniques. The two focuses of this section are the physical imaging and the computational analysis that can be conducted from the imaging techniques. LIF, a form of RIM fluorescent illumination, was evaluated for a couple of studies with some limitations and advantages. The quantitative method targeted was PIV which showed the ability to deal with texture over individual seed particle techniques like PTV. PIV was seen to have an advantage in stony debris flow imaging where the well graded nature and fines reduces the image quality.

Chapter 3. Methodology

This chapter describes the laboratory experiments designed to investigate the behaviour of laboratory debris flows for various moisture contents and change in slope. The chapter then looks at the PIV analysis procedure introduced in section 2.4.3.1.

Section 3.1 outlines the more specific research objectives of the thesis. Section 3.2 describes the context of the approach taken in order to give an overview. Section 3.3 then describes the major apparatus used in order to show what variables could be adjusted and the constraints on materials. Section 3.4 outlines the independent and dependent variables chosen for investigation in this thesis.

The next section, Section 3.6 shows the visualisation apparatus used for PLIF and exterior recording. This requires a particular type of substitute debris flow material described in section 3.4. Section 3.7 outlines the physical test procedure and Sections 3.8 and 3.9 discuss the issues of data collection and the challenges in the physical methodology.

The rest of this chapter looks at the analytical methodology using PIV. Section 3.10 describes how time and height variables were matched to ensure flow phenomena were comparable. Section 3.10 also outlines the data refinement process and the analysis procedure used to produce velocity profiles. Section 3.11 outlines the parameters that controlled the PIV outputs. The individual parts of this section look at the factors that impact PIV analysis including, the image quality, the patches size and patch spacing.

3.1. Research Objectives

Debris flows are hazardous, unique, and unpredictable by nature so, they need an innovative physical modelling technique in order to internally visualise their behaviour. High-speed video capture is now backed by powerful software programs that can offer quantitative data in addition to the qualitative information. The current laboratory based imaging methodology has been selected to compliment the developing field of PIV in this area.

Physical modelling has a number of advantages over field and numerical investigation. To find and investigate a natural debris flow as it flows is often an impractical, expensive and dangerous exercise, where the cost well exceeds the benefits. By nature, there is very little control over initiating, repeating or controlling a field event. Numerical methods currently

suffer from uncertainties around the driving mechanisms occurring internally and many models are empirically rather than analytically based.

3.2. Approach

The methodology is a continuation of the work of Sanvitale (Sanvitale, 2010; Sanvitale et al., 2010), conducted at the University of Canterbury. The same apparatus has been used but with modifications to adjust the slope and use of a high-speed camera with higher light-sensitivity to record the experimental flows. The key aspect of the laboratory methodology is the optical access to the interior of the flow which required matching of the refractive index between the fluid and transparent solid.

The imaging technique utilised in this thesis was planar laser-induced fluorescence (PLIF). In order to achieve PLIF, transparent materials were used to approximate opaque natural debris flow materials. The chosen methodology creates a non-intrusive way of viewing an otherwise highly opaque flow, via an interior plane.

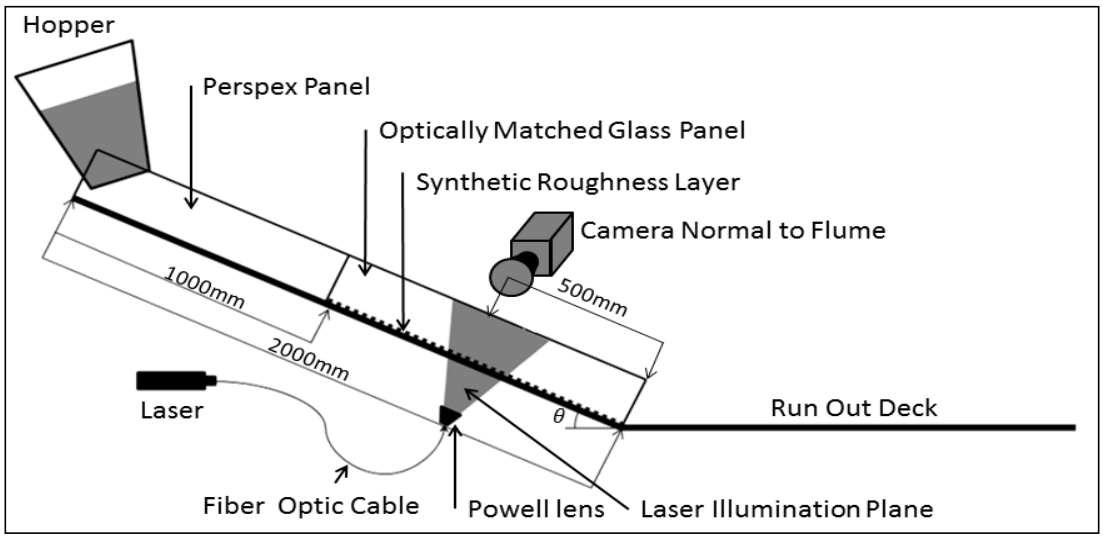

Figure 3-1: Schematic of the flume and PLIF setup used to record debris flows.

Figure 3-1 shows the schematic of the physical apparatus, illumination apparatus and recording equipment used. Following Sanvitale (2010), this method was newly applied to the field of granular flows and allows images of the interior flow to be taken by high speed camera. A more traditional exterior imaging recording method was also applied for comparing the exterior boundary conditions with the interior results. Post-processing of the images was then done using PIV methods.

3.3.Flume Apparatus

The main apparatus was a curved debris flow flume (Figure 3-2) with Duran (borosilicate glass) window panels made of the same optically matched glass used to represent the solid phase of the debris flow material in the experiments. The windows were located in the last section of the flume where recording was conducted. This was approximately 1500 mm downslope from the hopper. The borosilicate window for recording is shown in Figure 3-3 where the flume connects to the run-out deck.

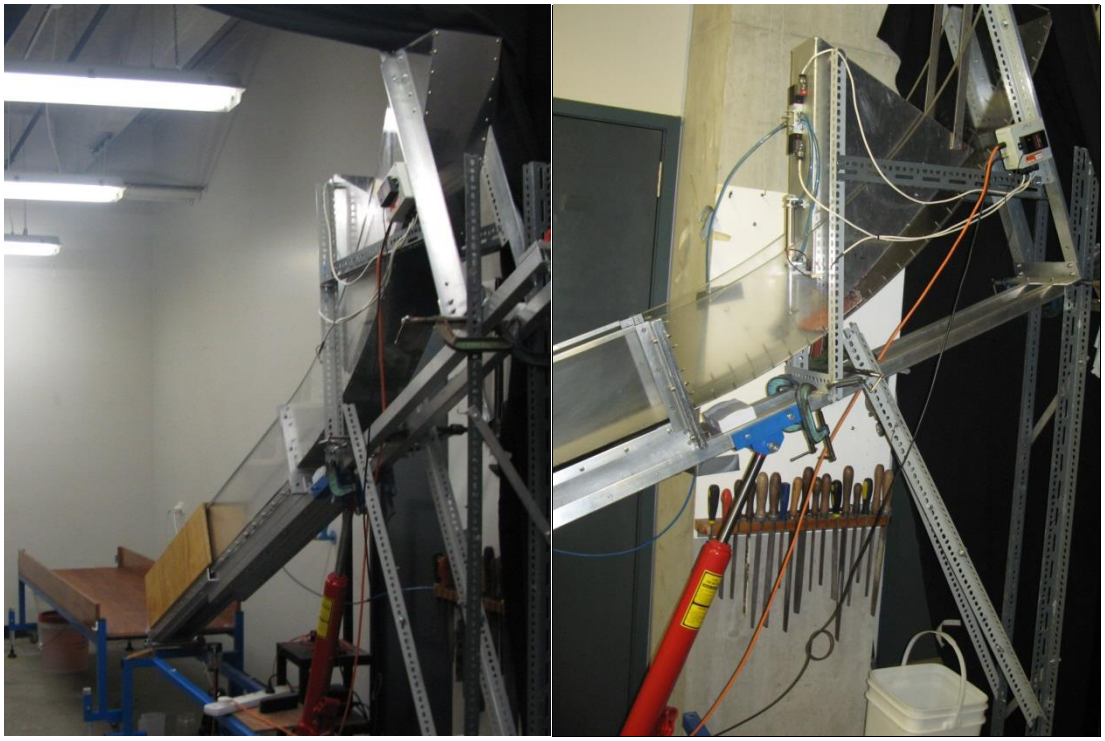

Figure 3-2: Flume experimental setup and close up of hopper showing red hydraulic jack.

Figure 3-3: Run-out deck with 50 mm grid inscribed on wooden deck.

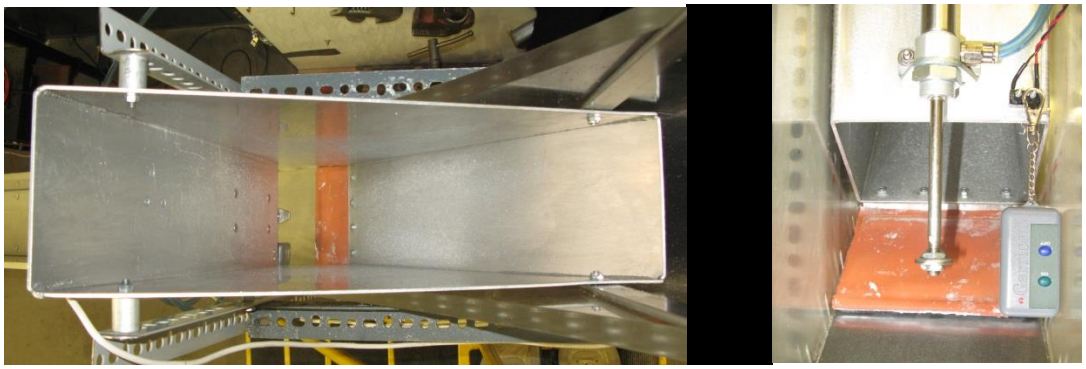

Figure 3-4: Hopper seen from above and the hinged gate and pneumatic piston with remote.

The experimental debris flow material was loaded and released from the trapezoid aluminium hopper seen in Figure 3-2 and Figure 3-4. The hopper angle could be adjusted so material was released at different rates and exit velocities. The hopper could also be adjusted so the material hit the flume vertically and was guided by a curved section. The gate shown in Figure 3-4 was hinged to open down onto the flume and the orange rubber created a seal to keep fluid in. The gate was pneumatically triggered and was linked by a micro switch to a camera, also shown in Figure 3-4.

The chute was curved to guide the material released from the hopper down the straight section of the chute and was 150 mm wide and 2000 mm long. The chute slope was able to be adjusted between 16°- 40° to the horizontal using the hydraulic jack shown in Figure 3-2. The jack released pressure over time due to the weight of the flume and the material. To prevent this at each slope a metal brace, also shown in the figure, was erected to support the flume and prevent motion.

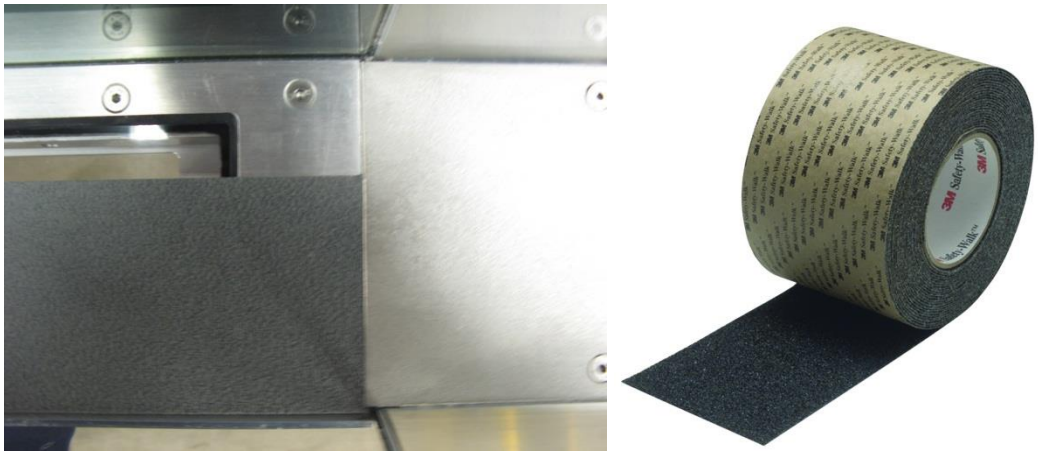

Figure 3-5: (Left) Roughness layer applied to base of flume. The glass window in the base can be seen partially covered by the 3M safety walk. To the right in the image is the steel base of the upper flume section. (Right) 3M Safety Walk.

The base of the chute was mainly steel with a borosilicate glass window over the last 1 m to allow the laser sheet to shine through from below. A sheet of rough rubber (3M Safety Walk 370) covered the entire based of the flume. This was limited to the last 1 m of the flume (as seen in Figure 3-5) and provided roughness that increased shear of the base of the flow. A narrow slit for the laser light was added for PLIF experiments. The chute emptied out on a horizontal wooden deck which was 700 mm wide and 2400 mm long, and was marked with a 50 mm square grid for outflow comparison. The flume run-out deck is shown in Figure 3-3.

3.4.Material Properties

The debris flow substitute materials required for PLIF were chosen based on their suitability to mimic the natural material (Sanvitale & Bowman, 2012), optical compatibility, ability to be safely handled and expense. The optical compatibility was judged, with regard to refractive index. The two materials chosen and tested were borosilicate glass (Schott Duran®) and a hydrocarbon oil (Cargille Immersion Liquid code 5095). Table 3-1 below shows the properties of a typical granular debris flow model material and the matched substitute materials used in experiments.

Table 3-1: Material Properties

Material Properties	Solid		Fluid	
	Debris	Duran Glass	Water	Immersion oil
Density at 25°C (g/cm^3)	2.65	2.23	1.00	0.846
Refractive index at ~21 °C λ = 589.3 nm		1.4718	1.3333	1.4718
Kinematic viscosity at 25 °C (cSt)			1.0	16

3.4.1. Scaling for Kinematic Viscosity

The increase in kinematic viscosity for the substitute fluid, compared with water, was accounted for in terms of settlement and drainage behaviour using Stokes' law for drag forces and the Kozeny-Carman equations for permeability behaviour. This was done by increasing the particle size of the natural material by a factor of four. In addition, the largest particle sizes were removed, as after scaling they were deemed to cause too greater risk of clogging.

The viscosity and density of the oil were different to that of water; therefore, the corresponding drag forces acting on the particles were different. Given that the glass had a density comparable with sand, a simple use of Stokes law showed the relationship between viscosity and particle size as;

$$\nu = \frac{F_d}{3\pi u \delta} \quad \therefore \quad \nu \propto \frac{1}{\delta} \tag{3-1}$$

where ν is the kinematic viscosity, F_d is drag force, u is the fall velocity and δ is the particle diameter. This showed that when changing fluid properties the diameter of the particles was inversely proportional to viscosity and needed to change in order to give the same settling velocity.

Scale analysis of the oil and glass showed that the ratio of viscosities was able to be used to determine a relationship for the length scales.

$$\frac{\nu_{oil}}{\nu_{water}} = \frac{\frac{l_{oil}^2}{t}}{\frac{l_{water}^2}{t}} = \frac{l_{oil}^2}{l_{water}^2} = \left(\frac{l_{oil}}{l_{water}}\right)^2 \tag{3-2}$$

where ν_{oil} is the viscosity of the oil, ν_{water} is the viscosity of water, l_{oil} is the modified length scale in oil and l_{water} is the length scale of natural particles in water,

Substituting values from Table 3-1 into (3-2);

$$\left(\frac{l_{oil}}{l_{water}}\right) \cong \sqrt{\frac{16 \times 10^{-6}}{1 \times 10^{-6}}} \cong 4 \tag{3-3}$$

Shows that that, in order to get comparative settling behaviour, the particles needed to be scaled up by a factor of four (Sanvitale et al., 2010) from the typical particle size in a representative debris flow deposit.

The permeability was also tested to ensure that the drainage through material was consistent. Permeability is a function of pore network and so PSD or particle diameter. In order to scale the particle size within a material Sanvitale (2010) used the Kozeny-Carman equation;

$$\mathrm{k} = \left(\frac{\gamma}{\mu}\right).\left(\frac{1}{C_{k-c}}\right).\left(\frac{1}{S_0^2}\right).\left[\frac{e^3}{1+e}\right] \tag{3-4}$$

where k is the permeability, γ is unit weight of permeant, $C_{k\text{-}c}$ is Kozeny-Carman empirical coefficient, S_0 specific surface area per unit volume of particles (cm^{-1}) and e is the void ratio. The Kozeny-Carman equation takes into account the shape and tortuosity of the pores and describes the behaviour of a cohesion less material (Barr, 2001).

The specific surface term was rewritten as;

$$S_0 = \left(\frac{SF}{\delta_{eff}}\right) \quad (3\text{-}5)$$

To include the effective particle diameter, δ_{eff} and shape factor, SF. This allowed a length scale to be incorporated into the Kozeny-Carman equation. Sanvitale (2010) verified that by up scaling by a factor of four the permeability was consistent. Verification was conducted in a constant head permeameter and showed laminar flow observations consistent with the natural material.

Another factor limiting the particle size distribution was a maximum restraint on the particle size due to the width of the flume. The restraint was caused by large particles combining to jam the flume. The maximum size was approximately 1/6th of the flume width, or 25 mm or 6.25 mm in natural scale. The hopper constructed to store the material was less than this so occasionally had some issues with jamming, especially at low slopes.

3.4.2. Solid Phase

The transparent material was required to represent a large variety of particle sizes based on a realistic natural shape. The particle size distribution used was taken from previous work by Sanvitale (2010) and reflected a natural debris flow event modified to take into account differences in viscosity and limitations of the flume dimensions.

3.4.2.1. Manufacture of Material

The same material was reused for each experiment. However, a small amount of fines were lost during the experimentation and cleaning procedures. The losses were approximately 50 g of 125 µm diameter particles and 20 g of other fine particles (less than 1 mm). This is consistent with previous experiments by Sanvitale. There were additional mass losses to larger particles due to collisions during experimentation. Repetitive use caused flat shards of glass to flake off the larger particles reducing their mass. These shards were removed as they were thin and elongated and therefore different from the initial material of a similar size.

In order to manufacture material, Sanvitale's (2010) method of manufacture was used. Tubes and rods of borosilicate (Figure 3-7) glass were crushed and chipped into various shapes and sizes, seen in Figure 3-6. The larger particle sizes were manufactured by hand from solid rods

of 4 mm-30 mm diameter. A press was used to cut the rods into roughly proportioned length-to-width cylindrical sections, the particles then had the edges chipped off by hand using a hammer. This process can be seen in Figure 3-8. This resulted in sub-rounded to sub-angular particles. There was some bias to rolling along one axis due to some retained cylindrical nature, but this was minimal. Smaller particles tended to be more angular and were shaped from crushing hollow glass tubes of wall thickness 0.8 mm- 2.0 mm. The process for this can be seen in Figure 3-8. Effort was made to remove, by visual inspection, the most elongated fine particles.

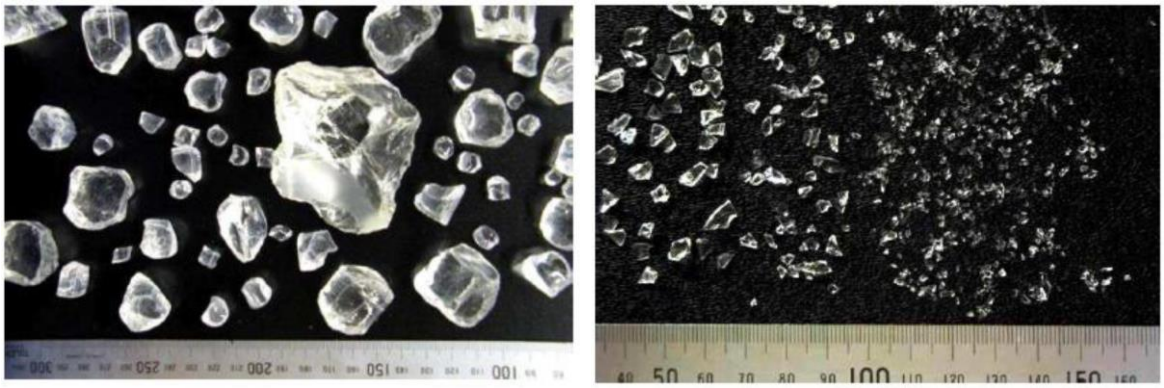

Figure 3-6: Particles used as transparent solid (Sanvitale et al., 2010).

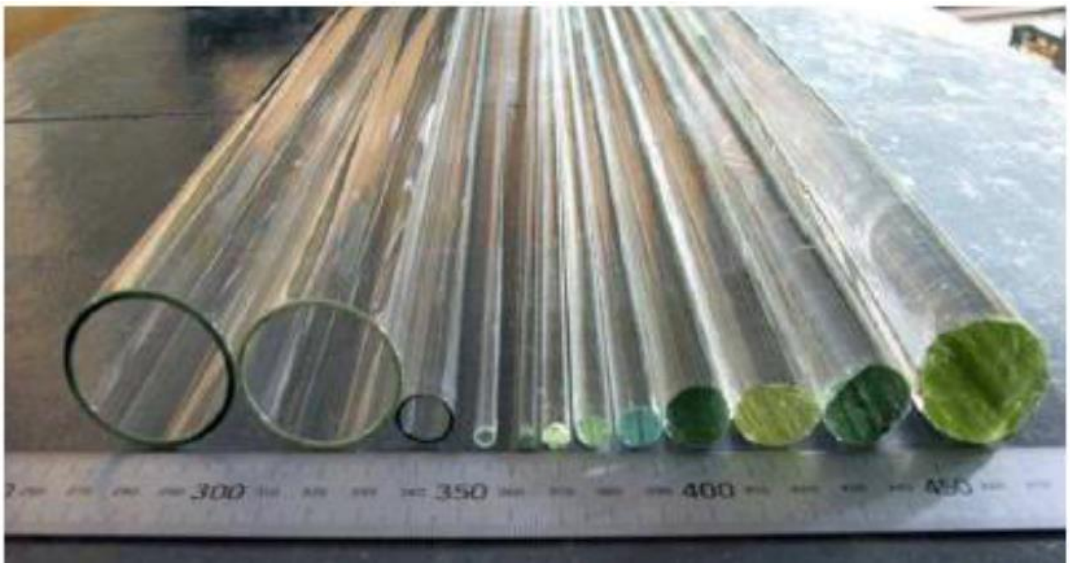

Figure 3-7: Stock of rods and tubes used for manufacturing material (Hunter 2012).

Figure 3-8: Large particle manufacturing. (Left) Press used to cut roads. (Top) cut rods. (Centre) hammer shaping of cut rods. (Bottom) shaped particles ready for use.

Figure 3-9: Small particle manufacturing. (Left) steel blocks used for crushing. (Centre) rods being placed in blocks. (Right top) glass resulting from 2-3 attempts to crush (Right bottom) final crushed particles ready for use.

3.4.2.2. Particle Size Distribution

An original PSD was selected from a variety of PSD's that Sanvitale (2010) created artificially. The PSDs were modified based on guidelines for natural granular debris flows PSD's, observed by Takahashi (1991). These PSDs were generally characterised as having a limited fraction of fine material. The PSD selected from Sanvitales (2010) experiments was PSD 9 (depicted in Figure 2-32). This was the PSD most used in small-scale experiments carried out by Sanvitale and was the one with the highest coefficient of uniformity. This PSD

needed to be modified to take into account scaling for viscosity and issues with jamming of large particles (see section 3.4.1). Table 3.2 shows the particle size characteristics of the debris flow modelled after scaling and truncation of coarsest fraction. The particle size distribution can be characterised as well graded and the PSD of the original and modified material is shown in Figure 3-10.

Table 3-2: Particle size distribution (PSD)

Particle Size Distribution	C_U	C_Z	D_{90} (mm)	D_{50} (mm)	D_{10} (mm)
Original Natural Material	21.0	1.1	11.9	1.76	0.135
Modified Substitute PSD	20.2	1.1	35.5	7.1	0.54

C_U, coefficient of uniformity; C_Z, coefficient of curvature; D_n, particle size at which n% of particles pass

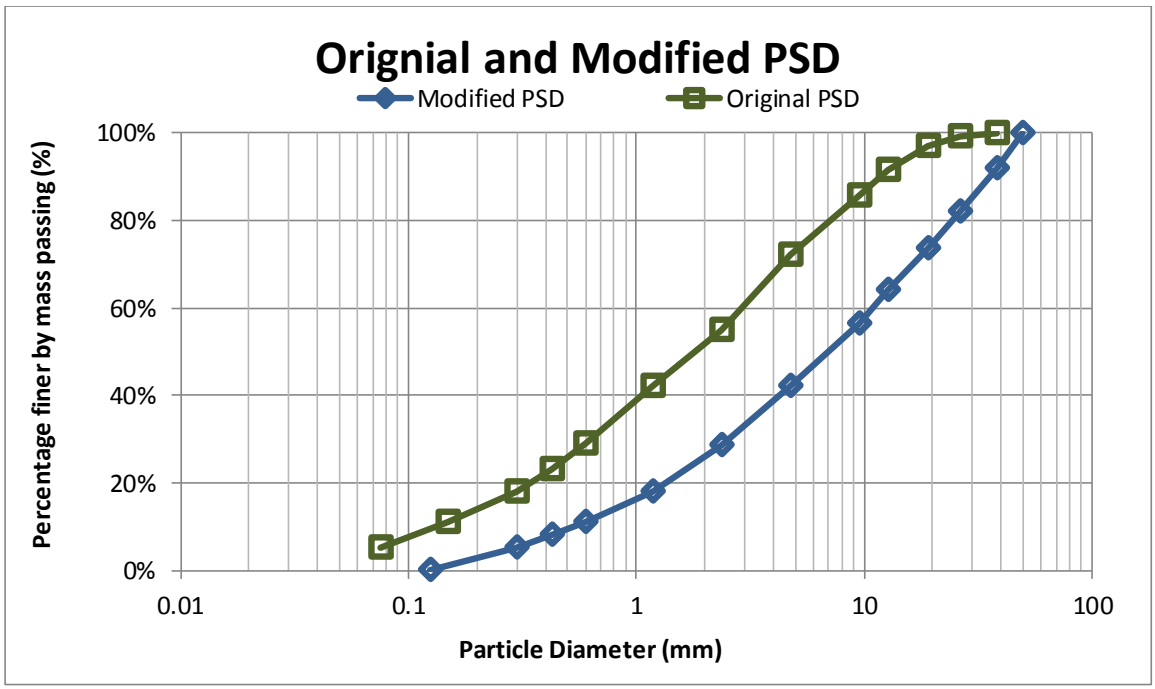

Figure 3-10: Particle size distribution of the original natural material and modified glass material (semi log plot).

3.4.3. Fluid Phase

The transparent fluid was required to optically match the solid particles requiring a refractive index the same as the solid particles within operating temperature range. The fluid must also contain a florescent dye which under laser light emission fluoresced to illuminate only the fluid fraction.

3.4.3.1. Theoretical RIM Errors

Patil and Liburdy (2012) investigated the errors associated with fluorescent particles in a refractive matched fluid. They described spherical particles acting as randomly distributed spherical lenses whose lens power depends on the level of mismatch in refractive indices. Patil and Liburdy (2012) focused on four types of errors: (1) particle position (Figure 3-11) (2) particle image degradation (3) attenuation of image light and (4) loss of particle image density.

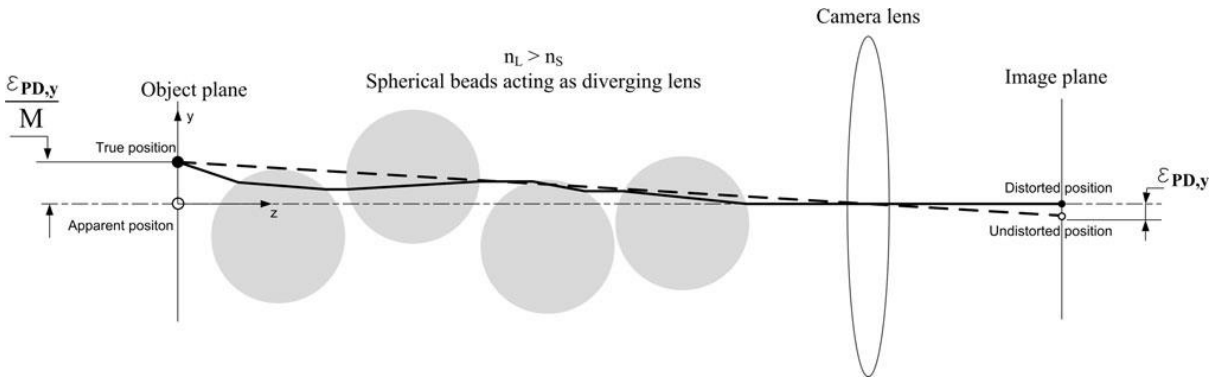

Figure 3-11: Illustration of light ray path through a randomly packed porous bed; the imaged position error, ePD, y, is shown on the right and the equivalent error on the object plane on the left. In ray tracing the beads were given random x, y positions over a range of ±DB/2 for each trace (Patil & Liburdy, 2012).

The position of the plane within the flow was dependent on the number of beads and bead size, and was acceptable to within a difference of index of approximately 0.002. The general model for particle degradation indicated that the difference in refractive indices is directly proportional to the error and that it was dependent on

$$\varepsilon_{PD} = |n_L - n_s|(1-c)L_{optical}\left(303(1-\varphi)\frac{L}{D_B} + 1,417\right)\left(\frac{M}{d_r}\right) \qquad (3\text{-}6)$$

where c was the solid concentration, $L_{optical}$ was optical axis length, D_B was bead diameter, M was image magnification and d_r was the camera pixel size.

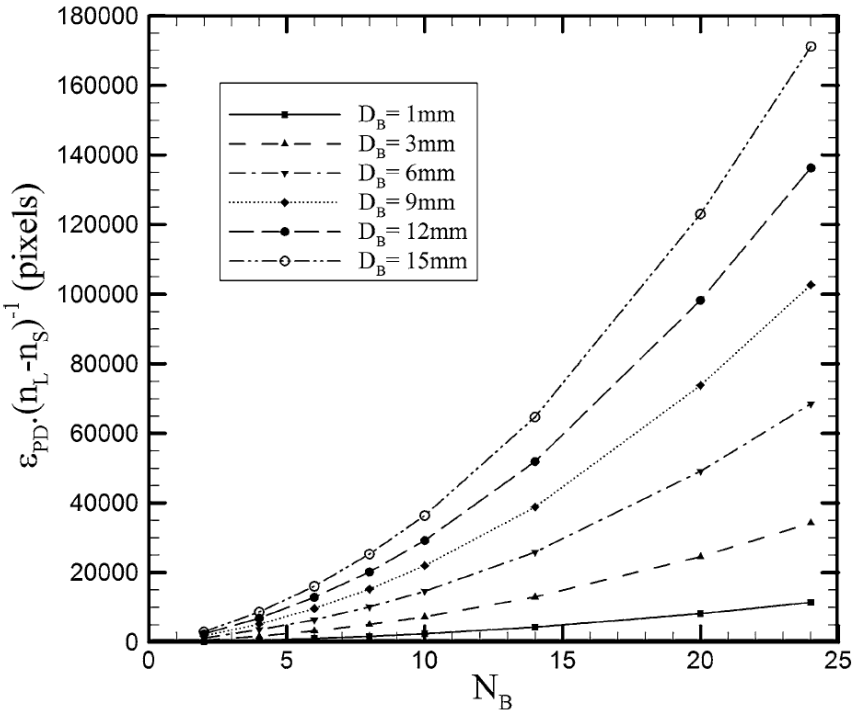

Figure 3-12: distortion in apparent location due to index mismatch versus number of beads, for a range of bead diameters (Patil & Liburdy, 2012).

The reduction in the imaged light flux is due to reflection losses at the solid/liquid interfaces and the defocusing effect introduced by the beads when the refractive indices are not matched in the porous bed. Larger beads gave larger errors which were exaggerated when increasing the number of beads (Figure 3-12). In general Patil & Liburdy (2012) showed a loss of 20% light for a mismatch of 0.001

Loss of particle density is relevant to systems where the fluid is illuminated as the non-illuminated particles become the seeds for PIV tracking and affects correlation strength in PIV data. If there is not enough texture due to seeds blurring into other parts of the image then correlation becomes more difficult. Particle seeding density was seen to have a rapid drop off with indices mismatch beyond 0.002.

The combination of all errors was inputted into PIV to determine a velocity measurement error values below 0.0016 were acceptable and values over 0.0036 were not, using 6 mm diameter spheres, a porosity of 0.47 and 20 mm LOV (Figure 3-13). Also there was a distortion in the laser plane at 0.0006 due to the particle interfaces. This may affect the position and parts of the particles illuminated as they no longer pass through a perfect two dimensional plane.

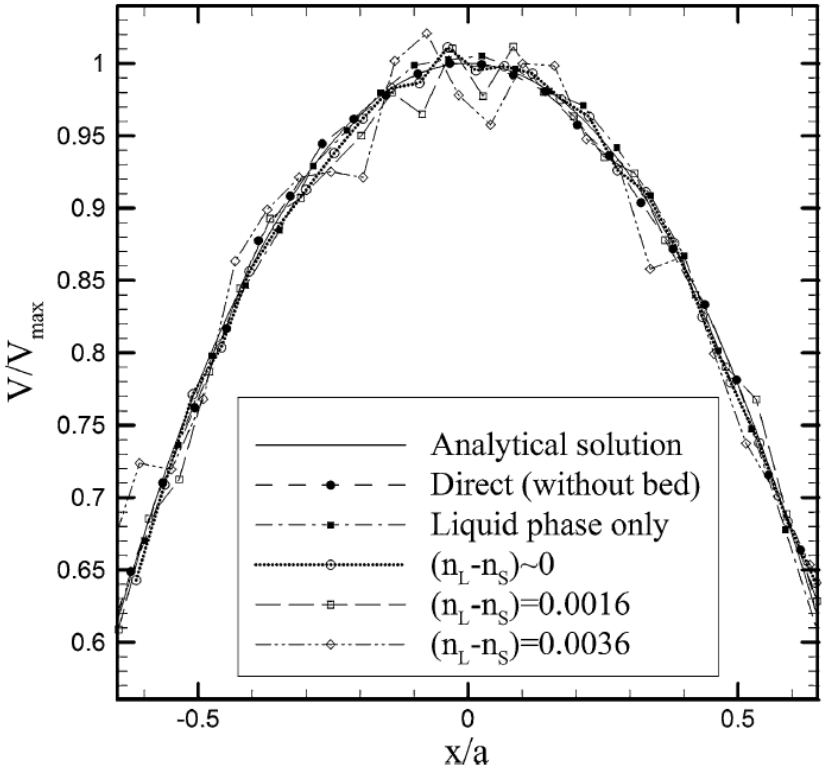

Figure 3-13: PIV measurements in a square channel seen through a transparent medium showing the effect of index mismatch. (Patil & Liburdy, 2012).

From the combination of data a guide for RIM states a minimum difference of 0.001 to give relatively unaffected images. This is, however, conditional on primarily the number of particle interfaces, but, also camera setup and level of impurities in the material (like air bubbles). The number of particle interfaces is generally a combination of the LOV of the plane under investigation and the particle size.

3.4.3.2. Laboratory RIM

From Table 3-1 the RIM for the solid and fluid are theoretically matched. But in a laboratory setting there are some factors that may influence the RIM. Therefore both the dye concentration and temperature of the oil were tested to see if they had a substantial effect on the refractive index and to find an optimum temperature for operation. An optimum temperature was defined as the point when the refractive index was the same for both the glass and oil.

It was decided to investigate the effect of temperature and dye concentration on refractive index, in order to ensure the refractive index of the oil was approximately that of the glass, at operating temperature. This was done with various samples of dye concentrations at different

temperatures to give a relationship that was then used to predict the refractive index, at a set temperature or concentration.

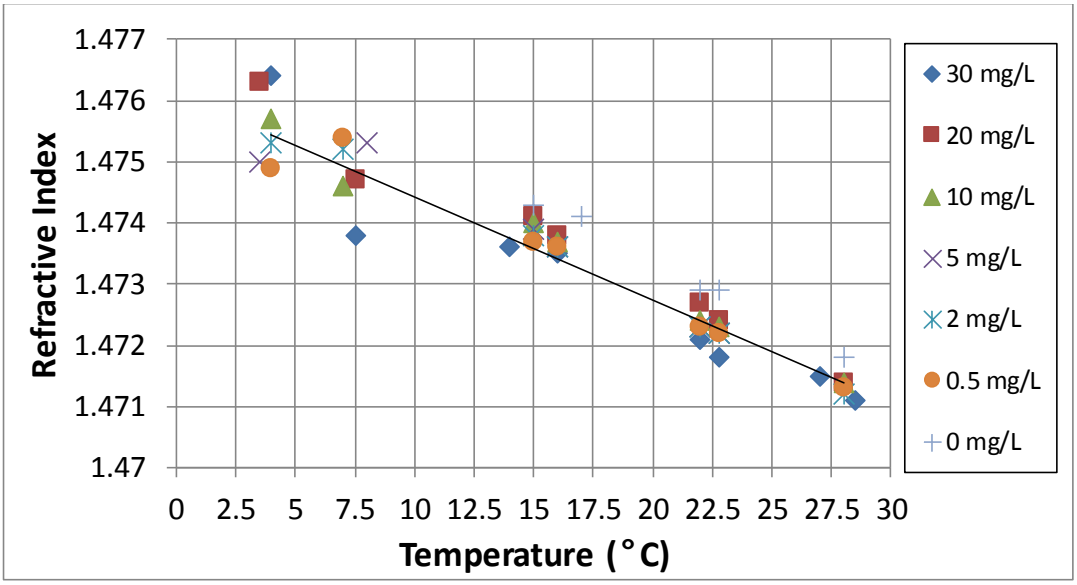

Figure 3-14: Graph of temperature effect on refractive index for various concentrations of dye.

It was found that in general the concentration of dye had a minimal effect on refractive index as demonstrated by the relatively small vertical spread in Figure 3-14. Figure 3-14 also shows that the refractive index was sensitive to temperature. A linear trend line was fitted to the values for a concentration of 0.25 mg/L to give

$$T = \frac{R_i + 1.4761}{-0.0002} \qquad (3\text{-}7)$$

where T is temperature in ˚C and R_i is the refractive index. Equation (3-7) has a R^2 (coefficient of regression) value of 0.944 indicating a good fit to the data. Given that the materials could be stored in a temperature controlled room at 21 °C, the refractive index was checked at this temperature. Using Equation (3-7) and the value of the refractive index of the glass at 21°C (Table 3-1) it was found that the difference in refractive indices of the oil and glass was within

$$\Delta R_i = -0.0002T + 1.4761 - 1.4718 \qquad (3\text{-}8)$$

$$-0.0002x21 + 1.4761 - 1.4718 = 0.0001 \qquad (3\text{-}9)$$

where ΔR_i is the difference in refractive index.

From section 3.4.3.1 it was deemed that a difference of 0.0001 was adequate to ensure transparency. Therefore it was deemed that if both glass and oil containing 0.25 mg/L dye was stored at 21 °C then the RIM was sufficient for testing.

3.4.3.3. Dye

The dye used was called Nile Red (Sigma-Aldrich) and had a suitable absorption and emission rate for the given laser wavelength. Sanvitale (2010) conducted research into the absorption and emission wavelengths of the dye in solution with the hydrocarbon oil. The dye used was selected for three reasons; in its non-aqueous state it is highly fluorescent, the dye is neutrally hydrophobic and can mix with both polar and non-polar fluids (this is important as the hydrocarbon oil is a polar solvent) and, once the dye was dissolved in a polar fluid it experienced a red shift in its emission spectrum. This meant that under excitation from the laser the wavelength of the emitted light increased in a polar fluid.

Figure 3-15 shows that the laser operates within the overlap between the absorption and emission spectra. The much brighter excitation light provided from the laser needs to be filtered out otherwise it overwhelms the weaker emitted fluorescence light and significantly diminishes specimen contrast. In order to ensure RIM of the solid and fluid the wavelength must be within the shaded region. The wavelength chosen for the laser is near the optimum RIM wavelength. A higher wavelength would mean less absorption and more of the emission spectra to be filtered out. A lower wavelength would reduce the RIM.

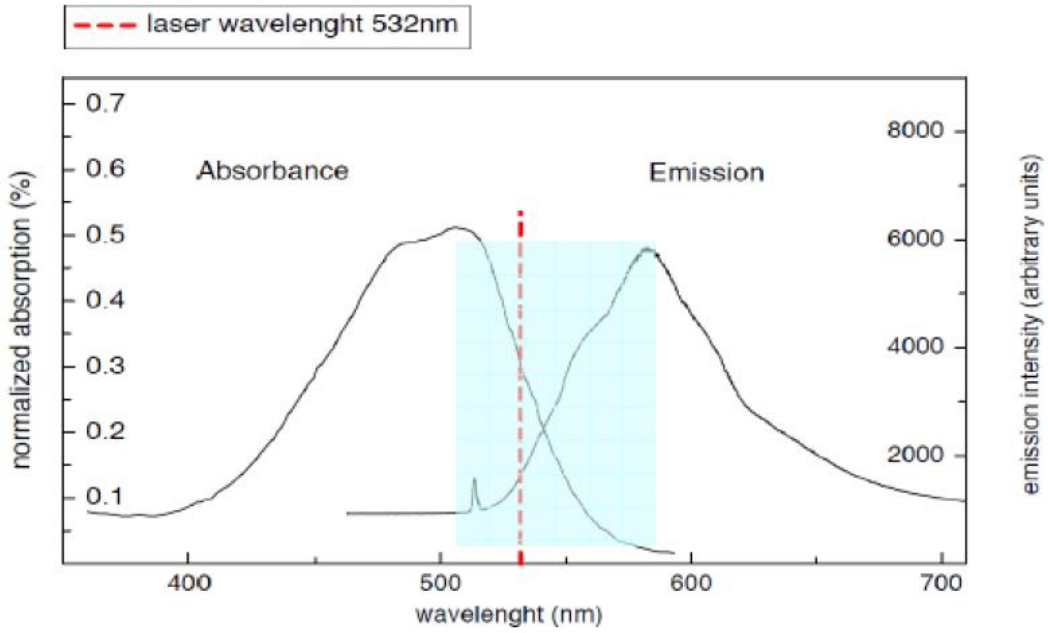

Figure 3-15: Absorption and emission spectra of Nile Red in a polar fluid. (Sanvitale 2010).

3.5.Variables

3.5.1. Independent Variables

There were a number of variables that could be adjusted within a laboratory experiment. The shape and dimensions of the flume were a basic representation of a straight, narrow, channel with a uniform slope. The material itself could have a number of different characteristics in terms of density, angularity, particle size distribution, uniformity and the maximum and minimum particle sizes. The fluid content could also vary dramatically depending on the type of debris flow.

In the case of this thesis it was necessary to substitute water, the natural fluid in debris flows, for another transparent fluid in order to match the refractive indices of the fluid and debris material. The substituted fluid was chosen based on its refractive index, resulting in a different viscosity and density to water. In addition to the effect of changing physical variables, it was of interest to see the difference in methods of filming. The two filming methods chosen, gave visualisation planes in different depths from the window. This was referred to as the location of view (LOV). The other independent variables chosen for this thesis were moisture content and slope.

3.5.1.1. Location of View

The LOV notates the position of the visualisation plane from the inside wall of the flume. It was an important factor in order to determine the effect on dependent variables of the boundary conditions imposed by the flume wall. The LOV was limited to two separate locations defined as the exterior (EX) and the interior (IN). Exterior visualisation was the boundary of the flume and was directly against the window. The exterior used a traditional method of filming, via a normally illuminated camera directed at the transparent window on the outside of the flume. Interior visualisation used PLIF to give a visualisation plane within the flow. The interior methodology could have given various slices into the flow, but the LOV chosen was 45 mm inside the flume. This was the distance constrained by a support beam between the flume wall and the window in the base of the flume that allowed laser light into the flume. This LOV represented a position deep enough within the flow to have a difference in observed behaviour, but close enough to the flume wall that there was no reduction in image quality.

3.5.1.2. Moisture Content

Moisture content was one of the factors that determined where on the continuum the flow located between fluid or solid-dominated flows. As debris flows sit at the turning point between solid and fluid flows, variations in the moisture content may capture changes in micro-behaviour as the flow moves toward a different regime. Four different moisture contents were selected at a constant interval of 4% starting at 23.8%. The notation for these variables is the percentage value rounded to zero decimal places: 24%, 28%, 32% and 36%.

3.5.1.3. Slope

As the slope increases the contribution from gravity creates a larger imbalance so larger acceleration results as slope increases. Two inclinations were chosen 24.5° (to replicate Sanvitales work) and 18.1° to simulate a slower flow. The slope was measured from the angle of inclination of the flume to the horizontal run-out bed.

3.5.2. Dependent Variables

The directly measured dependent variables were those used mainly to determine repeatability and conformation of expected debris flow behaviour. These were:

- Time for initial material to pass the camera
- Maximum run-out length
- Deposit edge shape
- Particle size distribution (PSD) of various locations relating to deposit
- Height of flow as it passes the camera (Eulerian approach).

The remaining dependent variables were obtained using PIV analysis:

- Average, maximum and minimum slope parallel flow velocity at a location over time
- Velocity with depth profiles at a location over time

3.5.3. Output Data

The raw data obtained from the experiments, in order to measure the dependent variables and provide the context for behaviour was:

- Photographs of any unusual deposit or ‘tide’ marks on the edge of the flume

- Run-out images used to determine the shape of deposit, showing how run-out was affected by changes in experimental variables
- Individual heights of the deposit at the intersections of a 50 mm grid, for use in showing the depth of the deposit and the location of any large particles
- PSDs of various locations within the deposit
- Large series of images at 1000-2000 frames per second. These images were adjusted to be used in PIV analysis.

3.6.Visualisation Technique

3.6.1. Interior Visualisation Plane

The PLIF technique (defined in section 2.4.2) required a transparent fluid that fluoresced, a laser light delivery system to a position within the flow and a high speed camera to capture images of illuminated fluid and dark solid particles. Each of the PLIF experiments needed to consist of transparent glass with refractivity matched immersion oil (see principles of RIM in section 2.4). The resulting mixture had the same refractive index, thus making the particles indistinguishable from the fluid. A dye was added to the fluid which was excited by a set wavelength of light emitted by a laser sheet. The fluorescence caused by the dye illuminated the fluid section of the sample and left the glass particles dark. The light produced from the fluorescing dye in the visualisation plane was able to be transmitted to the outer edge of the flume without picking up any material between it and the edge. A high-speed camera captured the light from the fluorescing fluid and a laser light filter was applied so only the light emitted by the fluid was captured by the high speed camera. The camera and laser set up is explained further in this section.

3.6.1.1. Laser and Optics Setup

The light source was an 800 mW solid state green laser. The laser had a wavelength of 532 nm and was coupled and focused into a multi-fibre optic cable transferring the laser light to a 30° Powell lens. A Powell lens is a lens that splits a beam into a sheet and was selected as it gave the most uniform intensity along the entire laser plane. The laser sheet was then directed through a slit in the rough surface of the channel bed to give an illumination plane approximately 2 mm thick (normal to the flow direction) and 100 mm wide (parallel to the

direction of flow) at the base of the flow. The laser was directed through the base of the flume because Sanvitale et al. (2010) found that orientation of the laser from the top played a large part in image clarity. By placing the laser sheet through the bottom rather than through the top free surface there was less refraction.

The laser light frequency was selected to ensure that it excited the Nile Red dye mixed into the fluid. Preliminary images showed that fine mixtures even in static conditions were much harder to identify than coarser distributions. This was solved by bringing the laser closer to flume wall. The laser sheet itself was, therefore, not located directly in the middle of the flow but 45 mm from the front wall as restricted by the base steel flume supports. This was common practice in the PLIF set up as it reduces the refraction of the image, leading to better quality images.

Figure 3-16: Example of illumination of static particles using PLIF. Images were taken in a sample box and were distorted at the base by silicon sealent.

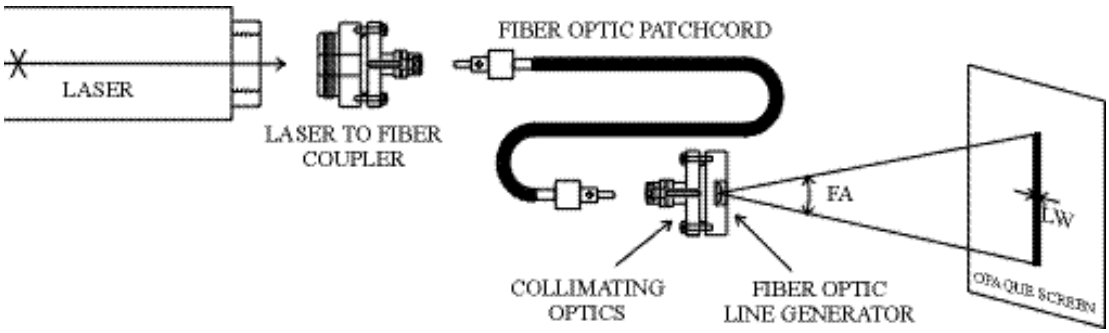

Figure 3-17: Laser fibre optic connection (Optics, 2005).

Figure 3-18: From left to right optic components used: Line generator, fibre cable, coupler and laser.

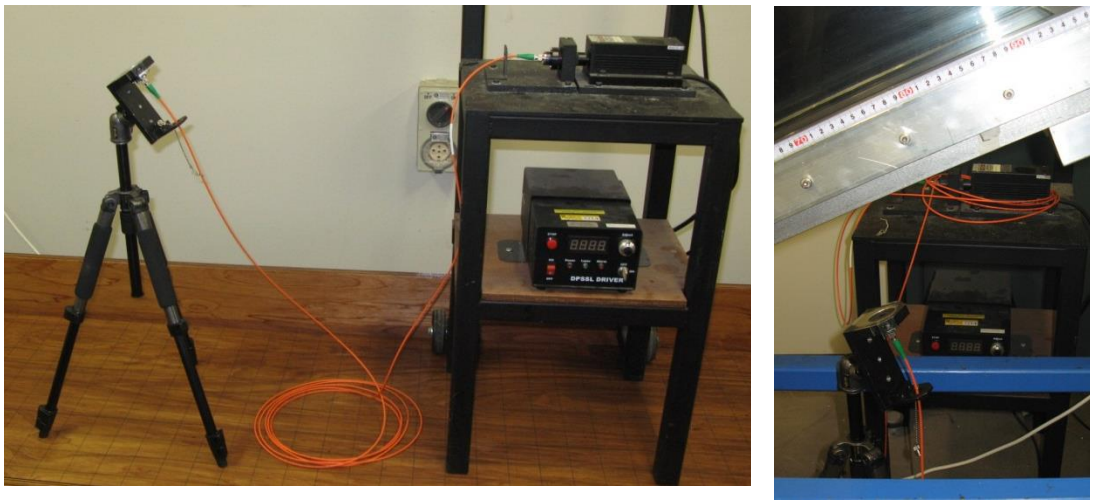

Figure 3-19: (Left) Laser and optics set up showing power box and mounts. (Right) Line generator setup located below the flume.

This optical system (Figure 3-17), was provided by Oz Optics Ltd and reduced the laser intensity by approximately 15-30% with the majority occurring when the laser beam was coupled to the fibre optic cable. The components, specifications and functions listed below and are shown in Figure 3-18 and Figure 3-19:

- **Laser** - light source for illumination of flow.
    - **Power:** 800 mW solid state
    - **Frequency:** 532 nm
    - **Model**: MGL-H-532 provided by Changchun New Industries
- **Laser to Fibre Coupler**,
    - **Model**: HPUC-23AF-532-M-13.9AS-11
- **Fibre optic cable**: multimode fibre for more light transfer
    - **Core size**: 25 µm – handles 10-20 Watts
    - **Length**: 3 m
    - **Model**: QMMJ-3AF3AF-UVVIS-25/125-3-3

- **Collimating Optics**: The output mount for the fibre optic cable and housing for Powell lens. A bracket was constructed so the re-collimator could be mounted on a tripod below the flow.
    - **Model**: FOLM-23AF-532-M4.5AS-60
- **Powell lens**: A Powell lens generated a vertical sheet of light that spread in a fan shape from the lens. The lens was mounted within the collimator.
    - **Thickness:** 2 mm
    - **Fan Angle**: 60°

3.6.2. Exterior Visualisation Plane

In order to fill the gaps in previous work by Sanvitale (2010), (that did not include a comparison of the material behaviour at the edge of the flow) a new method needed to be developed for recording the exterior experiments with the same physical setup and material. Due to the transparent nature of the flow material the only way to give texture to the material for PIV analysis was to oversaturate the material with light then rely on the discrepancy in refractive index at the various wavelengths of white light to produce texture between the solid and fluid phases at the flume window. Therefore, the laser was replaced with three high-powered spot lights placed around the camera aimed at the same section as the laser. The spotlights reflected enough light from the material to record an image directly against the flume side. This is demonstrated in Figure 3-20 during the calibration process.

Figure 3-20: Flood lights applied to exterior test camera calibration. Note, the high level of reflection off paper calibration target.

3.6.3. High Speed Camera Setup

The camera set up was relatively the same for both interior and exterior imaging (for exterior imaging there was no need to filter out laser light). Three high-speed digital cameras were used during experimentation to record images at a frame rate of between 600-2000 fps. Three cameras were used due to technical difficulties and had different light sensitivities. The following summarises the cameras used:

- SVSi Memview: Used for all preliminary test at 600fps
- Motion-Pro Used for most of the 18.1° slope experiments, at a frame rate of 1000-1200 fps and pixel size of 10 x 10 µm
- Miro M310: Selected for its performance in low light conditions. Used for all 24.5° slope experiments. The camera had 20 x 20 µm sided pixels for high light absorption. This gave the best illuminated and clearest images at twice the frame rate (2000 fps).

Figure 3-21: Miro camera with Ethernet cable, power adaptor and laptop used in experiments.

An orange 'long-pass filter' (Schott OG550) (seen in Figure 3-22) removed the laser light at a wavelength of 550 ± 6 nm, leaving only the fluorescent emitted light. In addition, the filter reduced the intensity of stray reflections of laser light which would have appeared as intense spots on the camera. Those reflections occurred most at and above the free surface but could occur internally, most likely as a result of air bubbles.

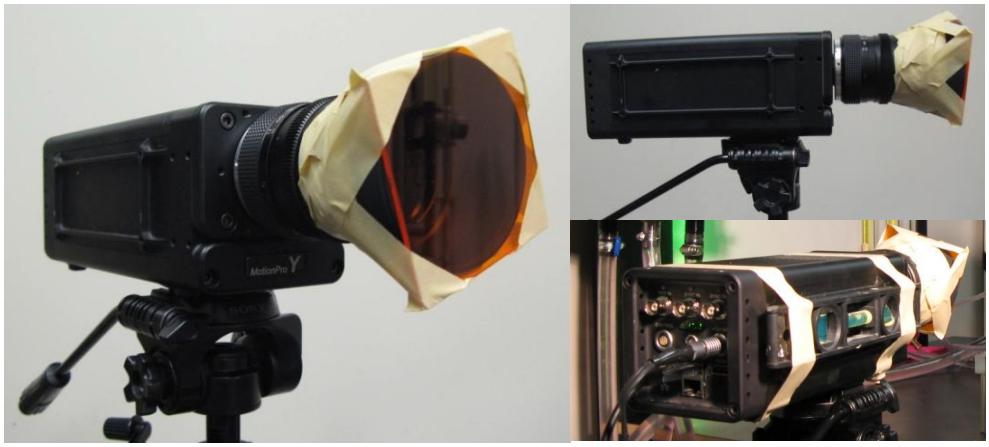

Figure 3-22: Motion-Pro Y4 camera with orange filter and spirit level for adjustment.

It must be noted that the camera aperture had to remain fully open for both the interior and exterior tests. This was to allow the maximum amount of light, narrowing the field of view and making it critical to focus properly to avoid blurring of images.

3.7.Test Procedure

3.7.1. Reuse of Material

Due to the time and effort taken to produce the material, it was important that a practical method of reusing it was available. The highly viscous, non-polar nature of the oil made it difficult to remove. It was necessary to remove the oil, particularly from the smallest particles, so that they could be sieved and the fines lost during an experiment, replaced. Appendix A outlines the time-consuming process required to prepare material after use for the next test.

3.7.2. Material Preparation

The solid dye was initially mixed with the immersion oil in a concentration of 50 mg/L. This stock solution was kept away from light as light degraded the florescent dye. The oil was then diluted to 0.25 mg/L dye concentration in the volume required for each experiment. This was added to the 12 kg of material used in each experiment. The materials were combined in buckets and left to soak overnight in a temperature-controlled room. Once the apparatus was set up including camera and illumination the sample mixture was agitated before and after being loaded into the hopper. It was mixed to minimise the amount of segregation and consolidation prior to the release of material down the slope.

3.7.3. Apparatus Setup

The following checks were made to ensure the flume was ready for a test:

- The glass window in the flume was clean and free of foreign particles
- Test trigger of pneumatic hopper door and camera were linked and operating correctly. This was done using rubber balls as a substituted for debris material
- Check the slope to ensure the jack had not released pressure. This was later replaced in later tests with a brace
- Angle of laser was the same as the slope and that reflection from flume aligned with Powel lens showing the laser plane was normal to the slope
- Check that camera was at level horizontally pointing toward the flume
- Check camera was tilted to the same angle as the flume bed, done by matched the lower edge of the image with the lower edge of flume
- Camera was pointed normally to the flume window and checked using a large set square
- Calibration and focus of camera. For PLIF experiments calibration required a sample of large particles and oil in the calibration box. The sample was used to check that the focus gave sharp particle edges.

3.7.4. Camera Setup and Calibration

The camera was connected to a laptop via an Ethernet cable during testing and ran the camera's own capture software. Figure 3-23 shows the Miro camera software interface during calibration. The resolution, frame rate (sample rate in figure) and post-trigger delay were set from here. The incoming light was maximised by setting the maximum exposure time. The longer the exposure time the more light was captured. However, maximum exposure time was an inverse function of the frame rate. This meant that the exposure was limited to one over the frame rate.

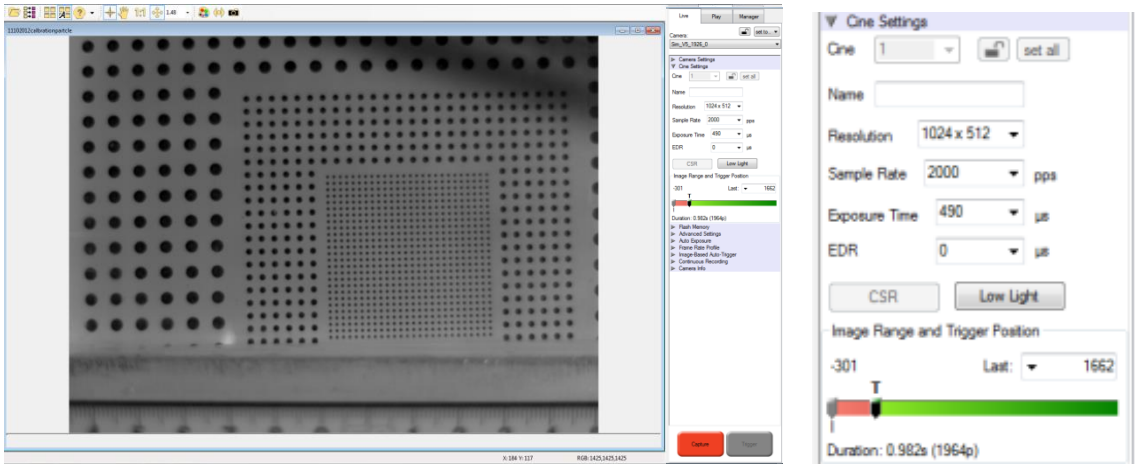

Figure 3-23: Screen print of calibration target, including enlarged camera settings

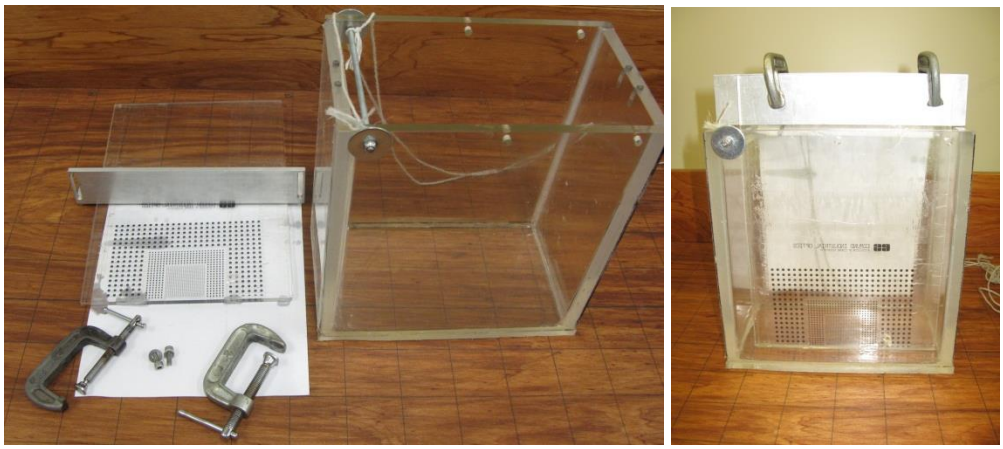

Figure 3-24: Calibration box and targets (Left) parts, clamps, screw, OHT target, Perspex board, Duran box and aluminium mounting bracket. (Right) assembled box.

A photogrammetric calibration target was used to form a reference and focus the camera. The calibration target is a series of spots spaced in a precise array that can be used to indicate scale and any distortion in scale sue to image capture. For PLIF calibration laser imaging a box made of the same Duran glass (see Figure 3-24) was filled with the oil in order to make sure that the target was under the same conditions as during the test. The target was printed on transparent film attached to a transparent plastic (Perspex) board. The board and target were adjusted so that the laser plane was just dimmed along the whole length of the target, as seen in Figure 3-25. This ensured the focus target was in the exact position of the laser plane. Failure to do this resulted in focusing on the wrong section and due to the very narrow field of view, unfocused images.

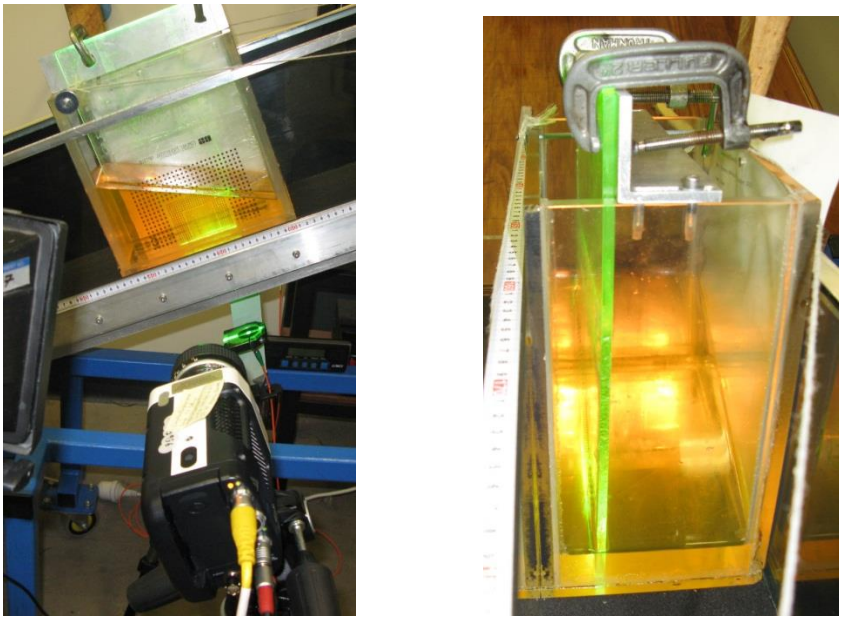

Figure 3-25: Calibration box with oil aligned along laser plane (Left) camera looking at target. (Right) target aligned along laser plane.

The camera was then focused on the target by ensuring that the smallest dots were clear and the entire target was sharp. In the case of the laser imaging, focus was checked by replacing the target with particles in oil. Setting up a stationary mock-up (Figure 3-26) particles in PLIF allowed a visual check to make sure the edges of the particles were in clear focus and enough light was being transmitted to the camera.

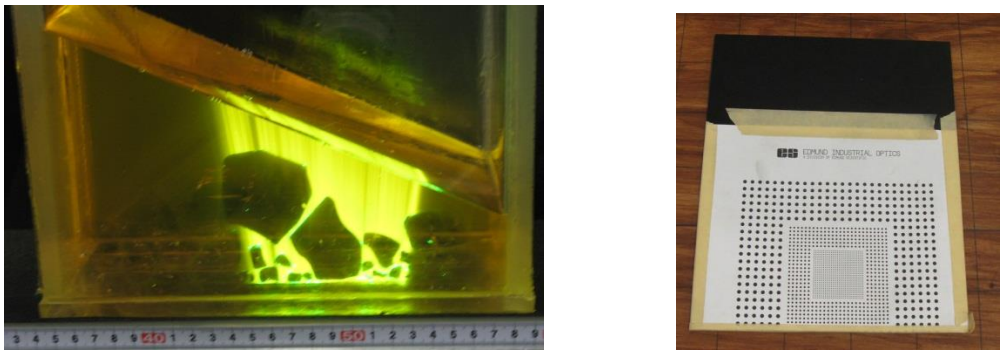

Figure 3-26: (Left) Calibration box set up with particle samples. (Right) Non-laser target.

For the non-laser imaging, the target was printed on paper and firmly pressed up to the inside of the flume (Figure 3-26). No additional lighting was required at this stage as the target was able to reflect enough ambient light even at the highest frame rate. Once the target was in focus, the additional lighting was directed to the middle of the target and it was removed. At this stage it was apparent that even the most superficial scratches to the glass window of the flume were reflected back to the camera. These were deemed a minor impact because when the fluid moved past the section it would fill the majority of the marks and return the window to a more refractively matched state.

3.7.4.1. Laser Setup and Stability

The laser had to be warmed up in stages in order to prevent damage to the equipment. Very small increments were avoided as this tended to increase instability. The laser warm-up procedure was to increase the power box readout by 0.5 units every 15 min to a value of 4.00 units.

The Powel lens mount was levelled in the transverse direction then adjusted to the slope of the flume using a digital inclinometer in the longitudinal direction. If the laser reflected back on to itself them it was deemed to be completely normal to the base of the flume (Figure 3-27). The laser mount was located at a set distance of 50 mm to base of the flume.

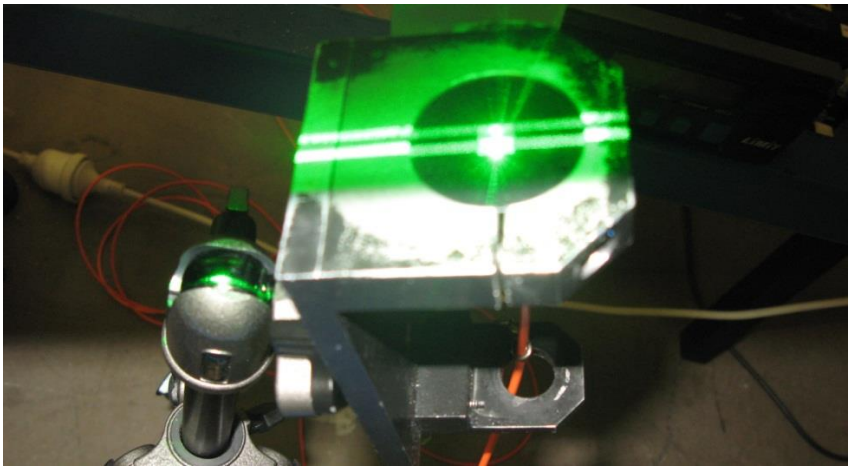

Figure 3-27: Laser beam reflecting back onto Powel lens.

Figure 3-28 shows that as the laser was warmed up there was fluctuation in laser power when the current was increased. If left the laser power would gradually increase over time. The laser power could therefore change between calibration and testing if not left long enough to stabilise. The laser did appear to become slightly unstable at high currents and small increases in current had large impacts on laser power. At a current setting of three on the power meter, the laser produced ~ 650 ± 100 mW. This corresponded to a power of approximately 440 mW at the Powel lens and 44 $mWcm^{-1}$ over the length of the laser sheet, at the base of the flume. This showed significant power loss but low sensitivity to small fluctuations in power of laser.

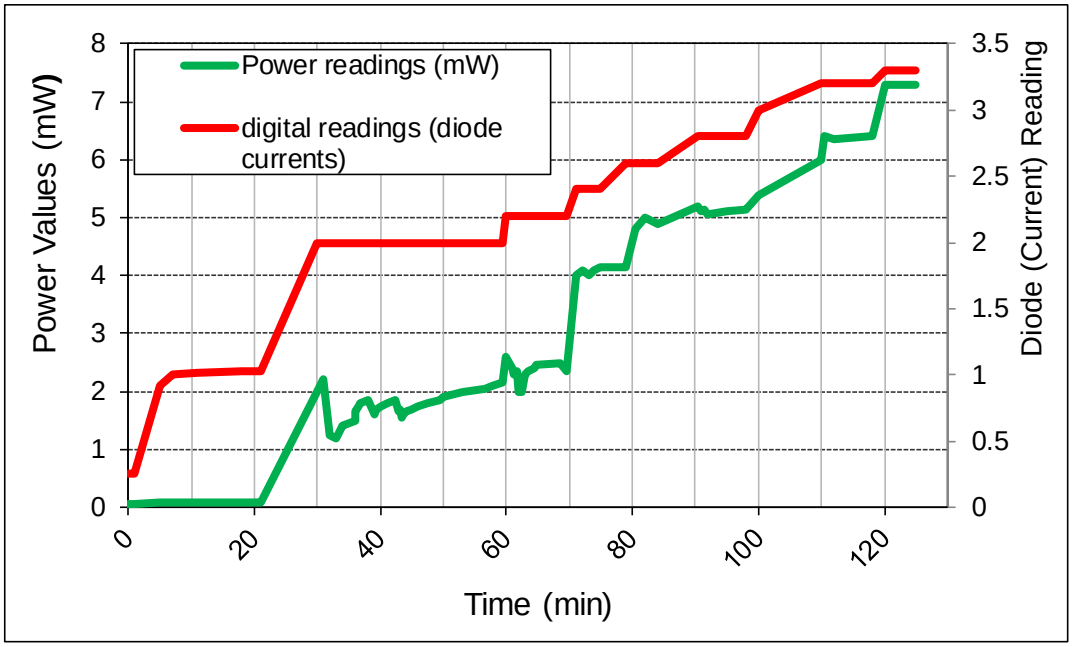

Figure 3-28: Laser power over time. The red line indicates the current and the green the laser power output.

3.8.Data Collection

After the experiment the following measurements and samples were taken:

- Spot heights (height of deposit at the intersection of grid lines) of grid points on run-out deck
- Samples for PSDs
- Photos of each run-out deposit to be used in shape analysis.

Spot heights from the deposits were obtained using a digital calliper. Spot heights were not measured until the majority of the oil was drained from the run-out deck. The actual measurement required some judgment if there were any large particles at the edge of a grid point. Where it was seen that a large particle was dominant or there was more than one large particle, the height was taken as the highest point within a 5 mm space around the grid point. The calliper end was gently pressed into contact with the run-out deck, this sometimes depressed the height close to the calliper and so measurements were taken level with the non-depressed height.

(a) **(b)**

(c) **(d)**

Figure 3-29: Areas clear for PSD sampling of deposit. (a) Front edge. (b) Centre. (c) Transition. (d) Tail.

Samples of the deposit used to produce PSDs of four locations of the deposit were collected. It was difficult to collect all of the wet fine particles with a brush as they stuck to the apparatus. The small number of fines not collected was consistent for all samples apart from the tail which drained making it easier to collect the fines. Each sample was individually cleaned, sieved and measured before being added back into experimental material stock. The areas collected (shown in Figure 3-29) were:

- The front edge - the front 1-2 square grids of material curving around until the deposit side was parallel to the wall of the run-out deck.
- The centre of the deposit- A square of the about 80 mm at the exact centre of the deposit
- The transition point - the two grids around the end of the flume where it meets the run-out deck
- The tail - the last 100-200 mm of the flume above the roughness layer.

3.9. Challenges to Methodology

There was need for an assiduous approach in order to maintain consistence between tests. The main challenge to observing and quantifying phenomena within the transparent debris flow was the consistency and quality of images. There is a large amount of inherent variability in the flow, particularly of large particles, which results in varying thickness and dispersion of fines which tend to cloud larger particles. Also getting the correct level of lighting was difficult in order to make sure that the individual particles were not over or under-exposed causing the particles to lose clarity and reducing the amount of texture in the images. The repeated use of the particles created some degradation that reduced the quality of the images. This degradation was mainly small chips and cracks in the edges that held thin air lenses. In addition, sieves left ground-in steel residue along the particle edges.

3.9.1. Consistency

Producing a good thickness of flow consistently, for a range of variables, was difficult. However, trial runs with used material showed that if variables were held the same the major challenge in producing a consistent height of flow was the mixing within the hopper and/or any potential jamming of particles during discharge of material. Due to the non-saturated front of the flow the height of the flow became a reference point for the development of the debris from the peak height at the front the shallow tail. While height of flow may not be the best indication of consistency it is a relatively important one as it is measured from preliminary analysis of the images.

3.9.2. Distortions in Imaging

The fine particles, in suspension, were often closely packed together. The finest particles were observed to be part of the fluid phase rather than as distinct particles. Particles that clump together allowed very little pore fluid to surround each distinct particle which made it difficult to distinguish individual particles and gave a clouded appearance.

In addition to the issue of fine particles clouding the images, air bubbles became entrained in the flow from the hopper and were seen as dark spots in the laser images and more distinct ovals with darker edges in the non-laser images. Because of the matched refractive index the air bubbles were a more prominent feature in the flow than the solid. In the laser images they diffracted the light and were difficult to distinguish. It was found that the air bubbles tended

to rise toward the surface and so were removed during PIV if the bubble had a large slope normal velocity component. The air bubbles were much more visible in the non-laser flow. They were much easier to distinguish because the air was able to reflect the light better than the optically matched material. However, because of their semi-transparent nature, air bubbles at other LOVs were also visible not just the ones at the wall of the flume. This was also seen in the interior LOV but to a lesser extent.

Careful adjustment of hopper positioning helped to reduce the entrainment of air bubbles. Preliminary work showed that the ability for the flow to entrain air was very sensitive to the location and adjustment of the hopper. It is unclear what the mechanisms behind this were, resulting in the setup being more trial and error than systematic. The larger number of bubbles in the non-laser images was not easily rectified and was left to post PIV analysis to remove.

3.9.2.1. Degradation of Particles

During the manufacturing of particles there was a considerable amount of chipping to the surface which resulted in fractures and distorted edges. Air was able to get into these fractures where the thick oil could not penetrate. This meant that in some of the larger particles, there was a pocket of air trapped close the surface. Soaking the particles the night before helped to reduce this effect.

The large particles lost their angular edges with repeated use and sieving, going from angular to sub-angular. This had the potential to change the rolling, contact and collisional performance of the particles during an experiment. Due to the particles being used in a prior experiment by Sanvitale the edge rounding had largely already occurred. Any new particles were put in the sieves first to attempt to remove the most angular edges.

3.10. PIV Analysis Process

PIV techniques adapted to use in geotechnical modelling (White et al., 2003) were performed at regular intervals throughout the flow. This analysis, specifically, used modified static mesh Geo-PIV (Sanvitale, Bowman, & Genevois, 2011) software developed specifically for this analysis. This analysis determined slope-parallel and slope-normal displacements which were converted into velocities using the time step between images. The procedure for the analytical methodology included:

- Measuring images manually to determine a zero time and max height
- Collating and processing images for analysis
- Create and apply a mesh that can be consistently applied to all batches of images.
- Process using Geo-PIV
- Calculate velocity values for each set of batch results and compare over time.

3.10.1. PIV Terminology

- Patch: The area of interrogation that is matched between two images. A patch represents a single data point for displacement.
- Mesh: A mesh is a grid of square patches set up over an image. The mesh width and length is defined by the operator and can be any size and any location within the image. It is set out in columns and rows with a set spacing between patches.
  - Columns: A column is each set of vertical patches
  - Rows: A row is each set of horizontal patches
  - Spacing: The spacing between the centers of the patches in each column or row. The spacing is set by the operator and can be adjusted so that patches overlap or have a gap between them.
- Batch: A batch is defined as the group of images selected at set time intervals for PIV analysis. The images are paired up so that the first and second images are analysed the second and third and so on. This gives one less comparison than the batch size.

3.10.2. PIV Methodology

The PIV methodology used in Geo-PIV is based on White, et al. (2003) and is conducted using the following procedure. Where a pair of flow images was divided into a mesh for analysis they are compared to measure the displacement of each test patch between the initial and secondary image. Figure 3-30 shows how the initial image (Image 1) was divided up into patches of size Lp x Lp. Each test patch, I_{test}, was converted into an image matrix with intensity values for each pixel.

To find the displacement of the patch in the second image, an expanded search patch, I_{search} (**U** + **S**), was increased by a distance S_{max} in the *u* and *v* directions making it larger than the original. This defined the zone, of dimensions $Lp+2S_{max}$ x $Lp+2S_{max}$, in which the original patch was assumed to have moved within.

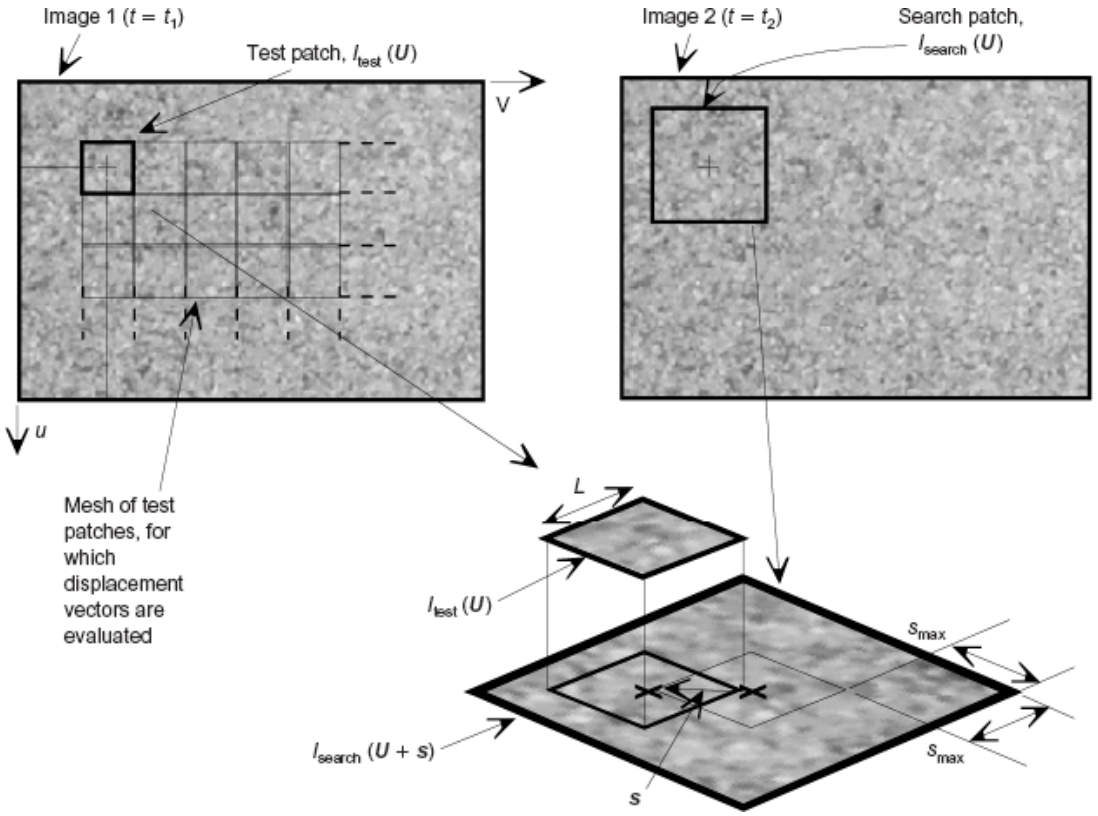

Figure 3-30: Image manipulation during PIV analysis where; t is time, v is horizontal direction. u is vertical direction, L is length of patch (pixels) U is the pixel intensity values, s is displacement between initial and secondary parches (White et al., 2003).

Cross-correlation was used to match the similarity U for the two subsections of the image matrices represented by the patches I_{test} and I_{search}. Cross-correlation took one matrix and multiplied it to obtain the integral, and then shift it along the horizontal and vertical axis over the entire domain of I_{search}. High values indicate the initial patch and search patch matched.

The resulting matrix of integrals was normalised to give the normalised correlation plane $R_n(s)$ over the offset range in the domain of **s** (Figure 3-31 (a)).

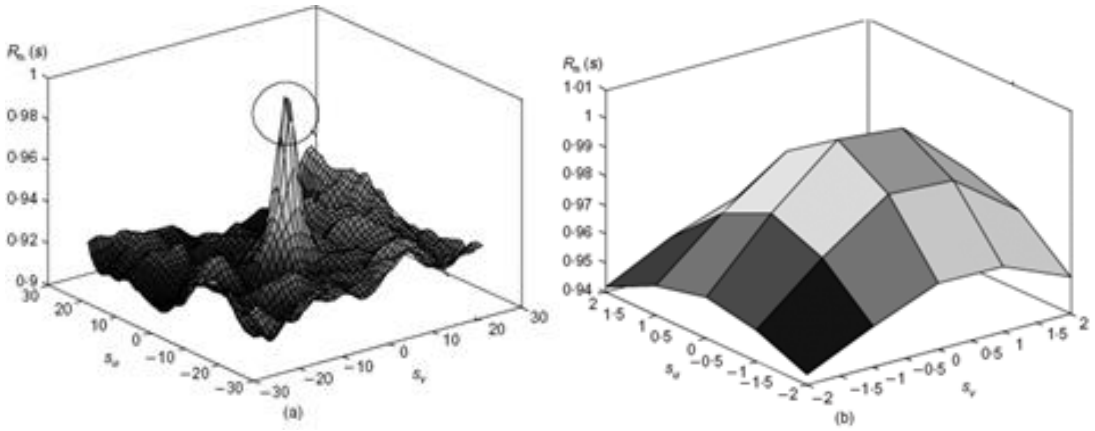

Figure 3-31: (a) normalised cross-correlation plane (b) enlargement of the peak under a fast Fourier transform (White et al., 2003).

To reduce the computational requirement the correlation operations were conducted in the frequency domain by taking the fast Fourier transform (FFT) of each patch and following the convolution theorem. The highest peak in the normalised correlation plane, $R_n(\boldsymbol{s})$, indicated the displacement of the test patch. The correlation plane was evaluated at single pixel intervals. By fitting a bi-cubic interpolation to the region close to the integer peak (Figure 3-31 (b)), the displacement vector could be resolved to within 1/200th pixel intervals. Greater resolution increased computational demand and the errors associated with, accuracy and precision reduced the effectiveness of the interpolation.

The flowchart for PIV analysis of an image series is shown in Figure 3-32. The procedure for calculating the displacement of a single patch was repeated for the entire mesh, producing the displacement field between the pair of images. The analysis was then continued by substituting the secondary image with another image at a larger time step from the initial image. The analysis was repeated by comparing the initial and subsequent images in the batch. As the analysis continues, image quality factors may reduce the sharpness of the correlation peak used to calculate displacement. If the correct correlation peak was indistinguishable due to random noise on the correlation plane a 'wild' vector was recorded as 'Not A Number (NAN)' indicating it did not have a real value.

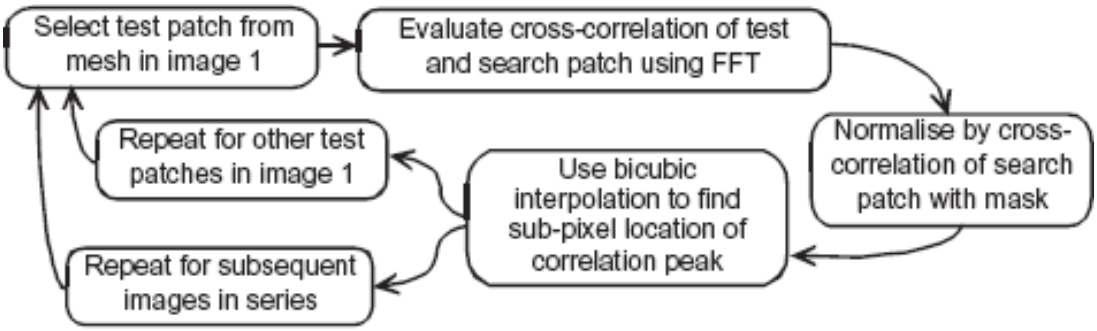

Figure 3-32: Flowchart of PIV analysis (White et al., 2003).

3.10.3. Selecting Comparable Reference Values

The variables of 'height of flow' and the 'time for front of flow to reach camera' were difficult to obtain due to limitations in the interior visualisation technique. This meant alternative methods needed to be used to select and obtain comparable reference points for analysis.

3.10.3.1. Height of Flow

The most real height is the absolute height of the flow at the middle of any particular image measured from the base of the flow in pixels and scaled to real space in millimetres. However, this introduced two issues - the first was noise, the other was related to the reliable imaging of the top potion of the flow. Noisy readings of height over time, were due to the large particles sitting high in the flow moving intermittently as part of the conveyor process. Noise could be removed by applying a moving average to the data to give an accurate representation of the actual trend. The period of the moving average should be large enough so that instantaneous fluctuations and variations do not significantly impact the values within the period.

In addition to noise, both the interior PLIF and exterior image techniques created unreliable readings for the height. An alternative reference height was chosen instead. The absolute height could not be reliably used for interior analysis as PLIF does not accurately illuminate the particles above the fluid. Above the saturation surface illumination relied on sufficient fluid attached to the particle sides. Often the fluid was insufficient giving a texture that rapidly changed with rotation and caused refraction and reflection. There were also flashes of laser light reflecting creating instantaneous bright spots only partially removed by the filter, which prevented image tracking.

In the exterior images the camera was focused directly at the window pane. Any large particles above the height of the saturation surface tended to sit further inward toward the centre of the flow and were out of focus. The blurring made it unreliable to measure these heights. Taking particles from within a different LOV of the flow was also inconsistent with the principle of taking a 2D slice of the flow.

So analysis for flow heights was based on a visible line in both the interior and exterior images where the fluid is saturated below and just coating the particles above. This level is referred to as the "saturation level or height." It must be noted that the flow above this height is important and removal means analysis is conducted only over reliable sections of flow rather than the entire flow depth. This will mean that comparisons with other research will have higher maximum height and velocities than those recorded at the saturation height. Both the absolute and saturation heights can be seen in Appendix F for all experiments.

3.10.3.2. Time Zero

Normally, the time taken for the initial material of the unsaturated flow front to reach the camera after a trigger would be used as the point of reference. This would then be used to align all of the experiments with respect to the time the flow was initiated. Due to malfunctions in camera triggers however, only the Miro camera had a reliable estimation of time taken for the front to reach the camera.

In addition, the unsaturated front was not easily illuminated for PLIF which requires significant fluid in order to provide resolvable images and analysis. Finding a zero time reference for comparison was based therefore on two considerations. The "saturation flow front" or point at which saturation first occurs was used to analyse the height as a function of time. This was the first reliable measurement but at this point no images were able to be processed through PIV.

For the selection of the first batch of images used in PIV the peak height of the flow was used. The '"peak height of saturation" was chosen rather than the "absolute height" as it was less-affected by large particles and it guaranteed proper illumination within the measured flow. The choice of peak height of saturation as the zero reference time gave a consistent point. However, sometimes the peak occurred well after the front of the flow. In this case further profiles were taken around the front. In terms of reference times this gave negative times before and positive times after the peak height of saturation.

3.10.4. PIV Analysis Procedure

The physical modelling produced between 8000 and 20,000 images that needed to be sorted and processed to give meaningful information. The following is the procedure to take the numerous images and produce accurate, consistent and relevant information.

1) Images were grouped into batches of 20 frames or images at regular time intervals starting from the peak saturation height
    - Slope 18.1˚ tests were sampled at 0.5 s intervals throughout test
    - Slope 24.5˚ tests were sampled at 0.5 s intervals. However, the body occurred completely within the first 0.5 s, this required additional profiles to be created at 0.1 s intervals for the first 0.5 s of the tests
2) Images were then processed to increase the light and image quality
3) The first batch of images was used to set the mesh and pixel sizes.
    - A series of meshes of different sized patches were created. These meshes had the patches located in a three-column 16 or 8 (depending on camera) pixels apart.
    - Geo-PIV software was then run for each patch size to create velocity profile estimates. Plots were produced to check for abnormalities.
    - These plots were: Max, mean and min velocities for each pair of images, to see if there were any discontinuities or outliers
4) The optimum patch size was evaluated based on level of noise and level of detail. For the Motion-Pro camera the typical patch size chosen was 32 pixels. For the Miro camera the typical patch size was 16 pixels
5) The remaining batches were processed using Geo-PIV software and the same mesh. This ensured all images and patch locations were consistent, particularly the base of the flow
6) Averaging was conducted on all results
    - At each height the horizontal velocities were averaged and a standard deviation calculated, which could be used to remove wild or inconsistent vectors
    - Once the wild vectors were removed the data was averaged again to produce a velocity at each depth
7) An upper and lower boundary were calculated. Patches not entirely contained in the flow were removed and the velocity profiles were plotted against depth

8) The velocity plots were normalised by the average velocity and the maximum height at each location within the flow
9) For each location in the flow, a depth-averaged velocity was calculated to give a representative value at that location. These values were used to make an approximation for flow rate and were plotted over time.

3.10.5. Averaging and Processing Data

3.10.5.1. Instantaneous Velocity Profiles

The Geo-PIV software produced a displacement for each patch in the '*x*' and '*y*' direction. The velocity of the patch ($u_{i,j,k}$) was the slope parallel displacement ($d_{i,j,k}$) divided by the time step between images ($t_{1/fps}$) converted from pixel to real space, using a scale factor derived from the calibration target.

$$u_{i,j,C} = \frac{d_{i,j,C}}{t_{1/fps}} \tag{3-10}$$

where *i* is mesh row (depth) *j* is the pair of images used in the calculation and *C* is the number of columns. A slope parallel velocity was calculated for each depth *i*. This was an average of all patches at the same depth for all pairs of images in the batch, *j* and columns, *C*, with columns calculated first

$$u_{i,j} = \frac{1}{C}\sum_{k=1}^{C} u_{i,j,k} \tag{3-11}$$

$$u_{i} = \frac{1}{(B-1)}\sum_{j=1}^{B-1} u_{i,j} \tag{3-12}$$

where B is the batch size and C is the number of columns of patches.

Wild or erratic vectors were removed based on two criteria. The first was if they displayed an unrealistically high slope-normal velocity. This was reasoned from the slope-parallel mean velocity being an order larger than that of the slope-normal case. Therefore, if a normal velocity vector was of the same order as the mean, it was deemed to be wild and removed.

The second refinement used the standard deviation at each depth, if a velocity was greater than two standard deviation either side of the mean, it was removed. Once the wild vectors were removed the average was recalculated. For each depth the standard deviation was calculated:

$$\sigma_i^2 = \frac{1}{(B-1)} \sum_{j=1}^{(B-1)} \left(u_{i,j} - u_i\right)^2 \quad (3\text{-}13)$$

3.10.5.2. Depth Average Velocity

The depth-averaged velocity allowed easy comparisons between different parts of the flow, for example, the body and the tail. For each instantaneous velocity profile a single velocity was calculated as:

$$u = \frac{1}{(P_{Total} - (P_{upper} + P_{lower}))} \sum_{i=P_{lower}}^{P_{upper}} u_i \quad (3\text{-}14)$$

where, P_{Total} is the total number of rows of patches in the mesh, P_{upper} and P_{lower} were the number of patches to be removed at the upper and lower bounds of the mesh. This included the removal of patches outside of the flow. The upper and lower bounds were calculated from a mesh which was larger than the flow, and was calculated in two parts. The overlap in the mesh to ensure all patch centres were within the flow and the patches whose centres were in the flow but were not completely contained in the flow

$$P_{lower} = \frac{(p_{Mesh\ lower} - p_{Base\ flume})}{P_{Size}} + \frac{1}{2} P_{Size}\ x\ Y_{step} \quad (3\text{-}15)$$

$$P_{upper} = \frac{(p_{Mesh\ upper} - p_{Sat\ surface})}{P_{Size}} + \frac{1}{2} P_{Size}\ x\ Y_{step} \quad (3\text{-}16)$$

where $p_{Mesh\ lower}$ is the pixel height at the bottom of the mesh, $p_{Base\ flume}$ is the pixel height at the base of the flume taken from the image, $p_{Mesh\ upper}$ is the pixel height at the top of the mesh, $p_{Sat\ surface}$ is the pixel height at the saturation surface for the majority of images in the batch, P_{Size} is patch size in pixels and Y_{Step} is the slope normal pixel step between patches.

3.10.5.3. Flow

The flow was approximated from the depth average velocity, width of the flume and the height of the flow. This assumes that the flow is uniform across in the transverse direction and that the average velocity is representative of the areas of the flow unable to be captured with PLIF and PIV.

$$Q = w.u.h_{max} \quad (3\text{-}17)$$

where Q is the flow in mm^3/s, w is the width of the flume, h_{max} is the maximum depth.

3.11. Analysis Software Parameters

Choosing the best combination of parameters for analysis required a complex interaction of factors and settings. Once each test had a time and height reference point the images were selected paying attention to quality and sampling. A mesh or grid was then derived to turn image texture into patches for matching. Sensitivity studies were undertaken to identify the effect of changes in parameters controlling the image selection (presented in Appendix B) and patch mesh that was used to obtain velocity profiles.

The parameters were:

- Image selection
  - Inversion or adjustments to image quality
  - Number of images over which to average
  - Time step between images
- Mesh
  - Cut off points for mesh height and base
  - Number of columns
  - Size of patch
  - The slope parallel spacing between patches; affects the distance between columns
  - The slope normal spacing of the patches; affects the number of rows of patches.

3.11.1. Image Selection

Image selection for analysis was based on the ability for sufficient texture to be obtained from the images for patch matching using PIV. Three tests had low light levels which limited height and PIV analysis. These were S18W28IN1, S18W24EX6 and S24W32IN7. The following section looks at the sample size of images for analysis and the type of processing that was available for those images. A sensitivity study demonstrating the effect of image processing is presented in Appendix B.

3.11.1.1. Time Step

The PIV software displacements between each image were averaged over a specific number of images analysed. Therefore, there was a choice of time step between each image, the number of images to combine into a batch and the time step between each batch. The following section looks at these time-step parameters.

The smallest time step between images was set by the frame rate. Analysis was carried out using the minimum time step possible. Reasonably instantaneous values were obtained for velocities due to a combination of averaging to remove the variability in PIV patch matching and carefully chosen mesh parameters that reduced blurring out any instantaneous phenomena.

For velocity profile analysis the time intervals between batches determined the level of continuity between profiles. Large sampling time steps missed detail and the profiles changed shape considerably. This missed the evolution in trends over time. A very small time step created too much information which made it difficult to see the trends. Optimally the time step should have showed enough profiles so the changes were clear and reasonably gradual over time but there were not so many profiles that they were all the same or overlap. Due to the computation work load this was taken as 0.5 s giving approximately 10 steps in total (dependent on length of film). The time step was reduced for the body of the 24.5˚ slope experiments whose body passed in the first 0.5 s. This is supported by the experiments conducted by Sanvitale (2010).

For the height analysis the time intervals between sample images needed to be small enough to show instantaneous change and variability. This could then have a moving average to suppress the fluctuation and give a smooth representation of height change over time. Due to computation effort the height analysis was limited to approximately the first second of flow and was sampled every 0.01 s. This gave a good representation of the variability. The rest of the flow, which was less variable, was sampled at 0.5 s to match the velocity profile sampling times and give approximate heights to show if the tail was stable of not.

3.11.1.2. Images per Batch

The PIV software located the same textured patch between two images that was used to find the displacement of the patch. The result was a matrix of slope-parallel and slope-normal strains. For a given number of images in a batch the PIV software created (one less than the number of images) strain matrices. The matrices were averaged and wild vectors removed to give a smoother velocity profile that had fewer instantaneous fluctuations. If the batch size was large then the instantaneous information was suppressed and detail was lost. In addition, an assumption was made that averaging can be made over a small time scale because the behaviour is steady. If the batch size was too large then the assumption did not hold. It was

found in sensitivity analysis that too many frames removed the localised nature of the behaviour and may have decreased the overall velocity recorded.

As batch sizes increases the standard deviation becomes more accurate. This is because there are more samples to use in comparison and calculation of the standard deviation. The standard deviation was used to check for wild vectors and indicate the error associated with each profile. Two sensitivity studies (Appendix C) were conducted to find the minimum number of images that still gave a non-erratic velocity profile. It was found in the first study that 30 images per batch were combined with a relatively sensitive mesh to give a reasonable balanced of detail without introducing significant amounts of noise.

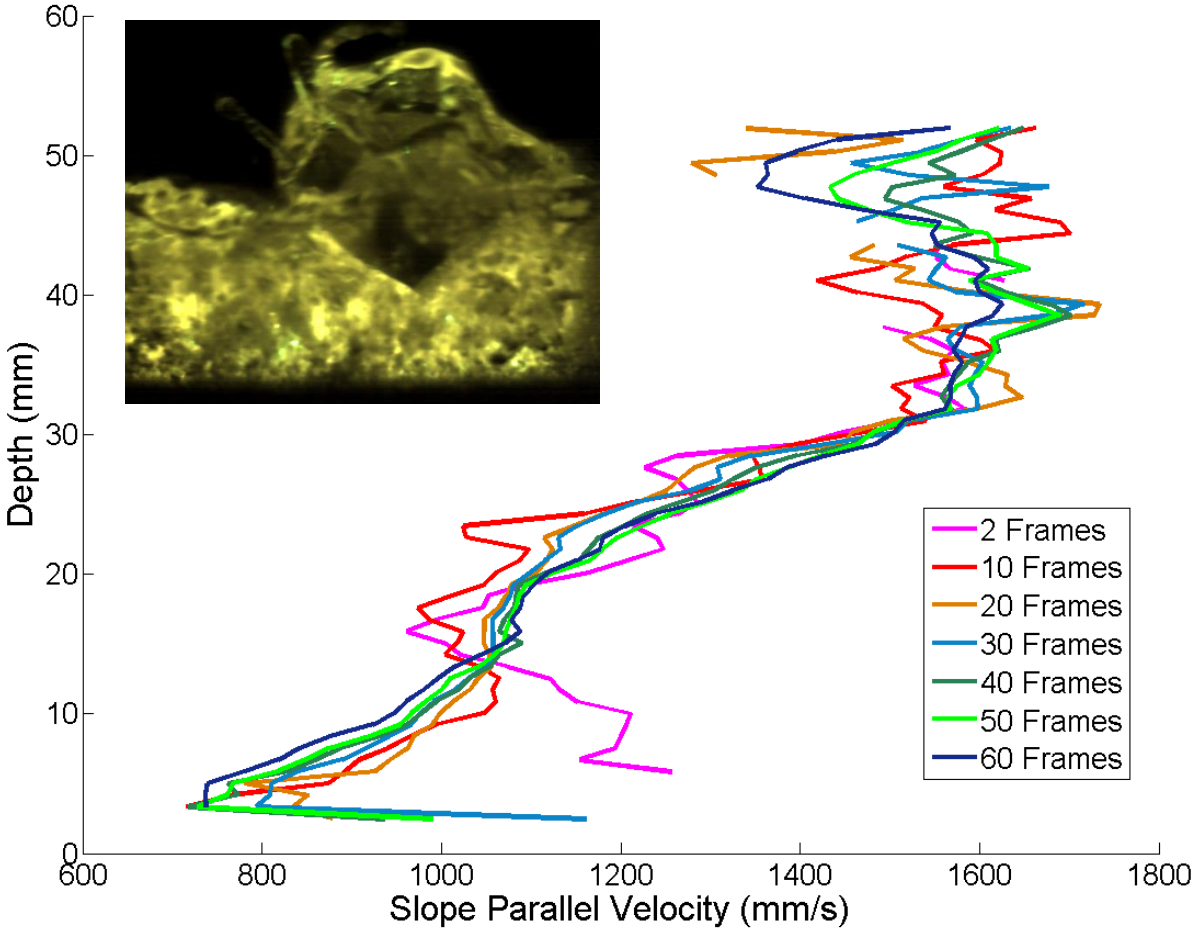

Figure 3-33: Effect of number of frames per batch on velocity depth profile. Using 3 columns, 32 pixel patch size and slope normal patch spacing of 8 pixels. Batch analysed was from S18W32IN8 profile, 0.5 s after peak saturation height with a suspended particle. Note above 32 mm the profile is reading the flow above the saturation level. (Insert top left) Image at the centre of each batches showing large particle.

Figure 3-33 represents the batch sensitivity analysis using images S18W32IN2 with a robust mesh (3 columns and 32 pixels per patch). This batch had a large particle suspended in the flow. In general there was low variation in profiles with batch size. This is attributed to the robust mesh. However, the 10 and two-frame batches showed more variability, particularly at the base of the flow. This can be attributed to the large particle moving at a depth between 20 and 30 mm. The instantaneous effects along the bottom edge of the larger particle were smoothed out for the high batch sizes. The effect of one large particle is an important observation for identifying the interior behaviour of debris flows but may influence comparisons between different flows. It was also notable that the small batch sizes had more data removed due to wild vectors. This resulted in the two frame profile being shorter.

3.11.1.3. Image Processing

Image processing was important to brighten the Motion-Pro images in order to allow manual measuring of flow heights and the identification of the saturation level within a flow. Sensitivity studies in Appendix B showed that post processing of images had no significant effect on PIV results. This was because the same information was present and scaling did not increase correlation between patches during analysis.

To overcome the low light levels the brightness and contrast had to be adjusted. For example, one of the tests (S18W32IN2) has brightness values between 0 (completely black) and 82 (dark grey). The brightness values were scaled so that the values were between 1 and 255 (completely white). Figure 3-34 shows the light intensity histogram and images pre and post processing.

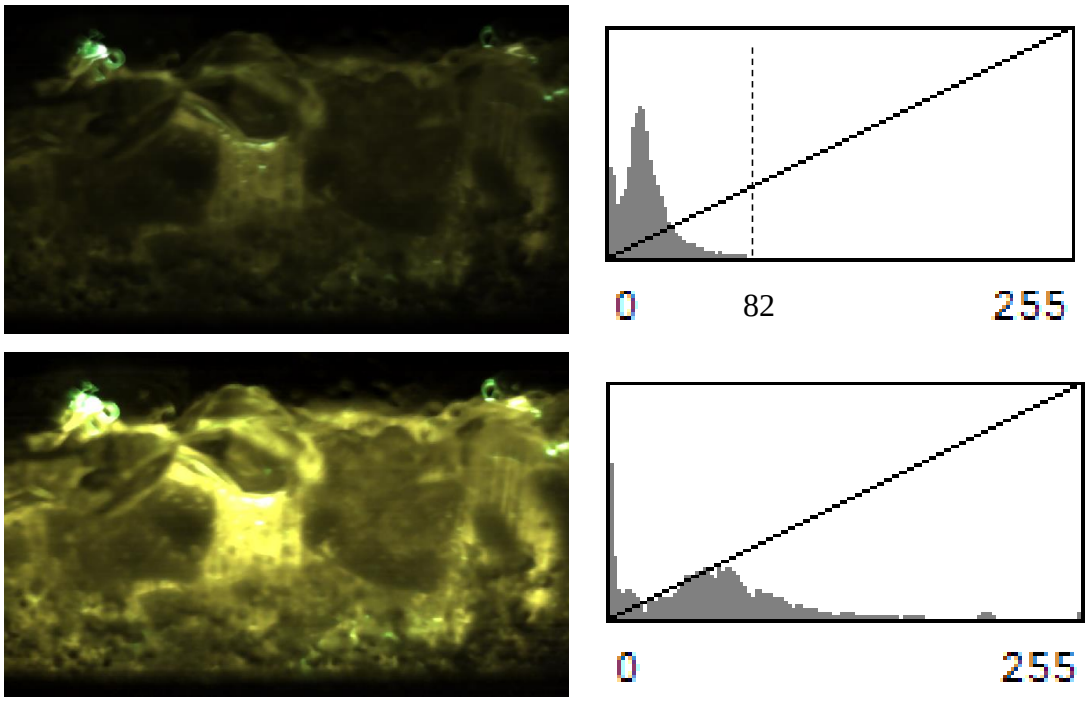

Figure 3-34: (Top left) pre-processed image. (Top right) pre-processed light intensity histogram. (Bottom left) post-processed image. (Bottom right) post-processed light intensity histogram

3.11.2. Mesh Parameters

There were a number of ways to alter the mesh or grid, all of which have a significant impact on the final results. The main adjustable mesh parameters relate to where in the flow normal direction to: cut off the grid, the width of the grid, the size of the patches and the number of patches in each column. The upper and lower bounds govern where to cut off the grid. The slope-normal and slope parallel spacing of the patches determine the amount of overlap and number of patches within the grid. Patch size influences overlap but is not determined by spacing of the patches themselves. This section looks individually at these parameters and their influence on the final reliability of velocity profiles.

3.11.2.1. Lower Bound of Mesh

The lower bound of the mesh was the flume bed. However, because the patches were positioned based on the location of their centre, they overlapped with the bed of the flume. This area of the image was normally completely black for PLIF or white for exterior imaging. This meant there was no texture to match, creating significant error in the PIV analysis and giving wild vectors. The patches at the base of the flow were removed so that only patches completely contained in the flow were used in analysis. Therefore, because the velocity was

approximated at the centre of the patch, as patches increased in size, so did the distance from top and bottom of the flow that could not be analysed. Figure 3-35 demonstrates the effect of changing patch size and patch spacing on the data obtained. At the tail of the flow the depth was limited so that as depth decreased, so did the number of velocities with depth. This reduced the smoothness of the profile. If the patch size was greater than the depth of the flow then no measurement was obtained.

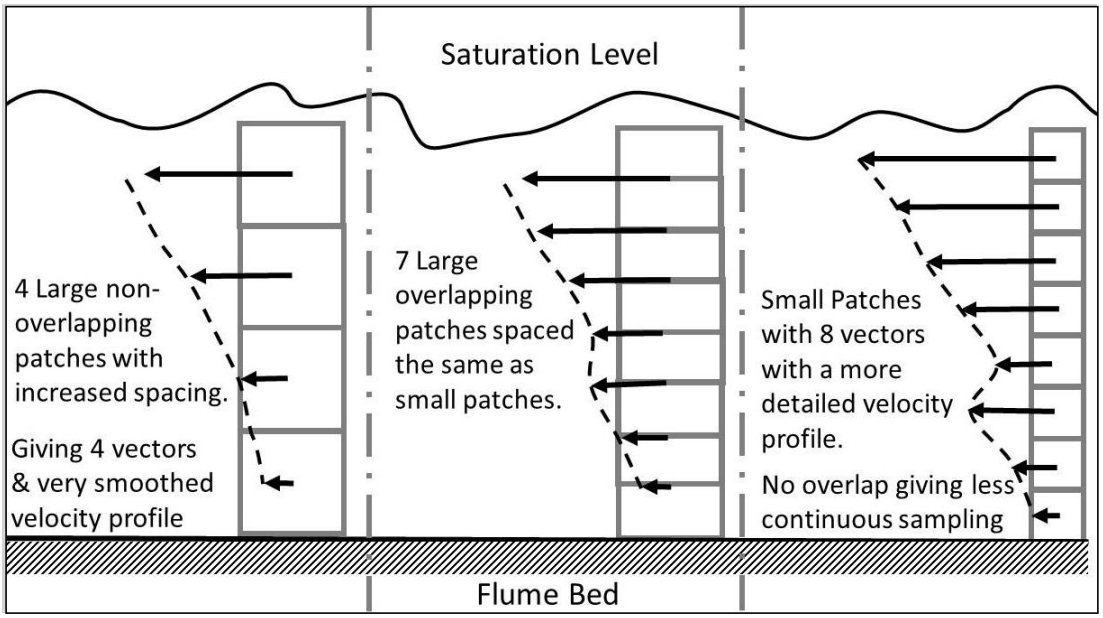

Figure 3-35: Diagram showing the effect of altering the patch size and spacing in terms of smoothing and the effective depth of analysis.

3.11.2.2. Upper Bound of Mesh

The upper bound of a velocity profile could be one of the three points given at each time by the absolute maximum height, height of saturation, or height at maximum velocity. Given that between the maximum and the saturation level the images were often of poor quality the saturation level was chosen. The height at maximum velocity was also calculated but it was not used to define the upper bound of the velocity profiles as it could remove important data and slip zones within the flow. The same blurring effect apparent in the lower bound was also a factor in the upper bound with patches overlapping regions above the saturation level. These patches were removed so that only patches fully in the flow were presented as part of the velocity profiles.

3.11.2.3. Selecting Patch Size

In order to determine the correct patch size for an experiment a range of patch sizes was analysed for the batch taken at the peak saturation level. The patch size that gave the best balance in instantaneous and clarity was then chosen for analysis of the rest of the batches. Patch size was the most significant influence on the outcome.

With increased patch size there were fewer wild vectors. However, this meant a loss of resolution with depth. Also the pixel size varied with the camera used, with the Motion-Pro camera having a smaller size per pixel (10 x 10 µm) than the Miro (20 x 20 µm). This had a similar effect as changing the number of pixels used in the analysis by a factor of two. For consistent scales 16 pixels was used for the Miro and 32 pixels for the Miro. Therefore the patch size was balanced so that a similar amount of real space was contained in each patch. This enabled the same number of patches per velocity profile regardless of the camera used.

3.11.2.4. Patch Spacing

Patch spacing is defined as the slope-normal and slope-parallel distance, in pixels between the centres of each patch. The patch spacing used in PIV analysis was always less than the size of the patch, resulting in overlapping patches. With more overlap there is more sharing of texture. This incorporates the same texture multiple times in order to give a more continuous profile in a similar manner to a moving average. The amount of overlap must be balanced with the computational demand as the overlap increases the number of data points and too many individual data points could also distract from the overall trend.

3.12. Chapter Summary

The key aspect of the laboratory methodology was the optical access to the interior of the flow which required matching of the refractive index between the fluid and transparent solid. The independent variables chosen for investigation were exterior vs. interior, moisture content and slope. The PLIF technique followed work by Sanvitale using a 2 m long flume fitted with optically matched glass windows. A new exterior imaging technique was developed to compensate for the optical matching of material and a more light-sensitive camera was used.

Optically matched fluid and solid were substituted and scaled to match typical debris flow material. The optimum operating temperature was investigated to ensure the best refractive matching. The method for manufacturing, cleaning and preparing material was refined. After each tests a range of non-imaging measurements were taken of the deposit to insure consistence and highlight any abnormalities in each test.

The PIV process was outlined and a frame of reference for the flows imposed due to issues with imaging unsaturated sections of flow. The PIV process inputs were discussed in terms of the velocity profile sensitivity to changes in image quality, inversion, patch size, slope-parallel and slope-normal spacing. The patch size was found to be the most significant input to the PIV process, particularly at the upper and lower limits of the flow.

The final combination of PIV parameters used initially in every test was three columns and 20 frames. The number of frames per batch and columns were kept constant and the patch size was adjusted to give balanced velocity profiles. A patch size of 32 pixels for Motion-Pro and 16 pixels for the Miro camera gave balanced results when combined with quarter slope-normal spacing and half patch slope-parallel spacing.

Chapter 4. Results

4.1. Results Introduction

The results presented in this chapter are broken into two parts. The first part presents the physical deposit and height over time measurements that are used to determine consistency with traditional debris flow behaviour and identify any exceptions in behaviour. The second part looks at the post-processed images and the data obtained from PIV analysis.

The first part is comprised of four sections. Section 4.2 summarises all of the data collected without the use of PIV software. Particular the run-out length heights of flows and the time between parts of the flow. Section 4.3 gives the overall behaviour of the deposit, in terms of: shape of deposit, spot heights of deposit and PSDs of samples taken at various locations within the deposit. Section 4.4 is the general behaviour of the height over time, looking particularly at the profile shape of the saturation level over time and actual peak heights. These two sections aim to show the typical representative behaviour obtained. Section 4.5 looks at the trends in deposit and height over time data with respect to changes in location of view (LOV), moisture content and slope. Appendix D has also been prepared to evaluate the consistency and exceptions of each test grouped by slope and moisture content.

The second part takes the representative tests from the first part and looks at the results produced from PIV analysis. Section 4.6 evaluates the typical shape of velocity profiles and how they change due to location within any given flow, base velocities and how the average slope-parallel velocities develop over time. Section 4.6 looks at the trends in velocity depth profiles, base velocities and average velocity over time data with respect to changes in depth of LOV, moisture content and slope.

4.2. Non-PIV Summary Tables

4.2.1. Summary Run-out Length

The simplest measurement for comparison is the maximum extent of deposit referred to as the run-out length. This was defined as the length from the end of the flume to the furthermost particle still in contact with the deposit along the longitudinal axis only. Table 4-1 summarises all the run-out lengths by moisture content and slope.

Table 4-1 shows that the interior and exterior run-out length is similar for similar variables. The run-out length increases with slope and moisture content this increase is of a similar magnitude for the range of variables tested. A 6.4° change in slope (from 18.1° to 24.5°) has approximately an increase of 402 mm on run-out length. A 12% change in moisture content (from 23.7% to 35.7%) has an increase of approximately 640 mm on run-out length.

Table 4-1: Maximum run-out lengths in mm grouped by type of test

	Moisture Content			
Experiments	***23.8% (mm)***	***27.8% (mm)***	***31.8% (mm)***	***35.8% (mm)***
Preliminary		*689 (S18W28IN0a)* *261 (S18W28IN0b)* *752 (S18W28IN0d)*		
Slope 18.1° Interior	*515 (S18W24IN5)*	*685 (S18W28IN1)* *685 (S18W28IN4)*	*808 (S18W32IN2)* *947 (S18W32IN6)*	*1200 (S18W36IN3)*
Slope 18.1° Exterior	*412 (S18W24EX6)*	*752 (S18W28EX1)*	*1027 (S18W32EX2)* *1038 (S18W32EX4)*	*1085 (S18W36EX3)* *1022 (S18W36EX5)*
Slope 24.5° Interior			*1299 (S24W32IN7)* *1382 (S24W32IN8)*	
Slope 24.5° Exterior		*1089 (S24W28EX8)*	*1046 (S24W32EX7)* *1390 (S24W32EX9)*	
Avg. Slope 18.1° excluding outliers	*463*	*713*	*955*	*1102*
Avg. Slope 24.5° excluding outliers	*-*	*1089*	*1357*	*-*
Slope 24.5° Sanvitale Interior	*-*	*850*	*-*	*-*

4.2.2. Summary Height of Flows

Table 4-2 shows that absolute maximum height and peak saturation height increase with slope and moisture content with a similar order of magnitude of approximately 4-8 mm with each step in variable. Deposit thickness at the transition point decreases with moisture content but not slope and there is no visible trend in the tail height. Tail height may be influenced by recording time and structures within the deposit on the deck and transition point between the flume and deck.

Table 4-2: Height of flow summary.

	Average Height of flows (mm)				
Slope and Moisture Content	*Number of Tests*	*Absolute Maximum*	*Peak Saturation*	*Saturation Tail Height*	*Transition Deposit*
S18W24	*1xIN*	*51*	*41*	*5*	*39*
S18W28	*5xIN*	*54 ± 13*	*39 ± 13*	*9 ± 6*	*29 ± 7*
S18W32	*2xIN 2xEX*	*57 ± 12*	*48 ± 9*	*8 ± 2*	*27 ± 3*
S18W36	*1xIN 2xEX*	*66 ± 15*	*52 ± 12*	*10 ± 3*	*26 ± 1*
S24W28	*1xEX*	*71*	*61*	*7*	*31*
S24W32	*2xIN 2XEX*	*66 ± 4*	*53 ± 9*	*6 ± 0.7*	*31 ± 6*

4.2.3. Summary Time Table

Table 4-3 shows there is no trend in first particle or the material that is seen to detach from flow and accelerate faster than the flow. The time between peak saturation height and the flow fronts increases with moisture content, this shows a change in the nature of the fronts. After removing outliers the changes in slope shows little difference in the difference between absolute or saturation fronts and peak saturation level showing that the shape of the fronts is similar.

Table 4-3: Time from peak summary.

	Average time between peak height and sections of flow (s)				
Slope and Moisture Content	Number of Tests	Trigger	First Particle	Absolute Front	Saturation Front
S18W24	1x IN	-	0.43	0.16	0.06
S18W28	5xIN	-	0.16 ± .1	0.14 ± 0.1	0.07 ± .04
S18W32	2xIN 2xEX	-	0.43 ± 0 .04	0.18 ± 0.2	0.17 ± 0.2
S18W36	1xIN 2xEX	3.28 ± 0.6	0.33 ± 0.03	0.31 ± 0.04	0.25 ± 0.06
S24W28	1xEX	2.90	0.77	0.67	0.21
S24W32	2xIN 2XEX	2.03 ± 0.4	0.34 ± 0.3	0.20 ± 0.05	0.16 ± 0.08

4.3. Deposit Behaviour

This section looks at the general behaviour of the deposits obtained from every experiment to give an indication of typical behaviour. The aspects of the deposit investigated are the shape of deposit, spot heights of deposit and PSDs of samples taken at various locations within the deposit.

The deposit measurements were taken after the material had time to settle and drain. All flow deposits were photographed and spot heights taken at each grid point. Once measurements were taken samples were collected and processed to give PSDs of various locations in the flow. The photographs of each deposit were used to create an outline of the outer extent the photo was used to infill this outline and show visually the arrangement of particles within the deposit. The outline was also used to give the maximum run-out length. All of the plots corresponding to every test can be found individually in Appendix E.

4.3.1. Deposit Shape

The deposits typically are elongated ovals where the flume end is narrow and the front edge is flattened and the widest part is in the centre of the deposit. The deposit edges are not smooth lines. The shorter run-outs had smoother edges with the longest being quite variable. Large particles especially distort the front edge from the centre forward as seen in Figure 4-1.

At the flume end the grain size is smaller and the deposit edge is a smoother line (but still not perfectly straight). Scaling all deposits by maximum run-out length indicated that the shape was non-dimensionally very consistent. So flows suffered from blockages that gave shorter deposits.

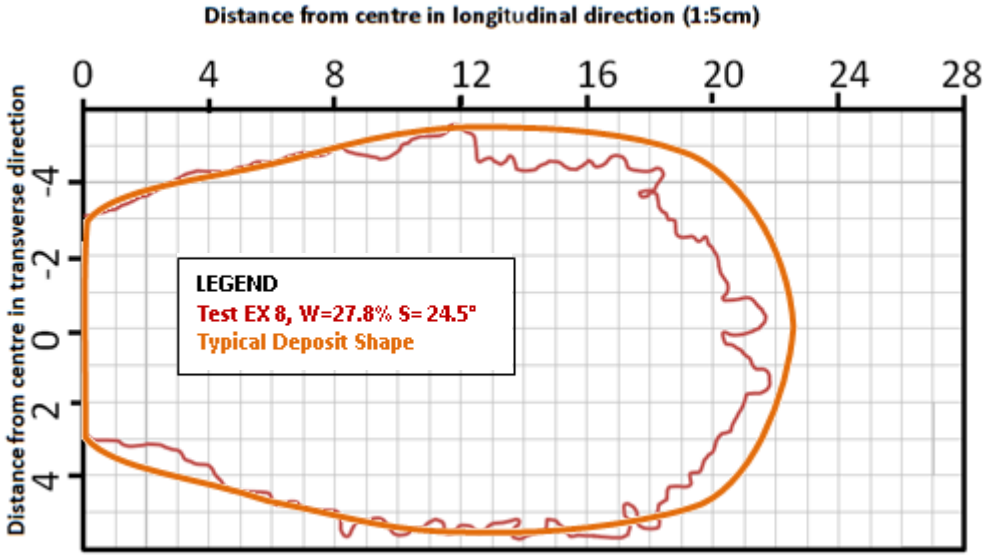

Figure 4-1: Outline in Red of S24W28EX8 deposit. Outline of typical shape in green. The longitudinal direction is parallel to the direction of flow. The flume releases at zero (longitudinal) and between 2 and -2 (transverse). Each square is 5cm x 5cm.

4.3.2. Particle Size Distribution of Deposition

Figure 4-2 shows typical PSD curves for samples at the front edge of the deposit, the centre, the transition point between the flume and the run-out deck, and the tail which was deposited on the highest extent of the flume. The largest particles tended to distort the upper fraction due to their scattered nature throughout the run-out deck deposit. The front edge and tail deposits are consistent and have much coarser or finer (respectively) PSDs than the original material. The transition and centre were more variable and could be gap graded, but they do follow a basic trend. The centre was generally coarser than the original but not more than the front edge. The PSD of the transition point was generally finer than the original but not more so than the tail.

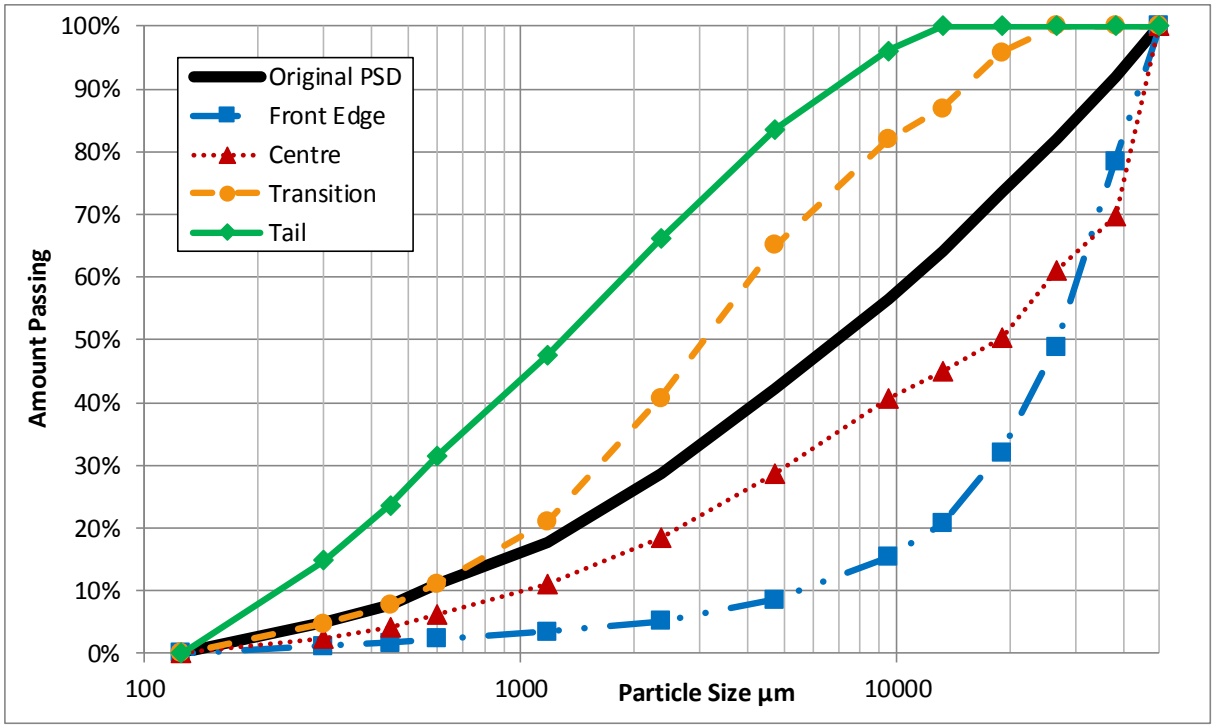

Figure 4-2: PSD of various locations of S18W36EX3 deposit, as labelled. The original PSD is the PSD of the material before conducting the test.

4.3.3. Deposit Spot Heights

Spot heights of the deposits showed graphically where the coarsest particles were within the flow and allowed showing of thin areas and the spread of material from the front to the flume. The coarse particles were scatted throughout the centre with a higher number at the outer front edge. The thinnest part was the centre and the tail deposited on the highest part of the flume. Figure 4-3 shows the spot heights the depth 'z' is the depth measured at the corners of the grid points on the run-out deck.

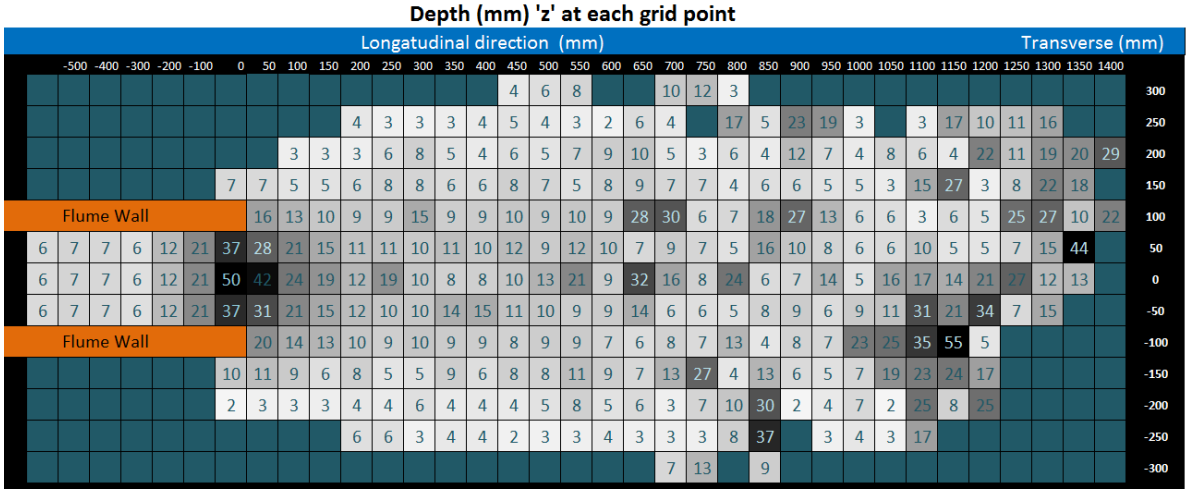

Figure 4-3: S24W32IN8 spot height graph, dark spots indicate a high level and white shallow heights. Each grid is 5 cm x 5 cm

4.4. Height of Flow over Time

4.4.1. General Debris Flow Description

The images show that in every case the physically modelled debris flows have a short dry front as seen in Figure 4-4. There are normally only a few particles that are separate and so faster than the front. Once the front edge has peaked the debris flow enters the body section of the flow. The front edge does incorporate a saturated core (Figure 4-4) that also rapidly increases in depth to become very close to the maximum height. The difference between absolute maximum height and saturation level is due to large particles "floating" in the flow.

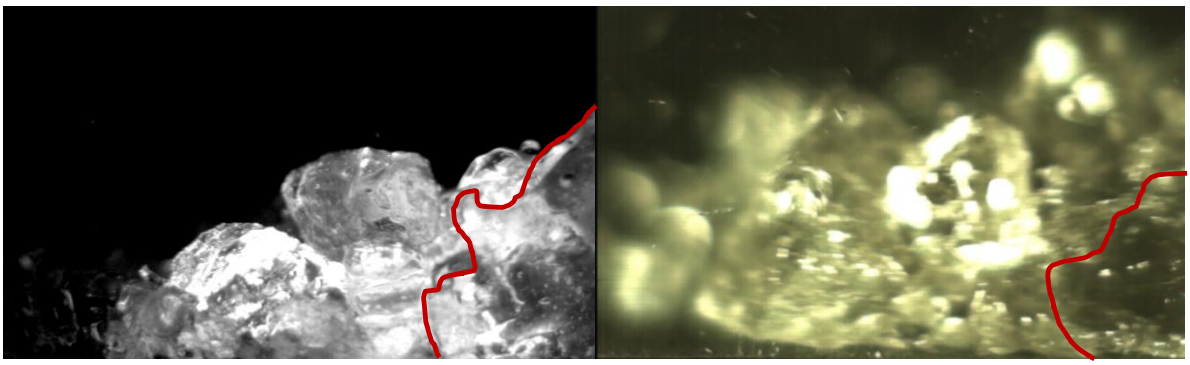

Figure 4-4: Unsaturated front of (left) S18W24IN5 and (right) S18W36EX5. Red line indicated the saturation front

After the front is the body is a deep section of flow that drops of in height quickly. In most cases the flow drops half the height in the first 0.8 seconds. There are lots of large particles incorporated into the flow at all levels but tend to move up through the flow. In general the floating particles in the body are intermittent and between particles the saturation level is at the absolute maximum height of flow. This indicated that the body was fully saturated. The floating particles become less frequent as the body develops into the tail section.

Once the body has rapidly dropped in height during the first 0.5-2 s the height becomes relatively stable. This is the tail section which is a long thinning section of flow. The flow in this section does not have many medium to large particles (above 3 mm in diameter). However, where there are these larger particles they can have a significant influence in the flow acting as obstructions in the flow, as seen in Figure 4-5. This description of the flow matches very well with other research (Ancey, 2001; Bardou, 2002; R.M. Iverson, 1997; Lorenzini & Mazza, 2004; Takahashi, 1991), presented in Chapter 2.

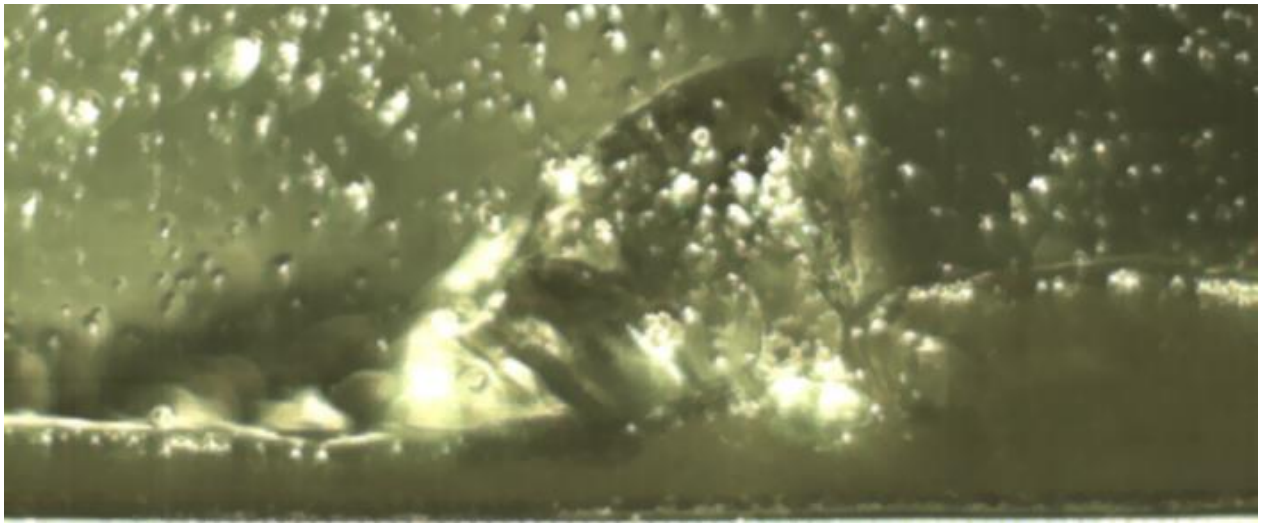

Figure 4-5: Image of damming caused by large particle in flow tail for S18W32EX4.

4.4.2. Shape of Height over Time Profile

4.4.2.1. Height of Front

The fronts for the low slope and moisture content are steeper, whereas the high slope and moisture content tended to have less well defined front sections which can be seen in Figure 4-6.

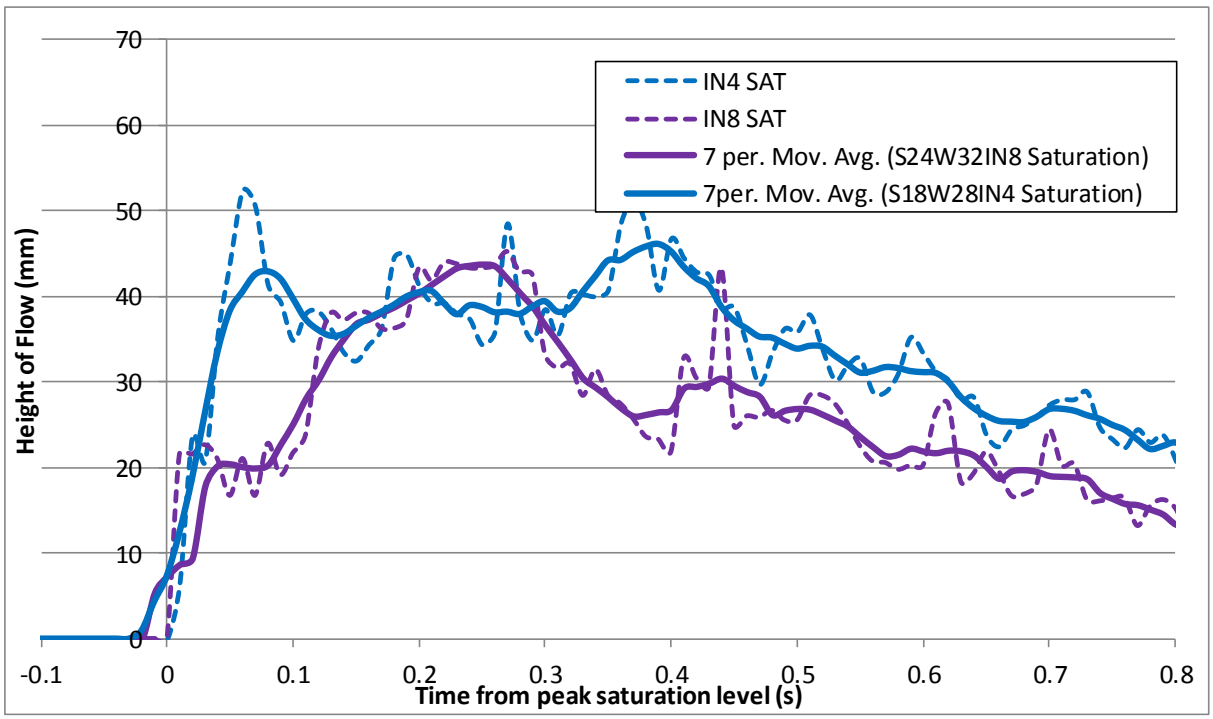

Figure 4-6: S18W24IN4 in blue and S24W32EIN8 in purple, height over time profiles. Time zero is the beginning of the saturation. The dotted line is the actual values the solid is a moving average of 7 points.

4.4.2.2. *Shape of Body*

Figure 4-7 shows the body drops off for fast for most high slope and high moisture content tests. However, the body can contain a relatively flat section and then drop height toward the tail.

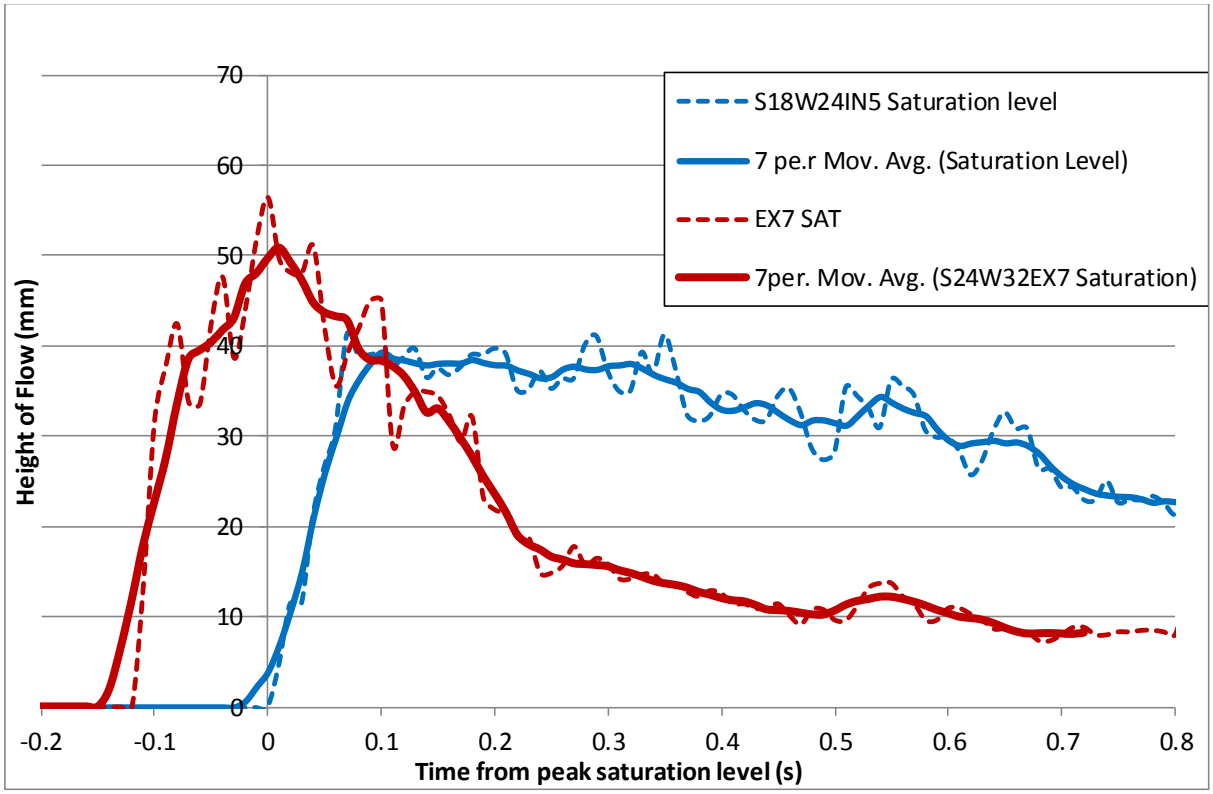

Figure 4-7: S18W24IN5 in blue and S24W32EX7 in red, height over time profiles. Time zero is the beginning of the saturation. The dotted line is the actual values the solid is a moving average of 7 points.

4.4.3. Saturation Level vs. Absolute Maximum Height

The height of the flow was taken from the still images at a rate of 0.01 s for the first 0.8 s after the images showed saturation. The absolute maximum is always greater than or equal to the saturation surface as seen in a typical height-over-time plot, Figure 4-8.

The saturation level is more consistent in shape for all the tests than the absolute maximum height which has more spikes due to the large intermittent particles. The absolute maximum before the saturation front might or might not have peaks in height and is sensitive to the light quality for interior experiments. The average saturation level is consistently between 5 and 10 mm lower than the maximum. The absolute maximum has much greater variability shown by the numerous large spikes oscillating around the moving average.

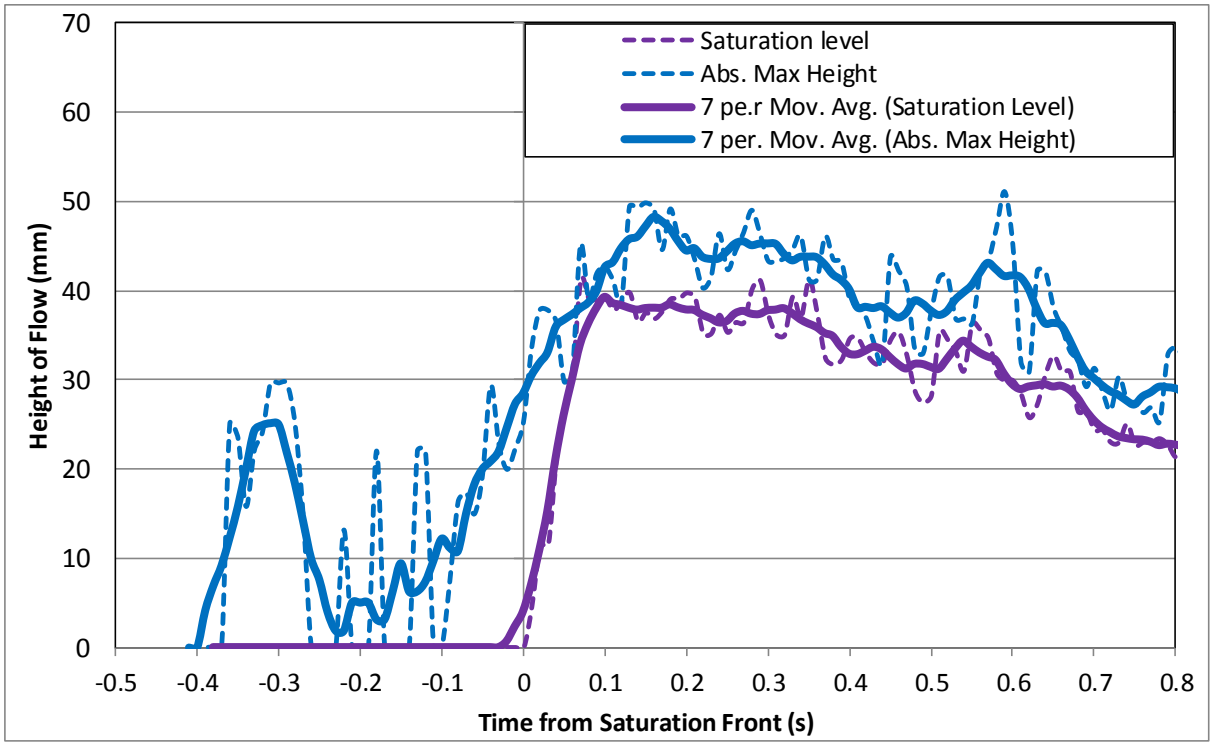

Figure 4-8: S18W24IN5 height over time profiles. Maximum in blue and saturation level in purple. Time zero is the beginning of the saturation. Note change in time scale to show maximum front.

4.4.4. Peak Saturation Level vs. Run-out Length

Figure 4-9 shows that there is no clear link between height of flow and run-out length. Some of the same flow heights gave very different run-out lengths. The slope and moisture content have a bigger effect on the run-out than the height. The slope appears to have less variability in peak saturation height, but that might be because of the sample size.

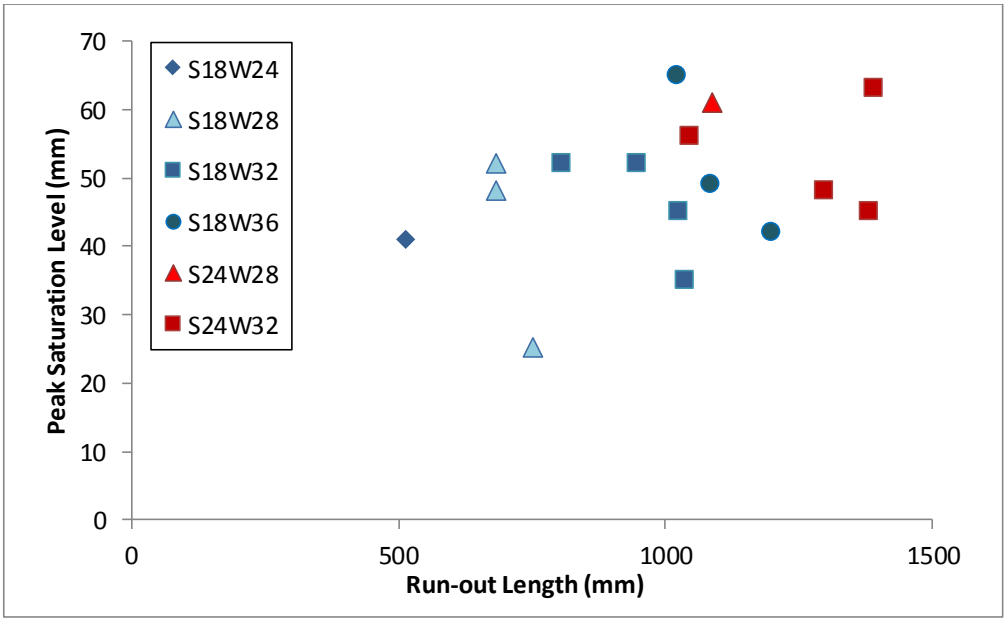

Figure 4-9: Peak Saturation level vs. run-out length.

4.5. Trends Relating to LOV, Moisture Content and Slope

4.5.1. Deposit LOV Comparison

The following pairs of tests were chosen to show the physical differences between interior and exterior LOV: S18W32IN2 vs. S18W32EX2, S18W36IN3 vs. S18W36EX3 and S24W32IN8 vs. S24W32EX9. These tests represent a selection of moisture contents and slopes.

4.5.1.1. Deposit

Shape

As LOV does not affect the flow at all there should not be any visible difference in deposit shape and length, any difference is therefore assumed to be from the inherent erratic nature of debris flows. Figure 4-10 shows the overlays of the deposits for the three pairs of LOV comparisons. In general the deposits are the same shape and have the same type of smooth or wavy edges. The exception is S18W32IN2 which had a much shorter run-out, comparatively S18W32IN2 has a shorter run-out than all test with the same slope and moisture variables and so is seen as an abnormality.

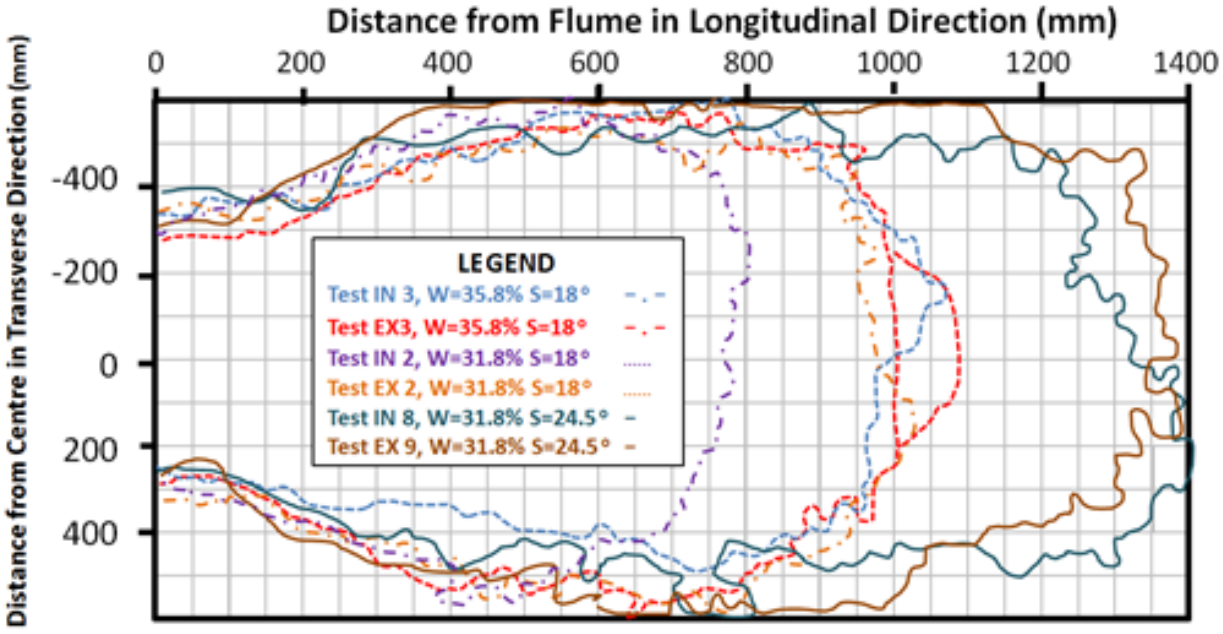

Figure 4-10: Comparison of deposit shapes between interior and exterior tests.

PSD

As LOV does not affect the flow at all there should not be any visible difference in deposit segregation. Any difference is therefore assumed to be from the inherent erratic nature of debris flows. The PSD curves (for example Figure 4-11) show that there was no visible difference that could not be attributed to the variation in sampling and general variability in deposit.

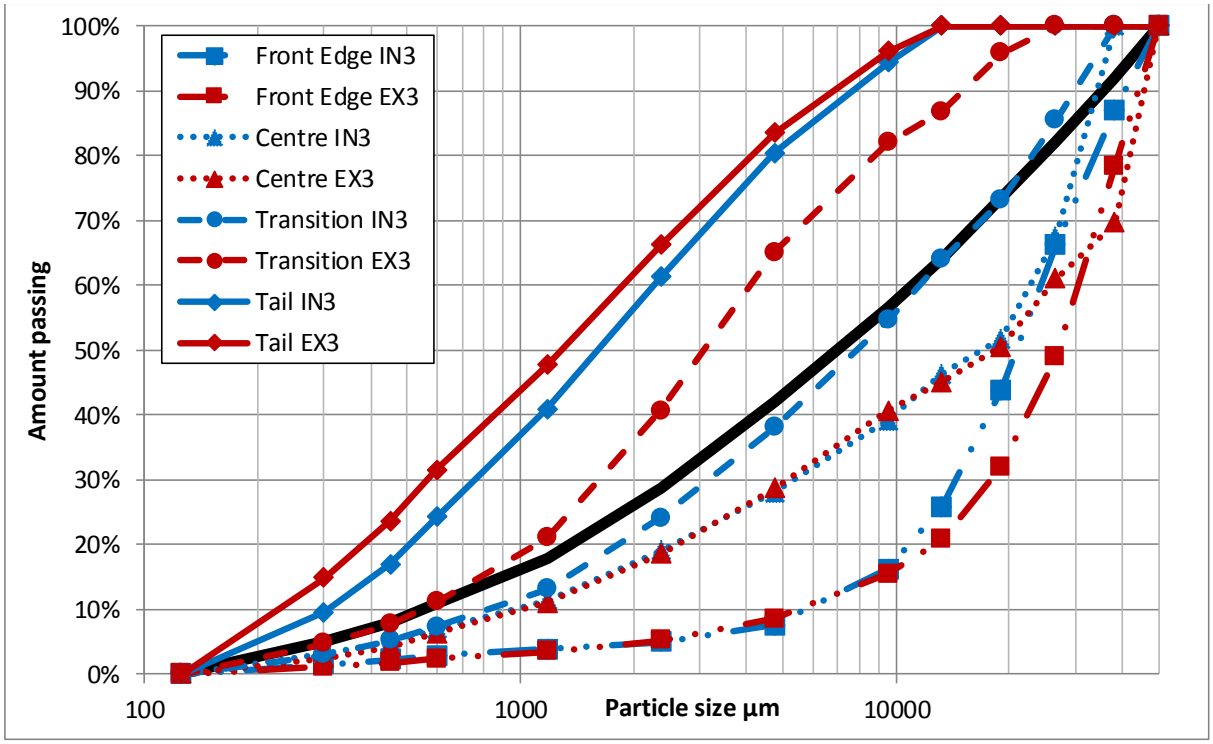

Figure 4-11: Graph of PSDs for various locations in the deposits of S18W36IN3 and S18W36EX3. Black line shows original PSD before experiment.

4.5.1.2. Height over Time

In general the height over time is similar or less for interior test than exterior tests. This is likely because of the boundary effect of the flume wall. Large particles cannot get close to the wall and there is friction along the wall as well as the base. This is likely to slow the material and so increase the height. This trend is the same for the absolute maximum and saturation levels as seen in Figure 4-12 and Figure 4-13. This has the following implication on PIV results. Because of higher depths in the exterior tests there is more depth to calculate velocity over which may mean it can reach higher maximum velocities. The flows unsaturated front being higher and faster might mean missing some of the fastest part of the flow as it is not saturated and so not visible.

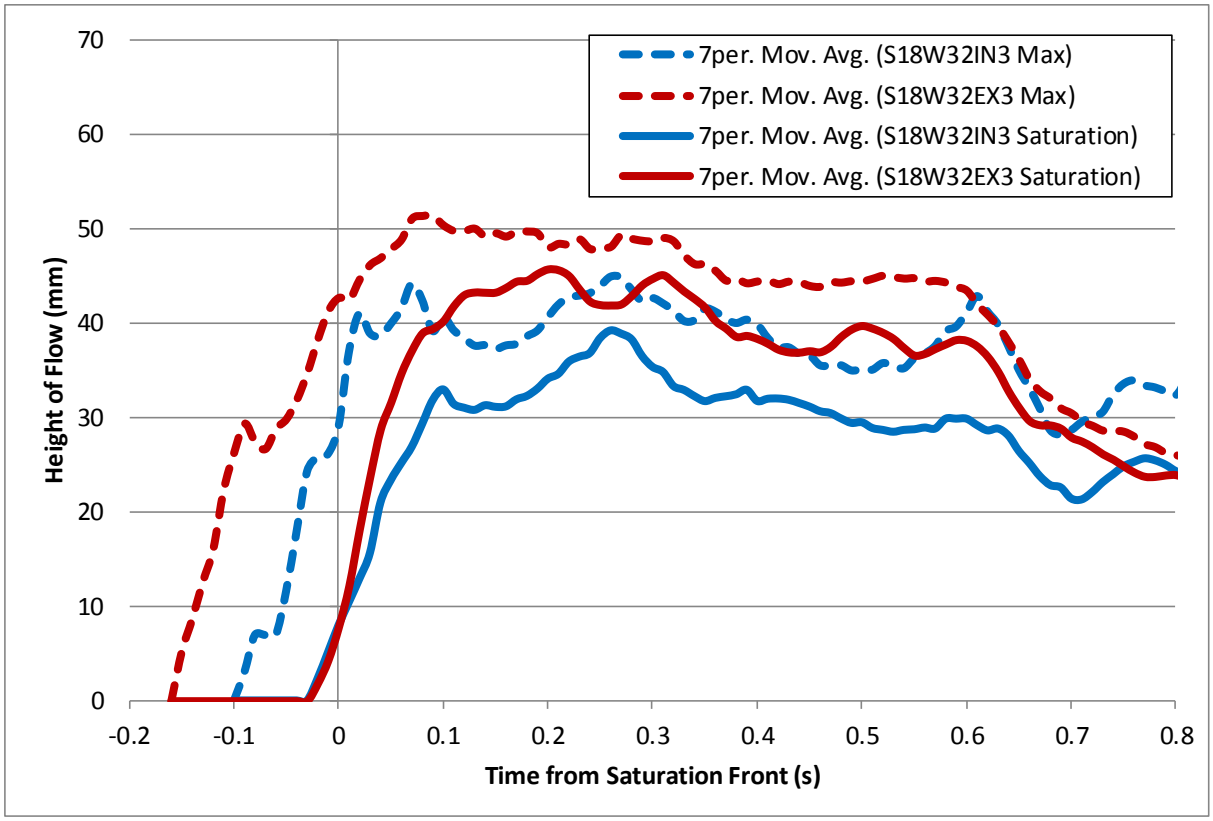

Figure 4-12: LOV Comparison of height over time. Maximum (dash) and saturation (solid) heights for S18W32IN3 vs. S18W32EX3.

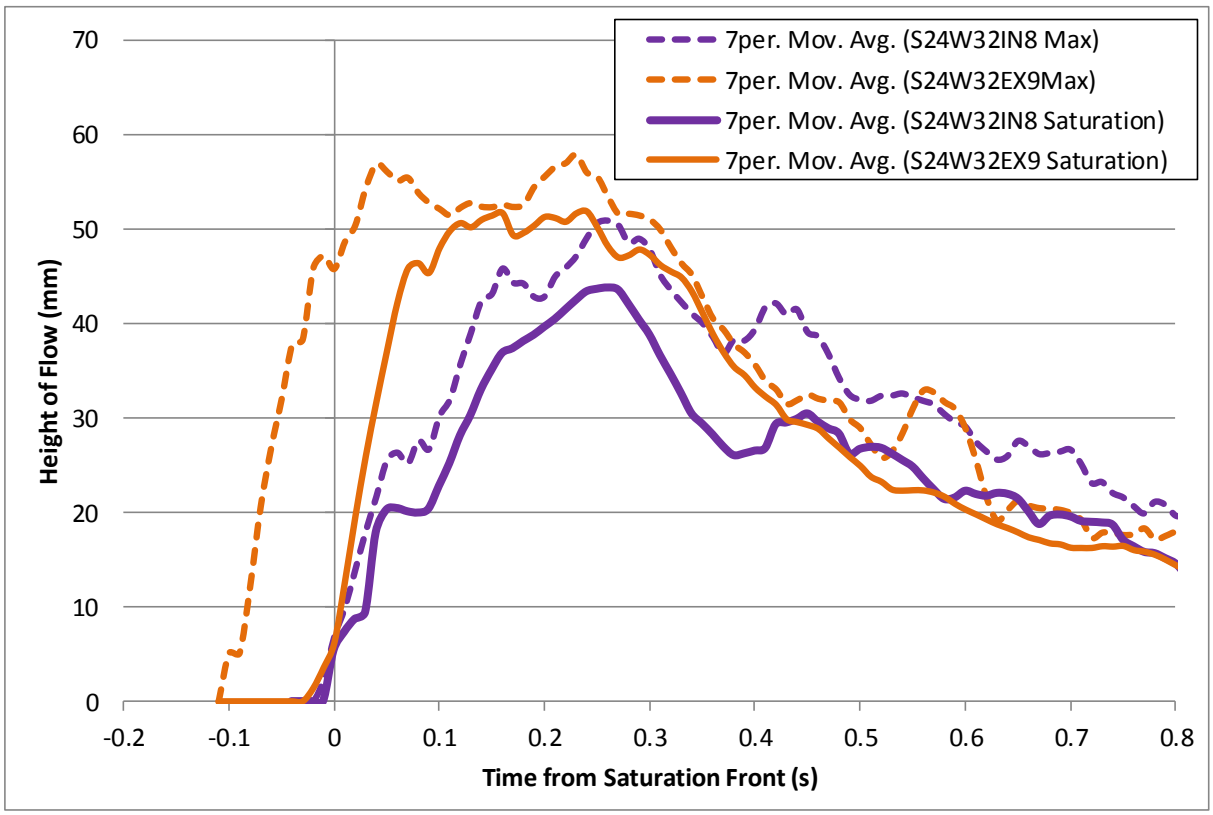

Figure 4-13: LOV Comparison of height over time. Maximum (dash) and saturation (solid) heights for S24W32IN8 vs. S24W32EX9.

The absolute maximum front is recorded as occurring earlier for the exterior tests. This could be one of two reasons; first in exterior test the fluidised section of the flow has a viscosity and so a no-slip condition or additional friction acting on the wall to delay the saturation front. The other more likely reason is that the PLIF technique is not able to illuminate the true interior front.

It does appear, however, that height over time is also dependent on flow development as some interior are greater than the exterior. This can be seen in Figure 4-14 where S18W32EX2 has a similar height over time and a lower peak than S18W32IN6. However, there were some issues with the interior tests deposit and flow characteristics. S18W32IN2 had a small run-out length and S18W32IN6 had a blockage and two front peaks. Both of these would suggest that the interior tests could have different front shapes.

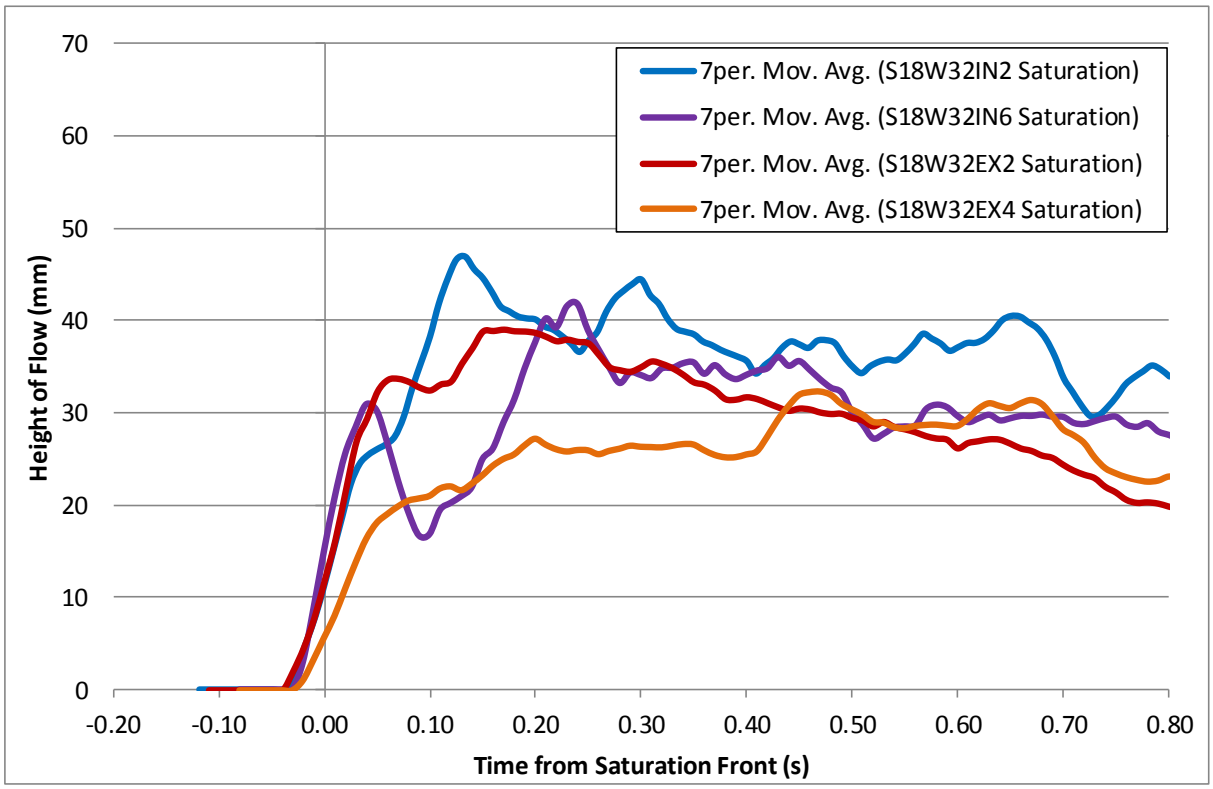

Figure 4-14: S18W32 Interior and Exterior tests. Height over time profiles are 7 point moving averages. Note: S18W32IN2 had a small run-out length and S18W32IN6 had a blockage and two front peaks.

4.5.2. Deposit Moisture Content Comparison

The following pairs of tests were chosen to show the physical differences caused by changing the moisture content: S18W24IN5, S18W28IN4, S18W32IN2 and S18W36IN3. All tests are interior and at the lower slope of 18.1°.

4.5.2.1. Deposit

Run-out Length

The moisture content shows a reasonably linear relationship to the run-out length presented in Figure 4-15. The statistical regression (R^2) value of 0.89 indicates that there is a good fit to the data over the range tested. The relationship indicates an increased run-out of approximately 200 mm for each 4% increase in moisture content.

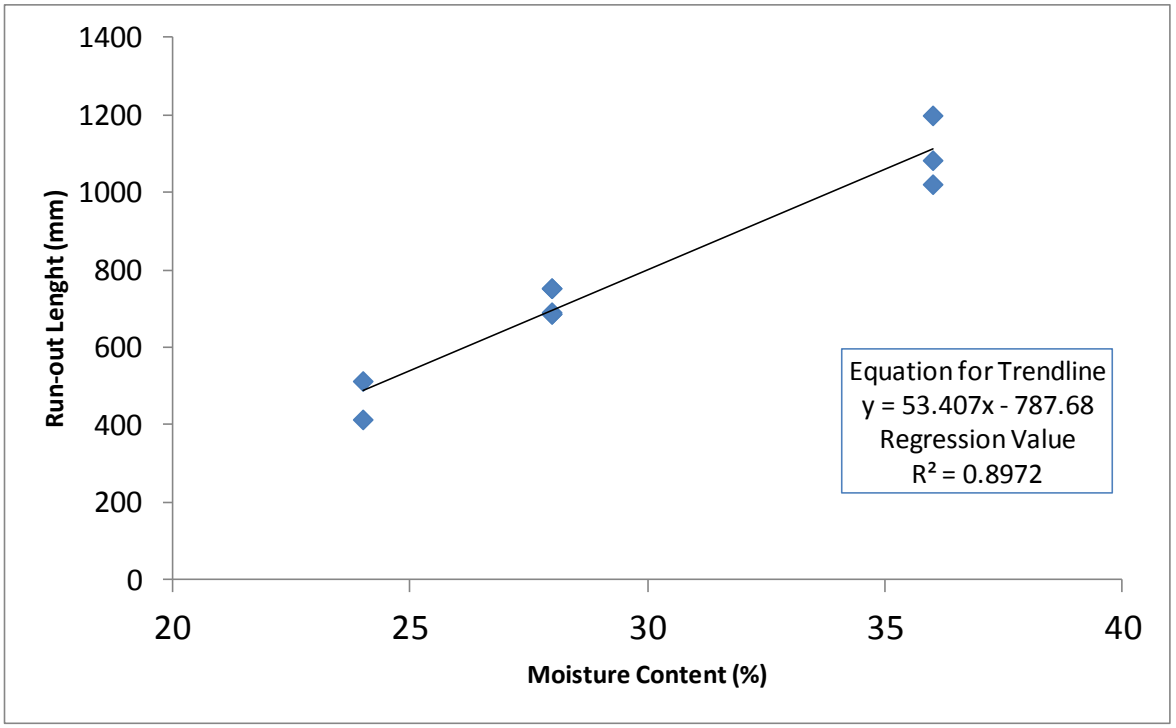

Figure 4-15: Run-out length vs. moisture content, for all tests conducted at slope of 18.1 °.

Shape

The maximum run-out lengths presented in Table 3-1 show that as moisture content increases so does the length of run-out. This appears to be approximately linear based on the average run-out length. The 35.7% moisture content had the most variability with the exterior tests giving lower than expected run-outs. The shapes also become wider with moisture content but the waviness of the edges seems to remain the relatively the same.

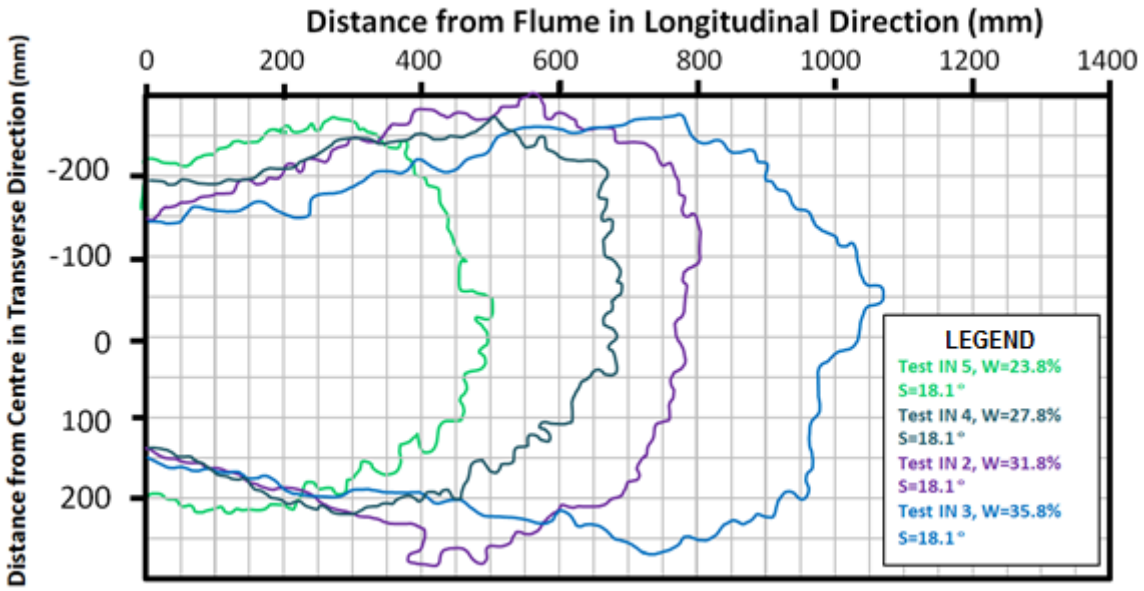

Figure 4-16: Comparison of deposit shapes for change in moisture content.

PSD

The PSDs in Figure 4-17 shows only the tail and front edge. Given the inherent variability in the centre and the transition points these were not plotted. The tests show that there is a small trend but overall the curves remain the same shape. The higher moisture contents gave a finer curve for both tail and front edge while the lowest moisture content was coarser. It is likely that as there is more fluid more of the fine particles are mixed in to the fluid phase and are so concentrated in the more fluid parts of the flow.

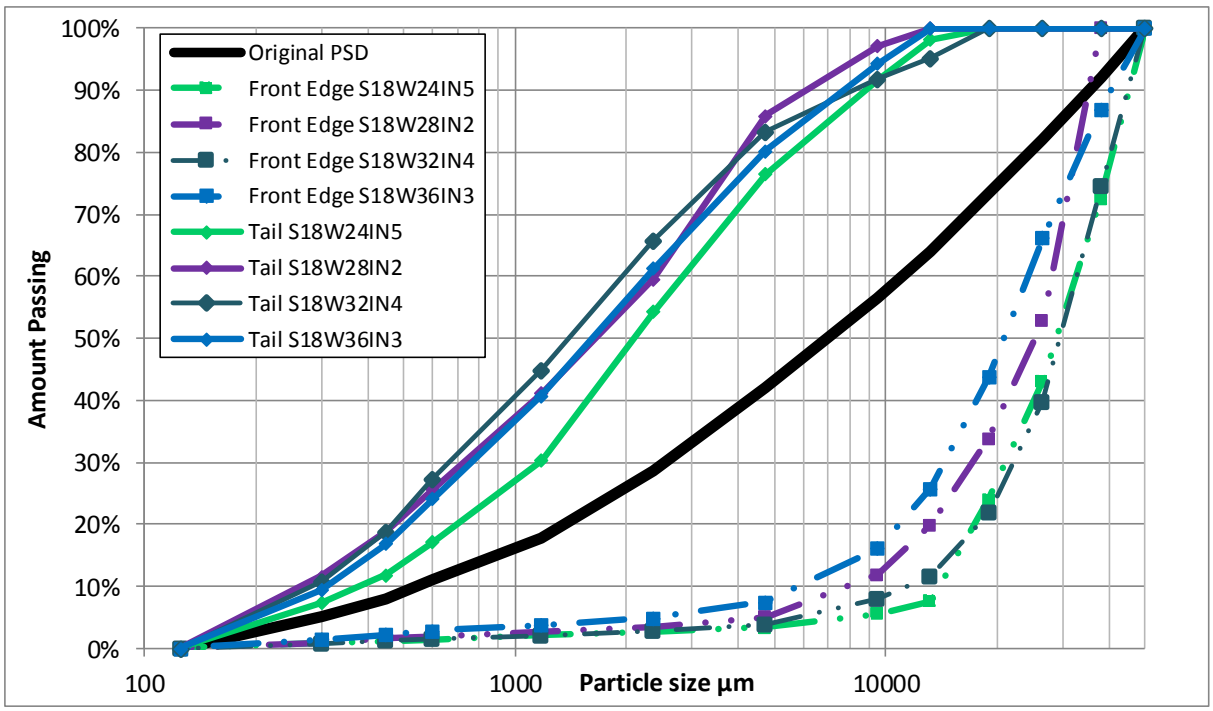

Figure 4-17: PSD's at tail and front edge of S18W24IN5, S18W28IN2, S18W32IN4 and S18W36IN3.

4.5.2.2. Height over Time

The shape of the height over time curve for all moisture contents is consistent, particularly for the saturation level (Figure 4-18). There is large degree of natural variation within moisture content which makes obtaining a trend in shape difficult. For example S18W36IN3, when compared to other exterior tests of the same slope and moisture content, has a lower flow height than expected. Just considering the other tests and the trend in peak heights shown in

Table 4-2 the higher the moisture content the higher the average absolute maximum and peak saturation height. Even though all of the moisture content profiles in Figure 4-18 are approximately the same, they give consistently different run-out lengths. This might show that the peak height of the flow does not give an indication of deposition. This is only true where the volume of the flow is the same. Suggesting that volume of flow should be investigated to determine if it is the leading factor determining peak height.

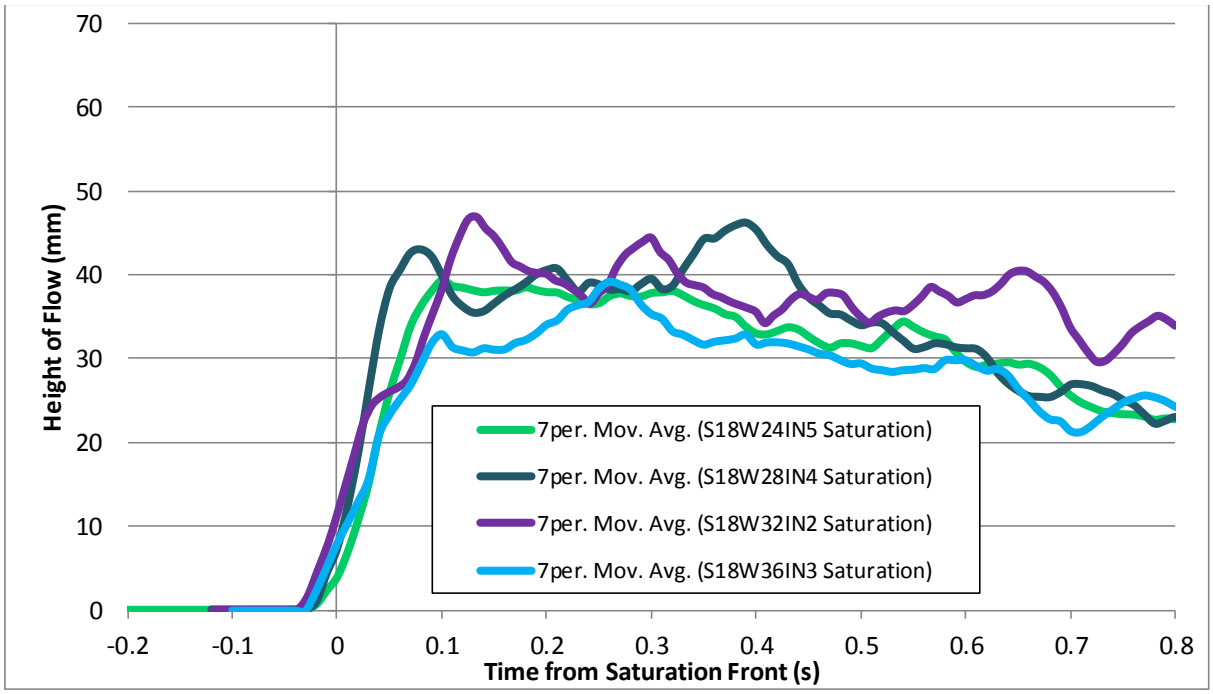

Figure 4-18: Saturation level using a 7 point moving average. Note S18W36IN3 was found to have lower height than expected.

The steepness of the saturation and maximum fronts in Figure 4-18 and Figure 4-19 is difficult to see. However, by considering the trends in times between the peak and fronts of the flow presented in Table 4-3 a trend is apparent. As the moisture content increases the times between the start of the front and the peak saturation height increases. This suggests that the front is less well defined and does not form the same barrier to the fluid as moisture content increases.

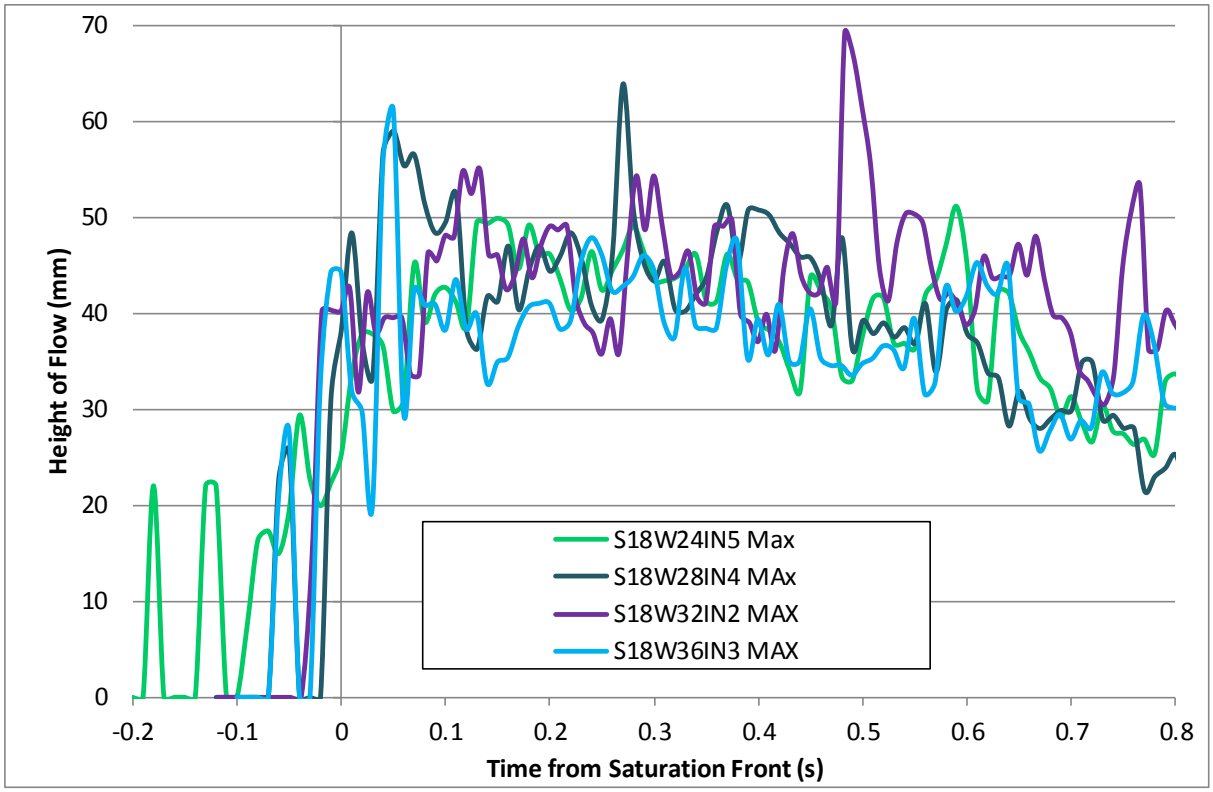

Figure 4-19: Real Absolute maximum heights sampled ever 0.01 s. showing erratic nature of real flow. Note S18W36IN3 was found to have lower height than expected.

It appears that the higher moisture contents also had the highest fluctuations in real measurements. In terms of absolute maximum height, the lowest moisture content varies less than 20 mm between peak and trough shown in Figure 4-19. In contrast, the highest moisture content varies by 40 mm between peak and trough. This suggests that more moisture increased the movement of large particles to the surface.

4.5.3. Deposit Slope Comparison

The following pairs of tests were chosen to show the physical differences caused by changing the slope: S18W32IN2 vs. S24W32IN8 and S18W32EX3 vs. S24W32EX9. One pair is exterior the other is interior; all tests are at a moisture content of 31.7%.

4.5.3.1. Deposit

Run-out Length

Even though there are only two slopes in Figure 4-20 the spread of the run-out values caused by the natural variation in testing is not so large as to obscure the increasing trend in run-out with slope.

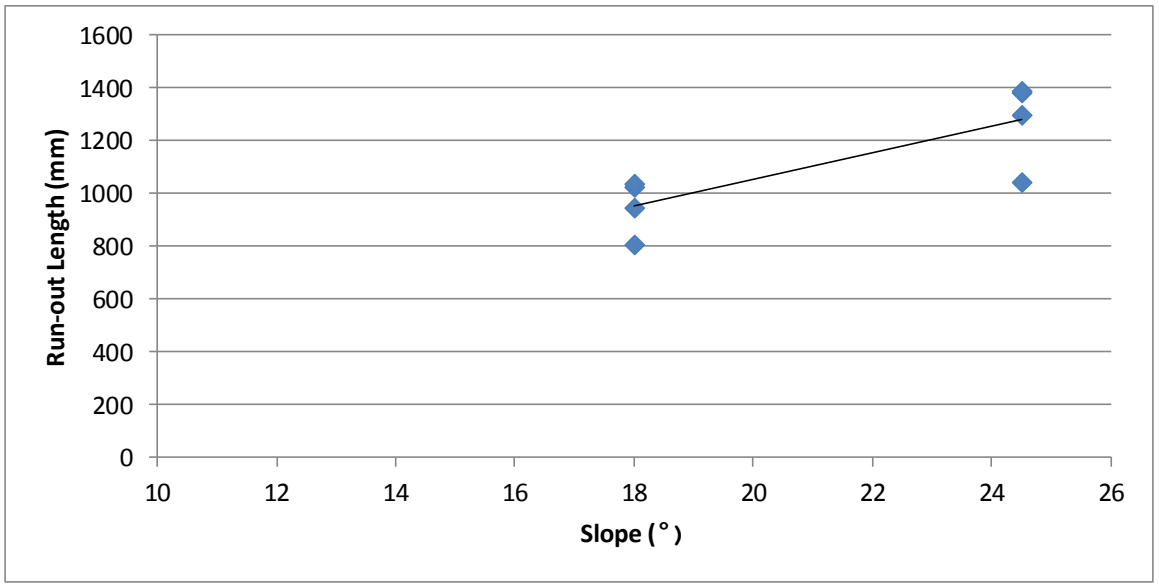

Figure 4-20: Run-out length vs. Slope, for four tests conducted at slope of 18.1 ° and four tests conducted at slope of 24.5 °.

Shape

Figure 4-21 shows that deposits become elongated and wider with a higher slope. For the higher slope, the front edge has a more erratic shape and the deposit touches the walls of the run-out deck. The deposit is also more spread out and thinner for the higher slope and there is still material on the flume itself so the volume has been spread over a larger area rather than all being deposited toward the front.

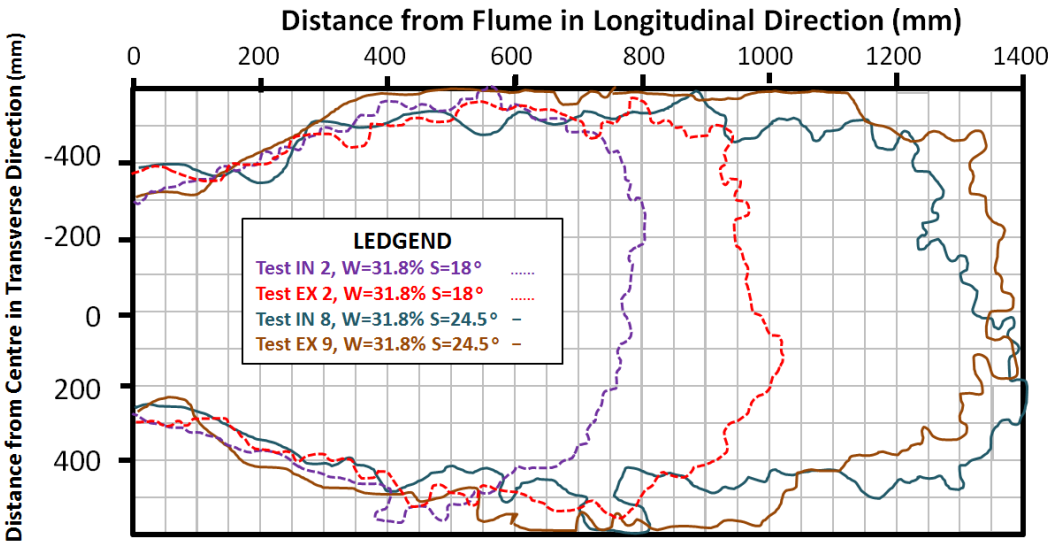

Figure 4-21: Comparison of deposit shapes for change in slope.

PSD

The PSD curves, in Figure 4-22, show that the deposits are similar. There is a small trend in the front and tail edges showing more segregation at a higher slope. This is likely a result of the thinning of the deposit making the segregation phenomena clearer.

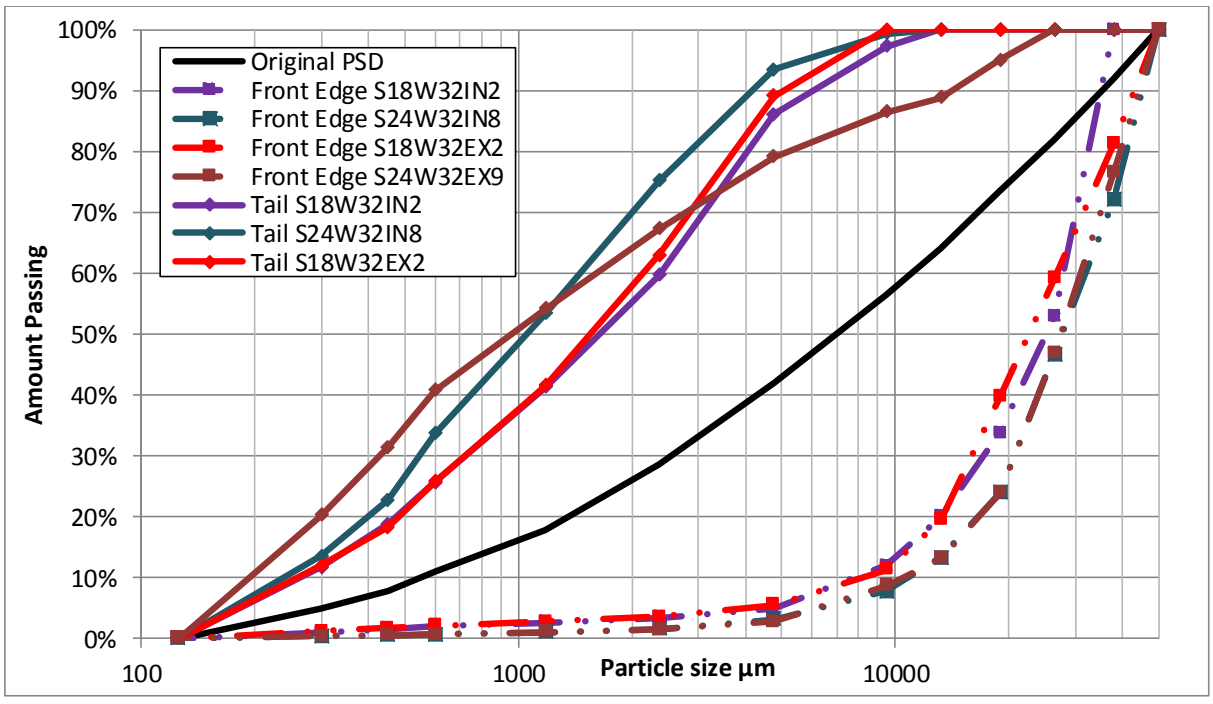

Figure 4-22: PSD comparisons for Slope 18.1° and a moisture content of 31.8%.

4.5.3.2. Height over Time

Figure 4-23 shows that there does not appear to be a trend in the level of erratic behaviour of the real absolute maximum height between the two slopes. This suggests that an increase in slope did not significantly promote the movement and transport of large particles to the surface of the flow.

Figure 4-24 looks at the moving average of the maximum height it shows that the exterior maximum was higher for a higher slope and the interior comparison gave similar flow heights. It is possible that S24W32IN8 did not develop fully. There is nothing in the deposit behaviour to support this but it does have a longer time between trigger and flowing past camera and the other high-slope moisture contents do not have as large a time difference between peak and saturation front.

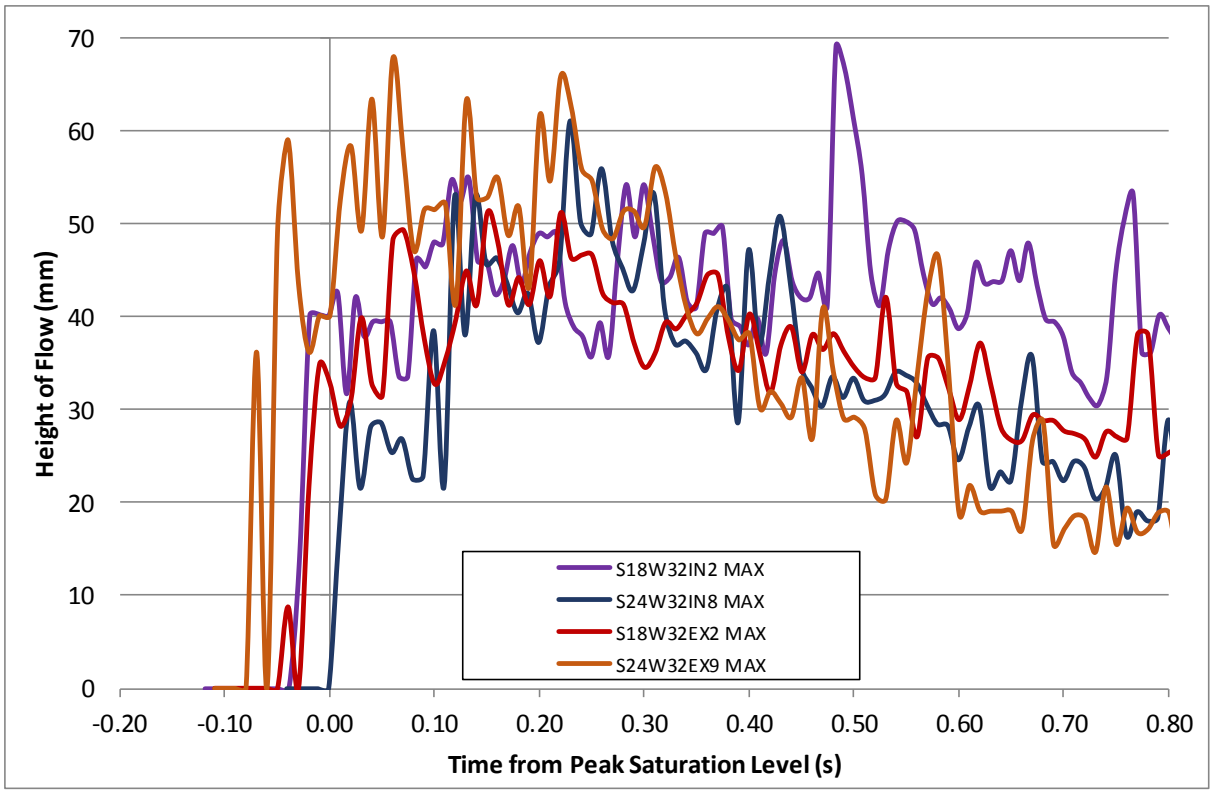

Figure 4-23: Real absolute maximum heights sampled ever 0.01 s. showing erratic nature of real flow.

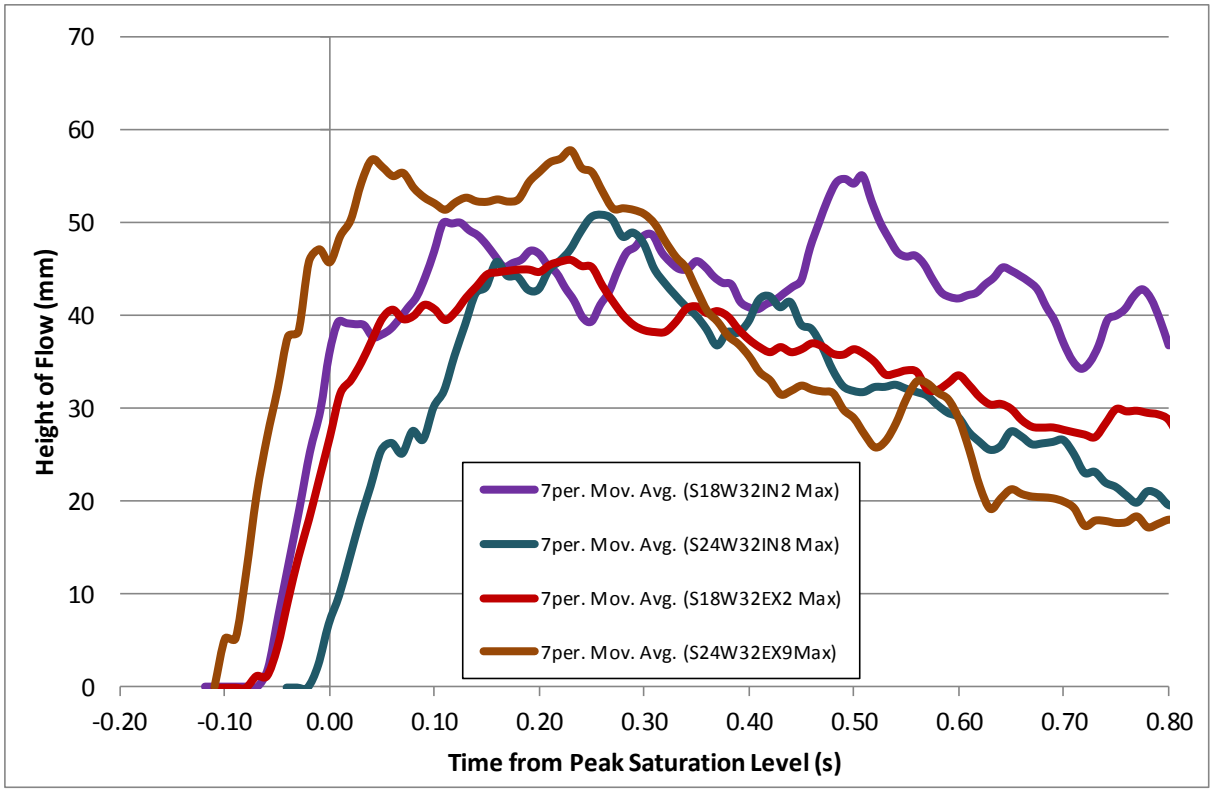

Figure 4-24: Comparison of height of absolute maximum height over time as a result of changes in slope. Tests shown are S18W32IN2 (green) vs. S24W32IN8 (purple) and S18W32EX2 (red) vs. S24W32EX9 (tan).

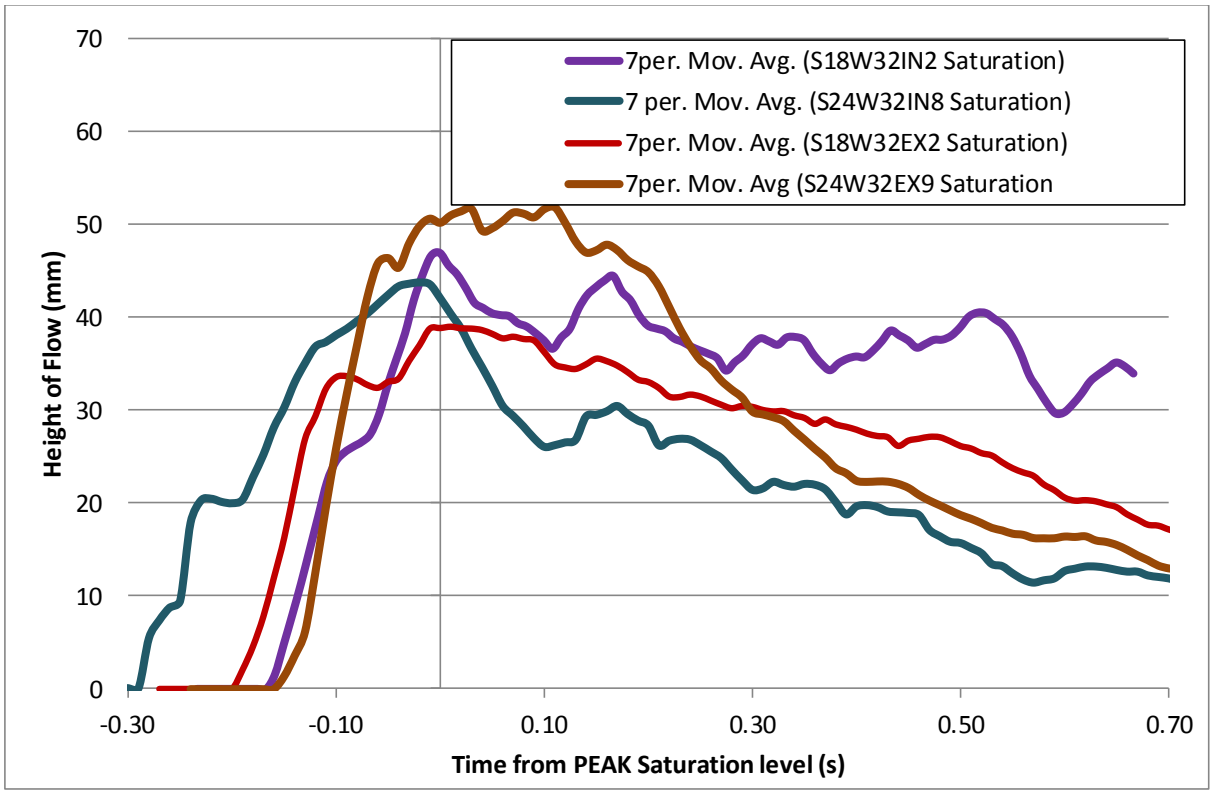

Figure 4-25: Comparison of height of saturation level over time as a result of changes in slope. Time scale changed so that peak height is aligned to time = 0 s. Tests shown are S18W32IN2 (green) vs. S24W32IN8 (purple) and S18W32EX2 (red) vs. S24W32EX9 (tan).

Figure 4-25 aligns the peak saturation levels so that they all occur at time equals zero. This allows comparison of peak height and shape of the front. The shape of the fronts is steeper for the higher slopes apart from S24W32IN8. The body height of the higher slope tests drop off quicker than the lower slope and have a lower average tail height. From Table 4-3 the time between peak saturation height and the absolute front is approximately 0.18 s for the lower slope and 0.2 for the higher. Once the peaks are shifted to overlap it is evident that the interior tests show a similar or lower peak saturation level and the exterior show an increase in height for the higher slope. This could be linked to increased friction at the flume wall increasing the height whereas within the flow this is not affected and there could be thinning of the saturation heights within the material as a super critical flow the height decreases with higher flow rates. This will be investigated further in conjunction with the PIV velocity and flow results.

4.6. General Behaviour of PIV Results

The shape of the velocity profiles, with depth, is generated at a specific time from the peak saturation level. This allows the profiles to be located in terms of front, body and tail for the flow. The velocity profiles are relatively consistent between locations in different flows. They do, however, change with respect to the location within the flow, mainly between the body and the tail. The reliability or quality of the data presented in the profiles can also be subject to depth of flow, patch size and variations in the saturation surface level. This section outlines the fluctuations and errors; the general behaviour over time of the depth-averaged velocity and, evolution in velocity profile shape.

4.6.1. Fluctuations and Errors (notes to interpretation of results)

The main sources of fluctuations are based on the variation picked up in PIV analysis. This is a reflection of the patch size and can be removed by increasing the patch size. It can be beneficial to note that the velocity is not smooth and there are small scale fluctuations occurring within the flow. The error bars in Figure 4-26 are based on a single standard deviation and show that as the fluctuations in the profiles increase then so does the error. It appears that the 16 and 32 pixel patches have more consistent error bands. The large patch size looks to have suppressed the fluctuations suggesting that the fluctuation scale is less than

32 pixels for this test using the Miro camera; in real scale this would be approximately 5.2 mm.

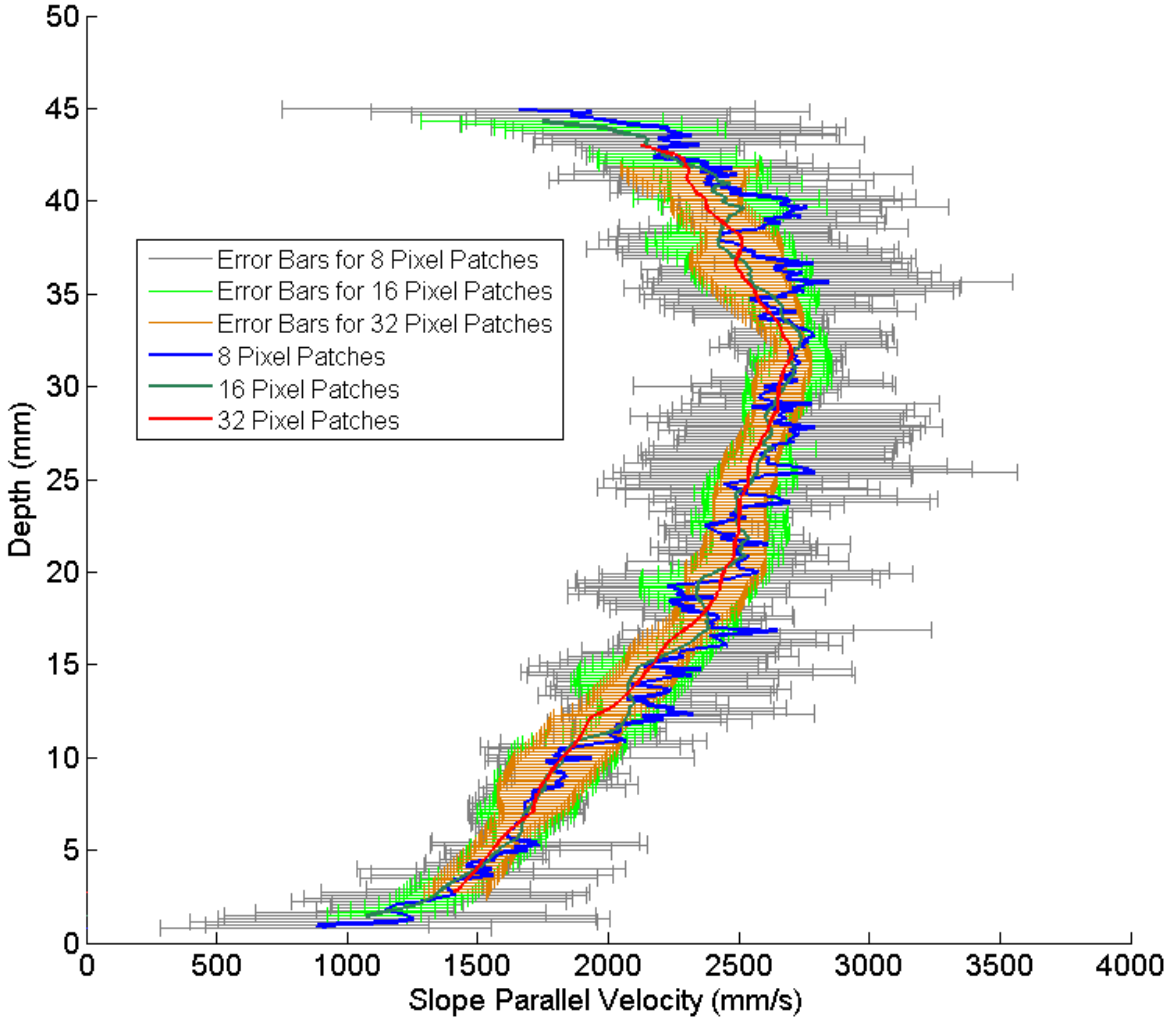

Figure 4-26: S24W32IN8 front velocity profile. Profiles include error bars at one standard deviation from the mean. Analyses using 8, 16 and 32 pixel sized patches are presented.

The bottom of the flow typically less than 5 mm is unable to be evaluated based on the patch overlapping with the stationary base of the flow. Depending on light intensity at the base of flow there may be some distortion of the base velocities. Figure 4-27 shows a blurred edge to the base common to most images particularly the front and body where the flow is rapidly changing. This distorting can result in a slower than true velocity as the patches pick up the stationary lower edge of the image.

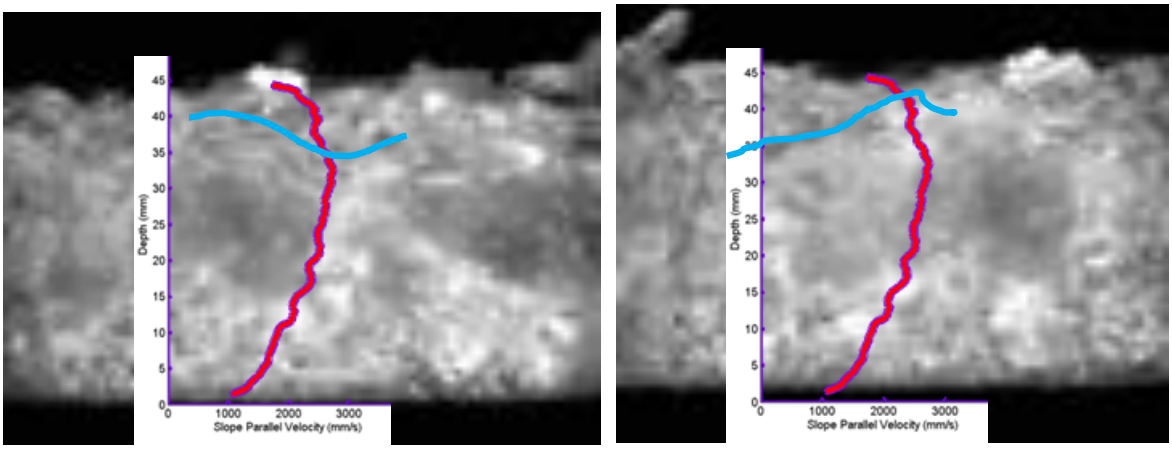

Figure 4-27: Images of peak flow for S24W32IN8, highlighting areas of multiple rippling saturation surfaces. (Left) first image in batch. (Right) last image in batch. Both images are overlaid with the velocity profile. The blue line indicates the lowest saturation level in rippled surface.

A similar issue to the base of the flow is the top of the flow. Most velocity profiles showed a curve back at the top of the profile (Figure 4-27). There are two reasons for this; areas of turbulence or fluctuations in saturation level between images. It can be difficult to identify a consistent saturation level due to the turbulence at the top of an image. This can create shadows that are similar to those produced at the saturation level. Also the saturation level changes between images in a batch. The saturation level in the body sections, particularly where the saturation level is close or the same as the absolute maximum height, can change rapidly so images pick up stationary area above the free surface or reflections of other particles not in the LOV.

4.6.2. PIV Summary Tables

Table 4-4: Maximum Saturation Peak Velocity

	Moisture Content			
Experiments	***23.8% (mm/s)***	***27.8% (mm/s)***	***31.8% (mm/s)***	***35.8% (mm/s)***
Slope 18.1° Interior	*1800 (S18W24IN5)*	*2030 (S18W28IN1)* *1850 (S18W28IN4)*	*1850 (S18W32IN2)* *2350 (S18W32IN6)*	*2100 (S18W36IN3)*
Slope 18.1° Exterior		*1450 (S18W28EX1)*	*2030 (S18W32EX2)* *1910 (S18W32EX4)*	*1850 (S18W36EX3)* *2200 (S18W36EX5)*
Slope 24.5° Interior			*3070 (S24W32IN7)* *2740 (S24W32IN8)*	
Slope 24.5° Exterior		*2400 (S24W28EX8)*	*4600 (S24W32EX7)* *3200 (S24W32EX9)*	

Table 4-5: Mean Saturation Peak Velocity

	Moisture Content			
Experiments	**23.8% (mm/s)**	**27.8% (mm/s)**	**31.8% (mm/s)**	**35.8% (mm/s)**
Slope 18.1˚ Interior	1285 (S18W24IN5)	1530 (S18W28IN1) 1560 (S18W28IN4)	1430 (S18W32IN2) 1900 (S18W32IN6)	1820 (S18W36IN3)
Slope 18.1˚ Exterior		1270 (S18W28EX1)	1610 (S18W32EX2) 1540 (S18W32EX4)	1360 (S18W36EX3) 1770 (S18W36EX5)
Slope 24.5˚ Interior			2780 (S24W32IN7) 2250 (S24W32IN8)	
Slope 24.5˚ Exterior		1530 (S24W28EX8)	3320 (S24W32EX7) 2400 (S24W32EX9)	

Table 4-6: Minimum Slip Velocity

	Moisture Content			
Experiments	**23.8% (mm/s)**	**27.8% (mm/s)**	**31.8% (mm/s)**	**35.8% (mm/s)**
Slope 18.1˚ Interior	800 (S18W24IN5)	1200(S18W28IN1) 975 (S18W28IN4)	1000 (S18W32IN2) 956 (S18W32IN6)	1240 (S18W36IN3)
Slope 18.1˚ Exterior		947 (S18W28EX1)	220 (S18W32EX2) 46 (S18W32EX4)	270 (S18W36EX3) 761 (S18W36EX5)
Slope 24.5˚ Interior			2530 (S24W32IN7) 1074 (S24W32IN8)	
Slope 24.5˚ Exterior		198 (S24W28EX8)	407 (S24W32EX7) 745 (S24W32EX9)	

Table 4-7: Maximum Flow Rate

	Moisture Content			
Experiments	**23.8% (m^3/s)**	**27.8% (m^3/s)**	**31.8% (m^3/s)**	**35.8% (m^3/s)**
Slope 18.1˚ Interior	0.009 (S18W24IN5)	0.010 (S18W28IN1) 0.007 (S18W28IN4)	0.004 (S18W32IN2) 0.007 (S18W32IN6)	0.007 (S18W36IN3)
Slope 18.1˚ Exterior		0.004 (S18W28EX1)	0.010 (S18W32EX2) 0.007 (S18W32EX4)	0.009 (S18W36EX3) 0.010 (S18W36EX5)
Slope 24.5˚ Interior			0.009 (S24W32IN7) 0.014 (S24W32IN8)	
Slope 24.5˚ Exterior		0.013 (S24W28EX)	0.027 (S24W32EX7) 0.022 (S24W32EX9)	

4.6.3. Height over Time

When looking at the heights of PIV analysis there are two heights that correspond to the velocities calculated. The first is the reduced height after patches are removed because of overlap with flow outside the saturation level which is the 'highest recordable patch height'. The second is the height at which the slope-parallel velocity is at its maximum. The "height of maximum velocity" could be a better indication of the true height once errors associated with variation in saturation level are accounted for. The highest recordable patch height and height of maximum velocity generally flow the same trend but the height of maximum velocity is lower. Both show that the height follows the trends in the physical heights shown in previous sections.

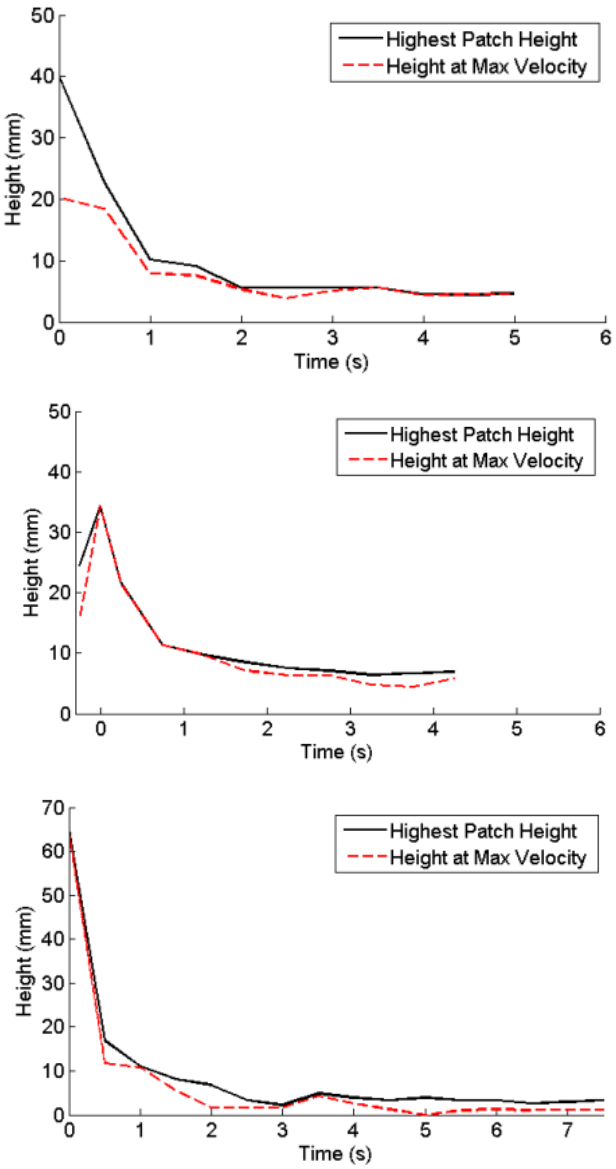

Figure 4-28: Height with time curves used in PIV analysis. (Top) S18W32EX2, (centre) S18W36IN3 and (bottom) S24W32EX9 (changed scale).

4.6.4. Velocity over Time

For the depth-averaged velocity over time, Figure 4-29 shows that all of the tests have a similar shape where they decrease rapidly with time as the front passes. The maximum follows the average curve with less of a gap than the minimum. The minimum is relatively large for the first second and then approaches zero. This shows the body has a slip velocity and the tail does not.

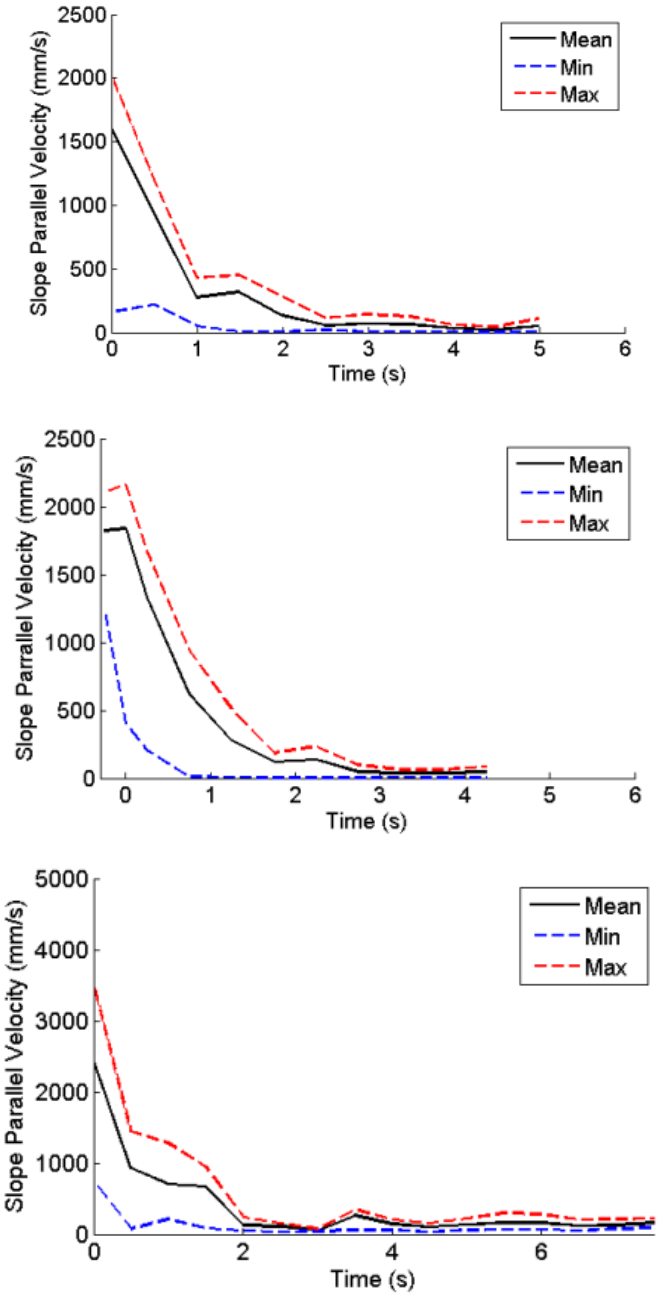

Figure 4-29: Velocity with time curves (top) S18W32EX2, (centre) S18W36IN3 and (bottom) S24W32EX9 (changed scale).

It was found that the maximum velocity followed that same trend as the mean depth-averaged velocity and generally always occurred near the peak saturation height. However, Figure 4-30 shows that the maximum and average velocities do not necessarily have a clear relationship with height. In some cases the highest flows were the slowest. The flow velocity is there for relatively independent of the height of the flow. The fastest flows do tend to be those with the higher slope and moisture level however the mean velocity is particularly erratic for these tests.

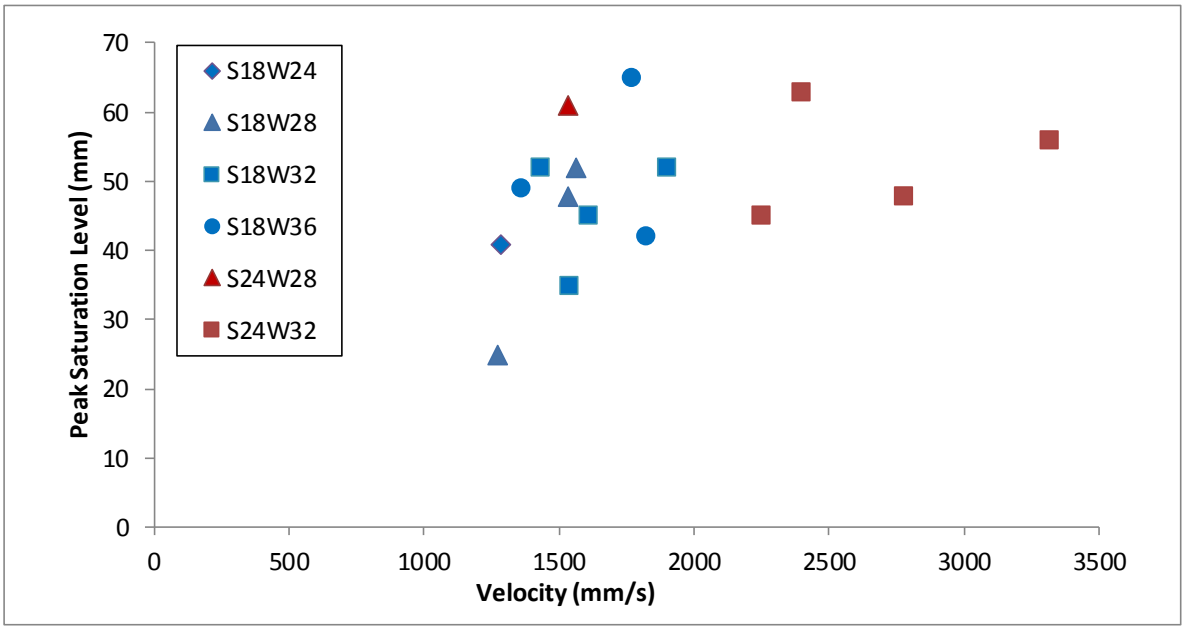

Figure 4-30: Scatter of mean velocity vs. peak saturation height of flow used to determine if there is a relationship between peak depth and velocity.

The velocity has a better relationship to run-out length (Figure 4-31) than the height of flow does to run-out length shown in Figure 4-9. It is still not clear if the relationship is linear or a square of the velocity. The slope shows a higher level of variation in velocity suggesting that the peak depth-averaged velocity may be harder to sample accurately. Test S24W32IN7 appears to be an outlier in terms of having a very fast flow for this material. Slope was seen to have a big influence on velocity

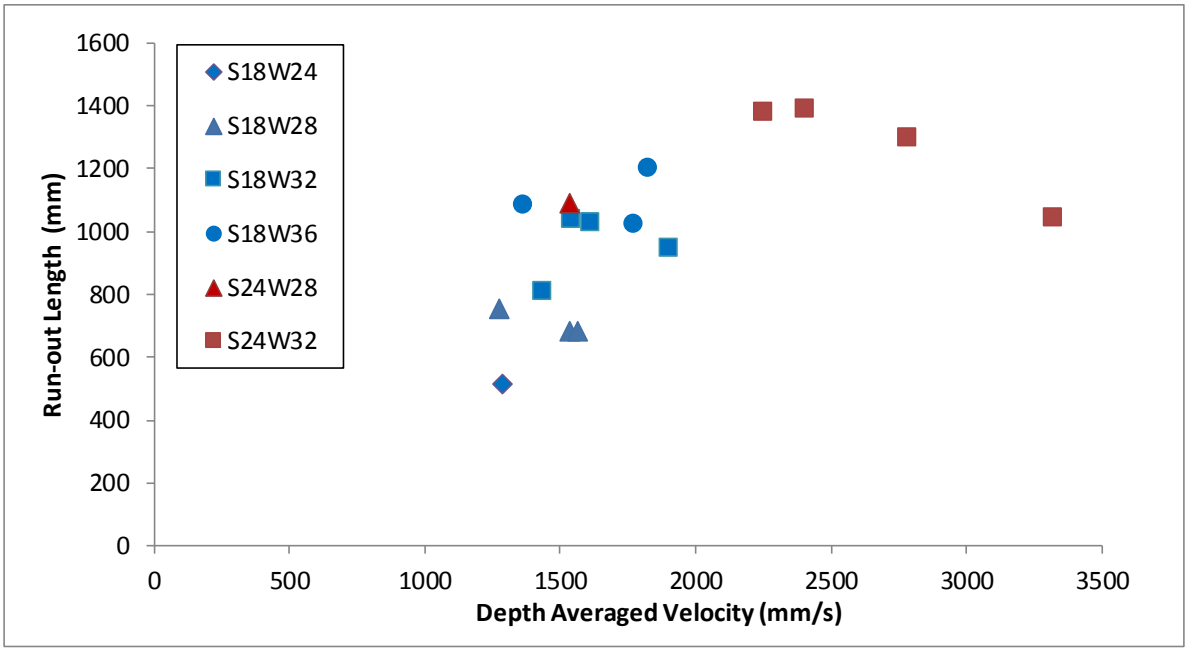

Figure 4-31: Scatter of Depth-averaged velocity vs. Run-out length used to determine if there is a relationship between run-out and velocity.

4.6.5. Flow Approximation over Time

Because both the height and velocity profiles over time have steep peaks which drop off rapidly the flow as the product of the two also has a very steep peak and relatively negligible flow rate after the body passes. This indicates a single surge flow due to the limited length and material in the laboratory tests. Figure 4-34 shows typical normalised flow profiles with time they all have a step peak which drops completely off by the 2nd second of flow, there is minimal flow after this as the tail drains downslope. The main peak is over after the first second. The fist second contains the bulk of the material in the body but perhaps there is a secondary more uniform body that is not stretching and maintains a relatively consistent flow.

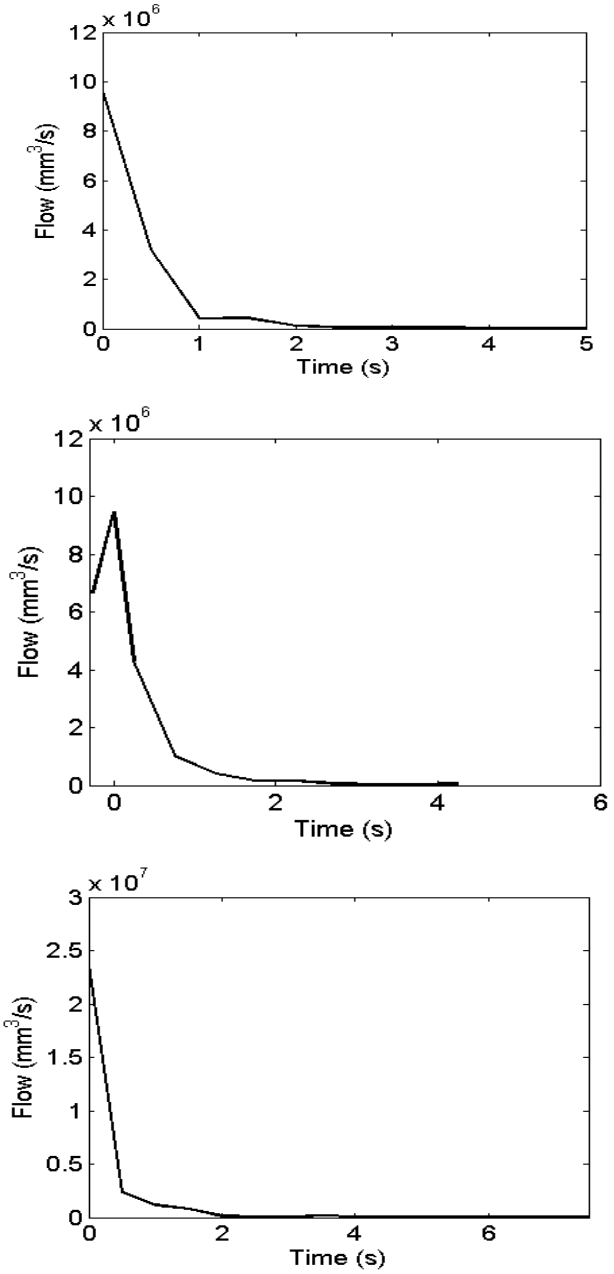

Figure 4-32: Flow curves (top) S18W32EX2, (middle) S18W36IN3 and (bottom) S24W32EX9.

4.6.6. Velocity Profile Evolution

Figure 4-33 shows three flow profiles from a high slope test at the front the body and the tail. Where possible the profiles were analysed at the very front of the body. The front of the body was fast and acted over a large depth. They often had a large slip velocity. At the middle and end of the body the profiles were shorter but still have the same shape of curve with a small apparent slip. At the tail the profiles became short and slow have no slip. Depth had a significant impact on the maximum velocities but less on the shape of the profiles and the average velocities.

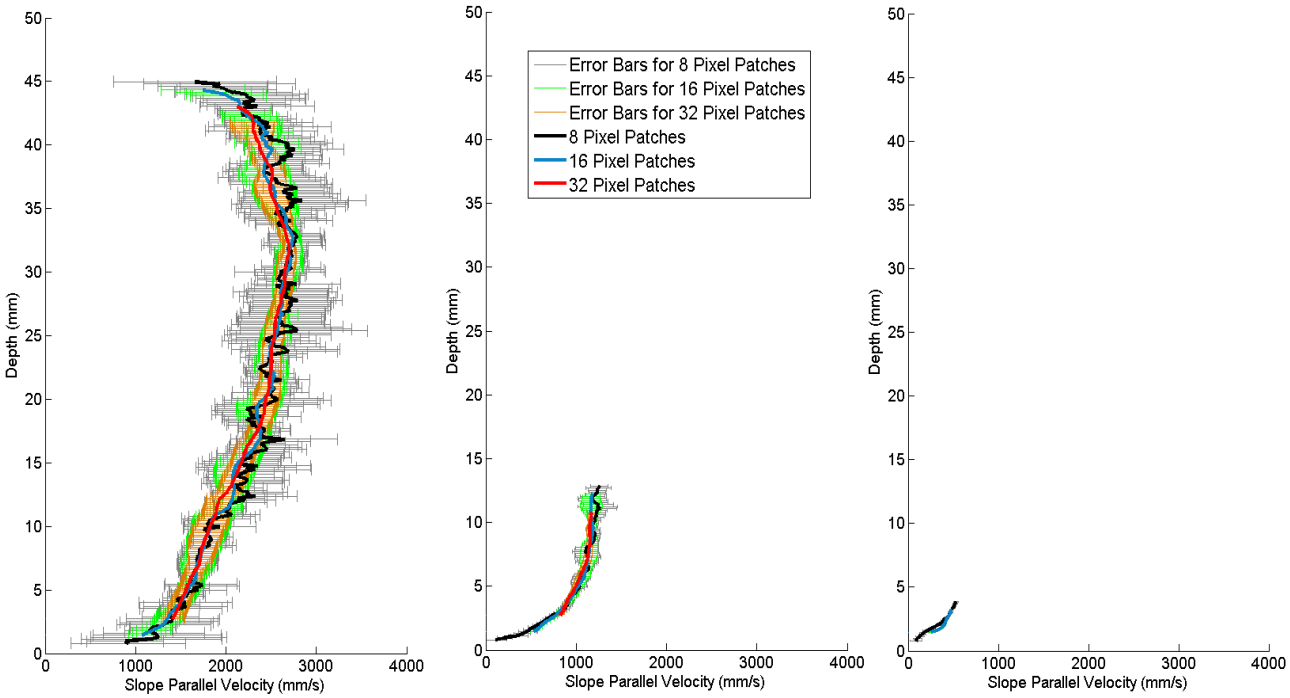

Figure 4-33: S24W32IN8 velocity profiles. (Left) Peak saturation (t = 0 s). (Centre) Body (t = 0.5 s). (Tail) Body (t = 2.5 s). Error bars show one standard deviation either side of the mean. The tail does not have 32 pixel patch profile as the depth was less than the patch size.

Figure 4-34 and Figure 4-35 show the normalised plots for two flows over time. They show two distinct shapes and profiles that appear to transition between the two shapes. The first type shows more shear at the base with a more uniform velocity at the top of the profile. These profiles correspond to the body of the flow which has the highest depths and the most rapid change in shape with time. The second type shows the height and velocity is more linearly related. These profiles correspond to the tail where the height of flow is more uniform. These flow sections are investigated separately to identify general flow characteristics and any abnormalities.

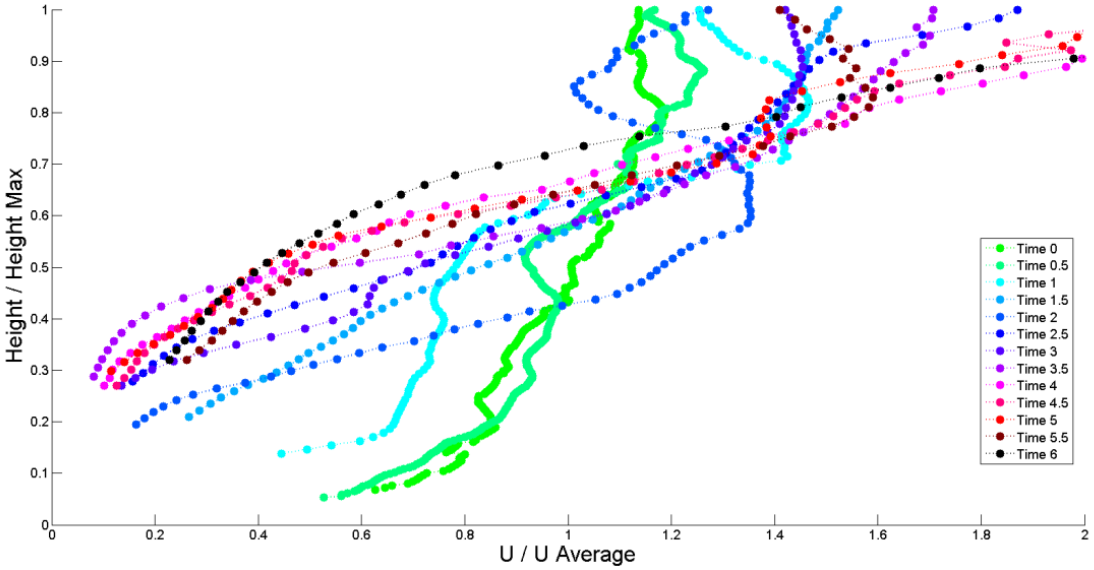

Figure 4-34: S18W28IN4 normalised velocity profiles.

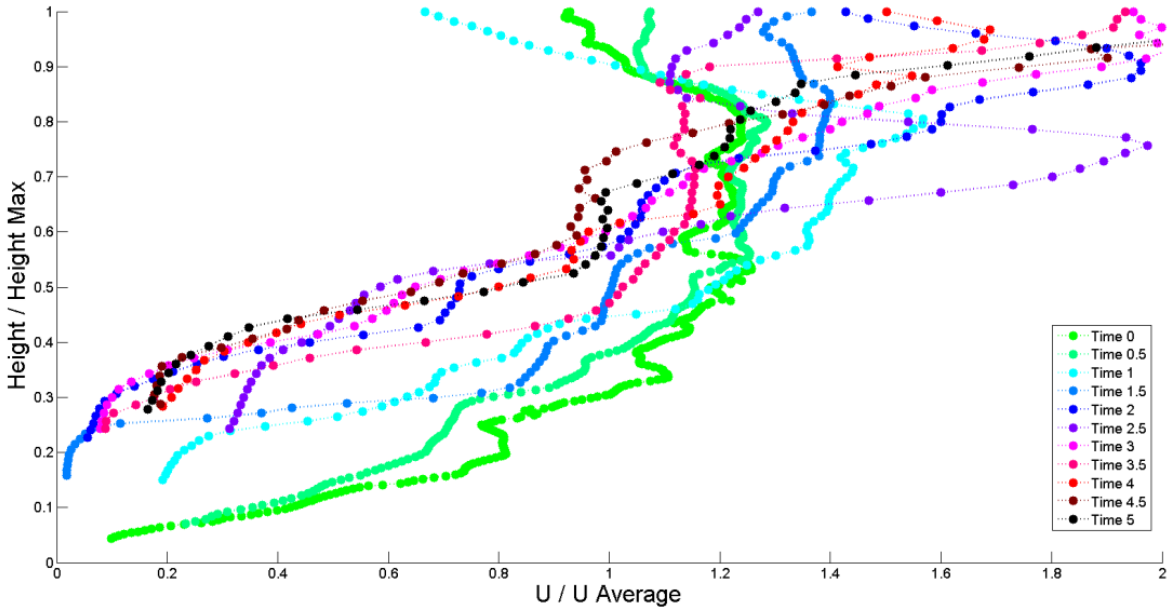

Figure 4-35: S18W32EX2 normalised velocity profiles.

4.6.6.1. Front

Figure 4-36 demonstrates the relationship between the front and the body of the flow. They show a profile in the front, the peak and a profile in the body 0.5 s after the first profile. These are all 18.1° tests and the middle two show an interior and exterior test at the same moisture content. In every case the maximum velocity is greater for the front compared to the body. However, in many cases the velocity profile is similar for the front to the peak. For S18W36IN3, S18W36EX5 and S18W32IN2 the velocity profiles overlap but S18W28IN4 is

faster. The reason is partly because of the larger time step between the peak and the front in S18W28IN4 and partly because (looking at the height over time) the peak occurred well after the steep front for S18W28IN4. In this case the -0.5 s is more likely the point at which the dry front ends and the saturated body starts.

For the other test in Figure 4-36 the shape is very similar. There is slightly more uniformity in the top of the front profiles with higher slip or boundary layer at the base. This is because the front is dryer and the particles are more likely to slide, bounce and roll.

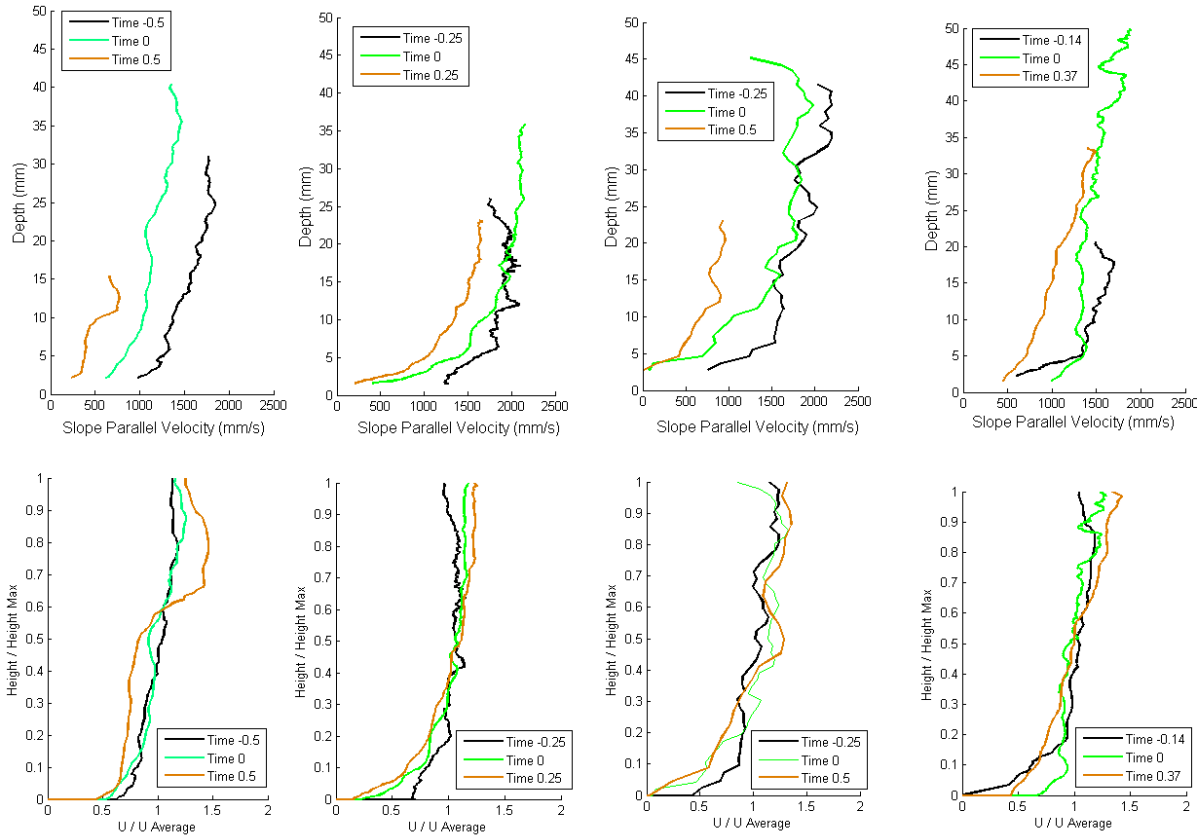

Figure 4-36: Left S18W28IN4 left centre S18W36IN3, right centre S18W36EX5 right S18W32IN2. (Top) Profiles (bottom) Normalised plots

Figure 4-37 shows the front and start of the body for two of the 24.5° slope tests. The front velocities are limited in analysis by the depth of saturation but from the assumption based on Figure 4-36 the dry sections are travel at the same velocities as the saturation from and the profiles are uniform in the top section of the profile (Figure 4-38). This assumption is logical otherwise the dry front would segregate from the flow if it were travelling faster. For the velocity profiles occurring before the peak there appears to be more fluctuations in the velocity which reduces once in the body. The normalised profiles are similar but as the maximum velocity of the peak profile (in blue) can be higher or the same as the dry front we see the top conveying material over the top. The velocity would be higher for the unsaturated

particles at the top of the flow, because they are barely visible this could not be captured and measured.

Overall the front appears to be travelling at a similar speed to peak of the saturation level and so the dry front does not segregate from the main flow. This supports the elongation of the body and the shortness of the front which does not travel faster and so does not elongate.

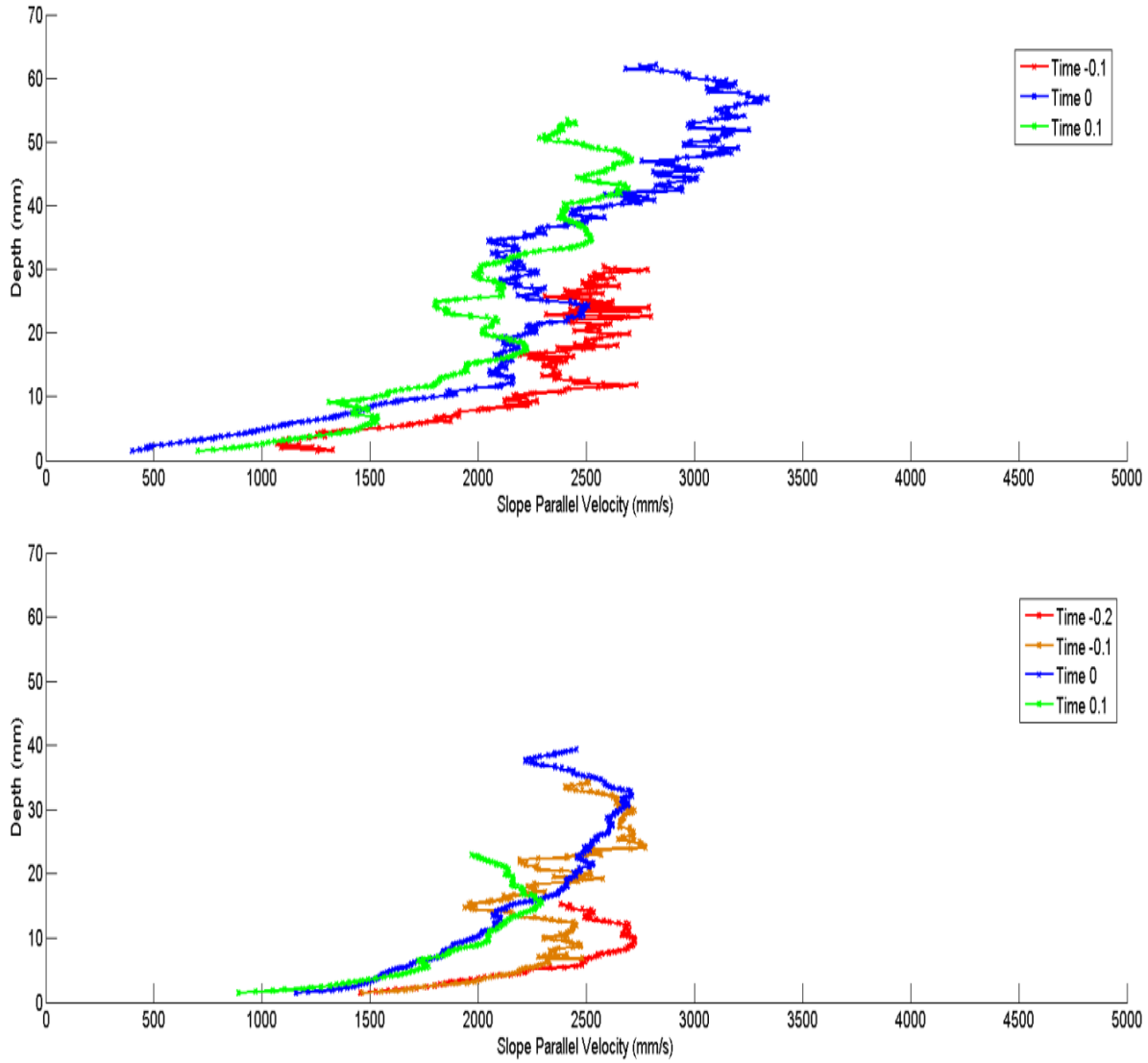

Figure 4-37: Front and first body profiles of S24W32EX9 (top) and S24W32IN8 (bottom).

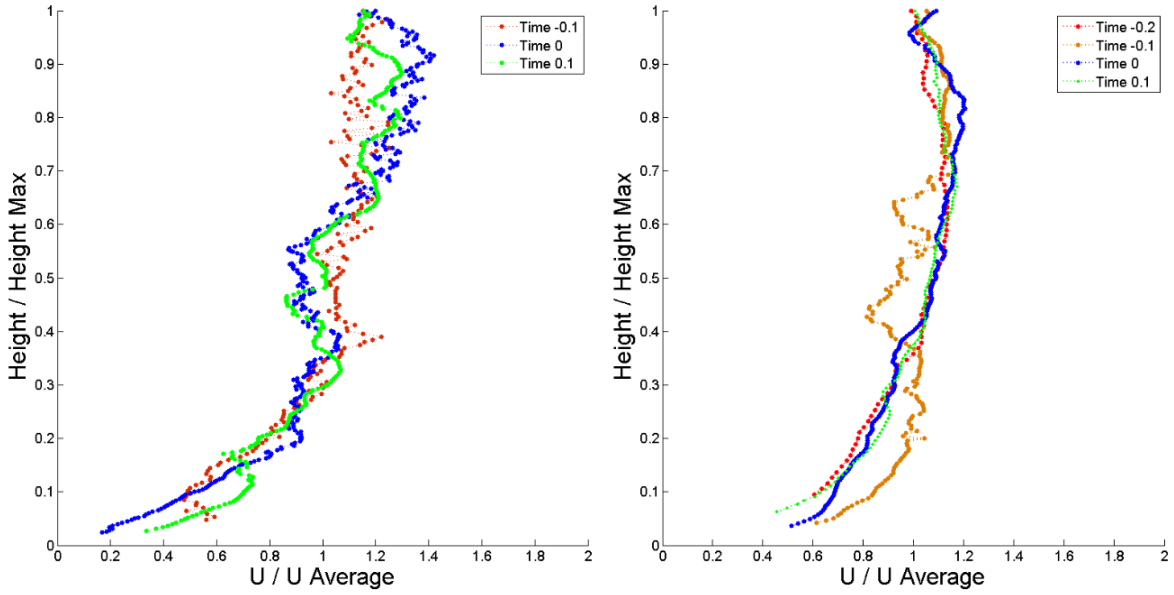

Figure 4-38: Normalised front and first body profiles of S24W32EX9 (left) and S24W32IN8 (right).

4.6.6.2. Body

The body of the flow represents the bulk of the flow material. Figure 4-39 and Figure 4-40 show velocity analysis just on the body of S24W32IN8 and S24W32EX9 respectively. These are both 24.5° slope test they are evaluated at 0.01 s intervals for the front (where able) and the first 0.5 s after the peak saturation level. The higher slope had a shorter body passing within the first 0.5-0.7 s. The lower 18.1° slope tests body passed between 0.5 and 2 s. The body height velocity and flow decayed rapidly after the peak in nearly every test.

Figure 4-39 and Figure 4-40 show that in the body the height and flow increased in the front peaked and dropped off within the first 0.5 s of the body. The velocities are more constant over the front and then drop off. The minimum velocity drops to less than 500 mm/s within the first 0.5 s showing that the body has slip but only over the short body.

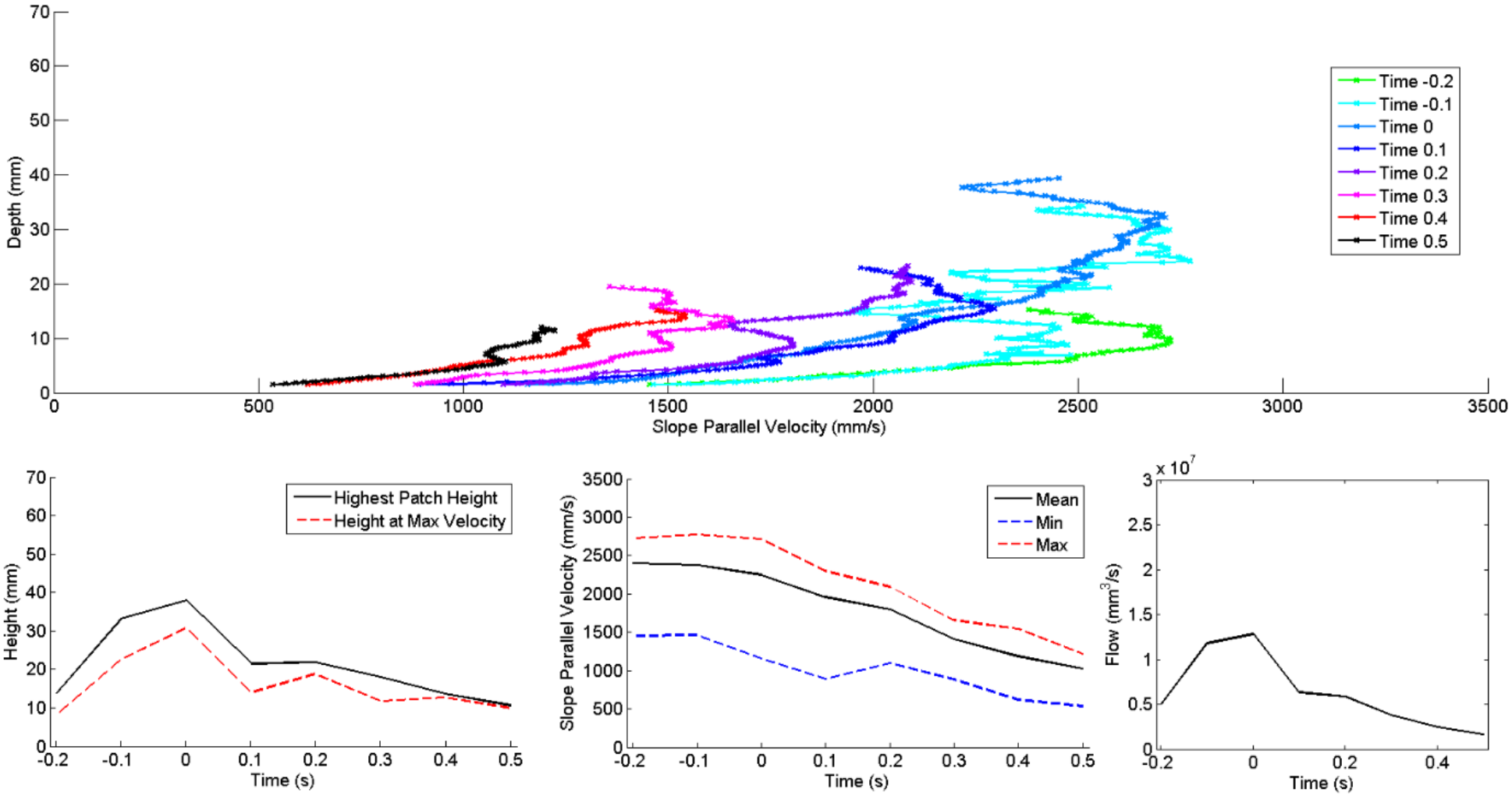

Figure 4-39: Body of S24W32IN8. Velocity profiles (top), (left) height over time from PIV analysis, (centre) velocity over time and (right) flow approximation.

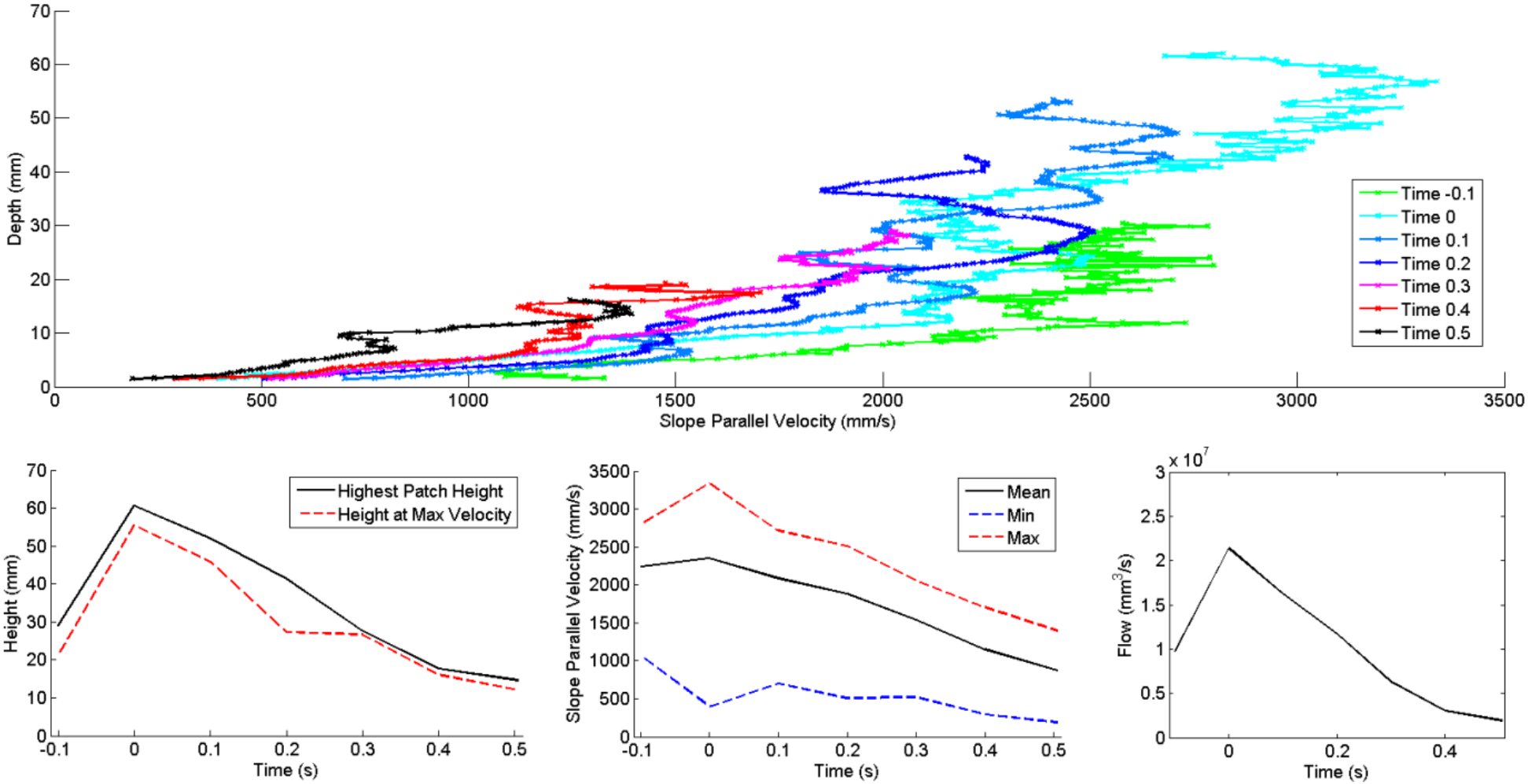

Figure 4-40: Body of S24W32EX9. Velocity profiles (top), (left) height over time from PIV analysis, (centre) velocity over time and (right) flow approximation.

4.6.6.3. Tail

Figure 4-34 and Figure 4-35 show the normalised velocity plots for the whole flows but from 2 s onward the shape has evolved into a much more linear shape with a distinct curving toward zero at the bottom of the profile. This shows that the flow is settling at the bottom of the flume and is likely to have a zero slip velocity.

Figure 4-41 shows the tail flow for S18W32IN6 which shows well behaved self-similar velocity profiles over a relatively constant height and flow velocity. The profiles at 1 and 1.5 s are transition from body and while the same shape has higher heights and velocities. This flow has the same normalised shape as seen in most of the tail flows.

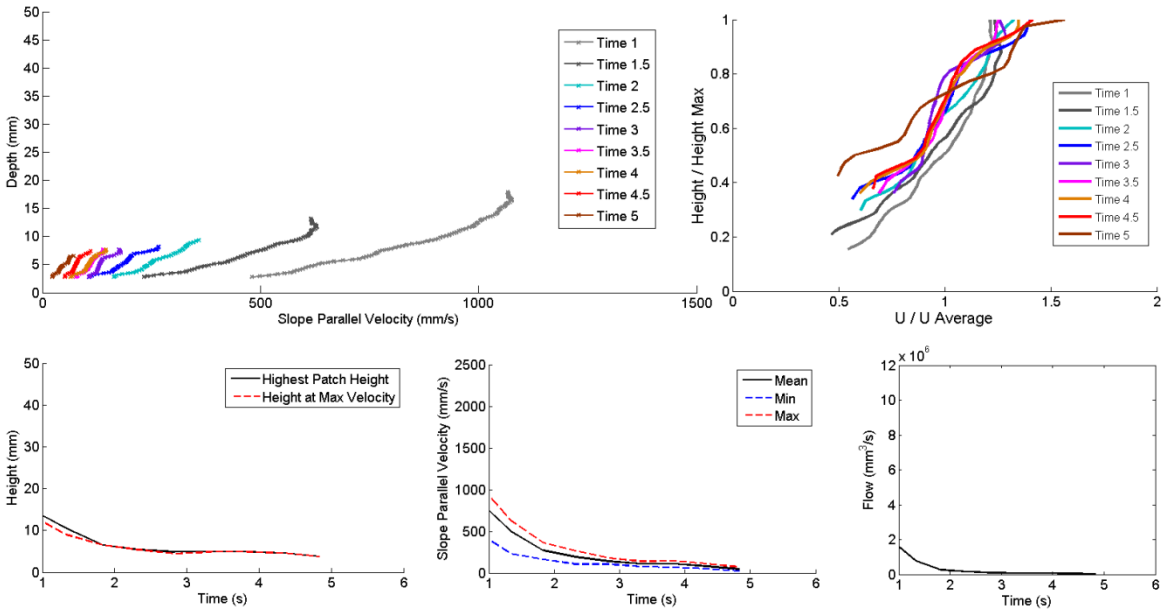

Figure 4-41: Tail flow of S18W32IN6 with (top left) velocity profiles, (top right) normalised profiles, (bottom left) height over time, (bottom centre) velocity over time and (bottom right) flow approximation. All flow before 1 s has been removed.

4.6.6.4. Drainage Paths

Some of the experiments showed a zone of faster flow through the middle of the tail section. Figure 4-42 shows the normalised plots showing that the maximum velocities occur in the middle of the flow from about 2 s onward. Looking at the images small particles can be seen to be draining with the fluid through the flow. This only once the flow has effectively finished and is a function of the deposition on the flume and drainage of fluid from the tail at a much slower rate showing separation of the fluid and solid phases.

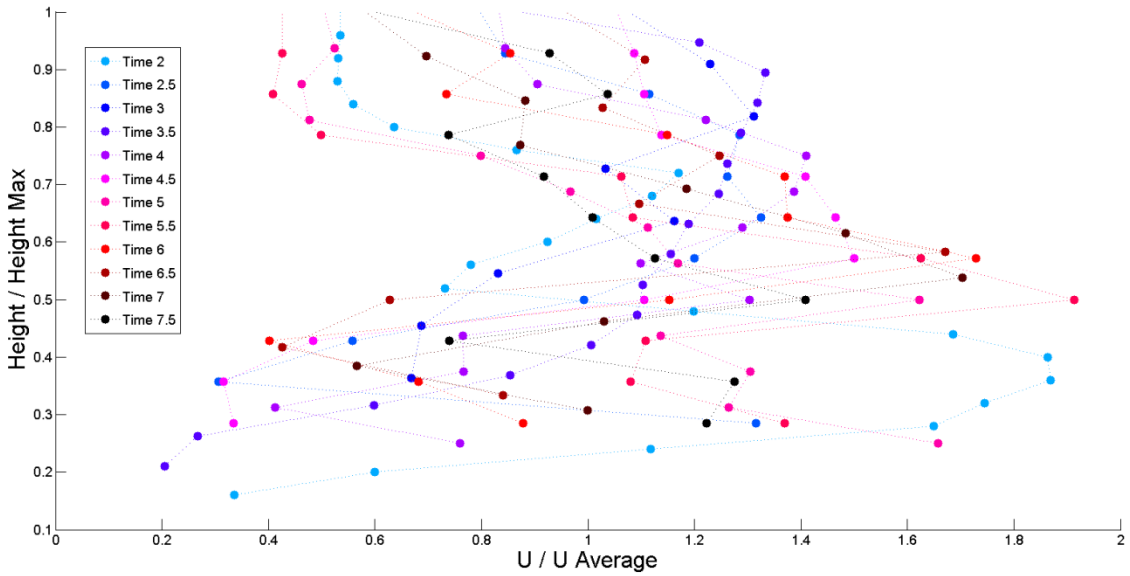

Figure 4-42: Tail flow of S24W32EX9 showing drainage through the middle of the flow.

4.6.7. Interior v Exterior Influence on Velocity

4.6.7.1. Profile Shape Plots

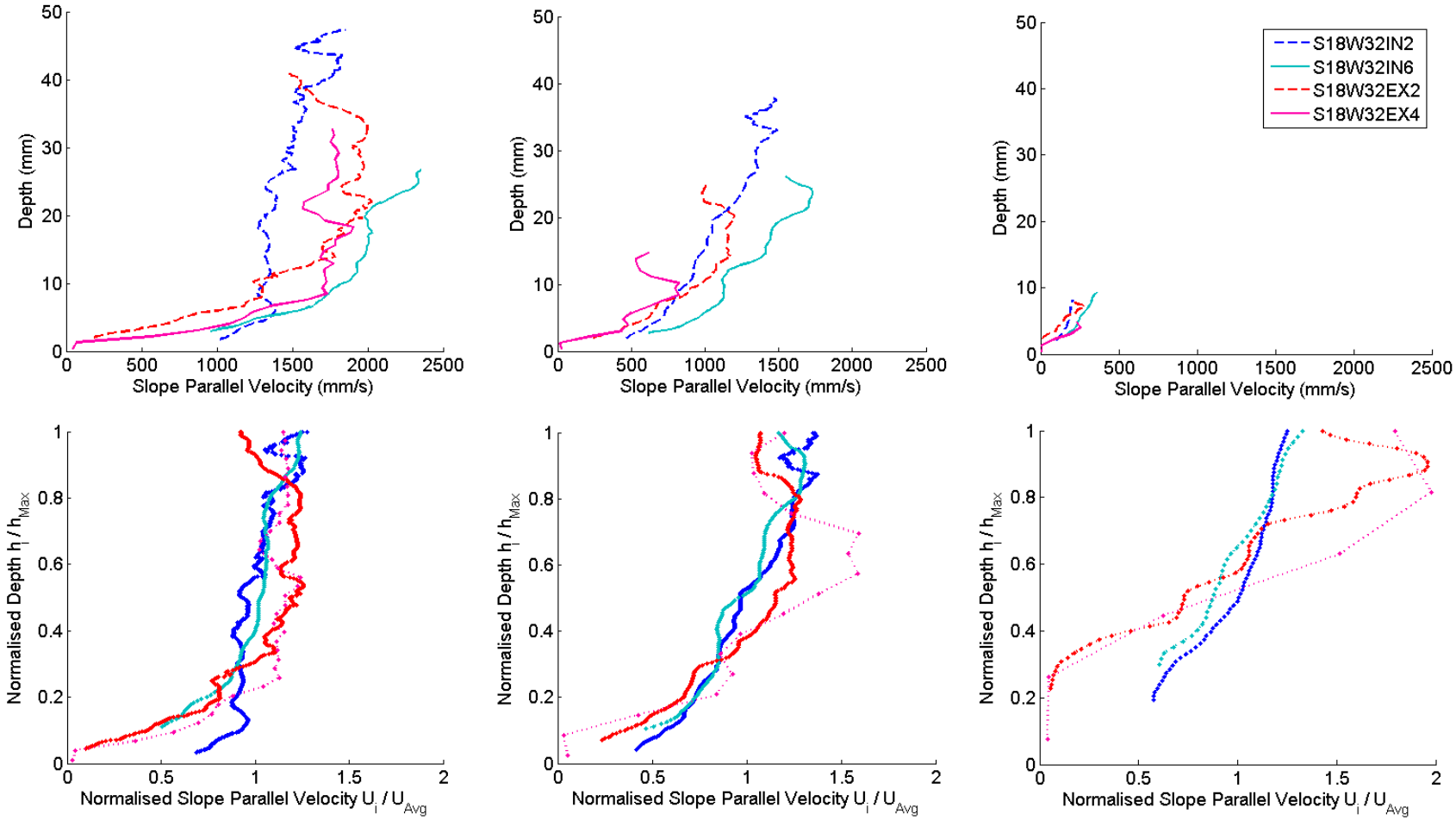

Figure 4-43: LOV comparison of S18W32IN2 vs. S18W32EX2. Velocity and normalised velocity profiles for peak, body and tail of flow.

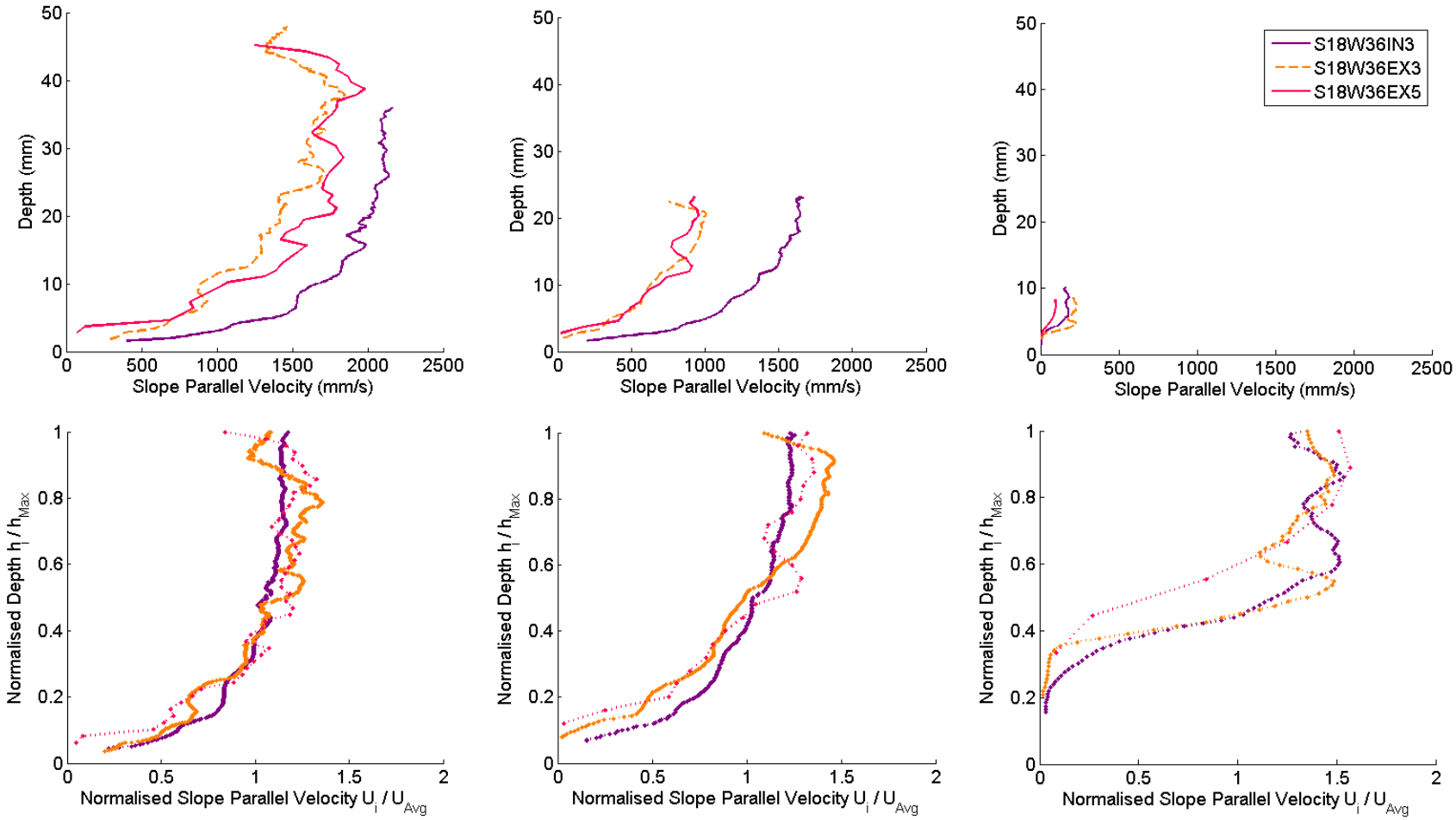

Figure 4-44: LOV comparison of S18W36IN3 vs. S18W36EX3. Velocity and normalised velocity profiles for peak, body and tail of flow.

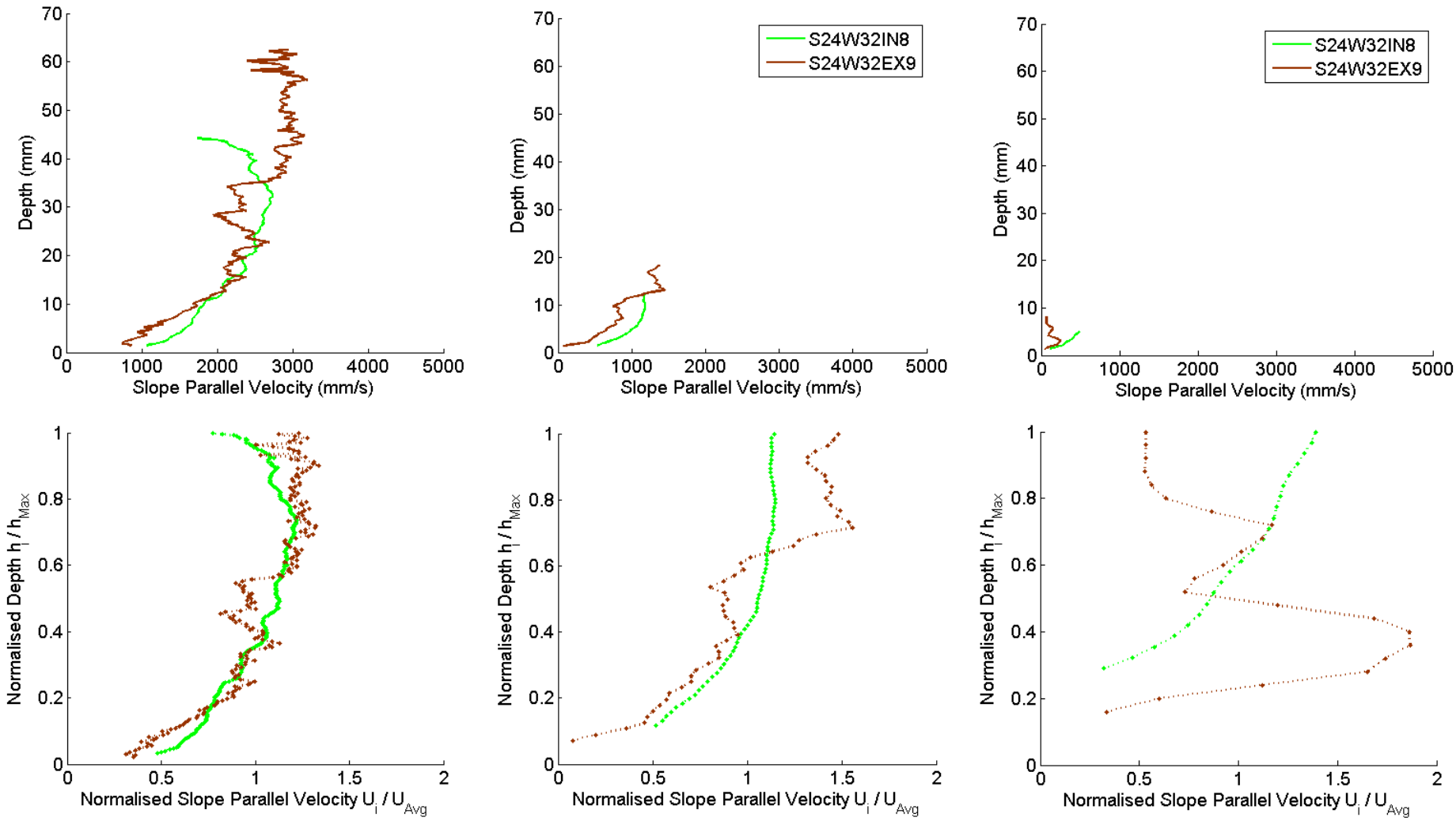

Figure 4-45: LOV comparison of S24W32IN8 vs. S24W32EX9. Velocity and normalised velocity profiles for peak, body and tail of flow.

4.6.7.2. Depth-averaged Over Time Plots

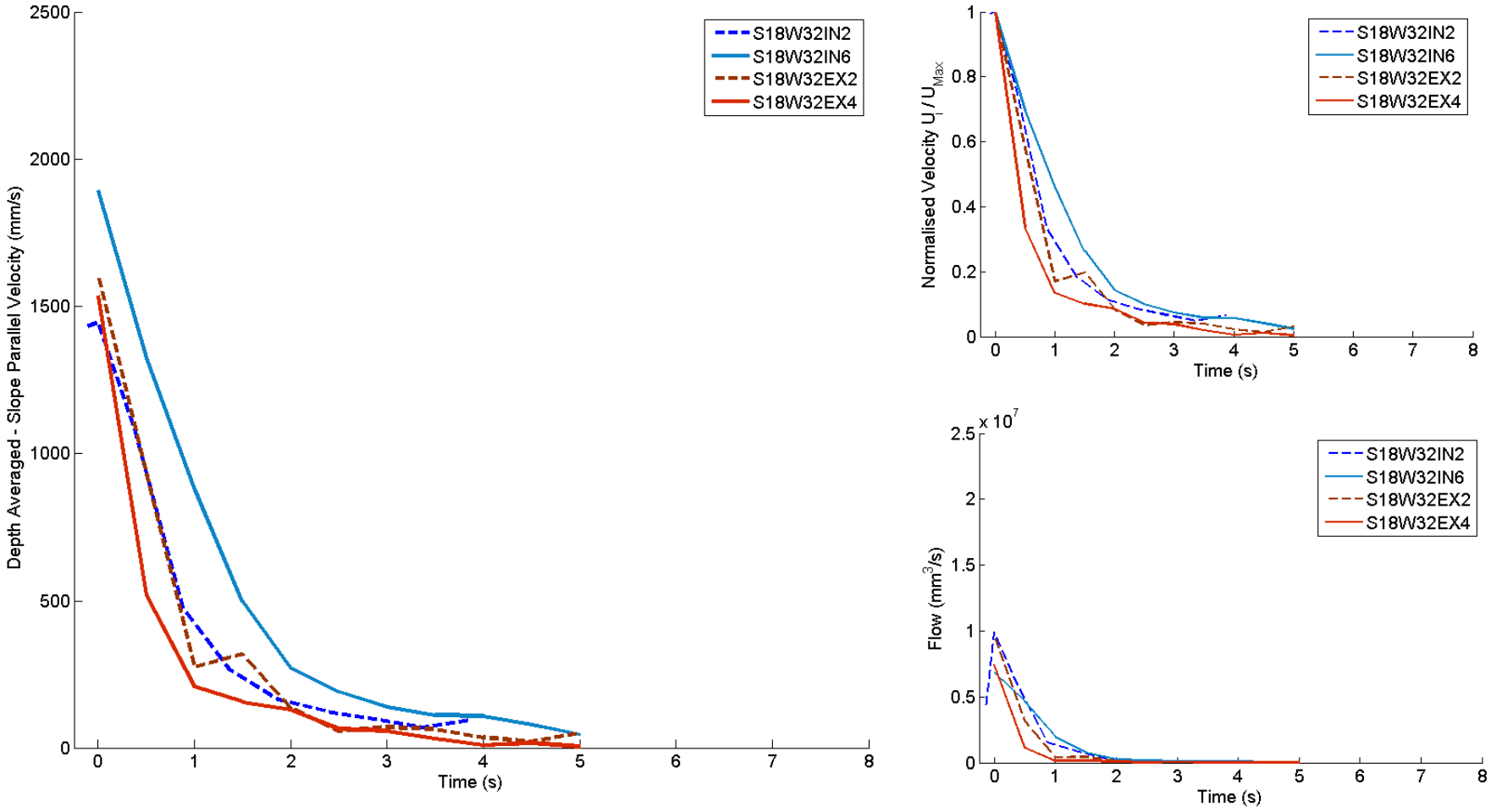

Figure 4-46: LOV comparison of S18W32IN2 vs. S18W32EX2. Depth-averaged velocity and flow approximation over time.

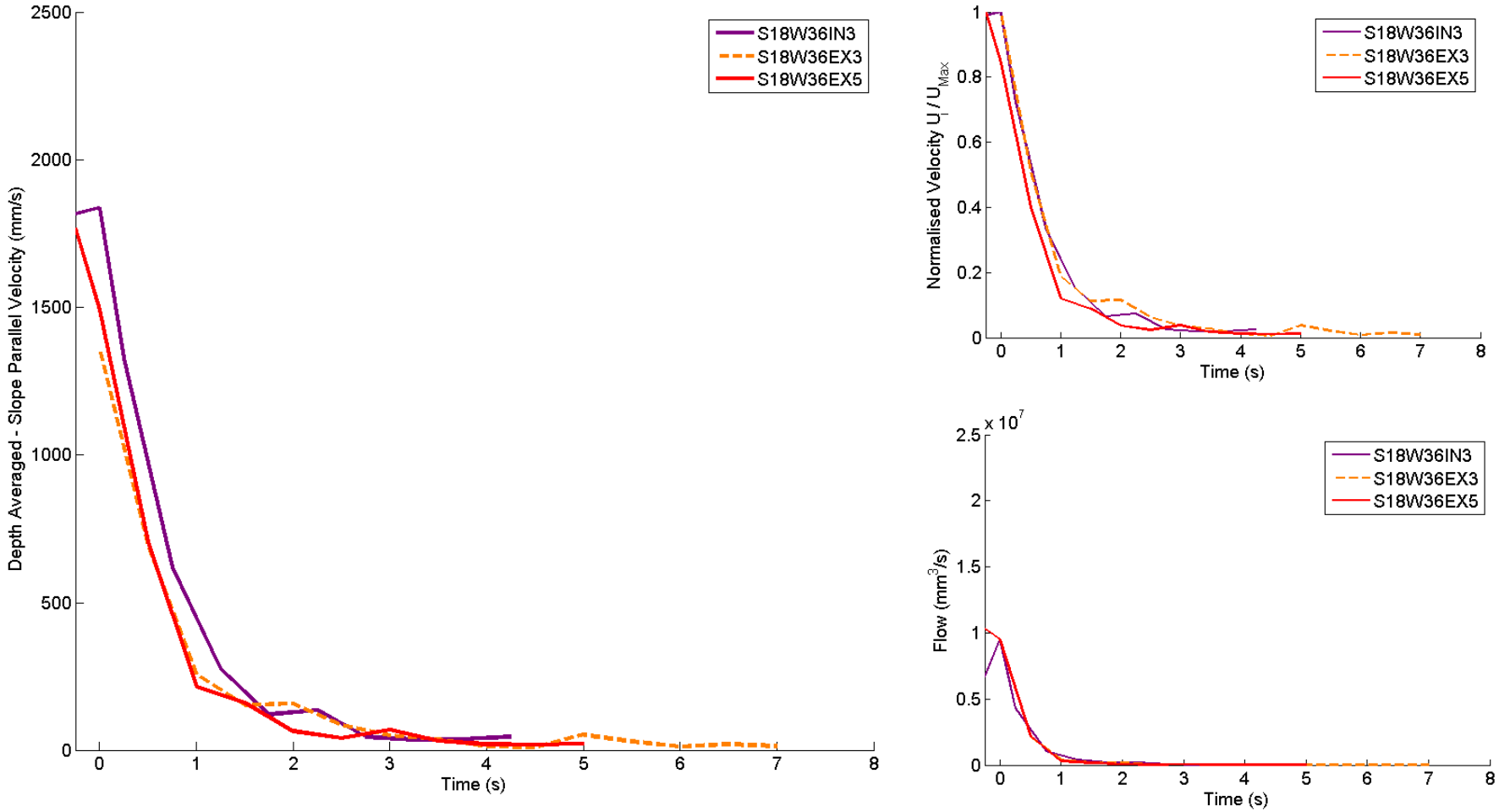

Figure 4-47: LOV comparison of S18W36IN3 vs. S18W36EX3. Depth-averaged velocity and flow approximation over time.

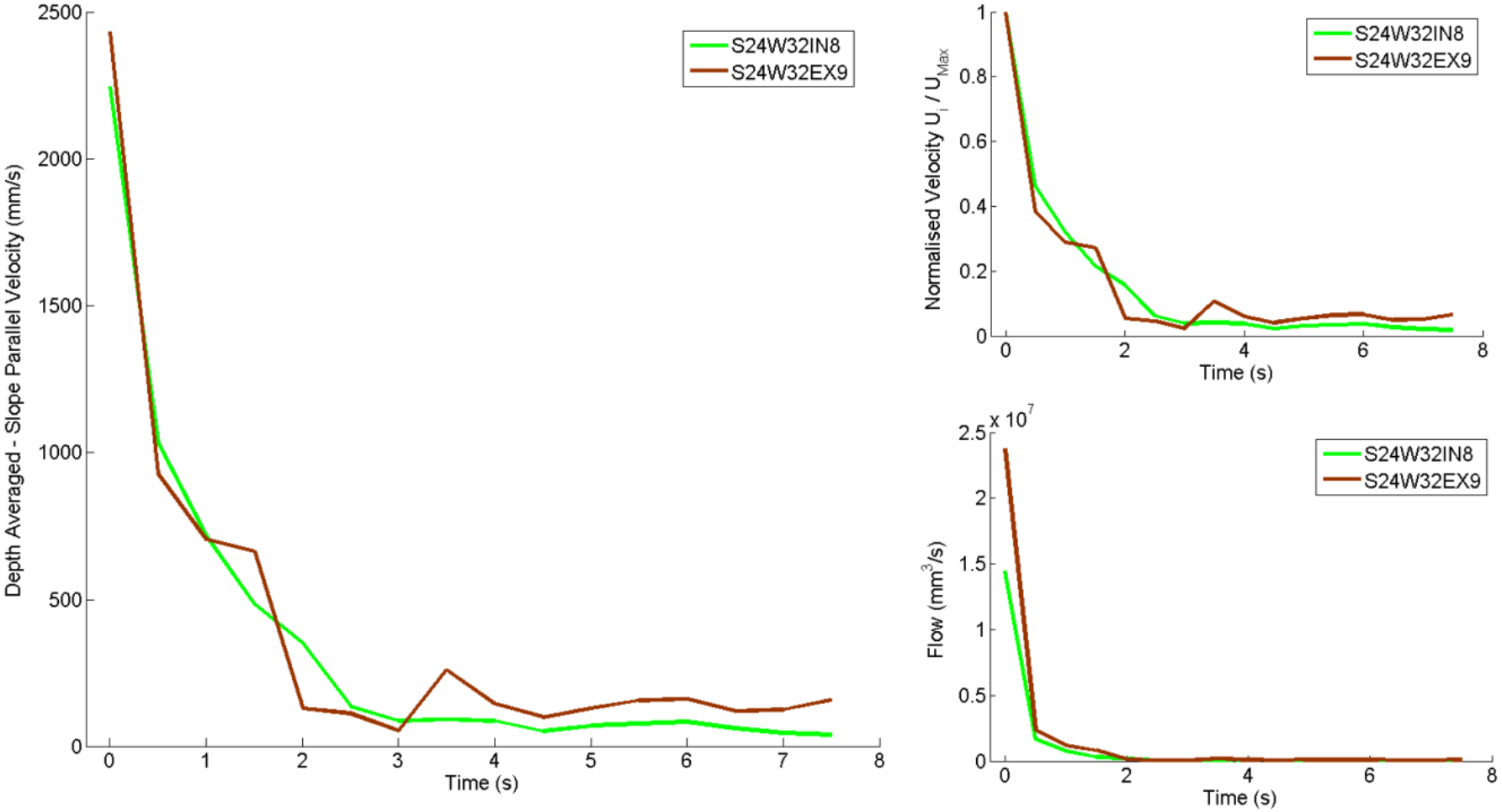

Figure 4-48: LOV comparison of S24W32IN8 vs. S24W32EX9. Depth-averaged velocity and flow approximation over time.

4.6.7.3. Comparison of LOV

Velocities Profiles

Figure 4-43, Figure 4-44 and Figure 4-45 are comparisons of the exterior and interior LOV. Each set of test has the same slope and moisture content. More than one test at each combination of variables has been present where possible to give an indication of variability. The velocity profiles and normalised velocity profiles show that there is a high level of variability in flows at the front which is less in the body. It is difficult to show if the velocity is over or underestimate from the exterior at the front. Table 4-3 and Table 4-4 show a slightly higher maximum and mean velocities at the peak. This might be linked to higher saturation flow levels.

Figure 4-43 shows slip for interior is much higher than the exterior. This is also seen in the other comparisons at higher slope and moisture contents but to a lesser extent. The value of the slip velocity at the interior front and body of the flows appears to be half the depth-averaged velocity this is supported in Figure 4-49 which slows a number of interior experiments. Table 4-6 shows the difference in slip velocity is five time less for the exterior than the interior.

In addition to the slip or no slip Figure 4-44 also shows that the body is faster for the interior than the exterior this is also seen in the other comparisons but to a lesser extent. Another point seen in all of the comparisons is that the normalised curves for the interior show less instantaneous fluctuations. This is most likely due to the presence of bubbles in the exterior images but needs to be investigated more.

Depth-averaged Velocities over Time

Figure 4-46, Figure 4-47 and Figure 4-48 show the depth-averaged velocity and flow over time. These measurements are less impacted by instantaneous fluctuations and show a general trend over time. Figure 4-46 and Figure 4-47 show that the mean velocity and flow drops off quicker for the exterior LOV than the interior. This could indicate friction at the walls is playing a bigger factor in decay of velocity as the more fine fluid tail passes. Figure 4-48 shows that the calculated values of average velocity are more erratic. This could be an indication of secondary surges seen in observations of the S24W32EX9 test. These surge fronts are likely evident at time 1.5 and 3.5 s. There are other possible surges in the other exterior test for example S18W32EX2 at 1.5 s.

4.6.8. Moisture Content Influence on Velocity

4.6.8.1. Profile Shape Plots

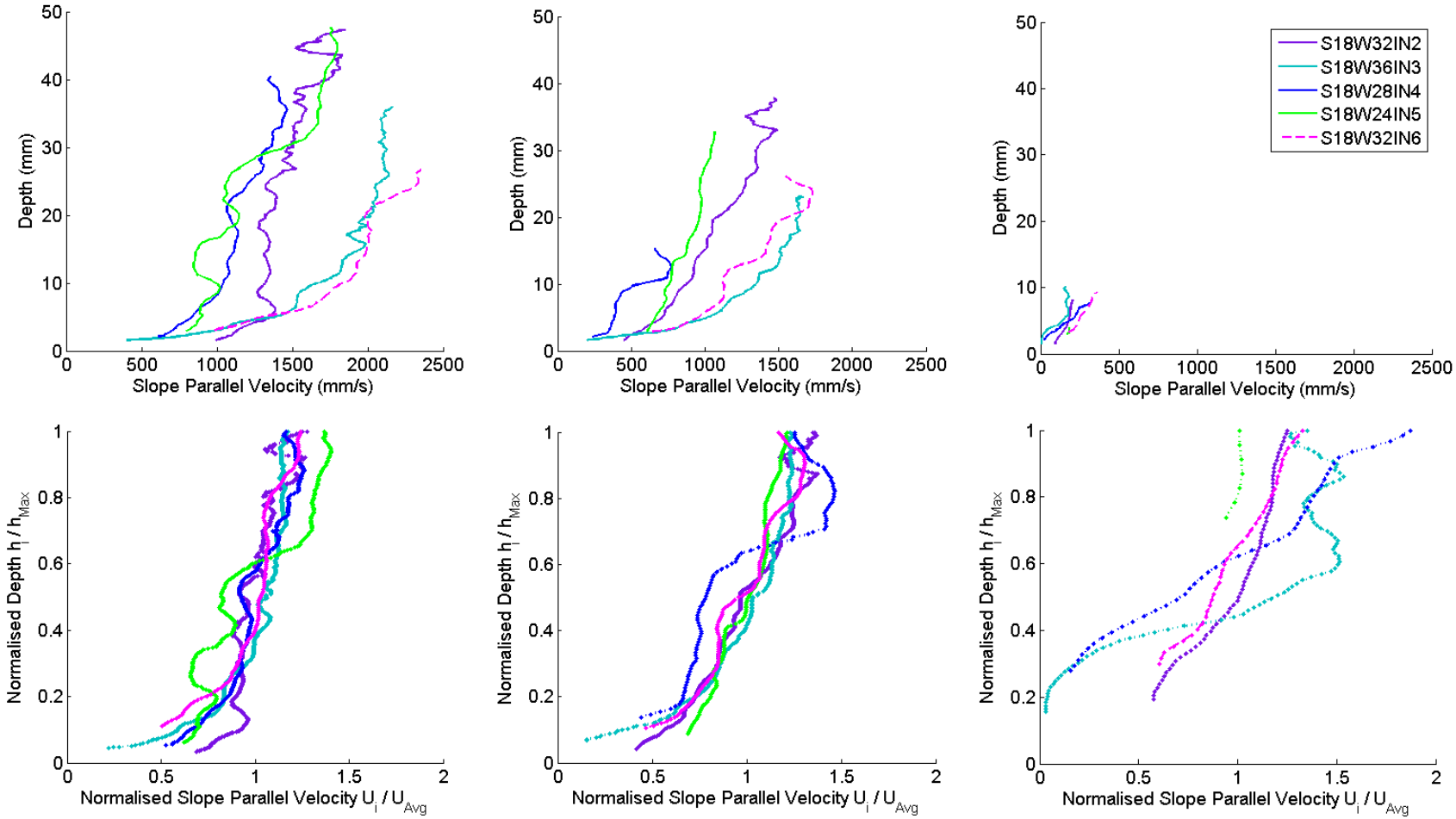

Figure 4-49: Moisture content comparison of S18W32IN, S18W32IN, S18W32IN and S18W36IN. Velocity and normalised velocity profiles for peak, body and tail of flow.

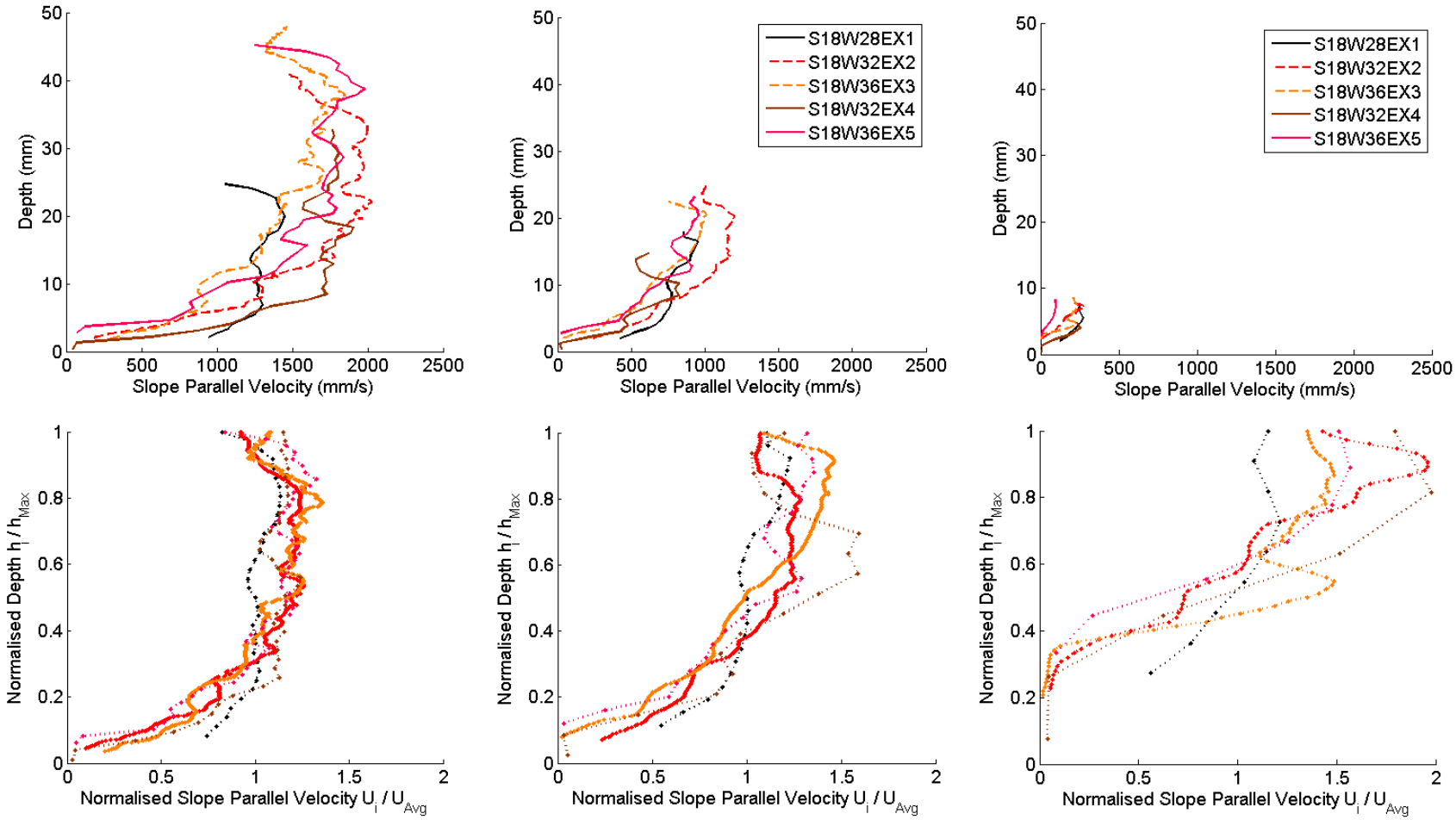

Figure 4-50: Moisture content comparison of S18W28EX1, S18W32EX2, S18W32EX4, S18W36EX3 and S18W36EX5. Velocity and normalised velocity profiles for peak, body and tail of flow.

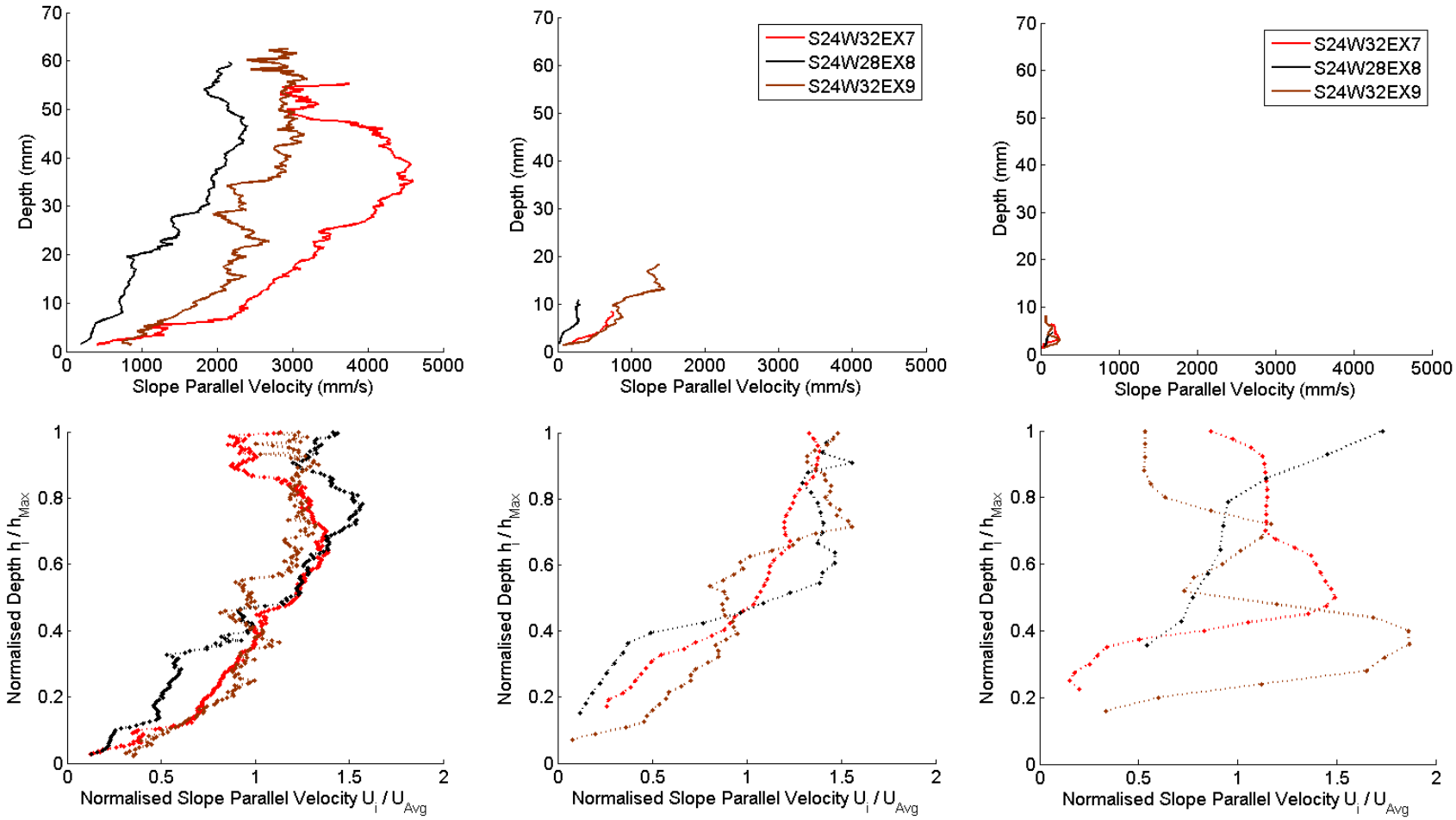

Figure 4-51: Moisture content comparison of S24W32EX7, S24W28EX8 and S24W32EX9. Velocity and normalised velocity profiles for peak, body and tail of flow.

4.6.8.2. Depth-averaged Over Time Plots

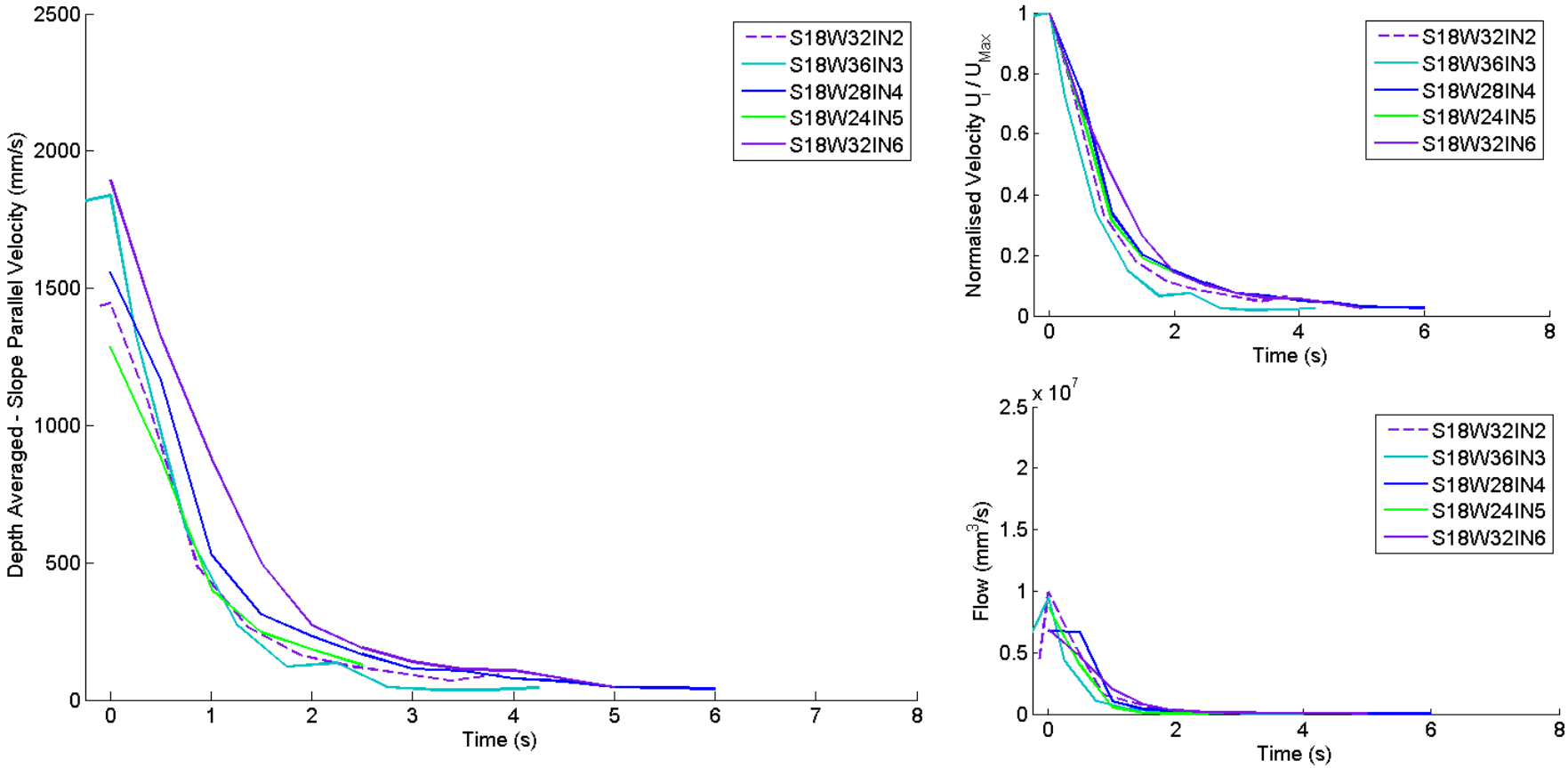

Figure 4-52: Moisture content comparison of S18W32IN, S18W32IN, S18W32IN and S18W36IN. Depth-averaged velocity and flow approximation over time.

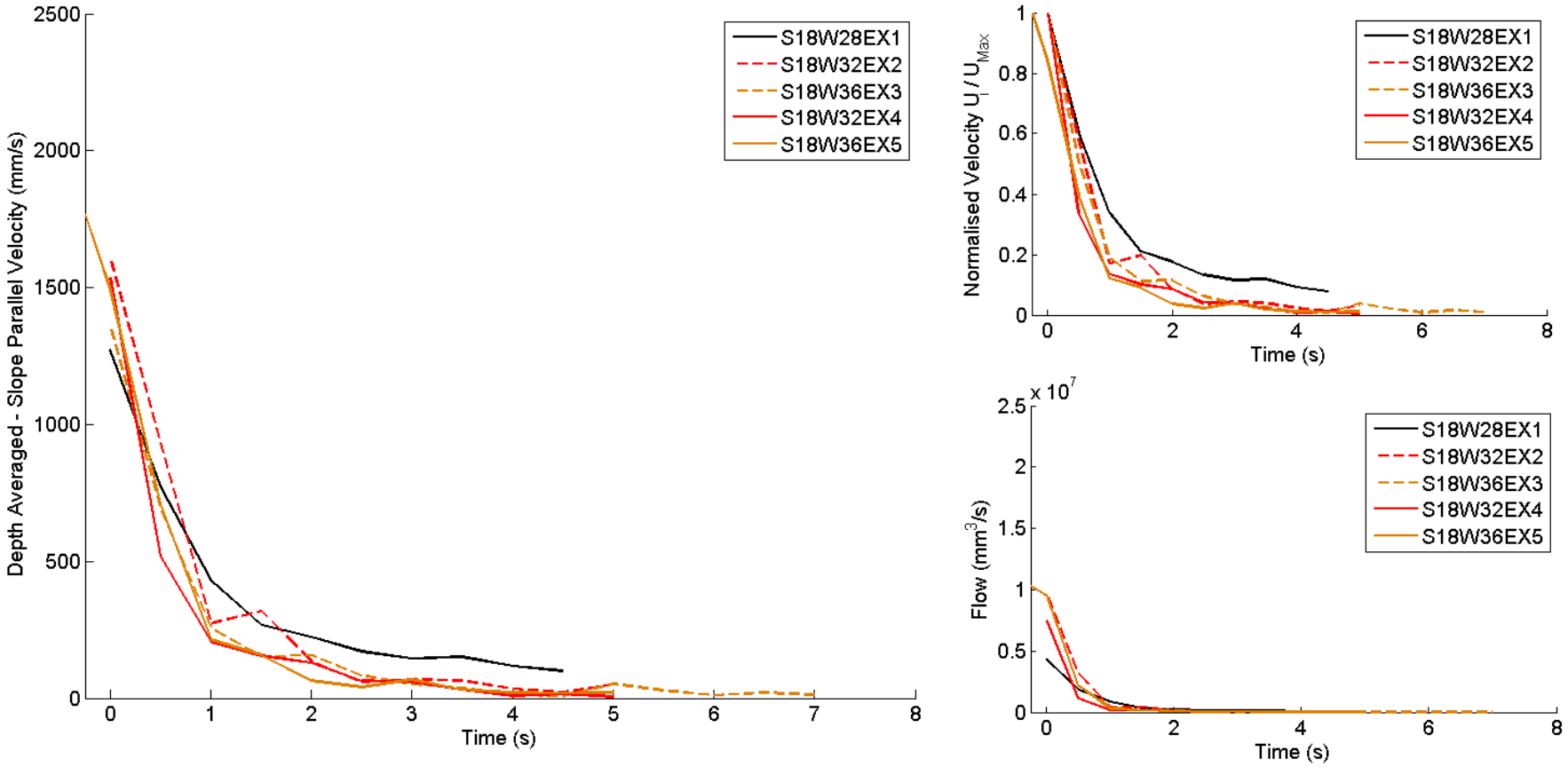

Figure 4-53: Moisture content comparison of S18W28EX1, S18W32EX2, S18W32EX4, S18W36EX3 and S18W36EX5. Depth-averaged velocity and flow approximation over time.

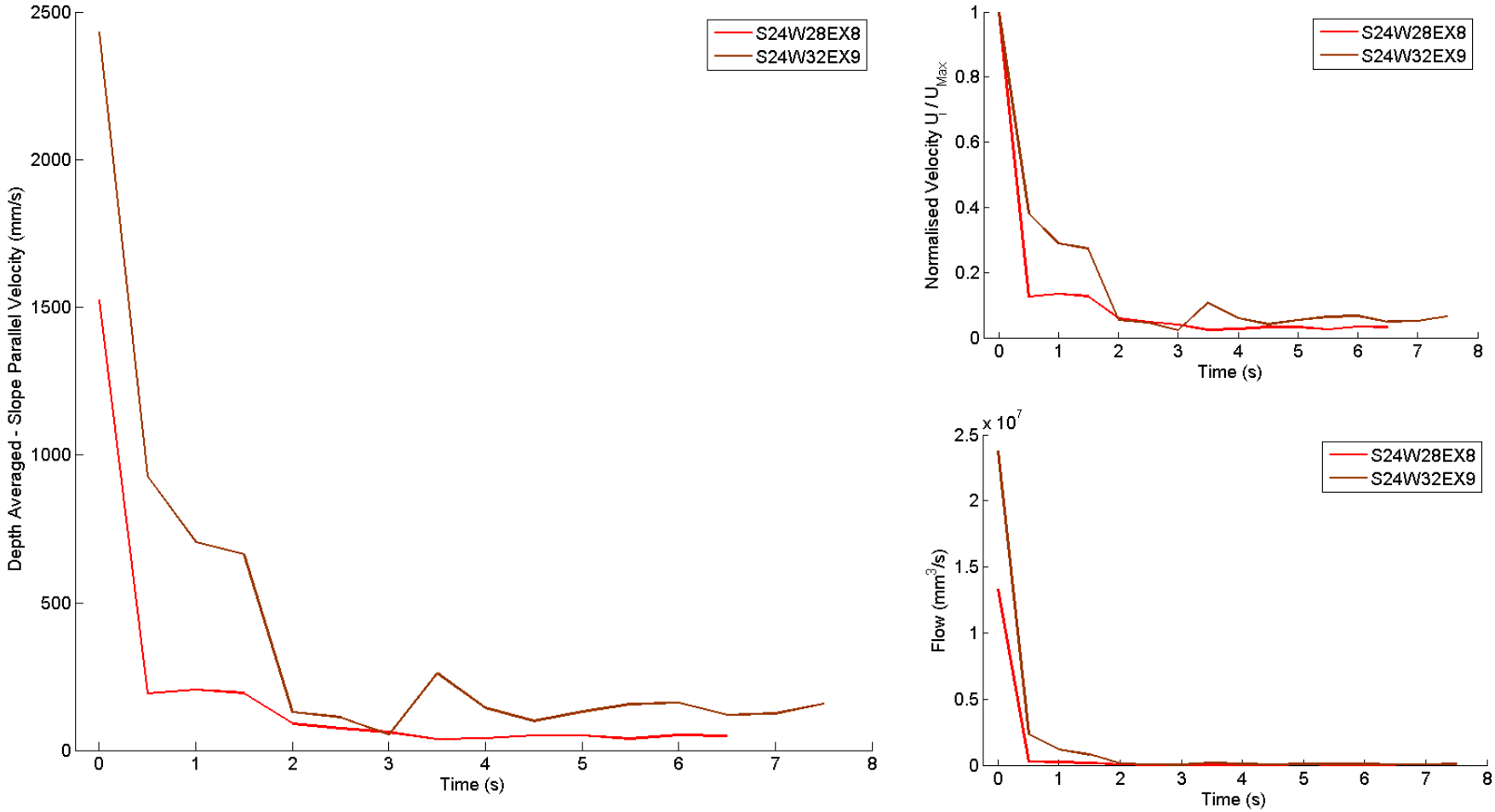

Figure 4-54: Moisture content comparison of S24W28EX8 and S24W32EX9. Depth-averaged velocity and flow approximation over time.

4.6.8.3. Comparison of Moisture Content

Velocities Profiles

Figure 4-49, Figure 4-50 and Figure 4-51 show comparisons of the velocity profiles with the same slope and LOV. Figure 4-49 shows four interior tests at slope 18.1° these tests represent four different moisture contents starting at 23.7% and increasing by 4% up to 35.7%. Figure 4-50 shows five exterior tests at 18.1° for three moisture contents, one at 27.7%, two at 31.7% and two at 35.7%. Figure 4-51 shows the two exterior tests at the higher slope of 24.5° the moisture contents are 27.7% and 31.7%.

In general all of the higher moisture contents results in faster flows Table 4-5. This is very evident in Figure 4-49 and Figure 4-50, However, Figure 4-50 and Figure 4-51 show there is a reasonable level of variability between flows of the same moisture content. As an approximate relationship each 4% increase in moisture content showed an increase of 15% in peak velocity. The normalised profiles for the front and body show a consistent shape with consistent slip or no slip velocities depending on LOV. The tail heights and velocities are similar but have different normalised shapes.

This indicates that the moisture content helps mobilise the flow giving faster velocity and longer run-out lengths. As the changing in moisture content does not seem to greatly impact the height and normalised curves shapes the moisture content does not appear to greatly impact the type of flow mechanisms

Depth-averaged Velocities over Time

Figure 4-52, Figure 4-53 and Figure 4-54 are the depth-averaged velocity profiles and flow approximations for the tests shown in Figure 4-49, Figure 4-50 and Figure 4-51. Figure 4-52 and Figure 4-53 show no obvious trend in the decay of velocity with time or the flow rate approximation. S24W28EX8 appears to have a very short body but there is nothing to suggest that the lower moisture content is the reason for this.

4.6.9. Slope Influence on Velocity

4.6.9.1. Profile Shape

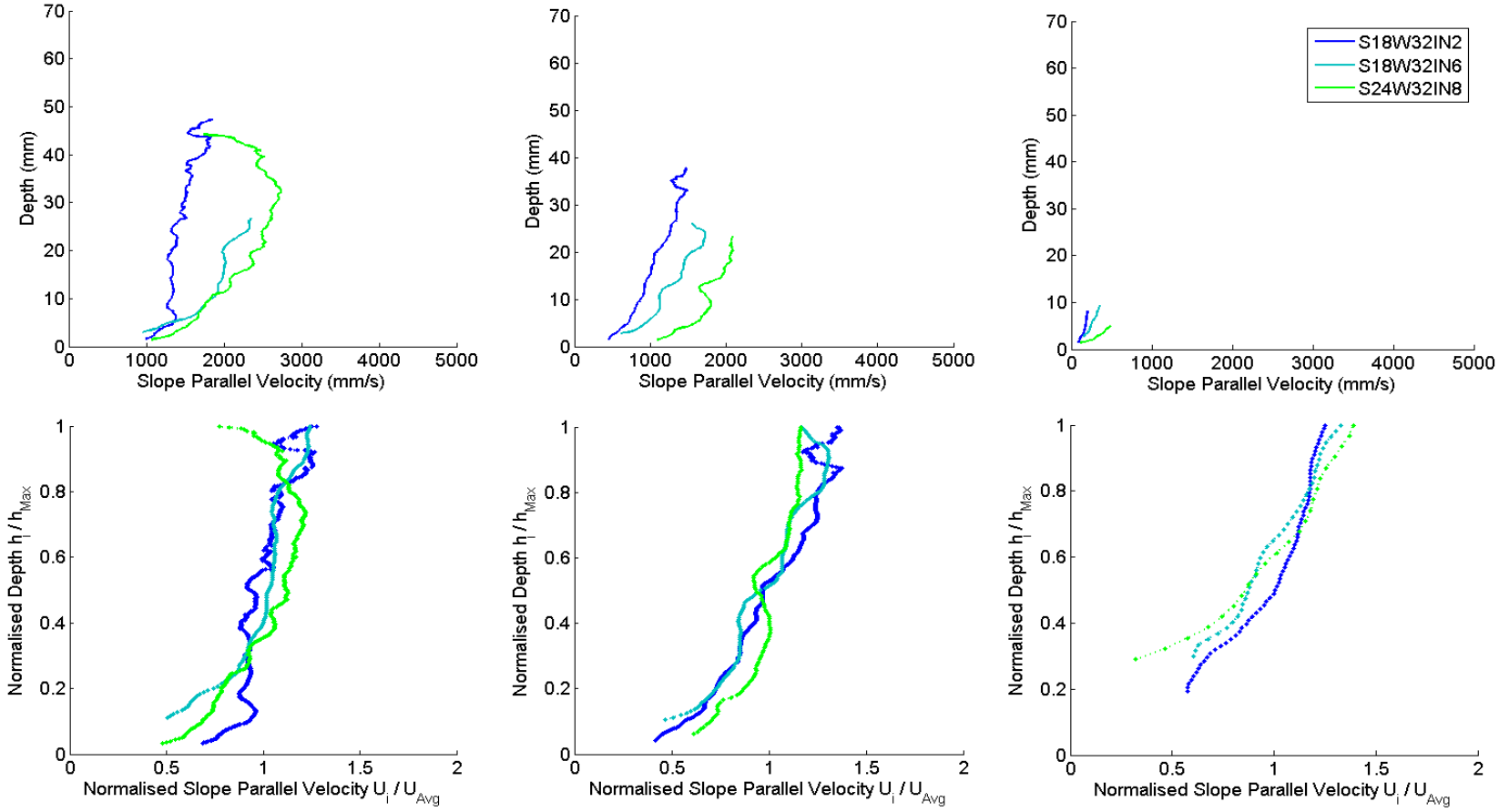

Figure 4-55: Slope comparison of S18W32IN2 and S18W32IN6 vs. S24W32IN8. Velocity and normalised velocity profiles for peak, body and tail of flow.

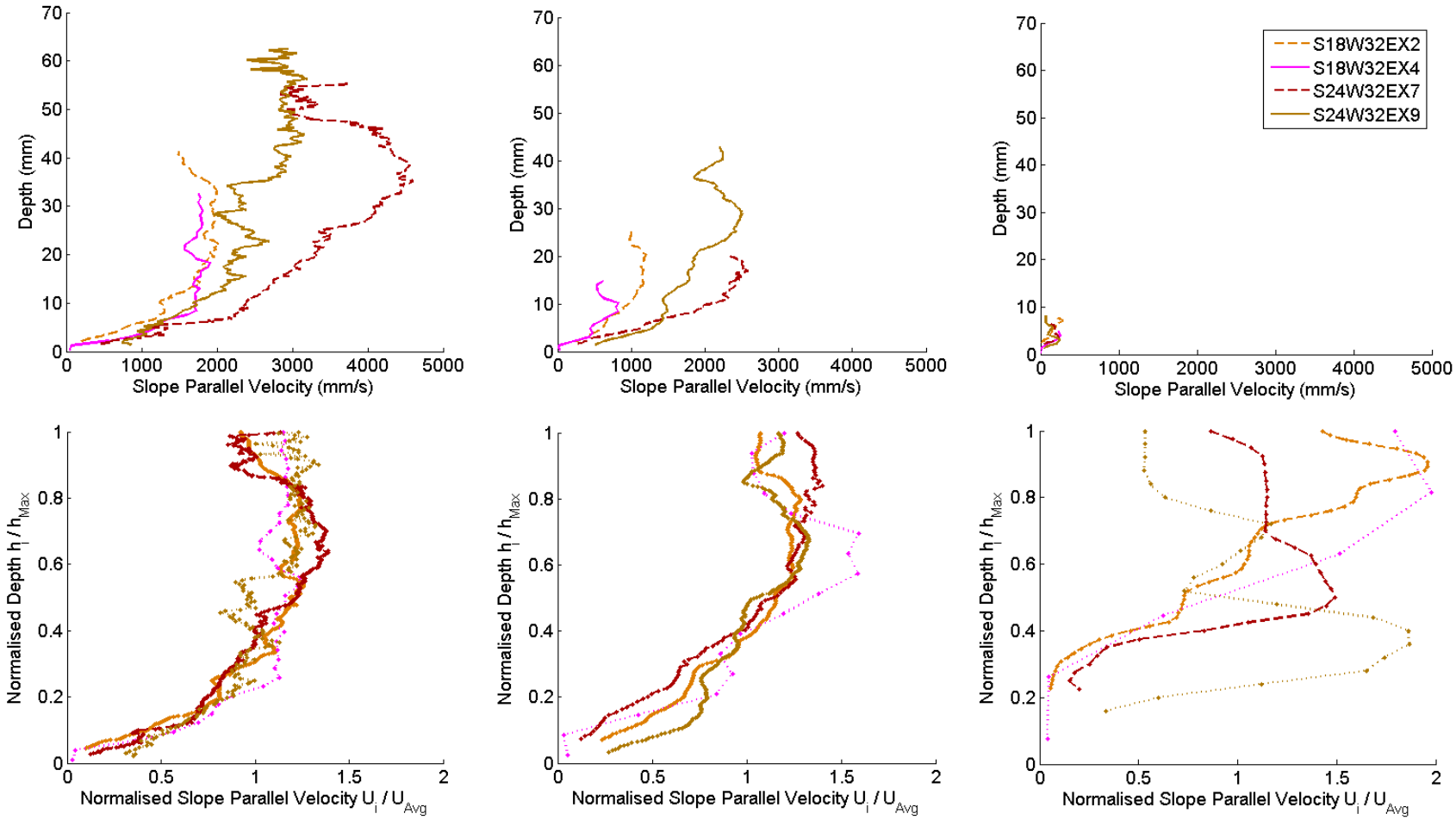

Figure 4-56: Slope comparison of S18W32EX2 and S18W32EX4vs. S24W32EX7 and S24W32EX9. Velocity and normalised velocity profiles for peak, body and tail of flow.

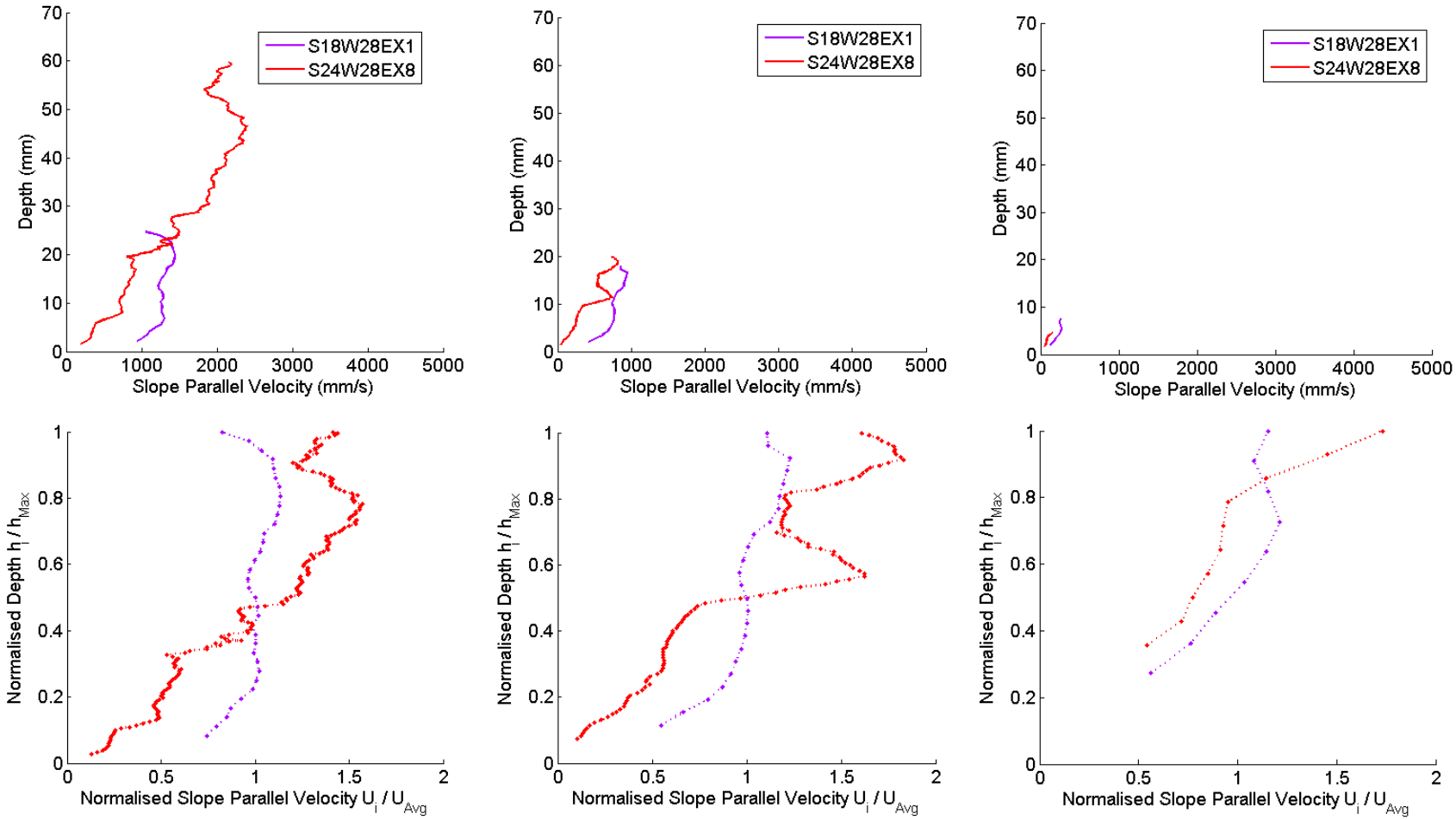

Figure 4-57: Slope comparison of S18W28EX1 vs. S24W28EX8. Velocity and normalised velocity profiles for peak, body and tail of flow.

4.6.9.2. Depth-averaged over Time

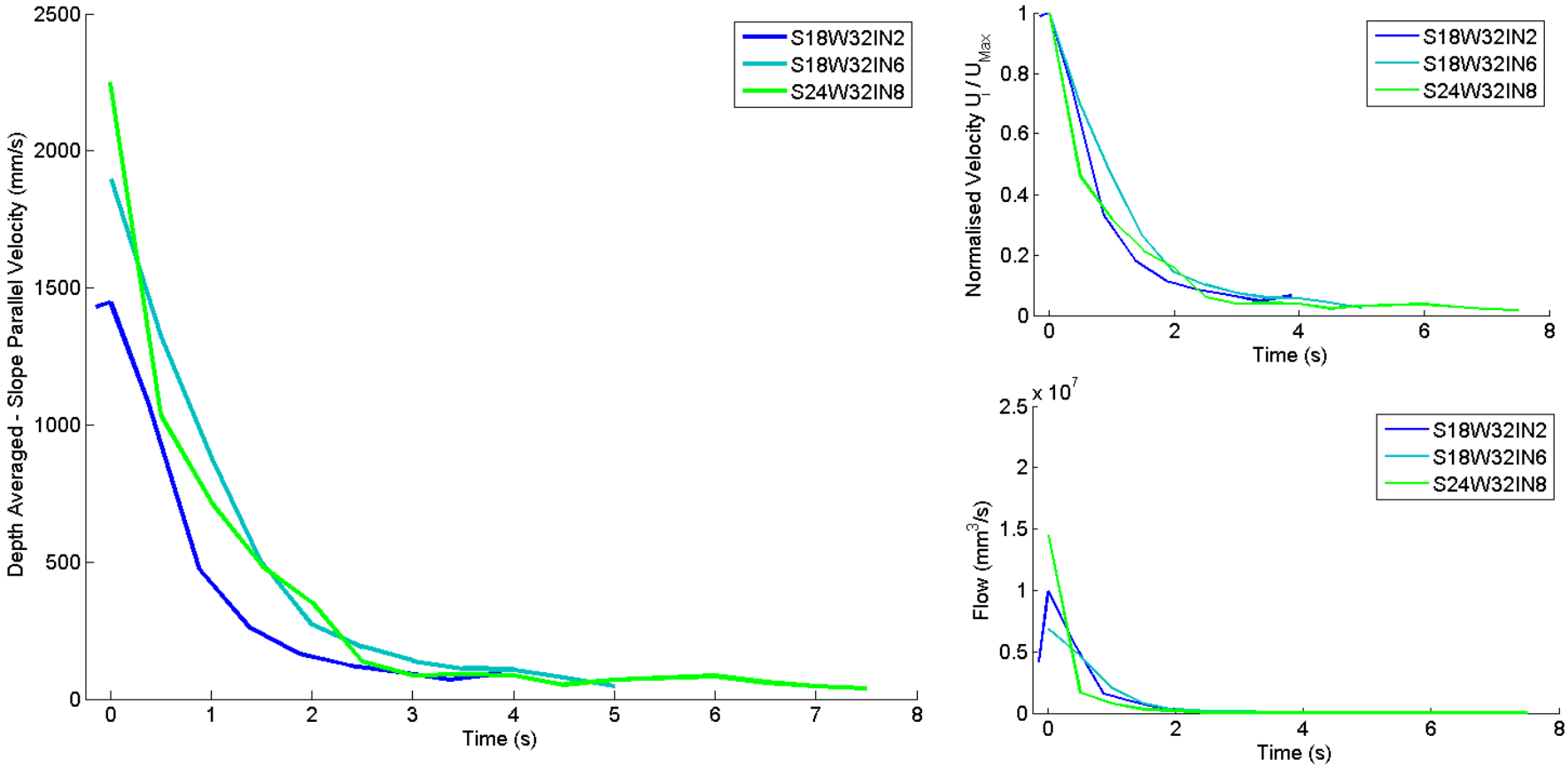

Figure 4-58: Slope comparison of S18W32IN2 and S18W32IN6 vs. S24W32IN8. Depth-averaged velocity and flow approximation over time.

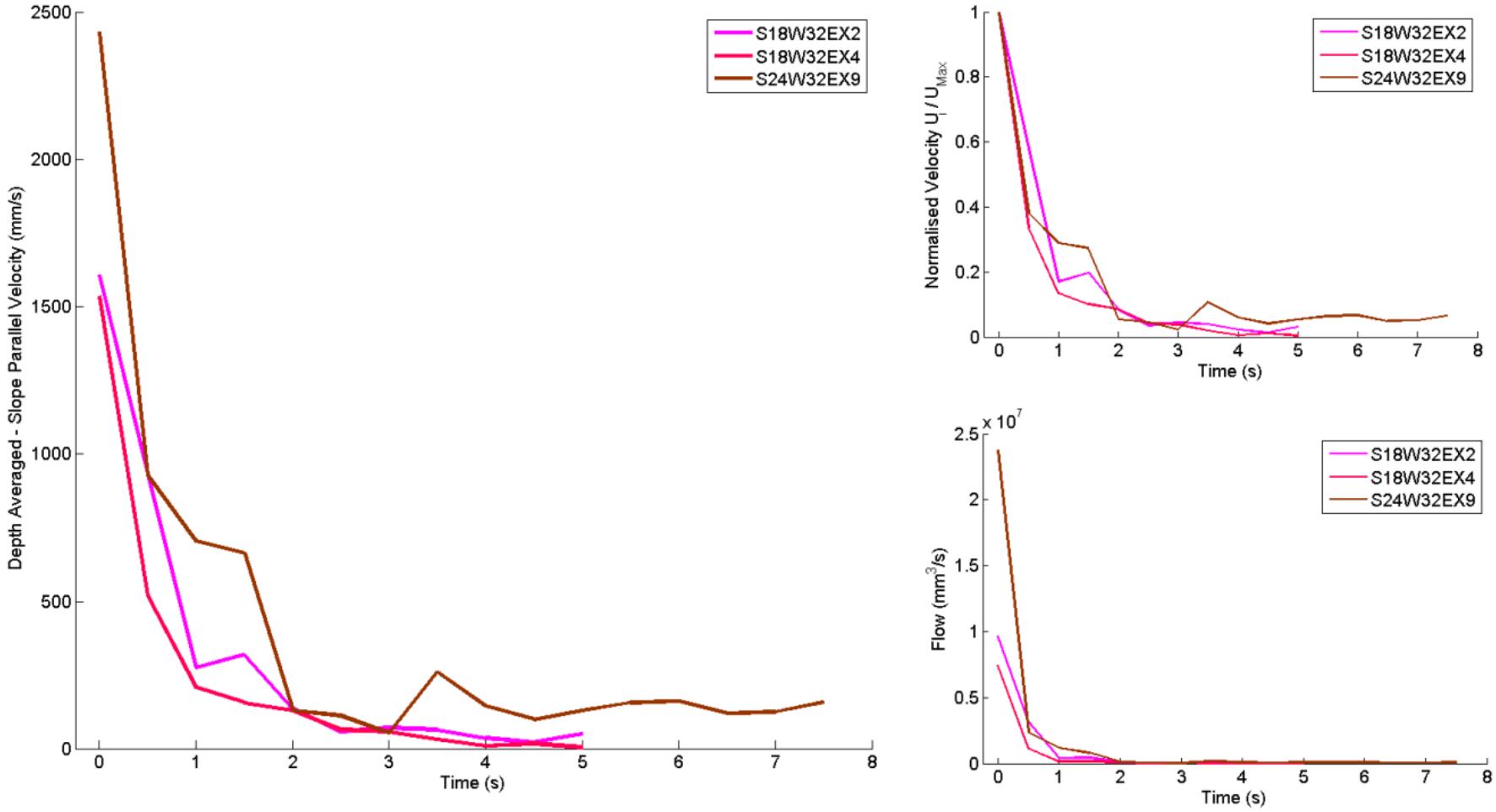

Figure 4-59: Slope comparison of S18W32EX2 and S18W32EX4 vs. S24W32EX9. Depth-averaged velocity and flow approximation over time.

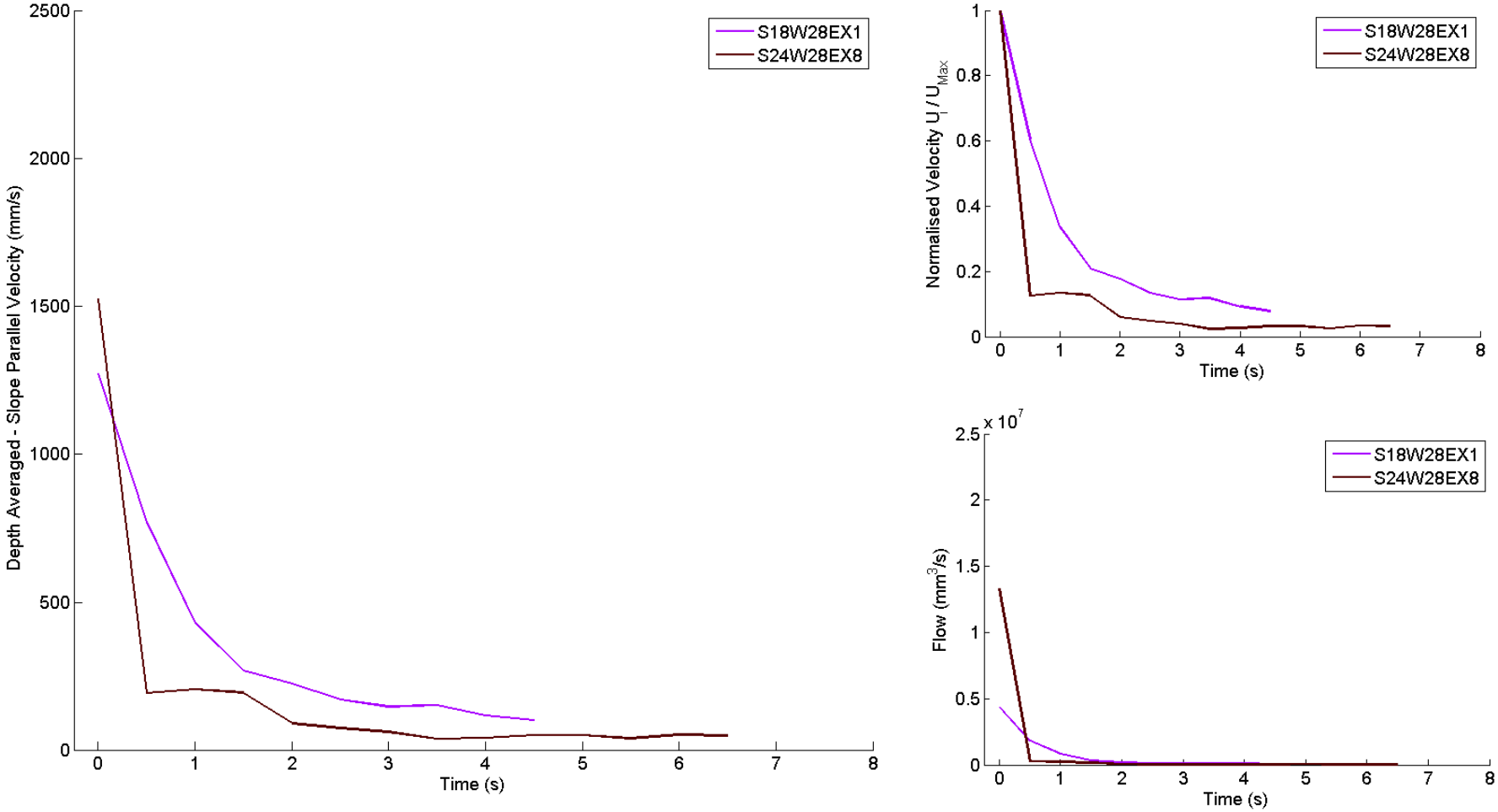

Figure 4-60: Slope comparison of S18W28EX1 vs. S24W28EX8. Depth-averaged velocity and flow approximation over time.

4.6.9.3. Comparison of Slope

Velocities Profiles

Figure 4-55, Figure 4-56 and Figure 4-57 show comparisons of the velocity profiles with the same moisture content and LOV. For the higher slope the body is 0.2 s after peak and is 0.5 s after, for the lower, as the body passes much quicker for the higher slope. This gave heights of flow similar for both sections of the body. The peak depth-averaged and maximum velocities are approximately 50% greater for the higher slope than the lower slope (Table 4-4 and Table 4-5). Table 4-6 shows there is less connection between slip velocity and slope.

In general the normalised curves show the same shape apart from S18W28EX1 which appears to be an outlier. This means that the mechanisms are the same over this change in slope and that the flow simply has a greater unbalanced force from a greater slope which results in a greater acceleration and velocity. These mechanisms include a slip velocity of half the average for the interior LOV and a high shear layer at the base of the exterior flows.

In the body of the flow the velocity is higher at a similar depth of saturated flow. It is difficult to say that these profiles are comparable as small time steps can have a large impact on the height and velocity in the body of the higher slope tests. The tails have greatly reduced velocities but the higher slope still gives greater velocities than the lower slope. Figure 4-55 shows that the normalised curves have the same shape when normalised by the average velocity showing similar flow type.

Depth-averaged Velocities over Time

Figure 4-58, Figure 4-59 and Figure 4-60 are the depth-averaged velocity profiles and flow approximations for the tests shown in Figure 4-55, Figure 4-56 and Figure 4-57. It is interesting that even though the velocity and height drop off quickly for higher slope the velocity over time shows very similar magnitude velocity curves after the first 0.5 s the velocity drops from the higher value at the peak to a similar value as the velocity transitions from rapid to slower. This could show that the end of the body and tail sections behave alike regardless of the slope. Perhaps the viscous fluid and settling solids restricts the flow velocity. It is, therefore, the high surge of material that is solely responsible for the longer run-out and not the tail of the flow. This surge

is higher and faster for the higher slope acting over a smaller time. This resulted in much higher peak flow rates.

4.6.10. Relative Variable Impacts

Slope showed the most and LOV the least impact on the peak values of the front velocity profiles. The 4% steps in moisture content have less individual impact on the velocity profiles than the 6.4° degree change in slope. However, the 16% change in moisture content is roughly equivalent to the 6.4° degree change in slope. LOV was the only variable that changed the normalised slip velocity in the front and body.

4.7. Chapter Summary

4.7.1. Consistency of Non-PIV Data

The non-PIV data comprised of the run-out lengths, shape of deposit, PSDs, spot heights, heights of flows and timing of parts of the flows was presented to show the general behaviour or each tests and provide a basis for identifying trends and abnormalities in the experiments presented.

The deposit shape of all tests had a consistent shape with a coarse front edge clearly evident in all cases. Spot heights also demonstrated the centre had scattered coarse particles. The PSDs showed the tail had the highest concentration of fine particles. This showed strong segregation of all flows thought out the length of the flow. In general the deposits indicated that the experiments were all of a similar nature and were classified as stony debris flows.

The images showed a very coarse unsaturated front flowed by a relatively short body that quickly tapered to a shallow tail. The front had a snout shape, the body contained the majority of coarse particles in a thick section and the tail was consistently highly fluid and shallow. Coarse particles were evident within in the flow and were seen to float on top of other particles which influenced the absolute height of the flow.

Saturation height was less than or equal to the absolute height and particles distributed throughout showed that there was no excess saturation in the body. The shape and nature of the front suggested a plug sliding down the flume. The saturation height was

found to be more stable but was affected locally by larger particles and other surge structures. The flow heights were not found to be a good indicator of run-out lengths.

The interior and exterior deposits are consistent as there was no intrusive mechanism to differentiate between the experiments. This gives an indication of the large inherent chaotic natures of the experiments that leads to inconsistencies in the deposits. The height over time is generally the same or less than the exterior tests which is likely a friction effect from the wall of the flume or the viscous nature of the material talking longer to recede after a surge.

Increased moisture content and slope increased run-out lengths. Within the parameters tested the trend in run-out length could be approximated as linear. The shape of the snout changed with slope and moisture content becoming a less well defined front which indicated the change from a block "wall" of material to a "ramp" shape at the snout. The increased combination of both also stated to introduce surges within the flow. Increased moisture content did slightly increase segregation of the deposit but not significantly. The moisture content did not affect the deposit shape except to enlarge the area. Higher moisture contents had more erratic heights over time for the body section due to the more mobile large particles moving through the flow. Increased slope gave wider longer run-outs and increased the waviness of the deposit outline as it became longer and thinner.

4.7.2. PIV Analysis Conclusions

The lack of saturation of the particles at the front and top of the flow reduced the effectiveness of the technique to measure the snout velocity. Large patches sizes were used to suppress fluctuations in the data but it was noted that there was a high level of small scale fluctuations. The height over time used for calculations was lower to the actual measured directly from images but followed the same trend.

Average velocity over time plots show that the average slope parallel velocities peak and then decay to a minimal value over time. The minimum recorded velocities over time show there is a high slip velocity present in the front with a smaller slip velocity in the body and none in the tail. The slip velocity at the front was approximately half the depth-averaged velocity. In general a higher velocity gave a higher run-out length

but the exact relationship was too random to give a clear trend. All tested showed a large initial flow rate that quickly decreased.

The normalised instantaneous velocity profiles calculated with depth of flow showed a development in the shape of the velocity profiles. The front profiles indicated a block like flow above a shear layer, the body showed a partially fluidised shape and the tail a fully fluidised shape. The snout and front of the body had similar magnitudes of velocity, but dropped to a relatively small value within the first 1-0.5 s depending on slope. The snout was made of the largest particles and the body showed inverse grading with depth showing segregation of solid within the flow.

For the LOV the slip velocity is much higher for the interior velocity at the front than the exterior. The body of the interior experiments were faster than the exterior values. Over time the velocity of the body decayed faster for the interior than exterior. The tail did not show a consistent trend.

In terms of the moisture content the higher moisture contents resulted in higher velocities. The magnitude of a 4% increase in moisture content gave approximately 15% increase in peak velocity; however, there was significant variation in values. The moisture content did not significantly affect the shape of the velocities profile at a given location or the ratio of slip velocity to depth-averaged velocity. The moisture content also did not significantly affect the decay of the velocity in the body or the trend in shape change of the normalised instantaneous velocity profiles with location in flow

The slope of the flow showed that higher slopes resulted in higher velocities. The 4° increase in slope resulted in an increase of approximately 50% in velocity showing relative sensitivity. The increased slope shortened the body and so the bulk of the mass passed quickly. The flow rate was therefore seen to be relatively sensitive to the change in slope compared to altering the moisture content. The normalised curves were consistent irrespective of slope at each location within the debris flow. At high slope and moisture contents experiments gave evidence of surges waves.

Chapter 5. Discussion

5.1. Introduction

This chapter looks at how the results presented in Chapter 4 correspond with previous research on natural debris flow materials. Findings on the regions of flow within the debris matrix and the difference between variables and rheologies have been highlighted. Evaluation of the methodology and recommendations for future research are made.

The chapter seeks, in section 5.2, to demonstrate the reliability of the results and to establish that the deposit information indicates that the substitute material used performs like natural material. Evidence of debris flow behaviour is identified and discussed in order to recommend how well and in what context these experiments fit within current research. Throughout section 5.2 the results are compare closely to the previous work by Sanvitale (2010) using the same apparatus, material and method. An evaluation of the potential difference and impact of changes from the preceding work concludes the section.

Section 5.3 looks at the specific data obtained through interior PLIF testing. It considers first the effect of interior compared to more traditional exterior testing. This is done through measurements of the height and velocity as well as qualitative observations from images. In section 5.3.2 observations of the large particle motion are depicted and how these particles relate to others within the flow is discussed. Section 5.4 is the discussion of suitable single phase rheologies based on the presented interior behaviour and region of flow.

In section 5.5 the methodology is evaluated in terms of natural variability, selected materials parameters, PLIF and PIV analysis. The evaluation of the technique identifies some of the limitations of the methodology and the relative impacts on the results. In section 5.6 future improvements based on this work are identified. There are also suggestions for future work that could be carried out using the data collected. Much of the future work focuses on the new areas of enquiry if image quality is improved.

5.2. The Nature of the Experimental Debris Flows

This section looks at how consistently the substitute debris flow material behaved and how well this behaviour is supported by previous research. The classification according to the observed behaviour, material parameters and Bagnold and Savage numbers show that the series of flows can be classified as "stony" according to Takahashi (1991), this would mean that they have strong levees and a high level of segregation and are more granularly dominant.

5.2.1. Comparison to Sanvitale

Comparisons to the previous work by Sanvitale (2010) using the same methodology, material and apparatus are spread throughout this section. Sanvitale's (2010) experiment of the same PSD, uniformity, 24.5° slope and 27.8% moisture content is referred to as PSD9-mod.

In general the behaviour is the same for Sanvitale (2010) as the research conducted here but the presented quantitative comparison is not always consistent. This is a reflection of the limited range of tests from Sanvitale (2010). Sanvitale (2010) only has one presented test with the same combination of slope and moisture content as this thesis, comparisons of one test will therefore suffer from the natural inherent variable nature of debris flows and any differences in methodology. Therefore the comparisons focus on the quantitative comparison of PSD9-mod with the four 24.5° slope experiments presented in Chapter 4. A concluding section (section 5.2.5) seeks to identify and explain the potential difference in tests.

Sanvitale (2010) produced a comparison between the substitute glass material and the natural material that the substitute material's PSD was based on. *"The artificial mixture (Duran glass and hydrocarbon oil) exhibits behaviour similar to that displayed by a mixture of soil and water in analogous tests. Sanvitale (2010)".* The run-out lengths and velocity trends in terms of normalised values were consistent when the uniformity was altered. *"Most important, the well graded (substituted) mixtures exhibit morphologic features common to many natural and laboratory debris flow fans. Sanvitale (2010)".* It is therefore inferred that if Sanvitale's (2010) data was similar to real world behaviour and the tests in this thesis are similar to Sanvitale's (2010) then these tests are similar to the behaviour of real world material. This is

more certain for trends and micromechanical behaviour than for the absolute quantified values due to the impacts of viscosity scaling for the substitute fluid. Sanvitale (2010) did show that the added viscosity of the fluid had a small effect, most likely from the additional viscous drag forces. The main impact was reduced run-out. The velocity did not appear to be strongly affected.

5.2.2. Consistency of Deposit

The results in section 4.3 showed that the deposit shape of all tests was consistent, with a coarse front edge and only fine material deposited on the flume. Evidence of segregation was present throughout the deposit. The flow heights were not a good indicator of run-out lengths. However, higher velocities resulted in longer run-outs.

5.2.2.1. Run-out Length

The run-out length can be compared with some semi-empirical relationships. From equation (2-6) (Rickenmann, 1999), the run-out on the deck links only to the volume of the flow. This indicates that the empirical coefficient A_1 would be 1.8 - 6.5 which is lower than the typical value of 15 quoted in Rickenmann (1999). However, the laboratory debris flows used in Rickenmann's (1999) empirical had run-out of ~1.3 m for a similar volume with more uniform material with a similar mean particle size (~1-2 mm) and a slope of 15°. The moisture content was not stated by it is implied that it was at the saturation level. The results showed a run-out of 0.4-1.4 m depending on slope and moisture content; this indicates that the run-out is therefore within realistic values for the volume of material, given the difference in PSD, slope and moisture content.

Sanvitale's (2010) 24.5° slope experiment at 27.8% moisture content (PSD9-mod) should give the same general deposit values. However, S24W28EX8 appears to have had a much wider and longer run-out. Sanvitale (2010) did comment that the run-out shape and length were not identical between repeated tests. The variation between Sanvitale's (2010) PSD9-mod test and S24W28EX8 showed a difference of 20% in the maximum run-out length. Sanvitale's (2010) PSD9-mod run-out length was approximately 850-1000 mm and S24W28EX8 was ~1000 mm as shown in Table 4-1. PSD9-mod's run-out length was greater than the slope 18.1° tests from this thesis showing that at least the trends in slope run-out relationship are consistent.

The reason for the difference in run-out length from Sanvitale (2010) may just be the inherent variability of the flows or the dismantling and reassembling of the flume which resulted in a different tilt to the hopper and possibly some change in levelling. Figure 5.1 shows the tests at the same slope including tests at higher moisture content. Here we can see that it is possible that the inherently variable nature of the flows can result in significant differences in run-out results for tests conducted with the same variables. The 31.8% and 27.8% tests in Figure 5.1 show that there may not be much difference in run-out length with a small difference in the moisture content as moisture content is less sensitive than change in slope.

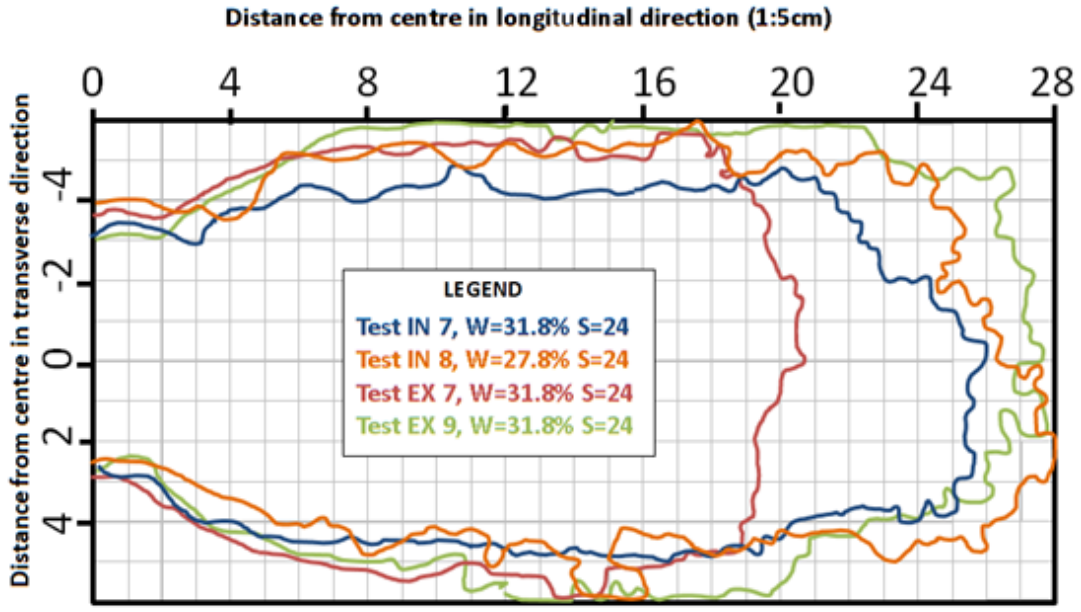

Figure 5-1: Outline of S24W32 deposits as taken from photographs of run-out deck. Grid is in 5cm squares.

Although Rickenmann (1999) related the height of flow to the run-out and travel distance of material, the results in this thesis did not show any indication that the height of flow was linked to travel distance or run-out lengths. This is likely related to the differences in volume of flows which has been seen to be the determining factor in height of flow. This means that Rickenmann's (1999) data taken for different volumes will have a wider range of variability and is a more general value. Additionally a difference might have arisen from the peak height being taken at a single location, combined with the evolving nature of the height which is discussed further in section 5.2.3.

In terms of the relationship between the flow velocity and run-out length, Figure 4-31 showed that in general as the velocity increased the run-out length increased.

Bowman and Sanvitale (2009) showed a relationship between the square of the velocity and the run-out length in Figure 2-23, original proposed by Hungr, Morgan et al. (1984). Sanvitale (2010) indicated that there was a constant uniformity coefficient required to apply this relationship. Figure 5-2 shows that the relationship cannot be applied to the results of this thesis. The 24.5° tests (in red) are too variable to compare between slopes, and the 18° tests (in blue) show that there is better fit to the velocity squared relationship but there is still much variability. It is possible to infer that changes in moisture content may not affect the relationship proposed by Hungr, Morgan et al. (1984), but no inference can be made in terms of slope.

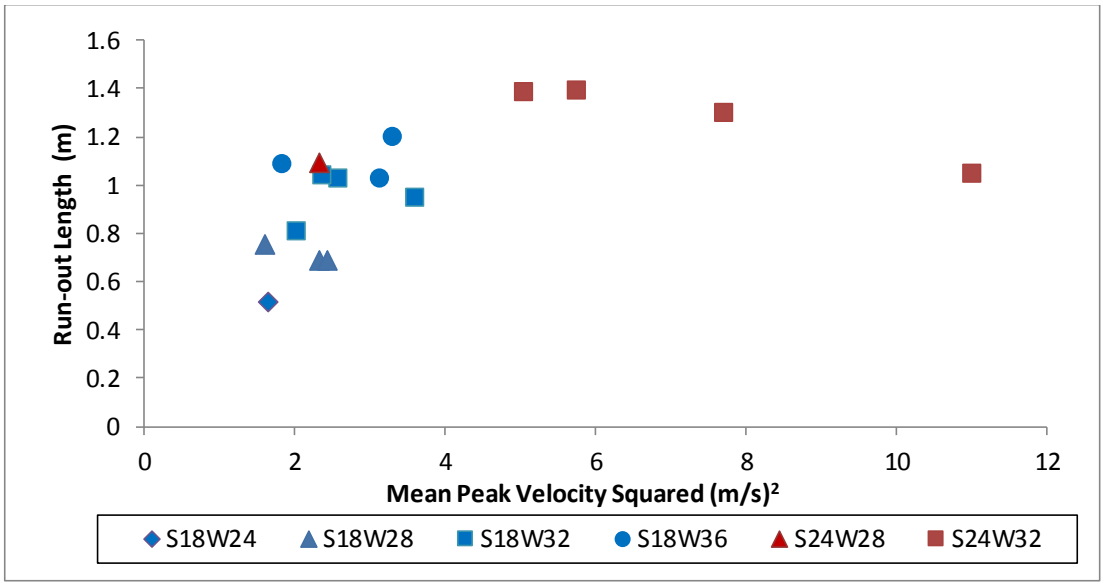

Figure 5-2: Velocity squared vs. run-out length. The legend indicates the approximate slope 'S' and the moisture content 'W'.

The relationship between moisture content and run-out length was well defined in Figure 4-15. Studies on moisture content (Chau et al., 2000; Legros, 2002; Major, 2000) agree that increased moisture content gives increased run-out within the range of tested values. The relative sensitivity of the run-out is the most interesting comparison to other studies. The findings of Chau, Chan et al. (2000), showed that run-out was highly sensitive to the moisture content. However, the results presented in this thesis were not as sensitive. In Chau, Chan et al. (2000) the slope and moisture contents were similar but the PSD was much more uniform with no coarse particles. This perhaps indicates that as the PSD becomes coarser the moisture content is a less-dominant factor unable to influence the largest particles in the flow.

The values in Figure 4-20 indicate that an increased slope gives an increased run-out, which is expected as a greater acceleration may be achieved on a steeper slope. The results of the tests showed the run-out was more sensitive to slope changes than moisture content changes when comparing the increased run-out length as a result of a 1% increase in moisture vs. a 1° increase in slope.

5.2.2.2. Deposit Shape

The deposit shapes presented in section 4.3.1 give a similar shape to other laboratory flows (Bardou, 2002; Liu, 1996) and show less variability than some of the USGS flume tests. The higher slopes had a more elongated shape similar to the higher slope (31°) USGS flume deposits. Results for higher slope showed the deposits were more elongated and had more chaotic edges. The edges are consistent with particles that have more energy. With regard to Sanvitale's (2010) experiments the similarity in shape holds as seen in Figure 5-3 of the outline of the of Sanvitale's (2010) experiments compared with S24W28EX8.

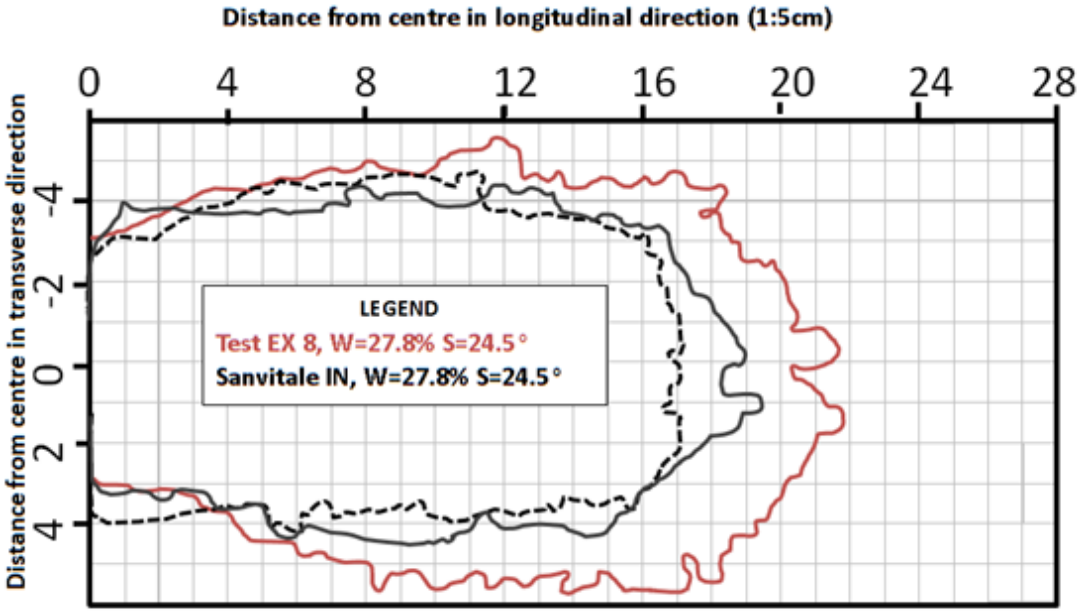

Figure 5-3: Outline of S24W28EX8 (red) deposit compared to two outlines (black) from (Sanvitale, 2010) as taken from photographs of run-out deck. Grid is in 5 cm squares.

The moisture content had a consistent effect on the shape of deposit and so was not seen to change the shape, just the scale. It is therefore assumed that it would not have just elongated as it increased in run-out length. The increased fluid might have allowed the increased spreading during deposition to occur at an equal amount in the transverse and longitudinal directions. The implication is that increase in longitudinal

run-out caused by added moisture will also allow spreading of the deposit. The moisture content did not affect the edges, suggesting that the solid and fluid phases do not separate with the changes in moisture.

The circular vs. elongated oval shapes are indications as to the type of deposition occurring. The circular shape would appear to show that the material slowed quickly at the transition to the 0° deposition deck and so spread out evenly without having the following material push through the coarse front. The elongated shape shows that there was considerable momentum and velocity at the base of the flume. This elongation thinned out the deposit which is supported by other laboratory experimentation (Liu, 1996).

The images, spot heights and PSD analysis showed well defined "Lobate" as described by Major (1997). The PSD of the various locations within the deposit agree with Sanvitale's (2010) conclusions for all experiments, particularly the coarseness of the front edge. The experiments presented in this thesis with a slope of 24.5° all had fines deposited on the flume to a metre up from the run-out deck. The depth of S24W28EX8 shown in Figure 5-4 shows that the deposit was typically around 10 mm deep which is lower than Sanvitale's PSD9-mod deposit (20 mm deep excluding individual large particles). The longer run-out means the same volume is spread over a larger area so the thickness is expected to be less.

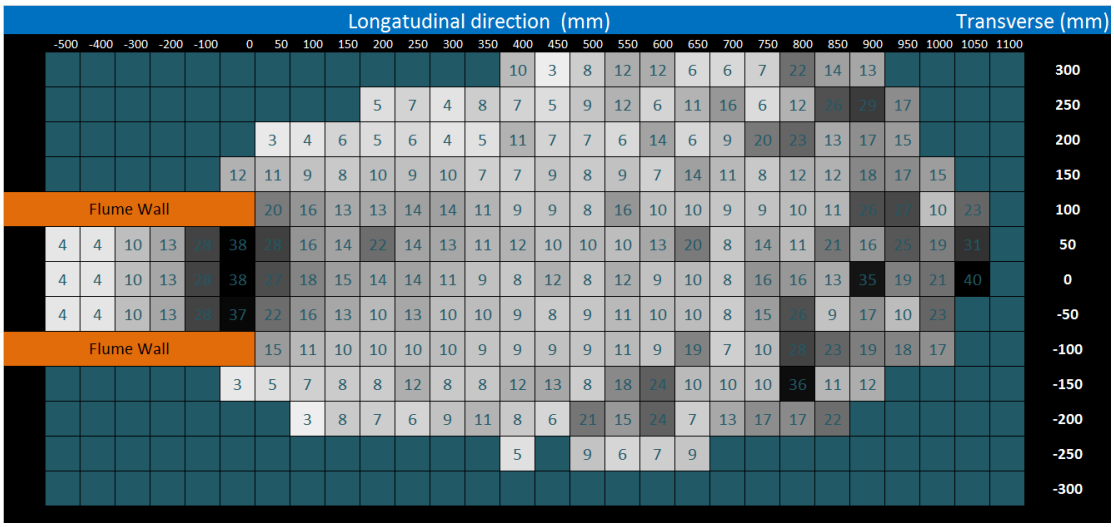

Figure 5-4: Spot heights of S24W28EX8. Shallow height trend to white and high spot height tend to black.

The effect of moisture content and slope on the deposits are supported by Major's (1997) findings where the deposit had a greater aspect ratio and a less variable margin

with a reduction in slope and moisture content. Comparing Table 2-1 the Major (1997) results show aspect ratios of 0.6-0.51 (over saturated) and 0.46-0.26 (approx. 100% saturated). The typical aspect ratio for low moisture content (27.8%) was 0.26 (EX8) and for the higher moisture content (31.8%) the aspect ratio was 0.42 (IN8, EX9). Considering that Major's experiments were conducted at a slope of 31 ° and the material was less well graded the corresponding aspect ratios indicates strong support for similar behaviour.

5.2.2.3. Deposit Segregation

Segregation was evident in all testing as seen in the spot heights and PSD analysis of the deposits. By exhibiting the most defining characteristics of debris flow deposits these flows can be reliably called debris flow. The segregation of the particles during the flow was evident in the images and will be discussed in section 5.3.2

There were no coarse levees on the sides near the transition point as suggested by Johnson, Kokelaar, et al. (2012); these sections of the deposits were actually dominated by fine material, particular in the longer deposits. This could indicate that there was mainly simple shear as in Figure 2-11, as the front did not push the coarse material out to the sides of the deposit. Alternatively there was no secondary surge front present to push the coarse particles to the side as it remobilised the deposit.

Sanvitale (2010) did not refer to the existence of any coarse levees but the observations of Sanvitale (2010) do support a large level of segregation in the deposit, particularly, the front edge which had a *"uniform coarse distribution with a significant increase in size of the mean diameter, in comparison to the source material. Sanvitale (2010)"*

5.2.3. Anatomy of Flow

5.2.3.1. General Flow Anatomy

The flow anatomy of the experiments was seen through velocity and height-over-time plots. The nature of these plots, how they compare to previous work and how they changed through the debris flows are discussed further in following parts of this section (Section 5.2.3.2 for height-over-time and Section 5.2.3.3 for velocity over time).

The summarised description of the flow anatomy, depicted in Figure 5-5, matches that from Section 2.1.3 but shows that there may be more distinguishable regions to the front and body which can be defined based on the particle behaviour and motion. These regions were consistently seen in all the tests regardless of the variables. In a eneral sense the flow anatomy, depicted in Figure 5-5, can be described as the following:

- **Free particles:** any particles that precede the flow. Sanvitale's (2010) images showed a few grains preceded the flow. In both cases the preceding particles' shape allowed rolling and bouncing rather than sliding allowing a faster transportation down the flow.
- **Coarse snout:** A blocky snout that was coarse and unsaturated was considered from the first particles that was constantly in contact with the flow to the beginning of the saturation of particles
- **Initial body**: A partially saturated front to the body that was coarse and increased in height; this section ended where the peak height occurred. The snout and this part of the body form the front and were often the same for the low slope and moisture content experiments.
- **Front**: the front is the traditional unsaturated or partially saturated section and is often defined as the part before the maximum height of flow
- **Body plateau:** The body contained the majority of coarse particles in a thick section that was well graded through the flow and inversely graded. The body was from the peak height to the point at which the velocity and or height stopped decreasing rapidly
- **Body to tail transition zone:** A transition area between the body and tail that had some velocity but low height of flow. This section is the point between a rapid decrease in height and velocity and the steady height and velocity of the tail and is represented by the curving part of the velocity over time plot.
- **Body:** the traditional body is the combination of the saturated part of the front and the bulk of the material and would finish half way through the transition region.
- **Tail:** The flow ended in a tail that was consistent, highly fluid and shallow.

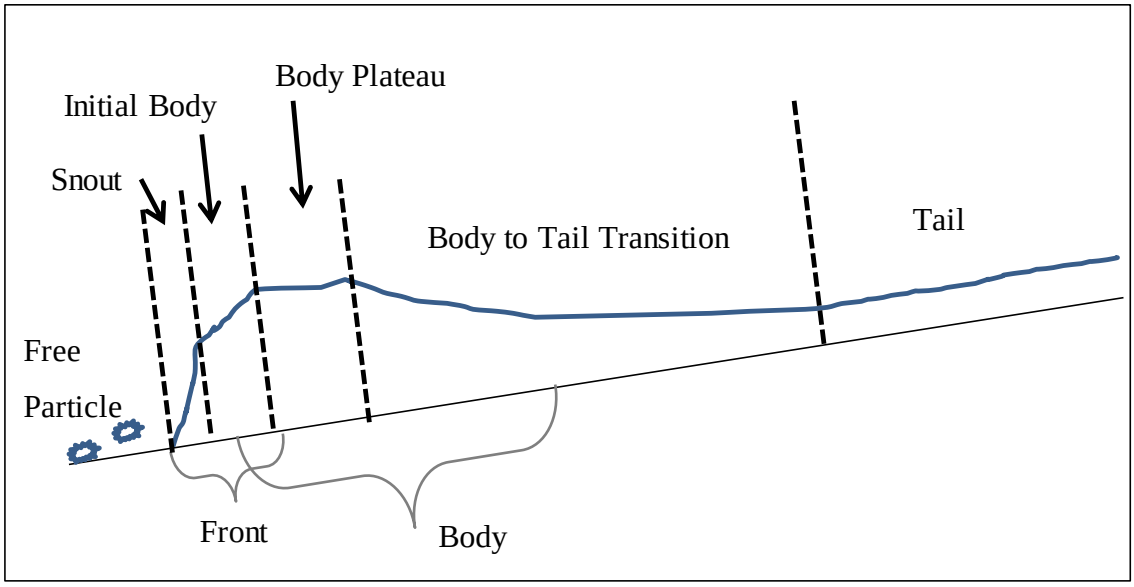

Figure 5-5: Regions of debris flow shown on a depth over length of slope. The debris flow is separated into specific regions of behaviour and material composition.

The bulk of the mass was fast and concentrated in the snout, initial body and body plateau, with a particularly peaked front in terms of velocity and height. These sections combine to form Takahashi's (1991) front and are reinforced by the same behaviour seen in Sanvitale (2010) where the PIV analysis of the flow showed the body as a high, fast, consistent surge that drops quickly to a slower thinner tail.

The micromechanical evolution between the various regions of the flow was continuous without very distinct transition points, showing why researchers tend to combine them. However, distinct regions of the flow can be more clearly seen in the velocity over time plots (particularly the interior plots) where the slope of the velocity over time profile reached inflection points. Table 4-3 shows the time steps between each part of the flow changed.

The separate regions have dramatically different PSDs and so will require different rheologies for modelling. Focusing on the quantifying of mass and PSD in these regions, particularly the body to tail transition, could help quantify the relationship between height, volume and the mass movement within surges.

5.2.3.2. Height with Time

Generally most researchers depict debris flows as smoother lengths when defining debris flows in idealised sketches. The height-over-time of these results is steeper with a distinct peak in height. This is likely the result of the flume's single mass being

released at a single moment directly on to the slope rather than developing via entrainment or continuous feeding of material from the top. The results show more of a bore that seems to represent all of the hazardous and destructive potential of the flow. This is still a realistic hazard scenario. For example, a large slip from a side wall of a valley that drops as a single mass into a non-erodible channel or steep valley, or a dam break scenario.

The height with time in Figure 2.21 for the USGS flume (Iverson et al., 1992) had a profile suggesting two surges. The USGS flume flows were conducted over a relatively longer length, higher slope and higher volume, which may have allowed for multiple surges to develop. Iverson and Vallance's (2001) experiments on the USGS flume show a profile (Figure 2-6) more consistent with the height-over-time of this thesis's laboratory experiments. There is even a slight plateau of the height at the beginning of the body which occurred enough in these results to create a separate region of the body. Iverson and Vallance (2001) has less instantaneous variation but the particles are relatively smaller compared to the depth of the flow so it is expected to be smoother.

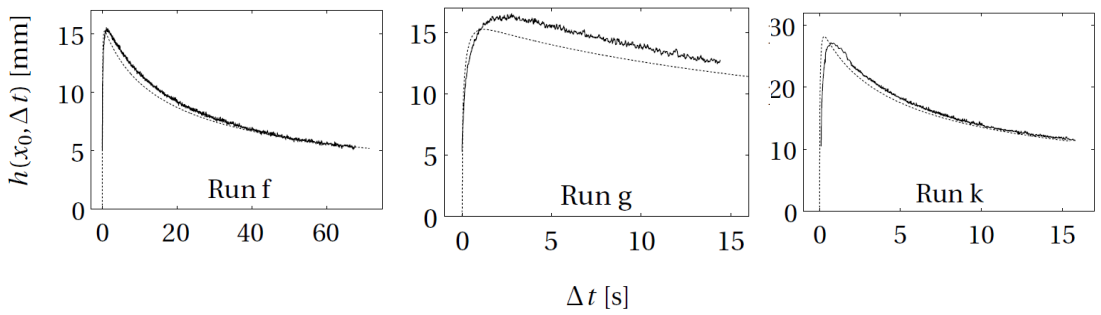

Figure 5-6: Height-over-time for slope 25° solid fraction 52-55 %. Run f and g have a mass of 3 kg. Run k has a mass of 6 kg. Note the variation in scales. (Andreini, 2012).

Andreini's (2012) interior recorded height-over-time gives a consistent smooth shape that decayed rapidly from a sharp peak (Figure 5-6). The time scale is very different (70 s compared to the 2-3 s of the thesis results) indicating a much more viscous flow, a reflection of the high level of fines in the flow. The smooth decaying height profile is likely due to the uniform fine PSD of Andreini's (2012) material that reduced the variability of a well-graded PSD. The comparison in sharpness of the peak height is a reflection of the ability of larger particles in a well graded material to form a more spread out body. Andreini (2012) proves that the height profile is not Newtonian in Figure 2-31.

The link between an absolute height and height of saturation has not been widely presented in research. This is likely due to the difficulty in recording the separate fluid and solid phases. In general the absolute height-over-time shows more instantaneous erratic movements as coarse particles, sitting high in the flow, move past the camera. There are some instances where the large particles are able to influence the saturation height but these are infrequent and limited to the later sections of the body and tail. Otherwise the saturation height follows the absolute height well. In the snout and body of the experiments conducted as part of this thesis, regardless of the moisture content, there was neither excess fluid above the particles nor unsaturated medium to fine material above the saturation surface. In the tail there was evidence of excess fluid. This shows that the shape and composition of the front adjusted so that there was close to 100 % saturation through the body.

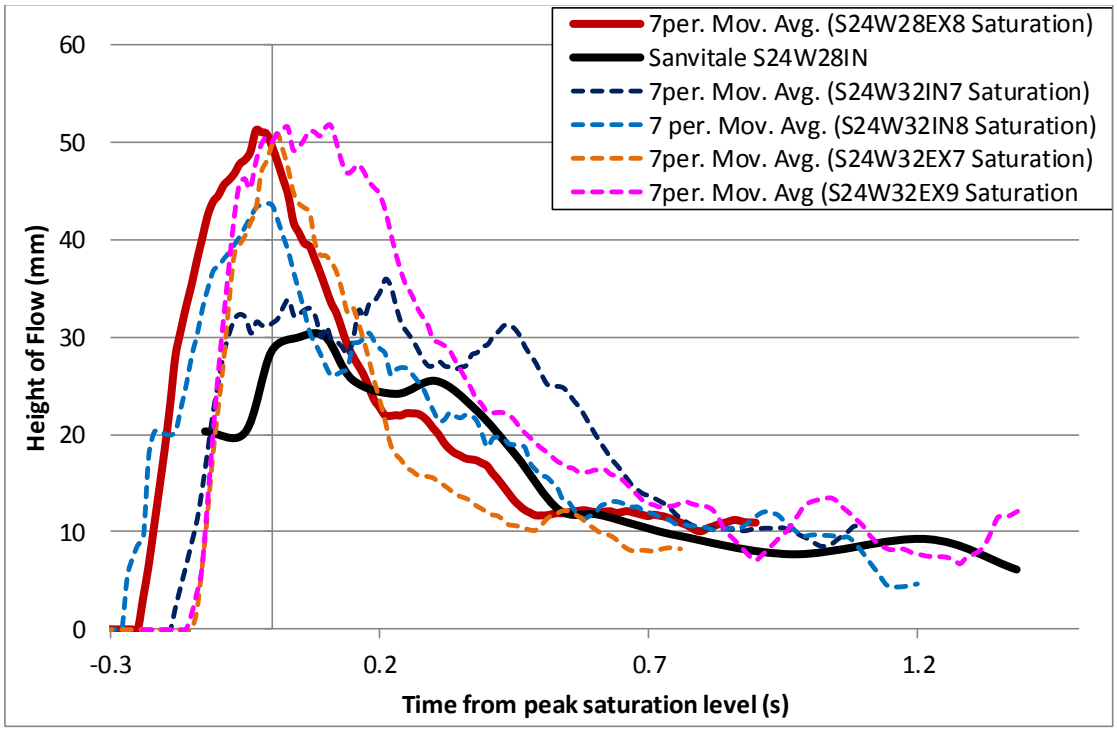

Figure 5-7: Saturation levels of slope 24.5 ° flows. Sanvitale's (2010) results have been shifted so that time zero occurs at the approximate maximum saturation height and the height cut from PIV analysis has been added approximately 2.6 mm.

The height-over-time comparisons with Sanvitale's (2010) PSD9-mod need two adjustments before they can be compared. The height in Sanvitale (2010) is the height used in PIV calculations and must be increased by the lower bound reduction due to patch centre trimming (2.6 mm). This value was calculated based on velocity profiles being analysed at a 32-pixel patch size. The lower bound is used as the reduction used

in PIV is the same at the base and free surface (see section 3.11.2.1). The other adjustment is to shift the time so that the peak saturation level corresponds to time zero. Sanvitale (2010) set the reference time of zero to correspond with the peak in absolute maximum height flow, so there was a lag correction between absolute and saturation level peaks. Figure 5-7 shows PSD9-mod's height-over-time after these adjustments. Figure 5-8 only needs the time shift and shows the heights used in PIV calculations.

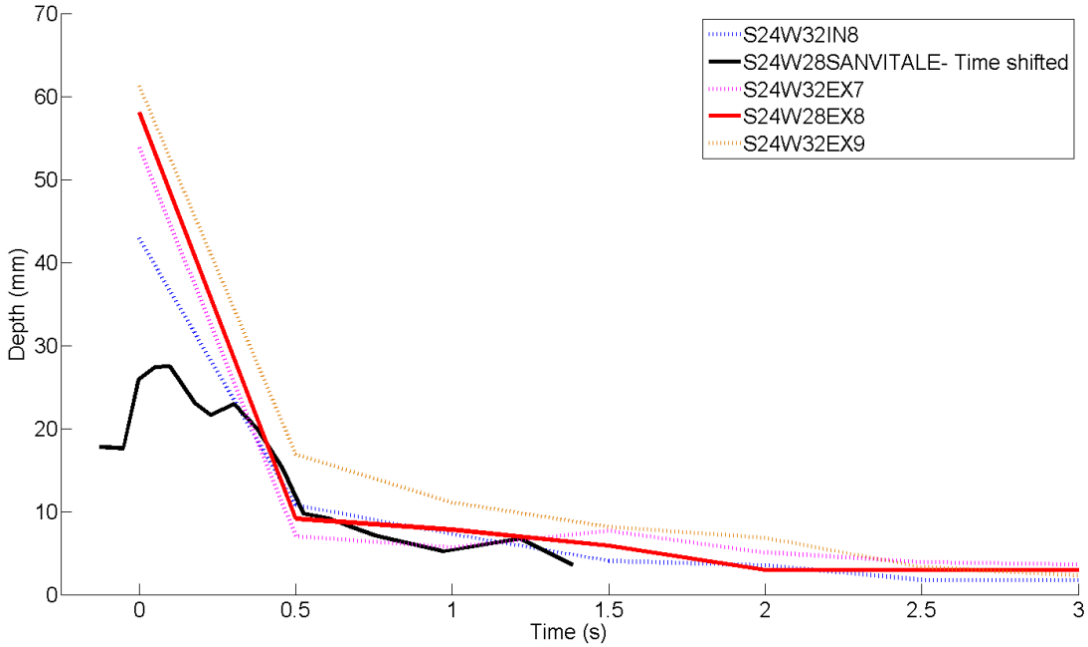

Figure 5-8: Height slope 24.5° of flows used for PIV calculations. Sanvitale's (2010) results have been shifted so that time zero occurs at the approximate maximum saturation height.

The heights match after the point where main part of the body has passed. It appears that Sanvitale's experiment did not develop the same peaked height and is similar to the S18W28IN1 and S24W32IN7 tests which had lower PIV heights. This may be due to relatively poorer illumination and image quality of Sanvitale's data. It is possible that the actual maximum height of the flow is higher and just not recorded due to being unsaturated.

5.2.3.3. Velocity with Time

The results show that the velocity over time matches the profile of the height-over-time with a more peaked front. Andreini's (2012) velocity profiles show that it peaks in the first ~1.5 s and then decays at a similar rate to the height. Again, this is a much longer time scale and lower velocity than these thesis results. The velocity over time

is a reflection of segregation where the coarse front material has relatively high dispersive pressures and low viscous pressures giving high mobility and the separated fine material being incorporated into the fluid, increasing its effective viscosity and reducing the velocity of the fluid.

Figure 5-9 and Figure 5-10 shows that even though Sanvitale's (2010) PSD9-mod's height did not reach the same peaked shape over time, the mean velocity over time did. PSD9-mod's velocity profile matches well with the mean velocity over time for S18W28EX8. This further supports the idea that the recorded height was not as high because of illumination issues. If the top was not properly illuminated then the higher faster top section would have not been calculated during PIV analysis. This could mean that Sanvitale (2010) underestimated the actual peak velocities.

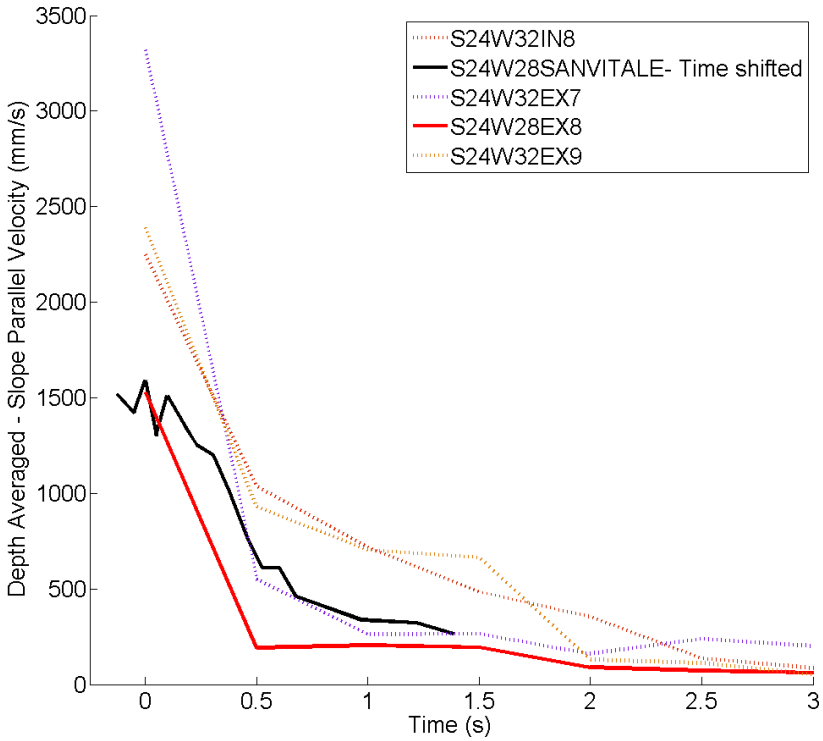

Figure 5-9: Comparison of depth over time of slope for 24.5° tests and Sanvitale's (2010) PSD9-mod results. Sanvitale (2010) results have been shifted so that time zero occurs at the maximum saturation height

The bottom graph in Figure 5-10 shows the approximated flow rate of material or the thesis results with Sanvitale's (2010) data. The flow rate of Sanvitale's (2010) data is significantly smaller because of the lower height. The tail and the transition section between body and tail show similar shapes and although it did not decay as quickly as S18W28EX8 it is within expectations based on the other tests at the same slope. The level of agreement in mean velocity means that the run-out length is expected to be close between the two tests which were found to be reasonably accurate.

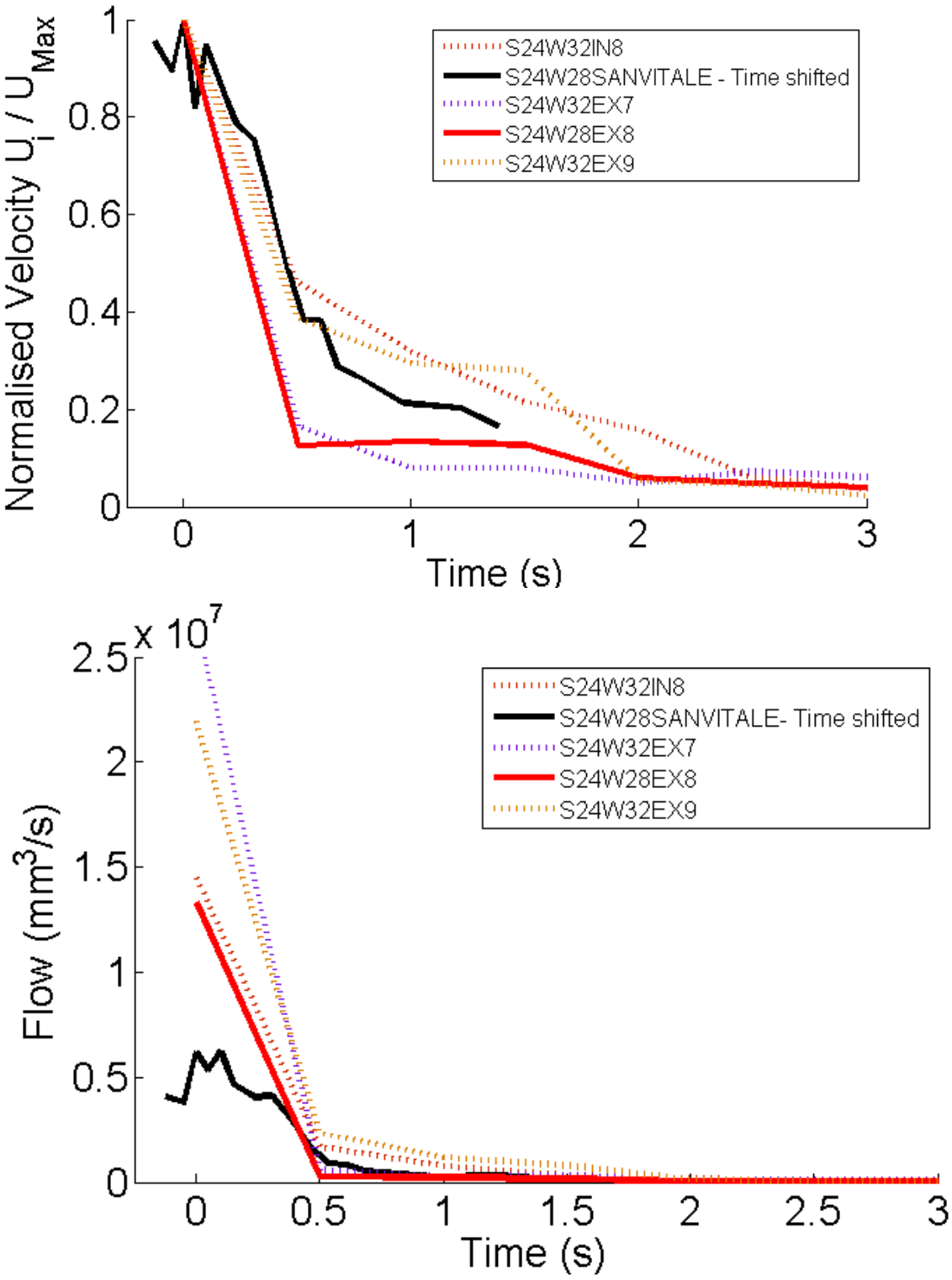

Figure 5-10: Comparison of depth averaged velocity over time (top) and flow rate over time (bottom) for slope 24.5° tests and Sanvitale's (2010) results. Sanvitale (2010) results have been shifted so that time zero occurs at the approximate maximum saturation height.

5.2.3.4. Effect of Moisture Content on Flow Anatomy

The moisture content shows a more noticeable difference on the snout and initial body shape than the body to tail transition and tail regions. At low moisture the snout was steeper indicating a more plug-like behaviour. This is expected as granular-only flows (Adrian, 2005) are more likely to form a shear layer at the base like Figure 2-5, which concentrates the shearing and does not transfer forces throughout the block of material above.

As the moisture content increases there could be larger pore pressures that could allow more dispersive pressures to separate the unsaturated snout and the saturated coarse section. The body becomes longer as well which created a more defined body plateau in height as the large particles have fluid and entrained finer particles in the voids contributing to pore pressures that prevent them from packing closer together, and act to push the front faster.

The tail heights in Table 4-2 may indicate that the tail became thicker as the flow progressed. The tail is fully to over-saturated by fluid and so additional moisture only dilutes the impact of the fines on fluid viscosity and, as discussed in 5.2.3.2, if the front and body are 100% saturated the extra fluid may be found in the tail, increasing its depth. The reason for the variation may be the occasional occurrence of large particles in the tail.

5.2.3.5. Effect of Slope on Flow Anatomy

It appears that the bore or snout at the front does not steepen with increased slope as a wave would, i.e. where the top moves faster than the base of the wave. This may be because the snout is being pushed and so the entire front, with depth, is travelling at the same velocity. The slope actually had a similar effect on the snout as moisture content resulting in a steeper snout at low slope. This could be an indication of more block-like behaviour but for a different reason. While moisture content affects the pore pressure, the slope will affect the granular collisions. The shallower slope allows the body to keep closer to the snout as less energy is being transferred into the particles so there is less dispersive pressure from the inter-granular collisions.

5.2.3.6. Abnormalities in Height and Flow Shape

There were some tests that had a different development in height they tended to elongate and not develop the same peak height. Sanvitale's (2010) front and body sections passed the camera in a time less than 0.45 s while Figure 5-7 shows that the bulk of the front and body of the S24W28EX8 test could be seen to have passed in the first 0.2 s.

The run-out is similar in most cases or is reduced. This suggests a potential under-development of the height or conveyor system that builds up the front. It is unclear whether these reduced fronts were a result of blockages in the hopper, were in a different stage of frontal collapse and build up, or were a result of different instabilities and small issues in release of material. These tests were S18W28IN1, S18W32EX4 and S24W28IN7 which are discussed in relation to the other tests with the same variables in detail in Appendix D.

It is seen that most of Sanvitale's (2010) work would have matched one of these stretched or under-developed results much better than the peaked ones. This would suggest that there could be something in the methodology that resulted in the difference. S18W28IN1 has issues with illumination using the same original camera as Sanvitale (2010). The illumination may mean that the top of these tests might not have been visible resulting in less height and depth. This does not, however, explain tests S18W32EX4 and S24W28IN7.

Possible causes for the other test differences are clogging or blockages in the release of the hopper. This is unlikely as S24WIN6 suffered from a large particles becoming lodged between the flume and pneumatic piston at the end of the hopper. This blockage did not result in any noticeable difference in flow behaviour. In order for blockages to be the reason it is possible that a bridge of material formed, letting some drop out before the rest. This was possible as some tests required a quick stir to initiate the release after the hopper door was opened. If this is the case then these tests show that material that is not released all at once can still give the same run-out and some may develop the same momentum by the time they reach the run-out deck.

Figure 5-6 also shows that in the case of Andreini (2012) the difference between run 'f' and 'g' (tests of very similar variables) there is a potential for a difference in trend

of the height-over-time. This is a case of a natural or laboratory variability in behaviour but the magnitude indicates something more than just the influence of random particle motion and interaction. This phenomenon should be further explored to see where the differences occur.

This is significant in that it shows that there is a mechanism in which the body does not form such a conglomerate mass but might be spread out more. The front of these cases will have less impact on obstacles than the more developed peak shapes. However, as engineering requires a prudent understanding of worst-case scenarios, protection and hazard management needs to be based on the steeper, higher impact, cases.

5.2.4. Instantaneous Velocity Profiles

The shape of the velocity profile is linked to specific regions of the flow and evolves over time. The following sections link the types of profiles to composition and demonstrate some implications on behaviour. The normalised velocity profiles offer the best indication of the different shapes of the velocity profiles. The results are split into the more traditional front, body and tail. The main visible factor differentiating these profiles is the presence of a slip velocity. Most fluid-based rheologies are based on a no-slip lower boundary condition whereas most granular rheologies have a slip condition. The reality is in a multi-phase mixture the fluid will have a no-slip boundary condition but the granular material will have slip. The actual resulting behaviour at the base of the flow is likely to promote some segregation of the phases.

5.2.4.1. General Comparisons

The velocity profile was seen to be more dependent on location within a flow than the effect of changing the LOV, moisture content, or slope. This can be seen in Figure 5-11 comparing Sanvitale's (2010) PSD9-mod results with the results from this thesis. Sanvitale's (2010) debris flow experiments on other particle size distributions show the same trend was indicated. Considering the velocity profiles for the front, body and tail of Sanvitale's (2010) work in Figure 5-11 against the higher slopes means comparing to exterior flows primarily. The effect of comparing to exterior tests will be discussed in section 5.3.1. However, given that the heights of the velocity profiles are quite different resulting in different velocities, only qualitative comparisons are

effective. The interior test S24W32IN8 matches PSD9-mod well in terms of velocity of the body to tail transition zone. Sanvitale's (2010) PSD9-mod and S24W32IN8 have different moisture contents but as discussed in the behaviour is not highly sensitive at this moisture content step of 4%.

What is most interesting is that the normalised curves for PSD9-mod follow the same shape as all of the interior profiles, particularly, the slip velocity value of half the depth-averaged velocity. The left panels of Figure 5-11 at the front show a slip velocity of 0.9 ms^{-1} which is approximately half the velocity of the upper uniform block part. This shows that there is a consistent difference in slip velocity regardless of the development of a steep front. Sanvitale did not make mention of secondary surges in the material but it is possible that some of the tests did have this phenomenon.

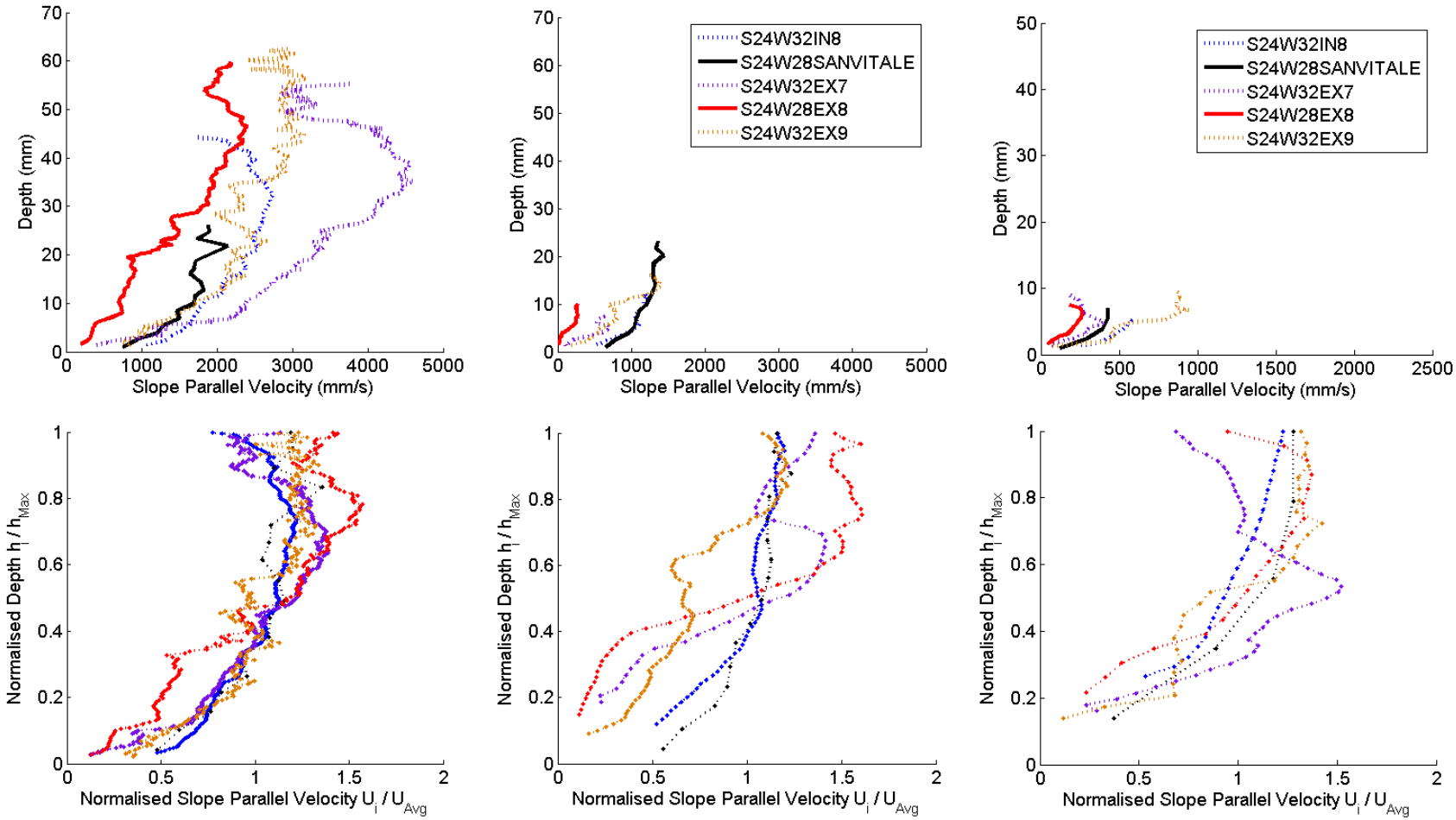

Figure 5-11: (Top) Real velocity and (bottom) normalised profiles for (left) front, (centre) body and (right) tail of flow. Black line represents data from Sanvitale's (2010) PSD9- mod.

5.2.4.2. Evolution of Profiles

The evolution of the velocity profile is best seen in the normalised velocity profiles like those present in Figure 4-32, which show a development throughout the length of the flow. The multiple regions may represent multiple rheologies, the tail being Bingham. The front tends toward a granularly dominated flow, with a short period transition between them. The timing of these changes reflects the passing of the body.

Samples taken within the defined area of the flow anatomy gave distinct profiles for the front, body and tail. This distinction was less evident in samples taken close to each other where the inherent natural variability was present. The evolution seems to be based on the level of saturation in each section of the flow. Figure 2-4 from Salm and Gubler (1985) can be used to demonstrate the idea of increasing saturation in a granular-dominated flow and how it affects the velocity profiles. Images and understanding of the composition of the front, body and tail allows a hypothesis to be made of the reason for evolving velocity profiles.

The nature of the different parts gives rise to an idea of "stretching" of the debris flow which means as the flow preferentially sorts the material with length along the flow, there is a difference in velocity that further forces the evolution of the profiles.

As the profiles evolve preferential sieving means that the larger particles move upward and so are no longer rolling or sliding along the base. The fines that replace these particles are more fluidised and flatter (see shape of particles in Figure 3-6) so they are less able to slide or roll. This shows why there are reduced slip velocities away from the coarse front. The velocity profiles show that the base friction is increasingly being transferred upward into the flow and this reduces the velocity, slowing that section of flow.

If the finer material finds it harder to move or move away from the base under viscous forces than the coarser particles the coarser fraction will move faster thus increasing the segregation. The finer material at the front now will have reduced forces acting at the base of the flow due to concentration of fluid concentrated with fine material. This effect further increases as the coarser material moves onward, and no longer contribute inertial forces. This slowing due to viscous drag increases the stretching of the flow making it longer and thinner. A thinner flow means less distance for the coarsest fraction to migrate to the faster free surface reinforcing the larger particles to move faster.

The unsaturated snout had the same velocity as the front of the body so did not stretch, while the coarse body and fine tail reduced in velocity so stretched out the flow beyond the front. The reason for the snout being at the same velocity as the initial body is that the snout which has collected the largest particles through the conveyor system does not have any fluid and so no additional pore pressures to increase mobility. It can be assumed that for these experiments the more mobile initial part of the body was unable to push through or over the snout as that would have resulted in surging as the mobile body was able to move faster until a new snout was formed. The fluid under viscous stresses is unable to travel faster than the initial body so does not seep out into the snout but is pulled back into the body plateau by the fluid's viscous forces and no-slip condition at the base.

5.2.4.3. Characteristic Snout Velocity Profile

The main difference between this study and historic studies is the presence of a slip velocity in the snout. The magnitude of these velocities themselves is consistent (see tables 4.7) at approximately half the depth averaged velocity of the flow. The variability of the slip velocity will be discussed further in section 5.3 on interior and exterior comparisons. The snout shows the highest slip velocity which reduces into the debris flow. The slip comes from the unsaturated and mainly sliding large particles. At this point the small gap in PIV analysis makes it difficult to determine exactly what the value of the slip velocity is, but is clearly present.

Figure 2-5 from Pudasaini and Hutter (2007) shows the best conceptual model to fit the velocity profile of the snout of these tested debris flows. The top is a block or plug that has little shear stress. The bottom boundary layer is the area of most shear and the above layer has a more constant velocity. Analysis of the snout shows that approximately the 0.1 s either side of the peak saturation height (or the separating point between the initial body and the plateau body) has similar velocity magnitudes to the profiles. However, as the analysis moves from the snout into the body plateau the velocity profiles have a similar upper shape but the bottom boundary layer loses the slip velocity as fluid begins to interact with the base material. This indicates that the fluid is acting predominantly at the base to affect the type of bottom boundary layer. The velocity profiles have reduced slip velocity and an increased shear gradient in the same thickness of boundary layer. The behaviour approaches something more like the bottom section of the block flow in Figure 2-4. The fluid can therefore either

not have penetrated into the upper sections of the flow or the fluid phase is not contributing to the behaviour.

The snout is the fastest part of the flow. The magnitude of the velocity (1.2-3.3 ms^{-1}) is similar to other laboratory experiments (Rickenmann 1999) of approximately 0.2 – 3.7 ms^{-1}. Sanvitale's (2010) PSD9-mod had a maximum front velocity of just over 2 ms^{-1} and a mean depth averaged velocity at the front of the body of 1.6 ms^{-1}. This is lower than the results presented here and is closer to the lower slope, high moisture content tests. Because all of the front regions appear to have the same velocity and the unsaturated snout section tended to be short and upright, it can be inferred that the snout is being pushed by the more fluidised initial or plateau body regions. If this was not the case the unsaturated snout would stretch away from the initial body or be less steep as the variously shaped particles began to move according to their rolling or bouncing nature.

5.2.4.4. Characteristic Body Velocity Profile

The latter regions of the body where it is beginning to transition to the tail show a partially fluid profile similar to Figure 2-4 and has a more non-uniform particle distribution with depth. Moving from the snout to the body the slip velocity reduces to a very low value. It appears to approach zero but cannot be determined due to PIV limitations. There is still an aspect of an upper block which could be the large particles moving as one. The bottom boundary layer increases in depth till it consumes the depth of the flow and the partially fluidised profile is established.

It is possible by transferring the stress into the material through viscous stress in the fluid at the base that the particles further dilate allowing more mobility and faster motion of the upper sections of the flow. The rheology of the body is the most complex as the solid and fluid phases are contributing to the behaviour.

5.2.4.5. Characteristic Tail Velocity Profile

The tail shows a fully fluid profile similar to what is expected of a laminar Newtonian fluid characterised by the nearly linear velocity profile. The velocity is low so the measure of turbulence and chaotic nature is reduced in theses sections, which is particularly apparent in these experiments as the substitute fluid has a higher viscosity which will reduce the Reynolds number at this velocity compared to the real fluid, water. This suggests that these experiments may have a tail that slows quicker but as the tail does not have large mass or

velocity and deposits on the slope, it is not as important a factor in evaluating the hazard produced by the debris flow.

The images show particles settling at the base of the flume, and fluid and smaller particles flowing over the top. The tail is now dominated by its ability to suspend the particles. As the velocity and depth reduces, the coarsest fraction drops out of the fast part of the flow and slides slowly until it backs, depositing on the flume slope.

Andreini (2012) shows the opposite trend in evolution of the tail in Figure 5-12. This is likely to be due to the settling and interlocking of the material as it slows, so the stress at the free surface is no longer enough to dilate the material. Because the tail of these experiments has only fine particles in an over-saturated case, the particles are more of a bed load and the fluid dominates.

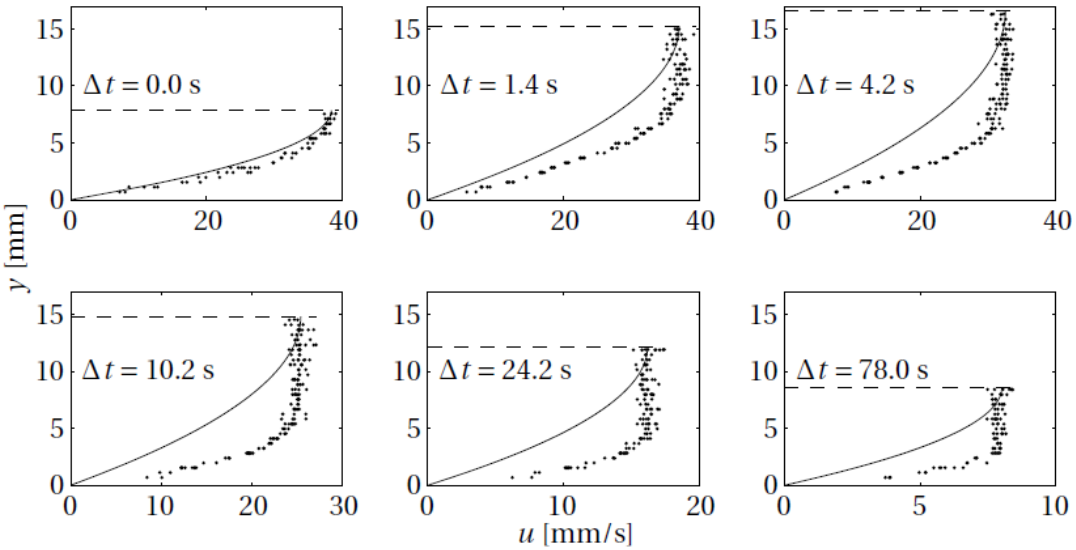

Figure 5-12: Instantaneous velocity profiles. Solid line is Newtonian profile spots are actual experimental results for a solid fraction of 56 % 25° and 3 kg. (Andreini 2012).

The top of the tail velocity profiles in Figure 5-12 seems to be forming a plug that is moving over the shear layer of the base. This could be due to the excess fluid above the particles that is able to flow faster at the free surface. As the excess fluid dissipates there is evidence at the end of the tails, in the longest recordings, of drainage within the tail material. The evidence of drainage paths in the flow of S24W32EX9 shows that in the exterior case the coarse particles are no longer moving, creating a network of pores that the fluid and finest particles can move through. This also indicates that the fluid is flowing out of the material deposited on the flume.

5.2.4.6. Effect of Moisture Content and Slope on Velocity Profile

In absolute terms, an increase in moisture content increased the velocity of the flows. But a change in moisture content did not appear to affect the velocity profile shape and devolution of the velocity profiles throughout the flow. This meant that the slip relationship of the snout was not particularly affected. This would support the idea that the fluid does not influence this part of the flow.

The moisture content might affect the rate at which slip velocity decreased, i.e. more moisture means the bottom layer is more fluid and so has less slip. But not the ratio of boundary layer thickness to depth. The tail was much more erratic in terms of profile which was mainly attributed to having such a thin flow to analyse since there were few data points which increased the erratic shape.

As the slope increased the velocity increased and the maximum and minimum velocities followed the same trend as the mean velocities. Unlike the moisture content, increasing the slope did affect the shape of the flow visibly shortening and thickening the body. The shortened body means an increase in slope quickened the evolution of the profiles. Because the snout, body and tail profiles were the same shapes, the increased slope did not affect the type of rheology and evolution of the velocity profiles, just the speed of the evolution. There was no visible effect on the actual slip velocity relationship or decay.

Schaefer, Bugnion et al. (2010) conducted slope-dependent tests on small particle dry granular flows and found that as the slope increased the front became steeper and the slip velocity increased. It is important to show that the slip velocity was not present throughout the flow and reduced to zero in the body in a similar evolution to the debris flow behaviour where the body velocity profiles showed a more constant shear rate. This material gave velocity profiles more like a debris flow than fluid flows, again suggesting that moisture content does not define the velocity profile.

Changing slope did seem to alter the thickness of the bottom boundary layer of the snout and initial or plateau regions of the body. At the high slopes the (compare to Figure 4-36) height of the bottom boundary layer had an approximate ratio of 0.3 to the maximum free surface depth of the profile, while the lower slopes had a (compare Figure 4-36) ratio of 0.2 for the bottom boundary layer.

An increase in slope meant more flow depth, so more material and range of particles sizes and more acceleration down slope. These are likely to combine to allow for more dilation of particles and so a thicker bottom shear layer. The amount of material above would add more weight, perhaps reducing the effect of the increased dilation.

Because moisture content and slope did not significantly affect the evolution of the velocity profile shape this can be seen as a characteristic flow of a well-graded debris flow and is a combination of the material properties and the presence of relatively similar volumes of fluid to solids. This should allow fitting of rheologies to parts of the flow that have only small impacts from slope and moisture content within the ranges tested.

5.2.5. Evaluation of Results Compared to Sanvitale (2010)

Over all, the results in Chapter 4 agreed with Sanvitale's (2010) data. The main difference was a lower run-out length, lower height and so slightly lower velocity for Sanvitale's data. The general nature of the behaviour and presence of a similar magnitude of slip velocity suggests the micromechanics were the same. The natural variability makes exact comparison difficult as only one of Sanvitale's tests is directly comparable with the same exact variables as used in this thesis. Other potential reasons for differences have been summarised below.

5.2.5.1. Initial Condition Sensitivity

The reason for the differences in height and run-out between Sanvitale's test and these tests with the same variables shows the sensitivity of laboratory debris flow testing. The same method, material and apparatus were used for both test arrangements. The velocities in the front show good similarity given the difference in height and the variability in the run-out can be partly attributed to the natural variation in testing. However, there is also some difference that can be attributed to small differences in the tilt of the hopper and the agitating of the material by the laboratory operator prior to testing.

The hopper used to store the material was adjusted and tilted during relocation of the apparatus. The original inclination of the hopper to the flume for Sanvitale was approximately 23˚ to the flume. This was increased and fixed to allow the material to drop freely from the hopper under lower slope conditions. The higher inclination may have resulted in the steeper surge front. The other factor was the agitation of material in the hopper prior to testing. This was conducted by the operator to prevent the solid and fluid phases to settle and separate. Given that this was an intensely physical task there will have been

differences in how vigorously and successfully different operators performed this task. It is likely this resulted in more agitation of the material than Sanvitale's experiments.

5.2.5.2. Illumination Levels

The only different piece of equipment used was the camera while the power level of the laser was increased in these tests. The increased power of the laser meant the flow depth was fully illuminated. It was found that the strength of the laser light reduces with depth, particularly areas of high fluid or fines concentration. This is likely due to the number of particles interfaces and the dye absorbing the emitted light.

The new camera had a sensor that had larger pixels which allowed more light to be captured. At the same resolution (number of pixels) the Miro camera would increase the captured light intensity by approximately double. This ensured that even the lower light parts of the flow were picked up and able to be distinguished. The more light captured by the camera, the higher the range in light intensity values, leading to more detail for the PIV programme to perform accurate correlations. Test S18W28IN1 (see Appendix G for image comparisons) showed the difference in light levels as it was conducted using the same Meme view camera as Sanvitale (2010). Given the difference between the original camera and the two subsequent higher quality cameras it is likely that there is at least some of this limitation in Sanvitale's (2010) work.

5.3. Interior Testing

Investigating the difference between the interior and exterior test is a key part of determining the benefit of an internally focused methodology like PLIF. There is no question that the motion of large particles cannot be easily seen in traditional opaque methods, as seen in studies like Sanvitale (2010), Hunter (2012) and Andreini (2012). This allows better theories, measurement of collisions and the relationship between the solid and fluid phases (e.g. pore sizes) to be seen. The other benefit is the ability to investigate the influence of a side boundary and how the interior may give more accurate results. As debris flows are channelized flows the interaction with a wall and the change in velocity and material composition perpendicular to the channel is a real and important factor. In this area there is little previous research with which to compare as it was not conducted as part of the previous work of Sanvitale (2010).

5.3.1. Boundary Conditions

This section focuses on the differences between interior and exterior tests. There was no significant difference in interior and exterior deposits but comparisons of all tests showed a high level of natural variability in experiments. This leads to a conclusion that the interior and exterior tests were the same but had chaotic and random factors that caused the differences.

The comparison between the exterior and interior behaviour was a key comparison in this work and showed that there are likely differences in velocity mainly in the front and initial sections of the body. The variability of testing means that quantifying the magnitude of the difference is difficult but the difference is visible in the results.

5.3.1.1. Height

The exterior saturation heights were similar or larger to interior, indicating that in most cases the height is consistent over the transverse direction of the flow. The reason for the slight edges may be the smearing of the fluid after large particles pass, making it hard to distinguish if the saturation surface level had dropped or not. Andreini (2012) had slightly upturned edges but these were likely a result of slowing due to friction at the wall backing up the flow directly adjacent to the window. Andreini's (2012) material is relatively fine and so is only affecting the particles directly pressed to the wall. This is not particularly likely in this research as the well- graded nature means that coarser particles are distributing forces throughout the flow as they interrupt the shear layers in the flow.

The absolute height or erratic height cause by passing large particles had less variation in the exterior tests than the interior tests showing the largest particles are concentrated more toward the centre of the flow. This is likely as they are too big to slide up against the window allowing finer material to move into this region. This would likely mean that the particle distribution at the wall has a slight boundary layer of fine fluid material against the window. This will be particularly evident in corners between the wall and base of the flume. This discontinuous corner is not typical of natural channels and so may add extra resistance that is not present in the real world.

5.3.1.2. Velocities

The interior of a model debris flow had higher body velocity than that measured externally. Because the front does not show the same difference in velocity and the height of the flow is consistent in the transverse direction there is a barrier to the movement of the interior material past the snout. Therefore, there must be transverse movement of the material. This indication of particles moving toward the outer edges supports the levee forming theories of (Johnson et al., 2012). Here the upper plug-like flow at the front may be pushing the material out to the edges.

The exterior appears to have a reduced length of body as the mean velocities decrease earlier. This may be a frictional or viscous drag effect at the wall of the flume. This additional force at the wall slows the flow while the centre is free to continue at a faster velocity. This may also mean stalling and sticking of particles and fluids at the edge of the wall until enough mass is built up to continue the flow. Another minor effect is the transverse movement similar to (Johnson et al., 2012) theories on migration of the particles, which is more evident in the plateau stage of the body.

5.3.1.3. Slip Velocity

The most obvious difference in investigating the LOV is the presence of a slip velocity in the interior flows that is considerably larger than the exterior tests. This was consistent regardless of the moisture or slope variables. Other experiments using base stress and pore pressure sensors (Iverson, Logan, et al., 2010) have shown that there is more shear stress in the interior of the flow than the exterior. This supports the findings of a faster slip velocity in the interior tests.

Less instantaneous fluctuation in the interior velocity profiles shows that the exterior material could have slipped differentially along the wall. Observations of this phenomenon are difficult in a Lagrangian approach as the front is not being tracked or recorded. This could be the case at the base as well but there is no ability to show this along the base. The slips could also indicate various coarse particles creating shear layers underneath them as fine particles align to allow the large particles to slide over them.

5.3.1.4. Images Supporting Interior and Exterior Effects

The following is a sampling of images that supports the difference in exterior and interior composition of large particles. Figure 5-13 shows how the smaller particles can be pushed up to the exterior wall and concentrate at the corner of the flume. The image shows a number of large particles that have either been pushed into the centre or pushed the fines to the exterior wall. This concentration of fine particles is followed by a more fluid section of flow.

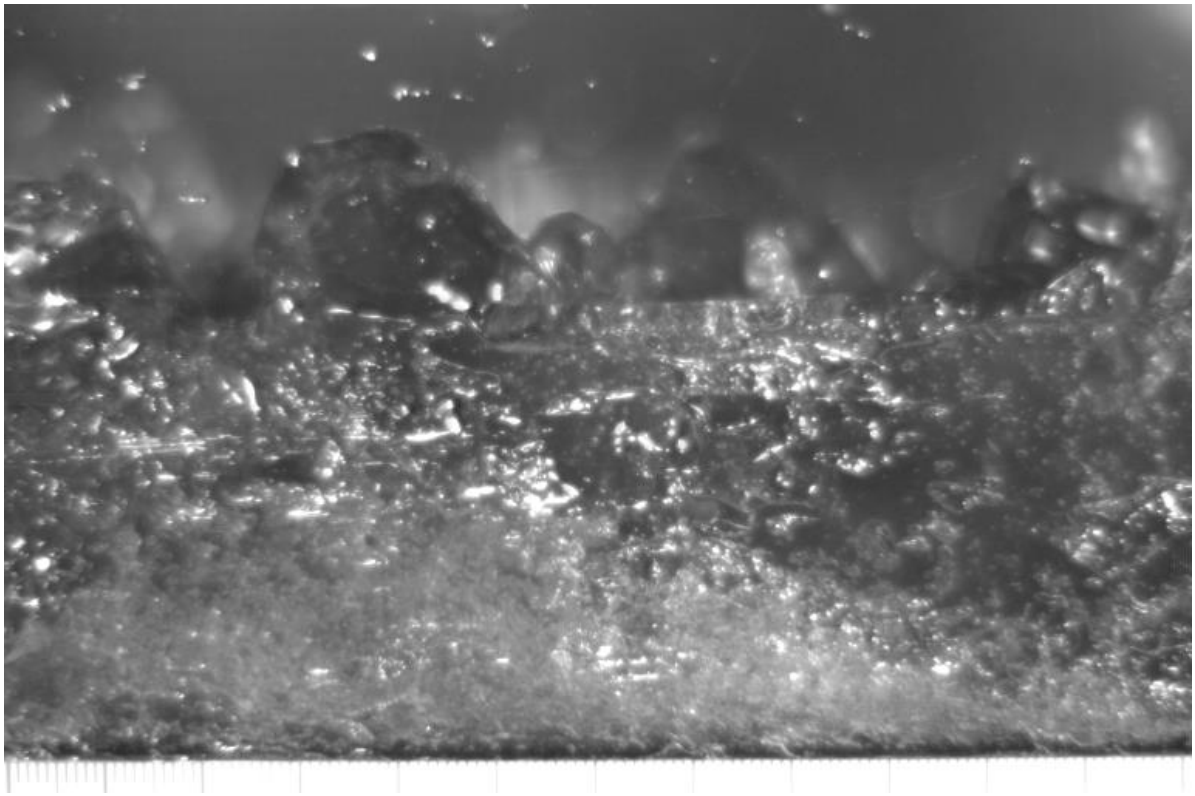

Figure 5-13:S24W28 EX 8 in the middle of the body section of flow. Large particles in the back ground and fine particles in foreground.

In general the large "floating" particles did not seem to significantly influence the exterior saturation heights. Figure 5-14 shows a large particle that cannot be seen to be influencing the saturation or absolute height at the wall. The level of focus of the particle suggests that it is relatively close to the wall. Figure 5-15 shows one of the largest particles in the background with a medium-sized particle at the wall of the flume. This large particle does not seem to influence the flow but the medium-sized particles precede a reduction in saturation height at the wall. The presence of the medium particles shows that large particles are unlikely to directly influence material at the wall but may push other smaller particles to the edge.

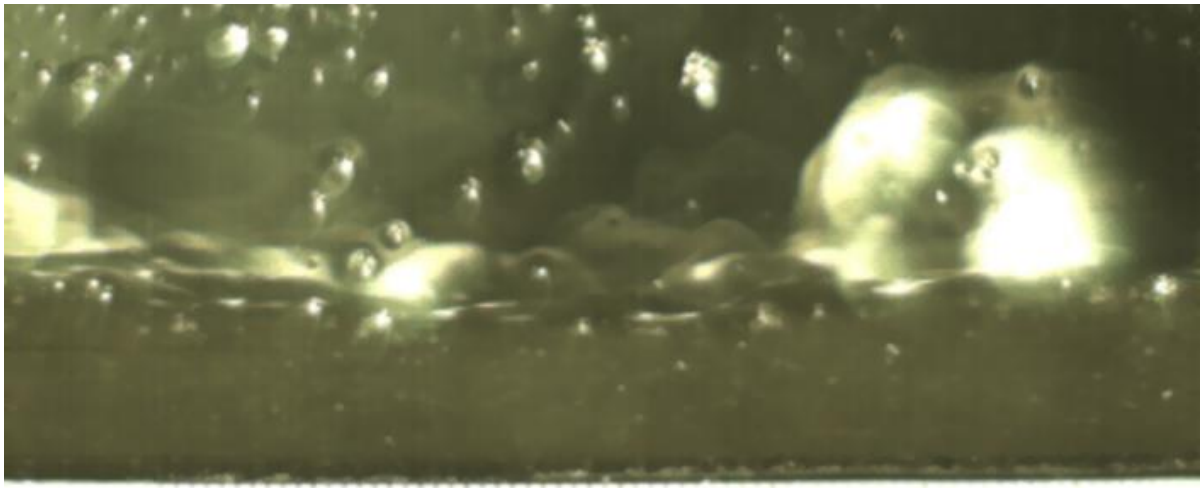

Figure 5-14: S18W32EX4 large particle not influencing the wall. Image in the end of body or start of tail.

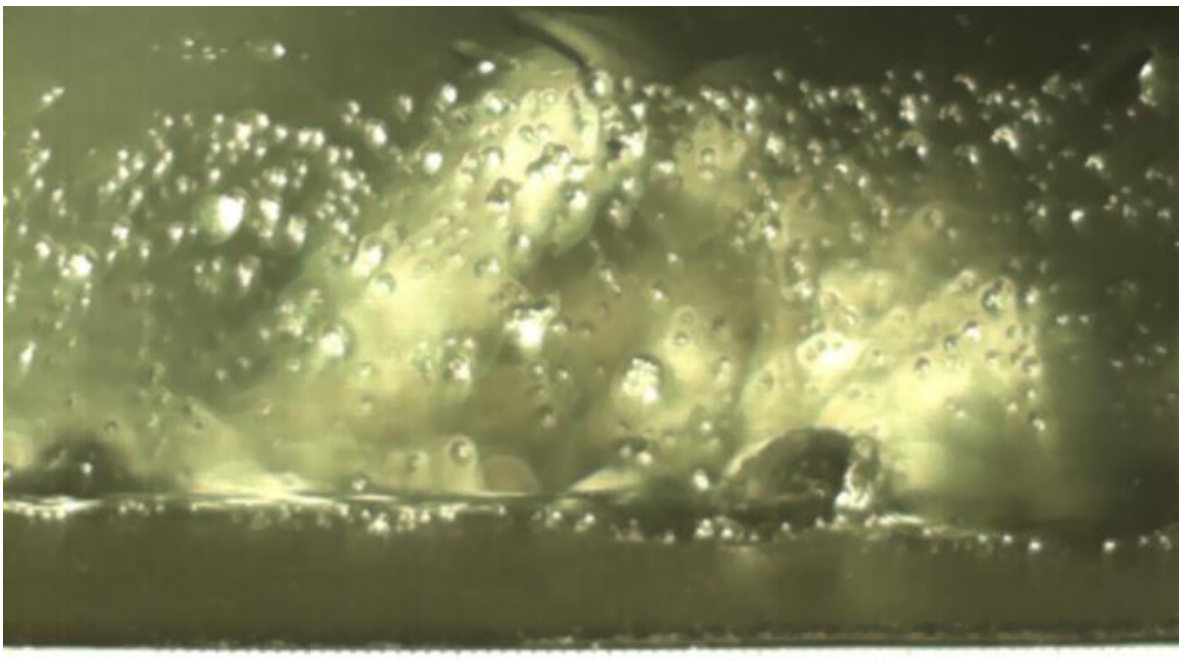

Figure 5-15: S18W32EX4in background and medium particle in foreground of an exterior test. Image located at the end of the body start of the tail.

5.3.2. Particle Motion within the Flow

Internal imaging through PLIF created images that distinguished fluid and solids throughout the debris flows. Even without inputting these images into a QI technique, to get quantitative results the qualitative data help to build a picture of the micromechanics of a debris flow. Being able to see the motion of the interior particles allows observations of motion, orientation, size distribution with depth and time, and short-term structures that form within the flow and the impacts these have on the flow in general. This section looks at these qualitative observations that have only been able to be recorded through the innovative application of PLIF.

5.3.2.1. Types of Motion

Many types of motion (Van Rijn, 1984) are seen in the model debris flows (1) Rolling and or sliding motion in the snout; (2) Saltation motion in the body; and (3) suspended particle motion in the body and tail. In addition results of work by Sanvitale (2010) show how large particles move upward within a flow. In general the largest particles migrated to the free surface and moved at a faster rate. Images showed that these coarse particles appeared to "float" and even bounced outside of the free surface as they moved upward through the flow; this was again supported by observations in Sanvitale (2010).

All tests tended to have a few preceding particles before the front, however, S24W28EX8 had more than the other tests. This is clearly seen in the results section where the unsaturated front occurred 0.8 s before the saturated front and the maximum height. This shows a potential abnormality in S24W28EX8 when comparing the size of the body as it is expected that this bulk of coarse unsaturated material would have typically been incorporated into the body of the flow, giving a more elongated shape similar to the other tests and the description of Sanvitale's (2010) flows (see section 5.2.3.6).

Observations of "floating" large particles (Figure 5-16) are evident in all tests, regardless of slope moisture content or LOV, supporting segregation of flow in motion. There are also large particles that escaped the free surface in some of the slope 24.5° tests. There are less instances of this energetic particle motion in the lower slope tests. Figure 5-17 shows a particle outlined in red 'bouncing' above the free surface of the flow. This occurred at the end of the body showing that even though the height and velocity has significantly reduced there is still a lot of slope normal motion. The particle is unfocused because it is sitting further into the flow than the saturated flow seen below. The mechanism or structure that produced this behaviour cannot be seen as it is an exterior test.

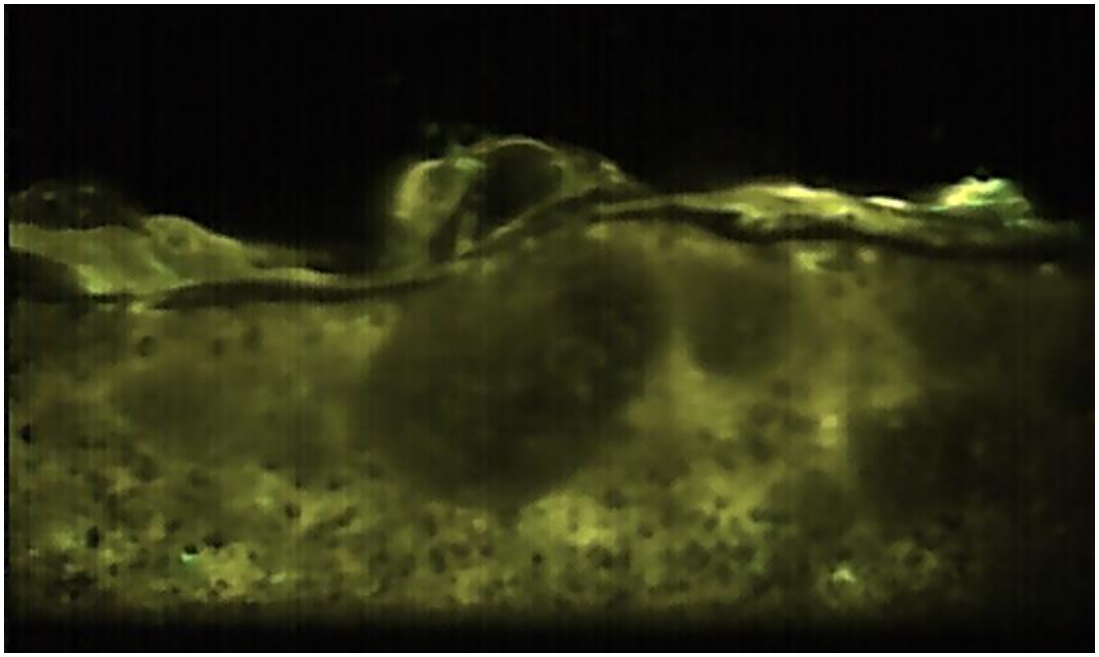

Figure 5-16: S18W28IN4 at time 0.022 s showing large particle moving over smaller particles

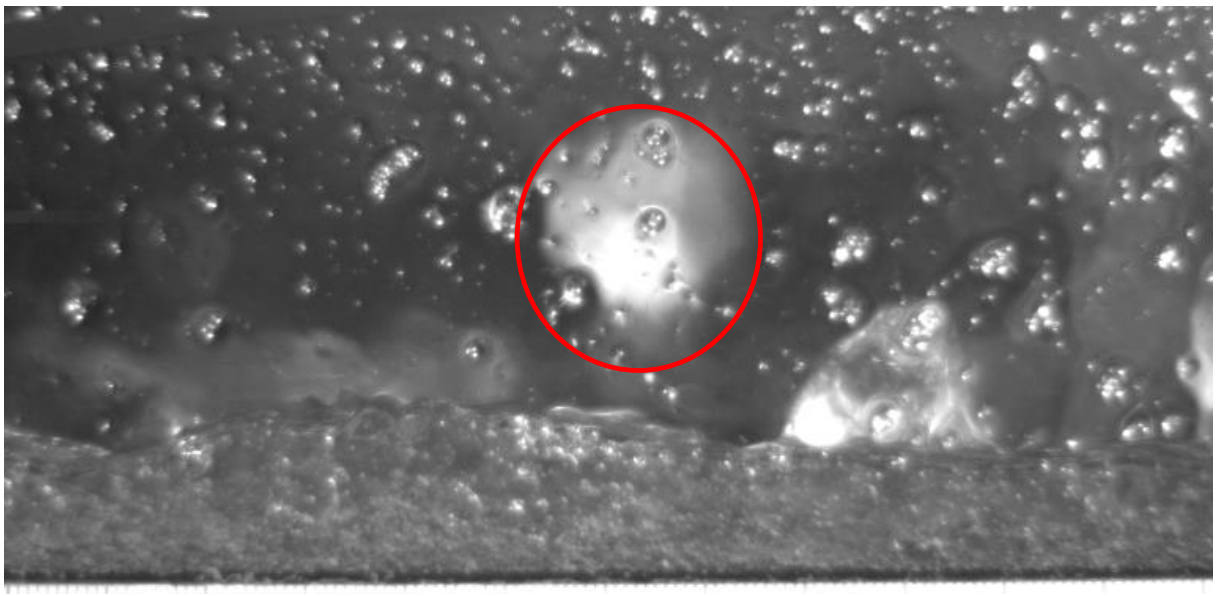

Figure 5-17: Image of (unfocused) particle leaving free surface of S24W28EX8 0.42 s after peak saturation level.

5.3.2.2. Segregation and Internal Particle Distribution

Figure 5-16 is an example of the inverse grading of the body sections. The grading shows evidence of segregation of particles and so supports the conveyor system for coarse particles. Figure 5-18, Figure 5-19 and Figure 5-20 show the more illuminated interior thick body section of the higher slope tests. The largest particles are dark and clearly close to the free surface with finer particles underneath. Figure 5-19 particularly shows some inverse grading at the left-hand side of the image, but in general the coarse particles dominate.

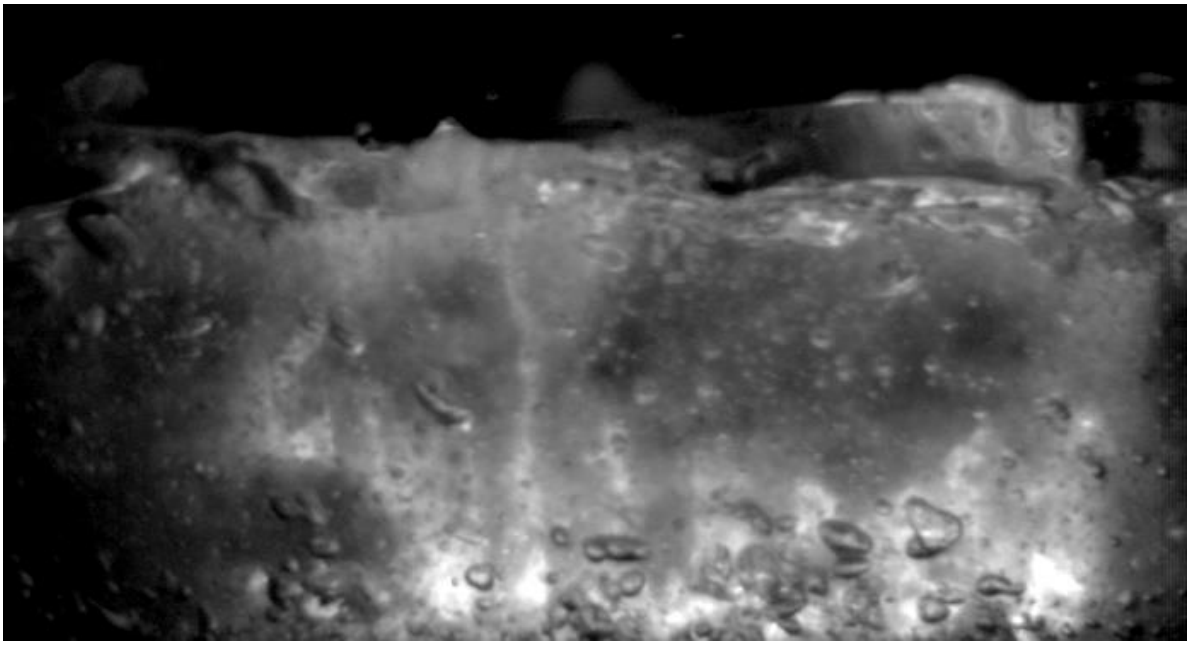

Figure 5-18: S18W24IN5 time 0.13 large particles longitudinal aligned above finer particles (Miro camera)

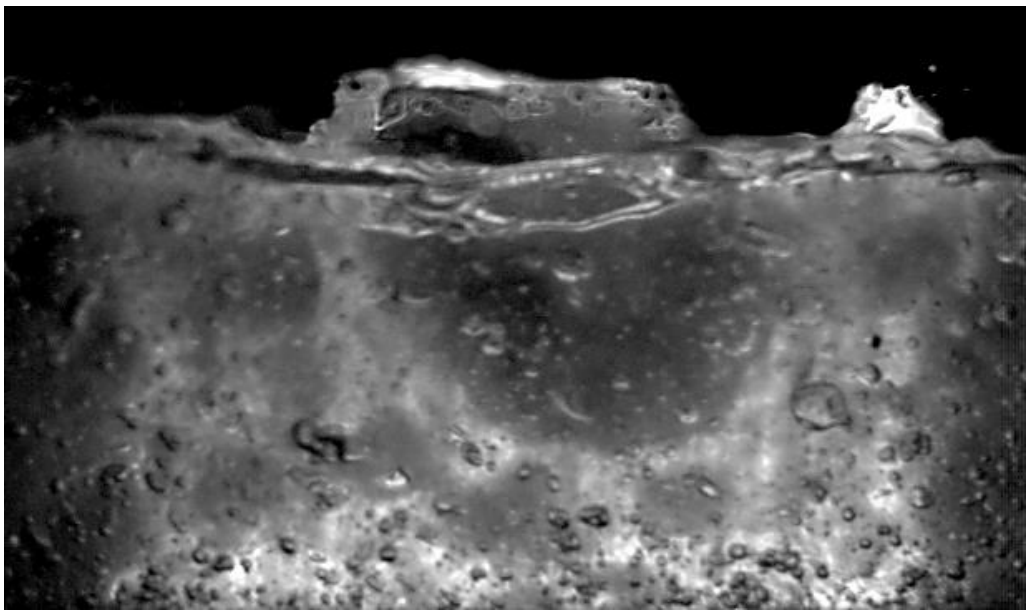

Figure 5-19: S18W24IN5 time 0.23 large particle point down with medium sized particles under the large particle. None of the particles appear to rotate (Miro camera).

The Miro camera allows better illumination of bubbles within the flow. The bubbles appear to have been trapped in the lowest parts of the flow underneath the largest particles. A mechanism that could explain this is the rolling over of coarse material at the snout, entraining air that cannot rise under density differences due to the flow of coarse particles over the top. The bubbles are greatly reduced in the tail and thinner sections of the flow, supporting the idea of being entrained at the front. The large size of the bubbles indicates the small bubbles have joined or are less likely to be able to expand in low pore pressure sections.

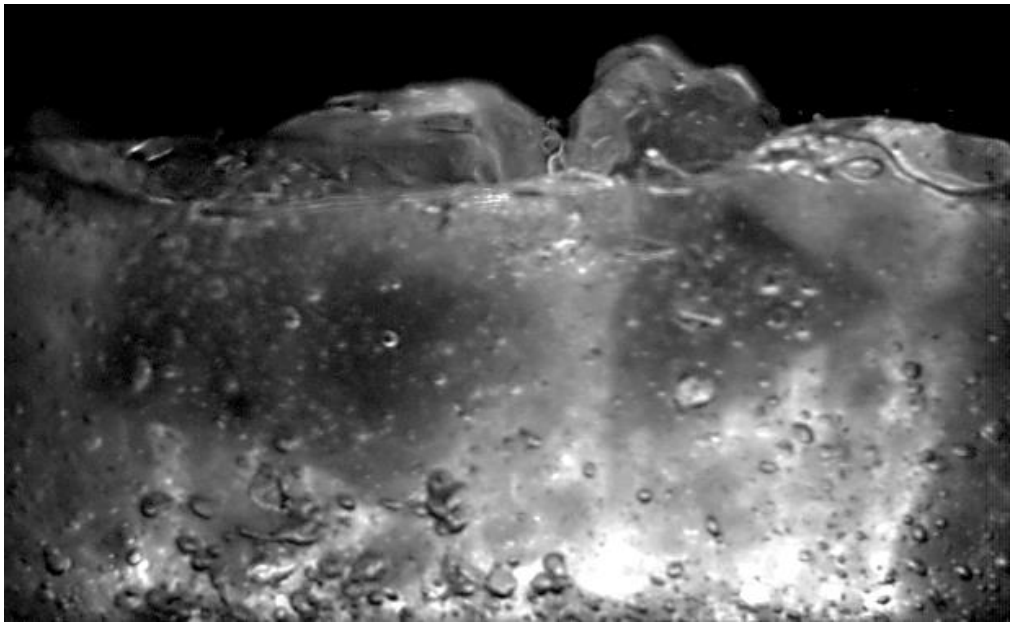

Figure 5-20: IN 5 time 0.23 large particle point down (Miro camera)

The images presented here (Figure 5-16, Figure 5-18, Figure 5-19, Figure 5-20, Figure 5-21, Figure 5-22 and Figure 5-23) are typical of the same floating particle observations seen by Sanvitale (2010). Sanvitale (2010) identified large ripples present in the body. These were attributed to large particles at the free surface moving faster than surrounding material. These ripples were better able to be distinguished in images like Figure 5-16.

The large particles push and accelerate the material in front of them, as seen by the higher concentration of the medium and fine particles at the "toe" of the large particle or the bottom edge that is digging into the preceding material. This observation is in agreement with Iverson's (2005) mechanism for development of grain segregation. It is possible that the increased fluid filled in the voids caused by the forward movement of the large particles. The accumulation indicates that the large particle is flowing faster than the other particles leaving a void for the fluid displaced from the flow in front of the particle. The large particle pushing may create higher pore pressures in the in front of the particle causing the fluid to flow around the particles. This indicates that the more large particles that get pushed forward the more acceleration due to the mass of the front.

5.3.2.3. Types of Orientations

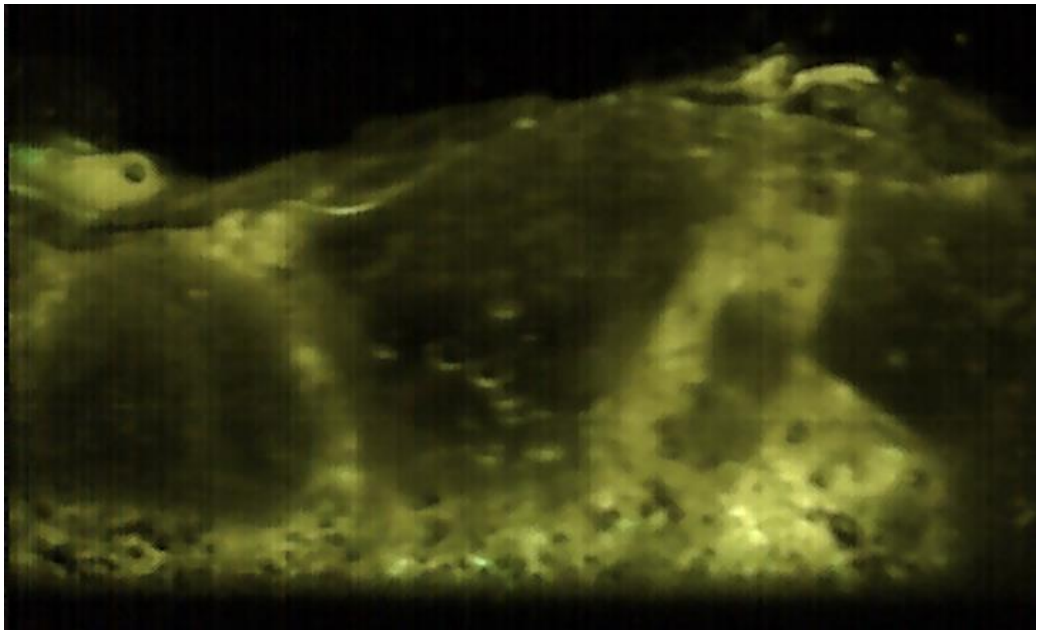

Figure 5-21: S18W28IN4 at time -0.24 s from peak saturation showing series of large particles affecting the saturation surface.

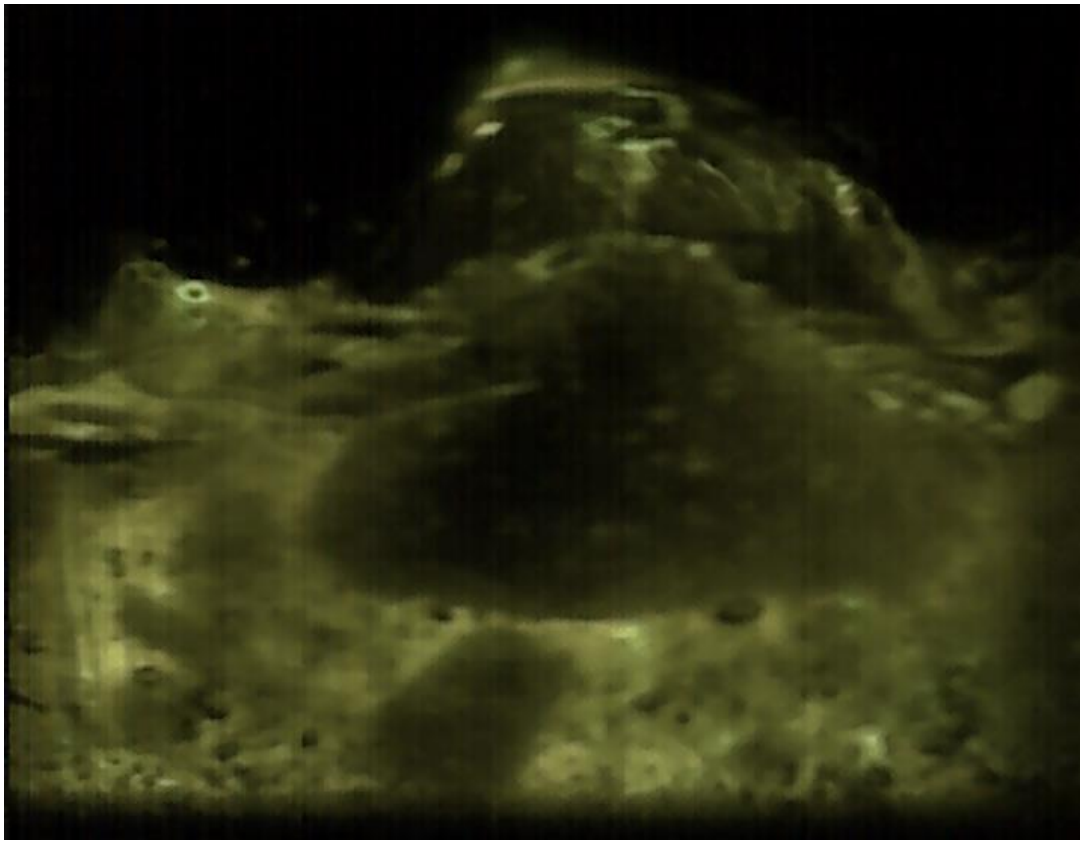

Figure 5-22: S18W28IN4 at time -0.14 from peak saturation. Particle shown with flat side down rolling over other smaller particles in the base of the flow.

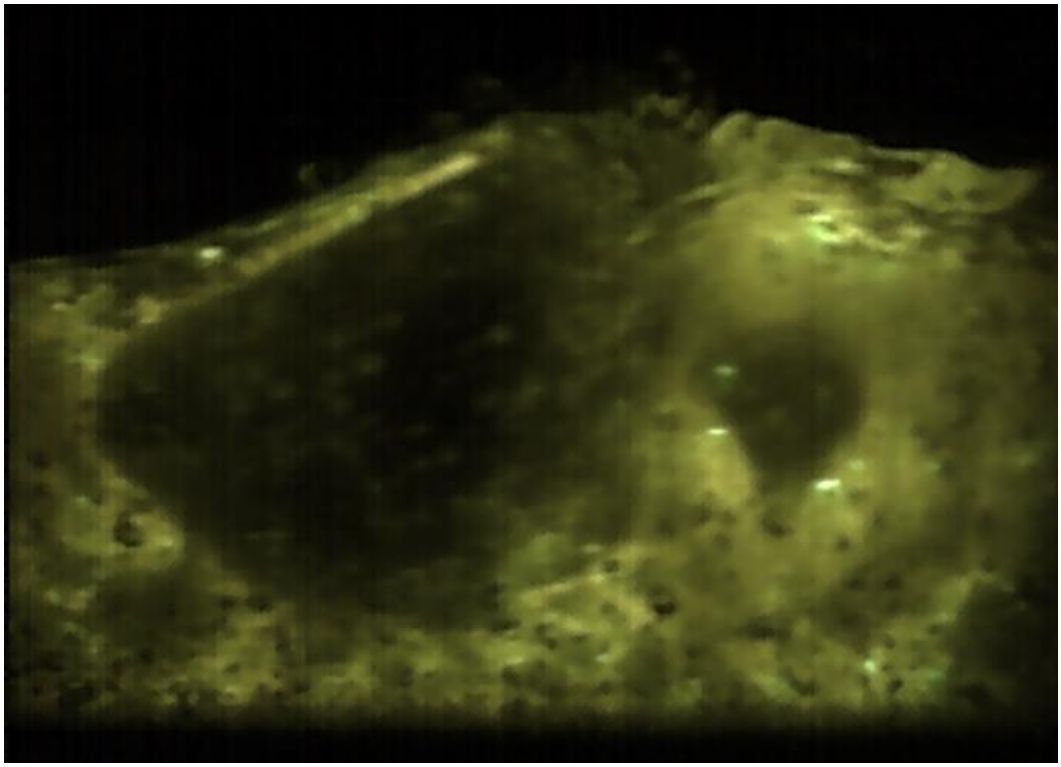

Figure 5-23: S18W28IN4 at time -0.01 from peak saturation level. Particles with point side down being pushed on angle shunting finer material forward and building up fluid behind.

The orientation of particles is useful for determining the interaction with the surrounding particles and the potential to shift within the flow. The orientation of the particle came in three variations based on two shapes, rounded and elongated. The rounded particles sat in the flow (Figure 5-21), the elongated particles rotated to orientate themselves with their longitudinal axis parallel to the flow direction. The rounded particles were free to rotate but were often constrained in a series of large particles as in Figure 5-21.

The elongated particles tended to stabilise with either flat side down (Figure 5-22) or point down (Figure 5-23). Those with flat side down had very little rotation and had particles underneath that exhibited a high level of rotation, allowing the larger particles to be more mobilised over the top of the base layer. The flat orientation also prevents the large particles from moving back down into the flow. Those with point side down did not have as many rolling particles underneath and could push material in front to form an accumulation at the toe of such particles. This could destabilise the large particles (as seen in Figure 5-23) causing them to rock from side to side in the flow or tip over. The destabilising seemed to affect the saturation level increasing the height of the flow. The combined accumulation of fines and large particle roll over could result in small cases of surge formation due to small damming of the flow in the body.

The orientation of the particles is significant because it shows that the largest particles tend to sit in a set way, indicating that longer flat particles may be more easily supported within a debris flow. Also the orientation may produce damming structures that could lead to surges within the flow. Where the large particles are not present, there is less indication of rotation in the medium or finer particles. Instead or rotation these particles exhibit the more stable floating movement of the large particles. This indicates the movement of large particles may be responsible for the rotations of medium particles which would otherwise slide over smaller particles.

5.3.2.4. Surging

In addition to an increase in the slope producing an increase in the run-out and flow velocity, the most evident change was in the inception of surge-like behaviour (Davies et al., 1988; Iverson, 1997) which started to occur in the higher energy, more mobile, fluid flows. The surges were small waves which were more prominent in the fluidised tail. Figure 5-24 shows the height-over-time for one of the tests that had small increases in height that appeared to be surge waves. The amplitude was relatively consistent above the saturation level of a few millimetres. The spot heights measured within the deposit did not show evidence of progressive surges remoulding it, where ridges through the deposit would have been evident. This suggests the surges were small and mainly affected the flow during transport and did not form secondary flow fronts. It might be possible to determine a representative period between the waves of approximately 0.5-0.8 s, but the chaotic nature means that this would require statistical analysis over many repetitions.

The surge-creating phenomena explained in section 1.3.2.3 would be exaggerated with a deeper faster body. The deeper flow gives more accumulation of material to for the damming structures caused by large particles pushing fines at the toe of the particle. The higher slope gives the large particles more ability to roll over the accumulation rather than stay constrained behind the accumulation.

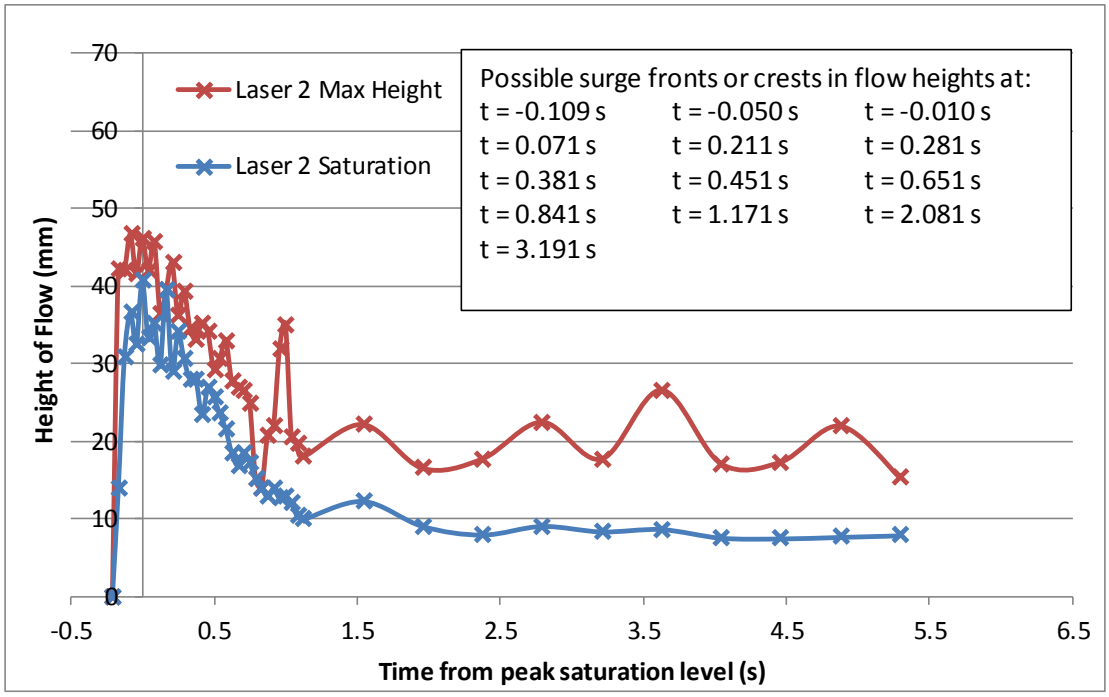

Figure 5-24: Height-over-time of S18W32EX2 with possible surge crests. Note that the tail after 1 s has been sampled at a reduced rate.

5.3.2.5. Observed Structures and Interactions with Other Particles

As well as the large particles rolling over the smaller ones there was evidence of chains of particles forming within the flow. Typically theses chains were about three particles in an arc as seen in the series of images in Figure 5-25. The arc of particles behaved like a larger particle pushing material forward creating areas of high fluid concentration behind the arc.

Figure 5-26 is a series of images that show a particle 'jumping' out of the flow. There has previously been little evidence recorded for any of the postulated mechanisms of this event occurring within a debris flow. Iverson (1997) proposed such a mechanism where roughness in the bed transferred slope-parallel velocity into slope- normal velocity. The series of images show that there is an accumulation of material which the particle appears to be in the process of rolling over. In addition there is a large particle moving into frame. This other particle seems to squeeze the fluid under the particle as it rolls over giving it added acceleration to 'jump' out of the flow. Perhaps it is the rare occurrence of an incoming surge to an existing damming structure that creates the mechanism for particles to leave the free surface rather than the particle itself bouncing against the base of the flow and being given enough rebound to jump out.

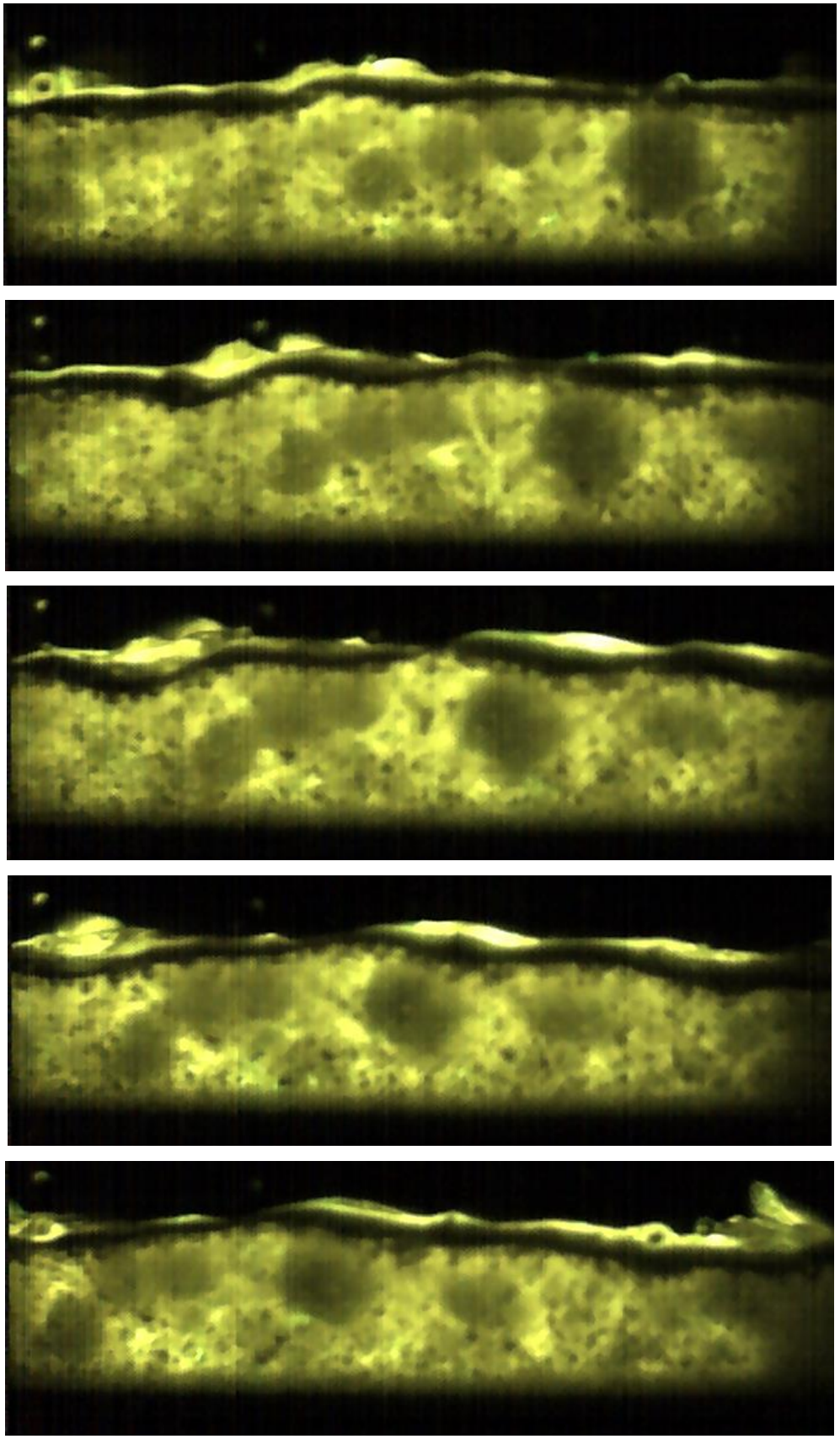

Figure 5-25: Arc of three small particles forming a fluid pocket underneath and pushing fins forward. Test images of S18W28IN4 at 0.64 -0.67 s from peak saturation height, in 0.01 s time intervals. (Motion-Pro camera).

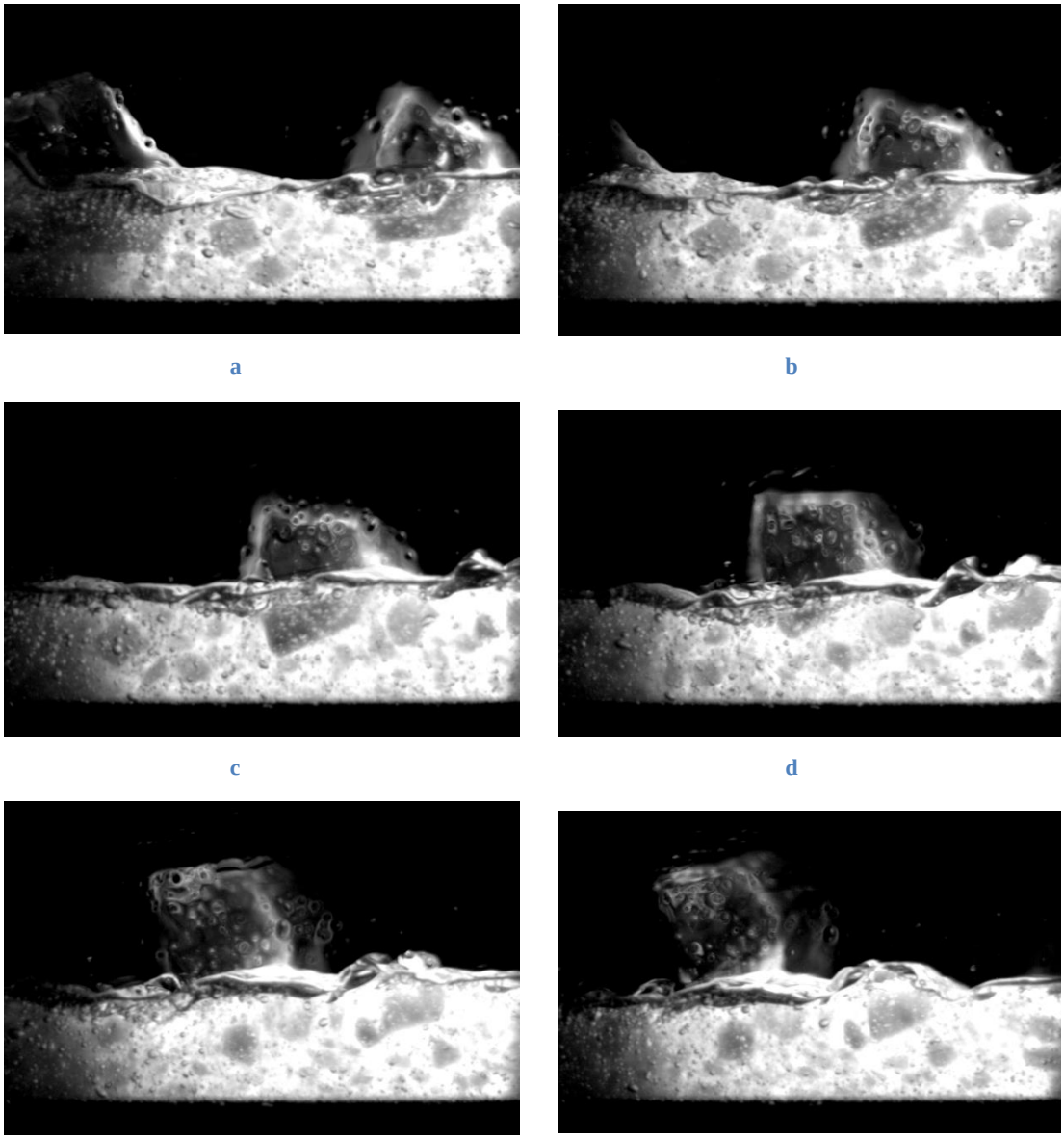

Figure 5-26: Coarse particle jumping out of flow for test S18W32IN6 at time 0.65 s from peak saturation with time step 0.01 s (MIRO camera).

In the tail a large particle that was released late had the potential to impact the thinner slower fluidised flow. Figure 5-27 shows the effect on the tail of a large particle. The effect is that the flow is reduced after the large particle. There are other instances in the body where the saturation level reduces after a large particle has passed. This indicates that the large particles are likely to have pushed material down slope and created a void behind the particle that forces fluid to flow around the particle to fill the void. The behaviour in the tail supports the movement of particles in the front and the proposed small surging mechanism.

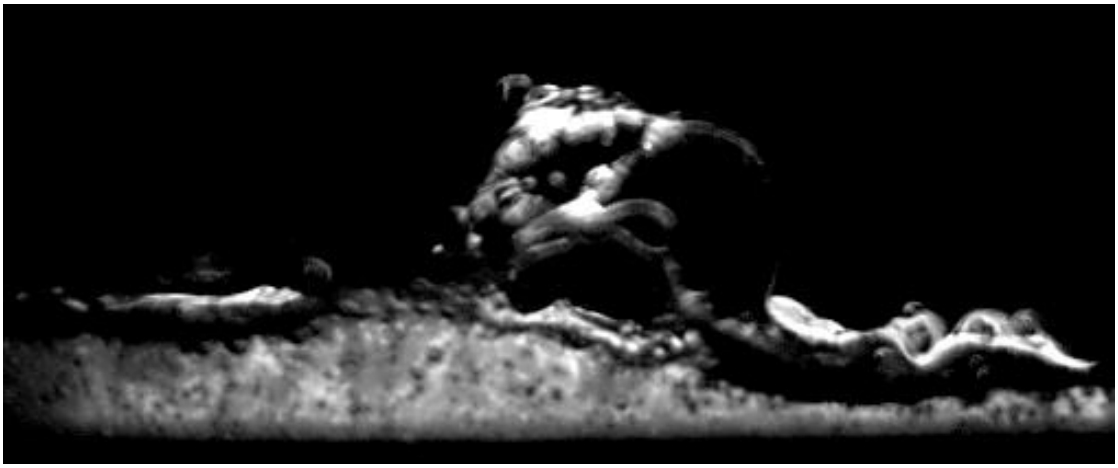

Figure 5-27: S24W28IN8 at time 1.075 s showing a large particle pushing and accumulating material in the tail (Miro camera).

5.4. Implication of Findings on Modelling and Rheology

The difference in body velocity between interior and exterior testing supports the possibility of transverse motion (Johnson et al., 2012) of particles during flow. However, this cannot be tested using only a 2D model of particle motion. It is likely that the viscous drag is a more determining factor on the magnitude of the velocity and shear at the wall. The no-slip condition within the flow means that exterior test underestimates slip and causes inaccuracy in base shear calculations.

The friction and particle interaction at the boundaries has an effect on the flow, even in a flume with glass sides with little roughness. The magnitude of this could be evaluated by comparing the difference in exterior and interior velocities. Historic methods of recording the exterior of the flow are likely to have under-estimated the true slip and longitudinal velocities as they would have been dampened by the friction at the boundary.

The PLIF technique also allows qualitative analysis of the particle distribution with depth. The motion and structures of particles within the flow that has otherwise only been implied by theories can be seen though the PLIF methodology. Section 2.2.3 seeks to explain that most rheologies proposed for debris flows are for a single region and composition during flow. Research often uses physical experiments that focus on fitting a single rheology to the bulk behaviour of a certain experiment. This research shows that the location in the flow also needs to be considered in determining the flow regime for a particular physical flow.

In the case of the tested material the snout is frictional, the body is stony and the tail tends to muddy or hyper-concentrated regime. An approach to modelling behaviour might therefore to

be to take each section and apply separate rheologies. The snout has body forces acting on it and so would require as a free body section to have a force contribution from the body. The tail does not appear to increase the velocity of the body of the flow as a result of stretching so can be assumed independent of the main bulk or hazard caused by the flow. However, breaking the sections into individual mass bodies does not help model how the debris flow evolves through a continuum from granular to hyper-concentrated over time and length. Finite element modelling could be used more prolifically after breaking the flow into the separate regions with individual rheologies. Each region can have a single-phase rheology but between regions the rheology changes so the finite element continuum assumption fails between regions. The results presented in the research suggest that the snout block is mainly self-contained and that the body is the section that needs the most analysis as it represents the most dramatic evolution of flow behaviour. This is supported by the methodology and techniques used in (Denlinger & Iverson, 2001) and (Iverson & Denlinger, 2001).

The interior vs. exterior findings show that slip velocity is higher than is usually modelled physically and is a defining feature of the snout. The orientation and impact of the large particles show that instantaneous collisions and random interruptions by other large particles are likely to dominate the flow and disrupt assumed modes of particle transport. The snout and body have the highest implications for managing debris flow hazards as they are the bulk of the mass and momentum of the material. Therefore the inclusion of the increased slip velocity is important and discounts many of the fluid-based models. The snout is likely to be granular but might be subject to additional forces from the body.

This research does not give a relationship between viscosity and stress and does not deal with the yield stress of the material as it is already assumed to be full dynamic at the point it passes the camera. This makes absolute determination of the true rheology in each section more dependent on the similarities in behaviour than quantitative relationships.
The following recommendations for (single phase) rheologies as applied to each section of the flow are:

Snout: Frictional or Voellmy flow (section 2.2.2.5 or Section 2.2.2.7) there is limited collisional behaviour and a defined lower boundary layer with minimal transfer of shear stress to the bulk of the material. Voellmy is likely to be a better fit as it would allow shear to be distributed into the full depth of flow as the snout develops into the body. The slip velocity is the main finding to support the use of a highly granular dominated rheology in the snout.

Body Plateau: Dilative Inertial (section 2.2.2.4) the more separated section of highly concentrated body allows particles to dilate and more collisional behaviour to occur.

Body to tail transition: Coulomb Viscous Flow (section 2.2.2.6), evolution of the body with a reduced concentration of large particles means more homogenous concentrations and fluid and solid interactions to dominate.

Tail: A hyper concentrated rheology like Bingham or Hershel-Bulkley (section 2.2.2.1 or 2.2.2.2) as the tail is more fluid it behaves more Newtonian during flow and then in a two phase it is consolidating, but as a one-phase model it indicates a yield stress in an otherwise Newtonian flow.

In general the complexities of a well-graded flow make application and validation of rheologies difficult. Models of motion assume layers of a particle diameter thickness (Lorenzini & Mazza, 2004) for the modelling of transfer of shear between layers. These image results show that the layers are mixed due to mixed particle sizes. There is a lower layer of fine material but as subsequent large particles move through they disrupt these layers impacting nearly the whole depth of flow.

The influence of coarse particles in the flow has been highlighted as a considerable factor in determining the micro-mechanical behaviour of the flow, particularly the formation of damming and surges. The orientation of the large particles shows that the shape factor of the large fraction may help determine the level surging behaviour. This will need to be further explored but it is likely that long thin or round particles have less inertial impact on the flow acceleration than angular ones. The ability of energetic expulsion of particles through squeezing of two accumulated large particles is a low frequency event but could increase the height of potential impacts for design of bridges and similar structures.

5.5. Evaluation of Technique

5.5.1. Variability

The physical modelling process produced qualitatively significant results and dealt with the large inherent natural variability in the debris flow phenomenon modelled. The material chosen in terms of PSD and initial conditions produced a more real world phenomenon than is typical for laboratory models that reflected the large natural variability in debris flow. The experiments were meant to be a snapshot of the phenomena and so suffered in terms of variability in outcomes. A more uniform material would have had less variation between tests in terms of run-out, height-over-time, and peak velocities. However, reducing this variability would have removed the real world connection. The observed image results show that there are phenomena that are directly linked to the variable nature of the material, particularly surging and snout formation. There is a trade-off between simplification and modelling real world behaviour. This research focuses on more realistic material and so has to be taken as an observation of the possible behaviour rather than an absolute example of model behaviour.

As the tests are at the most well-graded variable end of the phenomenon the results are consistent in terms of deposit behaviour, boundary conditions and velocity profiles. The results have been analysed within the context of the variable nature of the flows and care has been taken to identify the difference between effects of changing parameters and the natural variability.

5.5.2. Repeatability

The main limitation of this thesis was the limited number of experiments. This work was aimed at exploring the variables to determine if there were observable changes in behaviour. The exploratory nature of the work has investigated the flows in a qualitative manner rather than a statistically reliable quantitative manner. The research has highlighted how variable these flows really are and their ability to develop a range of body heights and micro-mechanic structures. There are some suggested changes to the methodology in section 5.6.2 that could be used to reduce the natural variability in order to make tests more reproducible. These include additional sensors and manufacturing methods for solids. However, these changes may affect the ability of the method to show the true complex nature of the flow.

More repetitions of work over a wider range of variables would have allowed a better understanding of the general behaviour of a single set of parameters and the likely range in

natural variability. However, that would have come at a loss of being able to vary parameters, limiting the scope of conclusions while providing a still inadequate number of tests, given the range of behaviour. The balance between conducting repeatable, and therefore reliable tests, and being able to see the effect of a range of parameters has to allow the magnitude of the parameter changes to be evident, otherwise no conclusions can be made. In terms of this balance, this research produced the expected trend caused by changes in slope and moisture content that are more than just the natural variability of the flows themselves. Therefore this method did show difference in behaviour in line with expected trends.

The taking of high-speed imaging over nearly all the flows means there were multiple data points within a test. This allows a high level of statistical analysis to be conducted on the PIV results, particularly velocities. Large numbers of patches particularly in the deep part of the flows allowed reliable estimates of the mean and standard deviation of the tests to be used in the identification of wild vectors. In terms of the PIV results the velocity results did become harder to capture as the depth decreased but this was not seen as a critical phase of the flow when put in context of real world hazards and impacts of debris flows.

5.5.3. PLIF Technique Evaluations

The PLIF technique worked well to illuminate the interior of the flow. There were limitations in terms of illumination, bubbles and distance within the flow.

Lack of pore pressure and dynamic viscosity measurements means that image clarity is particularly important in order to validate rheologies through the use of velocities obtained from the images. It was seen that the illumination levels of Sanvitale (2010) were insufficient, particularly at the snout of the flow, to give a full depth profile due to attenuation of laser light and lack of saturation in the coarse part of the flow. Preliminary tests showed that laser light was attenuated with distance travel through the fluid but not the solid. Therefore, sections of flow with coarse particles suffer less attenuation due to transfer through solid particles accounting for the irregular nature of the height in Sanvitale's data in Figure 5-7. The increased laser power and more light-sensitive Miro camera overcame the attenuation of laser light through the material and due to the viscous nature of the fluid there was enough dye to create outlines of the coarsest, unsaturated parts of the flow.

The bubbles were most evident in the use of the Miro camera as it had better low light sensors and so was able to pick up the bubbles clearly. The Motion-Pro or Memview camera

did not distinguish the bubbles. It was beneficial to have the bubbles clearly identifiable as their impact could be mitigated through sampling sections with lower bubble concentration; also the behaviour of the air in the flow was identified as being concentrated at the bottom of the flow. Air is likely a component of real flows but it is expected that the scale is much higher for the bubbles in the laboratory. The bubbles are all visible between the interior plane and the window, increasing the number of bubbles seen in images. The bubbles also had an impact on the transfer of light. The distortions gave the clear edges to the bubbles and did not seem too blur the images to much but will have introduced discrepancies in the velocity measurements where the PIV analysis tracked the velocity of the bubbles rather than the solids. It was seen that the bubbles tended to travel at the same, to slightly lower, approximate velocity as the material around them. This might have acted to slow some parts of the flow, particularly where the bubble was near the exterior window.

The distance that the plane could be projected into the interior was identified in Sanvitale, Bowman et al. (2010) as being limited past the point used in the thesis methodology. This was mainly due to light attenuation, contamination of the solid phase, the increased presence of bubbles and RIM mismatch causing blurring of the particle edges. In order to place the laser plane further into the interior, the emitted light would need to penetrate more of the fluid, attenuating the emission strength. The increased illumination levels from the Miro camera would allow capture of the light but does not solve the bubbles or RIM distortion. The main factor limiting the placement of the laser plane is the contamination of the edges of the fine material during sieving and the number of fine material interfaces which tended to concentrate at the base and exterior window. Solutions to this issue are discussed in section 5.6.2.

5.5.4. QI Technique

The use of the Geo-PIV software enabled the presentation of as much instantaneous data as needed at any location within the flow to a small time resolution of 500 µs for the Miro camera. The spatial resolution was also relatively small compared to the maximum particle size but was greater than the smallest 20% of particles. The amount of normal and perpendicular flow displacements allowed for reliable statistical values to be produced and allows for additional in-depth analysis of the flow covered in section 5.6.1. The ability of the PIV technique to absorb distortions in the images through capture of texture over actual particle identification made it highly versatile for this early stage of methodology

development. With increased image clarity this versatility could become a limitation as the tracking of individual particles becomes more viable. The use of other types of QI for higher quality images are covered in section 5.6.4.

There was a limitation in that there was a section of the base of the flow that was not able to be analysed and so was removed from the analysis (see section 3.11.2). This was identified as ~2-3 mm - which in the deep sections of the flow was relatively small. However, in the tail this became nearly half of the flow depth. The tail was seen as less hazardous and so the impact of the patch reduction is less significant to hazard management. The greatest influence of the base reduction is on the estimation and quantification of the slip velocity. This was the most significant difference between interior and exterior tests and so of the most importance. The use of increasingly small patch sizes would allowed this slip velocity to be better approximated but this become computationally very intense or selective of areas that can be analysed. In light of the requirement to cut off at the non-erodible bed this technique may be better suited to an erodible bed scenario. In an erodible bed scenario there would be no requirement for the lower bound patches to be removed.

The other limitation was the inability to distinguish precise slip-zone depths as the technique spreads the texture over an entire patch. For the front, the identified depth of the bottom boundary layer describes a lot about the size of the particles in this region and the mechanisms occurring. By having very small steps between patches in the slope-normal direction, it is possible to see a relatively accurate region within which to target the slip zones. Due to the well-graded nature of the material the slip zones would be constantly distributed by different sized particles and accumulations at the toe of large particles. Therefore, the low resolution of these slips zones was not seen as a significant limitation.

5.6. Future work and Improvements

5.6.1. Further Use of Current Data

The amount of PIV data collected allows for a wide range of future analysis to be undertaken. In the normal direction to flow there could be more frequent sampling. Increased modelling of the front and snout at smaller intervals will allow better identification of criteria for the transition from snout to body to tail. This research focused on sampling the flow at multiple points throughout. Targeting the front and snout will ensure capturing of the peak values and validation that the snout is travelling at the same velocity as the front of the body. This could

also focus on the toe of large particles to see how the velocity changes in the plane and other structures or slip layers within the flow.

Particularly in the perpendicular direction to the flow, the velocity is assumed to be due to the turbulent, collisional, chaotic random aspects of the flow. Focus on the perpendicular flow behaviour can be used to calculate a granular temperature (Aragon, 1995; Haff, 1983) or a measure of the solid phase's vibration or chaotic motion. This is similar to the concept of gases vibrating at higher temperatures as the energy is increased. Initial attempts to calculate this value using the same statistical techniques as Aragon (1995) could not deal with the well-graded nature of the material and the correlation depended on whether it is being sampled in areas of large and/or small particles.

5.6.2. Methodology

The methodology has proven itself to be versatile and innovative and can be applied to other scenarios and decreased levels of complexity. As mentioned in section 3.11.2 the lower bound caused by patch size may mean the methodology suits an erodible bed scenario more as the PIV technique is not limited by a lower bound. In general this research focused on the a more real world scenario and has produced some areas that could be simplified in order to show particular effects. One of these simplifications is the particle shape and PSD. In addition to simplifying the collisions and interlock of the particles the changes to the solid material may increase image quality. This is at the cost of reducing real world application.

Many rheologies assume that the fine fraction is part of the fluid. Studies could be conducted to see if the fine fraction can be removed and replaced with a more viscous fluid in order to reduce the effect of multiple particle interfaces in terms of RIM which causes distortion in the images. The idea that the fine material is part of the fluid is supported by the observations of the PSD of the coarse material that had similar amount of 125-300 µm particles as anywhere else in the flow but the 450- 600 µm were concentrated in the tail.

Adoption of single use prefabricated particles would reduce some of the shape factor issues and contamination from sieving and cleaning. Using glass beads that are manufactured to a range of sizes would reduce manufacturing time and ensure the particles are all the same shape. This reduction in shape factor to spheres is a simplification to remove some of the natural variability and make the application of theory simpler particularly when considering packing structures and pore geometry.

As the research found that there was no significant change in micromechanical behaviour over the tested parameters, increased levels of variation in moisture content and slope are needed to identify the transition of debris flows into other forms of flow. These will allow better determination of the inputs that vary debris flow behaviour and what the changing mechanisms are.

Additional sensors could be added to the flume apparatus to focus on pore pressure and shear stress along the flume bed both along and across the flume. This will help to identify the slip velocity and stresses in the snout at the base of the flow and the point at which they transition to the body. In addition, the current methodology has a single pulse of material from the hopper. A reservoir with more continuous release of material would allow the modelling of secondary surge phenomena which cannot be done at present. Once this is done the mechanisms that cause small-scale damming in the flow identified in section 5.3.2 of this thesis can be compared to see if they are the same that cause large-scale surges.

5.6.3. PLIF Imaging

The image quality was a limitation and while using the Miro camera did show an improvement over earlier cameras, further improvements could still be made. The laser operated at a wavelength higher than the optimum absorption wavelength of the dye at which the solid and fluid were optically matched so a better matching could produce a higher emission and the absorption could be filtered out without filtering any of the emission. It may be possible to introduce a second or third fluid that could be combined to create a mixture with a viscosity and density similar to water and a refractive index suitable for RIM experimentation. Andreini's (2012) application of plastic particles with a mixture of three fluid shows how multiple material properties can be adjusted while creating excellent RIM results, although relative density issues are also important to debris flow behaviour and this may be a limitation here.

5.6.3.1. Transverse Direction

By using a 2D plane there is an assumption that the laser is thin enough and that the material is not significantly moving in the transverse direction. However, there is likely to be variation in the transverse as well as the slope normal direction. The PLIF technique can be applied parallel with the base of the flume allowing a transverse plane to be recorded. This could be done at the same time with two laser planes and two cameras. It is suggested that if this is

attempted the laser plane is close to the base of the flume and recorded from underneath. This is due to the erratic changes in height of debris flows, particularly the front.

Use of 3D PIV or stereo PIV (Adrian, 2005) would allow calculation of variation in the transverse as well as normal and perpendicular directions at the same time. The limitation at this stage is the size of stereo PIV investigation volume and the additional complexity of the modelling.

5.6.3.2. Illuminating the Solids

Illumination of the solid phase using a fluorescent particle will allow the tracking of the snout and other unsaturated sections of the flow. Yu, Hsieh et al. (2010) shows that particles can be created by embedding a UV dye in plastic particles which allows a UV camera to take images of the solid phase. Alternatively fluorescent properties could be mixed into glass at its manufacturing. Illuminating the solid does not mean that the fluid needs to have the dye removed. By using different spectra of cameras, for example UV and white light, two images could or two different colours could be split using the colour filters after analysis.

This approach would allow targeting particular sizes of particles by seeding them with the plastic beads. Plastic beads can be easily removed and if the concentration is low enough will not affect the flow behaviour. This would require PTV or PSV. A combination of both the solid and fluid using difference emission spectra would allow the testing of the multiphase assumption to see if the fluid and solid move as one mass or is the fluid moves relatively slowly during flow. Different emission spectra mean recordings can be split or superimposed for analysis.

5.6.4. QI Technique

If the image clarity were improved, PTV could be applied to the PLIF analysis. PTV would allow the tracking of individual particles. The current versions of PTV software allow the measurement of rotations which could further contribute to improve on how the shape affects the orientation of the particles and the ability to dam the flow. PTV identifies the boundaries of particles by monitoring the amalgamation of the solid shadows such that a collision or contact measurement could be made. For example, the number of collisions and the time two particles are in contact could be determined. However, even with better image quality, it will be difficult to find and identify the finest fraction of the material without magnification.

If the image quality was improved then light intensities could be used to determine and track fluid pockets, as the higher the intensity of the light, the more fluid there is in the particular section of flow. This use of concentration or light intensity is called Image Correlation Velocimetry (ICV). By selecting patches at various depths the sediment density with depth and length of flow could be analysed. This would allow quantification of the location, saturation and concentration of the fluid phase. The laser light in an ICV experiment needs to be highly stable with minimal variation. Another challenge to adopting this form of QI is the attenuation of light which changes with particles moving through, so the base level of light without particles cannot be used as a reference for the attenuation of light.

Chapter 6. Concluding Remarks

This chapter provides a summary of the thesis and concludes the importance of researching the relatively real world laboratory experiments. This research has been on the interior mechanics and interior velocity profiles of debris flows through non-intrusive measurement of small-scale laboratory experiments.

The aims of this thesis were to refine the methodology, and measure velocity and height data. This was done in order to compare interior and exterior tests for a range of slope and moisture contents. Observations of deposit measurements, structures, height-over-time, instantaneous velocity and velocity over time, allowed instances of debris flow micro-mechanical behaviour to be seen in terms of the impacts on the type of flow rheology throughout the debris flow.

Research into the concepts, theories and physical modelling of debris flows showed that debris flows are non-Newtonian complex flows that have spatial and temporal evolving trends in behaviour. The combination of solid and fluid mobilises the mass creating a highly chaotic and fast-moving front that has the potential to destroy structures and development in its path. The methodology was an innovative combination of PLIV and PIV based on the previous work of Sanvitale (2010). The methodology was improved through the use of higher laser light intensity and more light sensitive cameras.

The deposit and height data results showed that the laboratory experiments using substitute materials were consistent with experiments conducted using real materials. It also highlighted that there was a considerable amount variation in the height and run-out, this was seen to be consistent with real world, well-graded, flows. The PIV data gave velocity over time and velocity with depth profiles. The profiles were normalised to show evolution over length of flow.

In this study on the interior behaviour and velocity profiles of debris flows the interior velocities had a significant no-slip condition not present in the exterior flow. Interior images showed the importance of large particles in the damming and surging of debris flows. Moisture content did not affect the normalised velocity profiles but did increase mobility velocity and run-out. The tests were less sensitive to moisture content than slope but both had the same general micro-mechanical behaviour seen in the interior images.

Even though most research does not account for such low saturation and high level of well-graded material the run-out, deposition and velocities of the experiments presented in this thesis are similar to within an order of magnitude with other laboratory tests, at similar volume and slope. Moisture content and slope do have a considerable impact on the run-out within the ranges tested. The results were more sensitive to slope than moisture content at the values tested. Analysis of Sanvitale's (2010) research showed similar behaviour, with hopper tilt and illumination levels the most likely reasons for differences in flow behaviour.

The flow anatomy analysis of height and velocity with time gave rise to a series of additional regions within traditional front and tail models of debris flows. The flow was seen to gradually evolve between regions. The instantaneous velocity profiles supported significantly different profiles at each region of flow. The snout was a block on a bottom shear layer. The body was a partially fluidised flow and the tail was fully fluidised. The slope and moisture content had less significant impacts on the velocity profiles than whether it was interior or exterior. The snout and initial body regions were found to have the same velocities and the other regions stretched due to velocity differentials caused by particle composition. Meaning that the unsaturated front is damming and constraining the body, but as preferential sieving occurs the finer tail is relative to the front slowing and stretching over the length of the slope.

The comparison of exterior and interior tests showed significant viscous and frictional forces are active at the boundaries to slow the flow. The height was less impacted by location of the analysis plane. The key difference is the higher slip velocity in the interior tests indicating that the front of the flow is much more granular and has little fluid impact. Observations of the large particles or chains of medium particles showed that they have significant inertial effects on the flow and tend to dominate locally. Depending on orientation, large particles tend to accumulate material in front of them, displacing fluid. This accumulation likely leads to surging and jumping of particles within the flow.

The rheology recommended is dependent on location in the flow more than slope and fluid content. Recommendations of rheologies were; for the snout, a granular rheology, for the body, likely a coulomb friction rheology, and the tail was most likely a Bingham rheology.

The debris flow experiments showed large levels of variability, which means a small test sample has limited statistical reproduction. Repeatability was not seen as a priority due to this high level of variability. The tests provided for qualitative assessment and so have been discussed within the limitations of instantaneous observations. The PLIF method was

effective at illuminating the interior of flow but was limited in terms of capturing bubbles, light attenuation and how far into the interior it could be located. The PIV analysis allowed a vast amount of data that allowed good statistical evaluation of the deep sections of flow. PIV was limited in terms of tracking individual particles but this was necessary in order to compensate for the image quality in some areas with multiple small particles. The measurement of the slip velocity was relatively accurate but could not be evaluated at the exact base of the flow.

Future improvements focused on three sections - current data, equipment, PLIF and QI. The main recommendation relating to the current data was to utilise the vertical displacement data in order to measure the granular temperature of the flow and how it evolves with time. The PLIF technique could be improved by simplifying the material PSD however this would limit real world behaviour. Other improvements include illuminating the solid phase and conduction transverse planes through the material. PTV and ICV were identified as new QI techniques that could add more information on the interior behaviour, but require increased image and testing quality.

Debris flows are an increasingly prominent hazard as commercial development of steep terrain increases. The research in this thesis highlights how variable and chaotic the material is. The observations show large particles disrupting flow as they pass. The effect of this interruption is dependent on the material around it. Given two of these interruptions occurring in close proximity in the correct manner a large particle may be forcibly ejected from the flow. Other surging and segregation micro-mechanical behaviours that occur at various intervals can be altered depending on the chaotic movement of the various-sized particles make it difficult to apply a single rheology to the actual behaviour. This unpredictable nature makes the modelling difficult as it requires the input of instantaneous structures that have only just been able to be visualised through this methodology.

Chapter 7. References

1. Adrian, R. J. (2005). Twenty years of particle image velocimetry. *Experiments in Fluids, 39*(2), 159-169.

2. Adrian R. J. (1984). *Development of pulsed laser velocimetry (PLV) for measurement of fluid flow.* Paper presented at the Proceedings of the 8th biennial symposium on turbulence, Rolla, Missouri.

3. Ancey, C. (2001). *Lecture Notes in Physics* (582 ed.): Springer.

4. Ancey, C., Andreini, N., & Epely-Chauvin, G. (2013). Granular suspension avalanches. Macro-viscous behavior. *Physics of Fluids, 25*(3).

5. Andreini, N. (2012). *Dam Break of Newtonian Fluids and Granular Suspensions - Internal Dynamics Measurements.* EPFL. Retrieved from http://infoscience.epfl.ch/record/175152 (last accessed April 2013)

6. Aragon, J. A. G. (1995). Granular-Fluid Chute Flow: Experimental and Numerical Observations. *Journal of Hydraulic Engineering, 121*(4), 355-364.

7. Arattano, M., & Franzi, L. (2003). On the evaluation of debris flows dynamics by means of mathematical models. *Natural Hazards and Earth System Science, 3*(6), 539-544.

8. Arattano, M., Franzi, L., & Marchi, L. (2006). Influence of rheology on debris-flow simulation. *Natural Hazards and Earth System Science, 6*(4), 519-528.

9. Bagnold, R. A. (1954). *Experiments on a gravity-free dispersion of large solid spheres in a Newtonian fluid under shear*. Paper presented at the Royal Society of London Proceedings, London.

10. Bardou, E. (2002). Methodologie de Diagnostic Des Laves Torren-Tielles Sur Un Bassin Versant Alpin. École Polytechnique Federale De Lausanne.

11. Barr, D. W. (2001). Coefficient of permeability determined by measurable parameters. *Groundwater, 39*(3), 356-361.

12. Bowman, E. T., Laue, J., Imre, B., & Springman, S. M. (2010). Experimental modelling of debris flow behaviour using a geotechnical centrifuge. *Canadian Geotechnical Journal, 47*(7), 742-762.

13. Bowman, E. T., & Sanvitale, N. (2009, 5-9 Oct 2009.). *The Role of Particle Size in the Flow Behaviour of Saturated Granular Materials.* Paper presented at the 17th International Conference on Soil Mechanics & Geotechnical Engineering (2009 ICSMGE), Alexandria, Egypt.

14. Breien, H., Pagliardi, M., Blasio, F. V., Issler, D., & Elverhøi, A. (2007). Experimental Studies Of Subaqueous Vs. Subaerial Debris Flows – Velocity Characteristics As A Function Of The Ambient Fluid. In V. Lykousis, D. Sakellariou & J. Locat (Eds.), *Submarine Mass Movements and Their Consequences* (Vol. 27, pp. 101-110): Springer Netherlands.

15. Chau, K., Chan, L., Luk, S., & Wai, W. (2000). *Shape of deposition fan and run-out distance of debris flow: Effect of granular and water content.* Paper presented at the Proc. of the Second International Conference on Debris Flows Hazards Mitigation, Taipei, Taiwan.

16. Chen, C.-l. (1988). Generalized Viscoplastic Modeling of Debris Flow. *Journal of Hydraulic Engineering, 114*(3), 237-258.

17. Chou, C. S. (2000). *Research on rapid granular flows of highly inelastic particles.* Paper presented at the *Proceedings of the National Sciemce Council Republic of China Part (A)*.

18. Coe, J., McCoy, S., Kean, J., & Tucker, G. (2011). *High-resolution measurements of sediment entrainment by a natural debris flow.* Paper presented at the AGU Fall Meeting Abstracts.

19. Coussot, P., Laigle, D., Arattano, M., Deganutti, A., & Marchi, L. (1998). Direct Determination of Rheological Characteristics of Debris Flow. *Journal of Hydraulic Engineering, 124*(8), 865-868.

20. Coussot, P., & Meunier, M. (1996). Recognition, classification and mechanical description of debris flows. *Earth-Science Reviews, 40*(3-4), 209-227.

21. Davies, T. R. (1990). Debris-flow surges-experimental simulation. *Journal Hydrology (New Zealand), 29*(1).

22. Davies, T. R., für Wasserbau, V., & und Glaziologie, H. (1988). *Debris Flow Surges: A Laboratory Investigation*: Versuchsanstalt für Wasserbau-Hydrologie und Glaziologie an der ETHZ.

23. Denlinger, R. P., & Iverson, R. M. (2001). Flow of variably fluidized granular masses across three-dimensional terrain: 2. Numerical predictions and experimental tests. *Journal of Geophysical Research: Solid Earth (1978–2012), 106*(B1), 553-566.

24. Duk. (2005). Laminar shear in a fluid. Retrieved 25/10/2010, 2010, from http://en.wikipedia.org/wiki/File:Laminar_shear.svg

25. Fannin, J., & Bowman, E. T. (2007). Debris flows - Entrainment, Deposition and Travel Distance *Geotechnical News, 25*(4), 3-6.

26. Fukushima, E. (1999). Nuclear magnetic resonance as a tool to study flow. *Annual Review of Fluid Mechanics, 31*, 95-123.

27. Gray, J. M. N. T., & Ancey, C. (2009). Segregation, recirculation and deposition of coarse particles near two-dimensional avalanche fronts. *Journal of Fluid Mechanics, 629*(1), 387-423.

28. Gray, J. M. N. T., & Kokelaar, B. P. (2010). Large particle segregation, transport and accumulation in granular free-surface flows. *Journal of Fluid Mechanics, 652*, 105.

29. Haff, P. (1983). Grain flow as a fluid-mechanical phenomenon. *Journal of Fluid Mechanics, 134*(1), 401-430.

30. Hart, D. P. (2000). PIV error correction. *Experiments in Fluids, 29*(1), 13-22.

31. Hsü, K. J. (1975). Catastrophic debris streams (sturzstroms) generated by rockfalls. *Geological Society of America Bulletin, 86*(1), 129-140.

32. Hsü, K. J. (1978). Albert Heim: Observations on landslides and relevance to modern interpretations. *Rockslides and avalanches, 1*, 71-93.

33. Hungr, O. (1995). A model for the runout analysis of rapid flow slides, debris flows, and avalanches. *Canadian Geotechnical Journal, 32*(4), 610-623. doi: 10.1139/t95-063

34. Hungr, O., Evans, S., Bovis, M., & Hutchinson, J. (2001). A review of the classification of landslides of the flow type. *Environmental & Engineering Geoscience, 7*(3), 221-238.

35. Hungr, O., Morgan, G. C., & Kellerhals, R. (1984). Quantitative Analysis of Debris Torrent Hazards for Design of Remedial Measures. *Canadian Geotechnical Journal 21*, 663-667.

36. Hunt, B. (1994). Newtonian fluid mechanics treatment of debris flows and avalanches. *Journal of hydraulic engineering, 120*(12), 1350-1363.

37. Hunter, R. P. (2012). Development of Transparent Soil Testing using Planar Laser Induced Fluorescence in the Study of Internal Erosion of Filters in Embankment Dams.

38. Hürlimann, M., Rickenmann, D., Medina, V., & Bateman, A. (2008). Evaluation of approaches to calculate debris-flow parameters for hazard assessment. *Engineering Geology, 102*(3-4), 152-163.

39. Innes, J. L. (1983). Debris flows. *Progress in Physical Geography, 7*(4), 469-501.

40. Iverson, R. M. (1985). A Constitutive Equation for Mass-Movement Behavior. *The Journal of Geology, 93*(2), 143-160.

41. Iverson, R. M. (1997). The physics of debris flows. *Reviews of Geophysics, 35*, 245-296.

42. Iverson, R. M. (2003). *The debris-flow rheology myth.* Paper presented at the *Third International Conference on Debris-Flow Hazard Mitigation: Mechanics Prediction and Assessment*. , Rotterdam.

43. Iverson, R. M. (2009). *Elements of an Improved Model of Debris-flow Motion.* Paper presented at the Powders and grains.

44. Iverson, R. M., Costa, J. E., & LaHusen, R. G. (1992). Debris-Flow Flume at H.J. Andrews Experimental Forest, Oregon U.S. Geological Survey

45. Iverson, R. M., & Denlinger, R. P. (2001). Flow of variably fluidized granular masses across 3-D terrain: 1. Coulomb mixture theory. *Journal of Geophysical Research*.

46. Iverson, R. M., Logan, M., LaHusen, R. G., & Berti, M. (2010). The perfect debris flow? Aggregated results from 28 large-scale experiments. *Journal of Geophysical Research: Earth Surface, 115*(F3), F03005. doi: 10.1029/2009jf001514

47. Iverson, R. M., Reid, M. E., Logan, M., LaHusen, R. G., Godt, J. W., & Griswold, J. P. (2010). Positive feedback and momentum growth during debris-flow entrainment of wet bed sediment. *Nature Geoscience, 4*(2), 116-121.

48. Iverson, R. M., & Vallance, J. W. (2001). New views of granular mass flows. *Geology, 29*(2), 115-118.

49. Jakob, M., & Hungr, O. (2005). Debris-flow Hazards and Related Phenomena *Springer Praxis Books, Geophysical Sciences* (pp. 739)

50. Jakob, M., & Jordan, P. (2001). Design flood estimates in mountain streams the need for a geomorphic approach. *Canadian Journal of Civil Engineering, 28*(3), 425-439.

51. Jan, C.-D., & Shen, H. W. (1997). Review dynamic modeling of debris flows *Recent Developments on Debris Flows* (pp. 93-116): Springer

52. Jesuthasan, N., Baliga, R., & Savage, S. B. (2006). Use of particle tracking velocimetry for measurements of granular flows: review and application. *KONA, 24*, 15-26

53. Johnson, C., Kokelaar, B., Iverson, R., Logan, M., LaHusen, R., & Gray, J. (2012). Grain-size segregation and levee formation in geophysical mass flows. *Journal of Geophysical Research: Earth Surface (2003–2012), 117*(F1).

54. Keane, R. D., & Adrian, R. J. (1992). Theory of cross-correlation analysis of PIV images. *Applied scientific research, 49*(3), 191-215.

55. Koch, T. (1998). Testing various constitutive equations for debris flow modelling. *IAHS Publication 248* 249–257.

56. Larcher, M., Fraccarollo, L., Armanini, A., & Capart, H. (2007). Set of measurement data from flume experiments on steady uniform debris flows *Journal of Hydraulic Research, 45*(extra), 59-71.

57. Legros, F. (2002). The mobility of long-runout landslides. *Engineering Geology, 63*(3-4), 301-331.

58. Lipman, P. W., & Mullineaux, D. R. (1981). *The 1980 eruptions of Mount St. Helens, Washington*: US Dept. of the Interior, US Geological Survey.

59. Liu, K.-F., & Chang, C.-W. (2010). Steady Mud Flow in Rotating Viscometer.

60. Liu, X. (1996). Size of a debris flow deposition: model experiment approach. *Environmental geology, 28*(2), 70-77.

61. Longo, S., & Lamberti, A. (2002). Grain shear flow in a rotating drum. *Experiments in Fluids, 32*(3), 313-325.

62. Lorenzini, G., & Mazza, N. (2004). *Debris Flow: Phenomenology and Rheological Modelling*. Ashurst, Southampton, UK: WIT Press.

63. Major, Jon J. (1997). Depositional Processes in Large Scale Debris Flow Experiments. *The Journal of Geology, 105*(3), 345-366.

64. Major, J. J. (2000). Gravity-Driven Consolidation of Granular Slurries: Implications for Debris-Flow Deposition and Deposit Characteristics. *Journal of Sedimentary Research, 70*(1), 64-83.

65. McLelland, S. J., & Nicholas, A. P. (2000). A new method for evaluating errors in high-frequency ADV measurements. *Hydrological Processes, 14*(2), 351-366.

66. McSaveney, M. J., & Beetham, R. D. (2006). The potential for debris flows from Karaka Stream at Thames, Coromandel (E. Waikato, Trans.). Lower Hutt, NZ: Institute of Geological and Nuclear Sciences Limited.

67. McSaveney, M. J., Beetham, R. D., & Leonard, G. S. (2005). The 18 May 2005 debris-flow disater at Matata: Causes and mitigation suggestions. (pp. 51 pp). Lower Hutt, NZ: Institute of Geological & Nuclear Sciences Limited.

68. Mills, P., & Snabre, P. (2009). Apparent viscosity and particle pressure of a concentrated suspension of non-Brownian hard spheres near the jamming transition. *The European Physical Journal E, 30*(3), 309-316.

69. Myles, F., & Parkin, E. (2008). *Debris Flows in the New Zealand Context: Influence of grain shape on runout behaviour*. (Honours Project), University of Canterbury, Christchurch.

70. Naef, D., Rickenmann, D., Rutschmann, P., & Mcardell, B. W. (2006). Comparison of flow resistance relations for debris flows using a one-dimensional finite element simulation model *Natural Hazards and Earth System Science, 6*(1), 155-165.

71. Nakagawa, M., Altobelli, S. A., Caprihan, A., Fukushima, E., & Jeong, E. K. (1993). Non-invasive measurements of granular flows by magnetic resonance imaging. *Experiments in Fluids, 16*(1), 54-60.

72. Nokes, R. (2008). ENCI638 Turbulence - Module 3 Notes: University of Canterbury.

73. Okamoto, K., Hassan, Y. A., & Schmidl, W. D. (1995). New tracking algorithm for particle image velocimetry. *Experiments in Fluids, 19*(5), 342-347.

74. Optics, O. Z. (2005). Delivery Systems for Flow Visualization. In O. O. Lts (Ed.). Ottawa, ON, Canada.

75. Pailha M, & Pouliquen O. (2009). A two-phase flow description of the initiation of underwater granular avalanches. . *Journal of Fluid Mechanics, 633*, 115-135.

76. Patil, V., & Liburdy, J. (2012). Optical measurement uncertainties due to refractive index mismatch for flow in porous media. *Experiments in Fluids, 53*(5), 1453-1468.

77. Paul, E. L., Atiemo-Obeng, V., & Kresta, S. M. (2004). *Handbook of industrial mixing: science and practice*: Wiley.com.

78. Phillips, C. J., & Davies, T. R. H. (1991). Determining rheological parameters of debris flow material. *Geomorphology, 4*(2), 101-110.

79. Phillips, D. T. (2008, April 5, 2010). The Physicsof Whipped Cream. *NASA Science: Science News*. Retrieved 26/10/2010, 2010, from http://science.nasa.gov/science-news/science-at-nasa/2008/25apr_cvx2/

80. Pierson, T. C. (1980). Erosion and deposition by debris flows at Mt Thomas, North Canterbury, New Zealand. *Earth Surface Processes, 5*(3), 227-247.

81. Pierson, T. C. (1981). Dominant particle support mechanisms in debris flows at Mt Thomas, New Zealand, and implications for flow mobility. *Sedimentology, 28*(1), 49-60.

82. Pierson, T. C., Costa, J. E., & Vancouver, W. (1987). A rheologic classification of subaerial sediment-water flows. *Debris flows/avalanches: process, recognition, and mitigation, 7*, 1.

83. Pouliquen, O., Delour, J., & Savage, S. B. (1997). Fingering in granular flows. *Nature, 386*(6627), 816-817.

84. Pouliquen, O., Forterre, Y. O., & Euml. (2002). Friction law for dense granular flows: application to the motion of a mass down a rough inclined plane. *Journal of Fluid Mechanics, 453*(-1), 133-151.

85. Raffel, M., Willert, C. E., & Kompenhans, J. (1998). *Particle Image Velocimetry: A Practical Guide; with 24 Tables*: Springer.

86. Rickenmann, D. (1990). Debris flows 1987 in Switzerland Modeling and sediment transport *IAHS Publications, 194*, 371-378.

87. Rickenmann, D. (1999). Empirical Relationships for Debris Flows. *Natural Hazards, 19*(1), 47-77. doi: 10.1023/a:1008064220727

88. Salm, B., & Gubler, H. (1985). Measurement and analysis of the motion of dense flow avalanches. *Ann. Glaciol, 6*, 26-34.

89. Sanvitale, N. (2010). *An experimental study on saturated granular flows and its application to the physcial modelling of debris flows.* (PH.D).

90. Sanvitale, N., Bowman, E., & Genevois, R. (2011). *Experimental Measurements of Velocity through Granular-Liquid Flows*. Paper presented at the 5th International Conference on Debris-Flow Hazards "Mitigation, Mechanics, Prediction and Assessment", Pradua, Italy.

91. Sanvitale, N., & Bowman, E. T. (2012). Internal imaging of saturated granular free-surface flows. *International Journal of Physical Modelling in Geotechnics, 12*, 129-142. http://www.icevirtuallibrary.com/content/article/10.1680/ijpmg.12.00002

92. Sanvitale, N., Bowman, E. T., & Genevois, R. (2010). *Optical investigation through a flowing saturated granular material*. Paper presented at the 7th international Conference on physical modelling in geotechnics, Zurich.

93. Sarikhan, I. (2007). Landslide Reconnaissance Following the December 3, 2007 Storm - Thurston County Cedar Flats Area. Retrieved 29/10/2013, 2013, from http://www.dnr.wa.gov/researchscience/topics/geologichazardsmapping/pages/landslides_thurstonslide2.aspx

94. Sassa, K., Kaibori, M., & Kitera, N. (1985). *Liquefaction and undrained shear of torrent deposits as the cause of debris flows.* Paper presented at the Proceedings International Symposium on Erosion, Debris Flows and Disaster Prevention.

95. Schaefer, M., Bugnion, L., Kern, M., & Bartelt, P. (2010). Position dependent velocity profiles in granular avalanches. *Granular Matter, 12*(3), 327-336.

96. Schroeder, A. (2008). *Particle Image Velocimetry: New Developments and Recent Applications; with 24 Tables* (Vol. 112): Springer.

97. Sharpe, C. F. S. (1938). *Landslides and related phenomena: a study of mass-movements of soil and rock*: Columbia University Press New York.

98. Shieh, C. L., Jan, C. D., & Tsai, Y. F. (1996). A numerical simulation of debris flow and its application. *Natural Hazards, 13*(1), 39-54.

99. Spaaks, Jurriaan H. 2010. Austria 2002 2002 [cited 9/11/2010 2010]. Available from http://staff.science.uva.nl/~jspaaks/files/fieldwork.html.

100. Sparks, R. S. J. (1976). Grain size variations in ignimbrites and implications for the transport of pyroclastic flows. *Sedimentology, 23*(2), 147-188.

101. Steffe, J. F. (1996). *Rheological Methods in Food Process Engineering* (2nd ed.). East lansing USA: Freeman Press.

102. Sutton, M., Chao, Y., & Taylor, C. (1983). Slope measurements using multiplexed diffraction gratings as shearing components in interferometry. *Experimental mechanics, 23*(4), 370-377.

103. Suzuki, T., & Hotta, N. (2006). *Resistance of the Debris Flow on the Roughness Boundary*.

104. Takahashi, T. (1981). Debris Flow. *Annual Review of Fluid Mechanics, 13*(1), 57-77.

105. Takahashi, T. (1997b). Dynamics of the Inertial and Viscous Debris Flows. In A. Armanini & M. Michiue (Eds.), *Recent Developments on Debris Flows: Lecture Notes in Earth Sciences, Berlin Springer Verlag* (Vol. 64): Springer

106. Takahashi, T. (Ed.). (1991). *Debris Flow*. Rotterdam: A. A. Balkema.

107. Takahashi, T., & Yoshida, H. (1979). Study on the deposition of debris flows, Part 1 - Deposition due to abrupt change of bed slope. *Annuals, Disaster Prevention Research Institute, Kyoto, Japan, 22*(B-2), 405-435.

108. Thornton, A., Gray, J., & Hogg, A. (2006). A three-phase mixture theory for particle size segregation in shallow granular free-surface flows. *Journal of Fluid Mechanics, 550*, 1-26.

109. Vallance, J., & Savage, S. (2000). Particle Segregation in Granular Flows Down Chutes. In A. Rosato & D. Blackmore (Eds.), *IUTAM Symposium on Segregation in Granular Flows* (Vol. 81, pp. 31-51): Springer Netherlands

110. Van Rijn, L. C. (1984). Sediment transport, part I: bed load transport. *Journal of hydraulic engineering, 110*(10), 1431-1456.

111. Wang, G., Sassa, K., & Fukuoka, H. (2003). Downslope volume enlargement of a debris slide–debris flow in the 1999 Hiroshima, Japan, rainstorm. *Engineering Geology, 69*(3–4), 309-330.

112. Wang, Y., & Hutter, K. (1999). A constitutive model of multiphase mixtures and its application in shearing flows of saturated solid-fluid mixtures. *Granular Matter, 1*(4), 163-181.

113. Watson, M. (2012, 237/08/2012). Volcano deris danger for drivers. *Stuff.co.nz*. Retrieved 15/4/2013, 2013, from (http://www.stuff.co.nz/national/7556422/Volcano-debris-danger-for-drivers)

114. Weber, D., & Rickenmann, D. (1999). *Physical Modelling of Debris Flow Surges and Related Erosion Processes*. Paper presented at the Hydraulic Engineering for Sustainable Water Resources Management at the Turn of the Millenium., Graz, Austria.

115. Westerweel, J. (1993). Digital particle image velocimetry. *Delft University*, 17-18.

116. Whipple, K. X. (1997). Open-Channel Flow of Bingham Fluids: Applications in Debris-Flow Research. *The Journal of Geology, 105*(2), 243-262.

117. White, D., Take, W., & Bolton, M. (2001). *Measuring soil deformation in geotechnical models using digital images and PIV analysis*. Paper presented at the 10th International Conference on Computer Methods and Advances in Geomechanics, Tucson, Arizona.

118. White, D., Take, W., & Bolton, M. (2003). Soil deformation measurement using particle image velocimetry (PIV) and photogrammetry. *Geotechnique, 53*(7), 619-632.

119. Wiederseiner, S., Andreini, N., Epely-Chauvin, G., & Ancey, C. (2011). Refractive-index and density matching in concentrated particle suspensions: a review. *Experiments in Fluids, 50*(5), 1183-1206.

120. Willert, C., & Gharib, M. (1991). Digital particle image velocimetry. *Experiments in Fluids, 10*(4), 181-193.

121. Yu, J. H., Hsieh, A. J., & Rutledge, G. C. (2010). *Novel Transparent PMMA Composites for Optical Tagging*. Aberdeen Proving Ground, MD 21005-5069, USA.

Chapter 8. Appendices

Appendix A: Material Preperation

A.1. Removal of Oil

Removal of oil was necessary in order to separate particles. This was done using methylated spirits baths and water rinses. All the material was collected and put in a perforated container to drain off the oil so that it could be re used. A methylated spirits rinse was used to wash the flume apparatus and brush the fines to the end where they were collected and drained. The fines were separated from the coarse particles using a kitchen sieve of approximately 2 mm openings. The coarse particles required less washing due to a reduced surface area. The fines were then placed in a 75 µm sieve, rinsed with methylated spirits and then water before being left to dry. This was repeated twice for the coarser fraction (>~2 mm) and three times for the finer fraction (see Figure A-1). A full face ventilation mask and thick chemically resistant gloves were required in a well-ventilated area in order to ensure the safety of the particle cleaner. It was observed that the best way to check if enough oil had been removed was to use a thin latex disposable glove to check by feel. This was more effective and safe than using touch by skin.

Figure A-1: (a) Initial 'dirty' material (b) rinse of large particles in methylated spirits (c) water rinse of material

A.2. Sieving and Final Wash

Once the oil has been removed the particles can be properly separated. There was a trade-off between ensuring that the particles had been sieved long enough to separate and to minimise abrasion caused by the steel sieves. The steel sieves, particularly those above 4 mm, abraded the edges of the particles changing the angularity of the particles, leaving a steel deposit on the edges. The deposits effectively outline the particle in the transparent material and so

reduce the imaging technique's effectiveness. Those below 4 mm used a wire mesh rather than a steel plate with a grid cut out; the smaller sieves were therefore less abrasive. Washing was done by hand for particles over 4 mm to avoid excess contact with the iron sieves. For particles below 4 mm, the particles were sieved for 10 min in a conventional sieve shaker, this was able to be done because the wire mesh had comparatively less abrasive effect. The large amount of fine material was more effectively and efficiently separated in a shaker. Amounts were limited under guidelines for the sieves to ensure accurate particle separation. Figure A-2 shows the clean weighed material ready for use in testing.

Figure A-2: Final sieved and cleaned particles ready for use in testing.

A.3. Foreign Particulates

During the methylated spirit baths and the final wash, a number of foreign particles were removed using tweezers. Common particulates and foreign objects removed are listed below:

- Brush bristles from cleaning sieves;
- Stray sediment particles from geo-mechanics lab;
- Paint chips from Earthquakes damage; and
- Plastic particles from abrasion by glass of buckets, tools and gloves.

The light foreign particles were easily seen in the purple dyed methylated spirits and the dark particles were seen in the water where the glass appeared white.

Appendix B: Image Processing Issues

B.1. Image Error Messages

The anaylsis software returned error messages when patches contain pure black space were atempedted to be analysied. This is due to the images being an 8-bit integer "byte image" with brightness values (or light intensity) ranging from 0-255. Where zero is pure black and absence of light and 255 is pure white light. Pure black areas therefore gave a zero intensity value.

Two solutions were considered to avoid this issue the first inverting the images. As the images contain large areas of pure black inverting converted these spaces to pure White which allows the Matlab programae to assigne a non-zero value to the patches. Sensitivity analysis was conducted to see if an inverted image gave the same value. The draw back to this method is that pure white areas are converted to pure black. There were much fewer areas of pure white but with small patch size these were picked up.

The alternative to this is to add a very small amount of light to all of the values in the image so there are no pure black areas. A brightness value of '1' is added to each image this slightly increasing the brightness for all patches.

Given that inversion appeared to have some effect at very low light levels and there were some sections of large pure white areas that inverted continued to cause issues, it was decided to use artificially addition to remove the issue of pure black areas.

B.1.1. Image Processing Sensitivity

B.1.1.1. Sensitivity Study Setup

One section of the second interior test was used to show the effect of adjusting the images. Figure B-1 shows the original image (a) and the adjusted or inverted images used in the sensitivity study. The patch size and mesh variables were kept constant at three columns of 36 pixel patches at spacing's x = 16 and y = 8. Figure B-1 show the original image and those adjusted using Image-J software. The adjustments to the images were either an inversion; or an increase in contrast and brightness; or both.

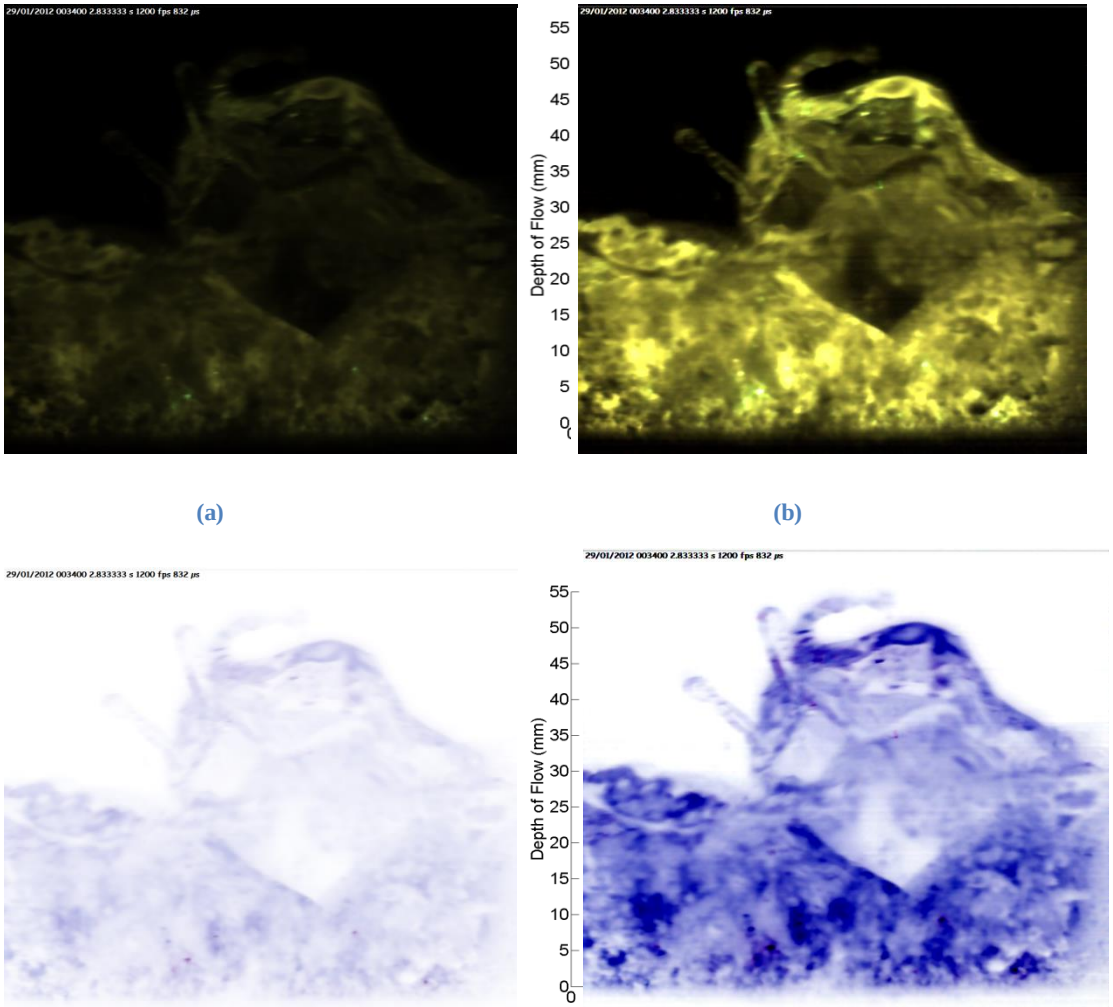

Figure B-1: (a) original pre-processed image (b) post-processed image (c) inverted pre-processed image (d) inverted post-processed image.

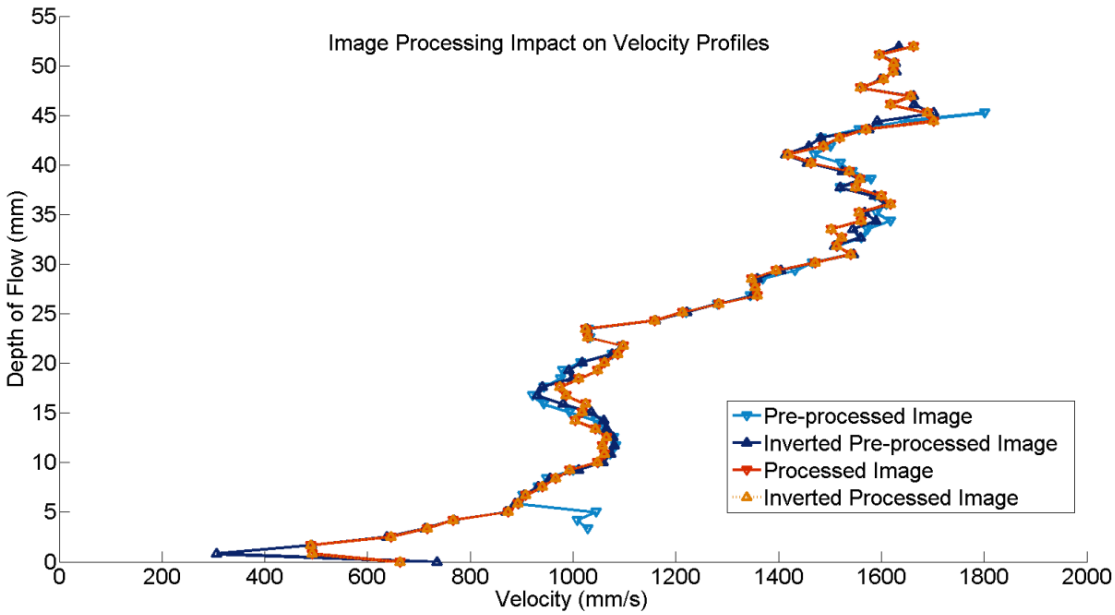

Figure B-2: Velocity profiles developed from original and adjusted images.

Figure B-2 is the result of the sensitivity study. This analysis used to produce the graph uses exactly the same mesh for all analysis. Velocity profiles for inverting and light adjustment are included on the same plot. The inverted post processed adjustment is based on the post processed image and so has the same range of light intensity.

B.1.2. Effect of Inversion

The inversion adjustment was considered as a potential solution to the software returning error messages when patches contain a zero intensity value. The Figure B-2 results show inversion did not materially affect the post-processed images at all, which can be seen as the red and orange triangles overlap to create a star. The pre-processed images showed a small difference in profile particularly around the base of the flow. The base of the flow is a particularly difficult section to accurately analyse due to the smearing effect of patches. As the inverted line matches the post-processed profiles (and the expected trends in profile) it follows that the inverted image does give a better indication of the true velocity profile. It is likely that the original image at low light levels does not give enough information to track patches or distinguish the base of flow from the dark flume base.

B.1.3. Effect of Adjusting Image Quality

Given that the inversion results gave reasonably similar results it is evident that the post processing adjustment of light levels is more significant to the profiles presented in Figure B-2. The post processed images seems to agree with the inverted pre-processed image in most sections of large changes in velocity with depth but are less consistent around the areas of consistent velocity over each step in depth. These areas seem to correspond to the base of the large particle moving through the images. The pre-processed patches could have been mismatched due to being similar to the texture around them, this is avoided when the differences in texture are scaled up. This would recommend that at the low values of light the program gives less reliable results.

Appendix C: Geo-PIV Sensitivity Studies

C.1. Number of Columns

There were three ways on which to apply number of columns: a single column, multiple columns set based on a set width, or a set number of columns regardless of other mesh parameters. Using a set width meant the number of columns was dependent on the other mesh parameter of slope parallel overlap. The graphical representation for each method of number of columns can be seen in Figure C-1. The mesh was constructed either with a single column at the center of the photo or 5 mm either side of the center to give multiple column's. The final number of columns is therefore dependent on the size of the patch. Single and fixed width options were analyzed based on the sensitivity analysis presented in Figure C-4, Figure C-5 and Figure C-6. Separate studies looked at the fixed number of columns and how this could be combined with other parameters.

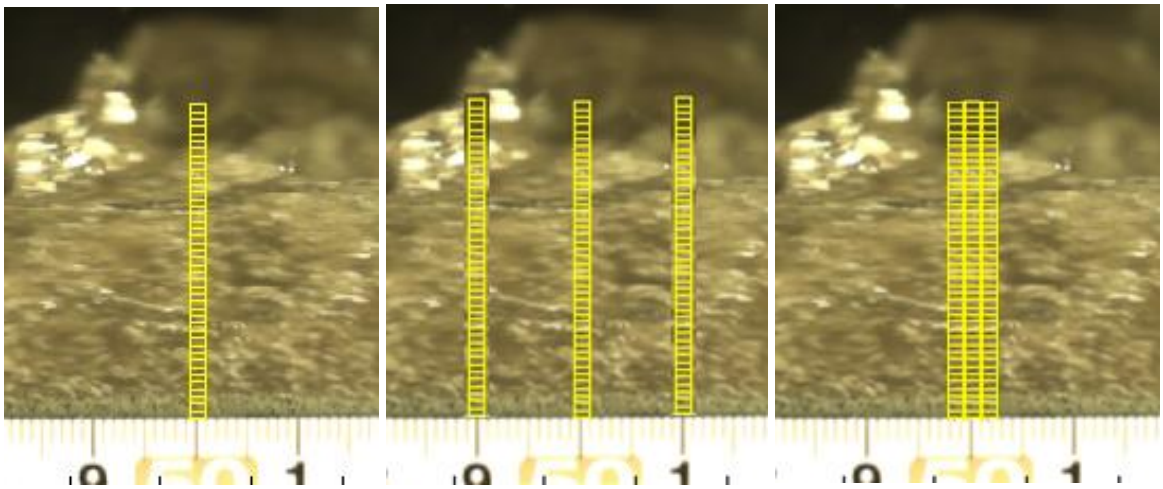

Figure C-1: (a) Example of single column, (b) columns over 10 mm width, (c) three columns no overlap

C.1.1. Using Single Column

Analysing over a single column like Figure C-1 with a small patch size (the analysis of which is shown in Figure C-6 (b)) shows a huge range of variability which is very much unsuitable. For each of the single versus multiple columns an average range in values was calculated. It showed that the single column was consistently more variable giving more distortion in the individual profiles from each of the ten photos than the multiple column analysis.

As the single profiles are averaged to give one representative profile over the batch, large instantaneous fluctuations can distort the mean value. This means that single column should only be used for instantaneous analysis over a small number of frames per batch of the information is lost.

C.1.2. Multiple Fixed Width

When looking at the increased slope parallel overlap (set to half the patch size) more columns were required to fill the set width. From the comparison of single to multiple it was expected that more columns tightens the range showing that as the patch size decreased for multiple columns the variability was similar.

Multiple columns averages the values of a single comparison of a pair of images removing fluctuations occurring with strain. The next columns could be the columns that moved to be at the datum in a small time step, therefore any change that will occur with time does not occur but the spatial difference has. When the next pair of fames is analysed there has been a time step and displacement step (displacement is again averaged to remove fluctuations). The further averaging of frames comparisons dependent on number of frames in the batch removes the fluctuations not removed already. This removal of fluctuations in time and space gives a better representation of the bulk behaviour (wider the columns less spatial fluctuation).

The width of the mesh gives the space scale over which the fluctuations are suppressed or averaged out. However, given the scales of particles compared to the depth of the tail it was seen that a wide set of columns was large enough to cause inaccuracies in the data. Restricting the number of columns to a set number allowed the removal of noise without losing detail.

C.2. Number of Frames per Batch

C.2.1. Sensitivity Study Setup

Two sensitivity studies were conducted to show the sensitivity of batch size at different mesh parameters. The first used the first batch of images of S18W28IN1. The second used S18W32IN2 and used a batch of images with and without a large particle. In order to conduct the studies the mesh was kept constant. S18W28IN1 used a single column of relatively small

patches (16 pixel) and was the most sensitive to batch size. S18W32IN2 used three columns and 32 pixel patches.

As more images were included in a batch, the extra images were added alternatively to the beginning and end of the batch. This was done to ensure the study was centred on the same instantaneous point. If images were just added to the end of a batch, it would invalidate the assumption that the flow is steady over small time steps. This is because the time step between the image of interest and last image would be doubled.

C.2.1.1. S18W28IN1 Sensitivity Study

The lowest batch size for PIV analysis was two frames. There must an original and a secondary image to calculate displacement this cannot be done with the original image alone. For the S18W28IN1 sensitivity study it was found that there was not enough consistent particle matching data to form a velocity profile from the differences between two images. A batch size of ten images was found to be the smallest batch size that gave a continuous velocity profile for S18W28IN1.

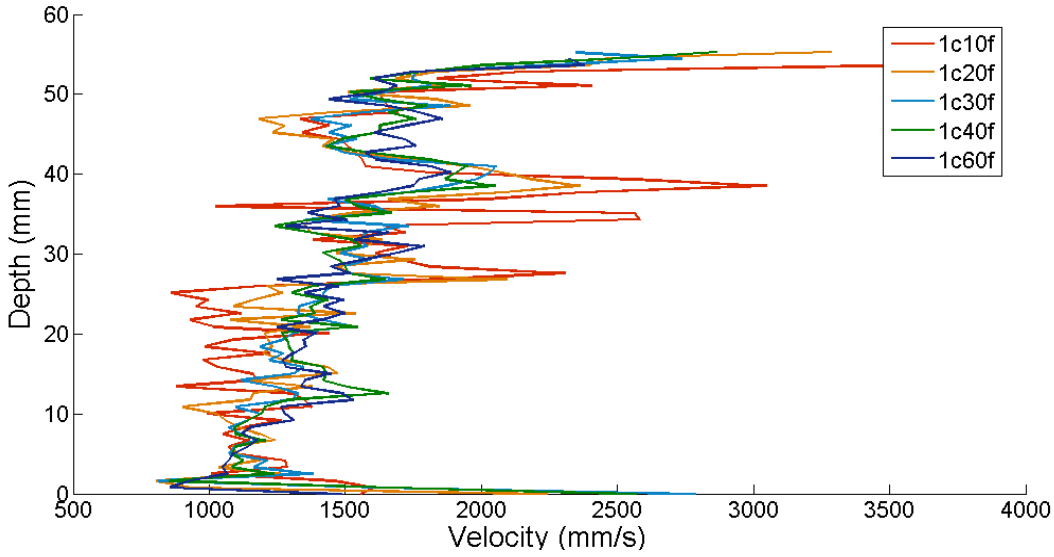

Figure C-2: Effect of number of frames per batch on velocity depth profile. Using 1 column, 16 pixel patch size and slope normal patch spacing of 8 pixels. Legend values correspond to 'c' columns 'f' frames.

Figure C-2 shows the velocity profiles obtained using 10-60 frames per batch. If the ten and twenty frame batch size profiles were removed, the rest of the data gave a consistent profile. Over a batch size of thirty, the velocity profile becomes relatively insensitive to batch size. Thirty images per batch were combined with a relatively sensitive mesh to give a reasonable balanced of detail and noise. Another sensitivity test was conducted to see what batch sizes were sensitive given a more robust mesh.

C.2.1.2. S18W32IN2 Sensitivity Study

Figure C-3 repeated the batch sensitivity analysis using S18W32IN2 with better quality images and a more robust mesh (three columns and larger patch size). The section of the flow studied was 0.5 s after peak saturation height. This batch had a large particle suspended in the flow. In general there was less variation in profiles with batch size. This is because of the higher number of columns averaged over. However, the ten and two-frame batches showed more variability, particularly at the base of the flow. This can be attributed to the large particle moving at a depth between 20 and 30 mm. The instantaneous effects along the bottom edge of the larger particle were smoothed out for the high batch sizes. The effect of one large particle is an important observation for identifying the interior behaviour of debris flows but may influence comparisons between different flows. It was also notable that the small batch sizes had more data removed due to wild vectors. This resulted in the two frame profile being shorter.

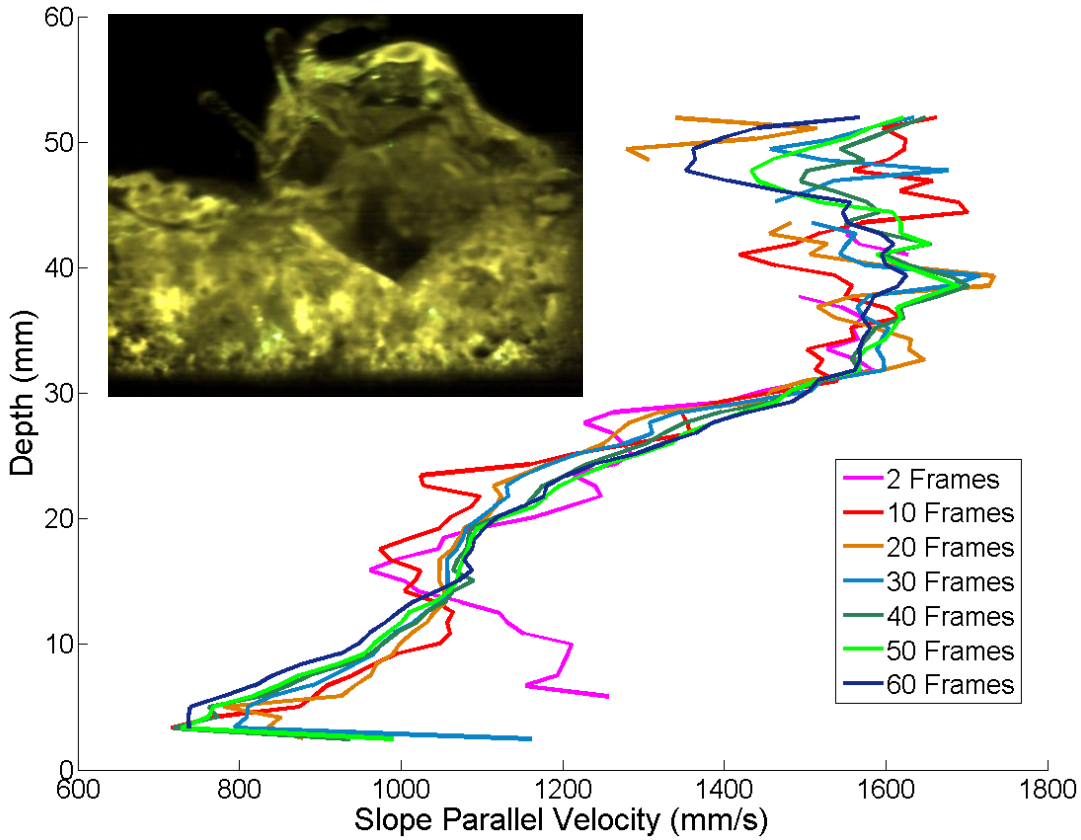

Figure C-3: Effect of number of frames per batch on velocity depth profile. Using 3 columns, 32 pixel patch size and slope normal patch spacing of 8 pixels. Batch analysed was from S18W32IN8 profile, 0.5 s after peak saturation height with a suspended particle. Note above 32 mm the profile is reading the flow above the saturation level. (Insert top left) Image at the centre of each batches showing large particle.

C.2.2. Sensitivity of Mesh Parameters

The three figures; Figure C-4, Figure C-5 and Figure C-6 graphically display a sensitivity analysis undertaken where size of patch and number of columns was changed. There were three patch sizes, 16, 32, and 64. It is important to note that this analysis was conducted on the images from the Motion-Pro camera for which pixels were smaller than the Miro camera (The equivalent sizes would be approximately 8, 16 and 32 for the Miro camera). The overlap in the 'x' direction is half the patch size in each size of patches used. The 'y' is kept at 8 pixels, this was smaller than the patch size in all cases.

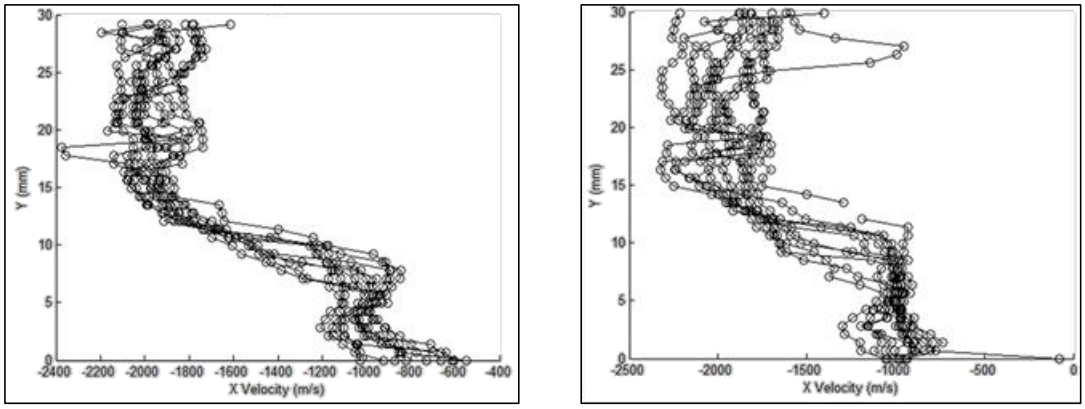

Figure C-4: Sample velocity profiles at Patch size =64 Interval 'x' =32 interval 'y'= 8 with (a) multiple columns or (b) single column.

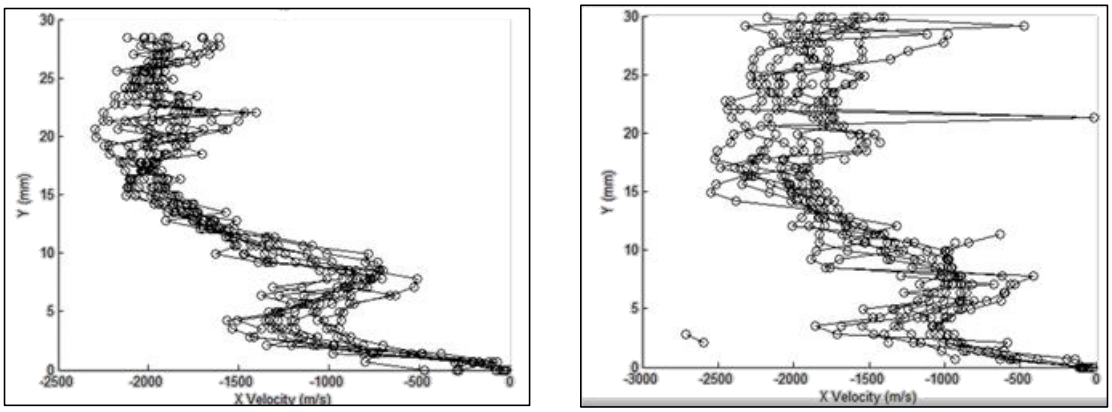

Figure C-5: Sample velocity profiles at Patch size =32 Interval 'x' =16 interval 'y'= 8 with (a) multiple columns or (b) single column.

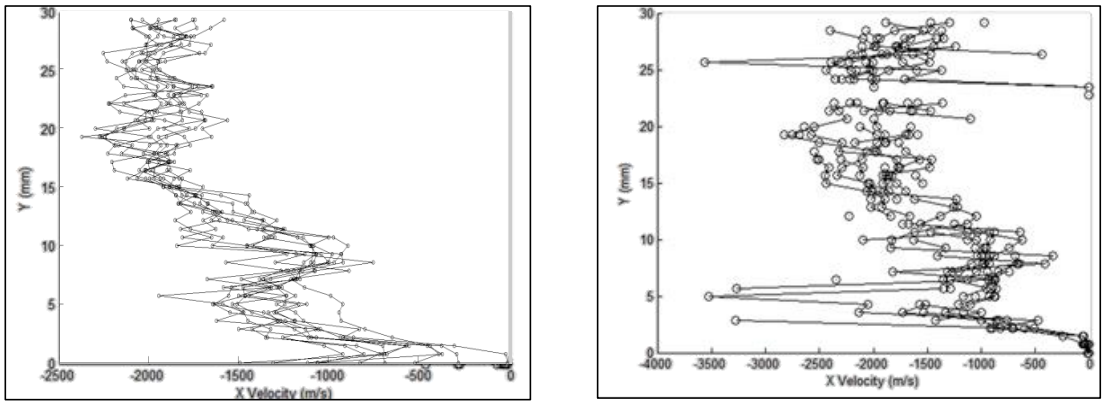

Figure C-6: Sample velocity profiles at Patch size =8 Interval 'x' =8 interval 'y'= 8 with (a) multiple columns or (b) single column.

C.2.2.1. Patch Size

For smaller patch sizes it was shown that Figure C-4 and Figure C-5 compared to Figure C-6 had better detail at the base area and a more pronounced shape with more exaggeration in the profiles. The 64-patch size in Figure C-4 suppresses the detail found in the 32-pixel profile in the bottom 10 mm. The same region for the 16-pixel patch profiles shows a lot of variability and a less-consistent profile. This shows that the smaller the patch size the better the detail. However, very small patches can lose similarity and become dominated by small-scale fluctuations. As the patch size decreased there were more wild vectors introduced. As the single column version in Figure C-6 demonstrates with a lack of a coherent profile and no data at a depth of 23 mm. The calculation time proportionally changes with changes in number of total patches applied. Small patches with multiple columns can therefore become computationally demanding.

C.2.2.2. Number of Columns – Fixed Width

The velocity profiles calculated using the average of multiple column gave less fluctuation then a single column analysis. Particularly looking at Figure C-6 with the 16-pixel sized patches, the multiple column width gives continues profiles with most profiles oscillating about a middle point. The single column patch profiles gave an incoherent picture of velocity with depth. All single-column graphs show increased noise, even the 64 pixel sized single column had a greater variability than the other multiple-column profiles for the top 15 mm of the profiles.

C.2.2.3. Patch Spacing Between Columns

The slope parallel spacing is an important factor tied to the number of columns. If the 'x' overlap is reduced from a half to a quarter (Figure C-7) for a set width of columns then the number of columns doubled. This increases the averaging and reduces variation. It was noted that the two graphs in Figure C-7 were very similar which suggests that 32 pixels per patch is showing accurate results for this test.

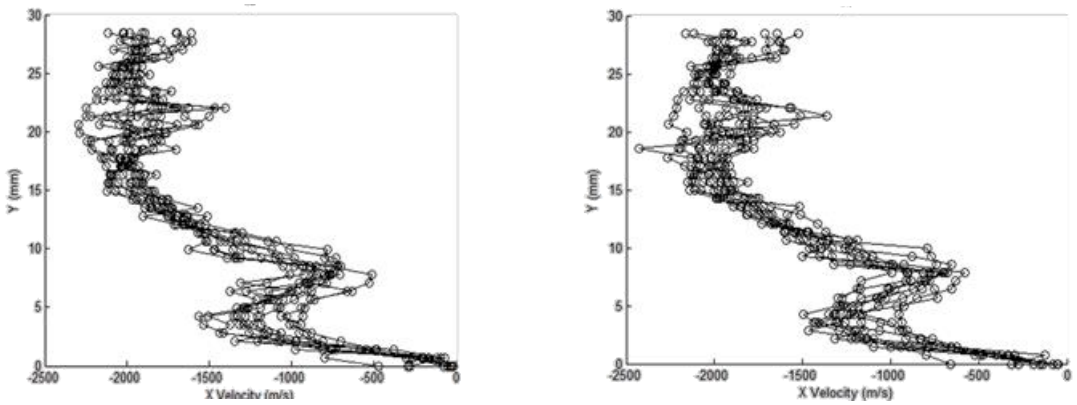

Figure C-7: Effect of altering the slope parallel spacing on a profile of 32 pixel sized patches (a) 'x' overlap of 16 (b) 'x' overlap of 8.

C.2.2.4. Number of Columns – Fixed Number

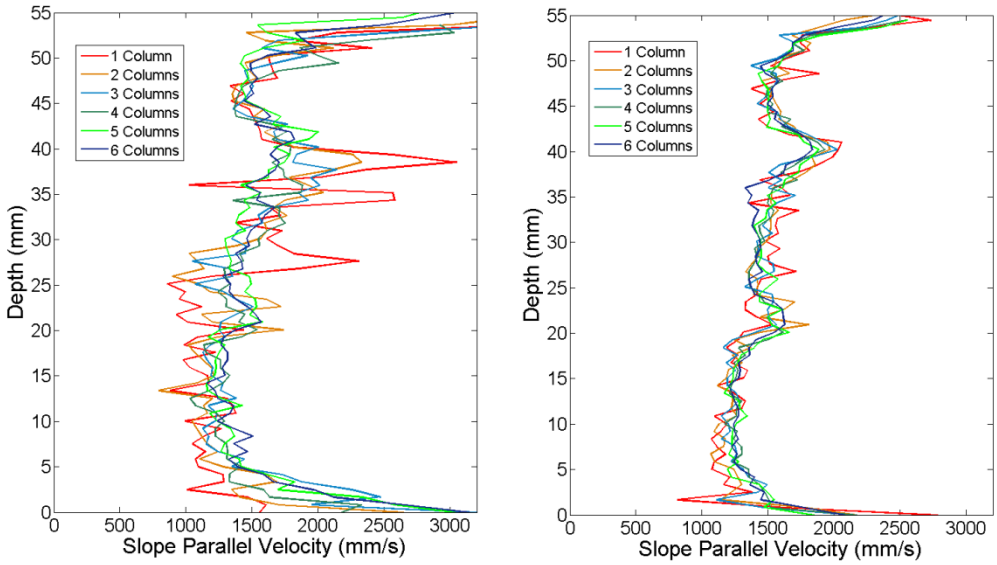

Figure C-8: Effect of change in set number of columns for (left) 30 frames (right) 10 frames. Columns spaced without overlap.

Using the sensitivity set up for section C.2, the number of columns was investigated with frame batch sizes of ten or thirty frames. All of the columns have the same patch size and patch spacing in the slope normal and parallel directions. The number of columns varies from

one to six and. Figure C-8 is of variable columns with thirty frames or ten frames. Only the one column profile seems to have some overly erratic behaviour with larger numbers of columns giving less spread in values. Three columns gave the best balance between detail and bulk behaviour for a batch size of thirty frames. When the batch size is increased to a sample of thirty images there is a noticeable decrease in variation for the same number of columns. This shows the number columns had the same magnitude of sensitivity as the number of images per batch.

C.2.2.5. Combined Columns and Batch Size Sensitivity

Because of the relationship between the sensitivity of the number of columns and batch size the ratio of the two was explored, in Figure C-9. Ratios tested were thirty and sixty and ninety. All curves do show the same general shape with a zone of more shear around 20 mm. This investigation showed that there was no significance of comparing the various ratios of columns to batch size. If either the number of columns or the number of frames was small then profile diverged from the trend. Too few frames gave a more erratic behaviour with generally a higher velocity profile. Too few columns also gave more erratic behaviour with a lower velocity profile. Too many columns shifted the profile most likely as it incorporated more images moving at a faster velocity.

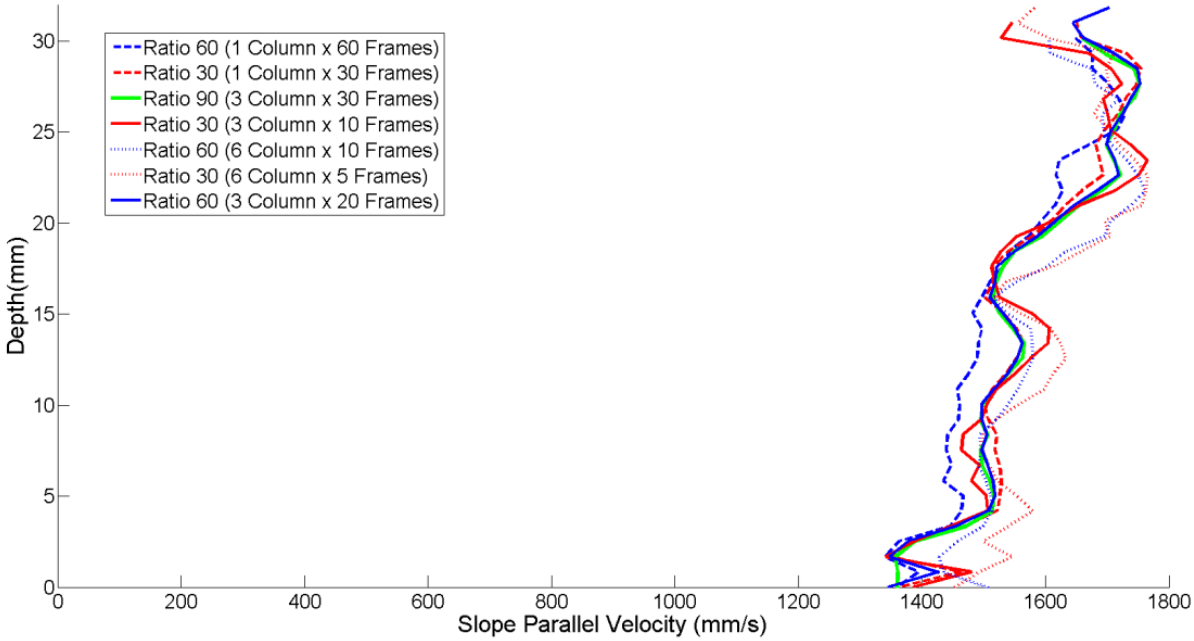

Figure C-9: Effect of altering the ration number of columns and number of frames.

C.2.2.6. Slope Normal Patch Spacing

In the case of velocity profiles with depth the slope-normal spacing, was kept small to increase the smoothness or detail between each point. The slope normal depth was often relatively close to the patch size, particularly in the tail sections. Small spacing ensured a higher number of points within the same depth which produced detailed curves and enough points to obtain enough average slope parallel velocities in the shallow tail sections. This is particularly evident in the normalized plots where the tail profiles can have as little as two velocity measurements. Figure C-10 and Figure C-11 shows the effect of running the slope normal spacing at half the patch size and one pixel. From this it was judged that the smoothness of curves, particularly the tail, justified the computation demand required for analysis at one spacing at one pixel.

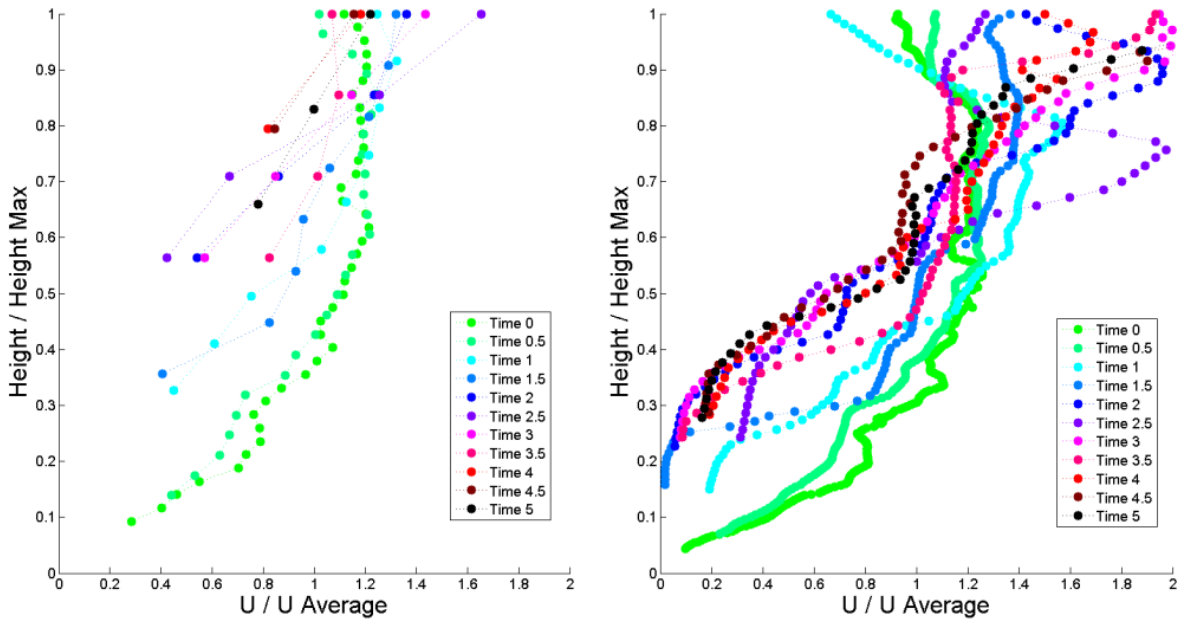

Figure C-10: Effect of altering 'y' overlap to normalized velocity plots of S18W32IN2. (Left) spacing 16 patches and (right) 1 patch spacing. Showing the smoothness of the curves

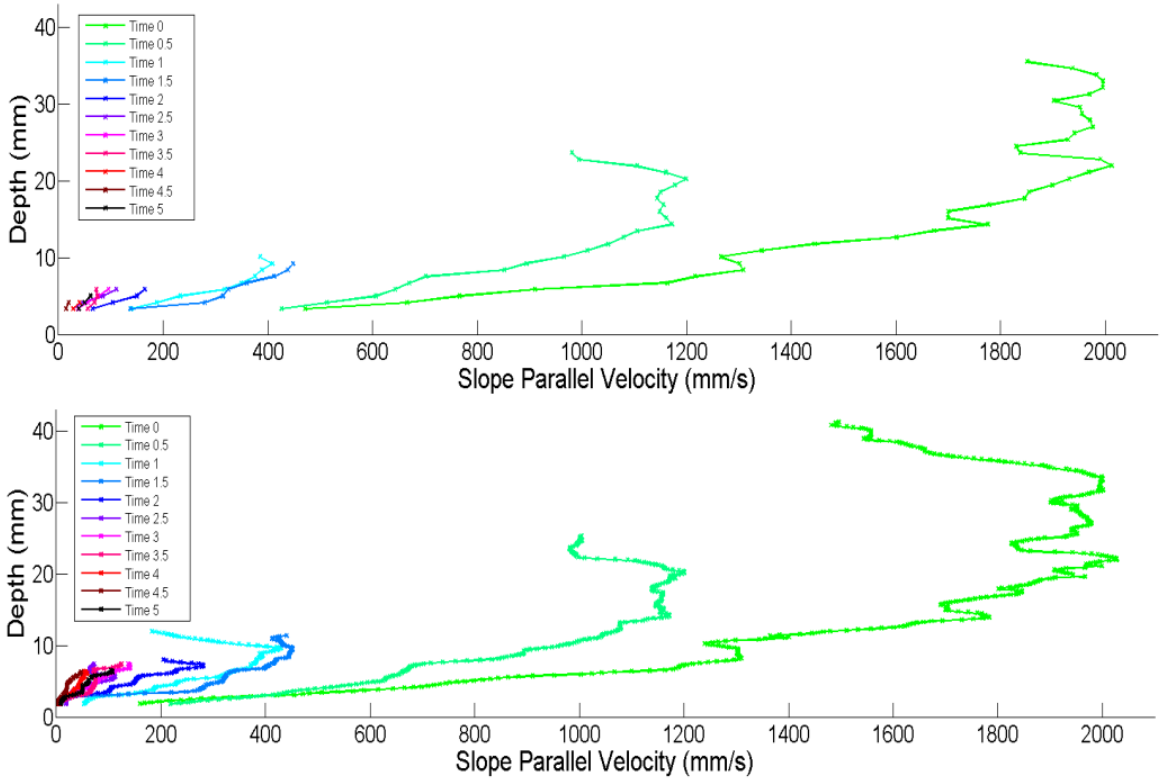

Figure C-11: Effect of altering 'y' overlap to velocity plots of S18W32IN2. (Left) spacing 16 patches and (Right) 1 patch spacing. Showing the smoothness of the curves.

Appendix D: Pre-PIV Results by Slope and Moisture Content

This section looks at each set of tests grouped by slope and moisture content to look at variability abnormalities and consistency in behaviour. Interior and exterior tests are presented together as the deposit data is not dependant on the LOV. Test comparability starts with the baseline behaviour shown for the S18W28 series where the slope is 18.1˚and moisture content of 27.5%. This series is chosen for comparisons of behaviour because it includes the most number of repeated tests.

D.1. Slope 18.1° and Moisture Content 27.8%

All of the preliminary experiments were conducted at slope 18.1˚and a moisture content of 27.5%. These experiments were used to give additional deposit information for use in analysing consistent behaviour of flows. None of the preliminary experiments were used for PIV analysis. Two tests (S18W28IN0b and S18W28IN0d) were simple repeats that were not cleaned giving inaccuracies in fines content and moisture content. In addition to the preliminary experiments two interior and one exterior were conducted, all three of these experiments gave good deposit data. However, the first interior experiments images were of a poor quality and their use has been limited to deposit analysis only.

D.1.1. Deposit

All of the preliminary and interior and exterior tests show good consistency in shape particularly longitudinally (in direction of flow), except S18W28IN0c) which was the most extreme example of the deposit resulting from blockages and segregation. Blockages and jamming in the hopper being the main phenomena that affected deposit run-out length and subsequent height profile over time of the flow. There was some variability in the transverse direction (perpendicular to the flow direction) this appears to be mainly on one side. The small changes in width are inversely reflected in the longitudinal direction giving a similar area for each deposit. The narrower S18W28EX1 is one of the longest and S18W28IN1 is a slightly more wide short shape.

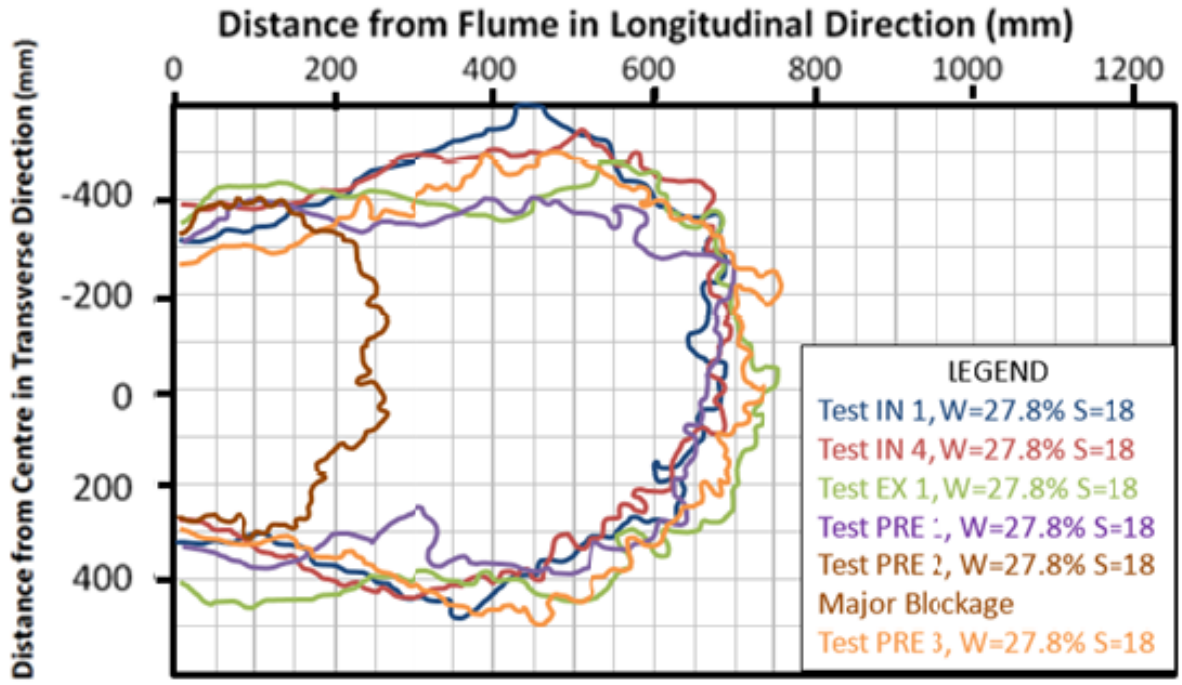

Figure D-1: Outline of S18W28 deposits as taken from photographs of run-out deck. Grid reference in 5cm lots.

The PSD curves for the preliminary experiments show very similar profiles for the tail and front edge for tests. The main discrepancies comes at the coarser end of the front edge samples for the centre and transition and is dependent on what coarse particles the sample space included. When this occurred the results were checked on spot height graphs to ensure the spread of large particles was not unusual.

In terms of the experiments, S18W28IN1 showed less impact of segregation through the centre and transition points with PSDs close to that of the original material. The larger particles appeared to be closer to the front edge than the centre indicating a high level of preferential movement of the coarse particles to the front. The centre sample was, therefore, not large enough to pick up this phenomenon.

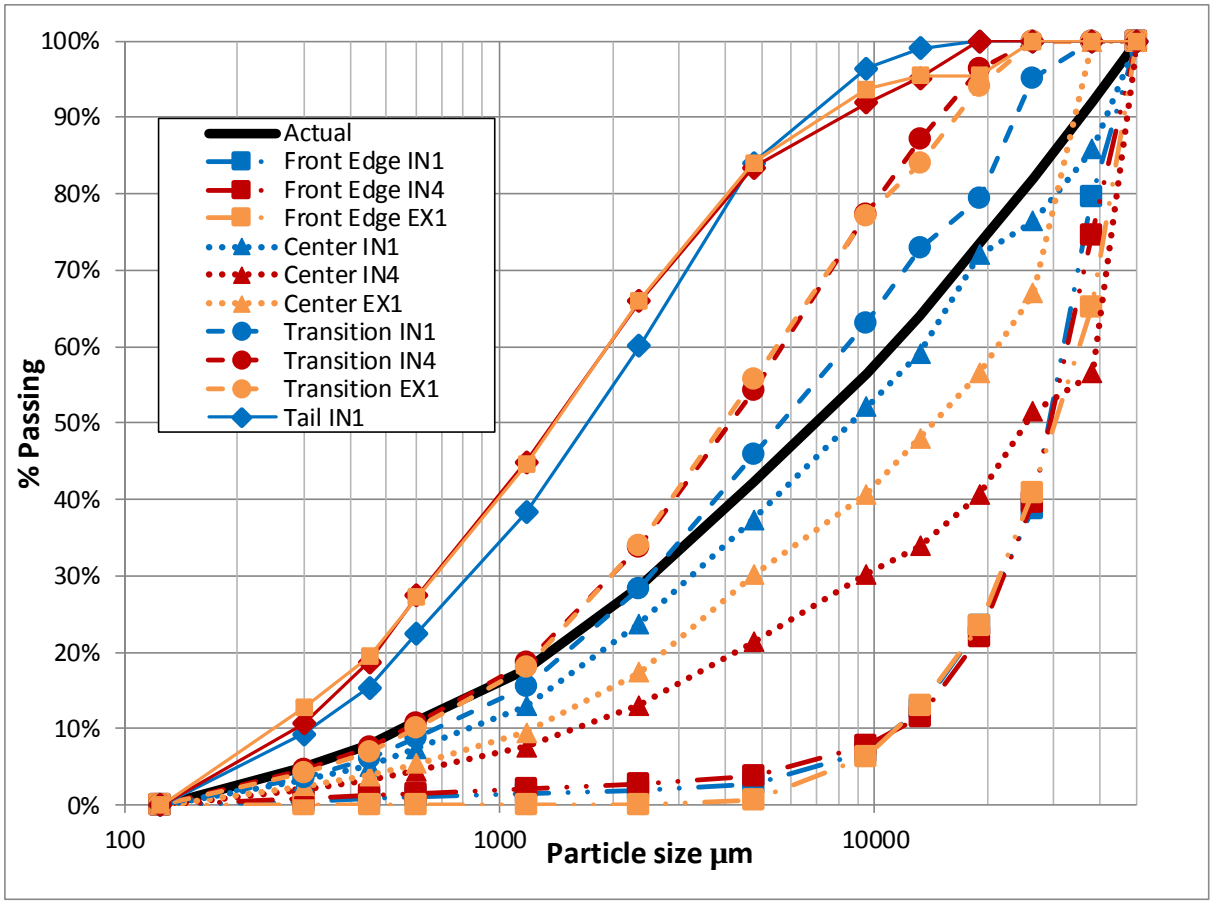

Figure D-2: PSD of S18W28IN1, S18W28IN4 and S18W28EX1, the actual is the PSD for the whole material.

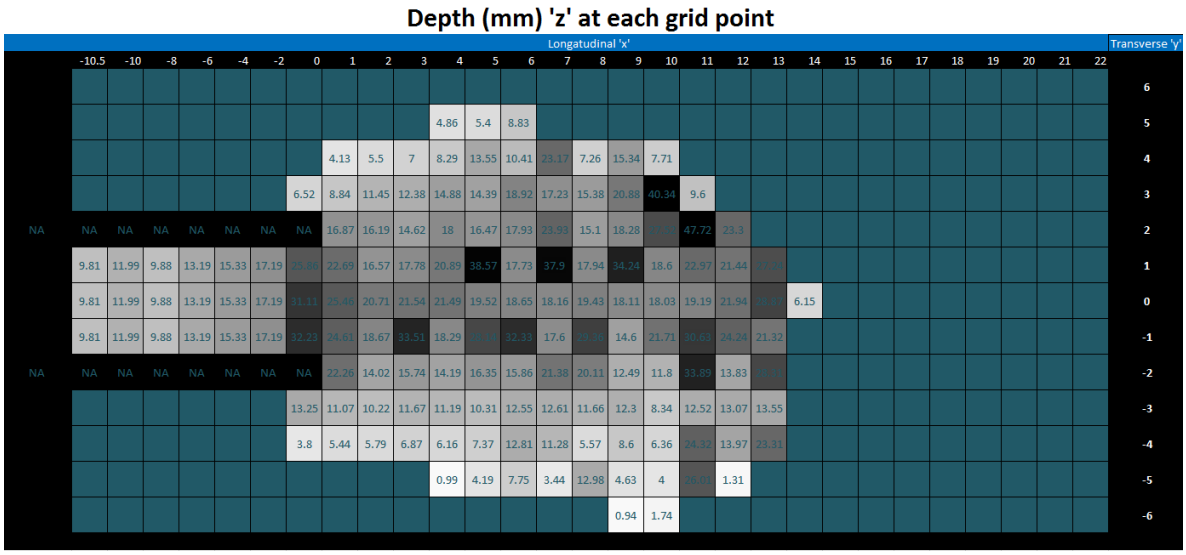

Figure D-3: S18W28IN4 spot height graph, dark spots indicate a high level and white shallow heights.

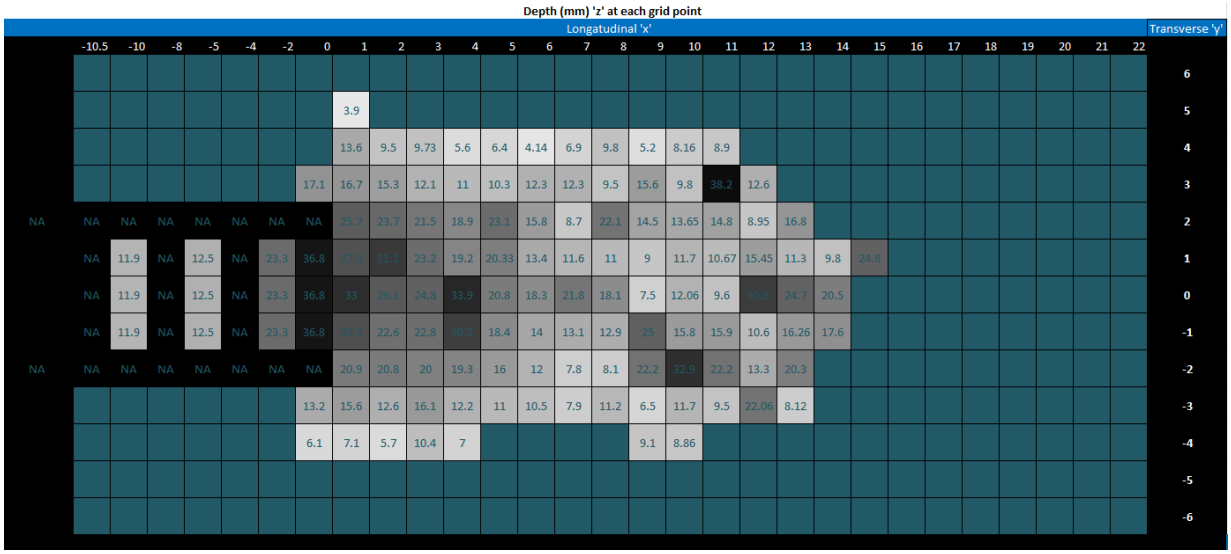

Figure D-4: S18W28EX1 spot height graph

Looking at the spot height plots for S18W28EX1 and S18W28IN4 we can see the likely locations of the largest particles are more evenly spread through the deposit for S18W28IN4. With S18W28EX1 having a shallower centre. This is reinforced in the PSD graph where the centre cure for S18W28IN4 is as a step as the front edge for the last 50% passing indicating high level of large particles similar to the front. The lower 50% is still much finer than the front outer edge. This is not significant as it takes only one or two large particles to cause this discrepancy

Over all the preliminary experiments the spread of the large particles has been seen to be random within the centre and flume sections of the deposits and is a function of surge and entrainment of these particles when the flow hits the run-out deck, perhaps also any jamming or delay in release. Large particles do make up the majority of the front edge and fines the tail section confirming flow segregation and debris flow behaviour.

D.1.2. Image Quality and Observations

All used the Motion Pro camera except S18W28IN1. Due to low laser light S18W28IN1 had a maximum light intensity of 32 out of 255, S18W28IN4 had double at 62. After the first test the laser light intensity was increased to compensate. A value of 32 meant that there was less information for use in image adjusting and so less texture. Reduced texture makes it harder to track patches in PIV. All tests apart from S18W28IN0c were clear enough to identify the saturation level in the body. The S18W28EX1 test had some bubbles but these were relatively limited.

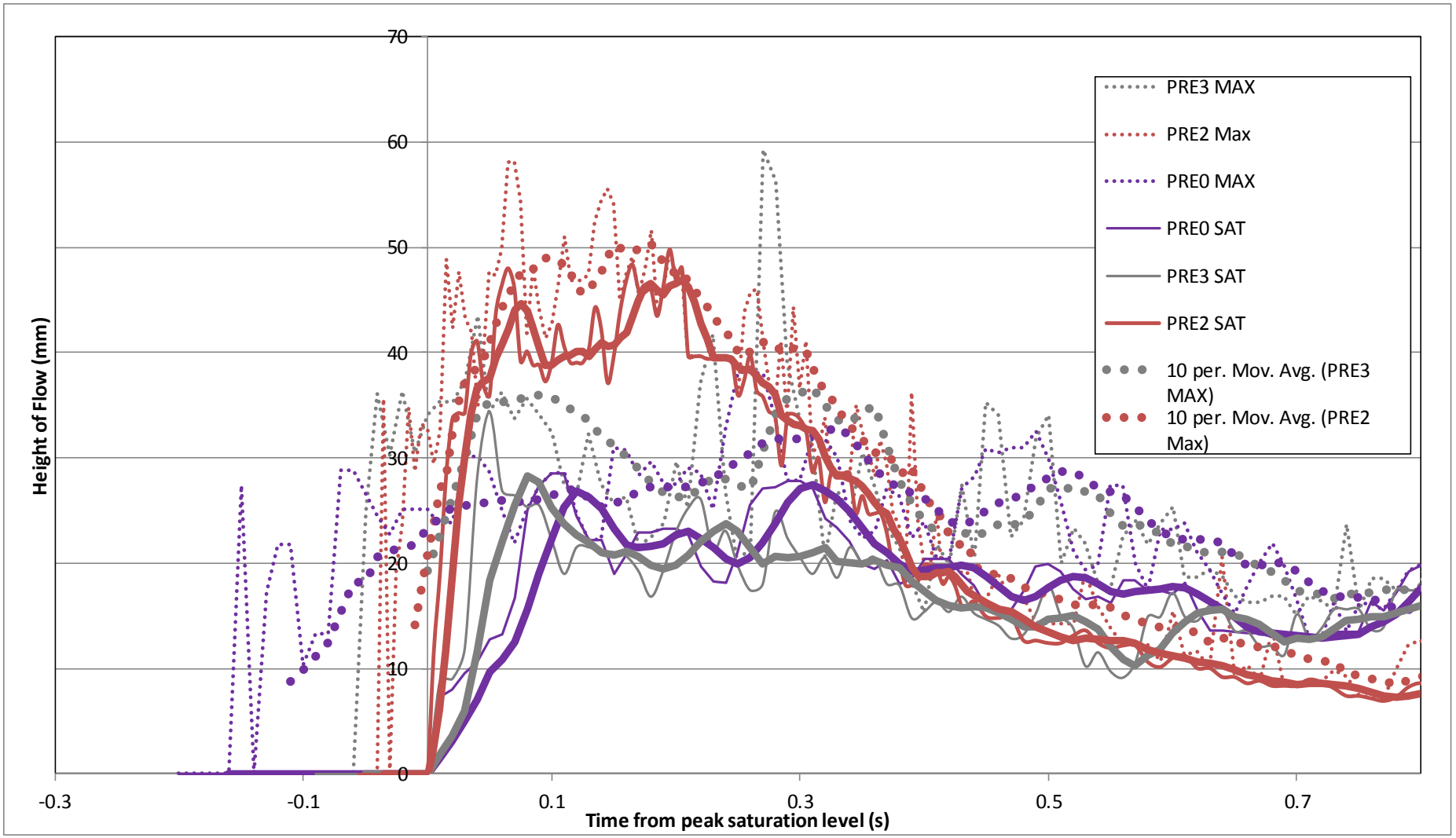

Figure D-5: Height with time for preliminary experiments, showing both saturation level and absolute levels with a moving average of 5 and 10 points respectively.

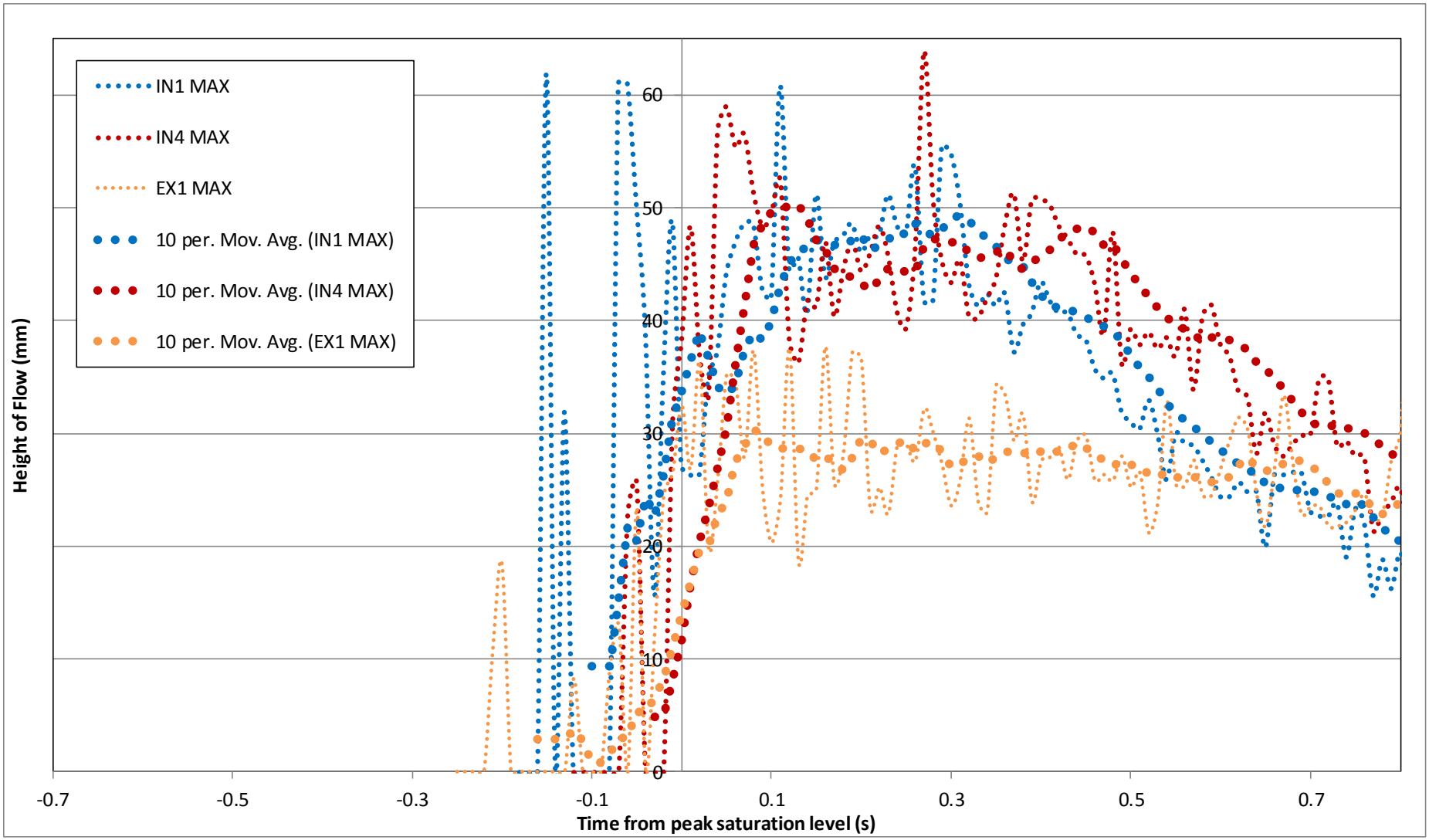

Figure D-6: Height with time for interior and exterior experiments, showing absolute levels with a moving average of 10 points.

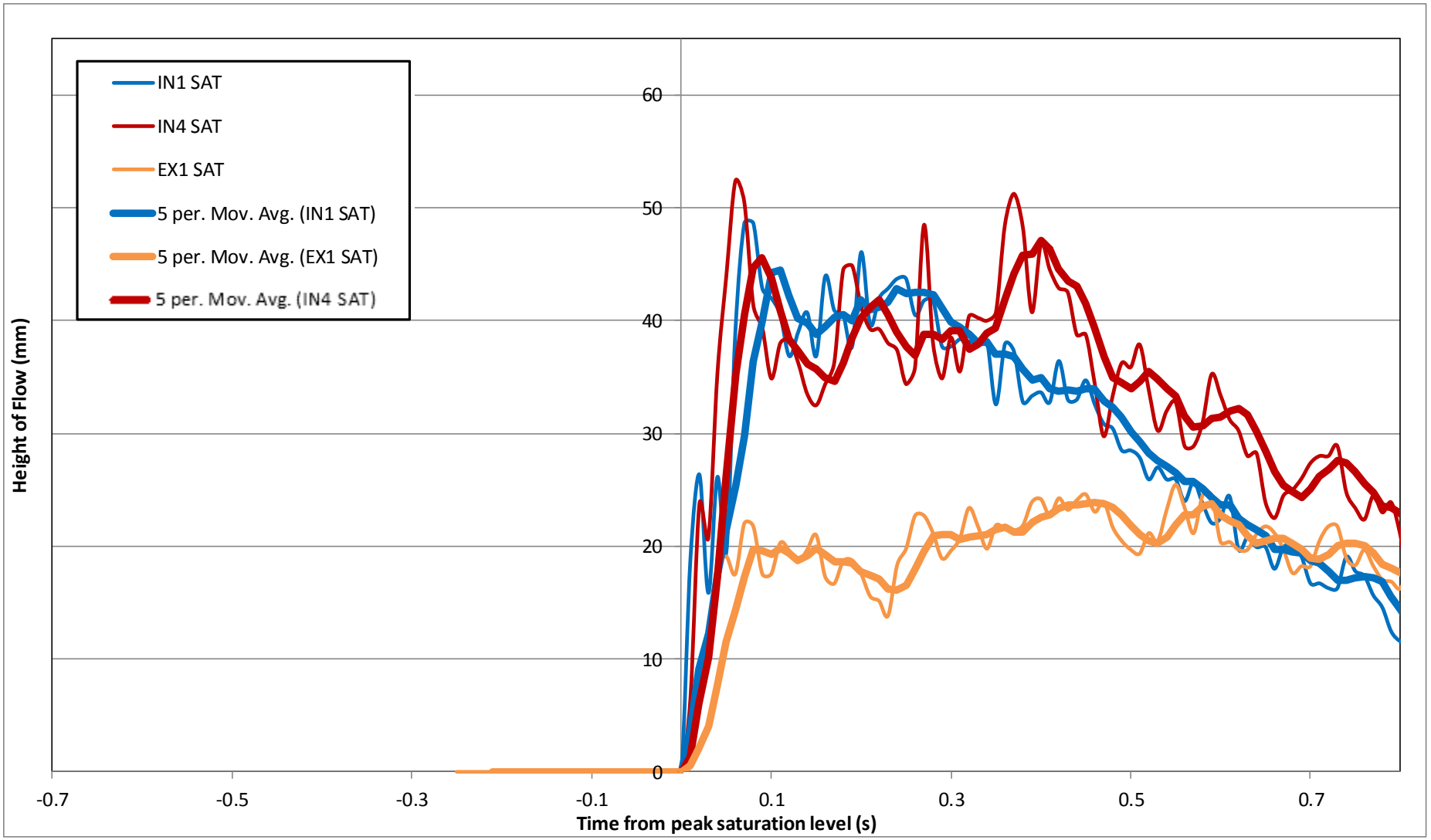

Figure D-7: Height with Time for interior and exterior experiments, showing both saturation level with a moving average of 5 points.

D.1.3. Height and Time Data

The height of the flow showed a lot more variability than the deposit information and is an important part of finding consistency. Figure D-7 shows the heights over time for first 0.8 seconds after the peak saturation for S18W28IN1, S18W28IN4, and S18W28EX1, these heights were sampled every 0.01s.

Table D-1: Height summary S18W28 series

	Height of flow (mm)			
Experiments	Absolute Maximum	Peak Saturation	Saturation Tail Height	Transition Deposit
S18W28IN0a	38.10	27.30	14.60	38.06
S18W28IN0c	58.16	46.10	5.70	25.07
S18W28IN0d	59.25	34.38	11.04	25.44
S18W28IN1	61.92	48.64	9.64	26.17
S18W28IN4	63.88	52.38	3.06	26.99
S18W28EX1	42.50	25.46	7.65	33.07
Average & Std. Error	**54 ± 13**	**39± 13**	**9 ± 6**	**29± 7**

D.1.3.1. Peak Height

There is no consistent link between absolute maximum and peak saturation heights in any given frame. Sometimes large particles push up through flow, sometimes they are submerged. However, the moving average does show that the maximum is on average 5-10 mm greater than the saturation level. The S18W28IN0a, S18W28IN0d and S18W28EX1 are low in terms of absolute and saturation levels. Figure D-7 shows S18W28IN1 and S18W28IN4 both show matching peak shapes that are steep before the maximum height then drop off rapidly. S18W28IN0c has the same shape but has lower peak heights and drops off quicker. S18W28IN4 does have a second peak in the moving average at about 0.3 s but this is linked to a large particle, the same doe S18W28IN0c at 0.1 s. S18W28EX1 has the steep front section but does not reach the same peak and has a longer shallower body. This indicates material did not leave the hopper as one mass but was jammed and was released over time.

Because the maximum is also lower than the other tests it is not just that the height is lower for the exterior tests.

D.1.3.2. Height of Tail

Table D-1 shows the average tail height based on the saturation height as it moves out to a relatively steady height. There seems to be a link between this value the height of the transition and the PSD of the transition point. The finer PSDs resulted from the tails with the deepest flow. If finer particles dam the transition point then lower permeability could result in a backup of flow and so height. S18W28IN0a and S18W28INd both have high tails which fits with the lower drawn-out shape of the body.

D.1.3.3. Timing

First particle and flow front are dependent on illumination for accuracy for the preliminary and interior experiments. The time is a good indicator of the steepness of the front. From Table D-2 the S18W28EX1 and S18W28IN0a experiments have the flow front occurring five and two times as early as the other tests respectively. The tests with the largest time since hopper opened had the long drawn out shape and so again indicating that there was some jamming or delay in material release.

Table D-2: Time references S18W28 series

	Time to Peak Saturation Height (s)		
Experiments	First Particle	Flow Front	Saturation Front
S18W28IN0a	-0.28	- 0.26	- 0.12
S18W28IN0c	-0.11	- 0.11	- 0.07
S18W28IN0d	-0.10	- 0.10	- 0.04
S18W28IN1	-0.22	- 0.14	- 0.06
S18W28IN4	-0.11	- 0.07	- 0.05
S18W28EX1	-0.76	- 0.55	- 0.45
Average (exl EX1)	**0.16 ± .1**	**0.14 ± 0.1**	**0.07 ± .04**

D.1.3.4. Summary of Behaviour

The S18W28IN1 test had good debris flow behaviour but poor image quality. S18W28IN4 had good behaviour and image quality. S18W28EX1 had some delays in material release from the hopper and so does not have the fully developed height behaviour during flow. S18W28EX1 did, however, have the same deposit behaviour and so behaved like a debris

flow. It is worth comparing this as an underdeveloped flow compared to S18W28IN4 but cannot be used for interior versus exterior comparisons or effects of slope and moisture content with other fully developed flows.

D.2. Slope 18.1° and Moisture Content 24.8%

Two experiments were conducted at a slope of 18.1° and the lowest moisture content of 24.5%, one interior (S18W24IN5) and one exterior (S18W24EX6). These experiments are expected to be near the point at which they cease to give the same type of debris flow behaviour as all the other experiments with a low slope and minimal moisture content. These experiments give a lower bound on slope and moisture content.

D.2.1. Deposit

From Figure D-8 both deposits have a semi-circular shape which is a shortening of the longer baseline of S18W28. It shows that the deposit's coarse front edge extends around the full edge of the deposit and has not been pushed fully out on to the run-out deck. There was some variability in the longitudinal direction (parallel to the flow direction) with a difference of approximately 20 mm. This is consistent with the absolute variability in the S18W28 deposits but as a percentage of the run-out length is a bigger variability. There is again the same one-sided variability to the right of graph which a slight tilt in the run-out deck could explain if seen in later experiments as well. There is no indication of major blockages based on the deposit shape.

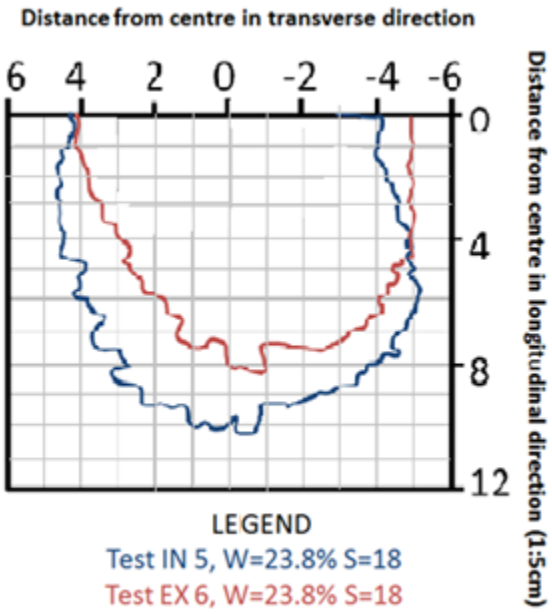

Figure D-8: Outline of S18W24 deposits as taken from photographs of run-out deck. Grid reference in 5 cm squares.

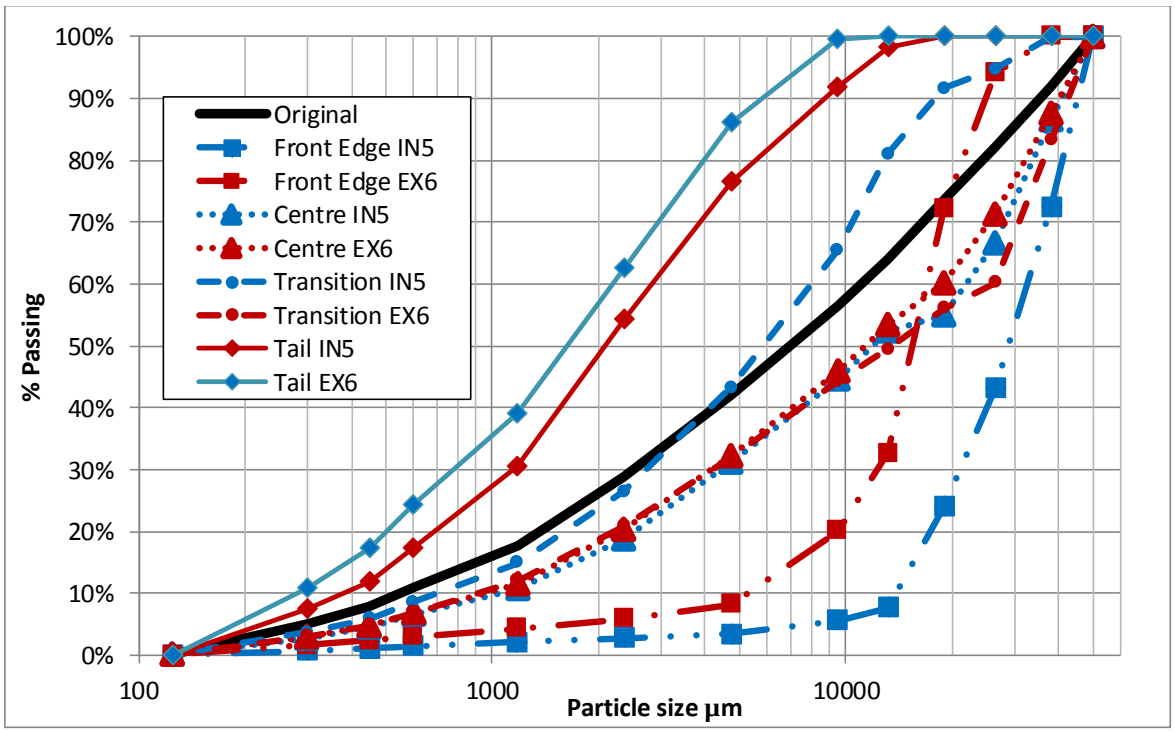

Figure D-9: PSD of S18W24IN5 and S18W24EX6, with original as the PSD for the initial whole material.

The PSD curves (Figure D-9) for the experiments show similar profiles for the transition. But more segregation in the S18W24IN5 test. This is partly because of the small size of the deposit the smaller deposit S18W24EX6 had more overlap of the samples compared to S18W24IN5 which being slightly longer would have had samples that showed these areas better.

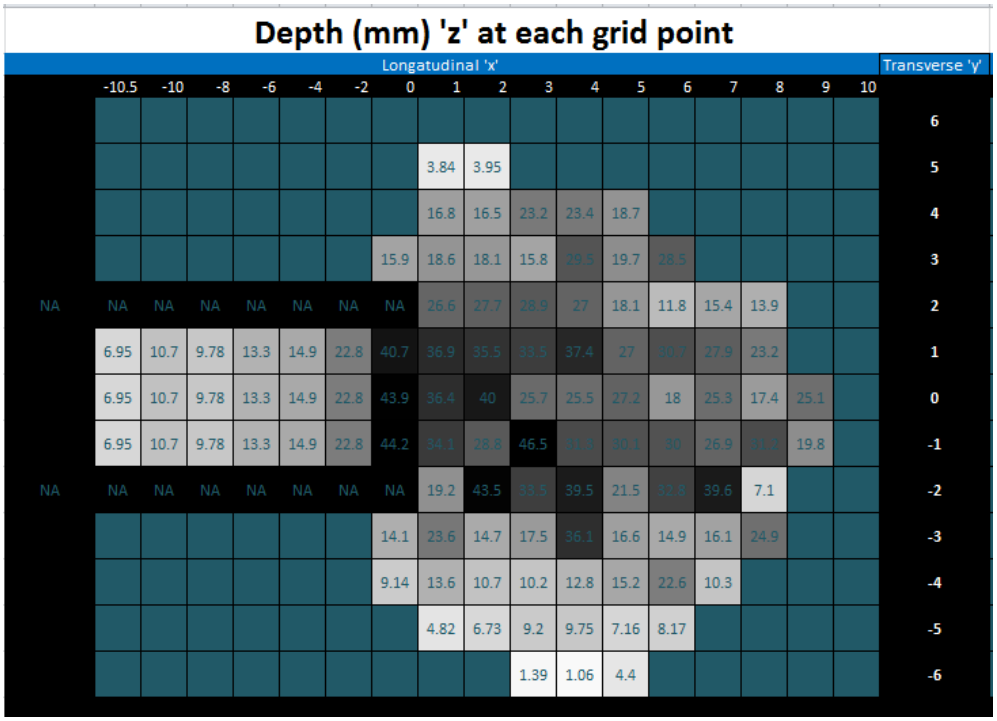

Figure D-10: IN5 spot height graph

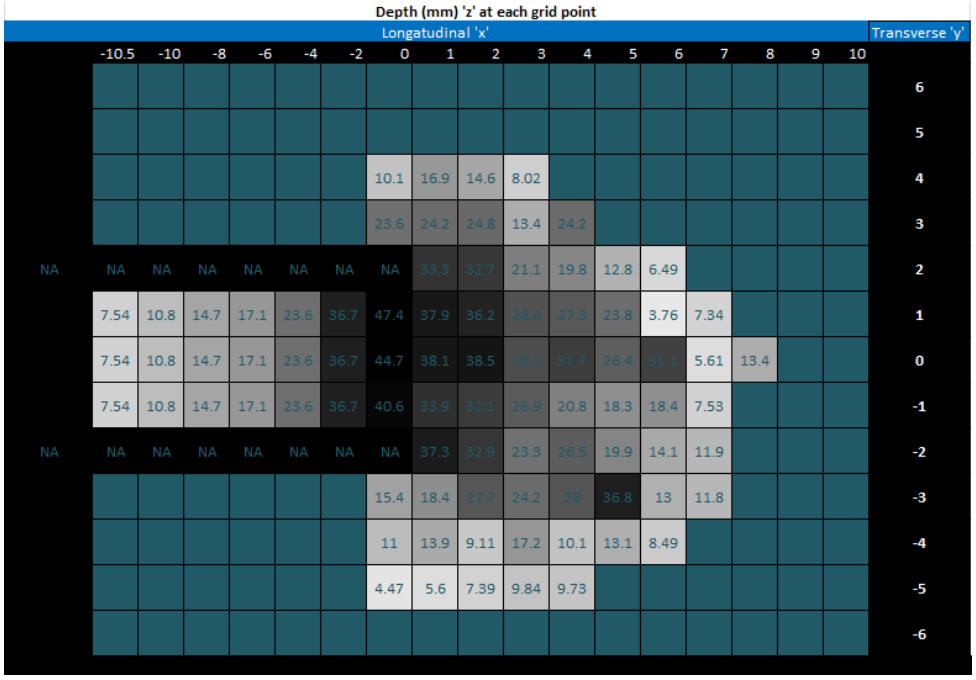

Figure D-11: EX6 spot height graph.

Figure D-10 shows that the front edge of S18W24EX6 is actually not the typical high blocky outer edge expected of a debris flow with a coarse front. This is reinforced by Figure D-9 that shows that the S18W24EX6 front edge had less coarse material than S18W24IN5. There is still the segregation but not to the same extent as S18W24EX6 or other experiments. Of particularly interest is that S18W**28**EX1 did not show this behaviour even though it was a blocked elongated flow. S18W24EX6 transition PSD curve is also much coarser than would

be expected as it is on the more coarse side of the original material. This may indicate that the coarse front material hit the run-out deck and was not pushed out due to a lack of momentum.

Looking at the spot height plots for S18W24IN5 and S18W24EX6 we cannot see the likely locations of the largest particles as the transitions are deep enough to make this difficult through the centre. However, there are a couple toward the front that show some spread of largest particles. The deposit data shows there were a few large particles at the front edge, with the coarse fraction concentrated at the edge and a fine tail section. This confirms flow segregation but less than the 27.8% moisture content and so is a more undeveloped type of debris flow behaviour. This is true for both tests, but particularly S18W24EX6.

D.2.2. Image Quality and Observations

Both used the Miro camera at a frame rate of 2000 fps. The S18W24EX6 did not have sufficient light for analysis of the exterior to be able to pick up texture at the window. S18W24IN5 had good quality images with a well spread light intensity distribution shown in the top left of Figure D-12. Bubbles were mainly at the bottom of the images and moved with the flow at the same velocity. By observation S18W24IN5 follows the steep shape with gradual reduction in height over body with a steady tail height. There are a few large particles in the body that slightly influence the saturation level but this is localised over the same length scale as the particle itself.

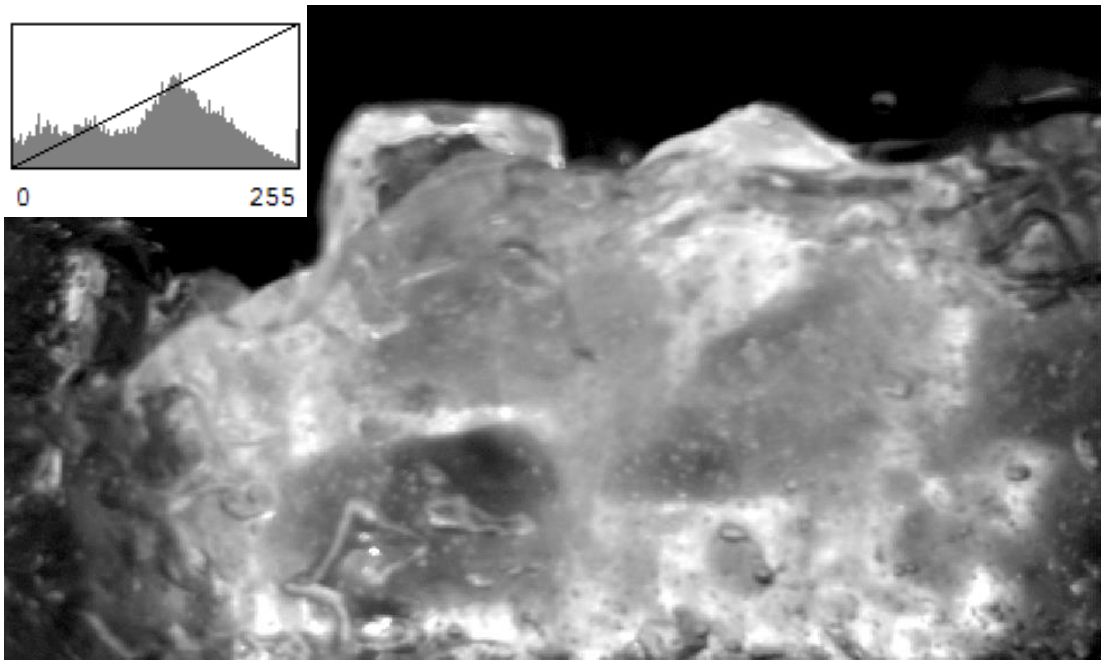

Figure D-12: Image of S18W24IN5 at peak saturation level, top left insert is light intensity graph.

D.2.3. Height and Time Data

The height of the flow is limited to S18W24IN5 due to the poor quality of S18W24EX6 images. Figure D-13 shows the heights over time for first 0.8 s after the peak saturation for S18W24IN5. The heights were sampled every 0.01 s.

Table D-3: Height summary S18W24 series

	Height of Flow (mm)			
Experiments	Absolute Maximum	Peak Saturation	Saturation Height	Tail Transition Deposit
IN5	51.06	41.24	4.09	39.4
EX6	-	-	-	40.4

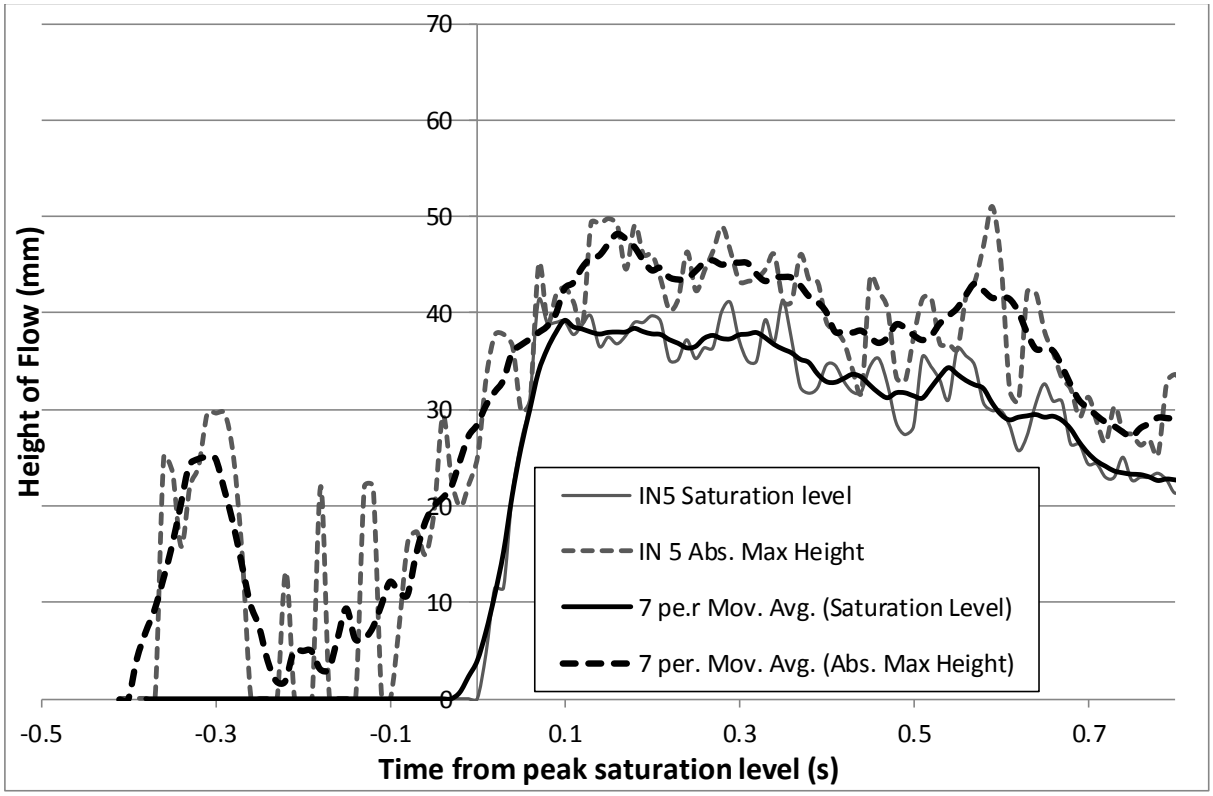

Figure D-13: Height with time for S18W24IN5, showing both saturation level and absolute levels with a moving average of 5 and 10 points respectively.

D.2.3.1. Peak Height

Compared with the 27.8% moisture content all of the height levels except the transition are lower for the 23.8% moisture content. This is about 10 mm less for the maximum and saturation and 5mm for the tail. The moving average shows that the maximum is on average 5-10 mm greater than the saturation level. S18W24IN5 shares the peaking shape of the 27.8% moisture content where the front is steep before the maximum height then drop off rapidly

before becoming steady over the tail. There is no evident secondary peak even with 3-5 large particles, shown in the maximum height line of Figure D-13.

D.2.3.2. Timing

Table D-4: Time references S18W24

	Time to peak height of … (s)			
Experiments	Trigger	First Particle	Flow Front	Saturation front
IN5	-	-0.43	- 0.16	- 0.06

Only the S18W24IN5 test had images clear enough to give time data. From Table D-4 the S18W24I times to saturation front and flow front are consistent with 27.8% except that the first particle arrived much earlier. This is likely just because the camera was able to pick up the particle better than the other cameras. Given the classic shape and the consistent timing of front we can assume there were no significant influences on the material as it was released from the hopper.

D.2.4. Summary of Behaviour

The S18W24EX6 test had okay debris flow behaviour but poor image quality and so was able to indicate that S18W24IN5 was consistent with expected vales at 23.8% moisture content. Therefore, S18W24EX6 was not able to be used for PIV analysis. S18W24IN5 had good behaviour and image quality. Segregation occurred but the deposit shape indicated that the flow did not reach high velocities and so might have had a different behaviour to the other debris flows. This test is consistent enough to compare with the other interior tests with different moisture contents. Because S18W24EX6 images were of poor quality there is no exterior test for interior versus exterior comparisons.

D.3. Slope 18.1° and Moisture Content 31.8%

Four experiments were conducted at a slope of 18.1°and a moisture content of 31.8%, two interior (S18W32IN2 & S18W32IN6) and two exterior (S18W32EX2 & S18W32EX4). All of these tests gave good deposit results and sufficient image quality for height analysis.

D.3.1. Deposit

From Figure D-8 both S18W32IN2 has a similar shape and length to the shorter S18W28 series. This shorter run-out length is an indication of some blockages in S18W32IN2 based on the deposit shape. The other tests have a more elongated shape and further run-out length. The longer shape fits with the trend moving from the semi-circular of S18W24 to the circular S18W28. The transverse direction matches well particularly in the centre about 500 mm from the flume.

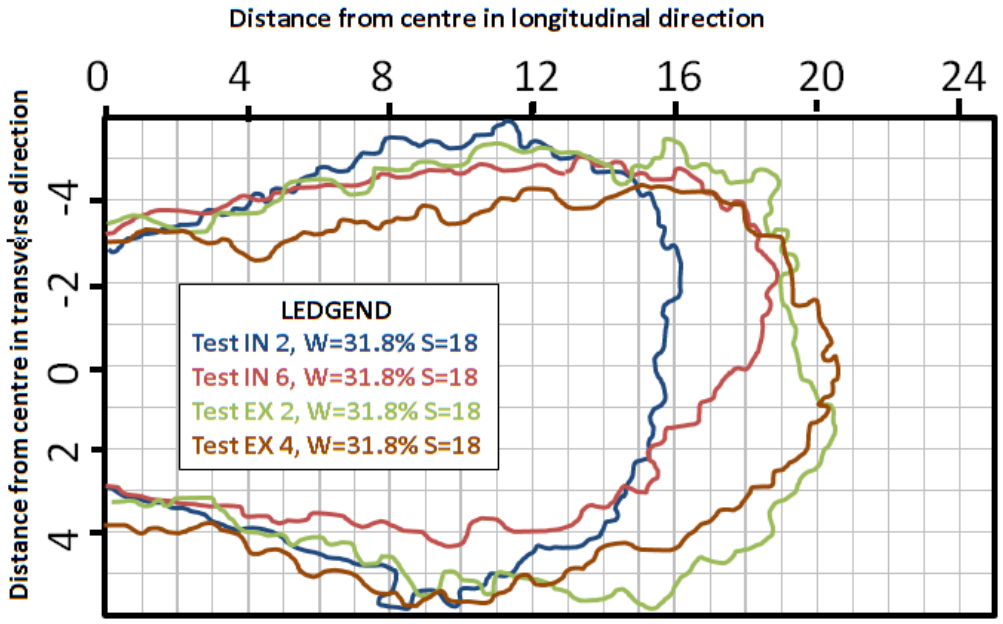

Figure D-14: Outline of S18W32 deposits as taken from photographs of run-out deck. Grid reference in 5cm squares.

There was more variability in the longitudinal direction on the positive side of the centre with the negative side giving consistent run-out lengths. This is most pronounced in S18W32IN6 which had a blockage at this side of the hopper where one of the largest particles lodged against the hydraulic piston that released the gate. Considering this blockage and loss of ~20% of the largest particles the deposit shows a good run-out length and spot height distribution. Figure D-16 shows that the spot height has some larger heights on the negative side and none on the blockage side. There are other tests with this same spread so it is not necessarily a direct reflection of the blockage.

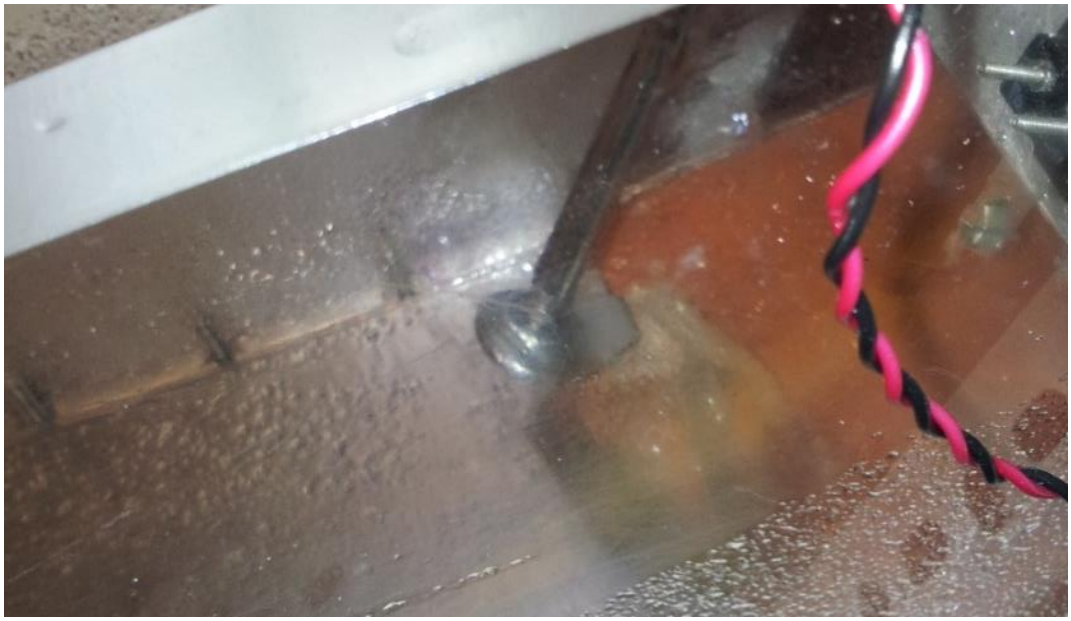

Figure D-15: Large particle causing blockage in test S18W32IN6.

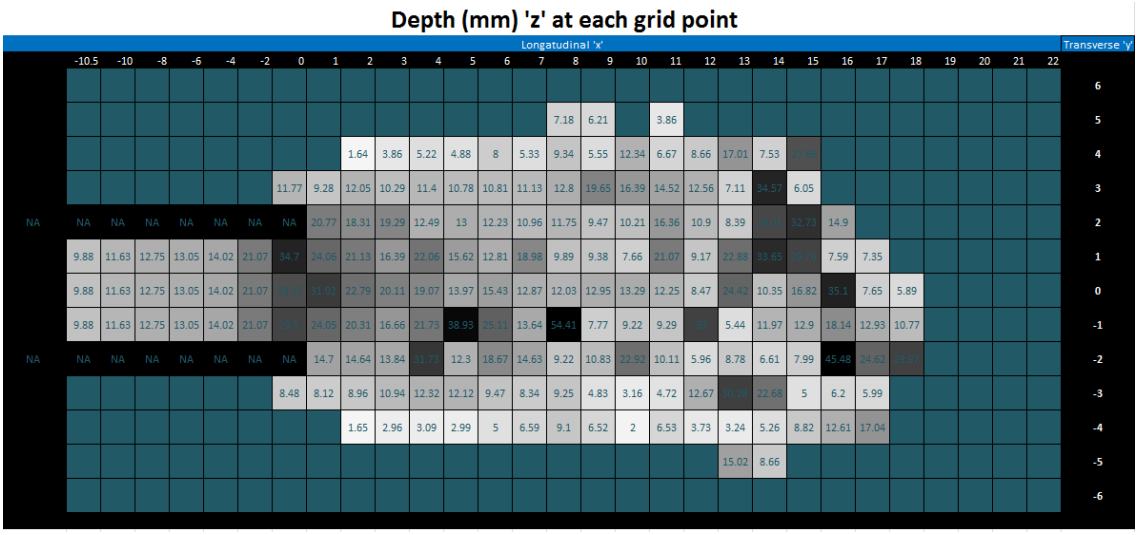

Figure D-16: S18W32IN6 Spot height graph, dark spots indicate a high level and white shallow heights.

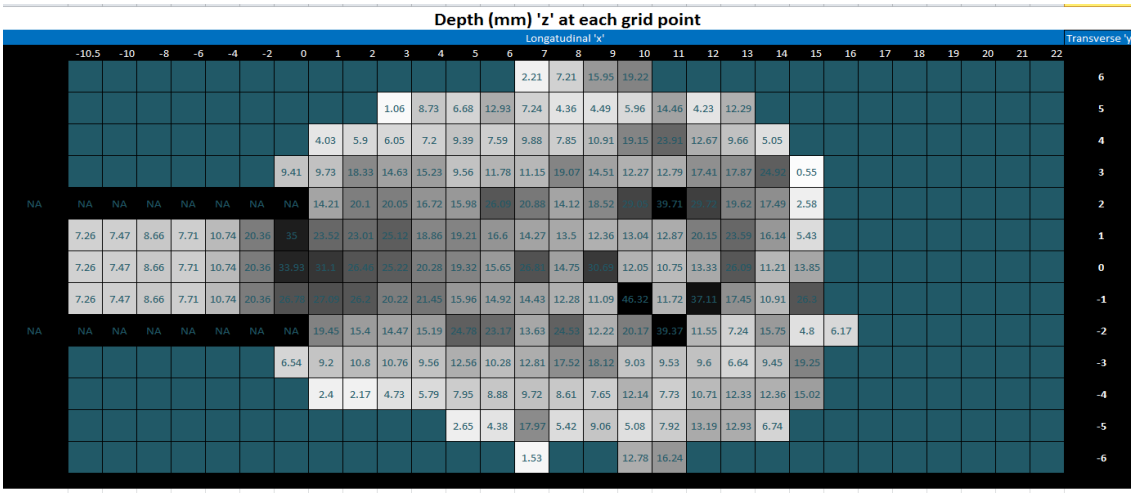

Figure D-17: S18W32IN2 spot height graph, dark spots indicate a high level and white shallow heights.

The PSD curves (Figure D-18) for the experiments show similar profiles for the front edge and tail. The transition is the most variable section but the curves are close to the original PSD or finer. The transition PSD for S18W32EX4 has included one (38.1-50 mm) large particles that has distorted the curve. These results indicate good segregation in deposit.

Looking at the spot height plots for S18W32IN2 in Figure D-17 the largest particles rest more in the centre than the front outer edge. This supports the blockage impact on the run-out length as the larger particles have not formed part of the high blocky edge to the same degree as the other experiments. The front edge was one of the least-coarse front edges but did not have many fines so even though it does not have the same amount of large particles it has formed a coarse front.

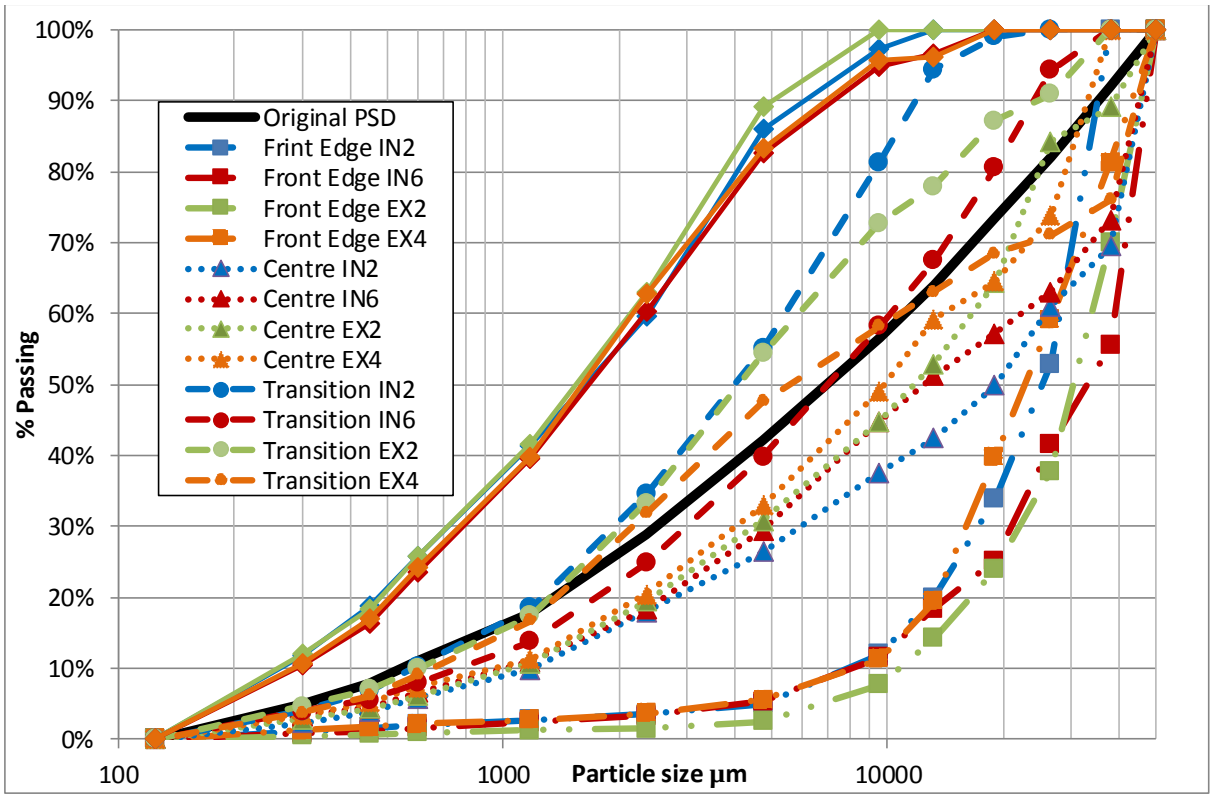

Figure D-18: PSD of S18W32IN2, S18W32IN6, S18W32EX2 and S18W32EX4, the original is the PSD for the whole sample before experiment.

D.3.2. Image Quality and Observations

S18W32IN2, S18W32EX2 and S18W32EX4 used the Motion-Pro camera at 1200 fps, S18W32IN6 used the Miro camera at a frame rate of 2000 fps. All of the tests had sufficient light for analysis but the Miro camera provided clearer, brighter, images that did not require any processing. The difference in raw image can be seen in Figure D-19. The drawback to the clearer images is that the bubbles in the moisture are also clearer. S18W32EX4 did have

significant bubbles and was slightly over-exposed, removing the texture of the smallest particles.

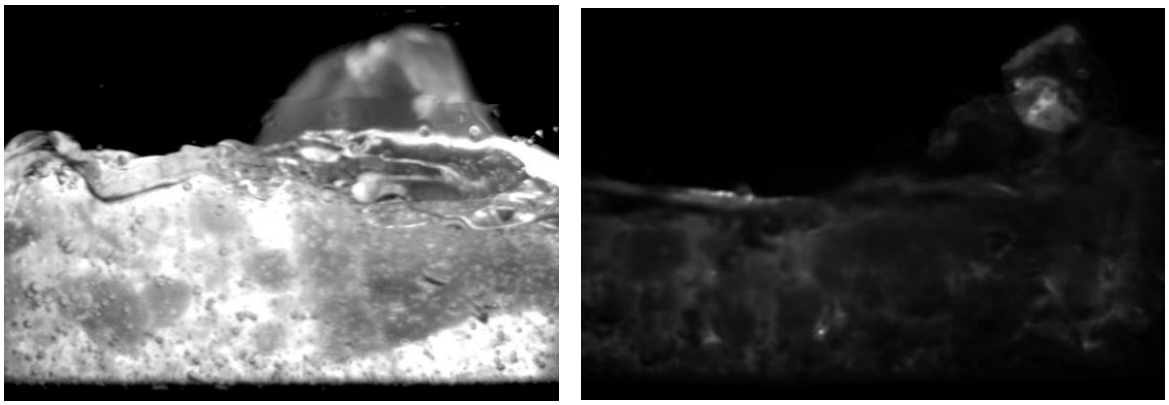

Figure D-19: Examples of raw images from (a) Miro camera S18W28IN6, (b) Motion-Pro camera S18W28IN2.

By observation S18W32EX4 had a number of large particles that directly influenced the saturation level around the particle is shown by the dotted red line in Figure D-20. These impacts are localised and do occur in other tests, but not as frequently.

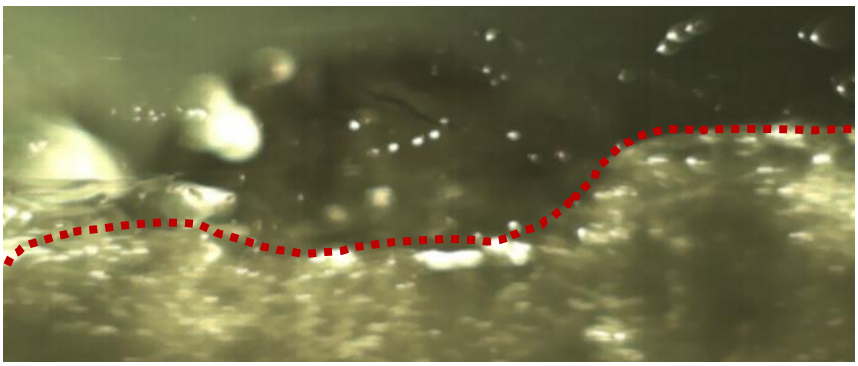

Figure D-20: Large particle influencing saturation level

D.3.3. Height and Time Data

Figure D-21 shows the height of the saturation level over time for first 0.8 s after the peak saturation height, these were sampled every 0.01s.

Table D-5: Height summary S18W32

	Height of … (mm)			
Experiments	Absolute Maximum	Peak Saturation	Saturation Tail Height	Transition Deposit
S18W32IN2	69.18	51.72	7.53	29.5
S18W32IN6	53.48	52.83	10.29	28.58
S18W32EX2	51.23	44.88	6.43	27.3
S18W32EX4	60.74	35.48	6.82	22.82
Average	**57.07 ± 12**	**47.82 ± 9**	**7.77 ± 2**	**27.05 ± 3**

D.3.3.1. Peak Height

The values in Table D-5 compared to the 27.8% moisture content show that the peak saturation and maximum heights were on average higher for the 31.8% moisture content. However, the range is high so the values are similar. S18W32IN2, S18W32IN6 and S18W32EX2 (Figure D-21) have a steep peak and high body but they did not exactly follow the same shape as the 27.8% moisture content. Overall S18W32IN2, S18W32IN6 and S18W32EX2 have consistent maximum height values and height over time curve shapes, however, they each have slight differences.

S18W32IN2 had the highest peak but the body did not drop off much suggesting there was something abnormal acting on the body. S18W32IN6 appears to have an early saturation peak. This peak is less prominent in the maximum height moving average (Figure D-22). This could have been caused by some material breaking away early from the hopper. S18W32EX2 has the best behaved heights but also has a peak before reaching maximum. This is similar to S18W32IN6 but much smaller.

S18W32EX4 was much lower in terms of absolute and saturation levels with a much longer shallower body. This indicates material did not leave the hopper as one mass but was jammed and was released over time. This is the same as S18W32EX1 and these two tests could be compared against each other, but not against the other tests and variables.

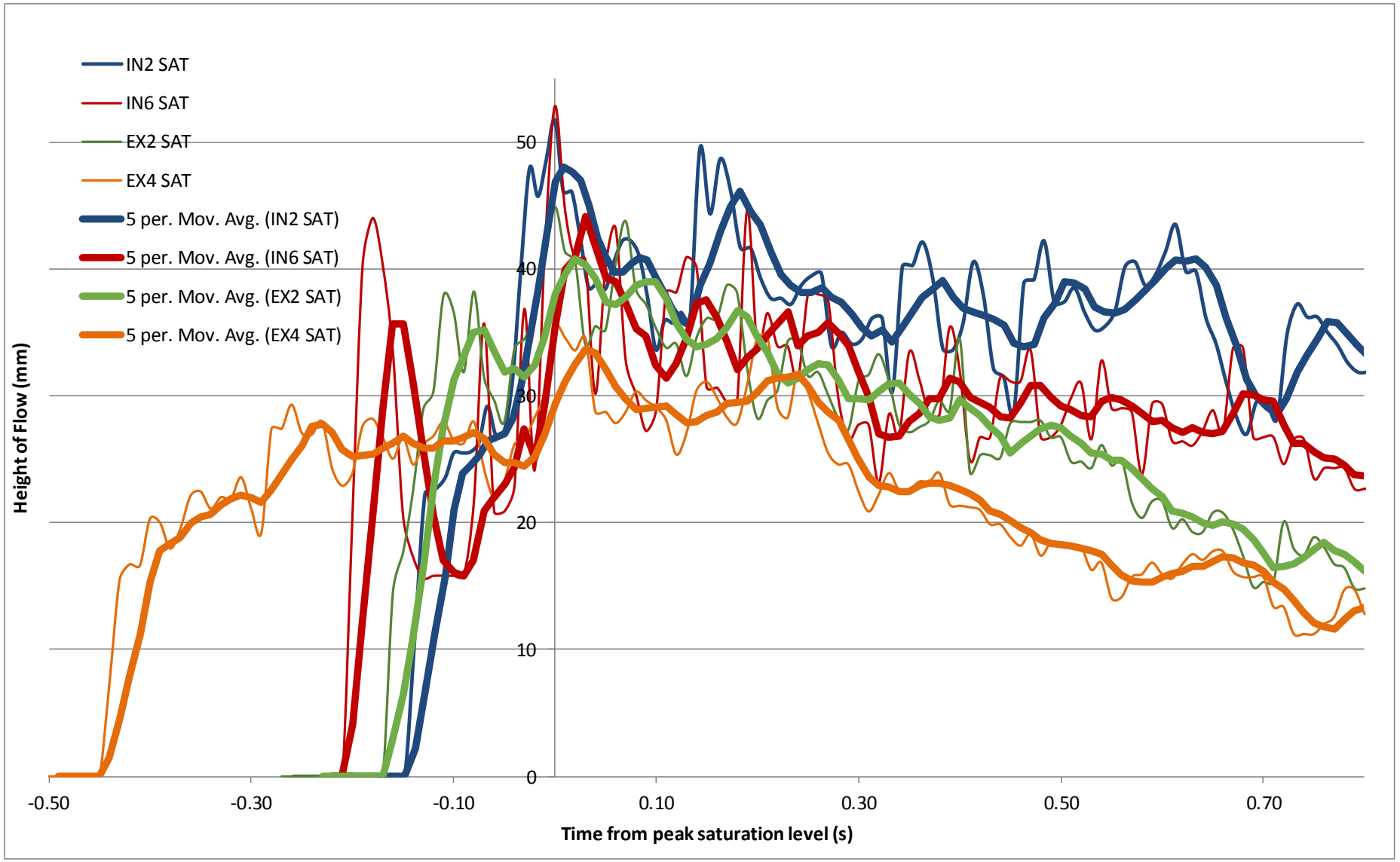

Figure D-21: Height with time for S18W32IN2, S18W32IN6, S18W32EX2 and S18W32EX4 experiments, showing saturation level with a moving average of 5 points.

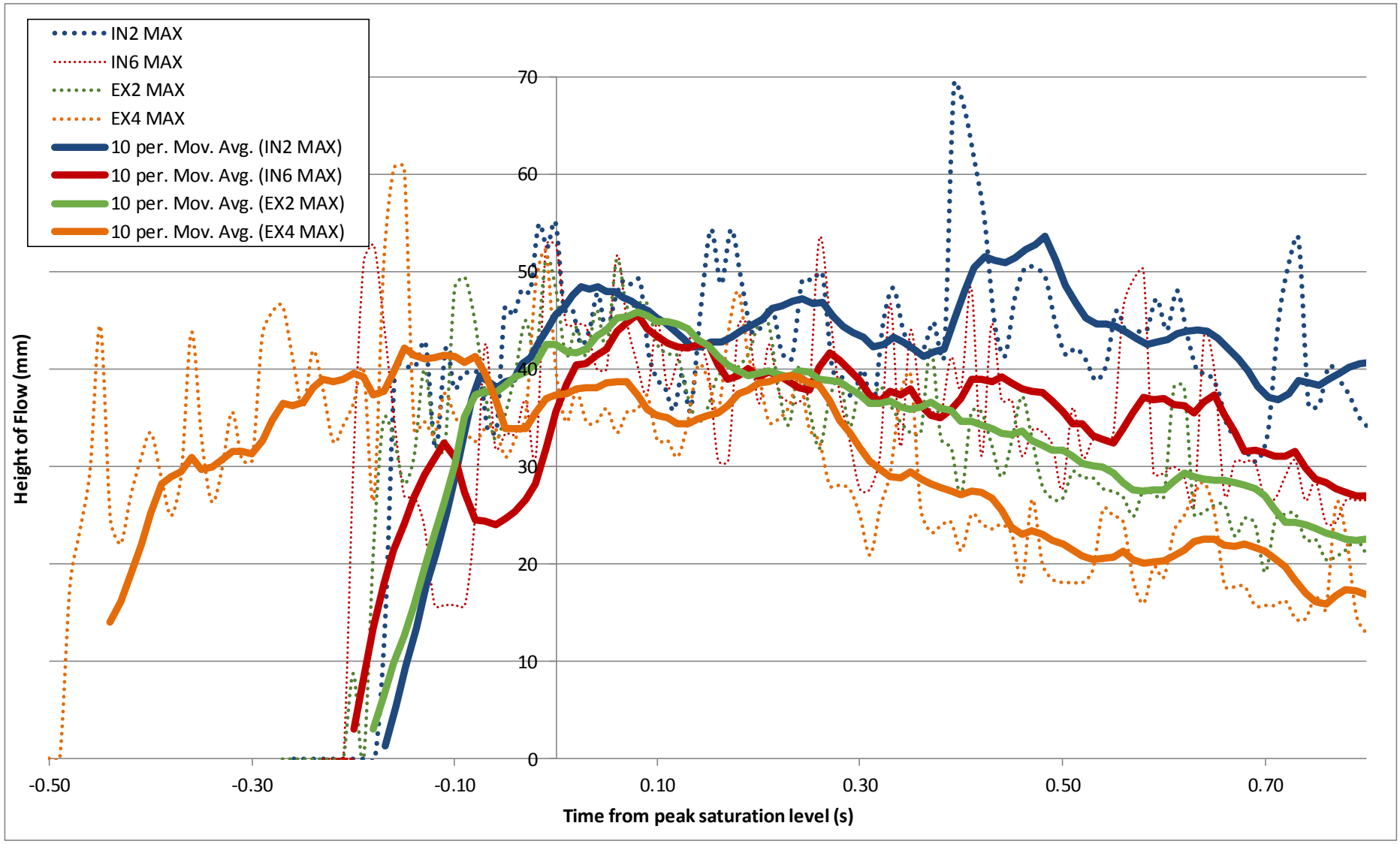

Figure D-22: Height with time for S18W32IN2, S18W32IN6, S18W32EX2 and S18W32EX4 experiments, showing absolute levels with a moving average of 10 points.

D.3.3.2. Height of Tail

Table D-5 shows the average tail height based on the saturation height is lower than the 27.8% moisture content, the height of the transition is also lower. The more moisture content the more fines are carried by the fluid allowing the highly fluid tail to flow more. In addition the longer run-out allows more coarse material to out on to the run-out deck so there is less coarse material to building up at the transition point.

D.3.3.3. Timing

Table D-6 shows that the front or the time between the first particles and the peak is longer than for 27.8% moisture content. This is reflected in the test heights not peaking as steeply. The reasons for this might be that the first peak is just not high enough to be the maximum as in the case of lower moisture contents.

S18W32EX4 is like S18W32EX1 and has a much higher time difference between the peak and the front of the flow. The difference between the front particles and the beginning of saturation (or the non-fluid portion of the front) is about the same size as the other tests based on the same small time gap between them. The time from trigger for S18W28EX4 is was similar to the other tests suggesting that the velocities were similar and that the height just did not develop.

Table D-6: Time references S18W32 series

	Time to Peak Saturation Height (s)			
Experiments	Trigger	First Particle	Flow Front	Saturation front
S18W32IN2	-2.60	-0.41	- 0.17	-0.14
S18W32IN6	-2.10	-0.48	- 0.20	- 0.20
S18W32EX2	-3.03	-0.41	- 0.18	- 0.16
S18W32EX4	-2.97	-0.76	- 0.48	- 0.44
Average	**2.87 ± 2**	**0.43 ± 0 .04**	**0.18 ± 0.2**	**0.17 ± 0.2**

D.3.4. Summary of Behaviour

All tests are of sufficient image quality for analysis. S18W28IN2 has inconsistent run-out length but a good height over time shape and consistent trimming results. S18W28IN6 had a blockage and had some impacts on the shape and timing of the front but showed consistent debris flow behaviour and the best image quality. S18W28EX2 has good behaviour and matches well with the other tests. S18W28EX4 had a peak well in to the flow but when

aligned with the saturation fronts it is of a similar shape with a lower height and more elongated body.

D.4. Slope 18.1° and Moisture Content 35.8%

Three experiments were conducted at a slope of 18.1˚and the highest moisture content of 35.8%, one interior (S18W36IN3) and two exterior (S18W36EX3 and S18W36IN5). All of these tests gave good deposit results and sufficient image quality for height analysis.

D.4.1. Deposit

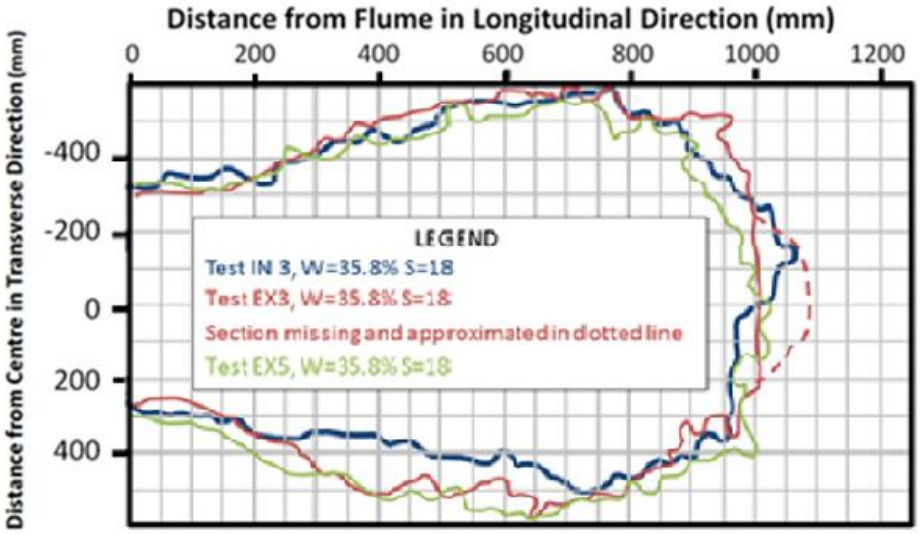

Figure D-23: Outline of S18W36 deposits as taken from photographs of run-out deck.

Figure D-23 shows that the tests have the expected elongated shape and further run-out length than other 18.1˚ slope tests. The transverse direction matches well particularly in the widest part which is at 800 mm from the flume rather than 500 mm for S18W32. In the longitudinal direction the tests are reasonably consistent. There is an approximated edge for S18W36EX3 due to poor imaging of the deposit spot heights obtained indicate that it was one grid (5 cm) longer than the other tests.

The PSD curves (Figure D-24) for the experiments show similar profiles for the front edge and tail. The centre is the most variable section but is less variable than other moisture contents samples. Also the transition section for S18W36IN3 is much coarser than the other tests it is similar to the original so does not indicate any abnormal behaviour. It is likely that because of the large spread of the deposit samples are less influenced by other parts of the

flow for example the centre does not contain any of the particles that stopped in the transition. Overall these results indicate the best segregation in 18.1˚ slope deposits.

Looking at the spot height plots for S18W36EX5 in Figure D-25 in conjunction with the centre deposit it can be seen that it has a number of the coarsest particles in the centre. The front retains the rest in the expected coarse front edge. This suggests that it is just that the centre sample captured more of these particles than is typical but the spread is still random.

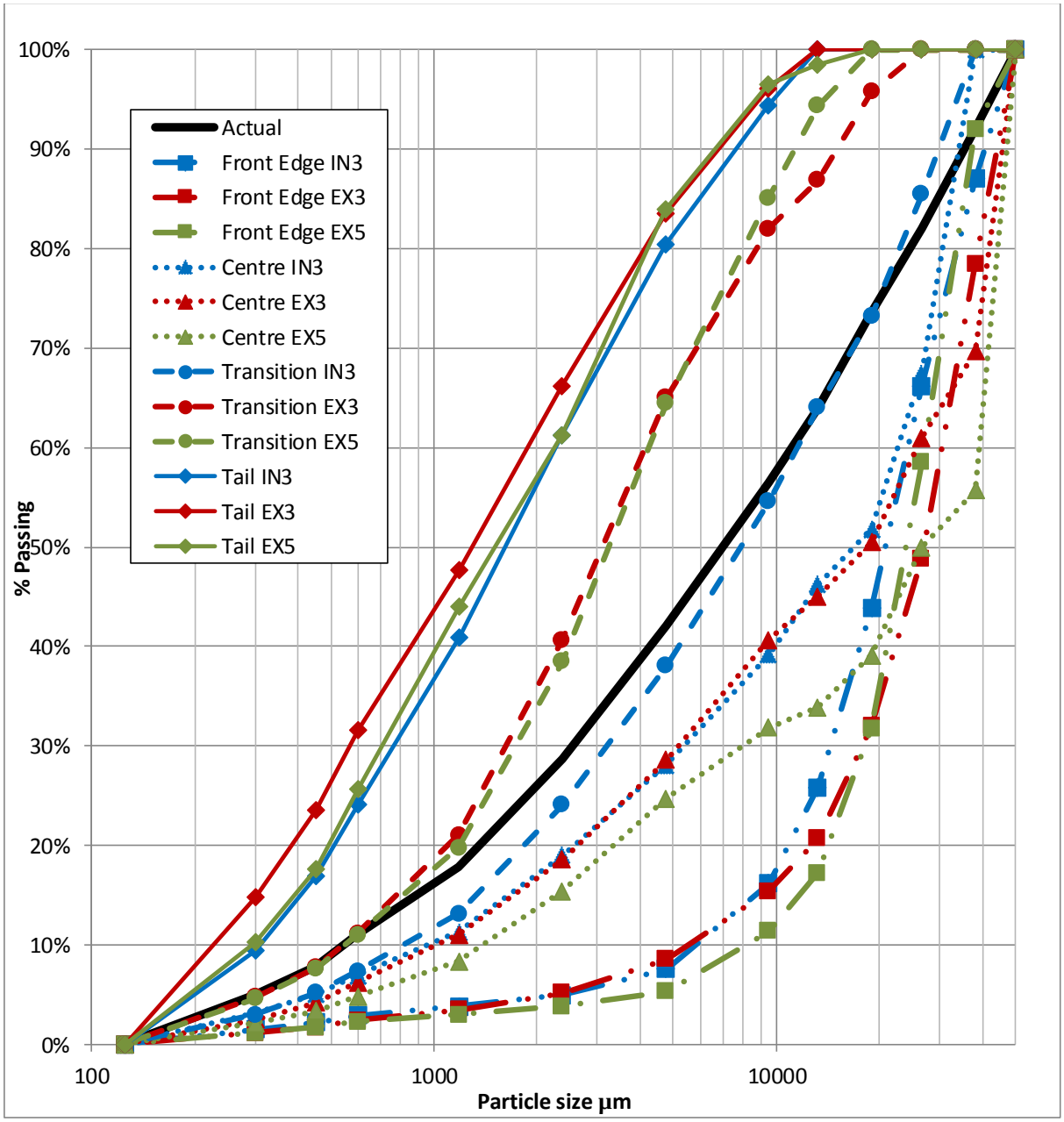

Figure D-24: PSD of S18W36IN3, S18W36EX3 and S18W36EX5, the original is the PSD for the whole sample before experiment.

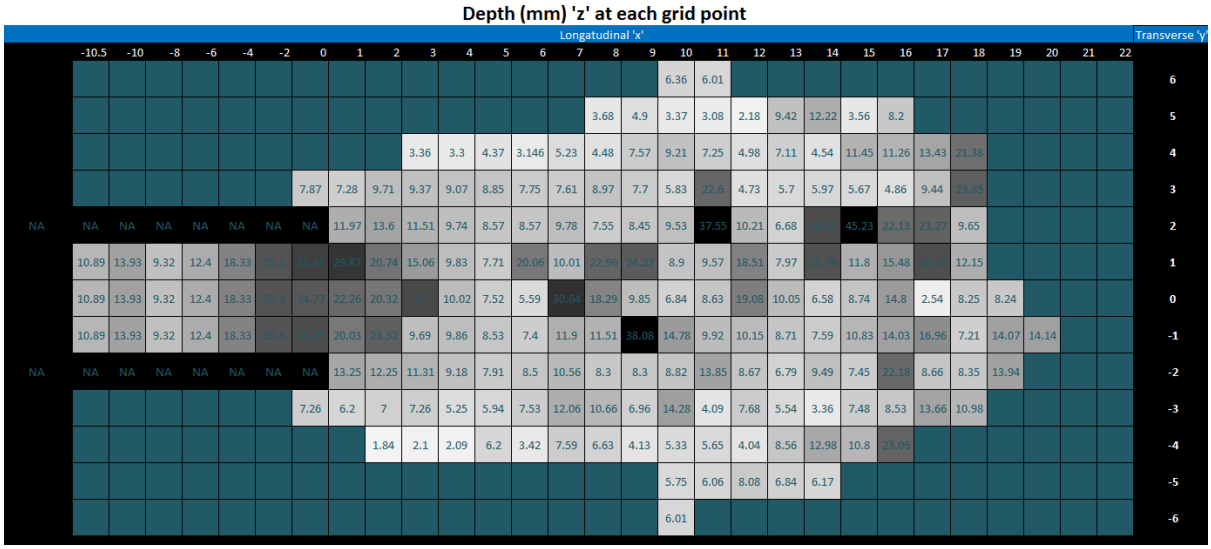

Figure D-25: S18W36EX5 Spot height graph, dark spots indicate a high level and white shallow heights.

D.4.2. Image quality and observations

All tests used the Motion-Pro camera at a frame rate of 1200 fps. They all had sufficient light for analysis. It was noted that there was more turbulence along the free surface as the other tests had given smooth wave forms but sections of these tests became turbulent. These sections had indistinct saturation levels and entrained bubbles in the exterior tests, as seen in image Figure D-26 (a) in the red oval area of the image. S18W36EX3 had more bubbles than the others limiting image quality for analysis.

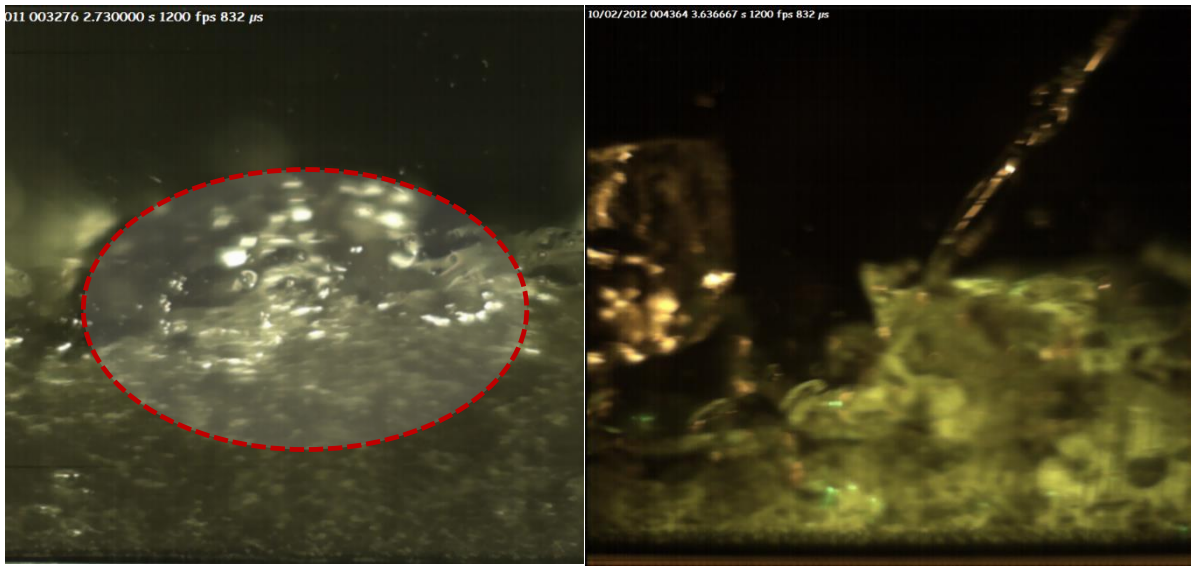

Figure D-26: Image quality (a) turbulent area in S18W36EX5 (b) light pollution in S18W36IN3.

S18W36IN3 had some light pollution from an exterior light source. This light pollution illuminated the orange tinted fluid covering the unsaturated particles (Figure D-26 (b))

resulting in visible particles above the surface. This was most prominent at the unsaturated front. The benefit of this light pollution is that it allows visualisation of sections otherwise not visible using PLIF. The illuminated front indicated that the shape of the front was the same as the exterior tests and there the camera was able to give some indication from stray laser light in the other interior tests.

D.4.3. Height and Time Data

Figure D-27 shows the height of the saturation level over time for first 0.8 s after the peak saturation. The heights were sampled every 0.01s.

Table D-7: Height summary S18W36

	Height of Flow (mm)			
Experiments	Absolute Maximum	Peak Saturation	Saturation Tail Height	Transition Deposit
S18W36IN3	61.15	42.12	12.53	25.29
S18W36EX3	52.86	48.99	6.43	26.48
S18W36EX5	82.70	65.22	10.55	27.3
Average	**65.57 ± 15**	**52.11 ± 12**	**9.84 ± 3**	**26.36 ± 1**

D.4.3.1. Peak Height

The values in Table D-7 show that the peak saturation and maximum heights were on average higher than the 31.8% moisture content showing an increasing trend with moisture content. However, the range is still very high. Figure D-27 shows that the height over time curves were similar for all of the tests with S18W36EX5 being the highest particularly in terms of the absolute maximum peak. This is due to a large particle sitting high in the flow in the middle of the body of the flow.

The height over time curves have much less distinct steep fronts, the front edge develops over twice the time as the 27.8% moisture content. This may be because the peak develops after this front where in other tests they occur at the same time or that. This is supported by the smaller peak at the front in S18W36EX5 that then builds to a maximum. The transition in this type of behaviour was evident around the 31.8% moisture content but seems to be more dominant at this higher moisture content. Overall the height curves show good consistency with a high range between them. This is expected at the higher moisture content where the flow is likely more mobile.

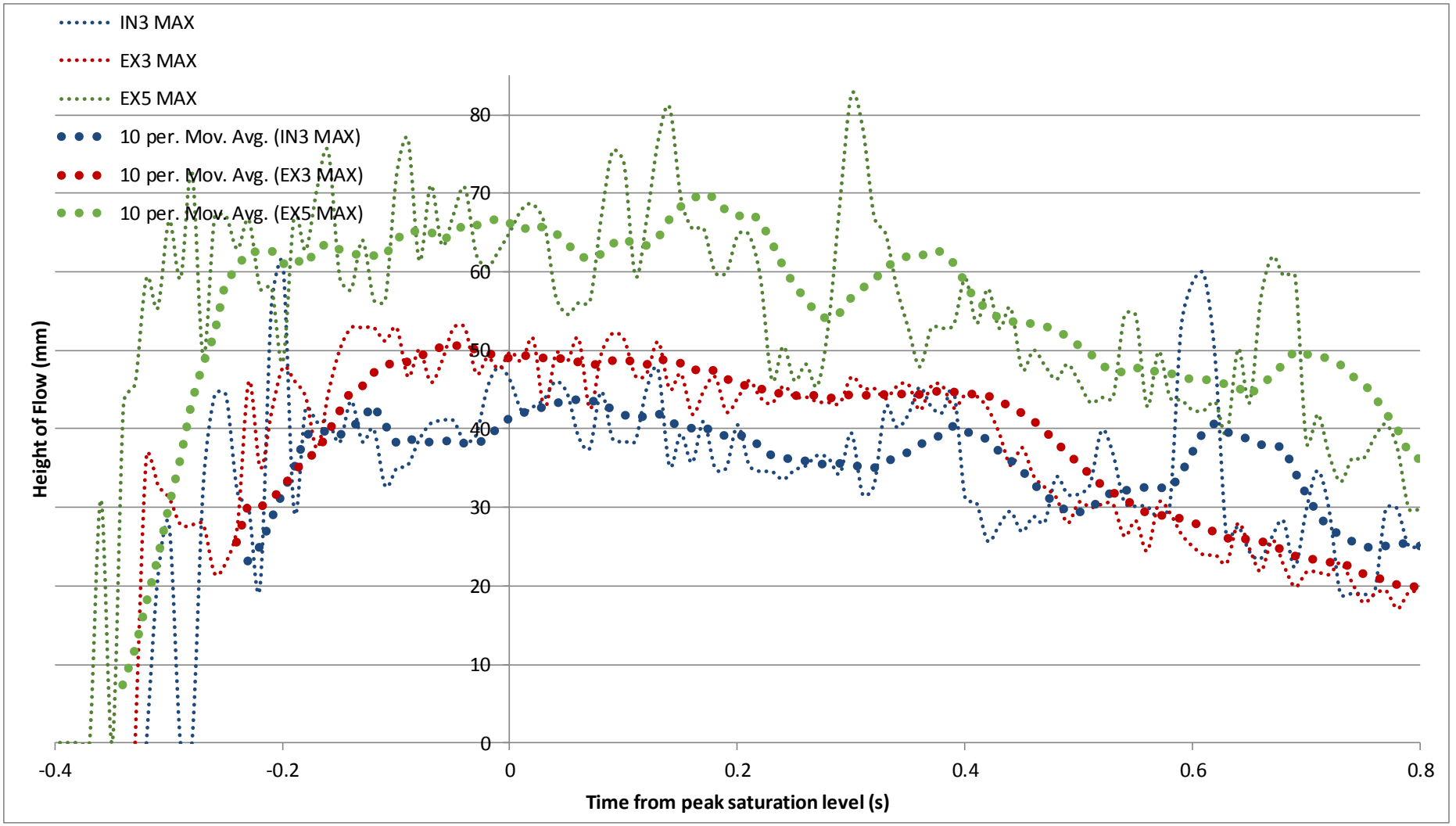

Figure D-27: Height with time for S18W36IN3, S18W36EX3 and S18W36EX5 experiments, showing absolute levels with a moving average of 10 points respectively.

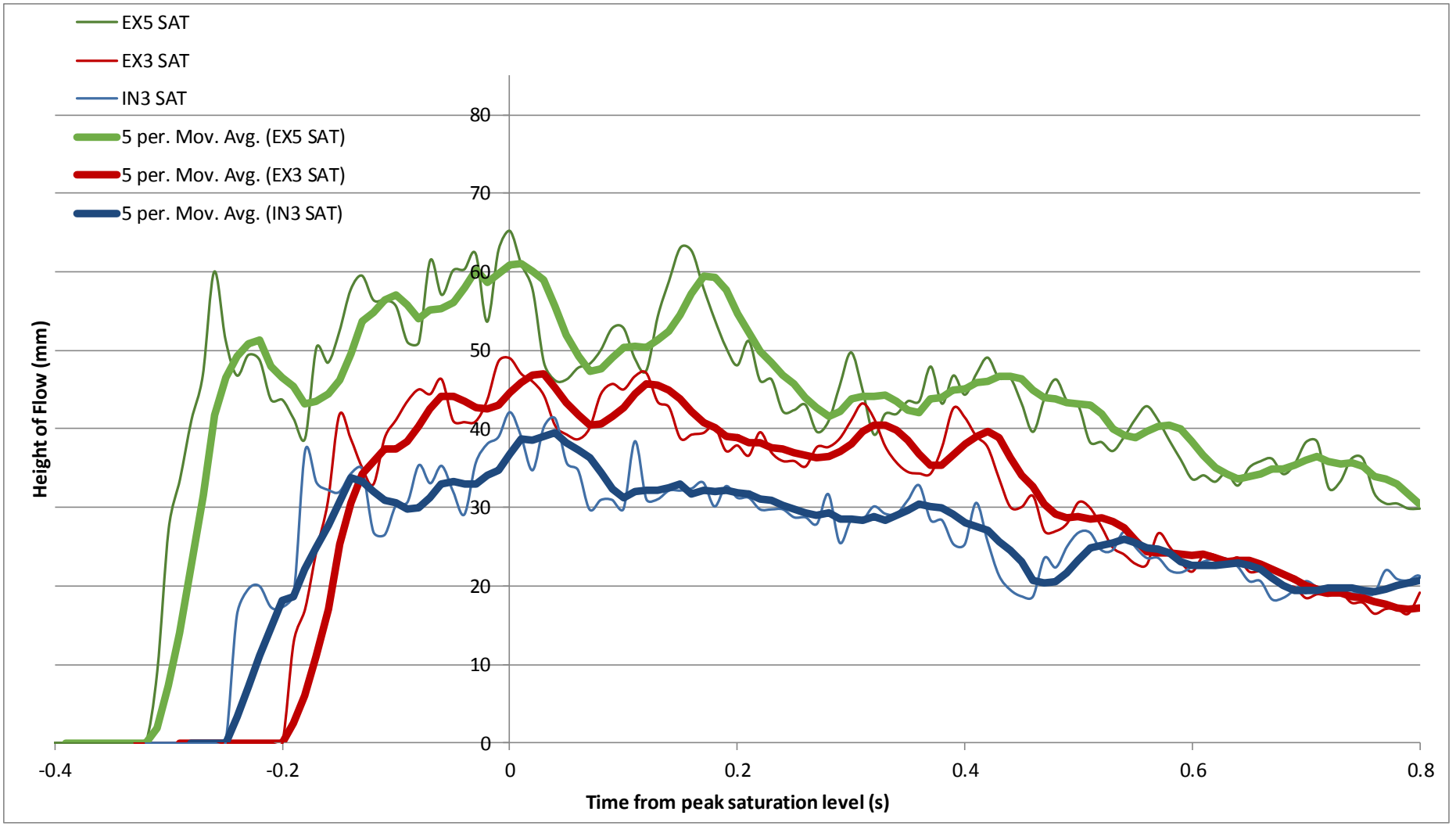

Figure D-28: Height with time for S18W36IN3, S18W36EX3 and S18W36EX5 experiments, showing saturation levels with a moving average of 5 points respectively.

D.4.3.2. Height of Tail

Table D-7 shows the height of the transition flow the trend of decreasing with increased moisture content. However, the average tail height does not seem to follow. Because this is linked to the limited recording time of these images it is assumed that the equilibrium tail height was not reached. As S18W36EX3 has a low value it is likely that these values would have developed to match the trend.

D.4.3.3. Timing

The change in height over time shape is reflected in the values present in Table D-8. The less steep front means that the flow front and saturation front occur earlier than for the other tests. The difference between flow and saturation front is also greater. Overall the times are more consistent with each other indicating that the behaviour is the same for all three experiments.

Table D-8: Time references S18W36

	Time to Peak Saturation Height of Flow (s)			
Experiments	Trigger	First Particle	Flow Front	Saturation front
S18W36IN3	-3.82	-0.31	- 0.27	-0.24
S18W36EX3	-2.58	-0.32	- 0.32	- 0.19
S18W36EX5	-3.44	-0.36	- 0.34	- 0.31
Average	**3.28 ± 0.6**	**0.33 ± 0.03**	**0.31 ± 0.04**	**0.25 ± 0.06**

D.4.4. Summary of Behaviour

All tests are of sufficient image quality for analysis; however, there is more turbulence and bubbles making the height level more difficult to distinguish. The deposit height and time data shows that the tests are all consistent but have a less steep abrupt front shape.

D.5. Slope 24.5° and Moisture Content 27.8%

One exterior (S24W28EX8) experiment was conducted at a slope of 24.5˚and the baseline moisture content of 27.8%. This test gave good deposit results and sufficient image quality for height analysis. The interior data for this combination of slope and moisture was taken from Sanvitale (2010) for comparison.

D.5.1. Deposit

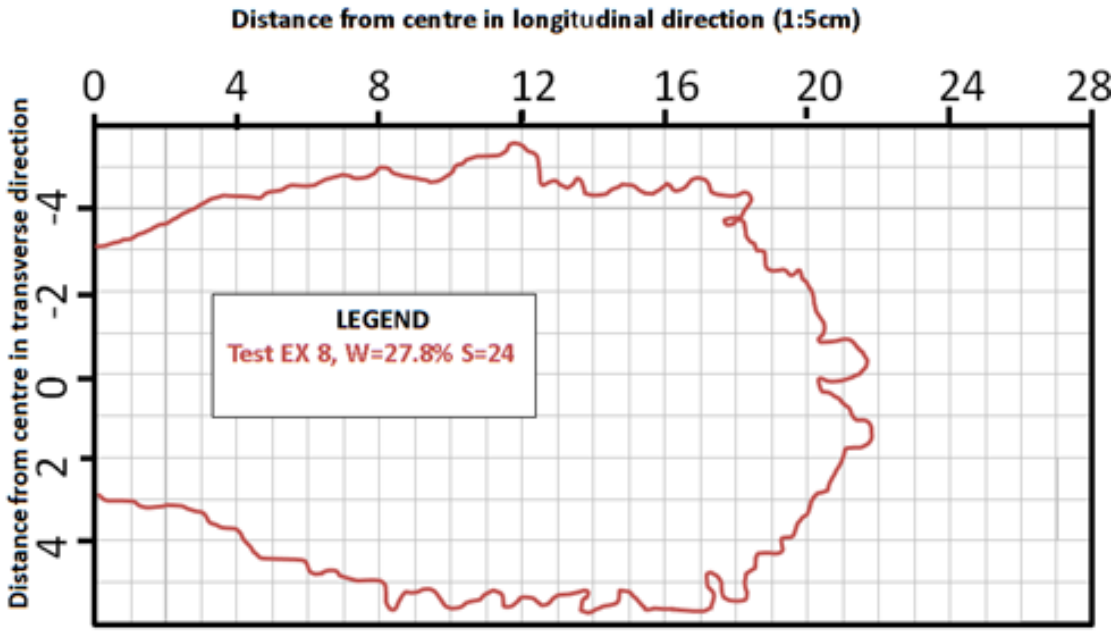

Figure D-29: Outline of S24W28EX8 deposits as taken from photographs of run-out deck. Grid reference is in 5 cm lots.

Figure D-29 show that the deposit fits with the trends and has a reasonably symmetrical shape. Figure D-30 also shows that in general segregation occurred, however, the centre is much finer than expected. This could be that the high slope and long run-out has meant that the large particles were all combined in the front of the deposit.

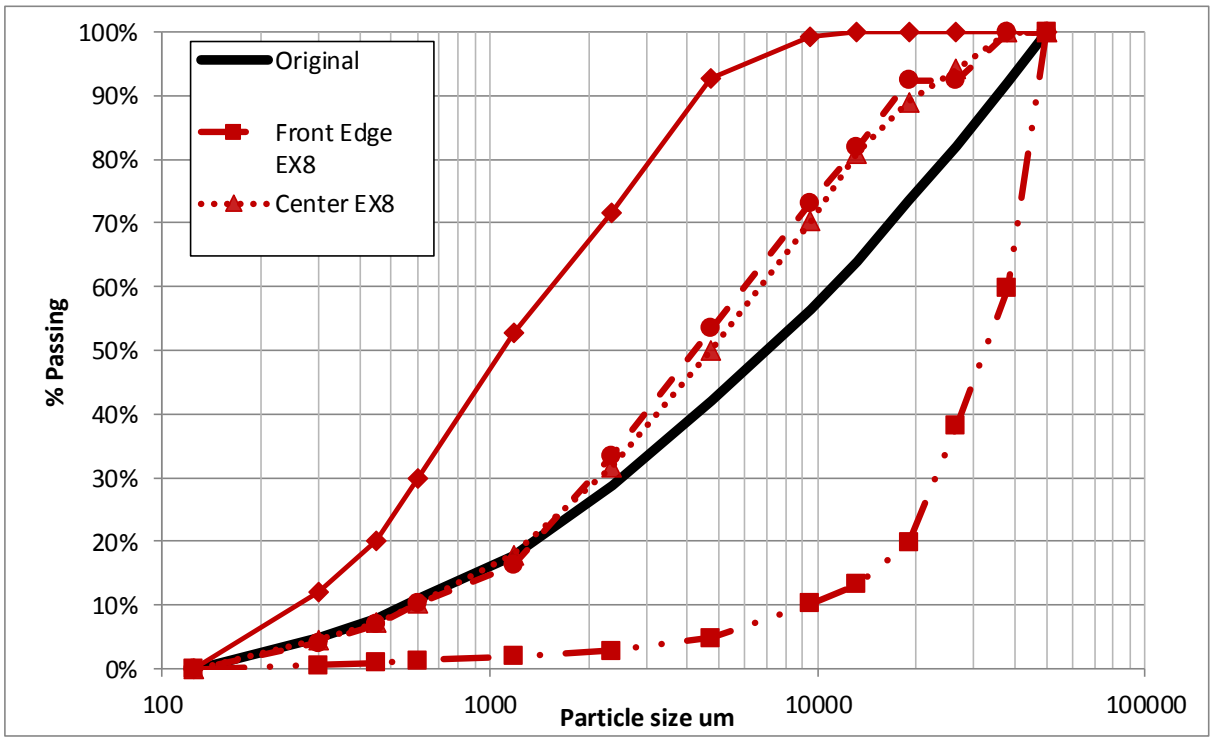

Figure D-30: PSD of S24W28EX8, the original is the PSD for the whole sample before experiment.

D.5.2. Image Quality and Observations

The exterior image quality for S24W28EX8 is slightly under-exposed at the wall. The level of light in the raw images reflects well off the air bubbles but is not intense enough to show particles in the upper areas of the image. The illumination results has clear air bubbles particularly after image processing (Figure D-31). The saturation surface is clear and there is a lot of texture for particle matching particularly at the base of the flow. Averaging patches over the three columns and 20-form batch size will remove the air bubbles as long as the patch size is not too small.

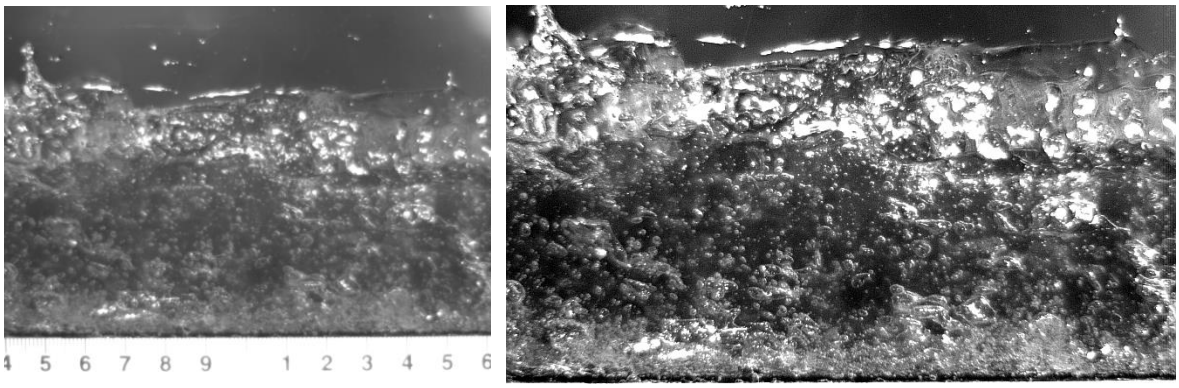

Figure D-31: S24W28EX8 image showing clear air bubbles. (Left) unprocessed. (Right) processed.

D.5.3. Height and Time Data

Table D-9: Height summary S18W36EX8

	Average Height of flows (mm)			
Experiment	***Absolute Maximum***	***Peak Saturation***	***Saturation Tail Height***	***Transition Deposit***
S24W28EX8	*71*	*61*	*7*	*31*

Table D-10: Time summary of S18W36EX8

	Time between peak height flow (s)			
Experiment	***Trigger***	***First Particle***	***Absolute Front***	***Saturation Front***
S24W28EX8	*2.90*	*0.77*	*0.67*	*0.21*

There is a lot of preceding material indicated by the high time between peak saturation height and the first particle. It is also seen in the approximate 20 mm height preceding absolute maximum. This preceding material had some large peaks caused by large particles sliding down the flume. This could indicate that some of the coarse unsaturated fraction dropped out of the hopper before the majority of the saturated material. This has implications depending on if the front was able to catch up to the preceding material. If the front did not catch up then

the PSD of the actual flow was significantly different to the other tests. However, based on the deposit having little large particles in the centre and transition, it is likely that the front did entrain this material.

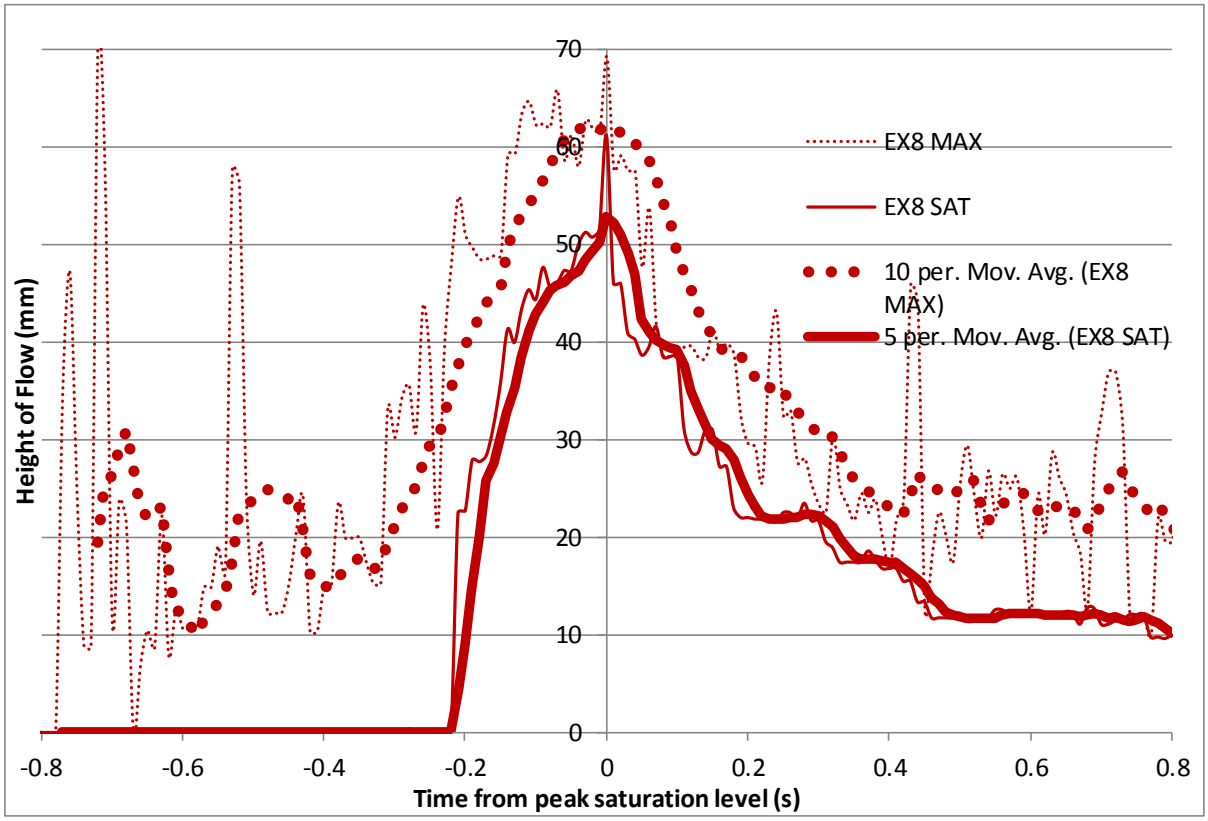

Figure D-32: Height with time for S24W28EX8 experiments, showing both saturation and absolute levels with a moving average of 5 and 10 points respectively. Centred on the maximum values.

The saturation level from S24W28EX8 is not that steep with a time between front and peak of 0.21 s which corresponds to the higher slope. However, the biggest abnormality is how quickly the body drops off. This could be because the material that would normally make up the body is in the preceding dry flow. The shape of this flow means that the velocity comparisons are likely to overestimate the peak and drop off faster than the other tests. Other tests have indicated that a steep short front produces a longer run-out and may produce higher velocities. Assuming the difference between the 28% and 32% moisture content at the lower slope the S24W28EX8 should be about ~250 mm shorter than the higher moisture content for the S24W28 series which is close to the ~270 mm actual difference.

D.5.4. Summary of Behaviour

S24W28EX8 has a well-developed front in terms of height. Based on the deposit data it is likely that the front contained most of the large particles. The body of the flow is very short. It is assumed that this flow was one of the fastest due to the shape of the front. The run-out length indicates that the influence of moisture content is potentially independent of the slope change for these magnitude tests.

D.6. Slope 24.5° and Moisture Content 31.8%

Four experiments were conducted at a slope of 24.5°and a moisture content of 31.8%, two interior (S24W32IN7 and S24W32IN8) and two exterior (S24W32EX7 and S24W32EX9). All of these tests gave good deposit results and were all, except for S24W32IN7, of sufficient image quality for height analysis. However S24W32IN7 only had enough texture to make an approximation of heights.

D.6.1. Deposit

Figure D-33 shows that the tests have the expected long elongated shape and further run-out length than any 18.1° slope tests. The transverse direction matches reasonably well particularly in the widest parts from about 400 mm to 900 mm. The S24W32EX9 test shows some evidence of being restricted by the walls of the run-out deck. However, none of the other tests show significant interaction with the walls.

In the longitudinal direction the tests are reasonably variable, particularly S24W32EX7, which could be affected by blockage in the hopper. The range is approximately 100 mm which is reasonably low. The wider flows appear to have gone further. By looking at the spot height diagrams for S24W32EX9 and S24W32IN7 we see that the wider longer flow has a thin centre were the narrower one has larger particles scattered throughout. This suggests that S24W32EX9's front held all the largest particles whereas S24W32IN7 had some spread throughout the flow. Figure D-36 shows that the PSDs of the centres are finer than the 18.1° slope tests in most cases.

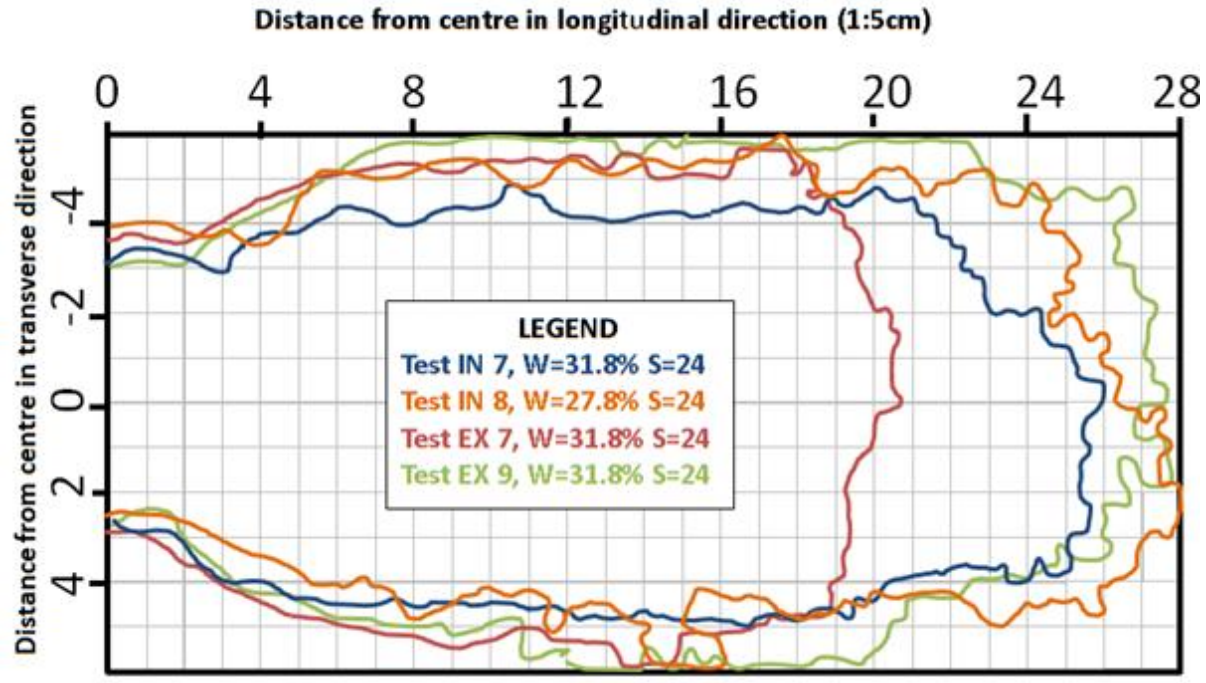

Figure D-33: Outline of S24W28 deposits as taken from photographs of run-out deck. Grid reference in 5cm lots.

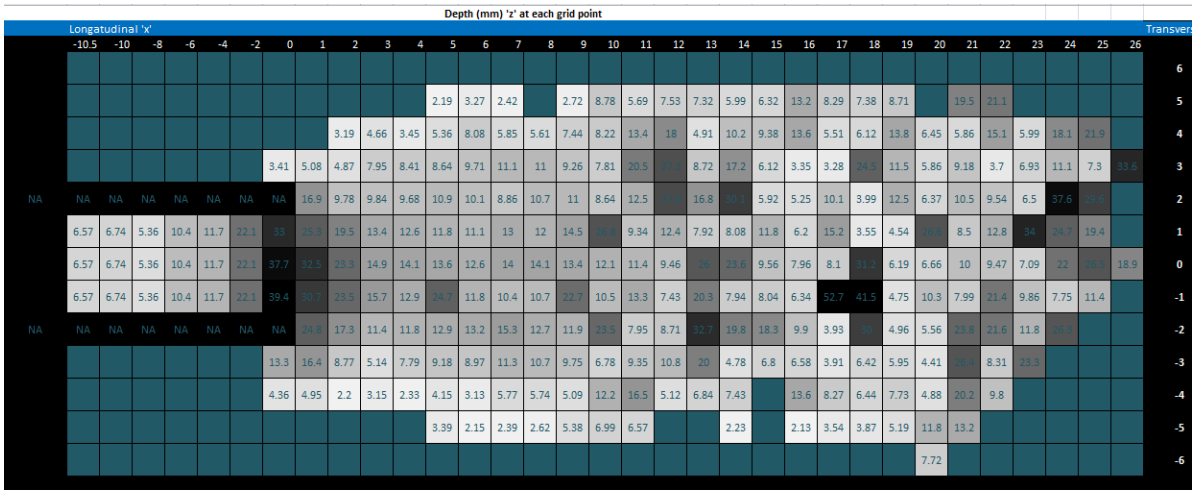

Figure D-34: IN7 spot height graph, dark spots indicate a high level and white shallow heights.

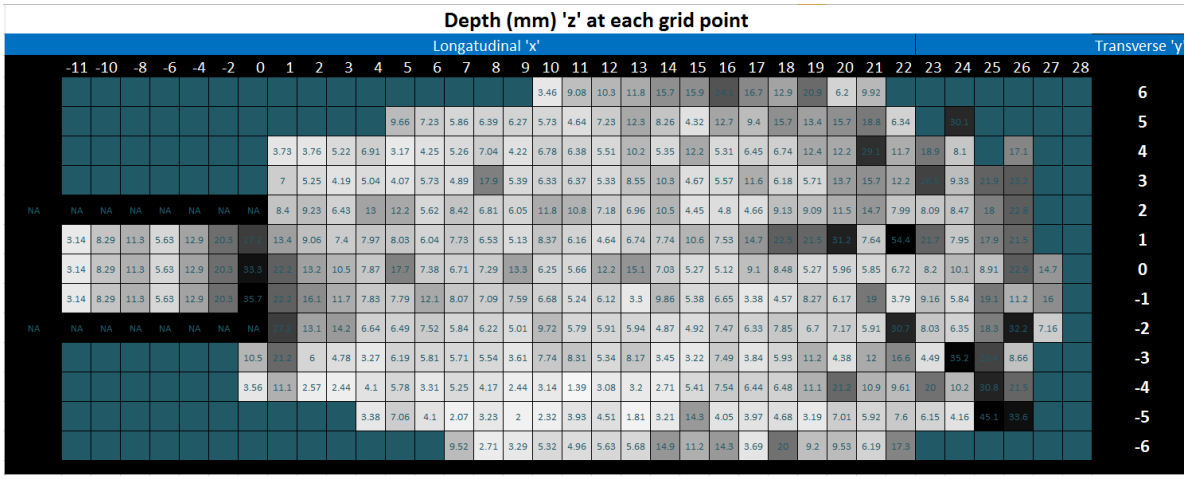

Figure D-35: EX9 spot height graph, dark spots indicate a high level and white shallow heights.

The PSD curves (Figure D-36) for the experiments show very similar profiles except for the centre and the transition curve of S24W32IN7. The longer deposit again means that there is some sensitivity to sampling in the centre where a large particle might influence smaller particles around it. In general the transition and centres are finer than the lower slope tests. S24W32EX7 has more medium-sized particles in the front edge than the other tests but still has the same trend. Overall these results indicate the very good segregation.

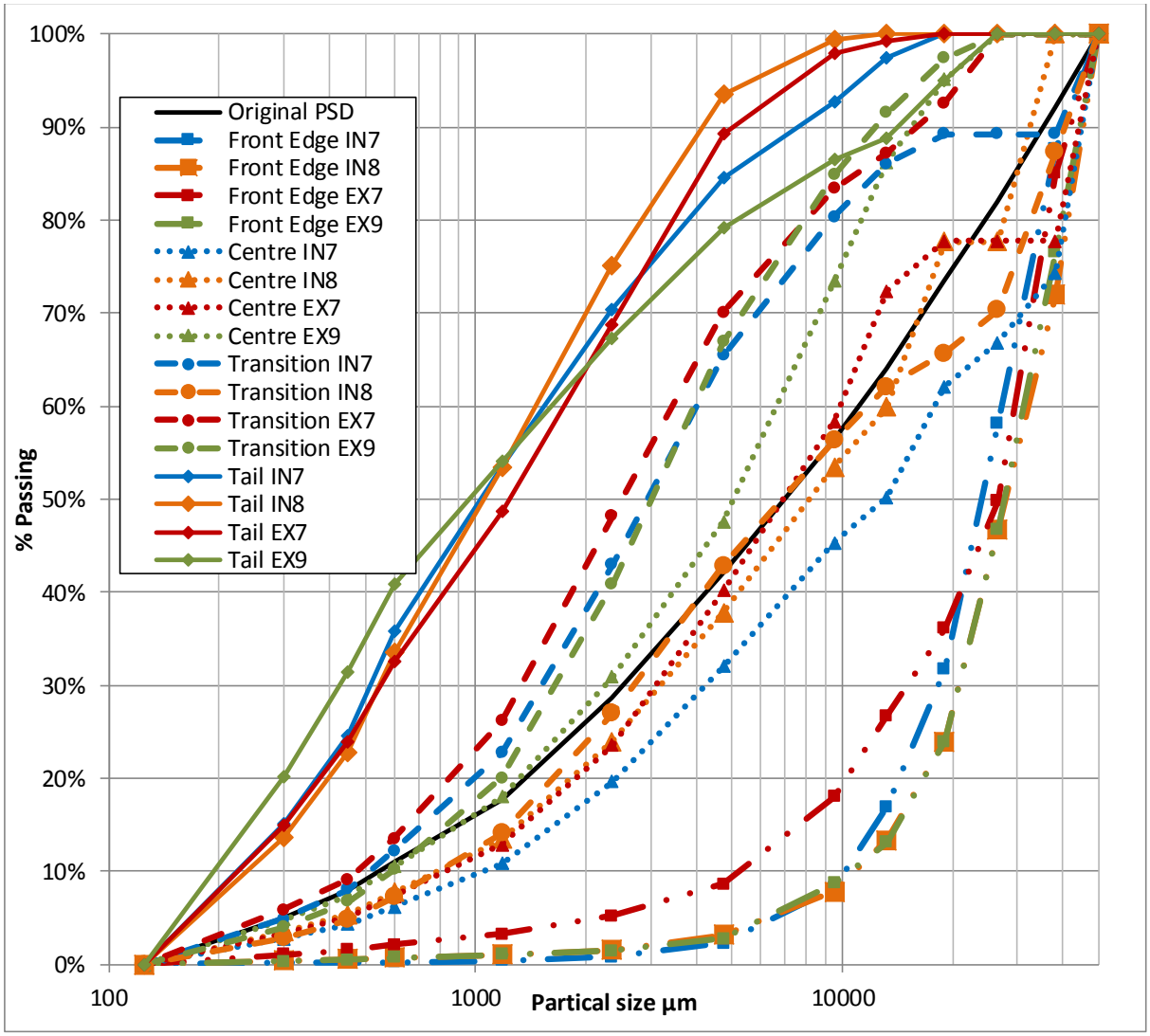

Figure D-36: PSD of EX8, the original is the PSD for the whole sample before experiment.

D.6.2. Image Quality and Observations

All tests used the Miro camera at a frame rate of 2000 fps which gave good image quality for all tests. The initial particles preceding the flow bounced more than the lower slope which tended to slide. The free surface was "energetic," changing in height quickly sometimes appearing to entrain some air. The tail sections had more apparent surge waves affecting the

height often pulling or pushing a medium to large particle with them. All of the tests had significant air bubbles in the body that moved up through the flow with positive buoyancy. S24W32EX9 like S24W28EX8 seemed to entrain air at the front as particles rolled over and collapsed on to the flume. This explains where the air bubbles concentrated at the base of the flume come from.

Figure D-37: Processed image quality of IN7 (a) Front, (b) Body (c) Tail

S24W32IN7 had poor quality illumination. There was reasonable information in the body but the tail was particularly dark and would not give enough texture for PIV analysis. Figure D-37 shows the front body and tail which shows the illumination got progressively worse as the depth of flow decreased. From flashes of light it is reasonable to assume that the absolute maximum was larger but the illumination was insufficient to capture the real front and height. S24W32EX7 had a large amount of material preceding the flow itself and once the front passed it was more fluid than typical lacking the large particles that define the front.

D.6.3. Height and Time Data

Figure D-27 shows the height of the saturation level over time for first 0.8 seconds after the peak saturation for S24W32IN7, S24W32IN8, S24W32EX7 and S24W32EX9, these heights were sampled every 0.01s.

Table D-11: Height summary S18W36 series

	Height of Flow (mm)			
Experiments	Absolute Maximum	Peak Saturation	Saturation Tail Height	Transition Deposit
S24W32IN7	-	47.48	6.21	33.11
S24W32IN8	61.12	45.28	6.01	37.49
S24W32EX7	68.97	56.20	6.89	29.00
S24W32EX9	67.83	63.26	5.55	25.67
Average	**65.97 ± 4**	**53.06 ± 9**	**6.17 ± 0.7**	**31.32 ± 6**

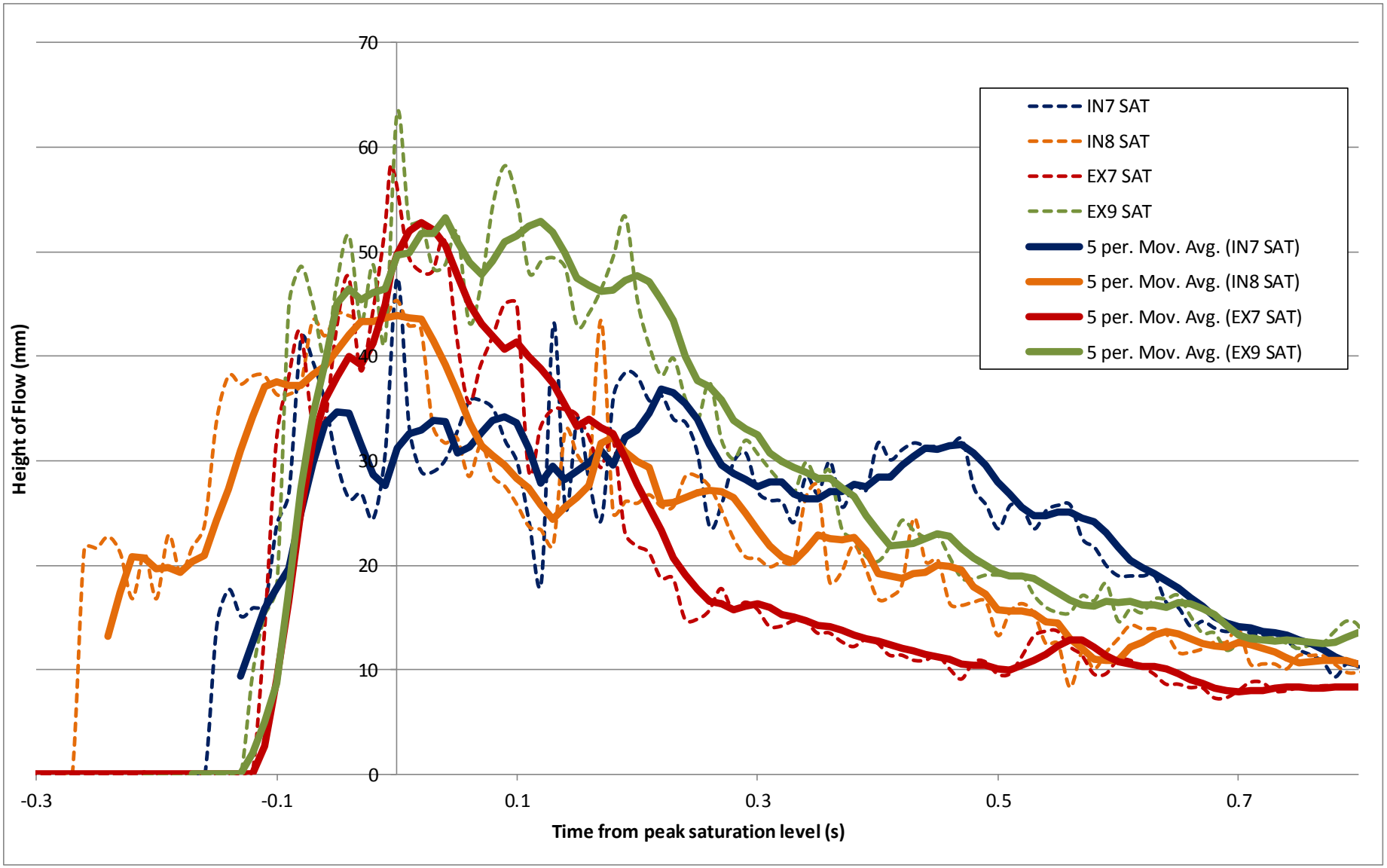

Figure D-38: Height with time for S24W32IN7, S24W32IN8, S24W32EX7 and S24W32EX9 experiments, showing saturation with a moving average of 5 points.

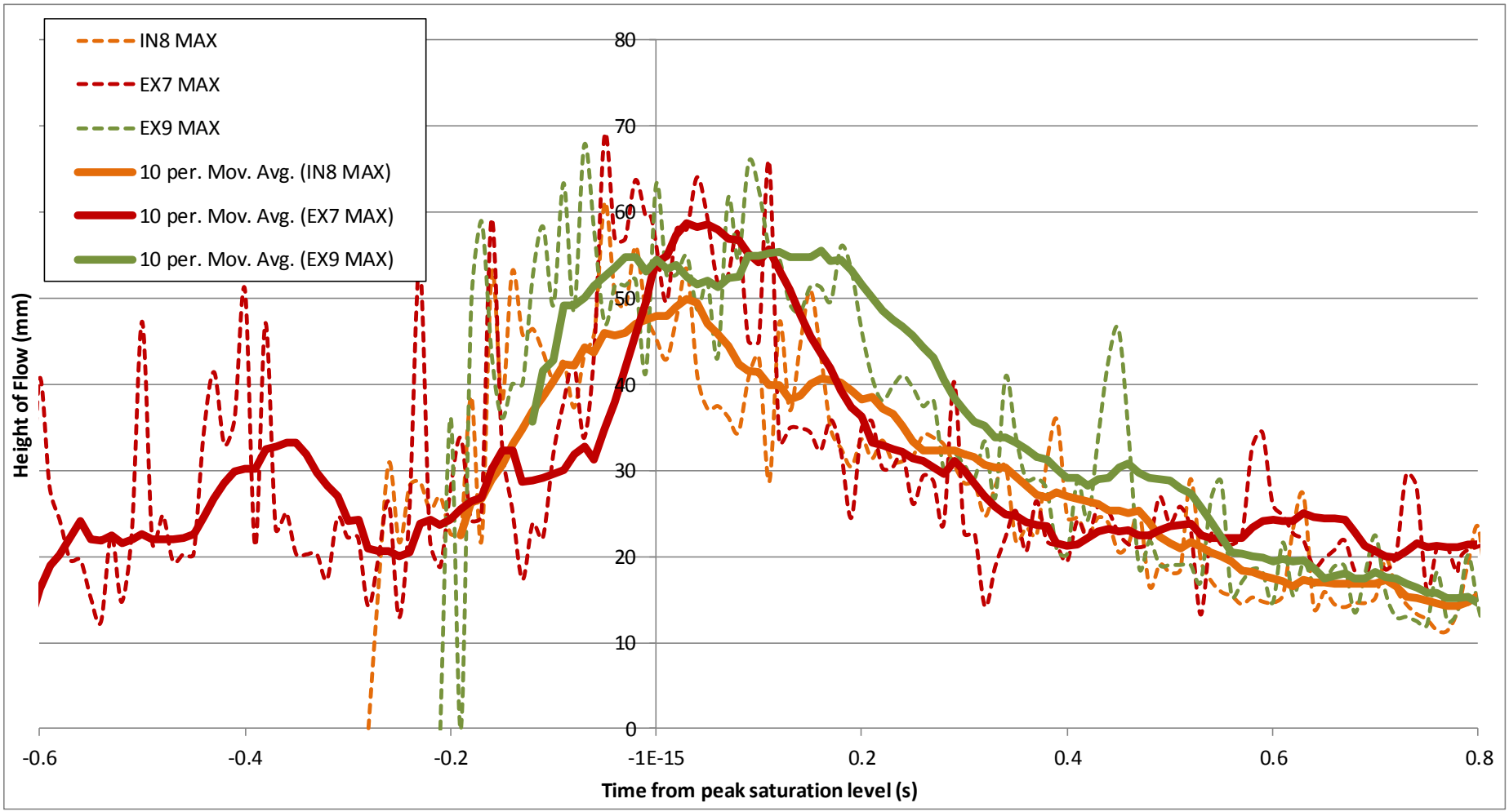

Figure D-39: Height with time for S24W32IN8, S24W32EX7 and S24W32 EX9 experiments, showing absolute levels with a moving average of 10 points. S24W32IN7 was removed due to quality issues.

D.6.3.1. Peak Height

S24W32IN7 had a low flow height which was slightly due to the image quality but linked to the slightly shorter run-out was also indicative of a slightly underdeveloped front flow. S24W32IN8 has the longest front with the peak and top of the front occurring nearly twice as long (Table D-12) after the saturation front as the other tests

S24W32EX7 has lots of proceeding material in the dry front, most of which seemed to be continuous with the flow. The saturated flow itself was the steepest but gave the shortest run-out length. This combination of results suggests some delay release of the material from the hopper perhaps caused by the fluid segregating from the solid before release.

All the tests have a similar decay in body shape which is more consistent in the absolute maximum height than the saturation level. The only abnormality in the body of the flow was a plateau in saturation height after the peak of S24W32EX9. All of the 24.5° tests show a flatter front than the lower slope.

D.6.3.2. Height of Tail

The tail height was relatively consistent and was lower than the S24W28EX8 and 18.1° tests in general. This is expected as the faster steeper flow is less likely to have as much material deposit on the flume.

D.6.3.3. Timing

The time between trigger and flow was longer for the S24W32IN8, this was not because the flow peak occurred well into the flow front, but because the flow front was not very steep. The high time between peak and first material in S24W32EX7 shows that there was a considerable amount of preceding material. But the front itself was quite steep.

Table D-12: Time references S18W36 series

	Time to peak saturation height of section of flow (s)			
Experiments	Trigger	First Particle	Flow Front	Saturation front
S24W32IN7	-	*-0.16*	*- 0.16*	*-0.15*
S24W32IN8	*-2.47*	*-0.27*	*- 0.27*	*- 0.26*
S24W32EX7	*-1.68*	*-0.74*	*-0.65*	*-0.11*
S24W32EX9	*-1.94*	*-0.2*	*-0.18*	*-0.11*
Average	***2.03 ± 0.4***	***0.34 ± 0.3***	***0.32 ± 0.3***	***0.16 ± 0.08***

D.6.4. Summary of Behaviour

S24W32IN7 had poor quality image which likely is the reason for the low flow height. There was large amount of variation in run-out length and shapes of the fronts of the tests. S24W32EX7 had issues with preceding material that might have resulted in a reduced run-out length and steep shape. S24W32IN8 had a less steep flow front but all tests had a similar decay in body shape leading to consistent tail heights.

Appendix E: Deposit Results

E.1. Photos of Run-out Deposition

E.1.1. S18 – W24

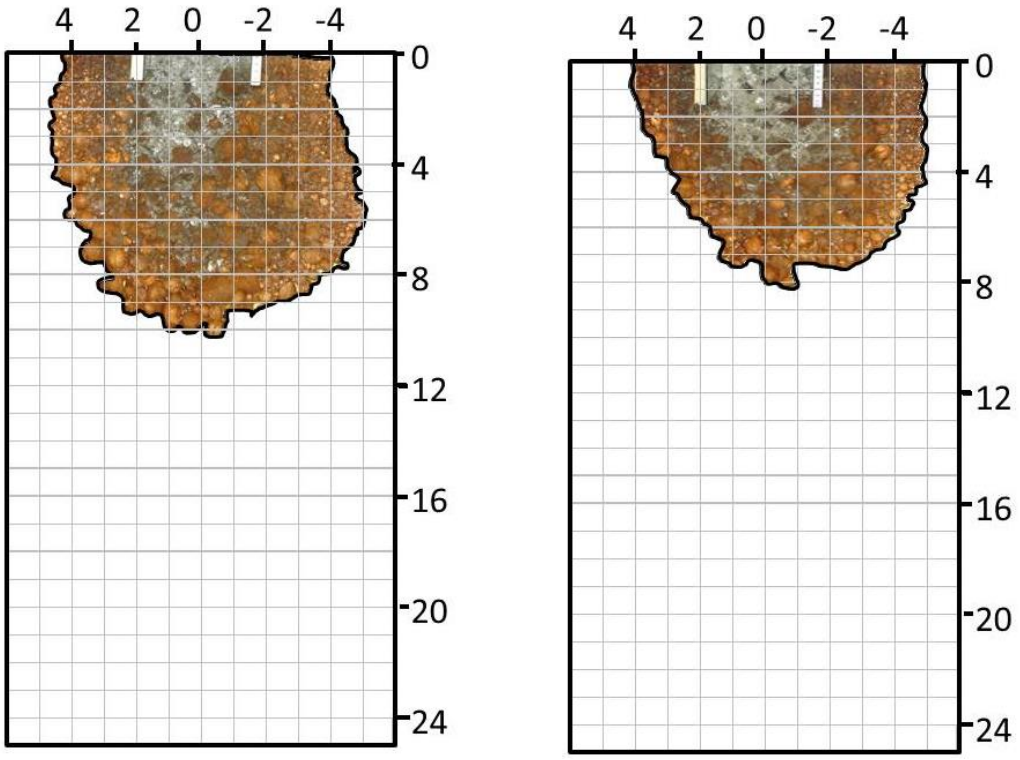

a) Internal Test S18W24IN5 b) External Test S18W24EX6

Figure E-1: Deposit shape for tests with slope 18.1° and moisture content of 23.8%.

E.1.2. S18 – W28

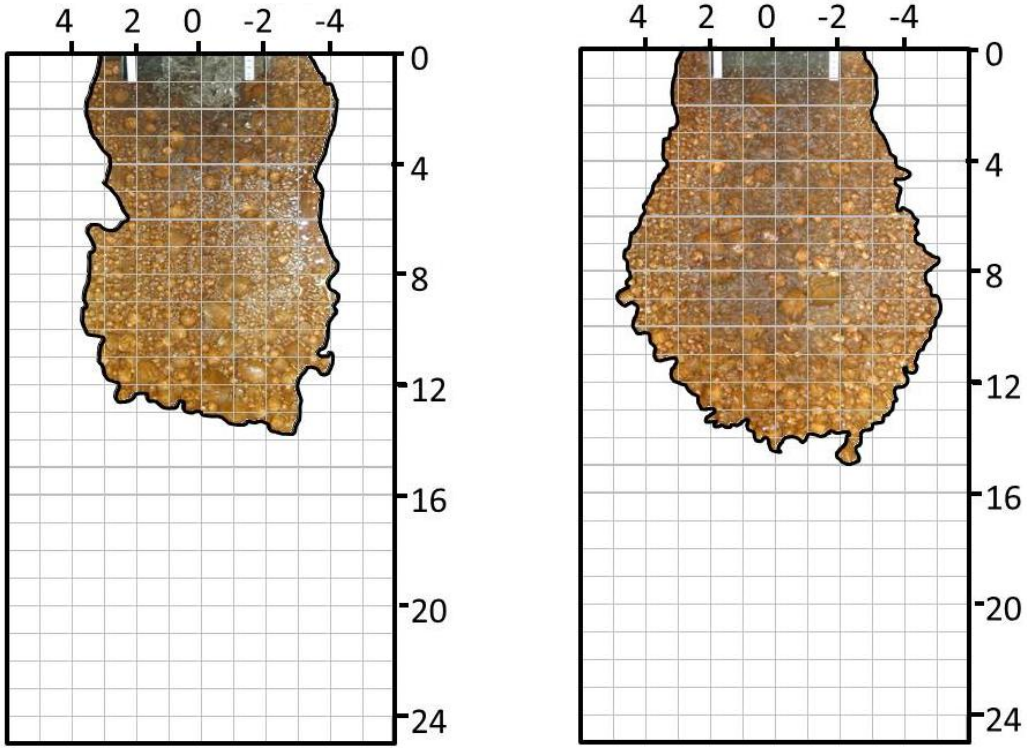

a) Preliminary Test S18W28IN0a

b) Preliminary Test S18W28IN0b

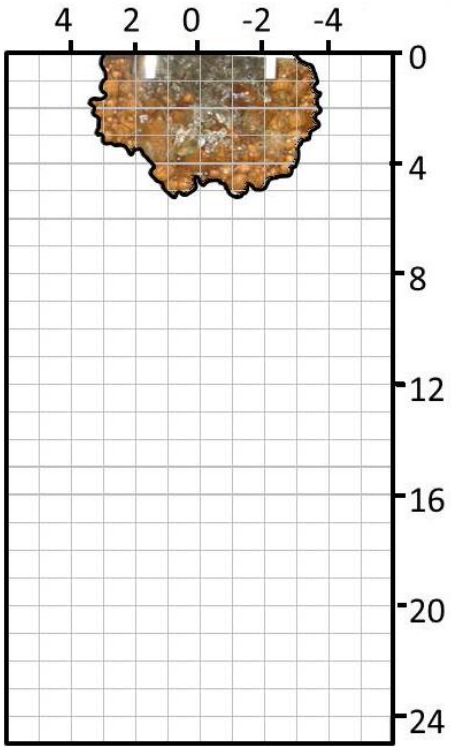

c) Preliminary Test S18W28IN0c with a major blockage during testing

Figure E-2: Deposit shape for preliminary tests for slope 18.1° and moisture content of 27.8%.

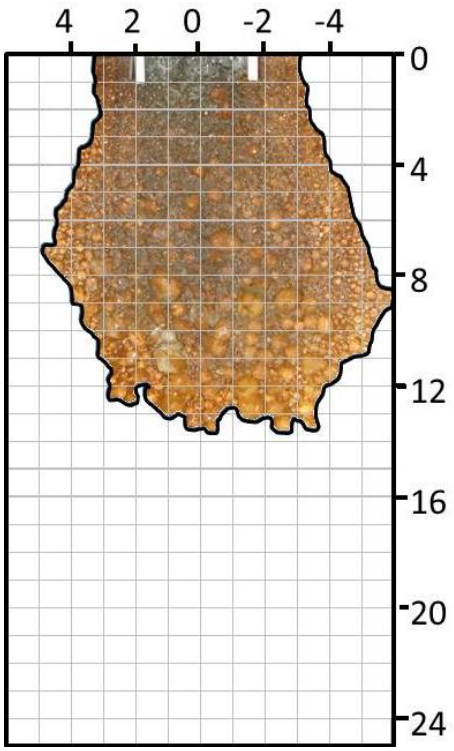

a) Internal Test S18W28IN1

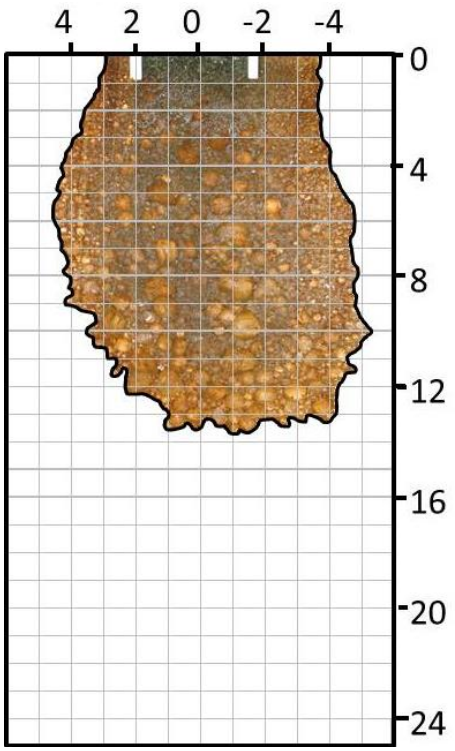

b) Internal Test S18W28IN4

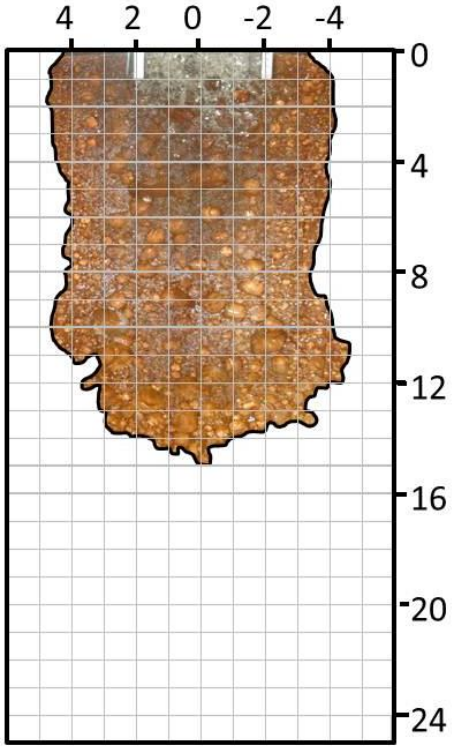

c) External Test S18W28EX1

Figure E-3: Deposit shape for slope 18.1° and moisture content of 27.8%.

E.1.3. S18 – W32

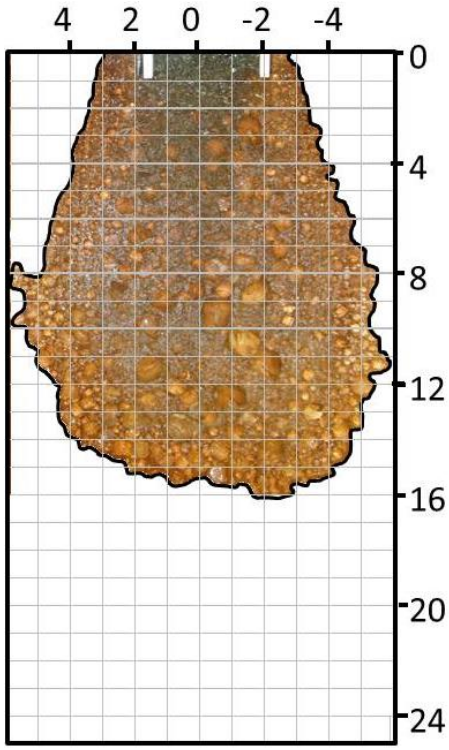

a) Internal Test S18W32IN2

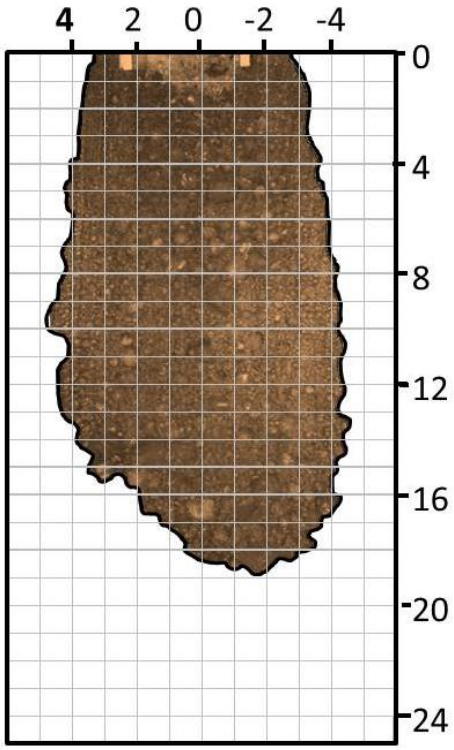

b) Internal Test S18W32IN6

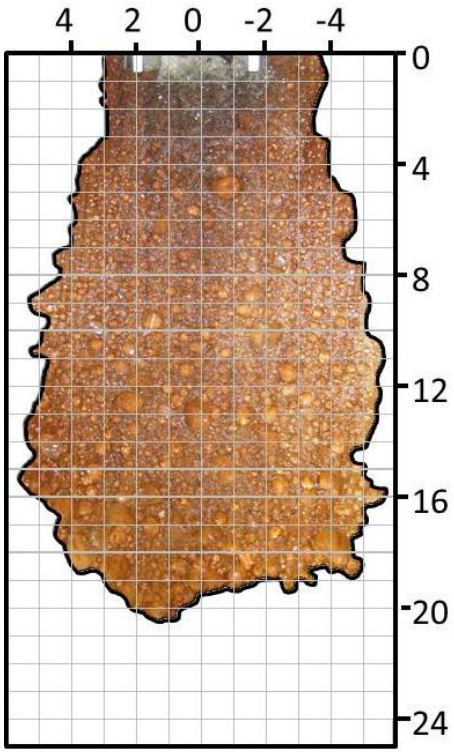

c) External Test S18W32EX2

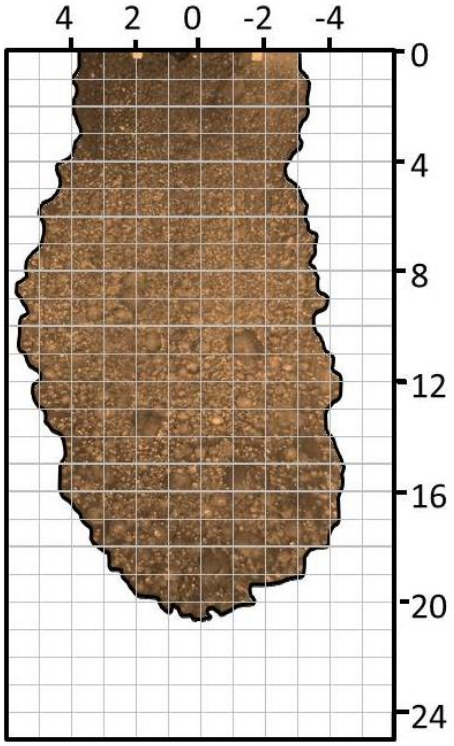

d) External Test S18W32EX4

Figure E-4: Deposit shape for tests with Slope 18.1° and moisture content of 31.8%.

E.1.4. S18 – W36

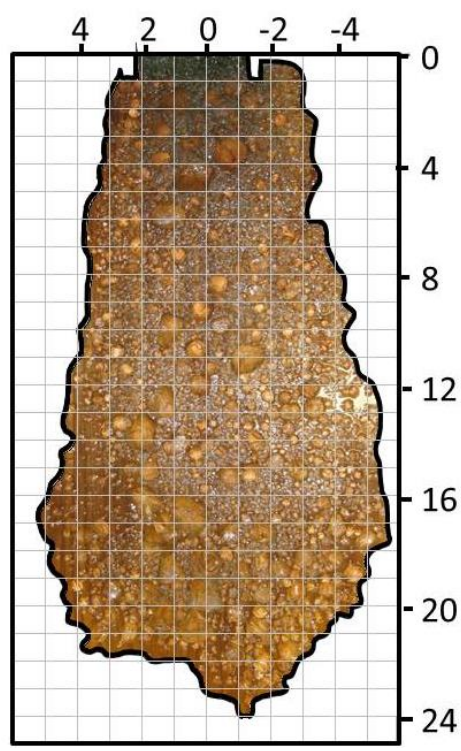

a) Internal Test S18W36IN3

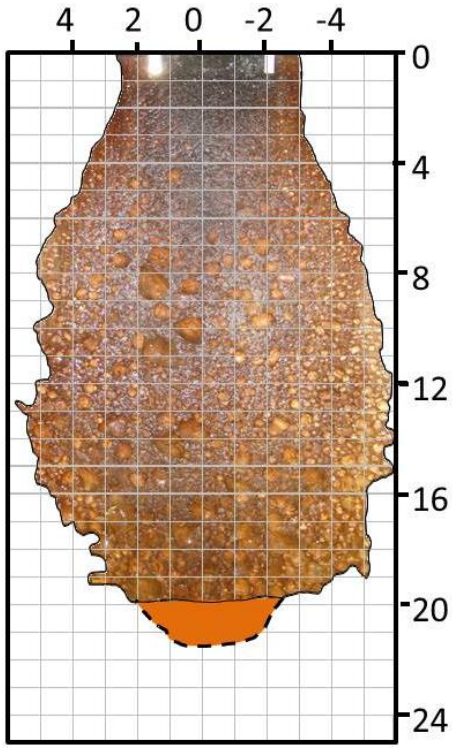

b) External Test S18W36EX3

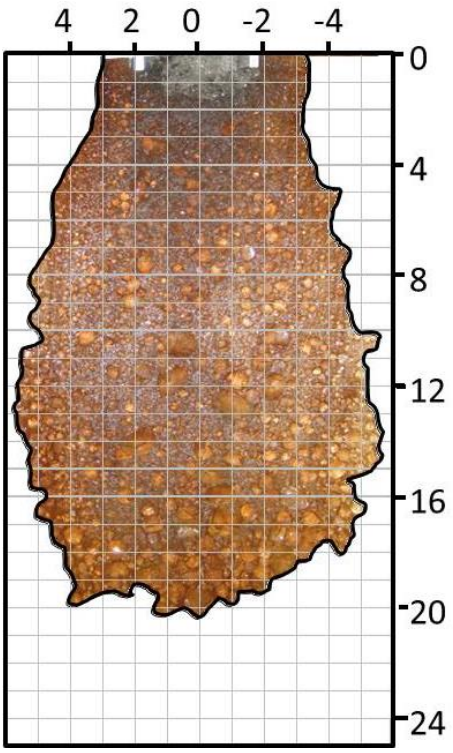

c) External Test S18W36EX5

Figure E-5: Deposit shape for tests with slope 18.1° and moisture content of 35.8%.

E.1.5. S24 – W28

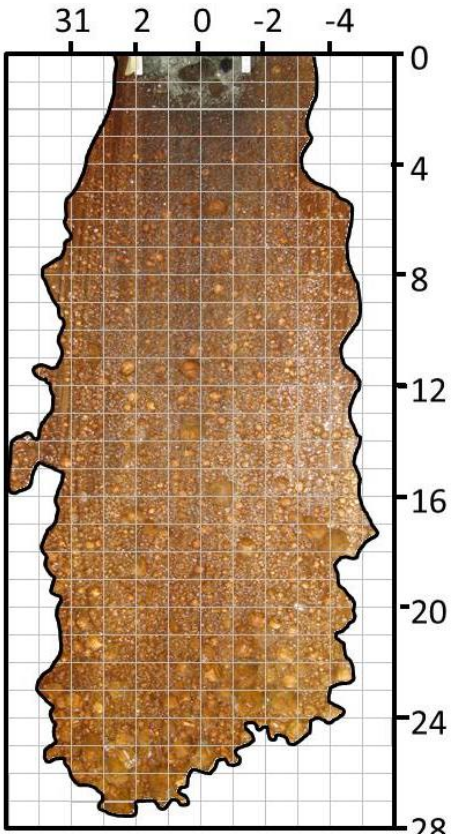

Figure E-6: Deposit shape for External Test S24W28EX8 with slope 24.5° and moisture content of 27.8%.

E.1.6. S24 – W32

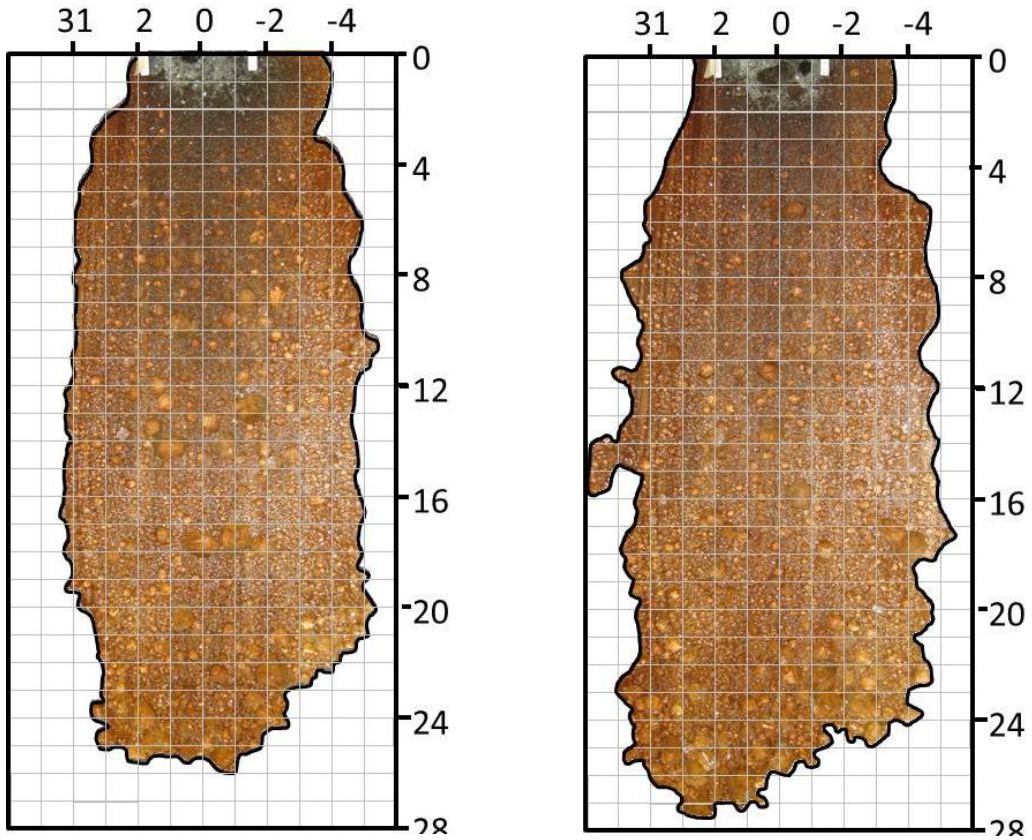

a) Internal Test S24W32IN7

b) Internal Test S24W32IN8

c) External Test S24W32EX7

d) External Test S24W32EX9

Figure E-7: Deposit shape for tests with slope 24.5° and moisture content of 31.8%.

E.2. Spot Height Diagrams

E.2.1. S18 – W24

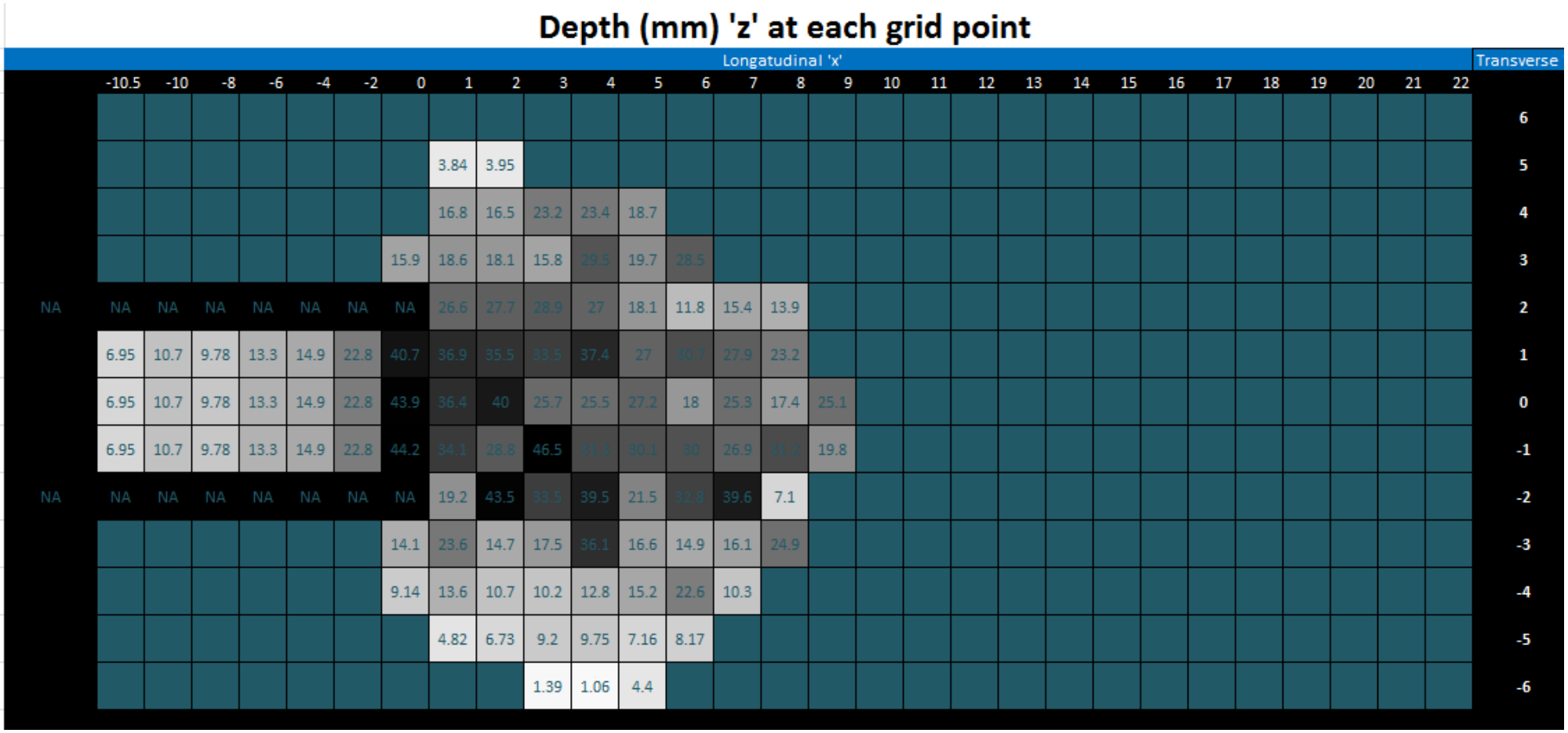

Figure E-8: Spot heights for Internal Test S18W24IN5 with slope 18.1° and moisture content of 23.8%

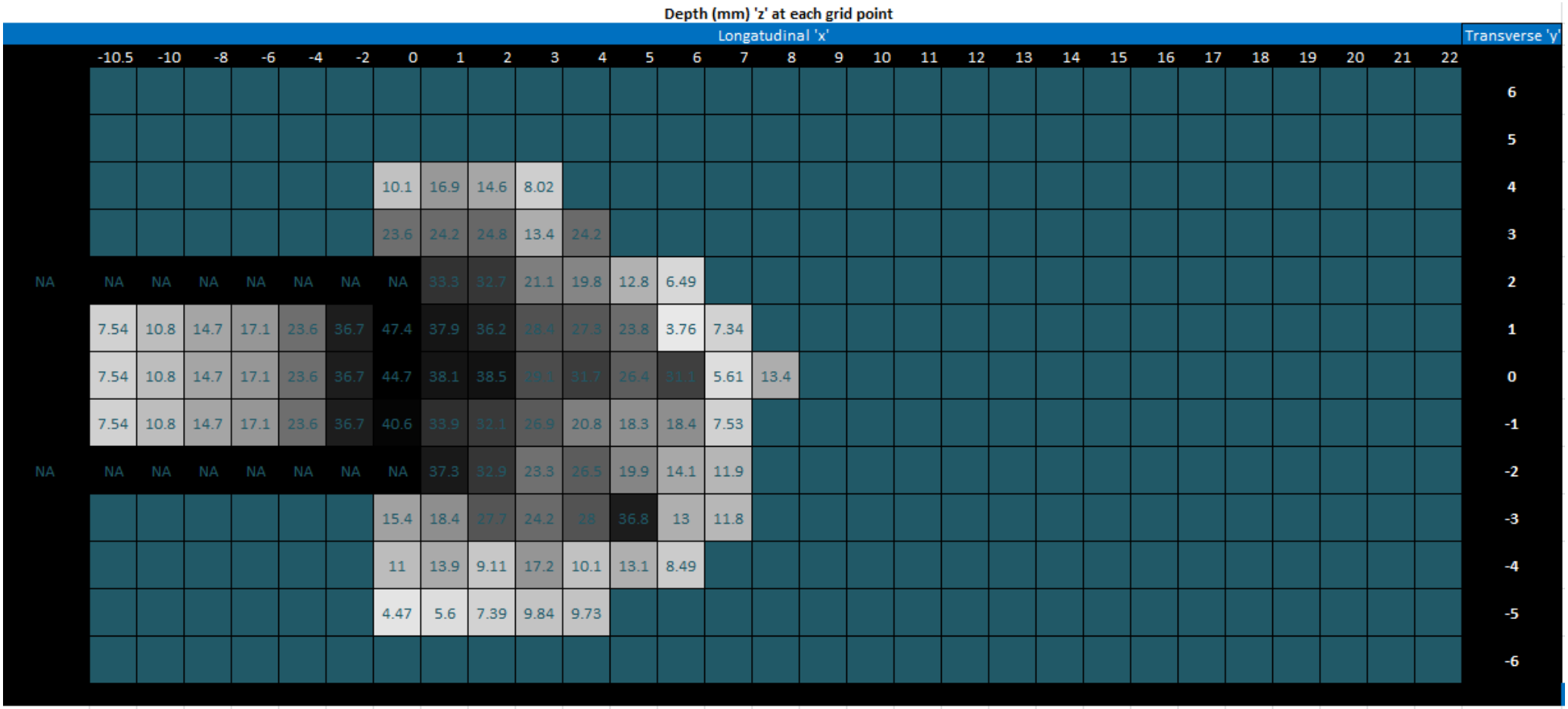

Figure E-9: Spot heights for S18W24EX6 with slope 18.1° and moisture content of 23.8%

E.2.2. S18 – W28

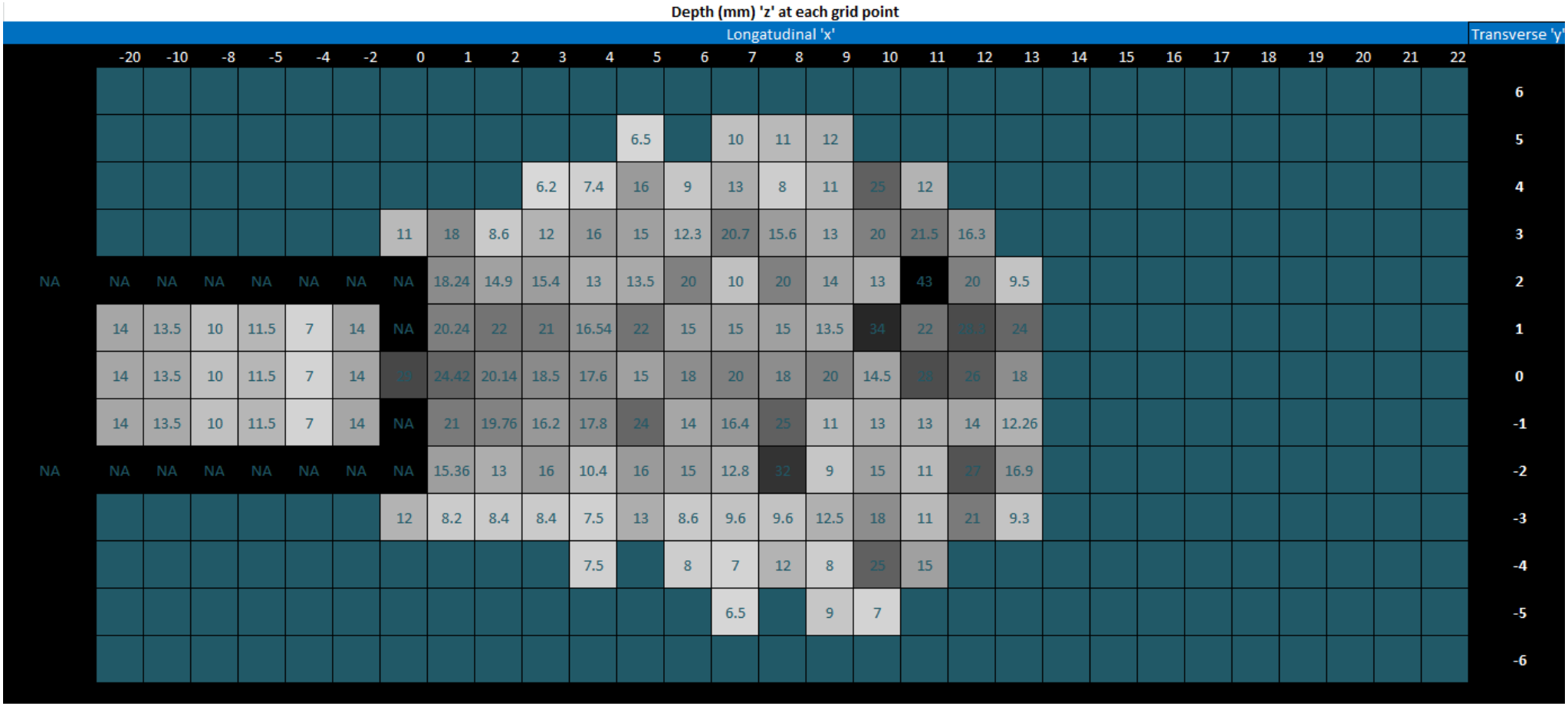

Figure E-10: Spot heights for S18W28IN0a with slope 18.1° and moisture content of 27.8%.

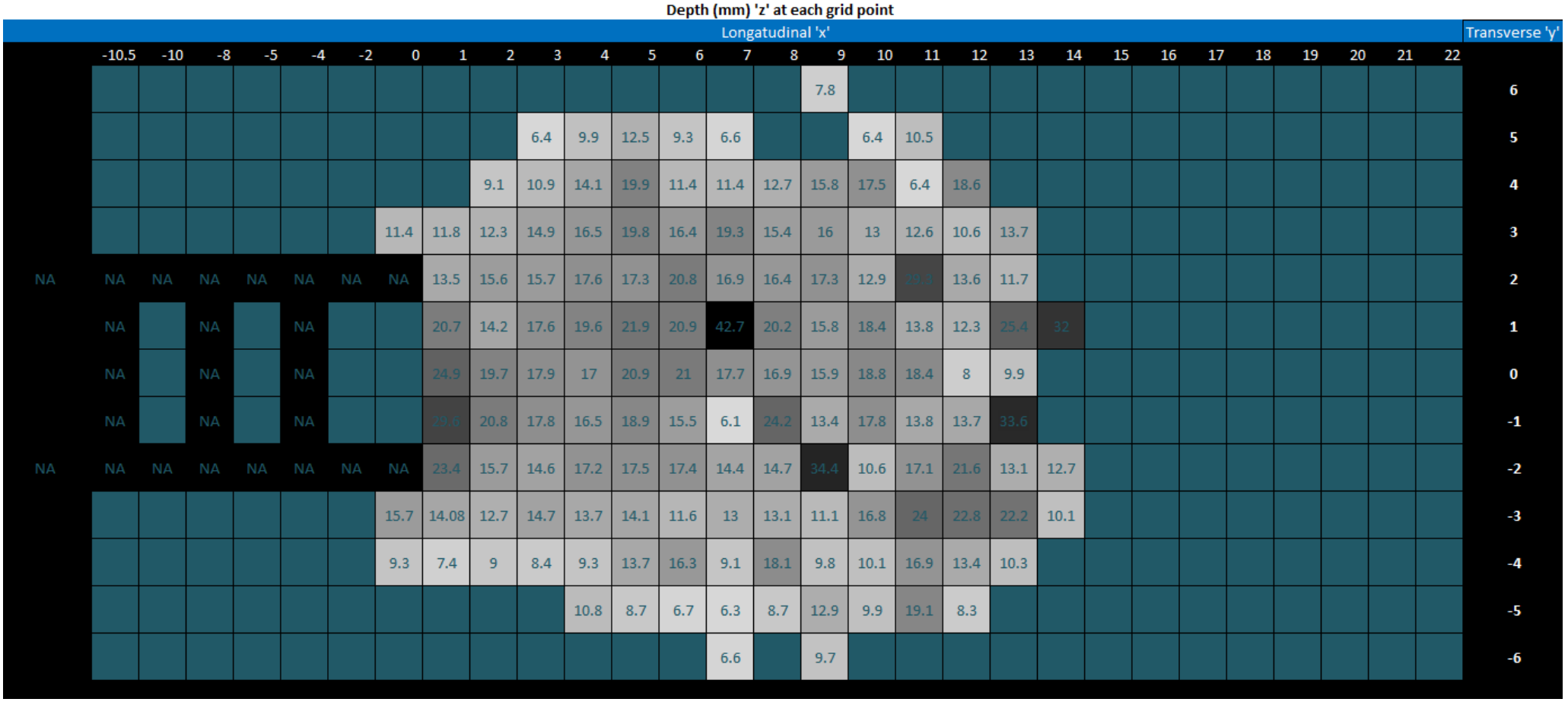

Figure E-11: Spot heights for S18W28IN0b with slope 18.1° and moisture content of 27.8%.

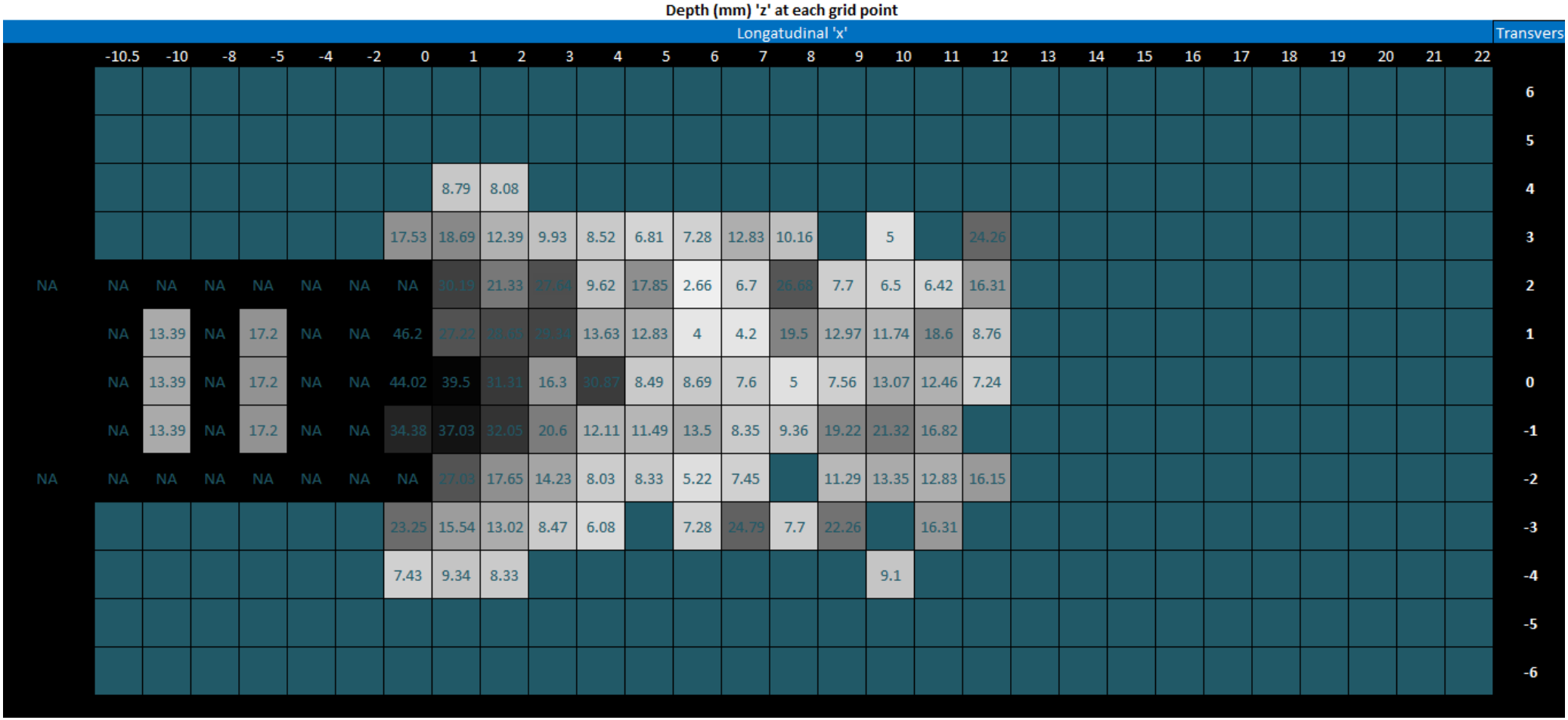

Figure E-12: Spot heights for S18W28IN0c with slope 18.1° and moisture content of 27.8%. Some of the depth measurements for the shallowest depths were inaccurate due to poor drainage of test.

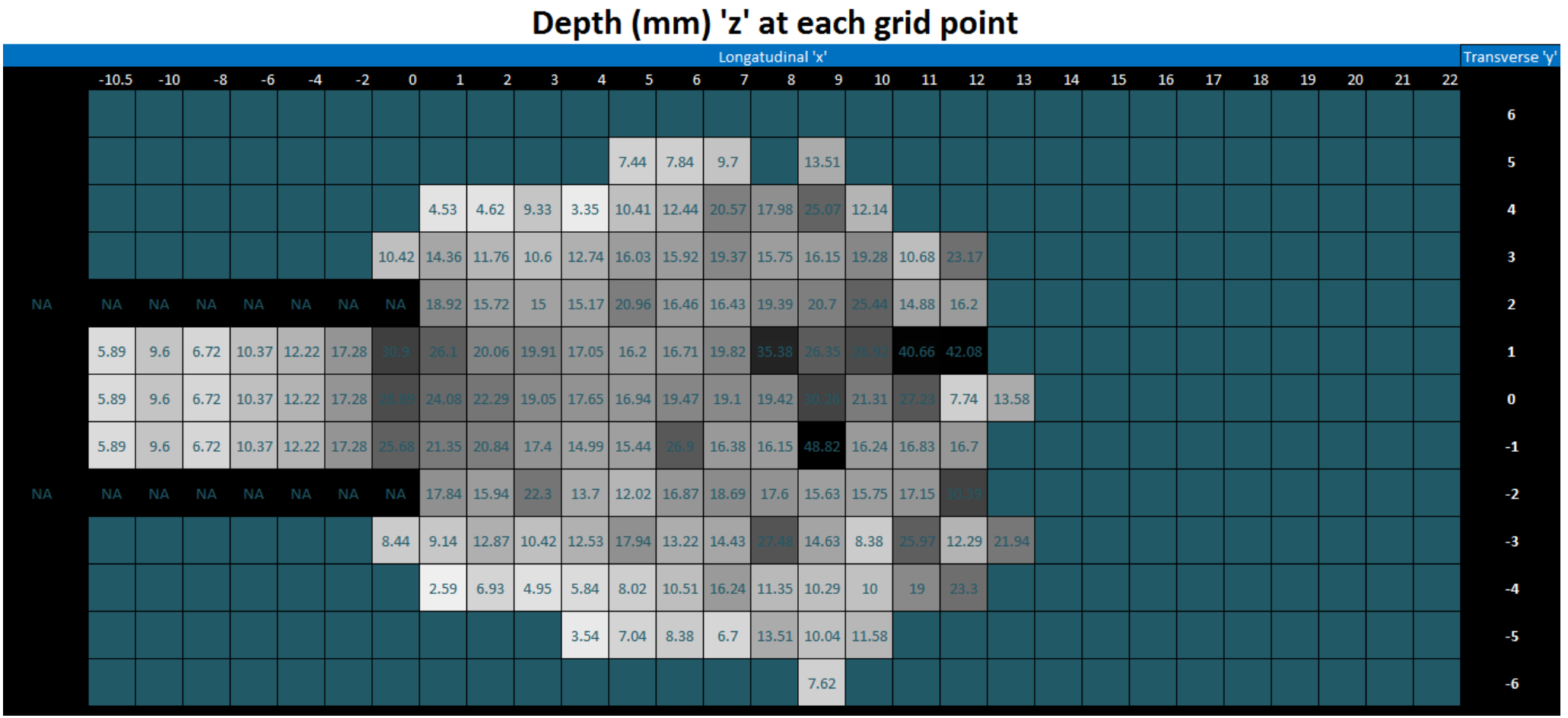

Figure E-13: Spot heights for S18W28IN1 with slope 18.1° and moisture content of 27.8%.

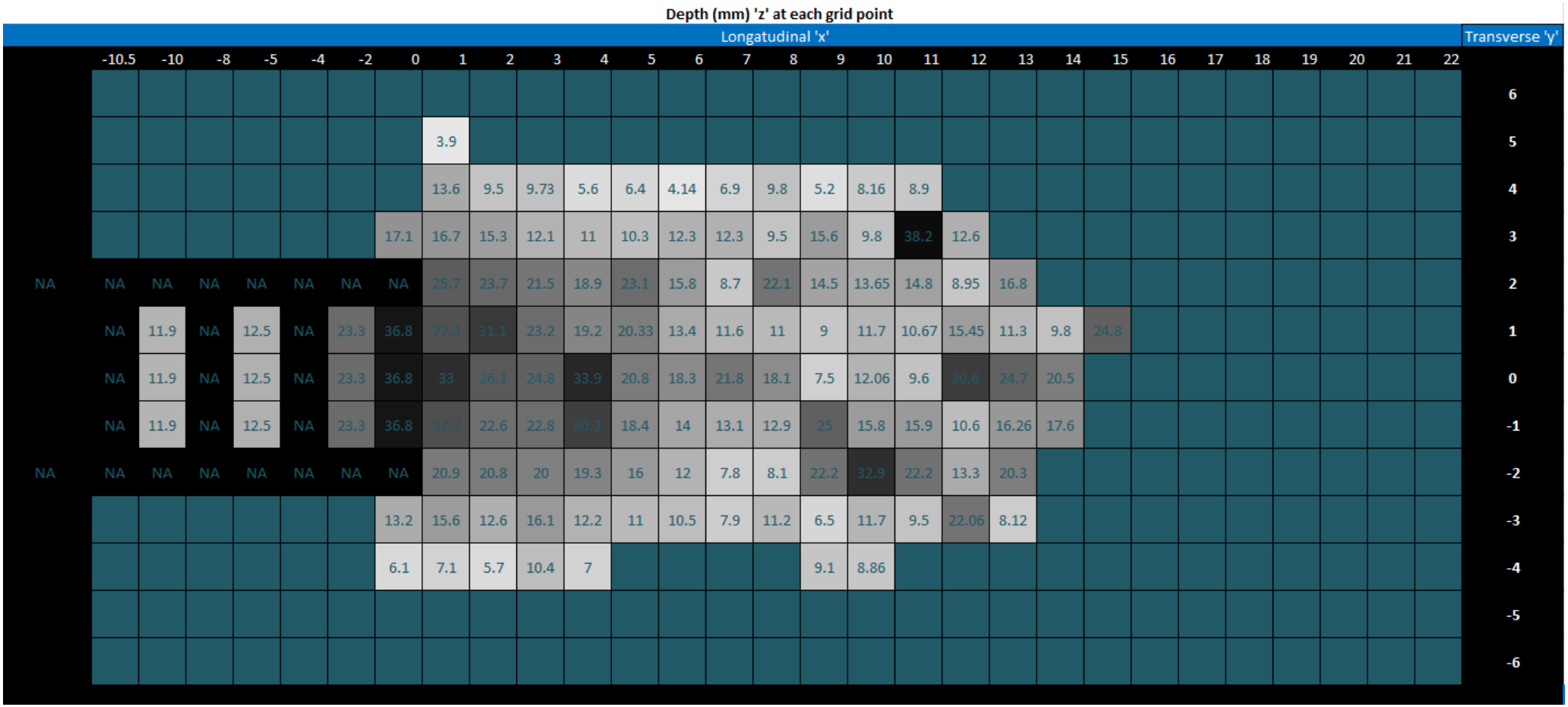

Figure E-14: Spot heights for S18W28EX1 with slope 18.1° and moisture content of 27.8%.

Depth (mm) 'z' at each grid point

Transverse 'y' \ Longatudinal 'x'	-10.5	-10	-8	-6	-4	-2	0	1	2	3	4	5	6	7	8	9	10	11	12	13	14	15	16	17	18	19	20	21	22
6																													
5											4.86	5.4	8.83																
4								4.13	5.5	7	8.29	13.55	10.41	23.17	7.26	15.34	7.71												
3							6.52	8.84	11.45	12.38	14.88	14.39	18.92	17.23	15.38	20.88	40.34	9.6											
2	NA	NA	NA	NA	NA	NA	NA	16.87	16.19	14.62	18	16.47	17.93	23.93	15.1	18.28	27.52	47.72	23.3										
1	9.81	11.99	9.88	13.19	15.33	17.19	25.86	22.69	16.57	17.78	20.89	38.57	17.73	37.9	17.94	34.24	18.6	22.97	21.44	27.24									
0	9.81	11.99	9.88	13.19	15.33	17.19	31.11	25.46	20.71	21.54	21.49	19.52	18.65	18.16	19.43	18.11	18.03	19.19	21.94	28.87	6.15								
-1	9.81	11.99	9.88	13.19	15.33	17.19	32.23	24.61	18.67	33.51	18.29	28.14	32.33	17.6	29.36	14.6	21.71	30.63	24.24	21.32									
-2	NA	NA	NA	NA	NA	NA	NA	22.26	14.02	15.74	14.19	16.35	15.86	21.38	20.11	12.49	11.8	33.89	13.83	28.31									
-3							13.25	11.07	10.22	11.67	11.19	10.31	12.55	12.61	11.66	12.3	8.34	12.52	13.07	13.55									
-4							3.8	5.44	5.79	6.87	6.16	7.37	12.81	11.28	5.57	8.6	6.36	24.32	13.97	23.31									
-5											0.99	4.19	7.75	3.44	12.98	4.63	4	26.01	1.31										
-6																0.94	1.74												

Figure E-15: Spot heights for S18W28IN4 with slope 18.1° and moisture content of 27.8%.

E.2.3. S18 W32

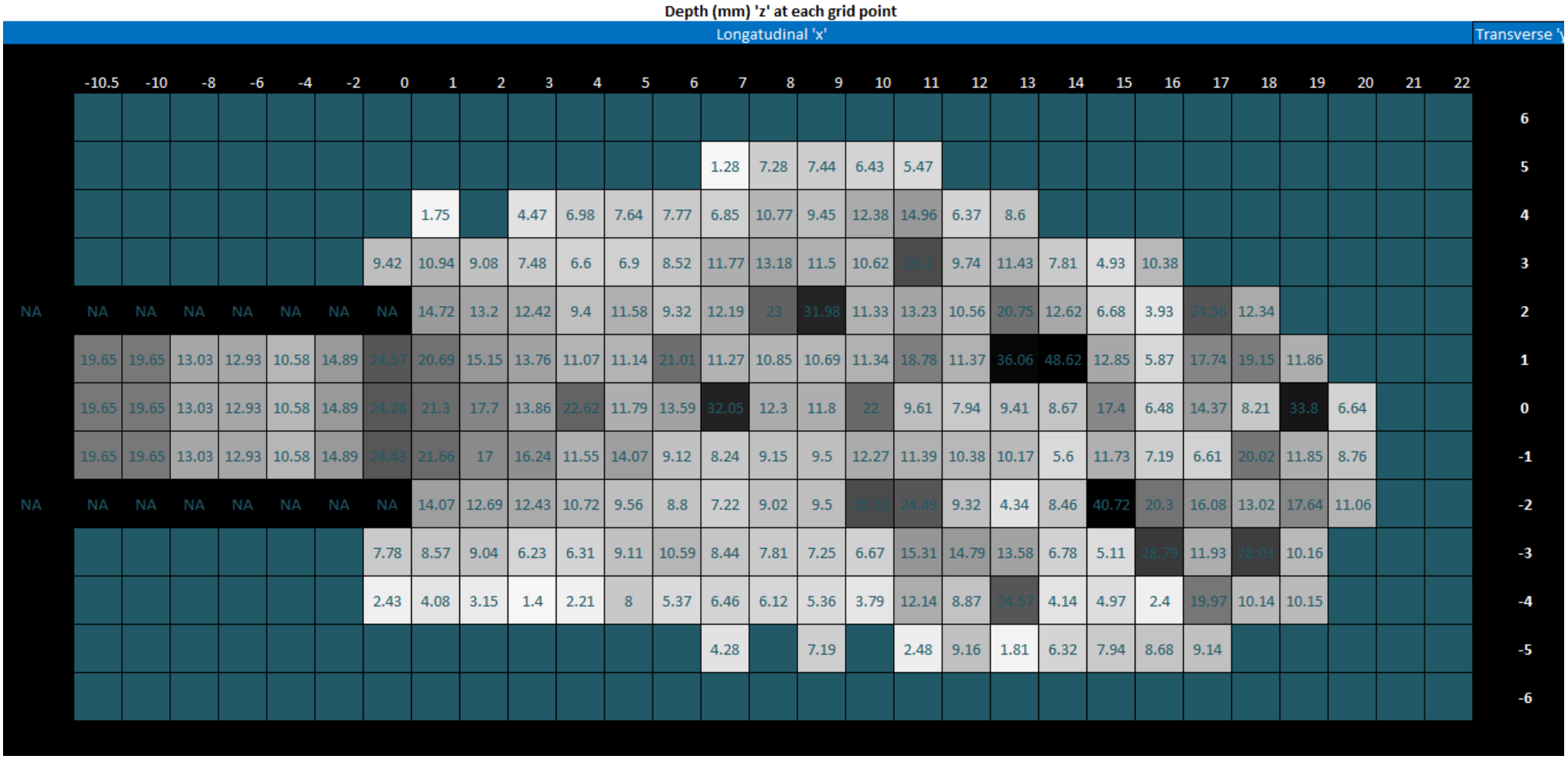

Figure E-16: Spot heights for S18W32EX4 with slope 18.1° and moisture content of 31.8%.

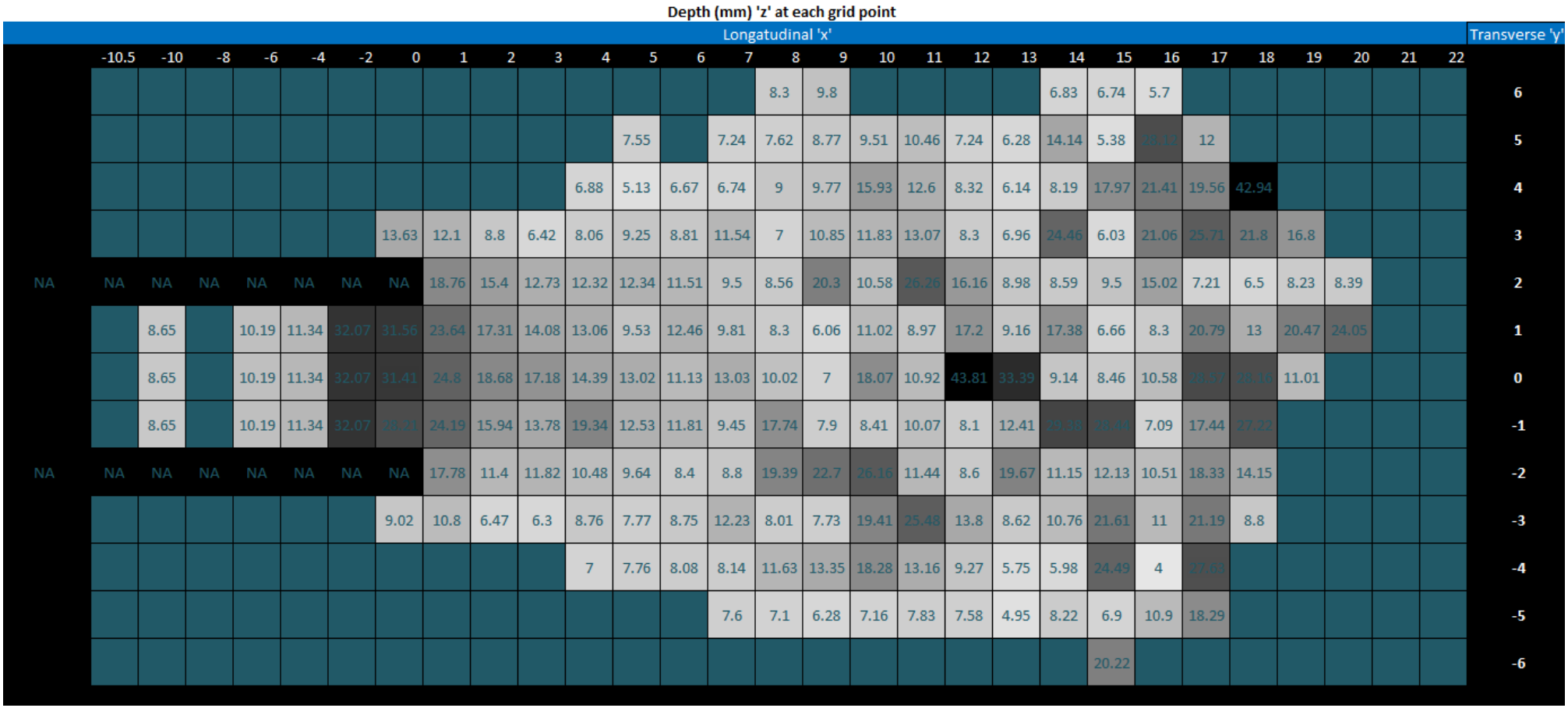

Figure E-17: Spot heights for S18W32EX2 with slope 18.1° and moisture content of 31.8%.

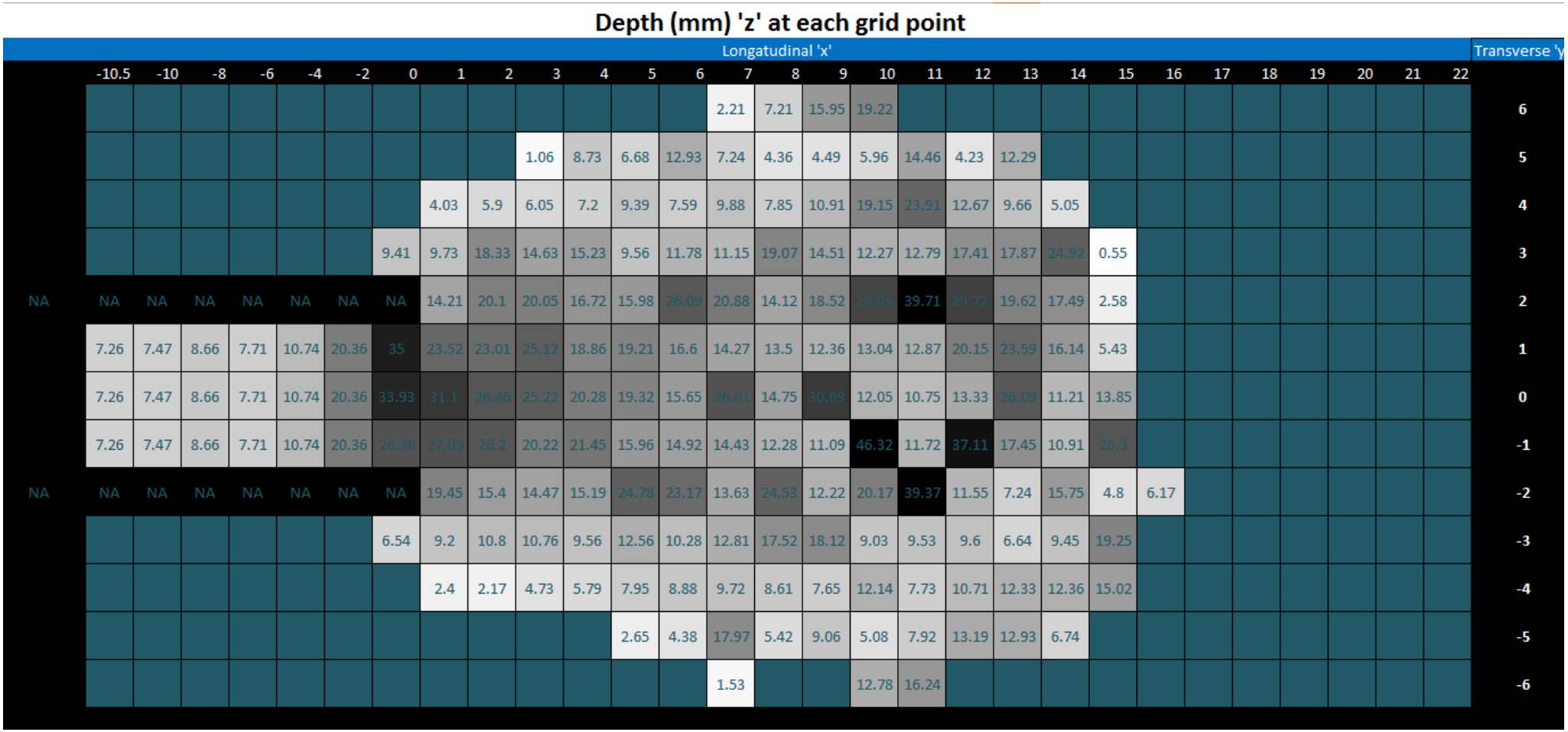

Figure E-18: Spot heights for S18W32IN2 with slope 18.1° and moisture content of 31.8%.

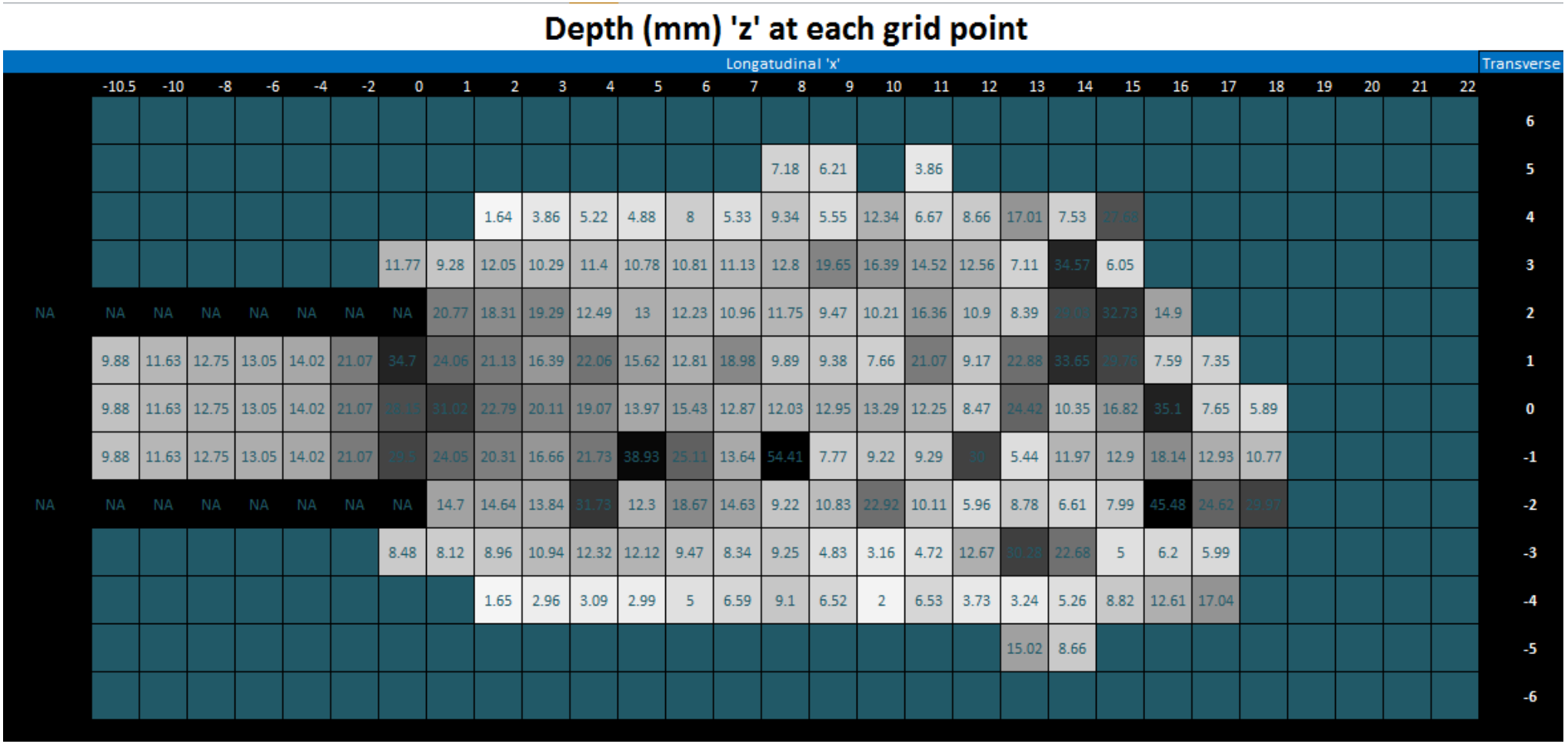

Figure E-19: Spot heights for S18W32IN6 with slope 18.1° and moisture content of 31.8%.

E.2.4. S18 W36

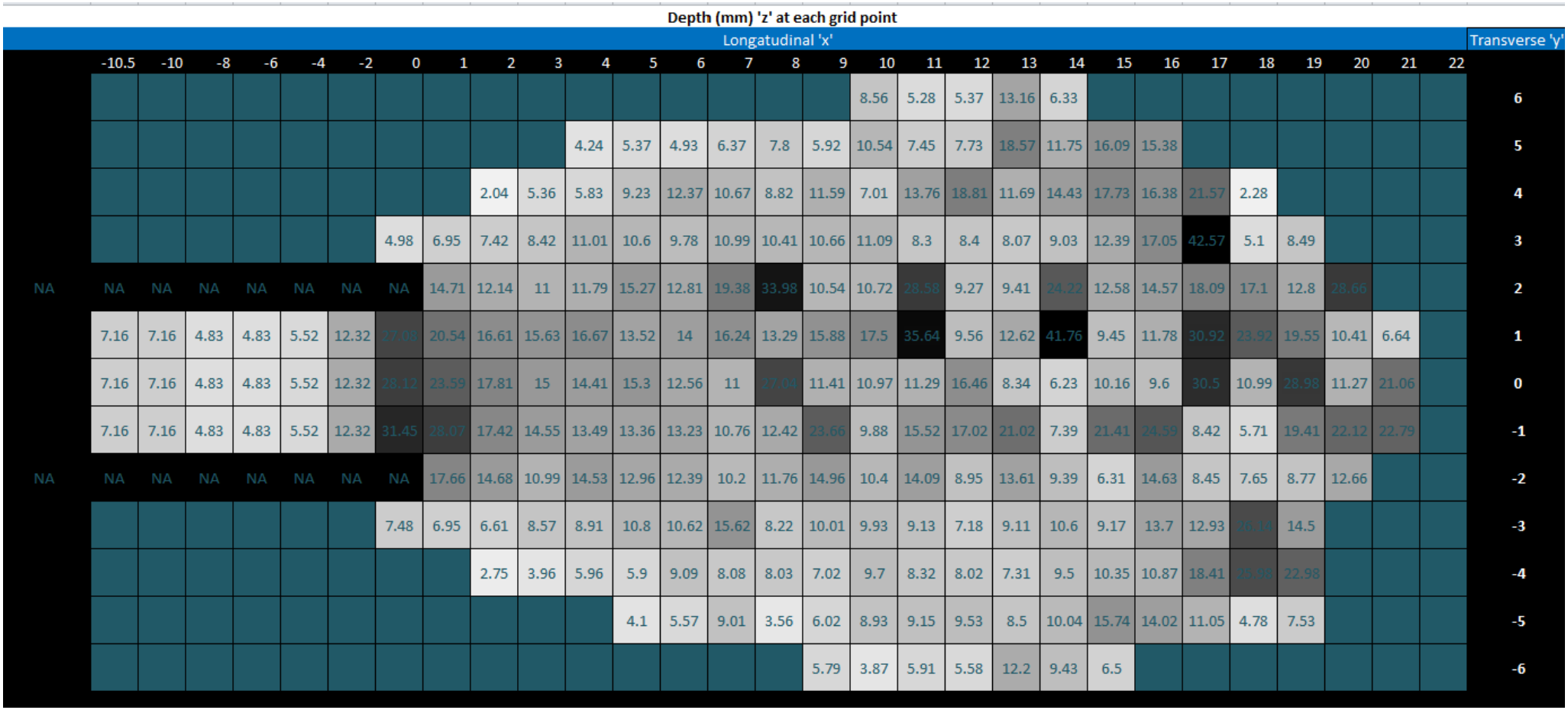

Depth (mm) 'z' at each grid point																													Transverse 'y'
Longatudinal 'x'																													
	-10.5	-10	-8	-6	-4	-2	0	1	2	3	4	5	6	7	8	9	10	11	12	13	14	15	16	17	18	19	20	21	22	
																	8.56	5.28	5.37	13.16	6.33									6
											4.24	5.37	4.93	6.37	7.8	5.92	10.54	7.45	7.73	18.57	11.75	16.09	15.38							5
									2.04	5.36	5.83	9.23	12.37	10.67	8.82	11.59	7.01	13.76	18.81	11.69	14.43	17.73	16.38	21.57	2.28					4
							4.98	6.95	7.42	8.42	11.01	10.6	9.78	10.99	10.41	10.66	11.09	8.3	8.4	8.07	9.03	12.39	17.05	42.57	5.1	8.49				3
NA	NA	NA	NA	NA	NA	NA	NA	14.71	12.14	11	11.79	15.27	12.81	19.38	33.98	10.54	10.72	28.58	9.27	9.41	24.22	12.58	14.57	18.09	17.1	12.8	28.66			2
	7.16	7.16	4.83	4.83	5.52	12.32	27.08	20.54	16.61	15.63	16.67	13.52	14	16.24	13.29	15.88	17.5	35.64	9.56	12.62	41.76	9.45	11.78	30.92	23.92	19.55	10.41	6.64		1
	7.16	7.16	4.83	4.83	5.52	12.32	28.12	23.59	17.81	15	14.41	15.3	12.56	11	27.04	11.41	10.97	11.29	16.46	8.34	6.23	10.16	9.6	30.5	10.99	28.98	11.27	21.06		0
	7.16	7.16	4.83	4.83	5.52	12.32	31.45	28.07	17.42	14.55	13.49	13.36	13.23	10.76	12.42	23.66	9.88	15.52	17.02	21.02	7.39	21.41	24.59	8.42	5.71	19.41	22.12	22.79		-1
NA	NA	NA	NA	NA	NA	NA	NA	17.66	14.68	10.99	14.53	12.96	12.39	10.2	11.76	14.96	10.4	14.09	8.95	13.61	9.39	6.31	14.63	8.45	7.65	8.77	12.66			-2
							7.48	6.95	6.61	8.57	8.91	10.8	10.62	15.62	8.22	10.01	9.93	9.13	7.18	9.11	10.6	9.17	13.7	12.93	26.14	14.5				-3
									2.75	3.96	5.96	5.9	9.09	8.08	8.03	7.02	9.7	8.32	8.02	7.31	9.5	10.35	10.87	18.41	25.98	22.98				-4
												4.1	5.57	9.01	3.56	6.02	8.93	9.15	9.53	8.5	10.04	15.74	14.02	11.05	4.78	7.53				-5
																5.79	3.87	5.91	5.58	12.2	9.43	6.5								-6

Figure E-20: Spot heights for S18W32EX3 with slope 18.1° and moisture content of 35.8%.

Depth (mm) 'z' at each grid point

Transverse 'y' \ Longatudinal 'x'	-10.5	-10	-8	-6	-4	-2	0	1	2	3	4	5	6	7	8	9	10	11	12	13	14	15	16	17	18	19	20	21	22
6														2.02	6.41	7.86	7.48	7.15	5.69	9.82		3.95	4.93						
5												4.49	2.97	6.79	6.55	4.88	4.51	7.66	11.65	11.22	10.99	6.53	2.21	12.23					
4									2.53	3.26	3.81	5.23	7.56	9.06	9.87	9.16	10.03	7.85	9.94	14.65	9.45	9.34	9.08	6.72	15.77	6.2			
3							8.32	7.36	7.55	9.13	9.34	7.33	8.98	11.7	7.24	10.26	17.1	13.02	9.63	8.38	15.99	9.86	10.63	10.65	15.53	6.82			
2	NA	NA	NA	NA	NA	NA	NA	16.28	13.05	12.53	13.31	12.26	13.38	20.53	18.05	6.88	8.54	13.19	7.44	8.5	23.67	9.83	16.71	26.39	14.87				
1	8.74	8.74	10.86	8.74	10.61	17.36	29.86	22.11	16.98	27.02	14.04	12.11	13.28	9.7	8.7	6.73	35.62	27.94	13.47	11.06	9.22	9.49	24.6	30.52	23.87	21.9			
0	8.74	8.74	10.86	8.74	10.61	17.36	30.94	24.75	19.01	15.77	16.38	15.98	13.12	13.91	9.61	6.75	9.17	9.06	8	10.39	22.94	20.44	6.3	7.58	16.32	8.01	19.1		
-1	8.74	8.74	10.86	8.74	10.61	17.36	30.48	24.4	17.65	16.01	14.41	12.58	11.81	10.06	8.11	15.68	15.69	26.14	28.29	7.97	23.44	23.44	47.29	11.79	15.29	15.33			
-2	NA	NA	NA	NA	NA	NA	NA	20.16	14.02	13.61	13.56	10.02	11.64	11.09	8.08	8.45	6.83	7.14	20.02	7.38	7.18	16.77	9.03	12.62	21.98	17.12			
-3							10.15	11.83	6.47	10.04	9.18	12.41	13.58	14.5	17.75	8.09	22.38	7.44	12.4	8.73	7.46	6.67	19.07	23.79	38.91				
-4							4.22	3.97	2.61	4.1	3.63	5.4	10.65	4.41	5.79	5.8	13.95	14.98	4.45	14.22	28	5.24	6.36	21.95					
-5											1.64	3.41	4.26	5.34	8.07	3.9	4.34	6.89	3.68	10.29	19.37	2.72	15.35	9.78					
-6																1.22	10.99		2.57	11.42	9.6		26.54						

Figure E-21: Spot heights for S18W32EX5 with slope 18.1° and moisture content of 35.8%.

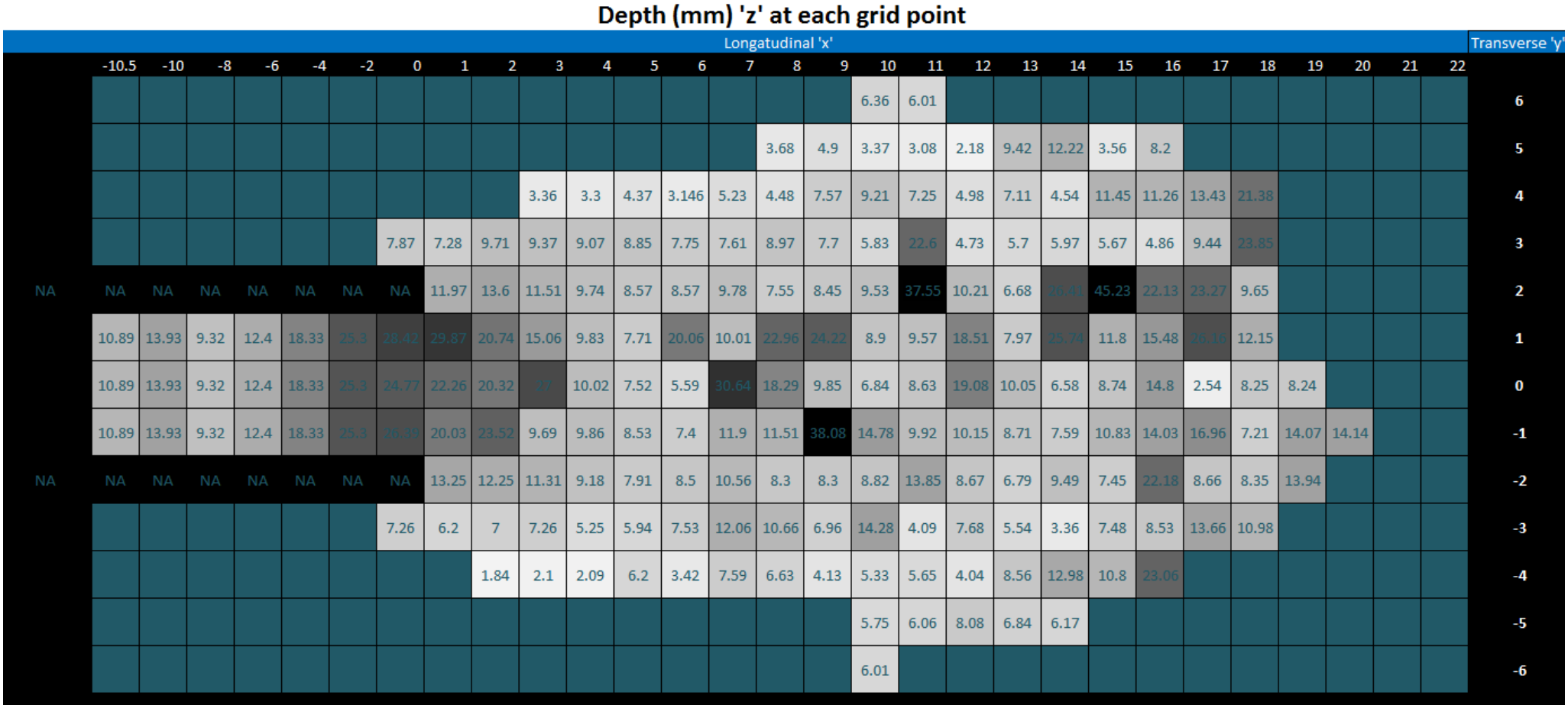

Figure E-22: Spot heights for S18W32IN3 with slope 18.1° and moisture content of 35.8%.

E.2.1. S24 W28

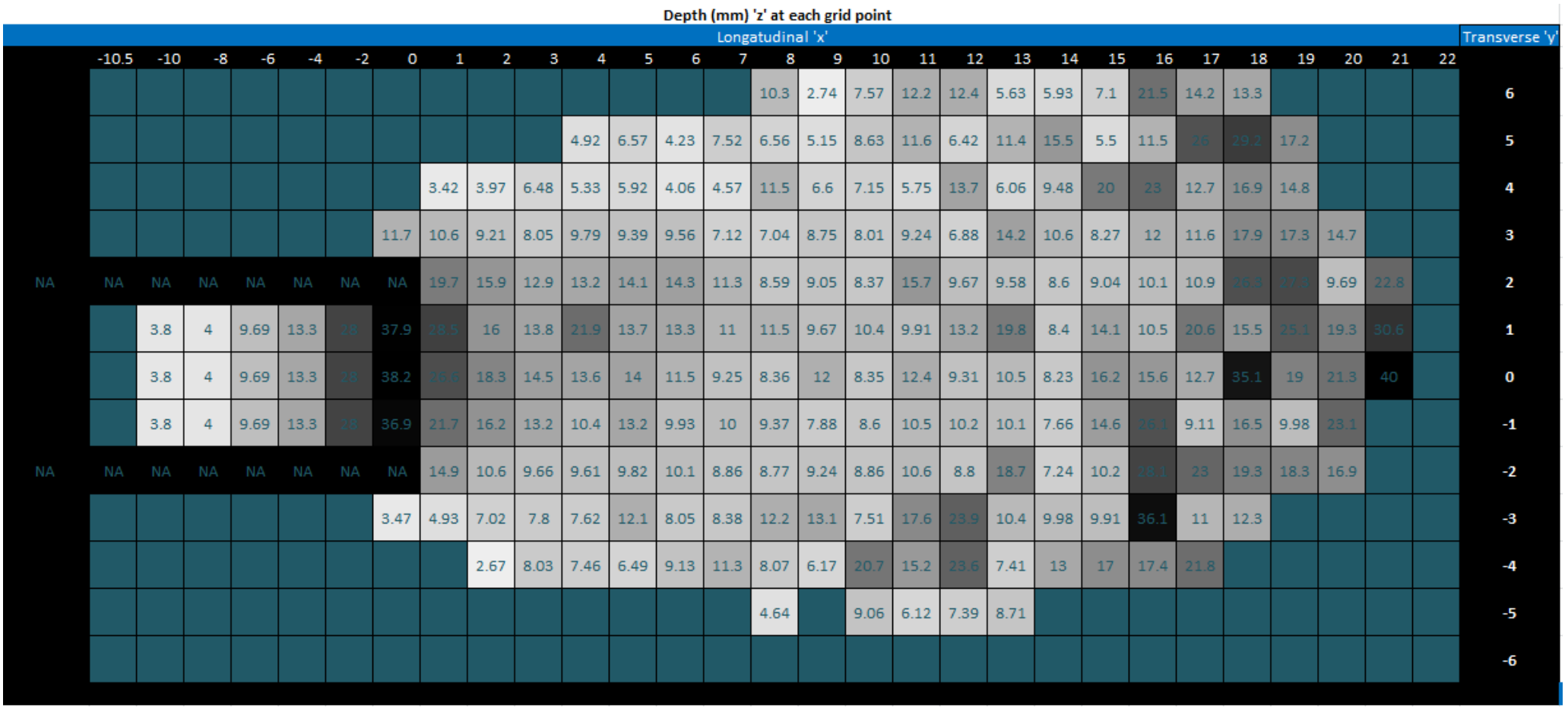

Figure E-23: Spot heights for S18W28EX7 with slope 24.5° and moisture content of 27.8%.

E.2.2. S24 W32

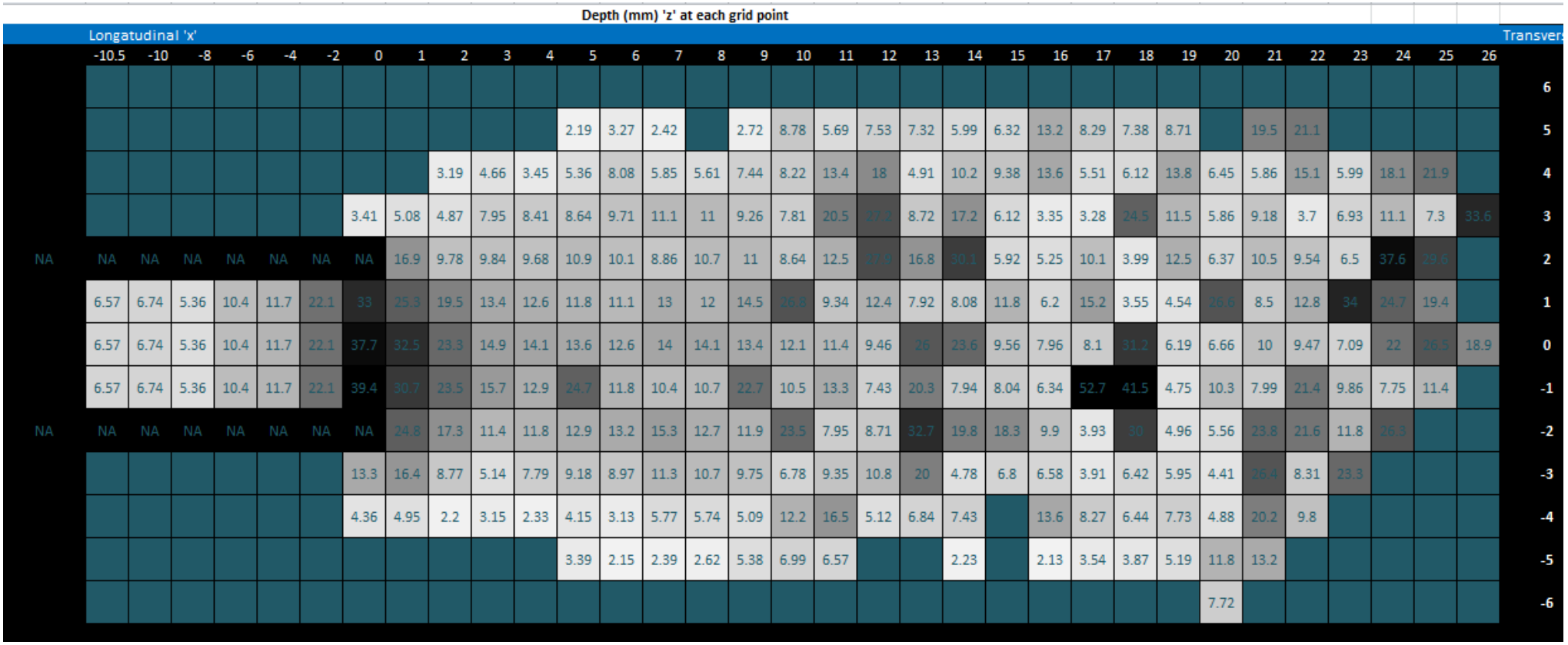

Figure E-24: Spot heights for S18W32IN7 with slope 24.5° and moisture content of 31.8%.

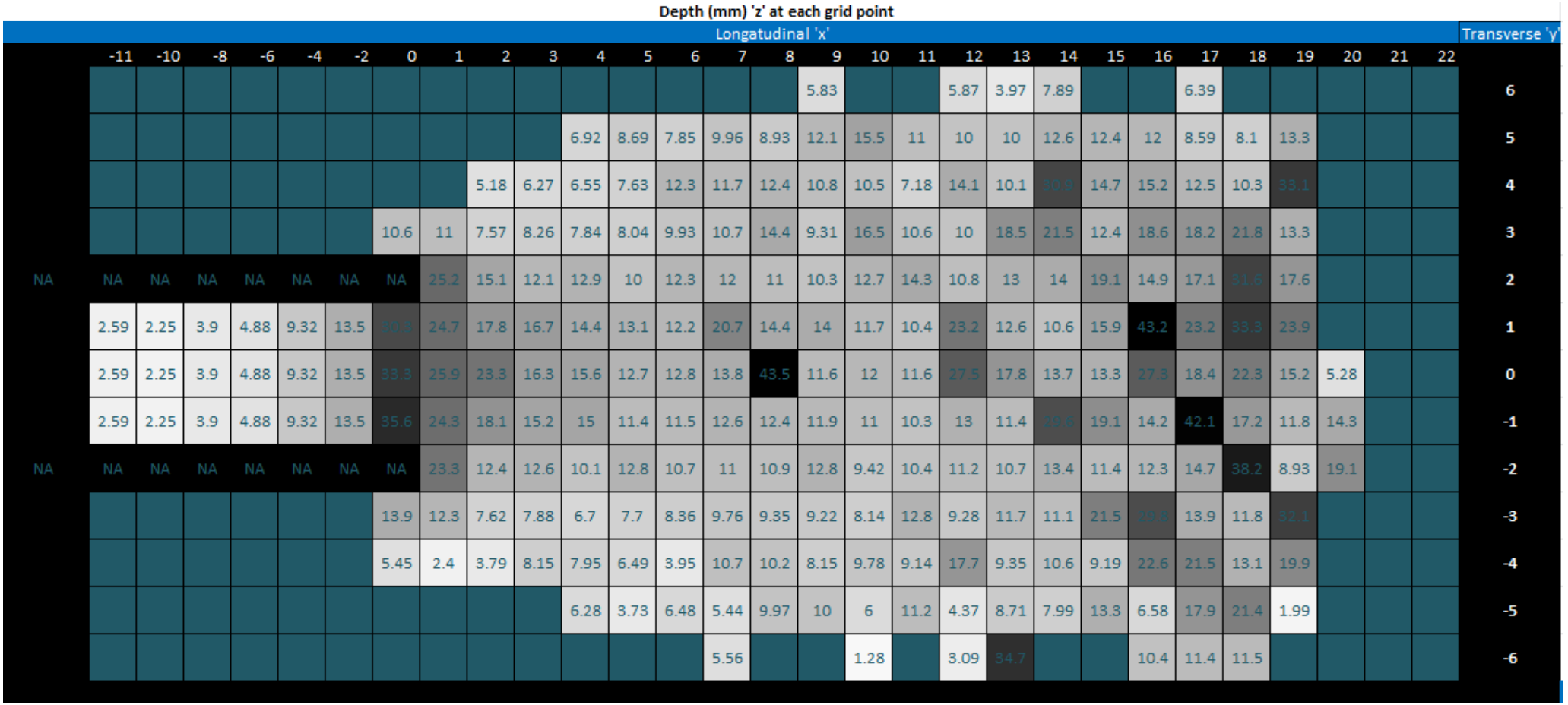

Figure E-25: Spot heights for S18W32EX7 with slope 24.5° and moisture content of 31.8%.

E.3. PSD

E.3.1. S18 – W24

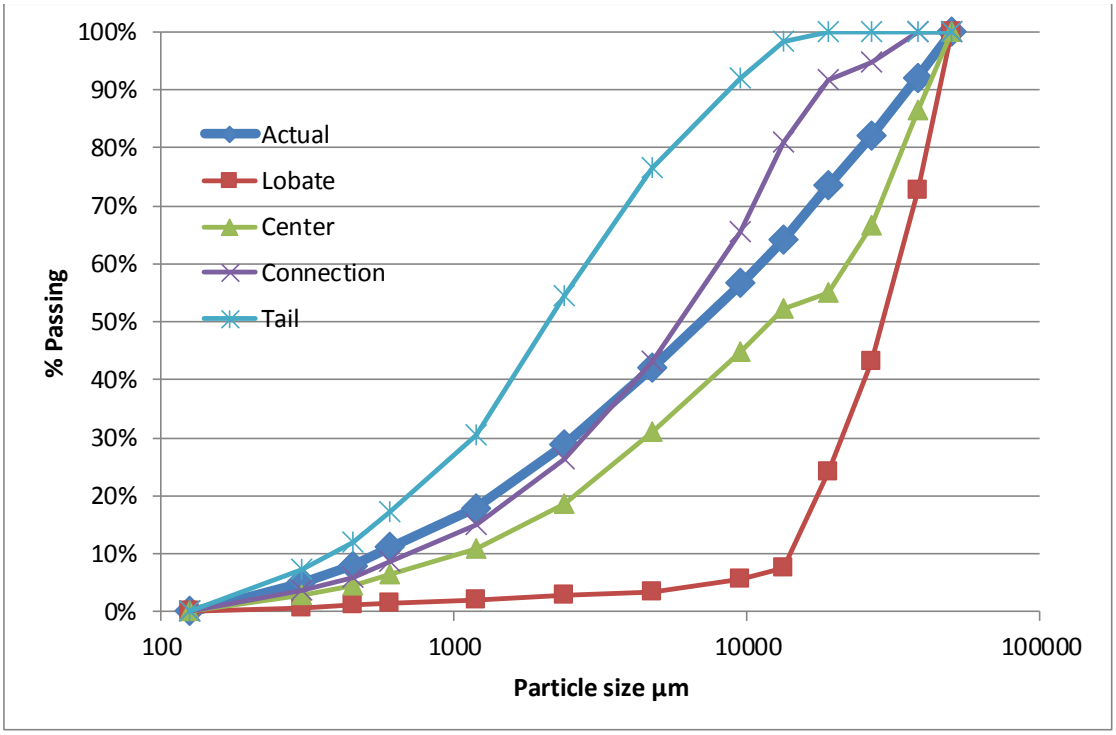

Figure E-26: PSD for S18W24IN5.

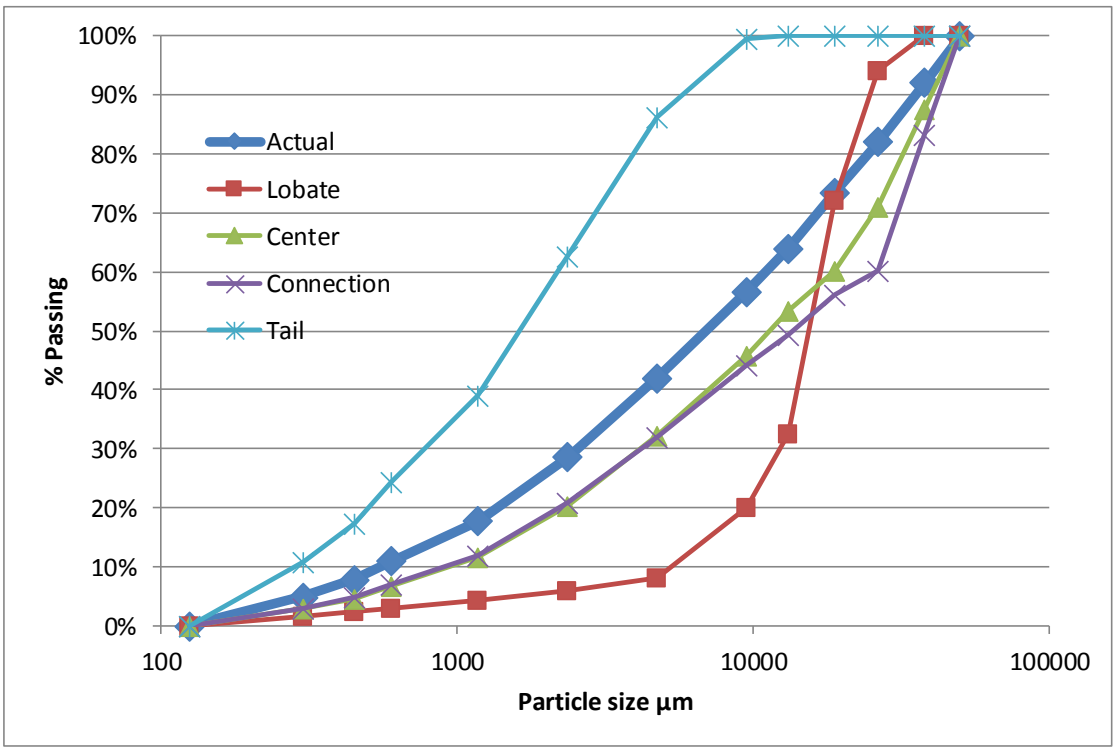

Figure E-27: PSD for S18W24EX6.

E.3.2. S18 – W28

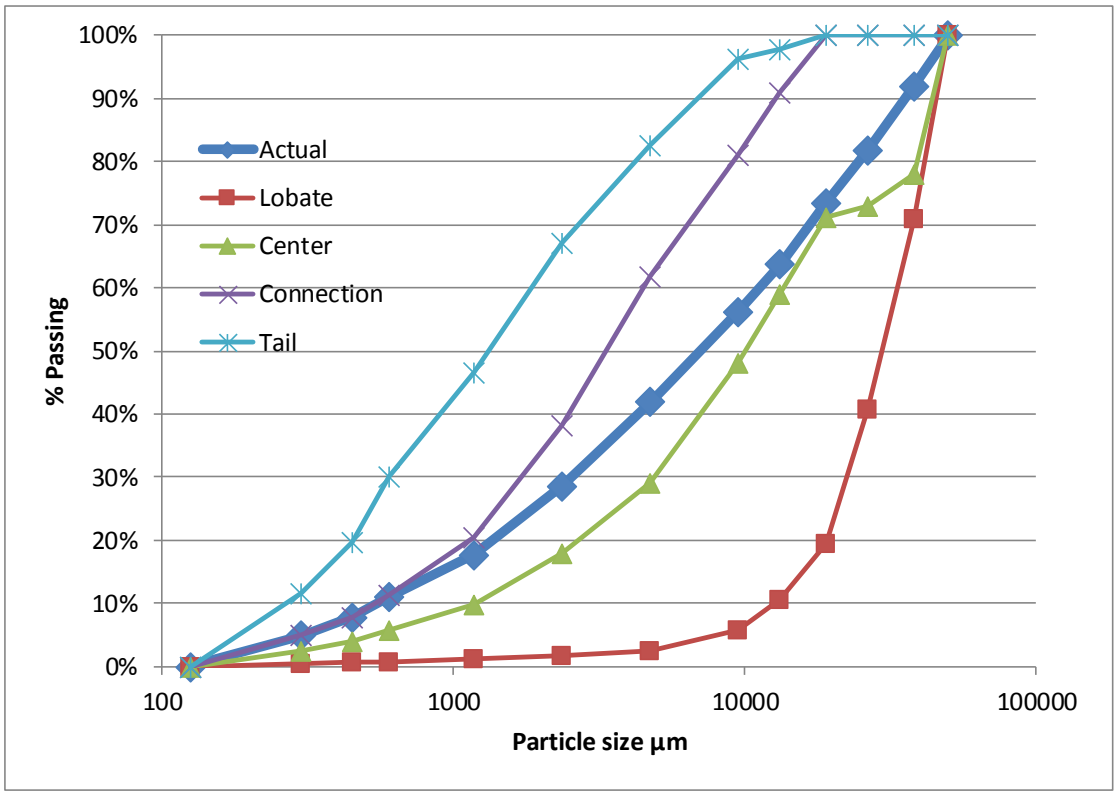

Figure E-28: PSD for S18W28IN0a.

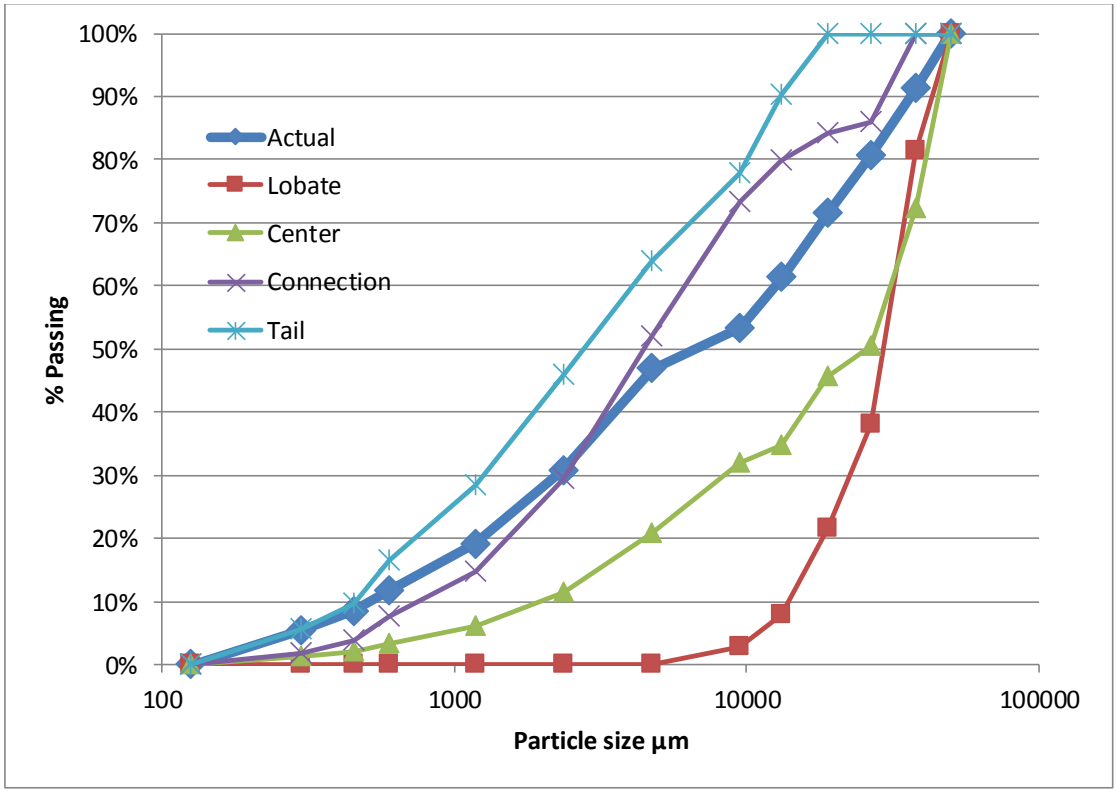

Figure E-29: PSD for S18W28IN0d.

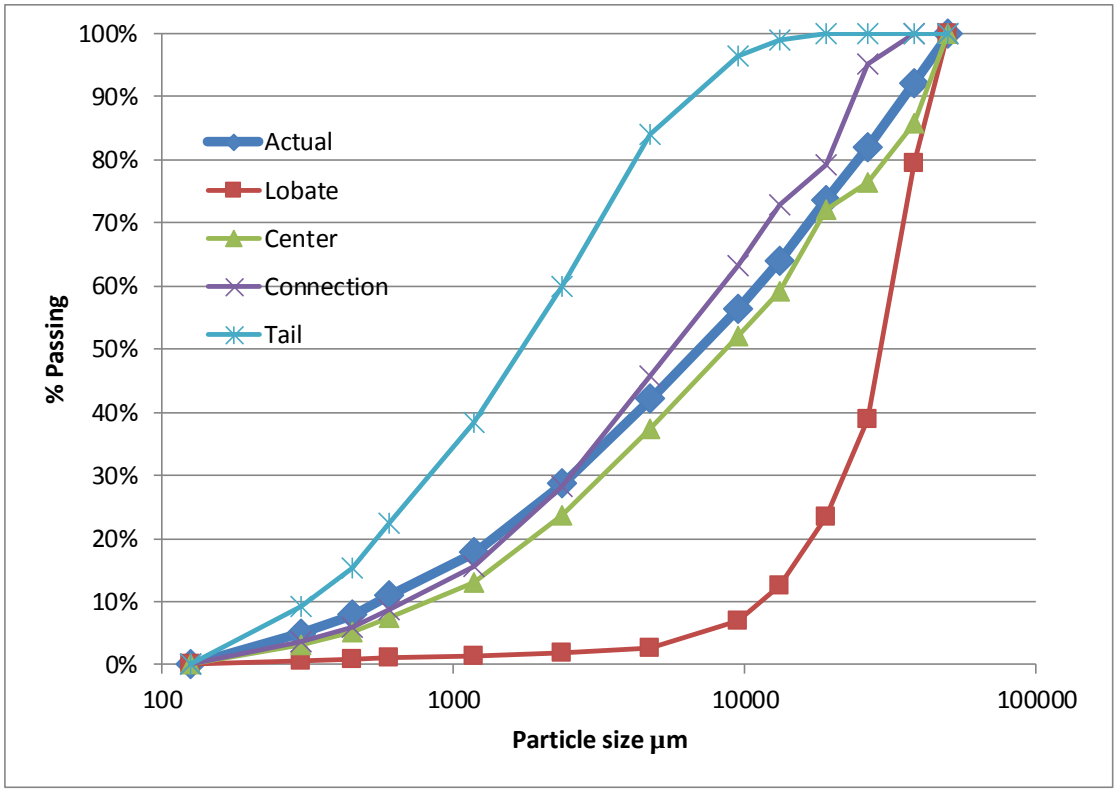

Figure E-30: PSD for S18W28IN1.

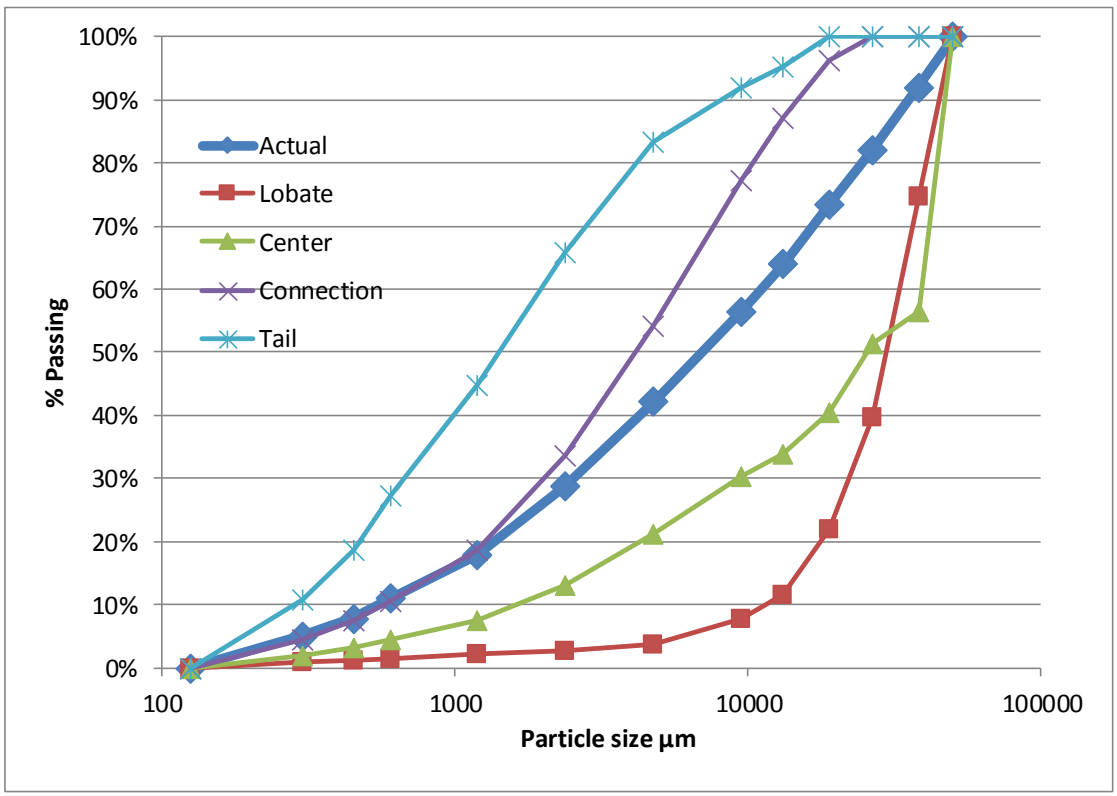

Figure E-31: PSD for S18W28IN4.

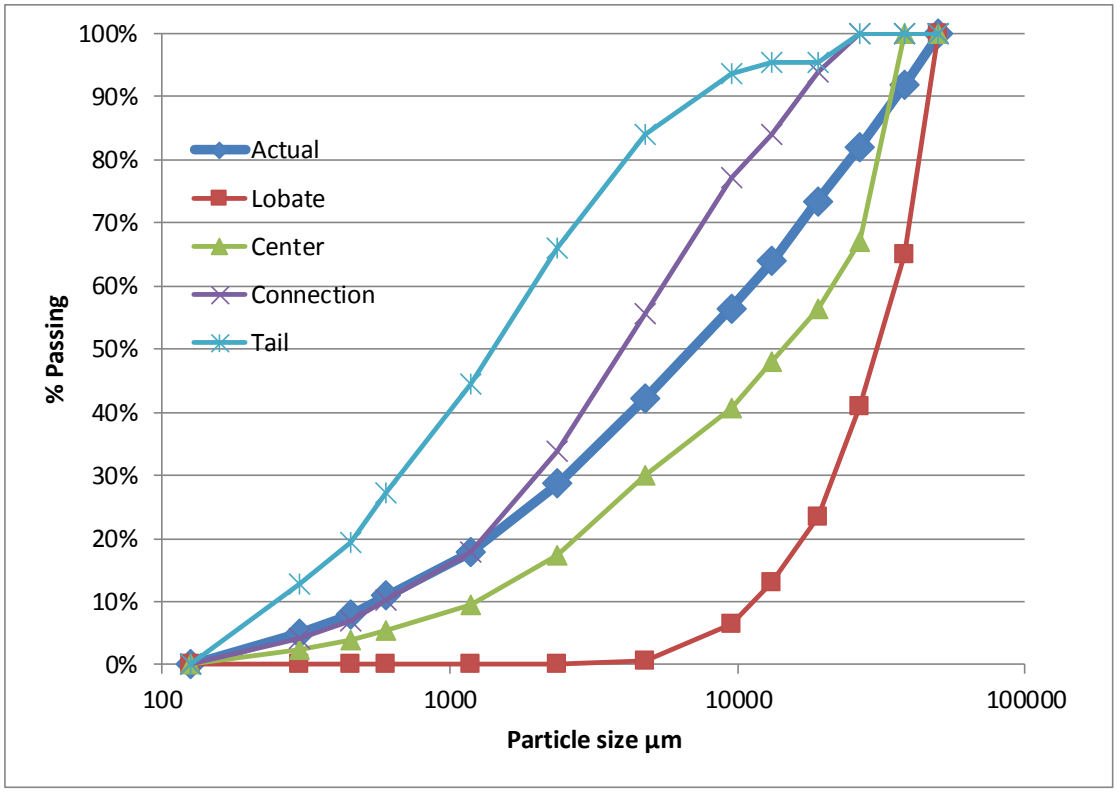

Figure E-32: PSD for S18W28EX1.

E.3.3. S18 – W32

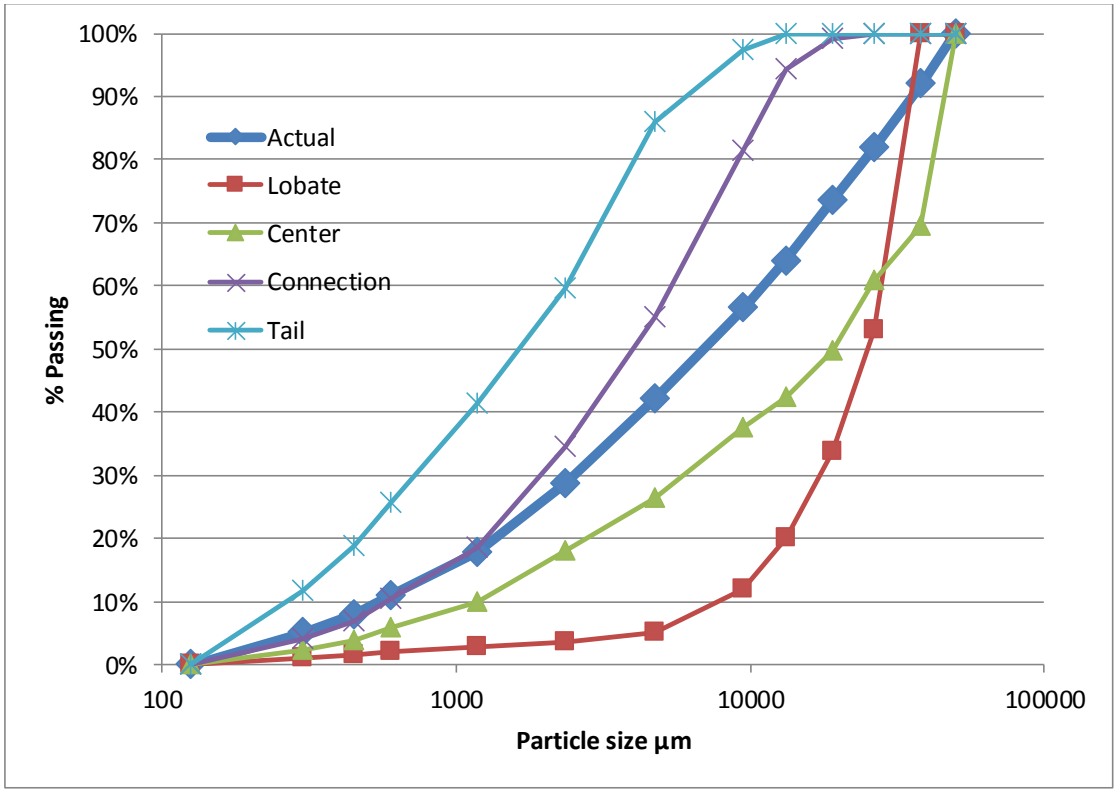

Figure E-33: PSD for S18W32IN2.

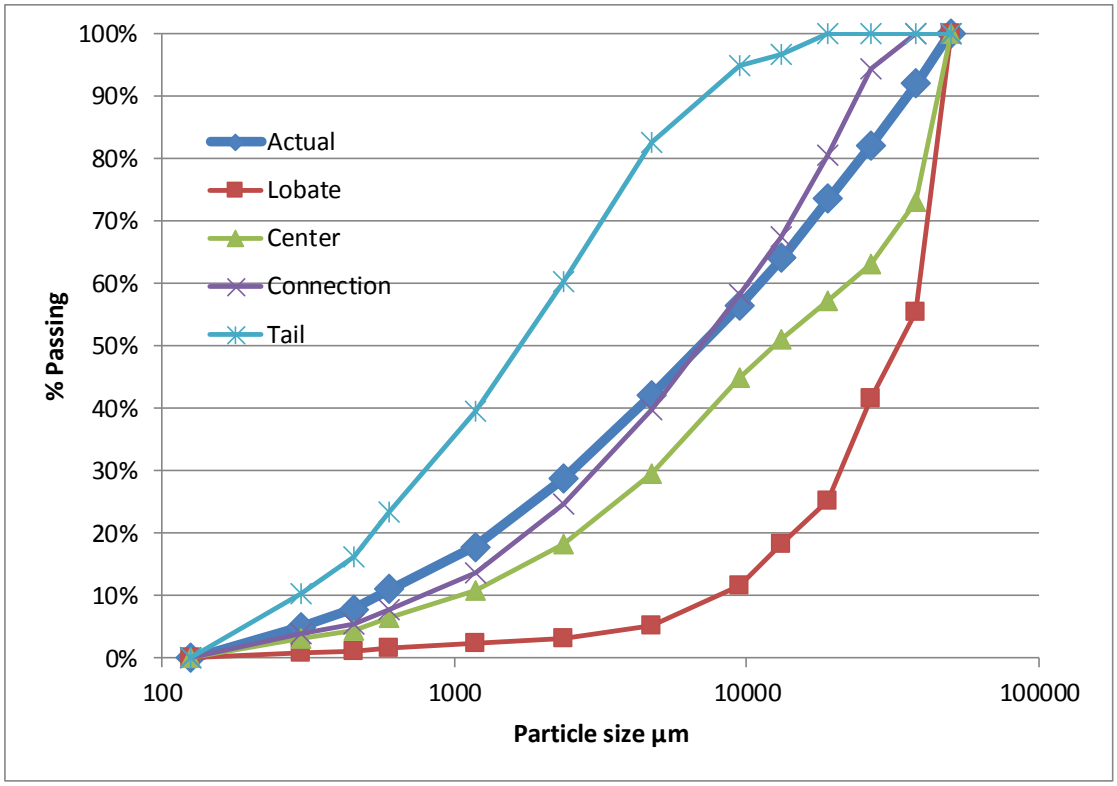

Figure E-34: PSD for S18W32IN6.

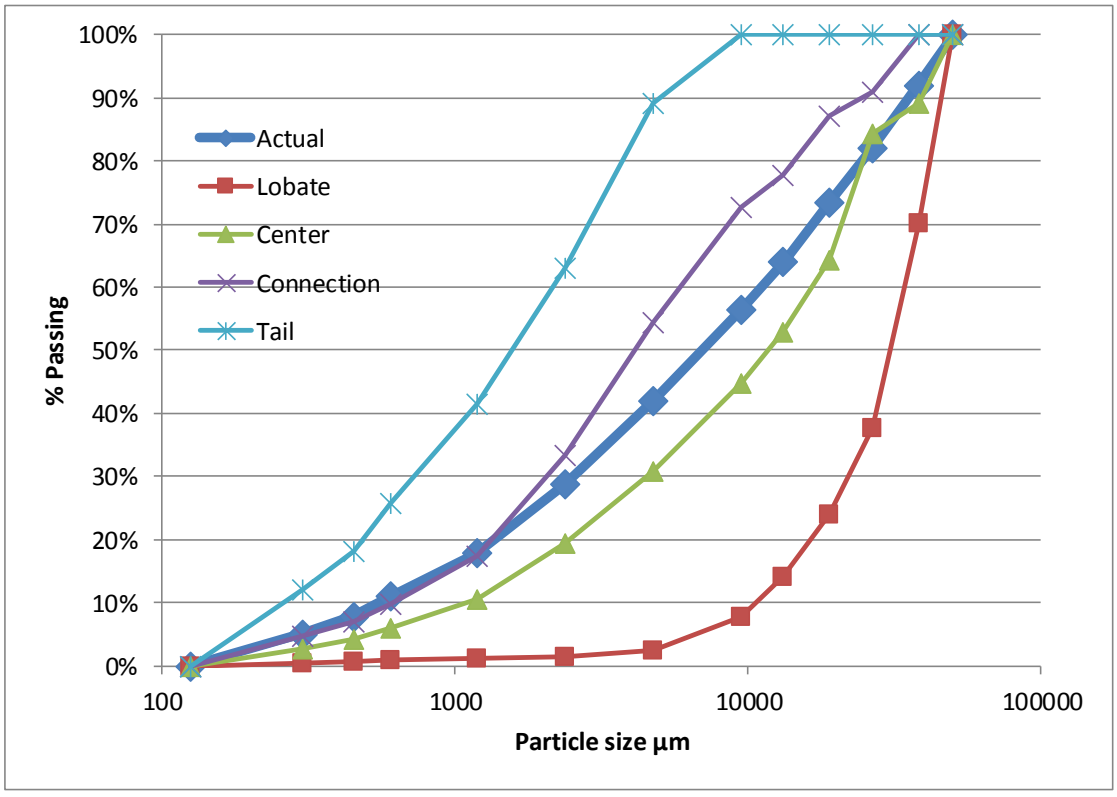

Figure E-35: PSD for S18W32EX2.

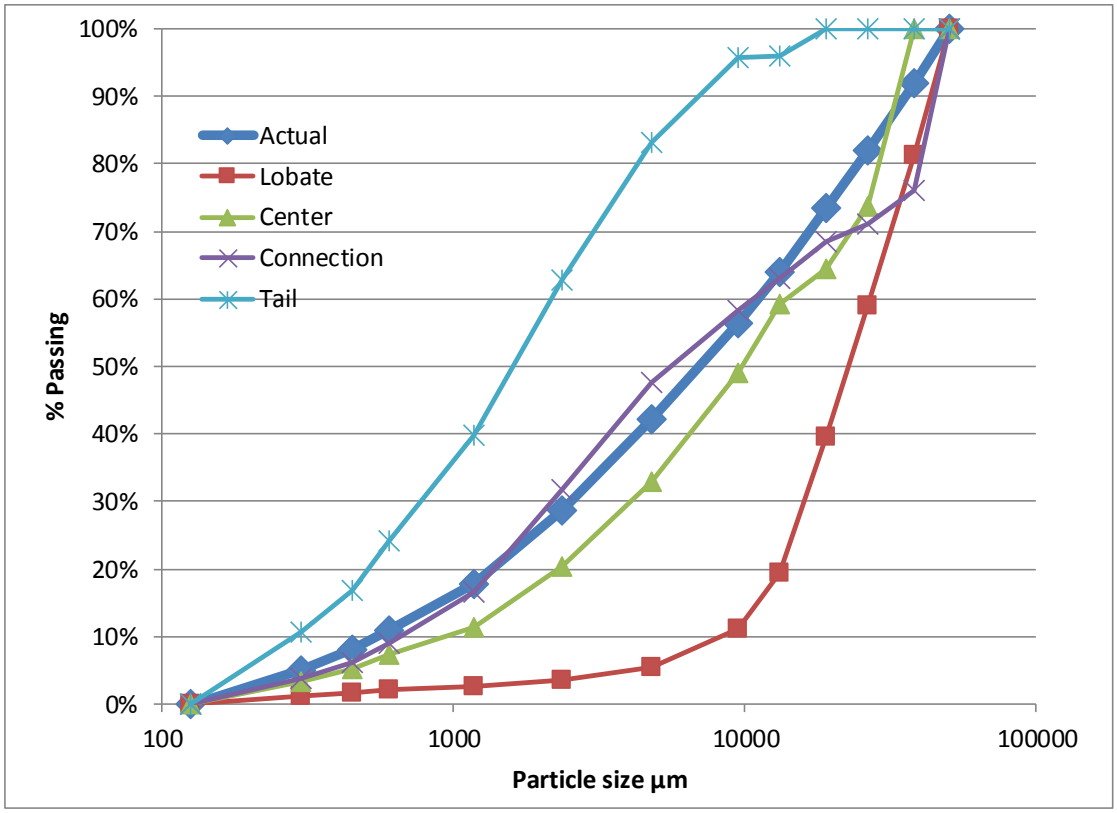

Figure E-36: PSD for S18W32EX4.

E.3.4. S18 – W36

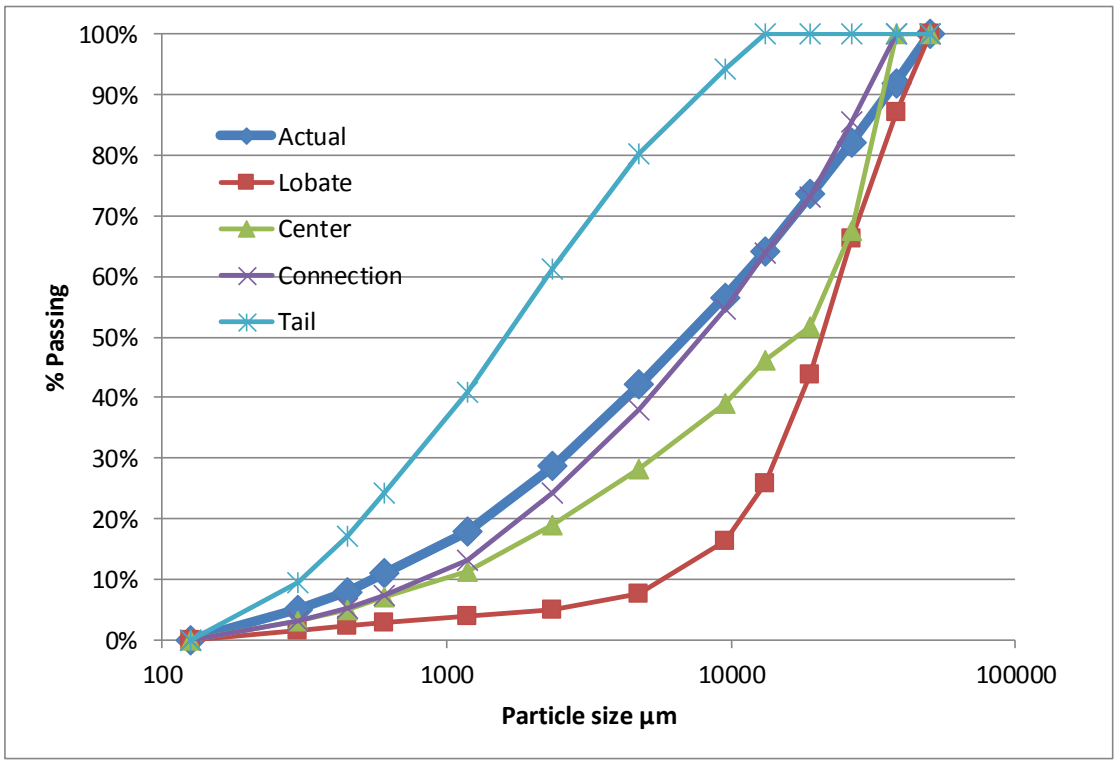

Figure E-37: PSD for S18W36IN3.

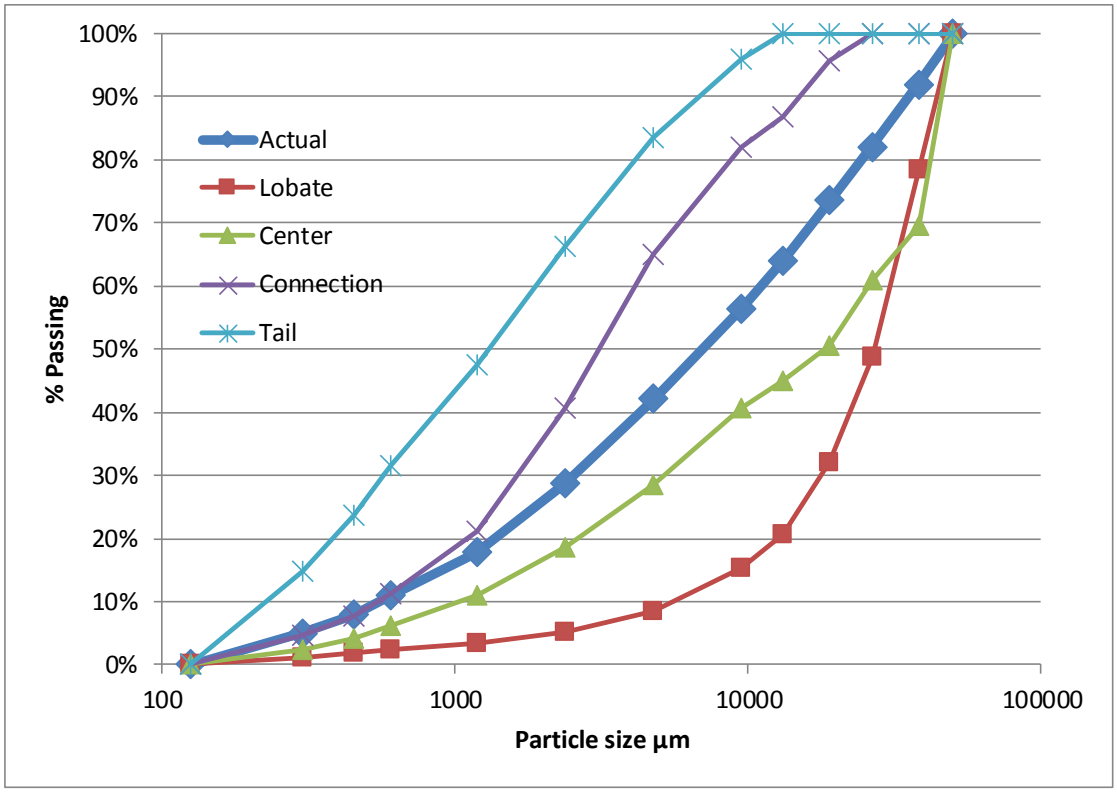

Figure E-38: PSD for S18W36EX3.

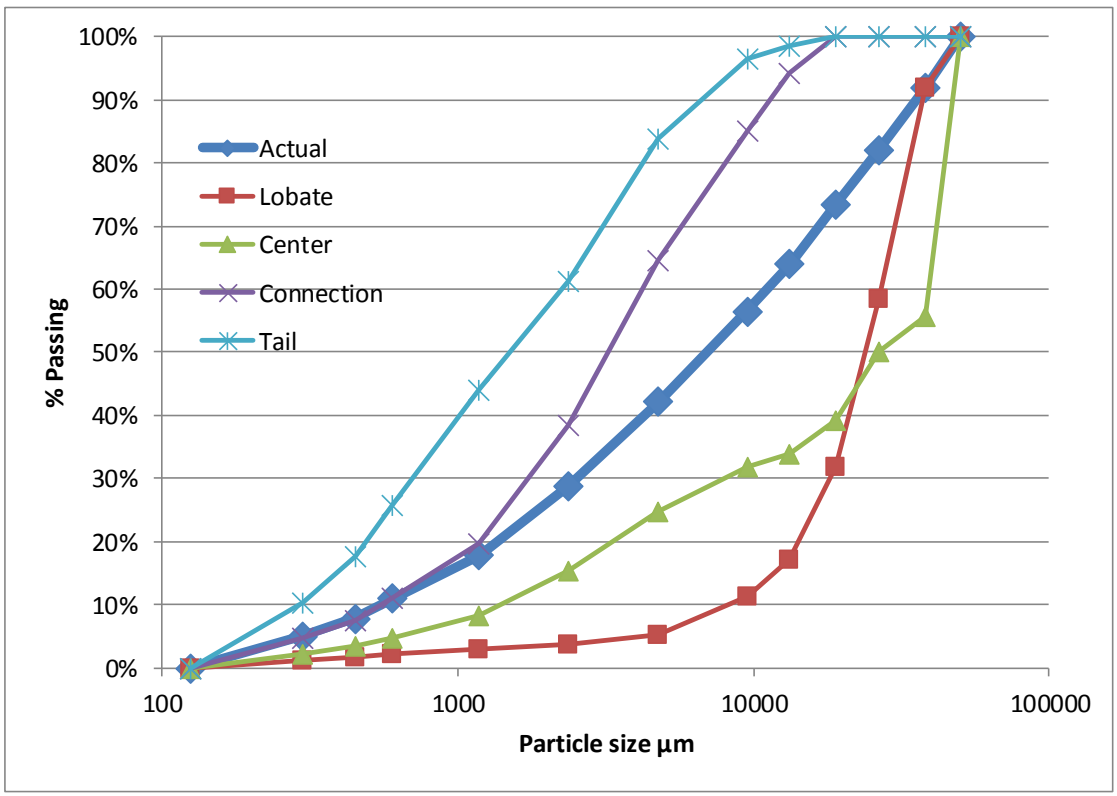

Figure E-39: PSD for S18W36EX5.

E.3.5. S24 – W28

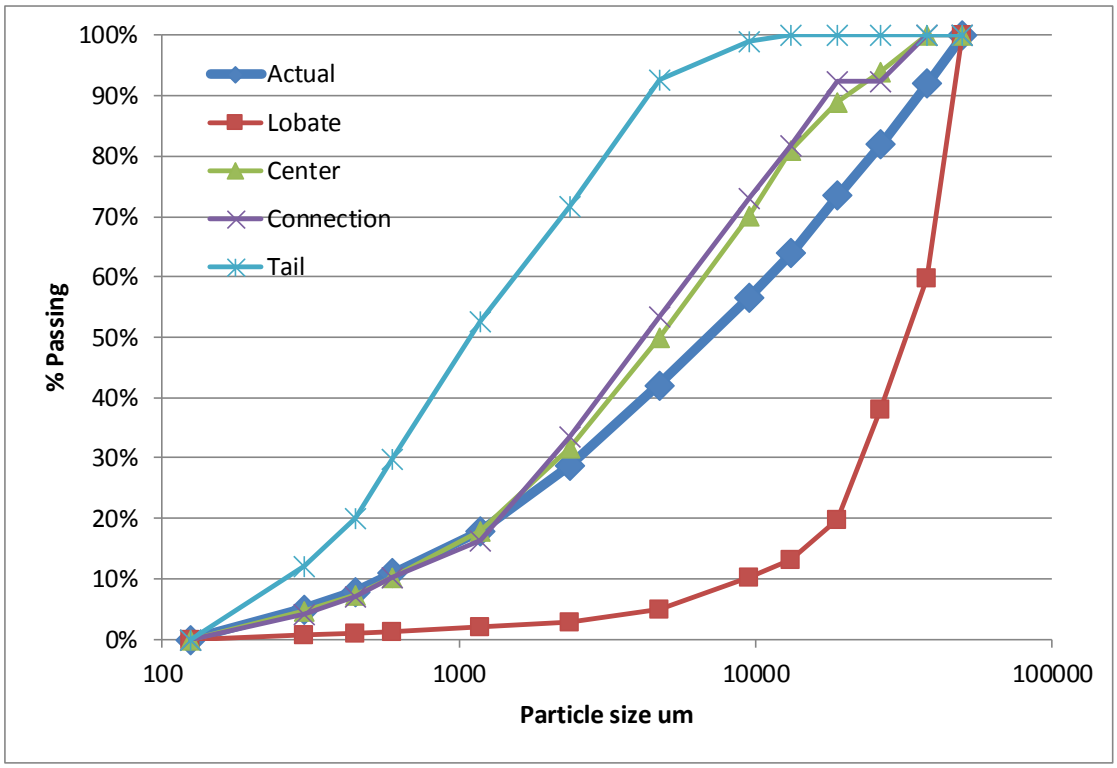

Figure E-40: PSD for S24W28EX8.

E.3.6. S24 – W32

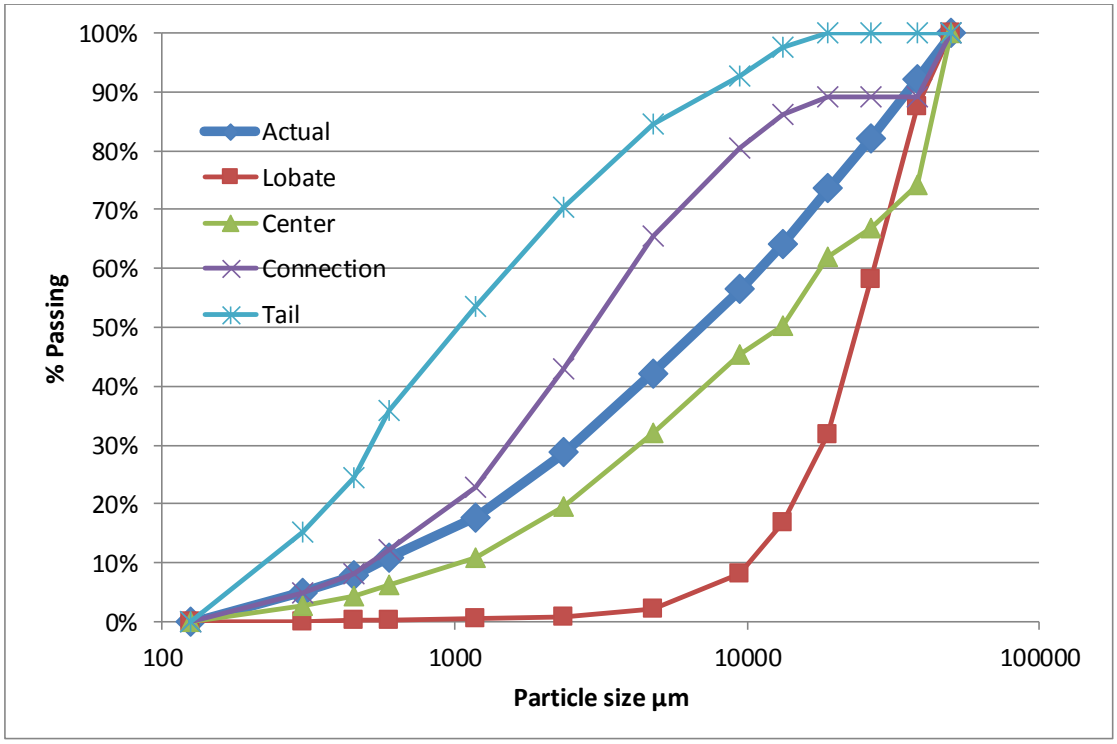

Figure E-41: PSD for S24W32IN7.

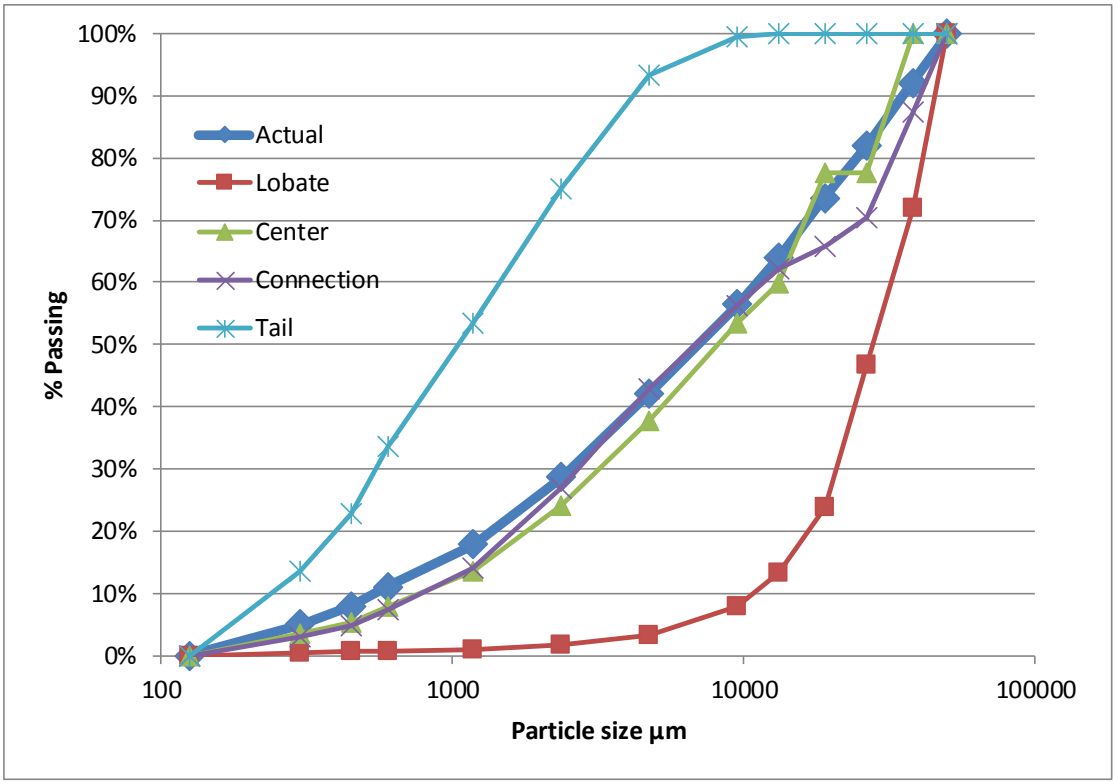

Figure E-42: PSD for S24W32IN8.

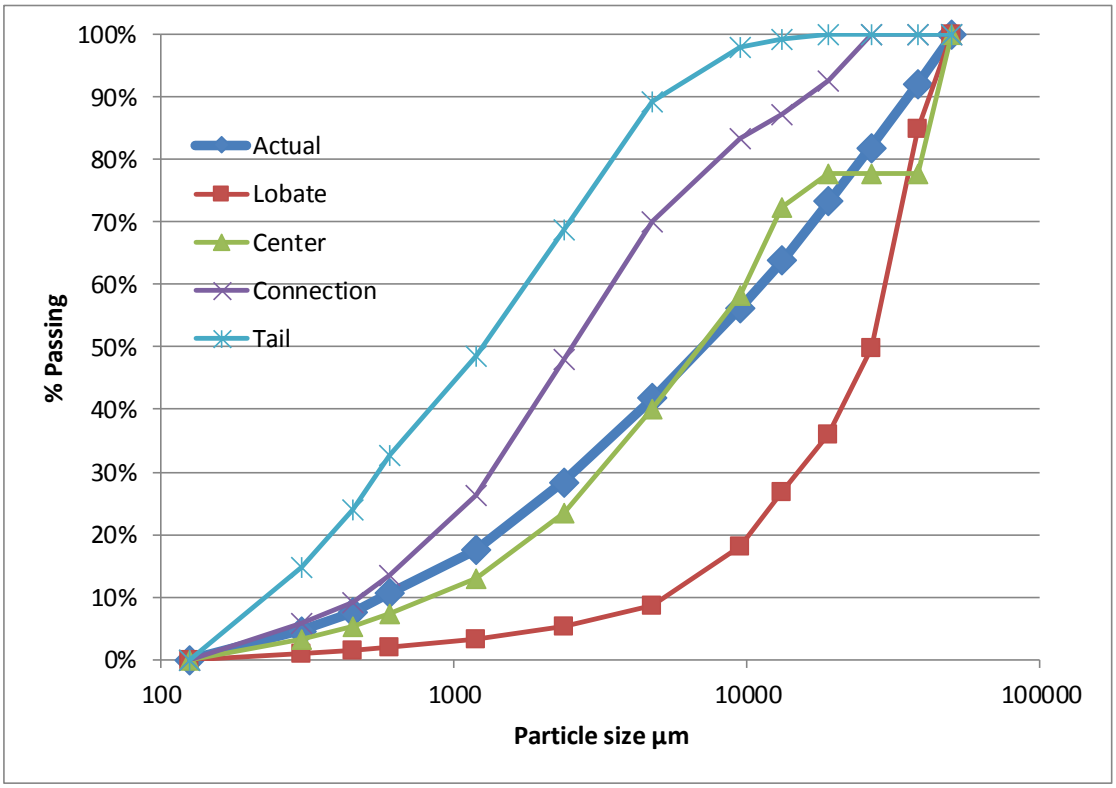

Figure E-43: PSD for S24W32EX7.

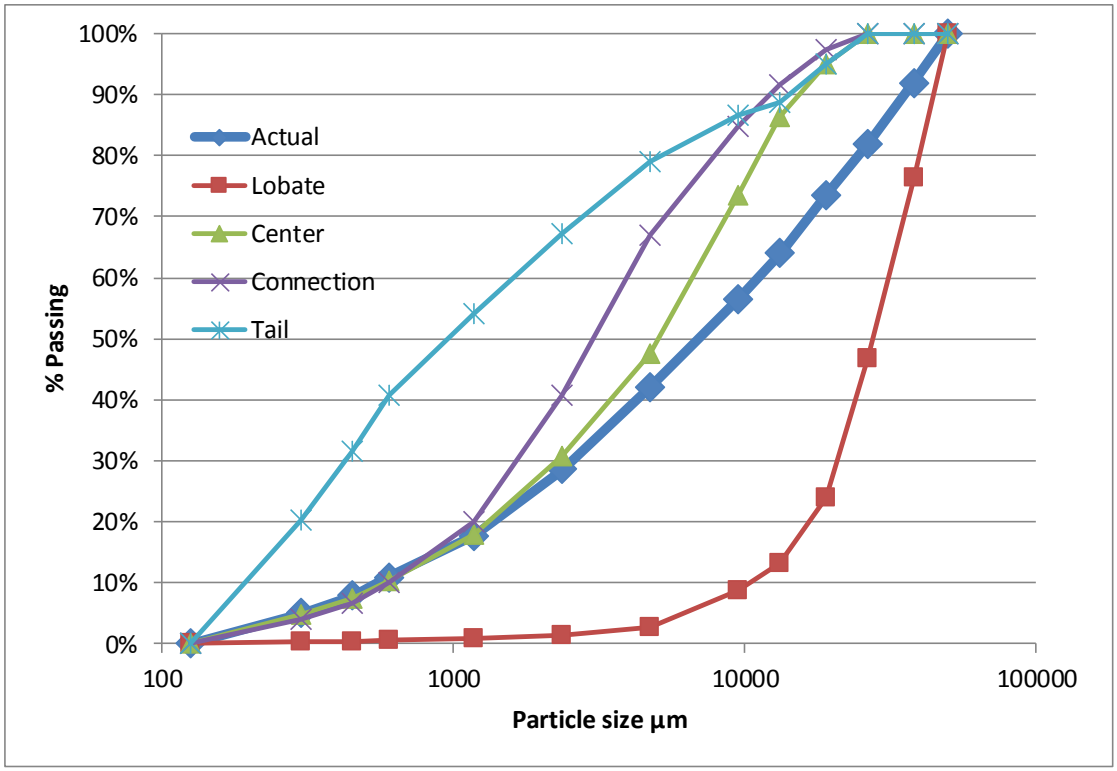

Figure E-44: PSD for S24W32EX9.

Appendix F: Height Over Time Analysis

F.1. Saturation and Absolute Maximum Heights for Recorded Flow

Note that the graphs in this section have different time sampling rates. The front and body are samples at 0.05 or 0.1 s and the tail is samples at 0.5s.

F.1.1. S18 – W24

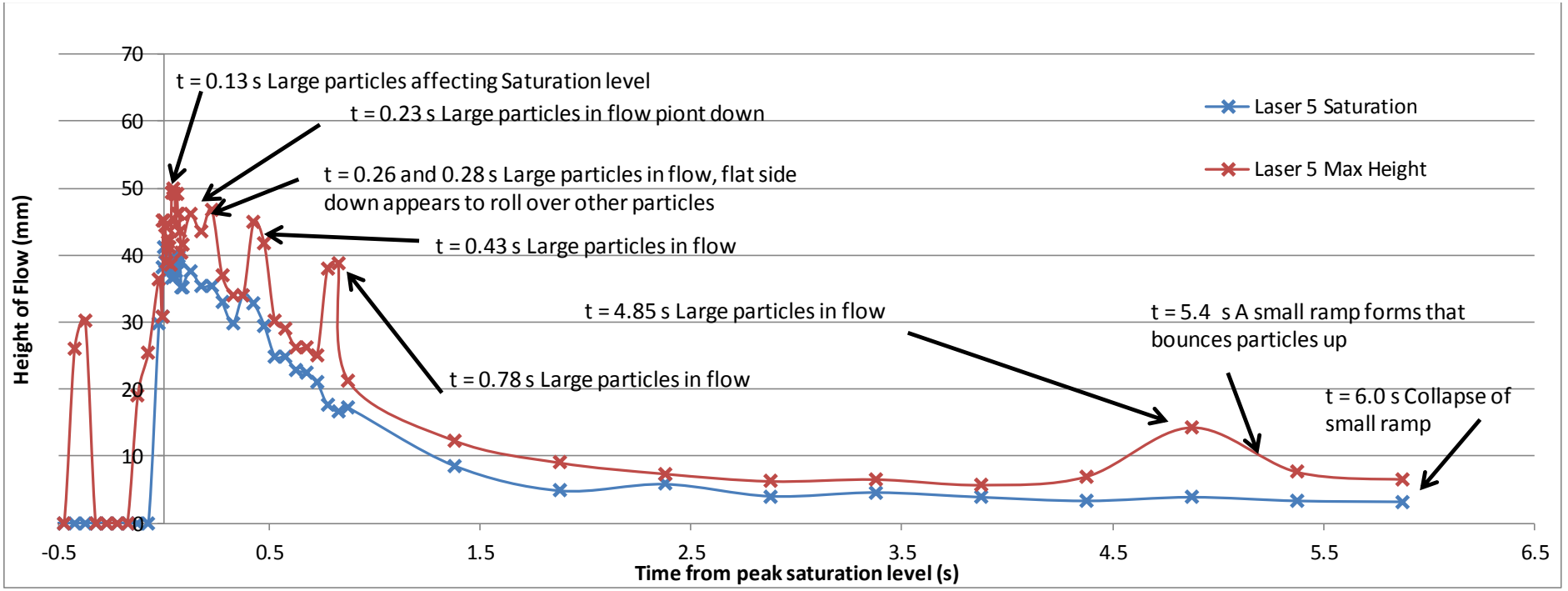

Figure F-1: Heights for S18W24IN5

F.1.2. S18 – W28

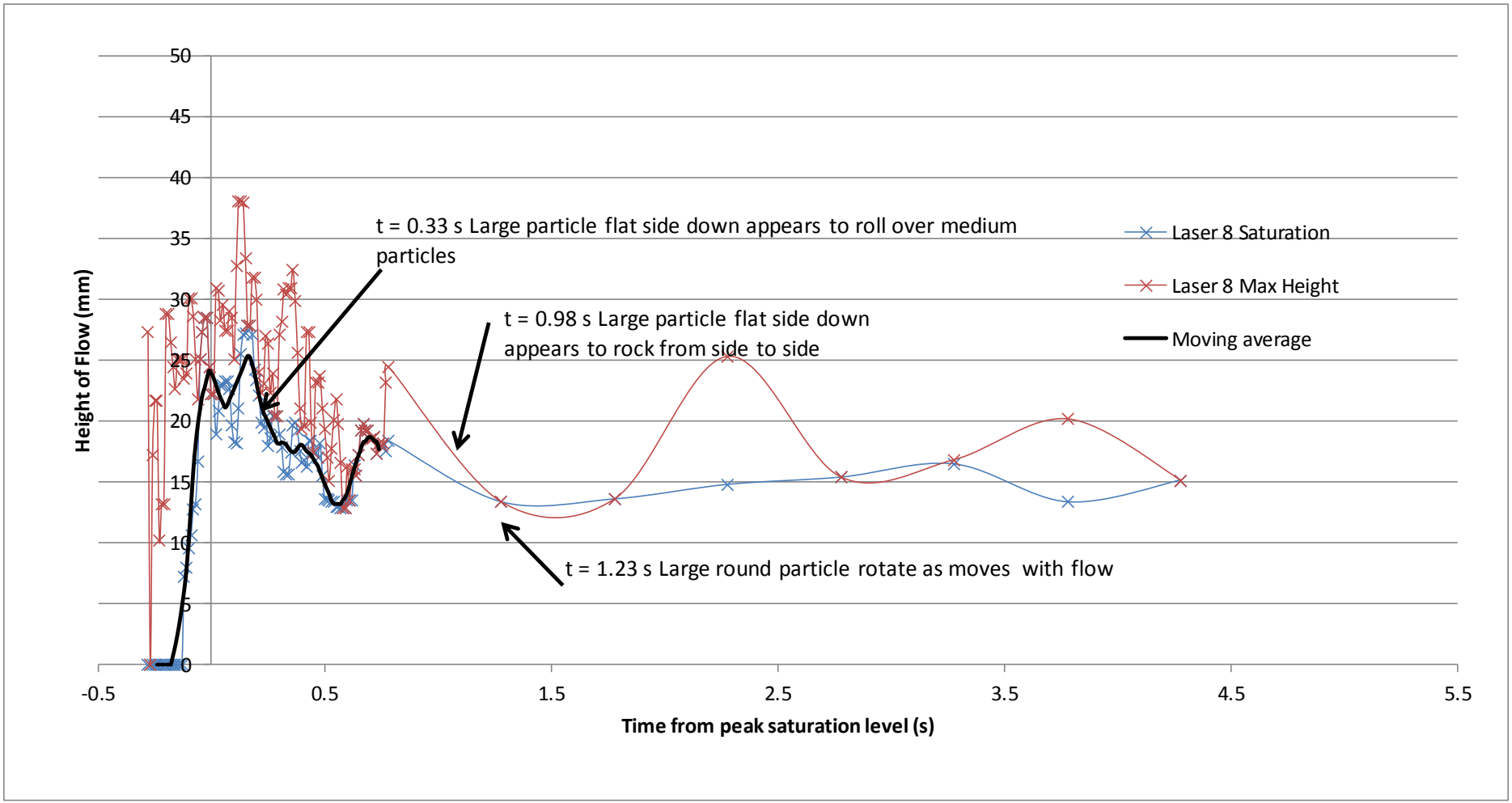

Figure F-2: Heights for S18W28IN0a

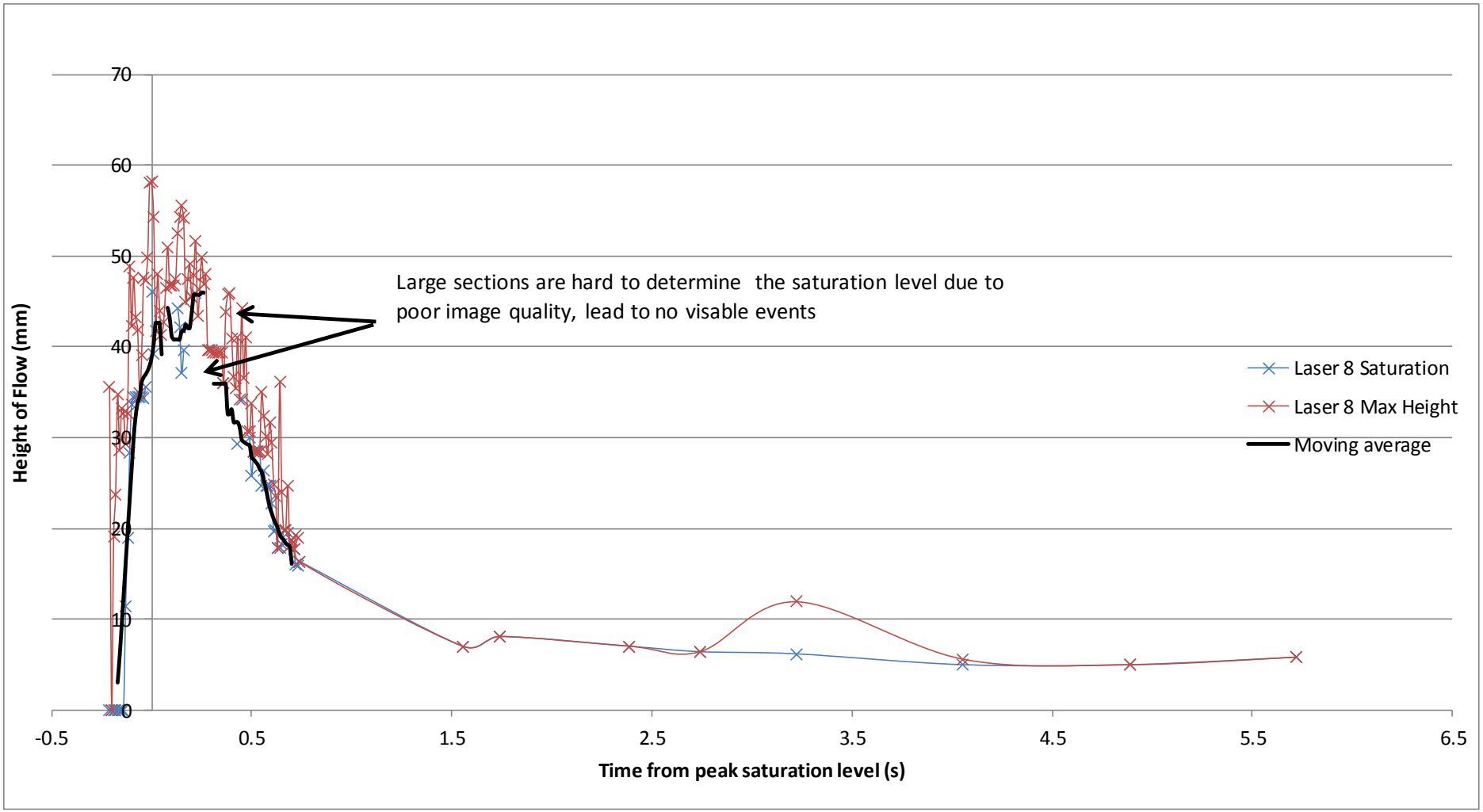

Figure F-3: Height for S18W28IN0c

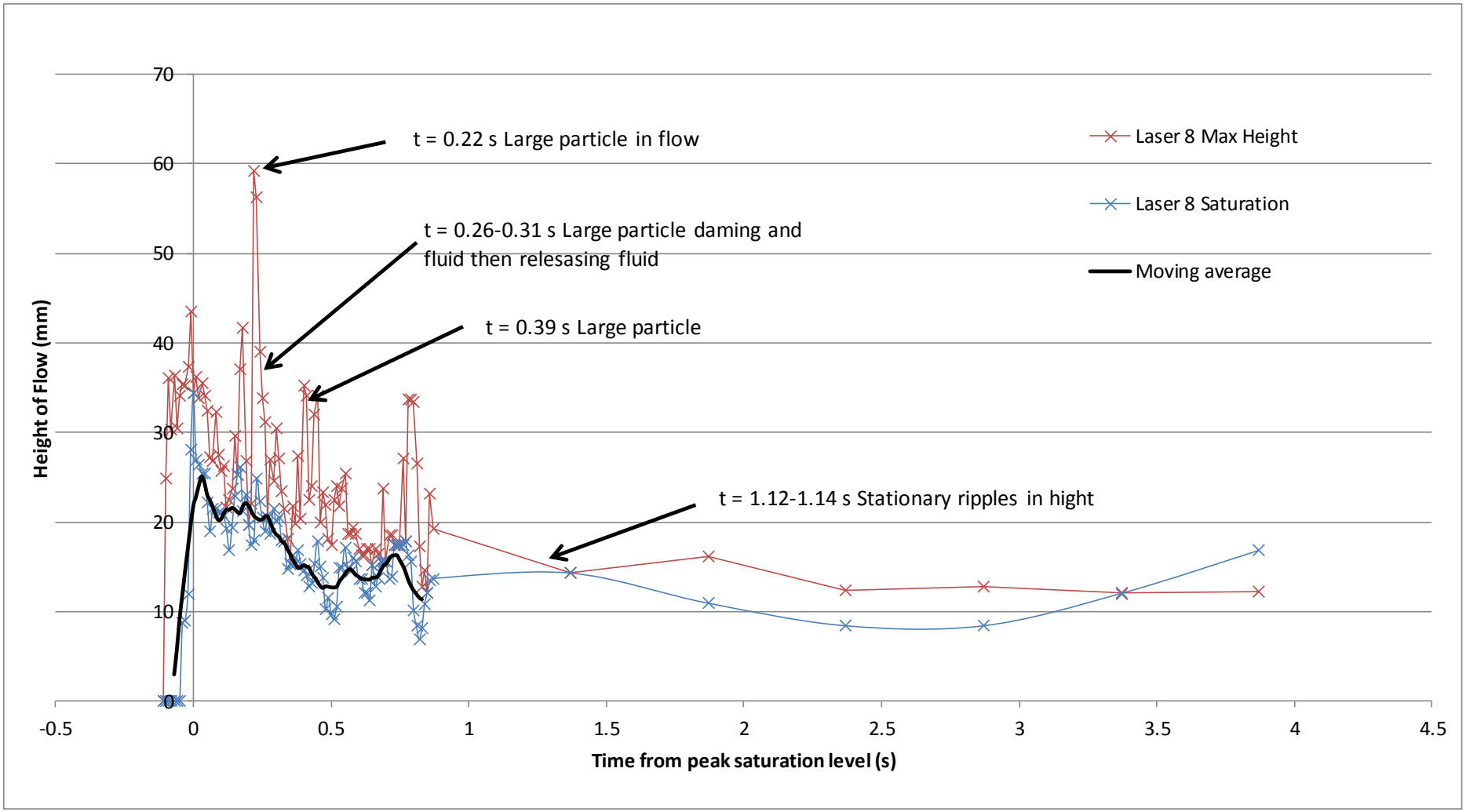

Figure F-4: Height for S18W28IN0d

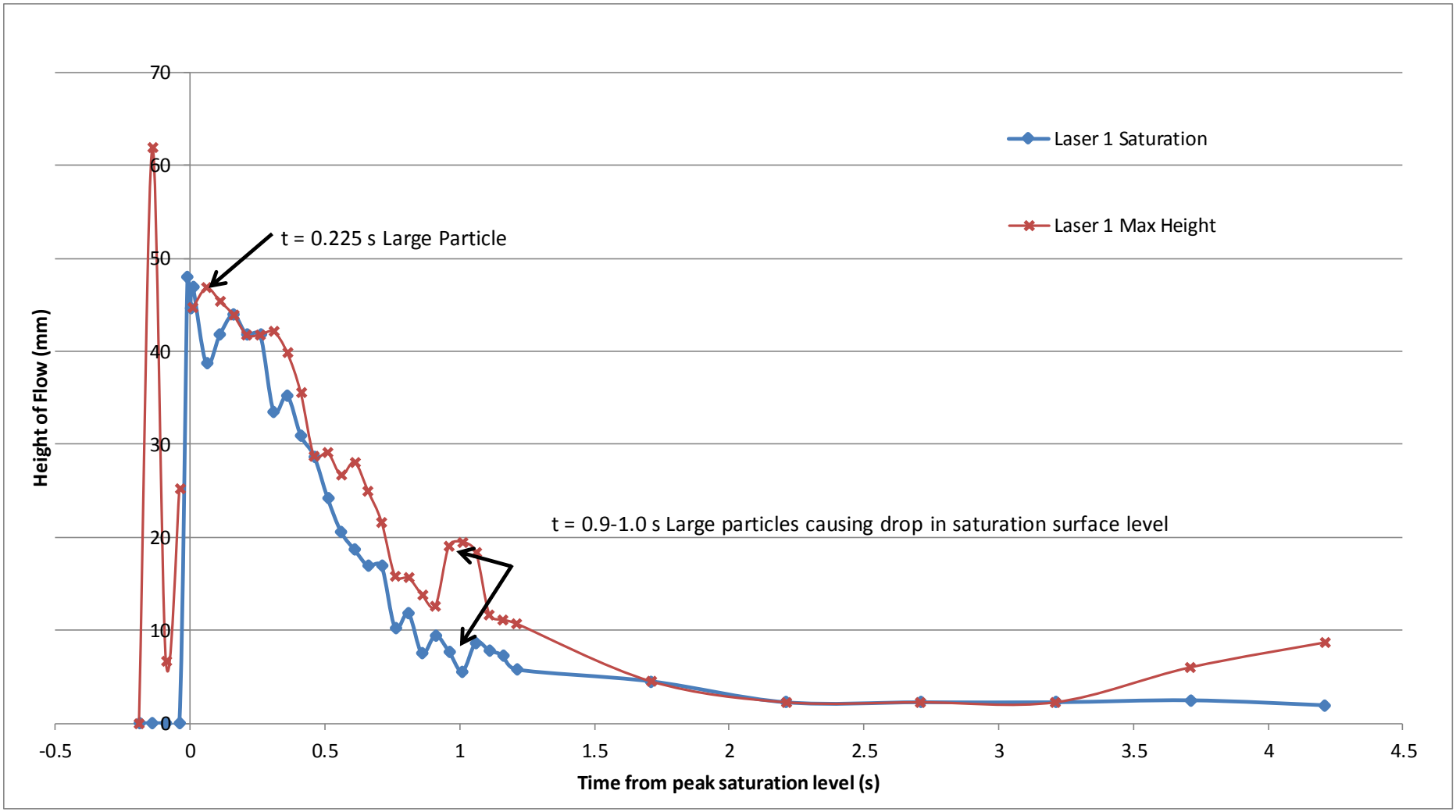

Figure F-5: Height for S18W28IN1

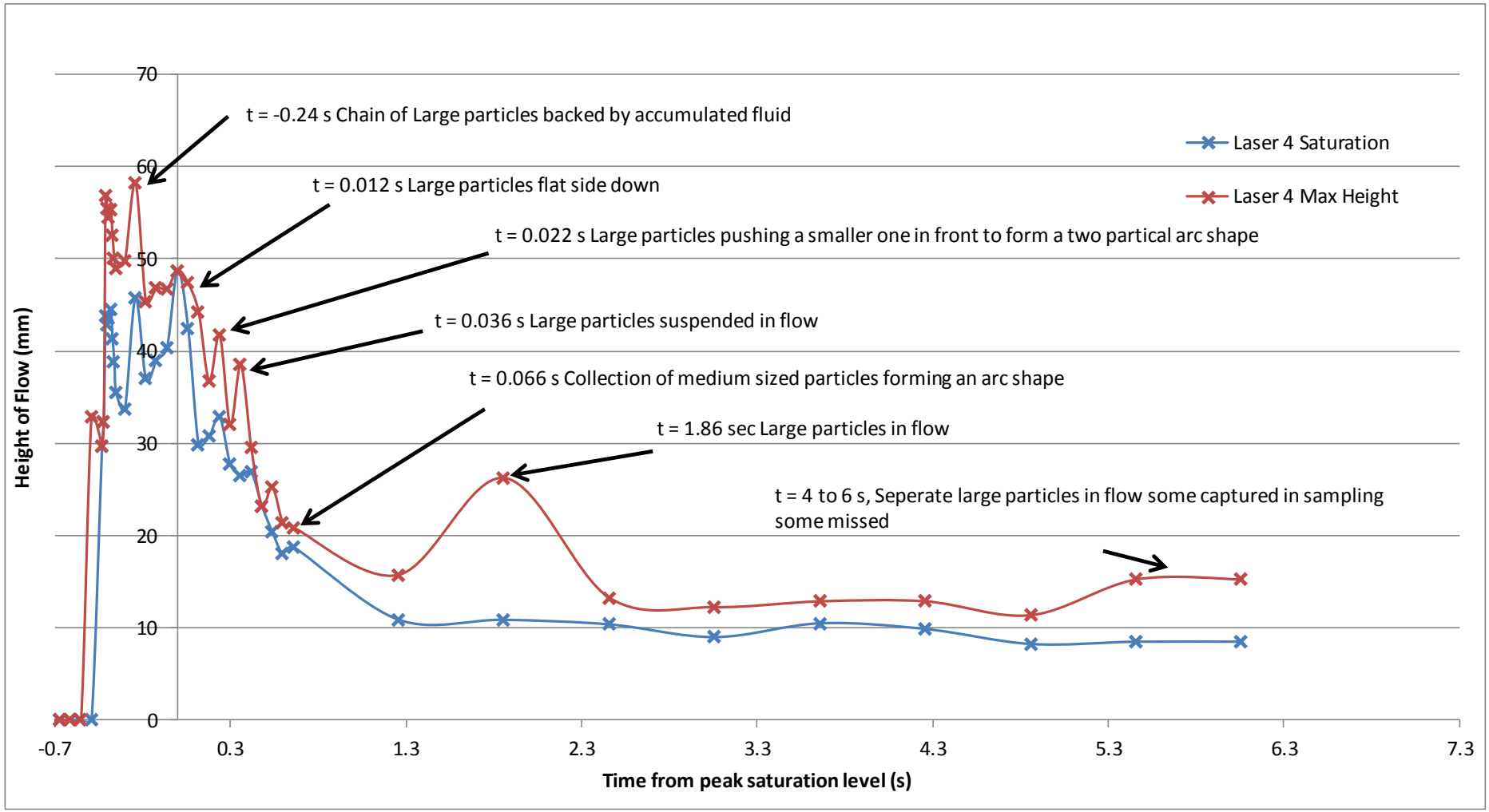

Figure F-6: Height for S18W28IN4

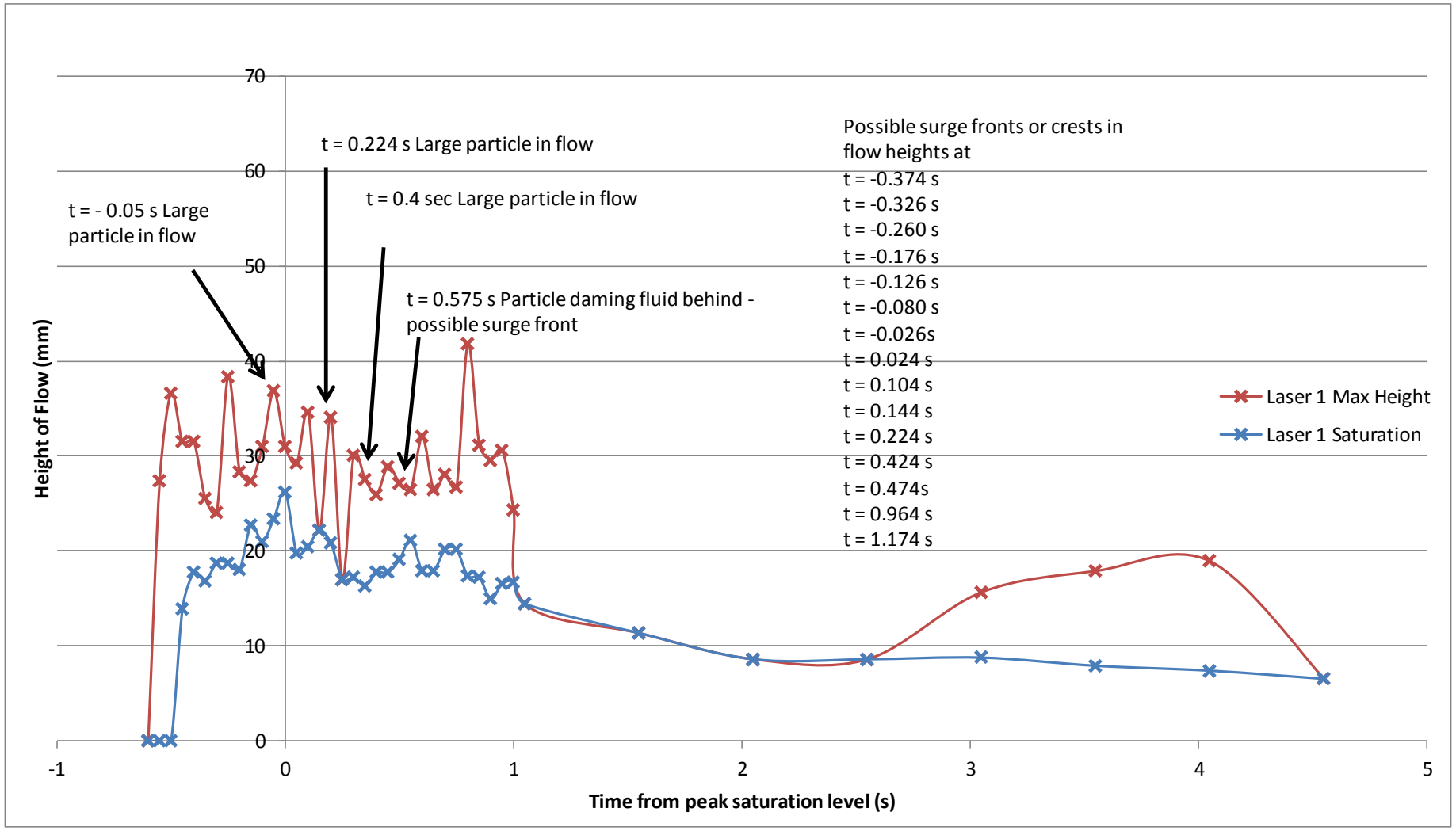

Figure F-7: Height for S18W28EX1

F.1.3. S18 – W32

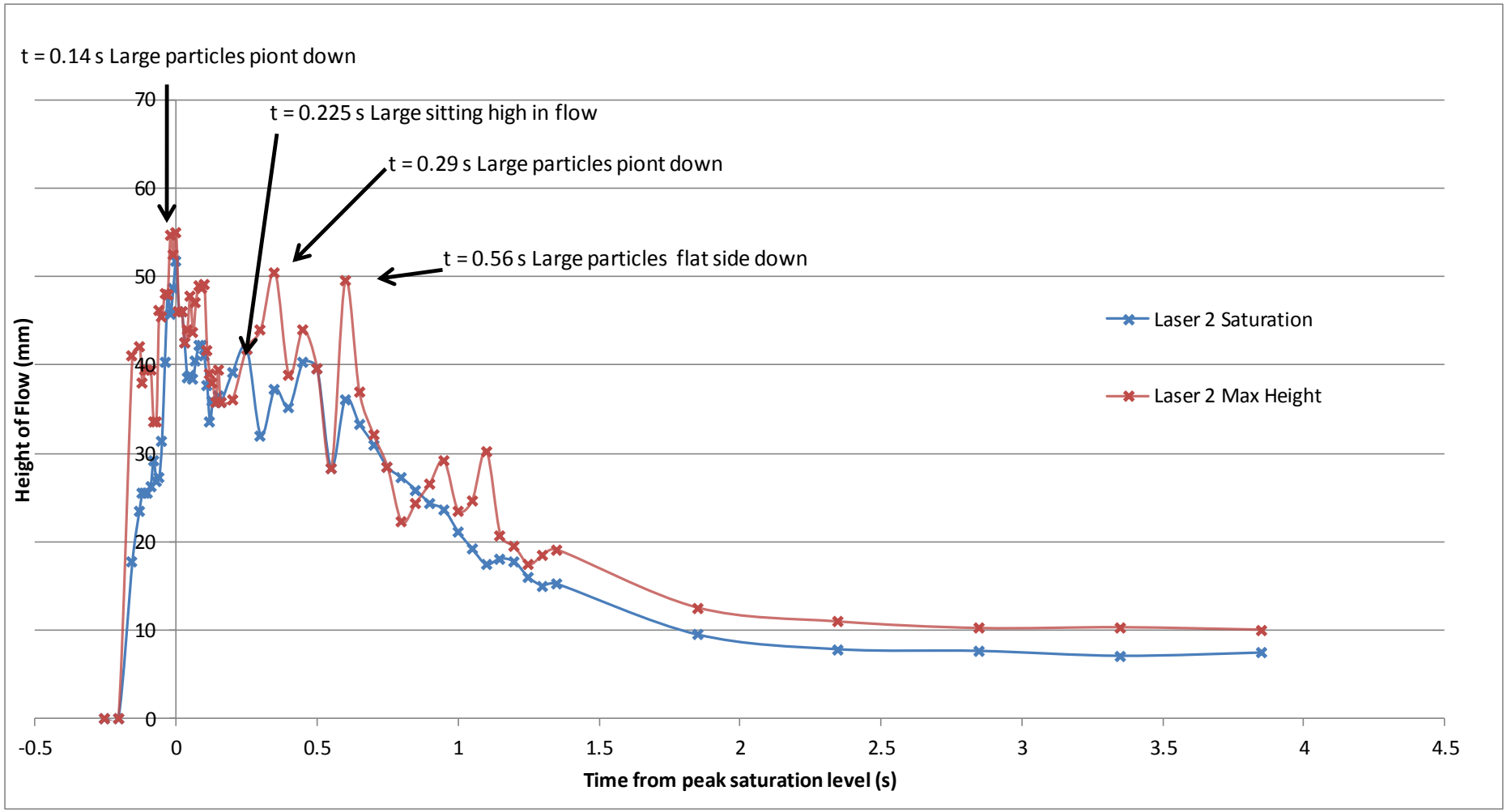

Figure F-8: Height for S18W32IN2

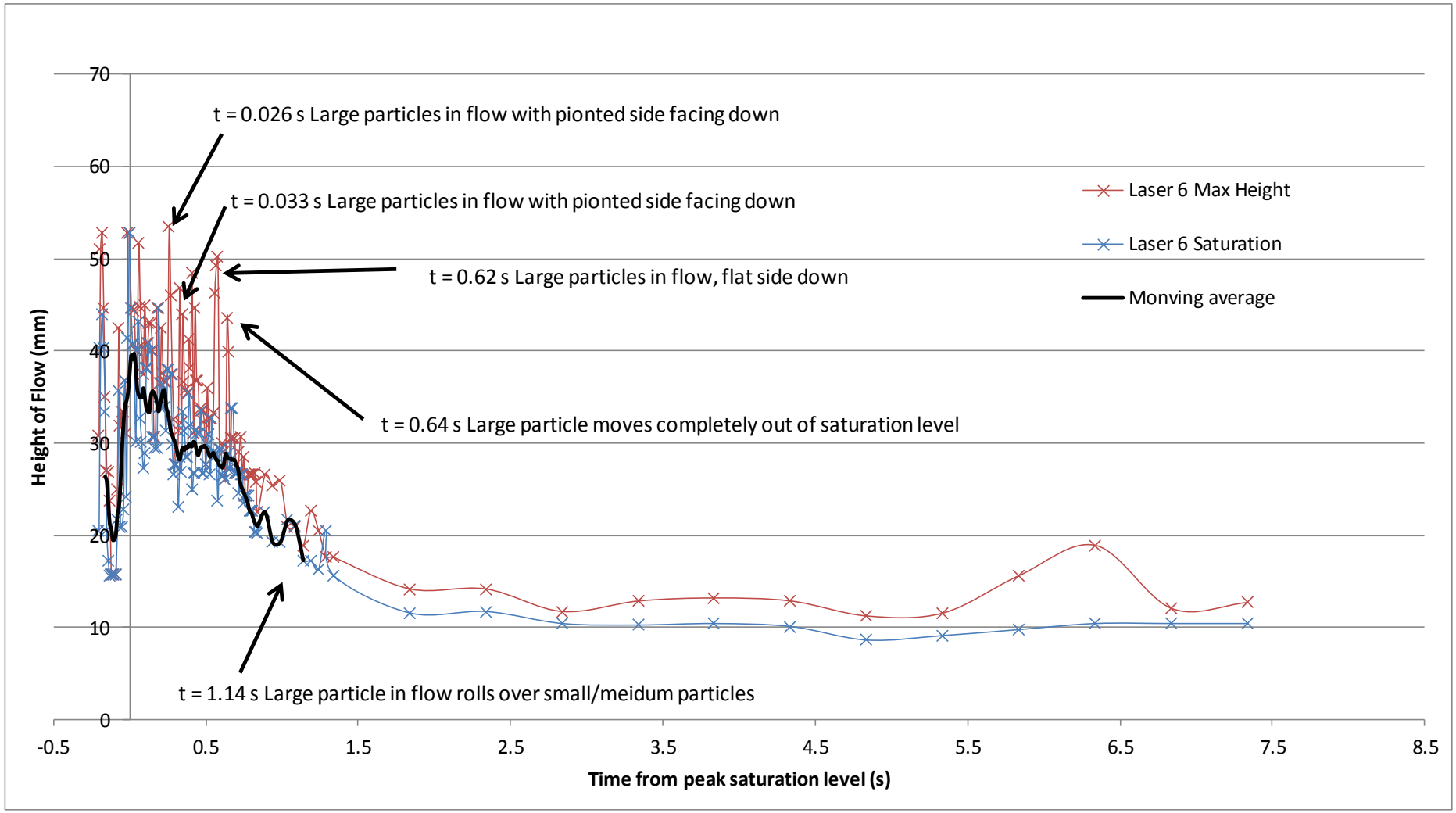

Figure F-9: Height for S18W32IN6

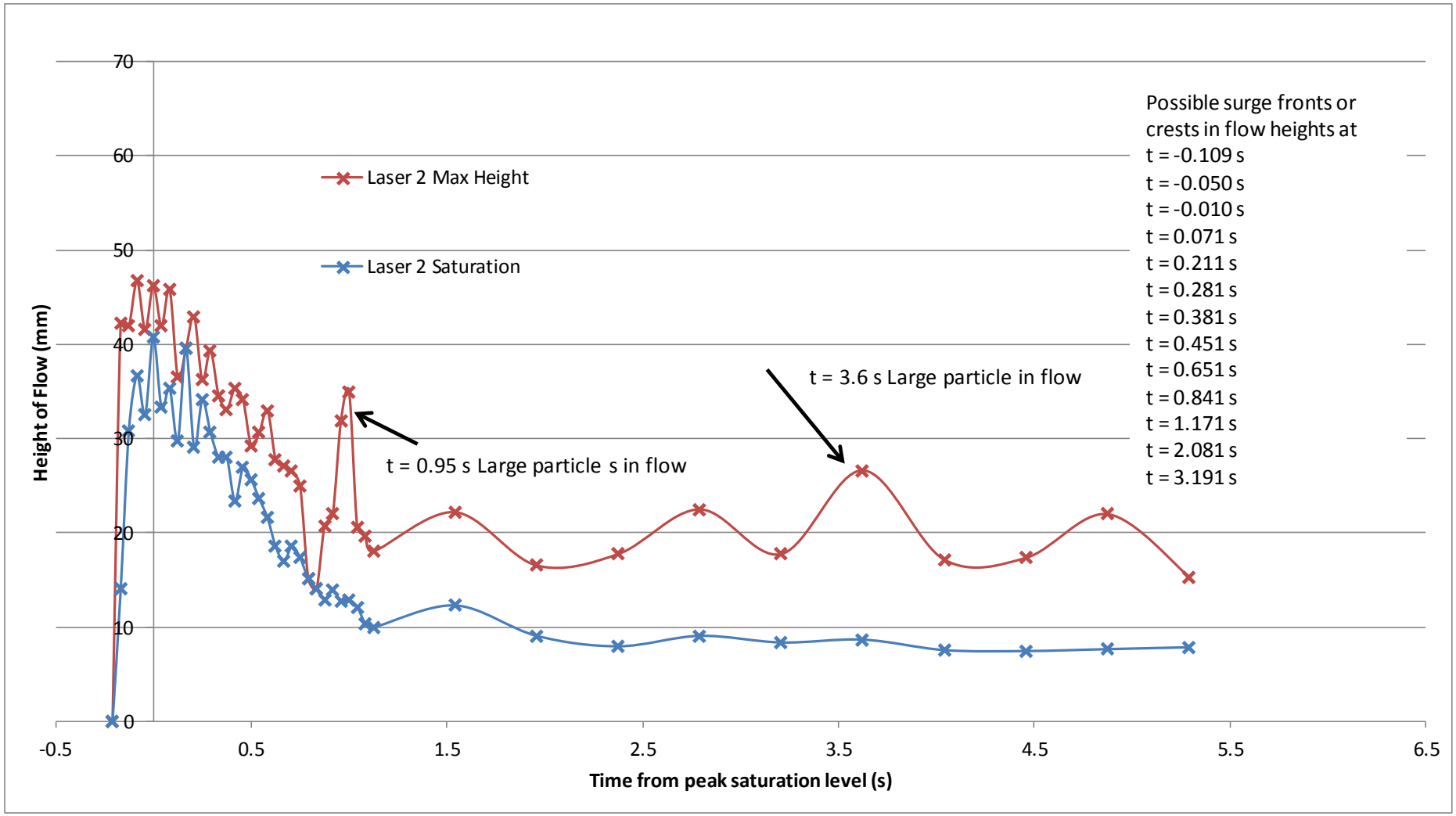

Figure F-10: Height for S18W32EX2

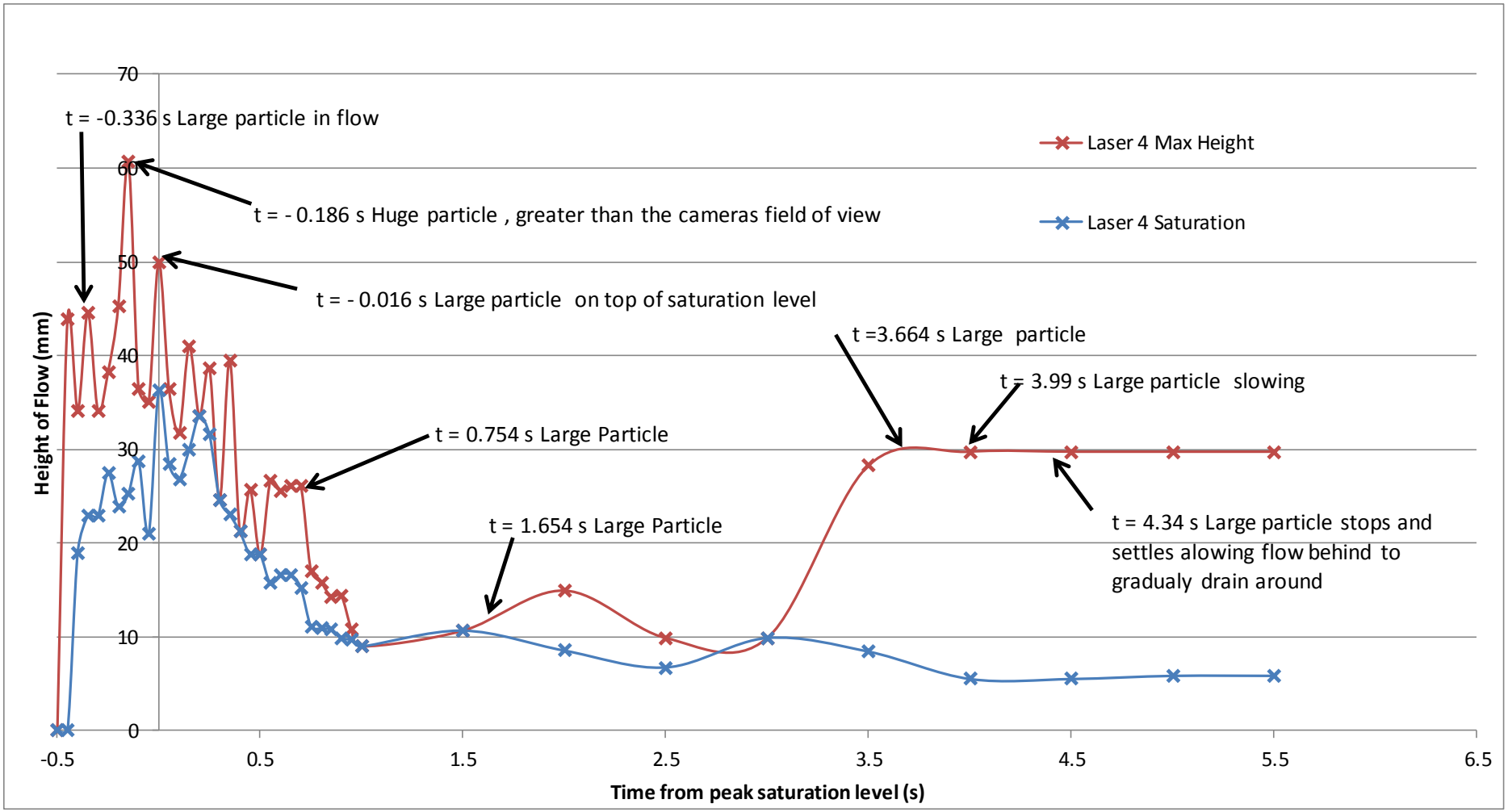

Figure F-11: Height for S18W32EX4

F.1.4. S18 – W36

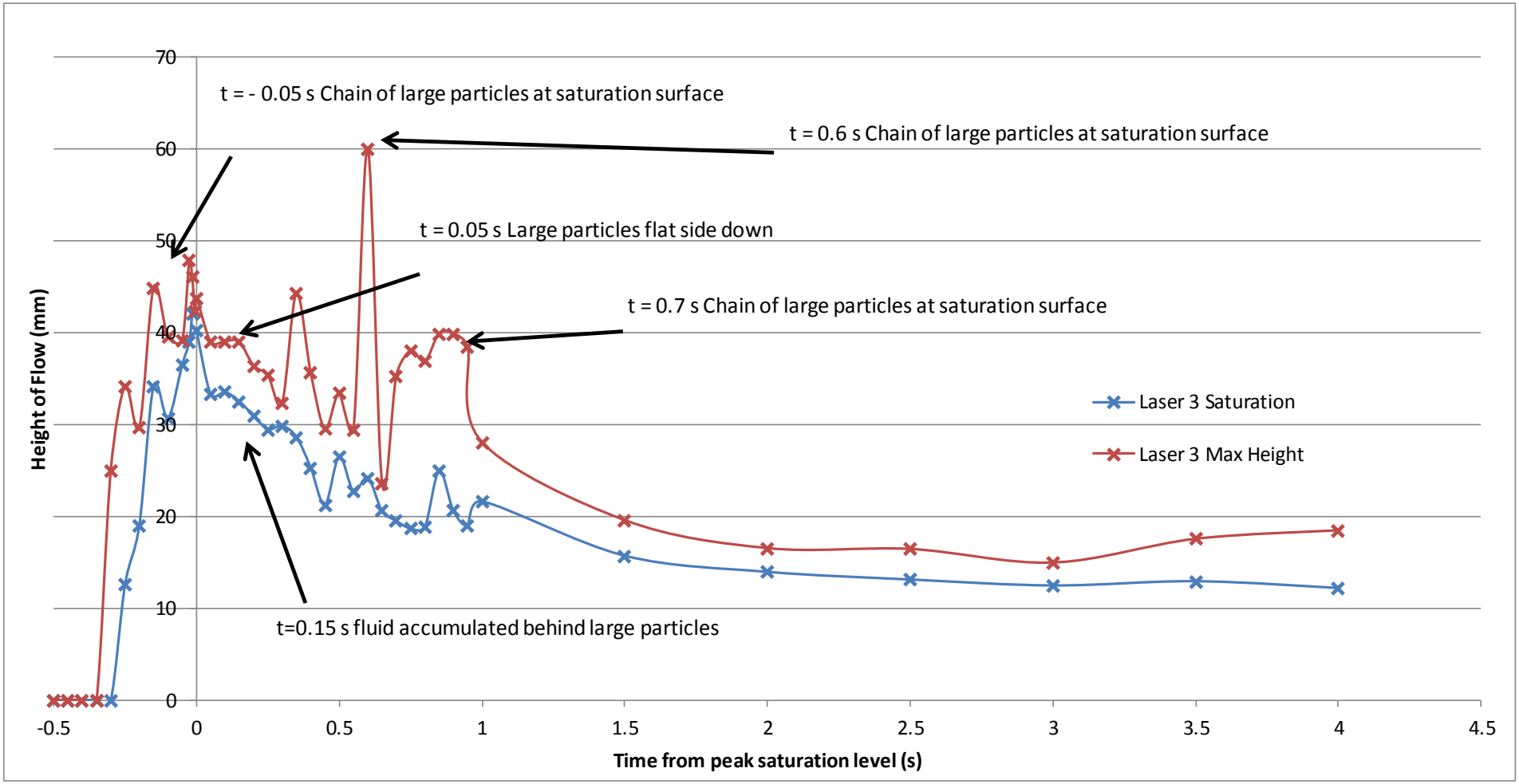

Figure F-12: Height for S18W36IN3

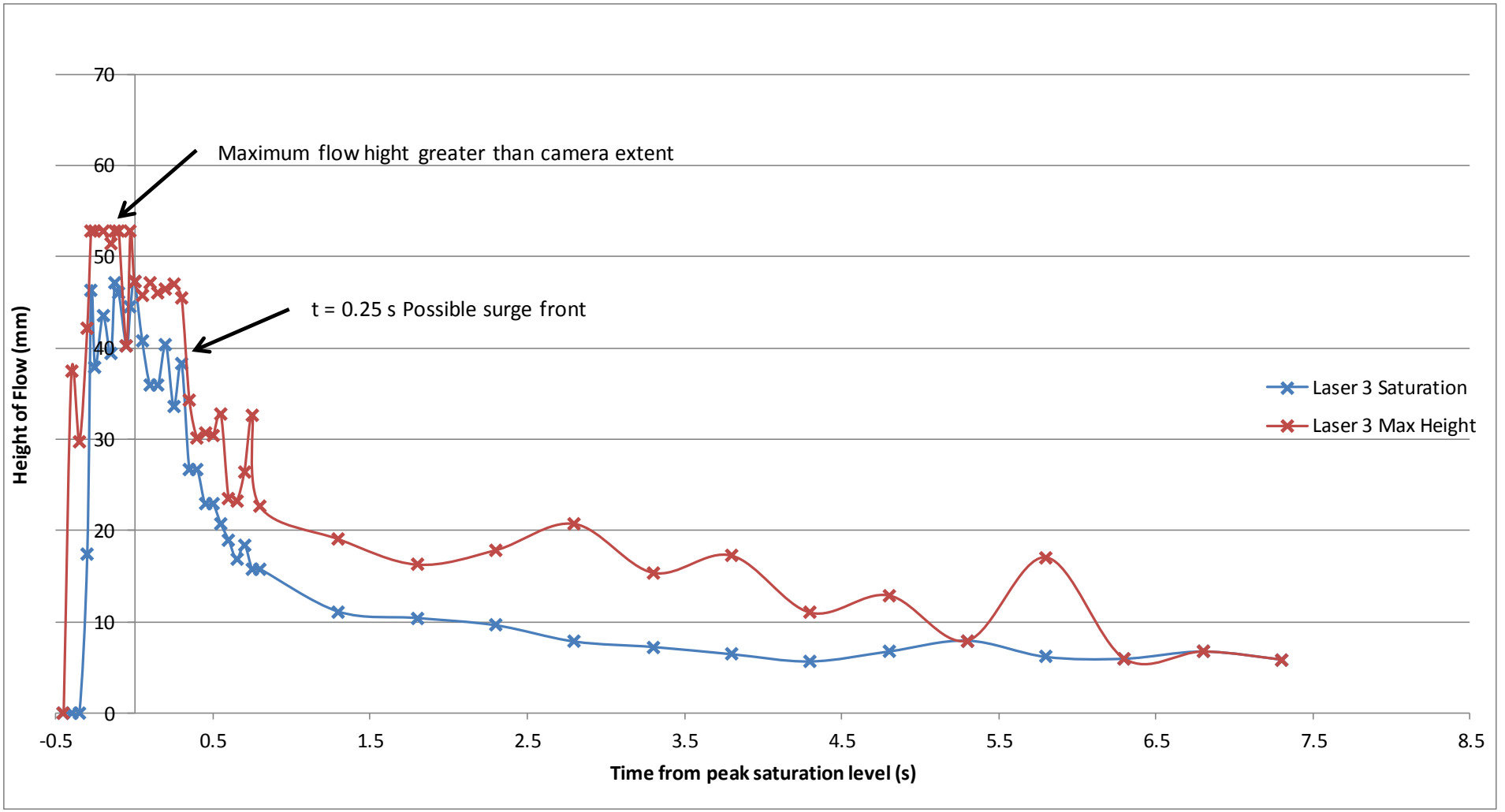

Figure F-13: Height for S18W36EX3

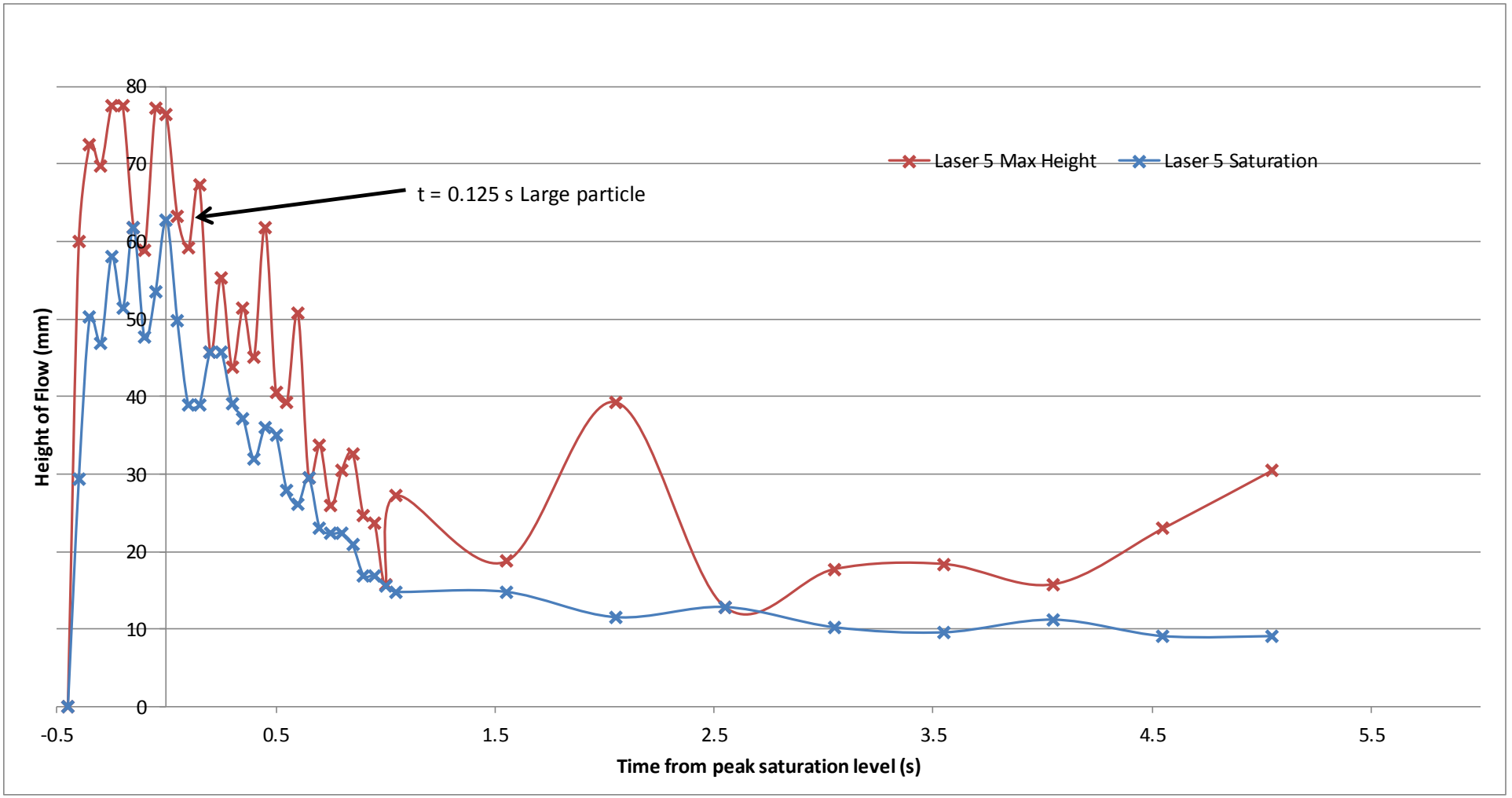

Figure F-14: Height for S18W36EX5

F.1.5. S24 – W28

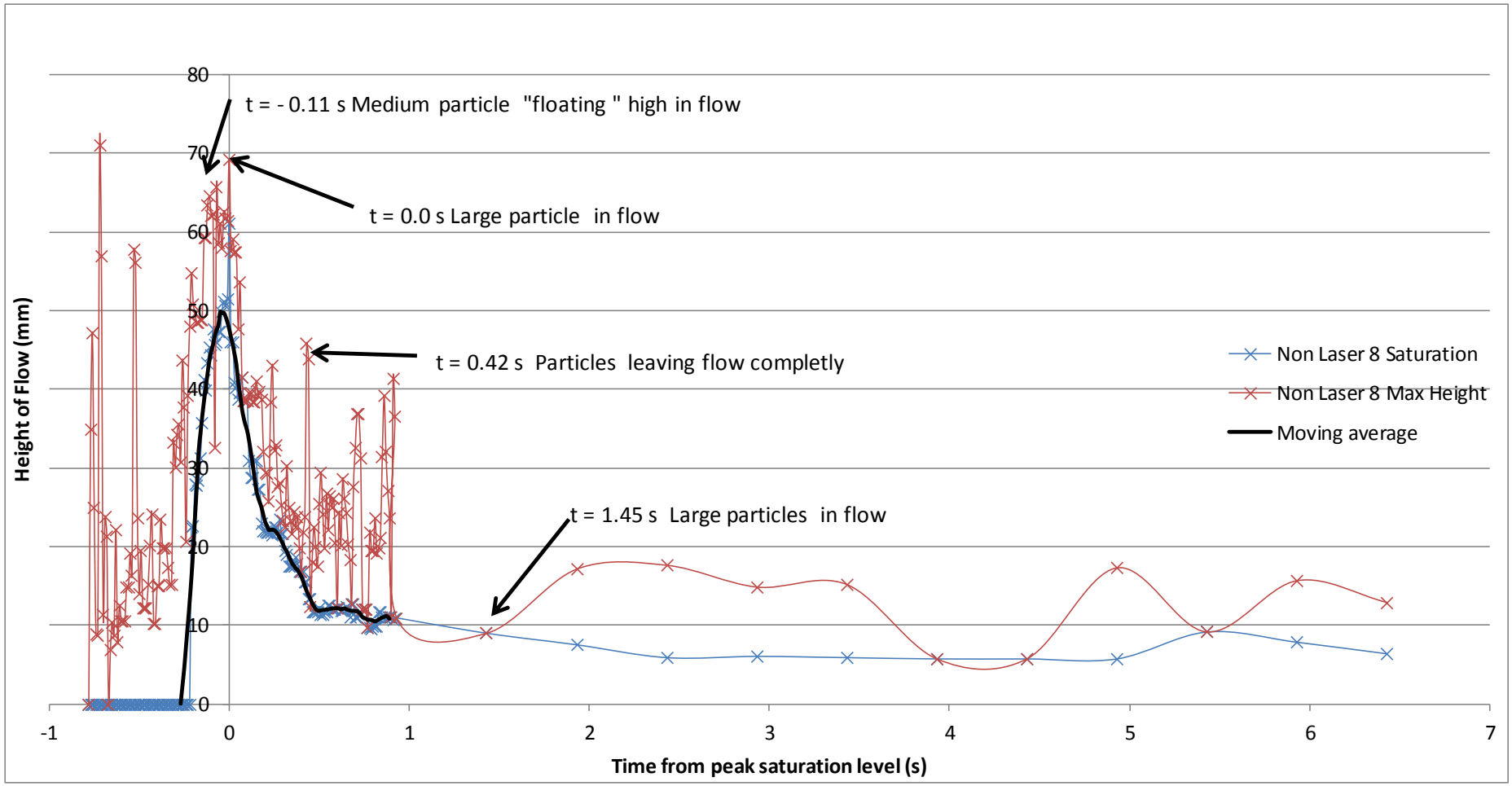

Figure F-15: Height for S24W28EX8

F.1.6. S24 – W32

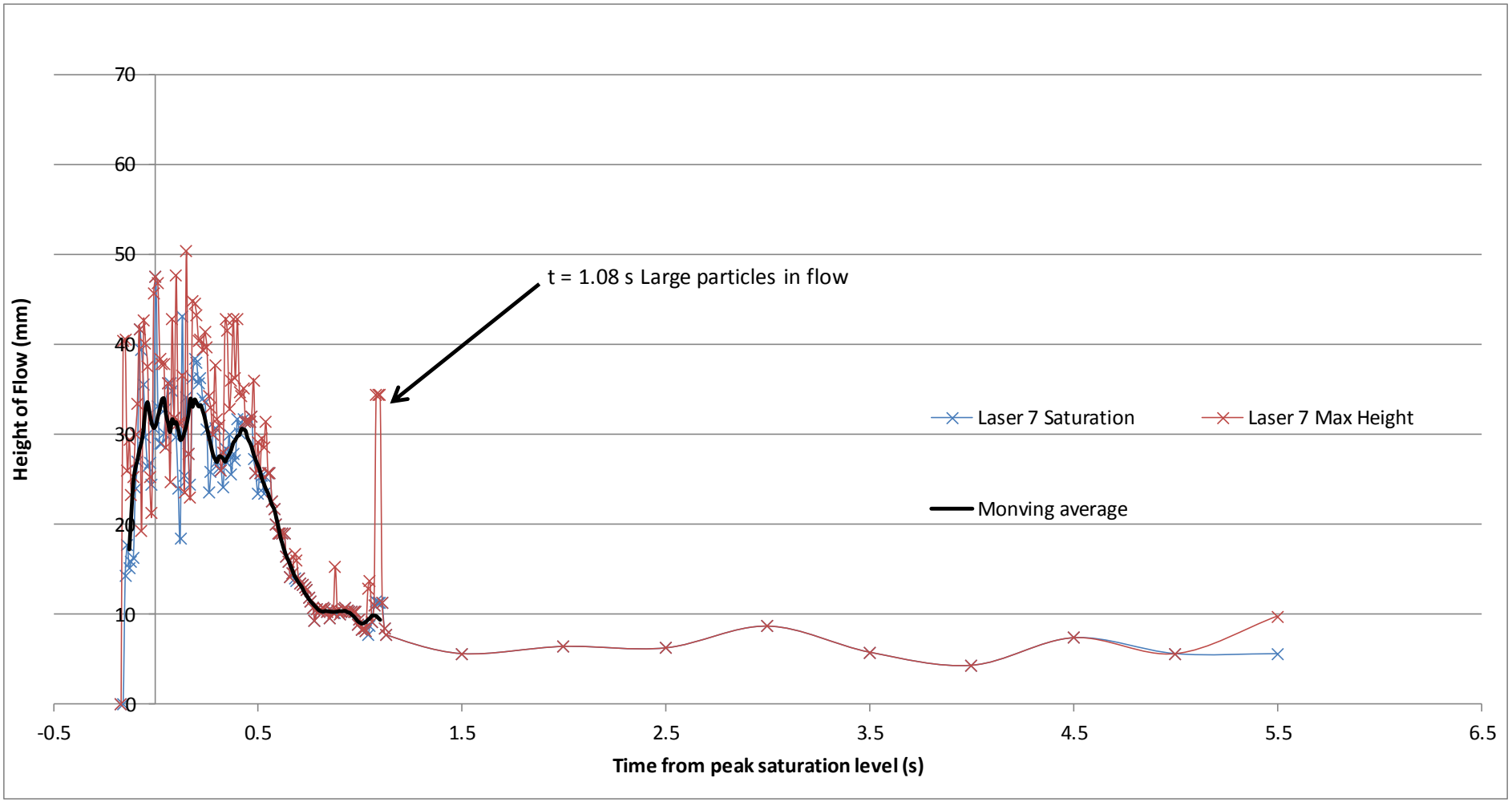

Figure F-16: Height for S24W32IN7

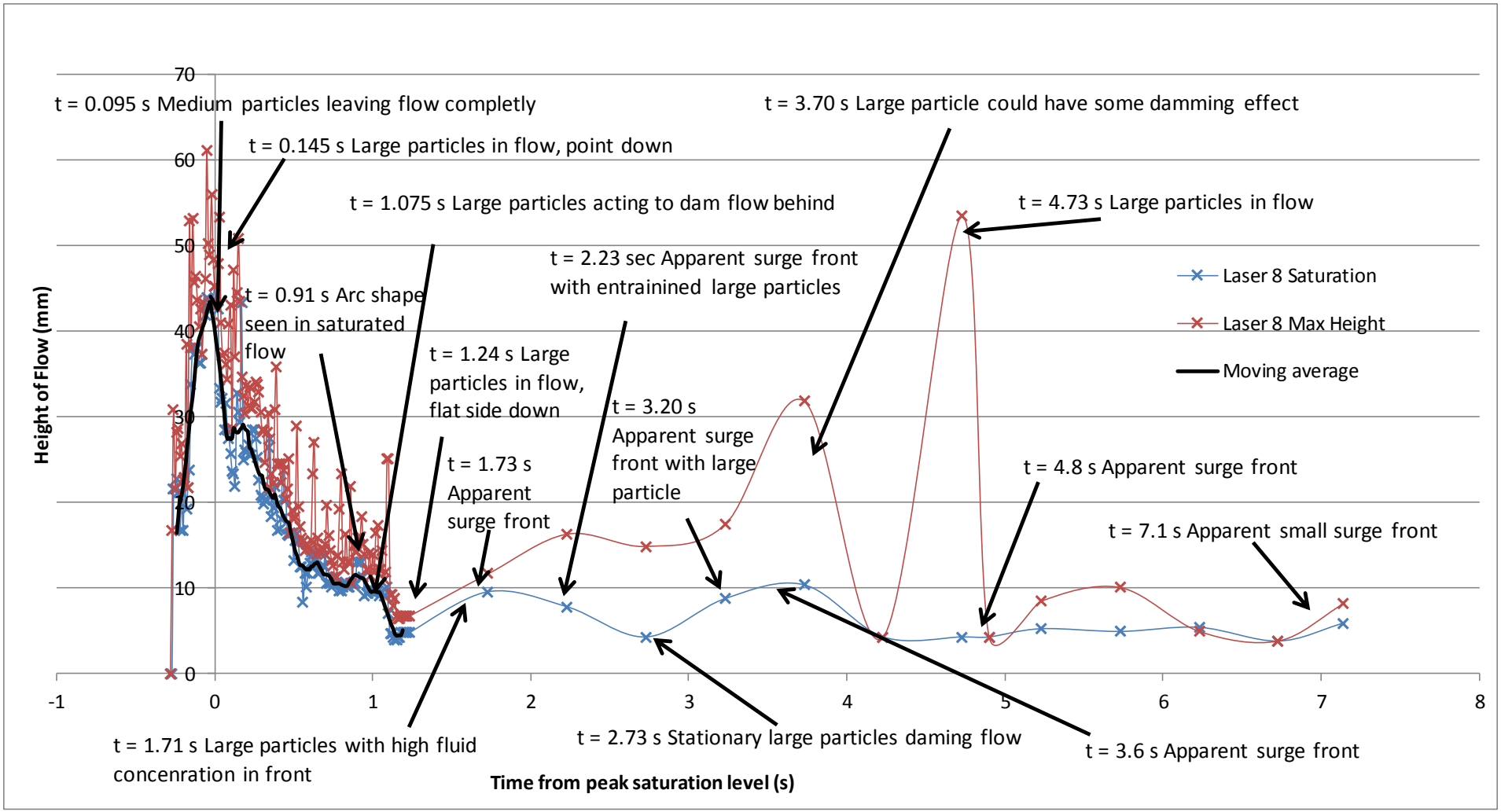

Figure F-17: Height for S24W32IN8

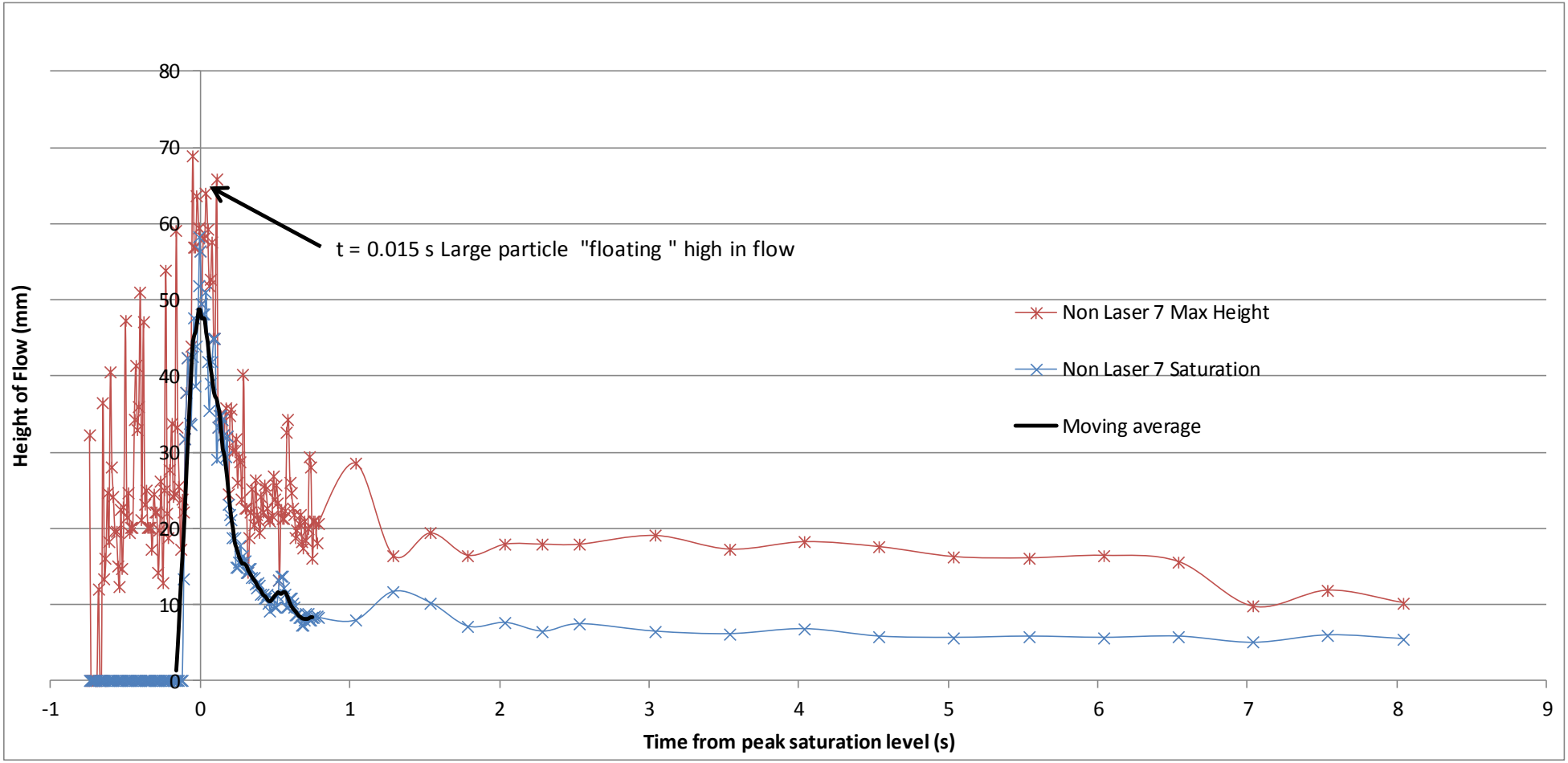

Figure F-18: Height for S24W32EX7

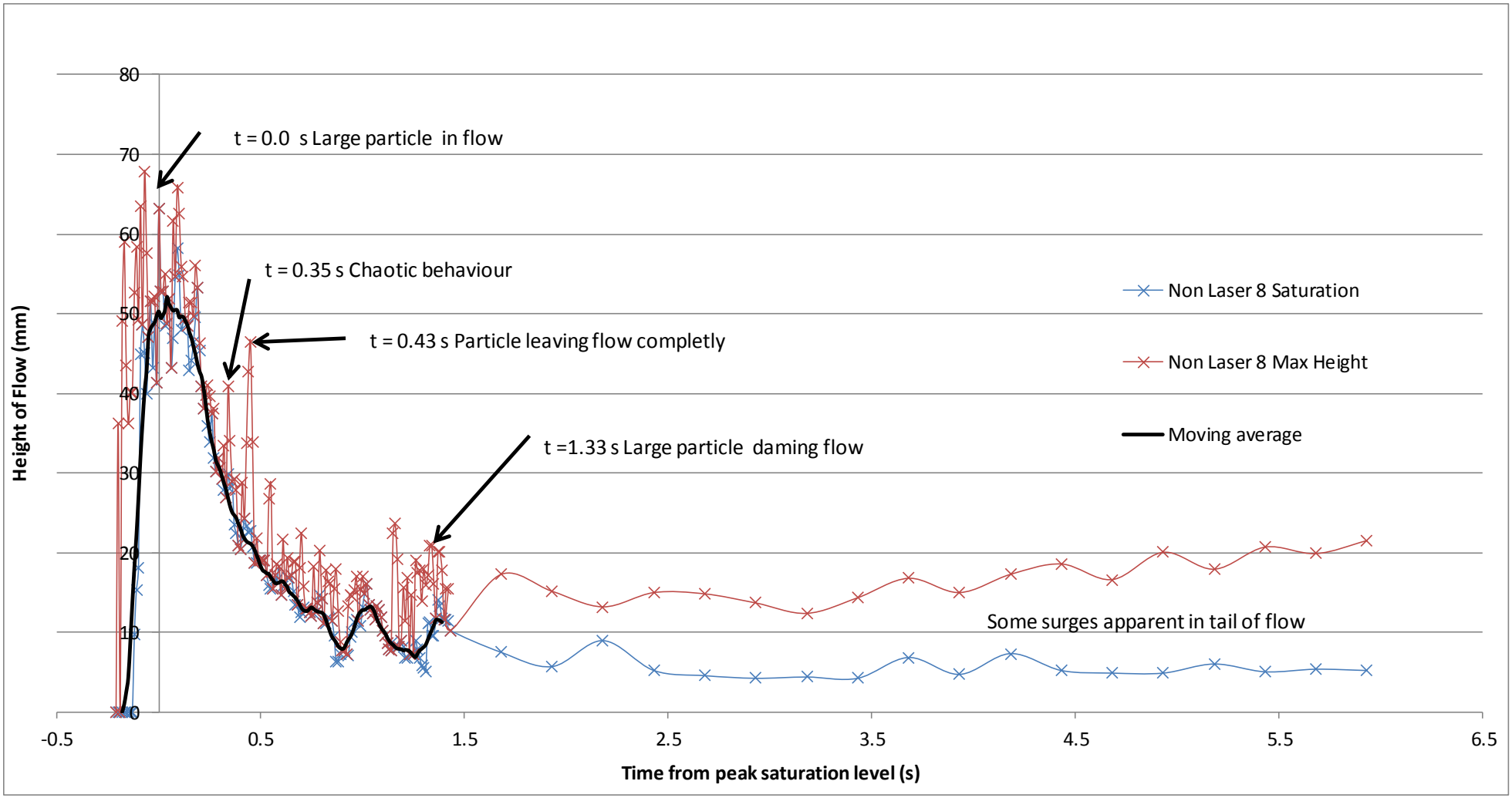

Figure F-19: Height for S24W32EX9

F.2. Front and Body, Absolute and Saturation heights

For all height-over-time graphs present in this section time zero is beginning of saturation level. The graphs show all maximum heights before time zero point and the first 0.8 seconds after time zero. Absolute maximum height of flow is in dashed lines. Saturation level is in solid line. Moving averages over seven points in bold line black. Actual values at taken at 0.01 s intervals and are presented as grey lines.

F.2.1. S18 – W24

F.2.1.1. S18W24IN5

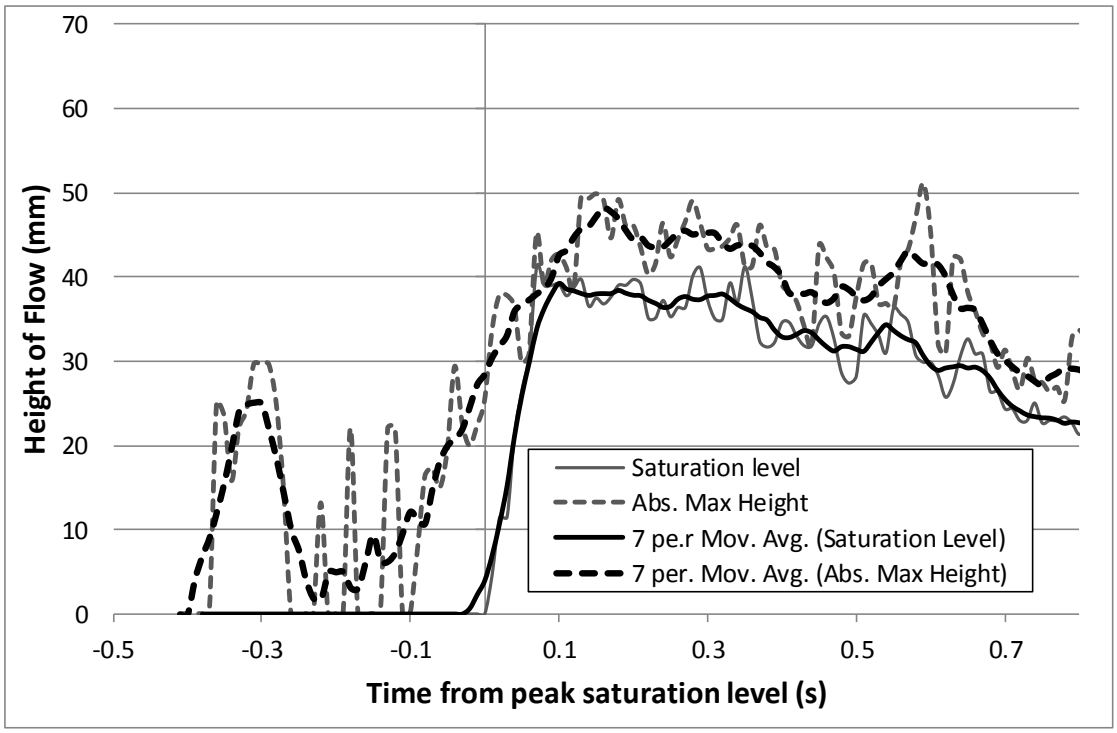

Figure F-20: Height over time of S18W24IN5. Note scale change on negative side.

F.2.2. S18 – W28

F.2.2.1. S18W28IN0a

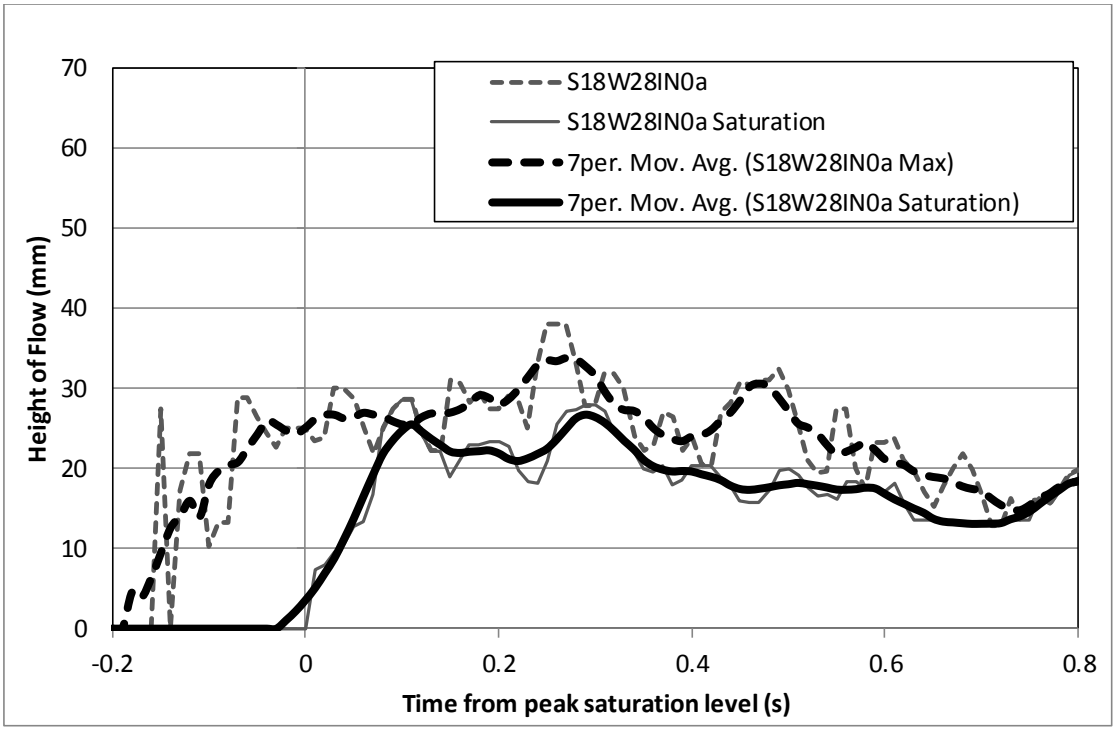

Figure F-21: Height over time of S18W28IN0a.

F.2.2.2. S18W28IN0c

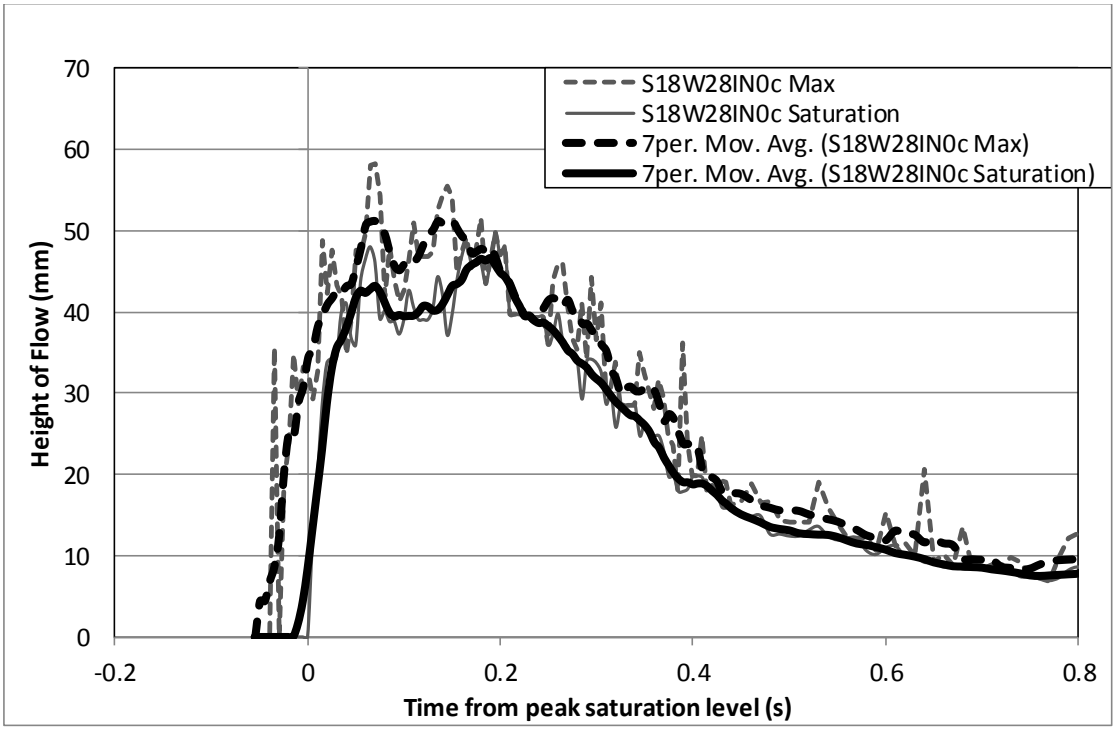

Figure F-22: Height over time of S18W28IN0c.

F.2.2.3. S18W28IN0d

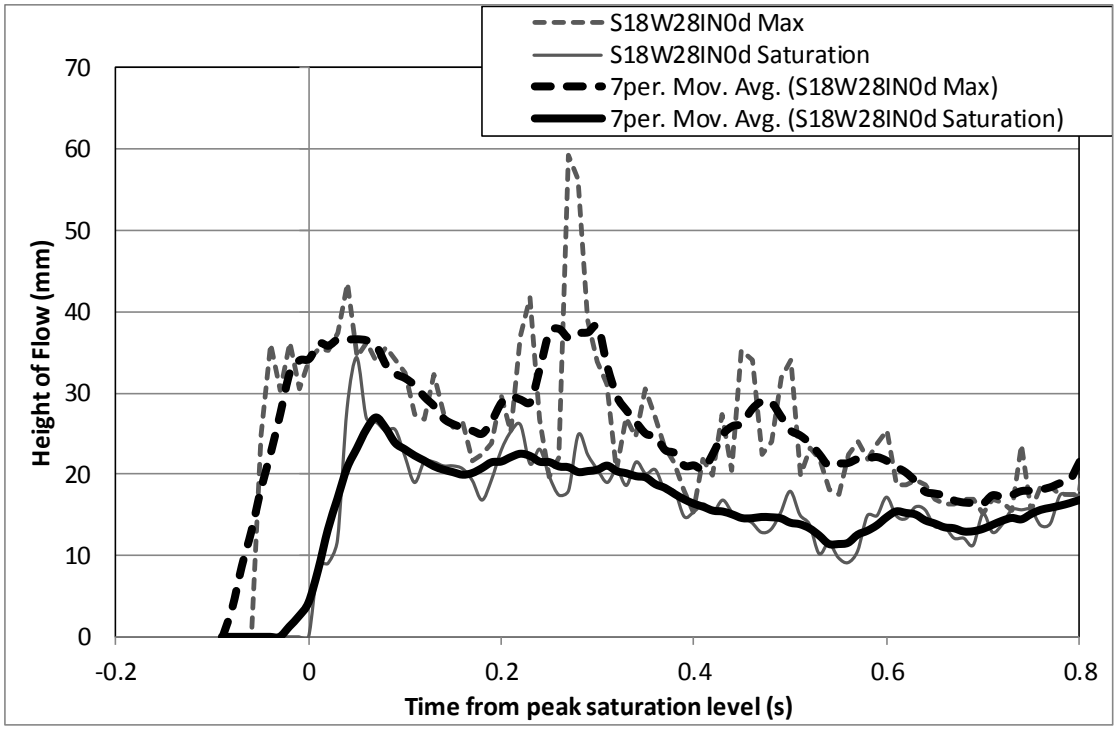

Figure F-23: Height over time of S18W28IN0c.

F.2.2.4. S18W28IN1

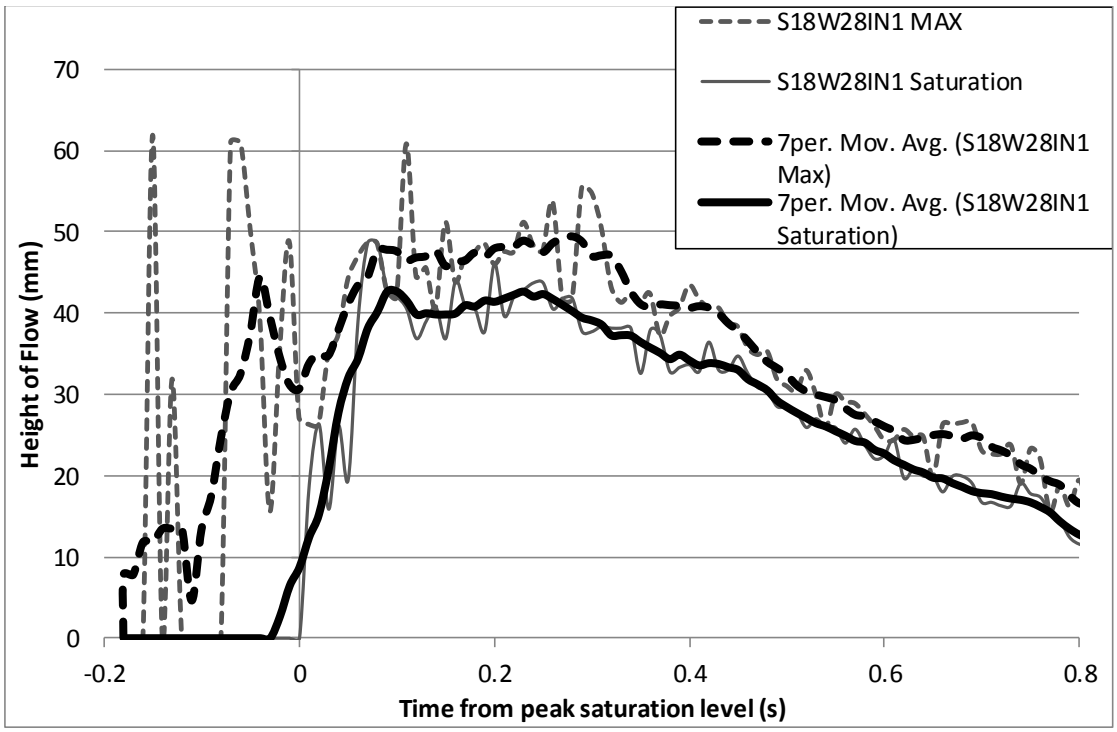

Figure F-24: Height over time of S18W28IN1.

F.2.2.5. S18W28IN4

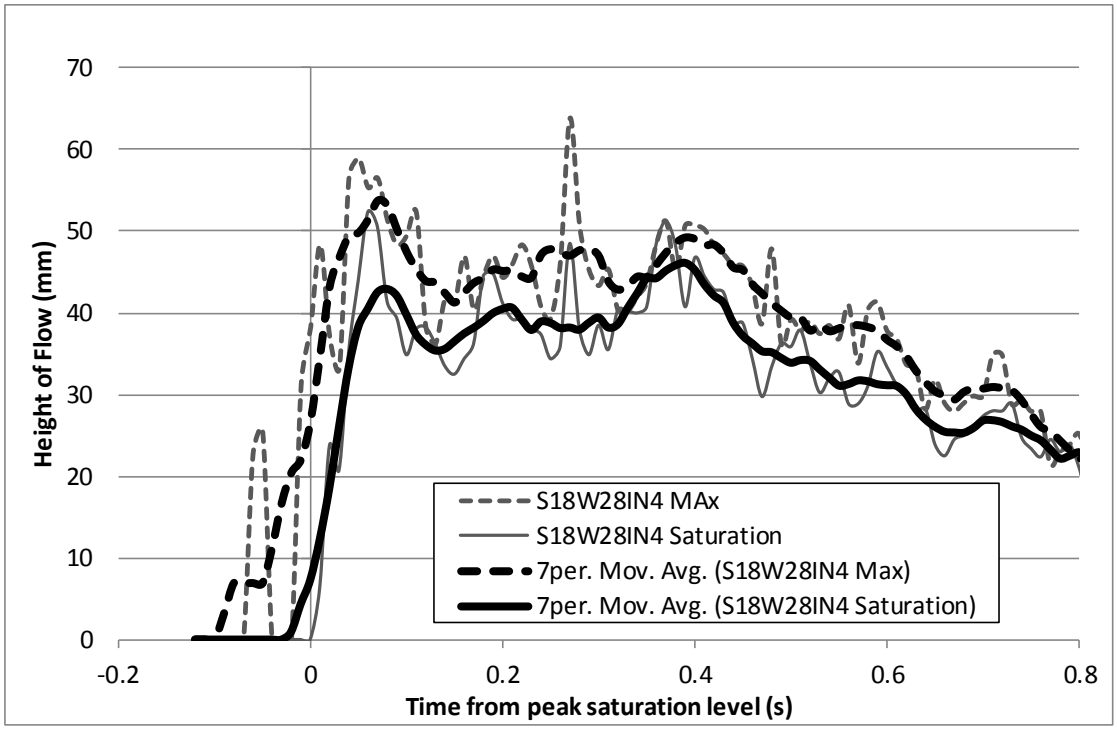

Figure F-25: Height over time of S18W28IN4.

F.2.2.6. S18W28EX1

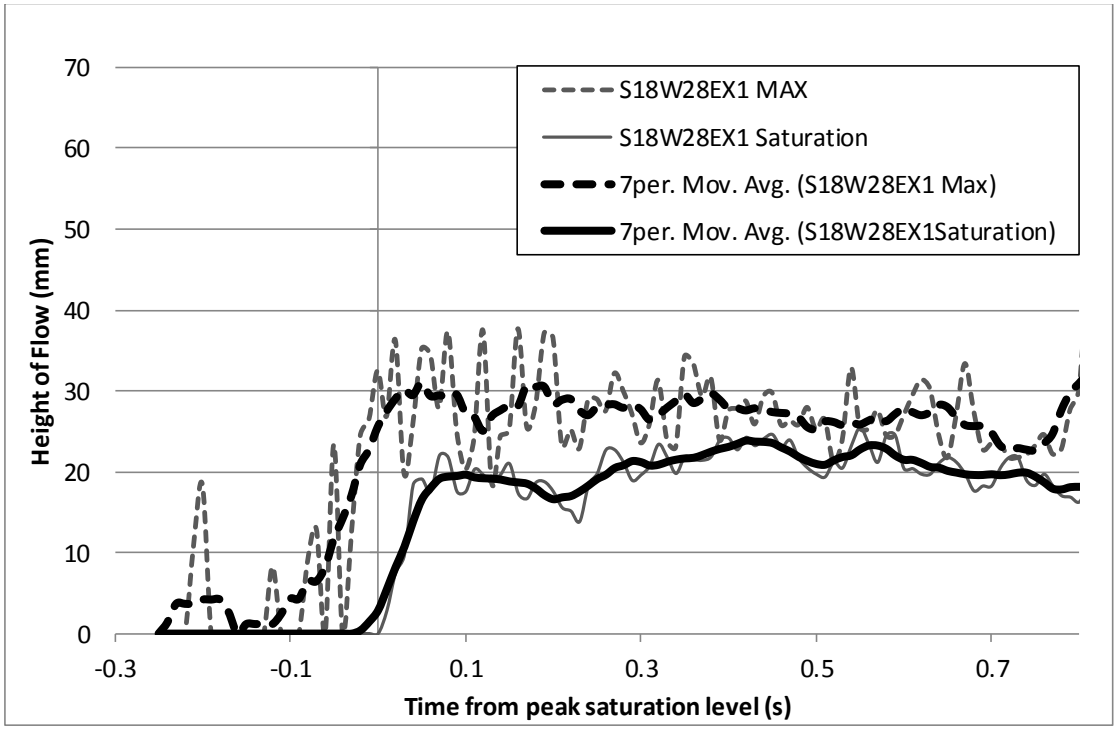

Figure F-26: Height over time of S18W28EX1. Note scale change on negative side.

F.2.3. S18 - W32

F.2.3.1. S18W32IN2

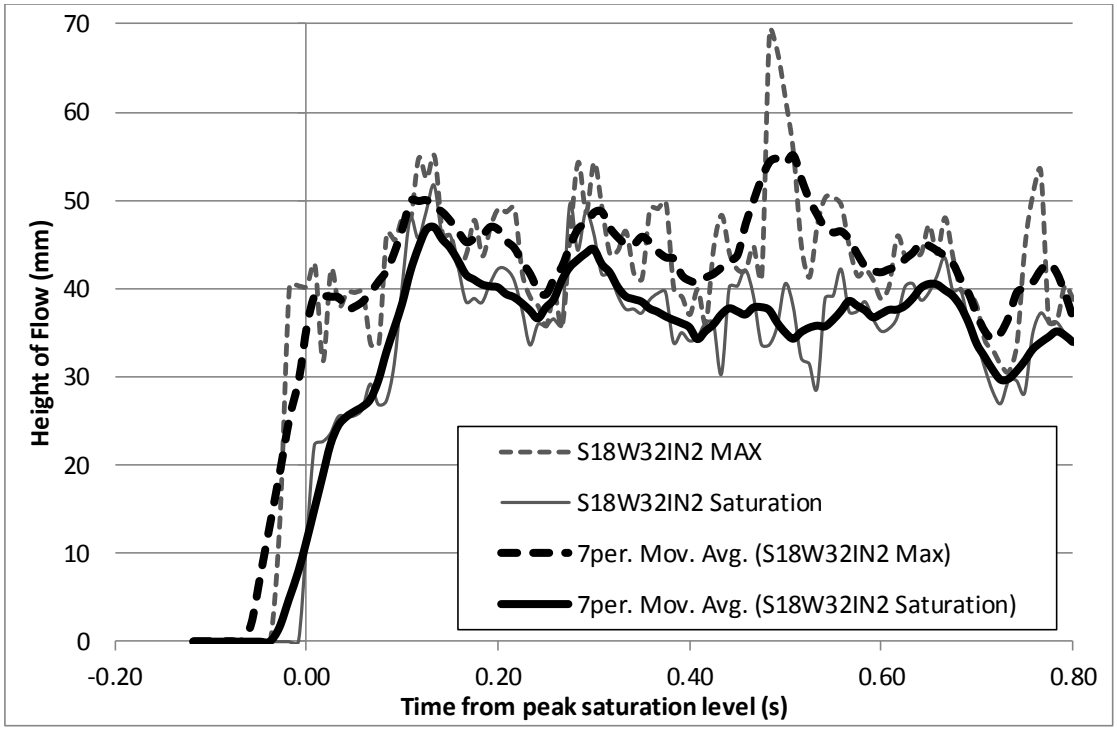

Figure F-27: Height over time of S18W32IN2.

F.2.3.2. S18W32IN6

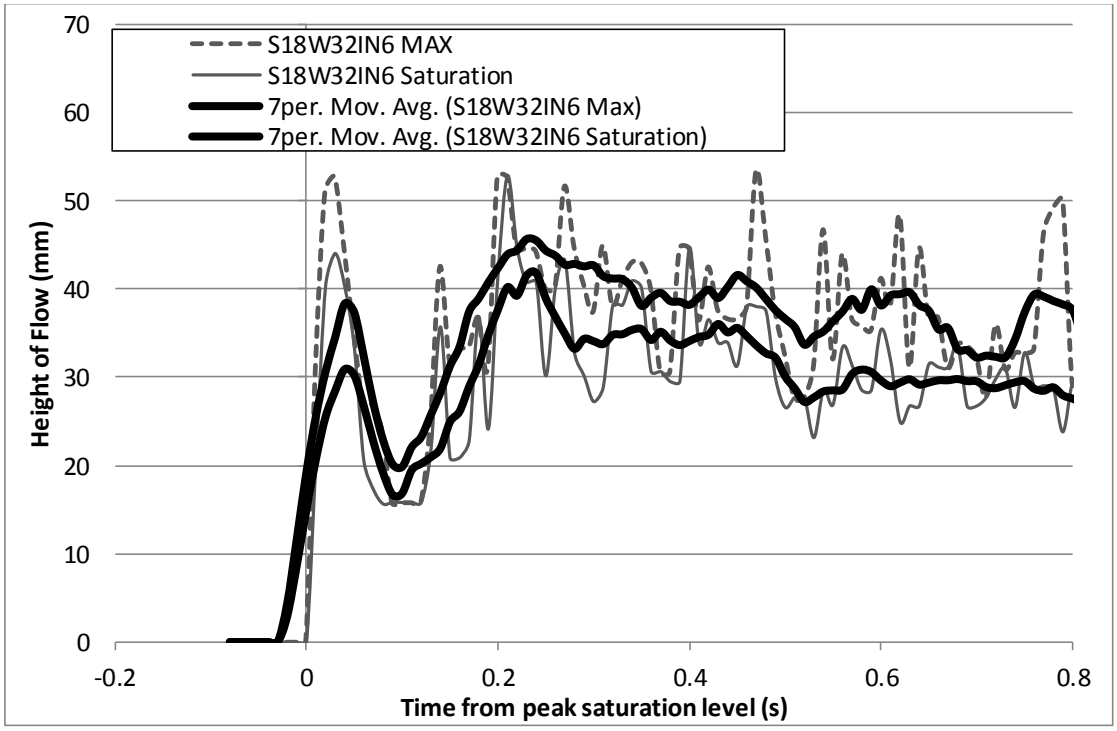

Figure F-28: Height over time of S18W32IN6.

F.2.3.3. S18W32EX2

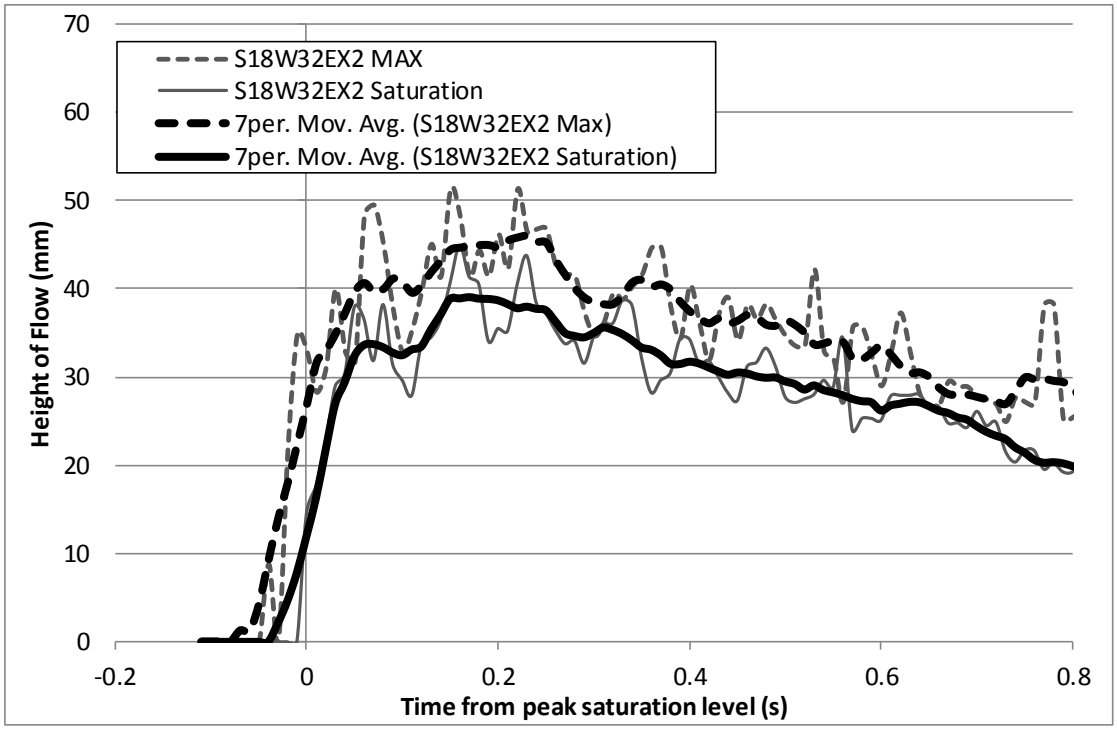

Figure F-29: Height over time of S18W32EX2.

F.2.3.4. S18W32EX4

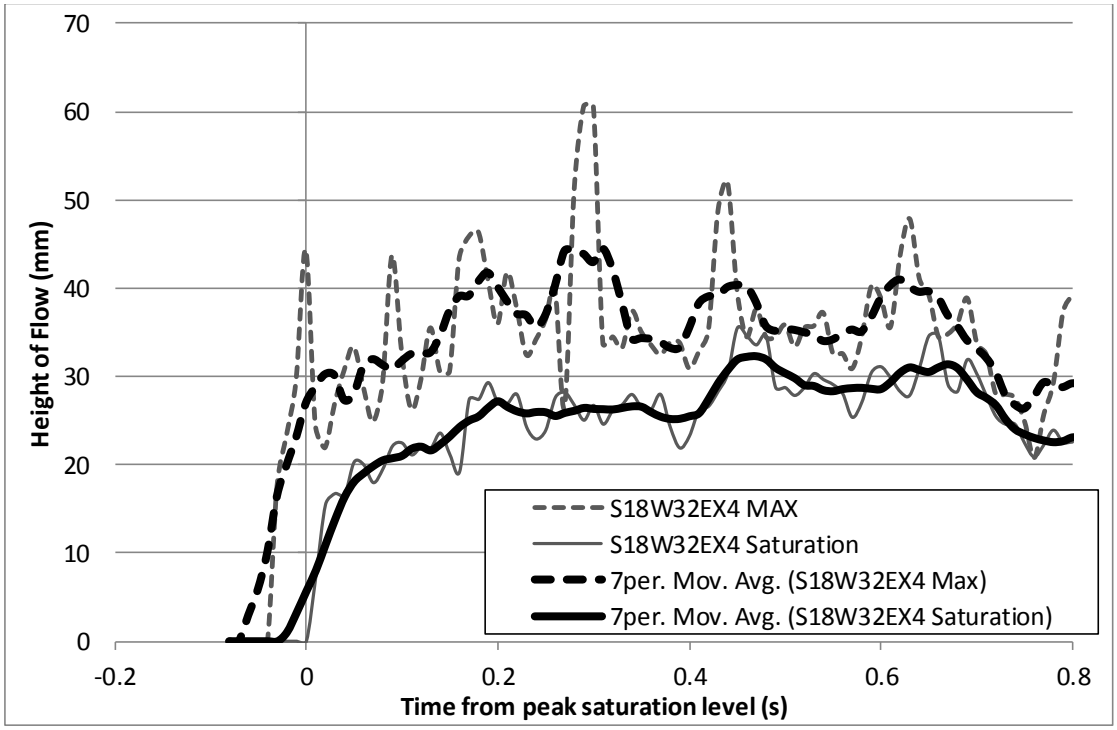

Figure F-30: Height over time of S18W32EX4.

F.2.4. S18 - W36

F.2.4.1. S18W36IN3

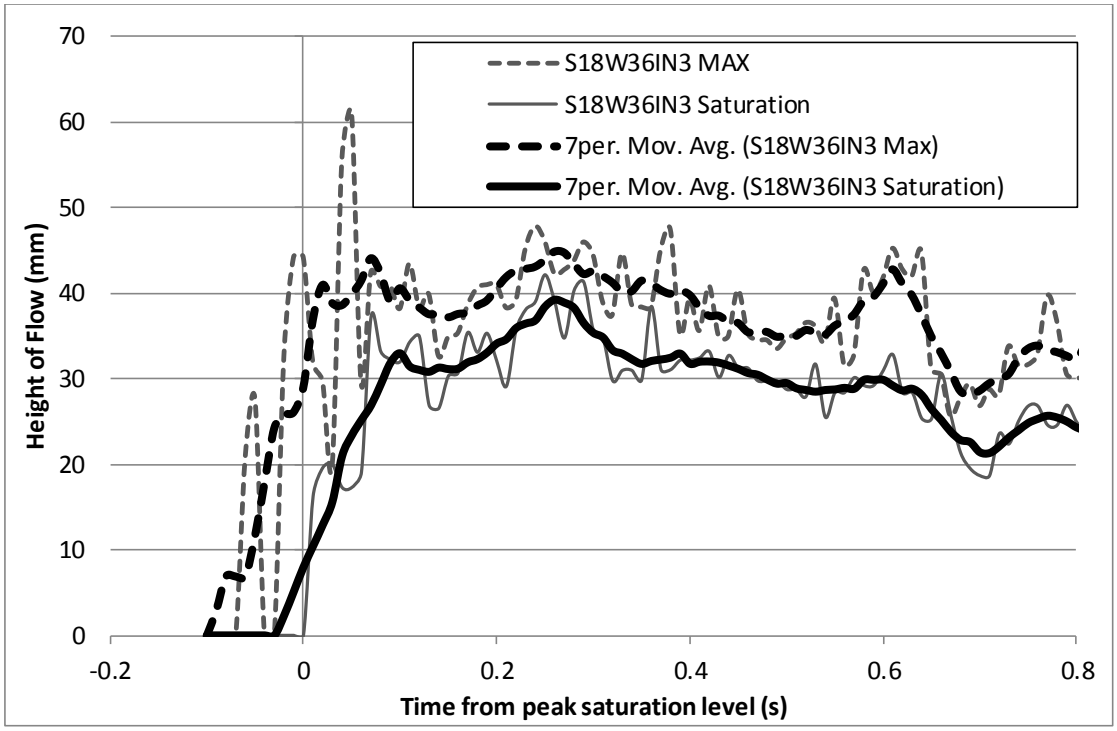

Figure F-31: Height over time of S18W36IN3.

F.2.4.2. S18W36EX3

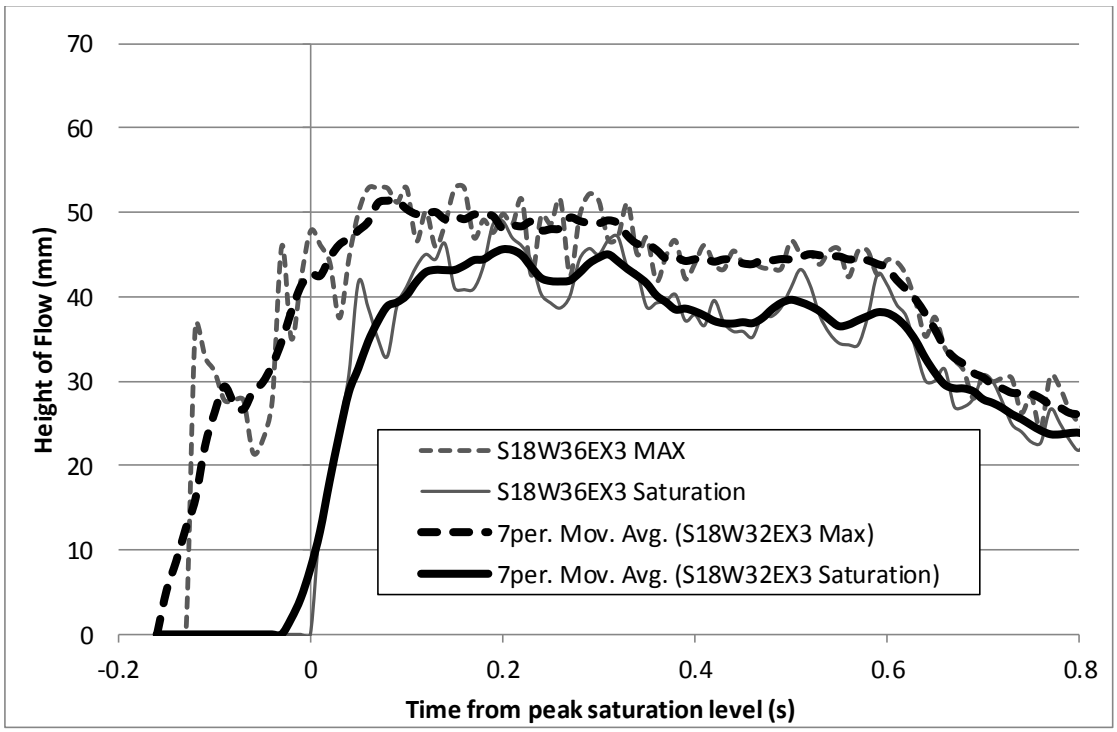

Figure F-32: Height over time of S18W36EX3.

F.2.4.3. S18W36EX5

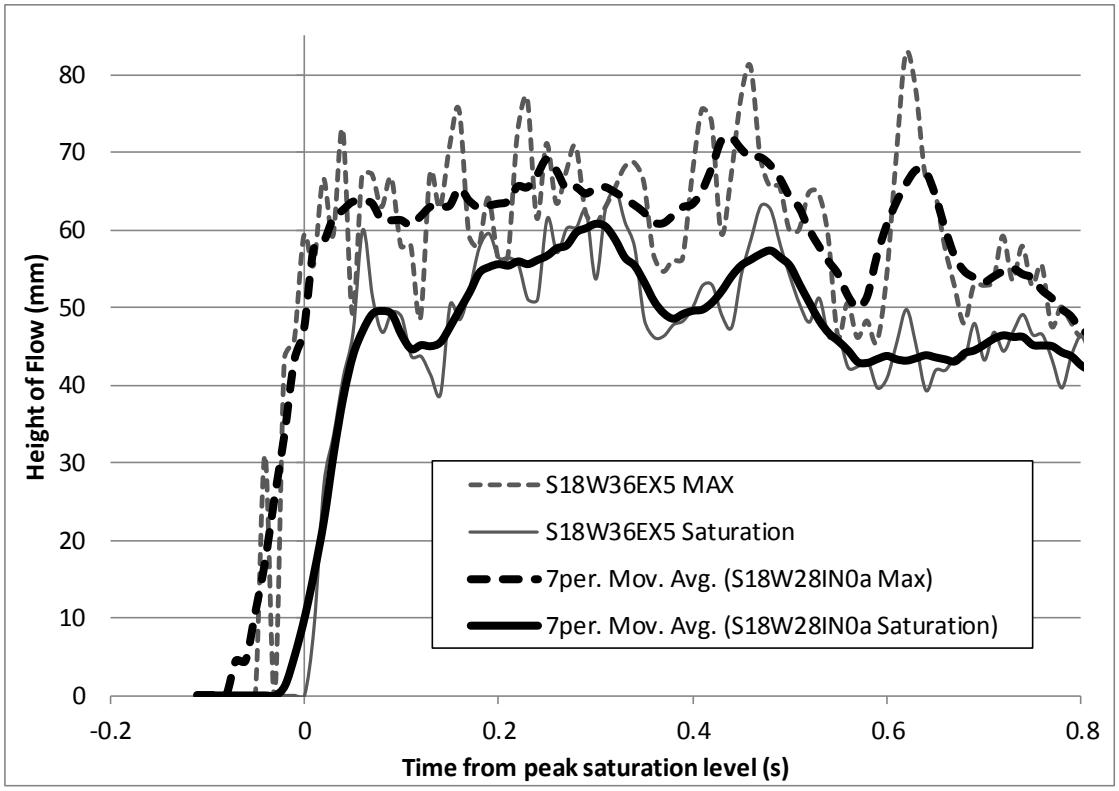

Figure F-33: Height over time of S18W36EX5. Note Change in vertical axis up to 85mm from 70mm

F.2.5. S24 – W28

F.2.5.1. S24W32EX8

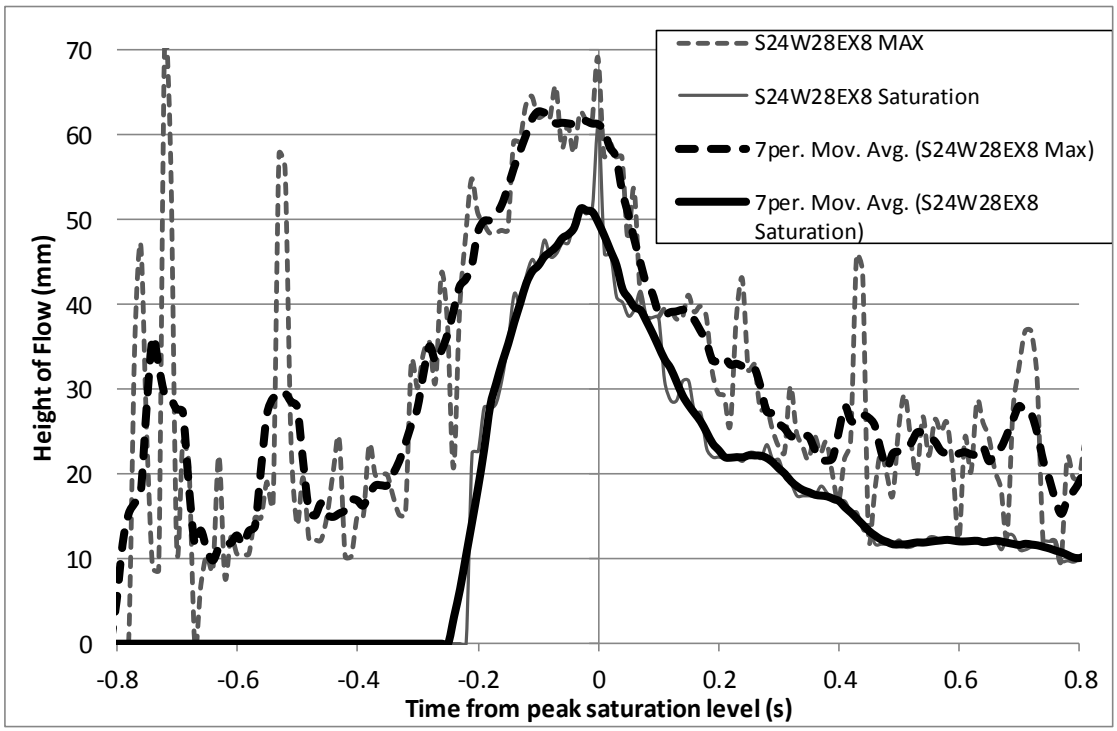

Figure F-34: Height over time of S24W28EX8. Note scale change on negative side of horizontal axis.

F.2.6. S24 – W32

F.2.6.1. S24W32IN7

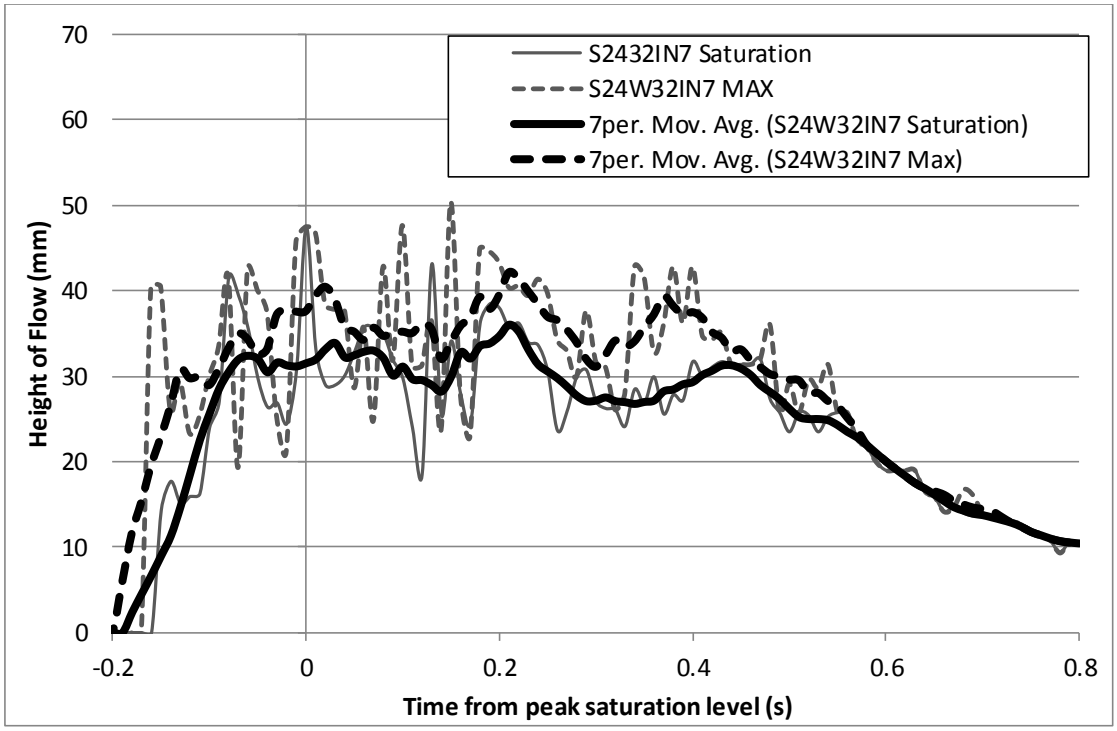

Figure F-35: Height over time of S24W32IN7.

F.2.6.2. S24W32IN8

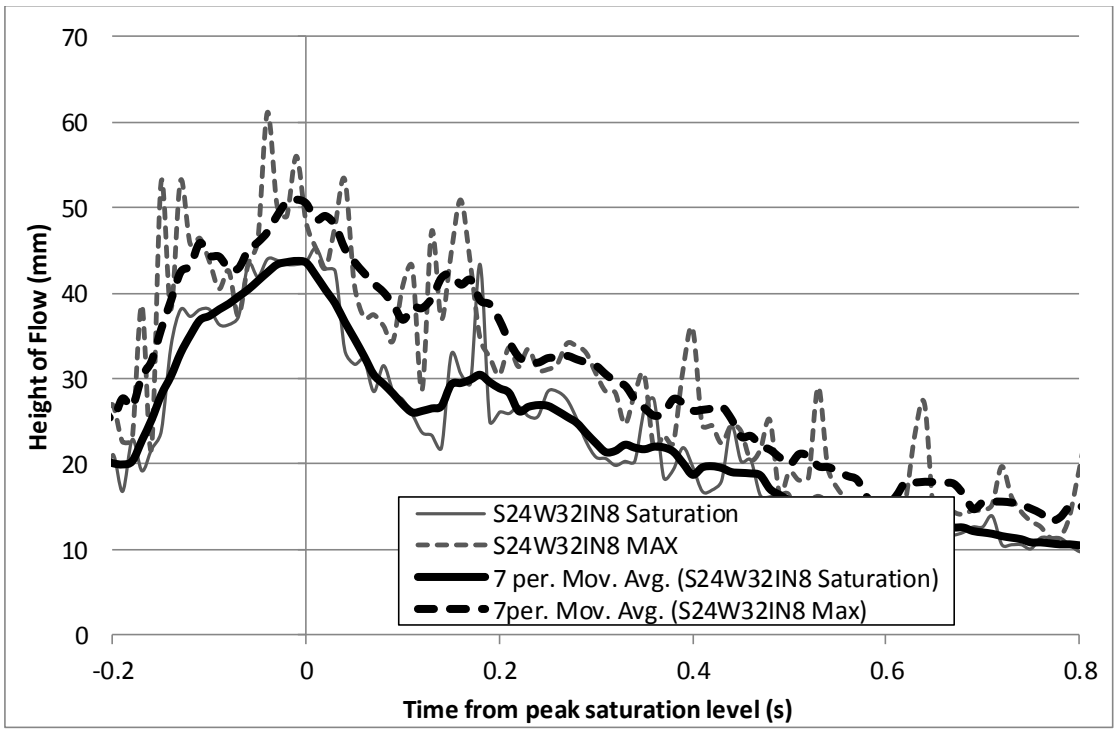

Figure F-36: Height over time of S24W32IN8.

F.2.6.3. S24W36EX7

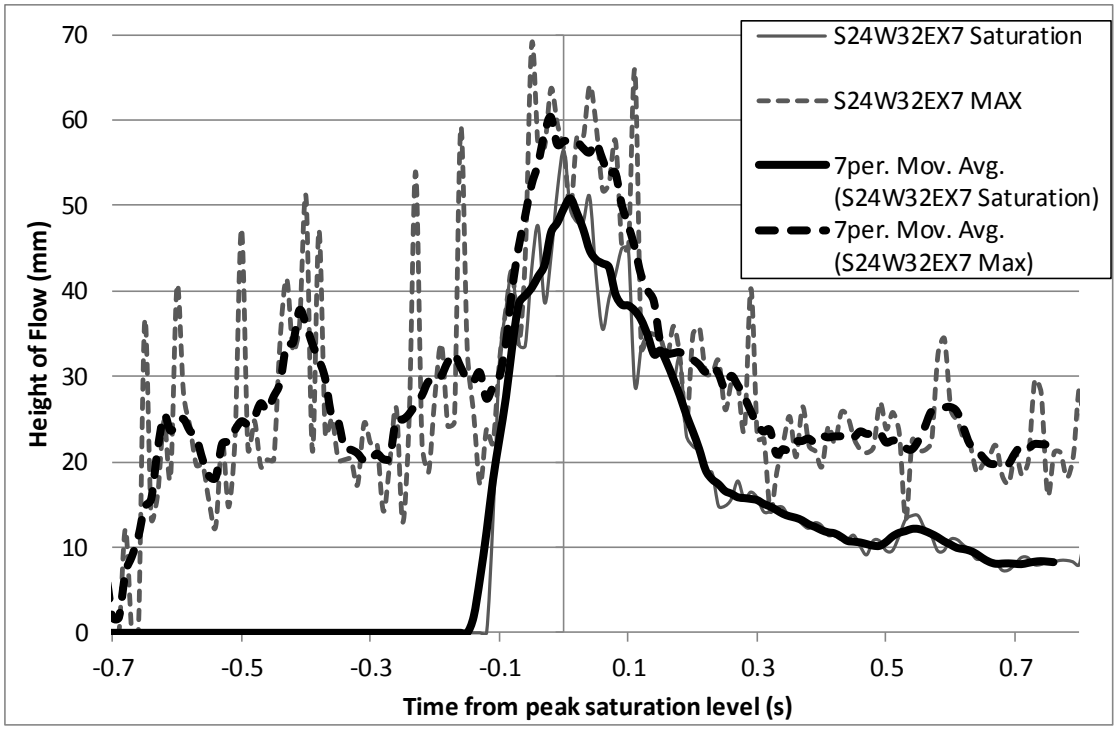

Figure F-37: Height over time of S24W32EX7. Note scale change on negative side of horizontal axis.

F.2.6.4. S24W36EX9

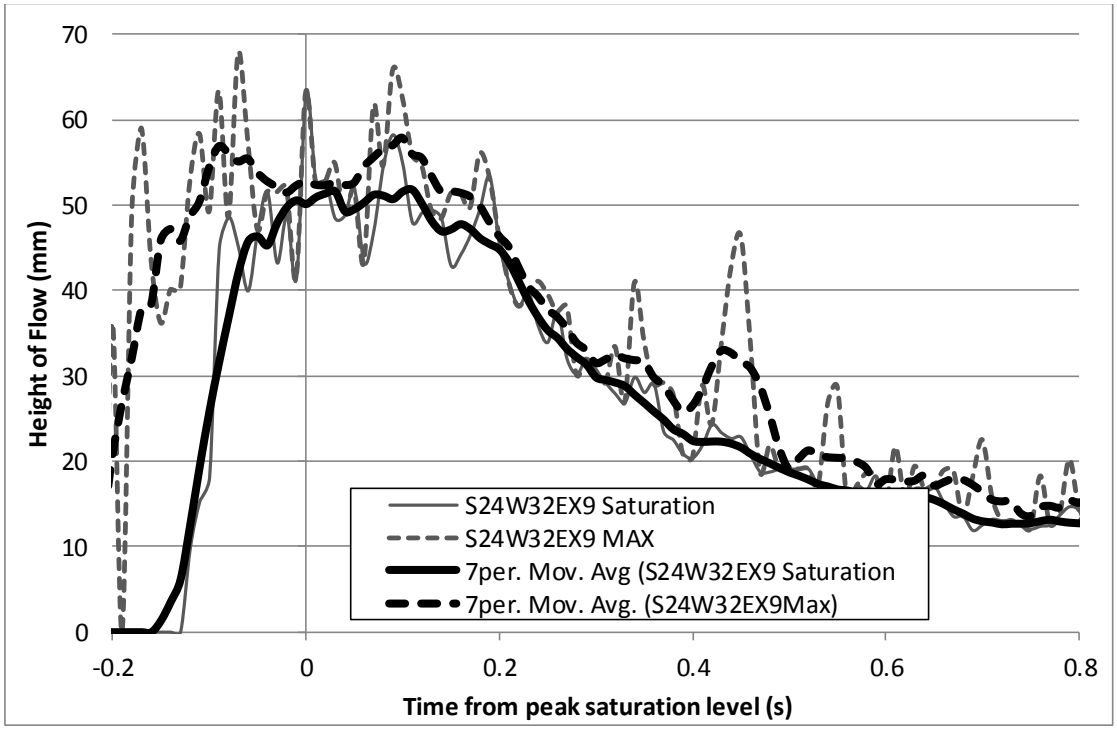

Figure F-38: Height over time of S24W32EX9.

Appendix G: PIV Results per test

G.1. Velocity over time

G.1.1. S18 – W24

G.1.1.1. S18W24IN5

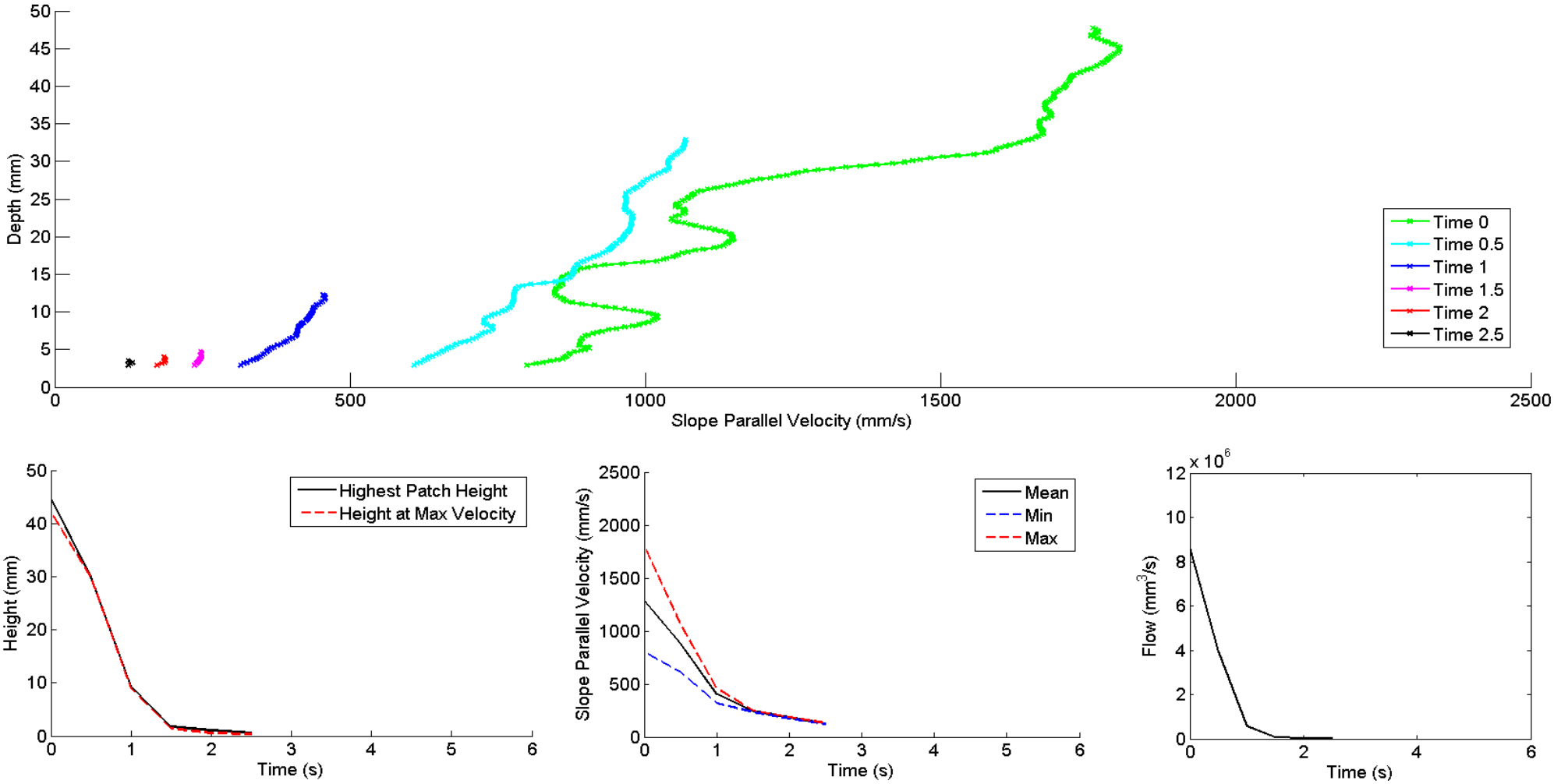

Figure G-1: Velocity profiles, height over time used in analysis averaged velocity over time and approximated flow of S18W24IN5. Depth of tail profiles was less than patch size so are omitted.

G.1.2. S18 – W28

G.1.2.1. S18W28IN1

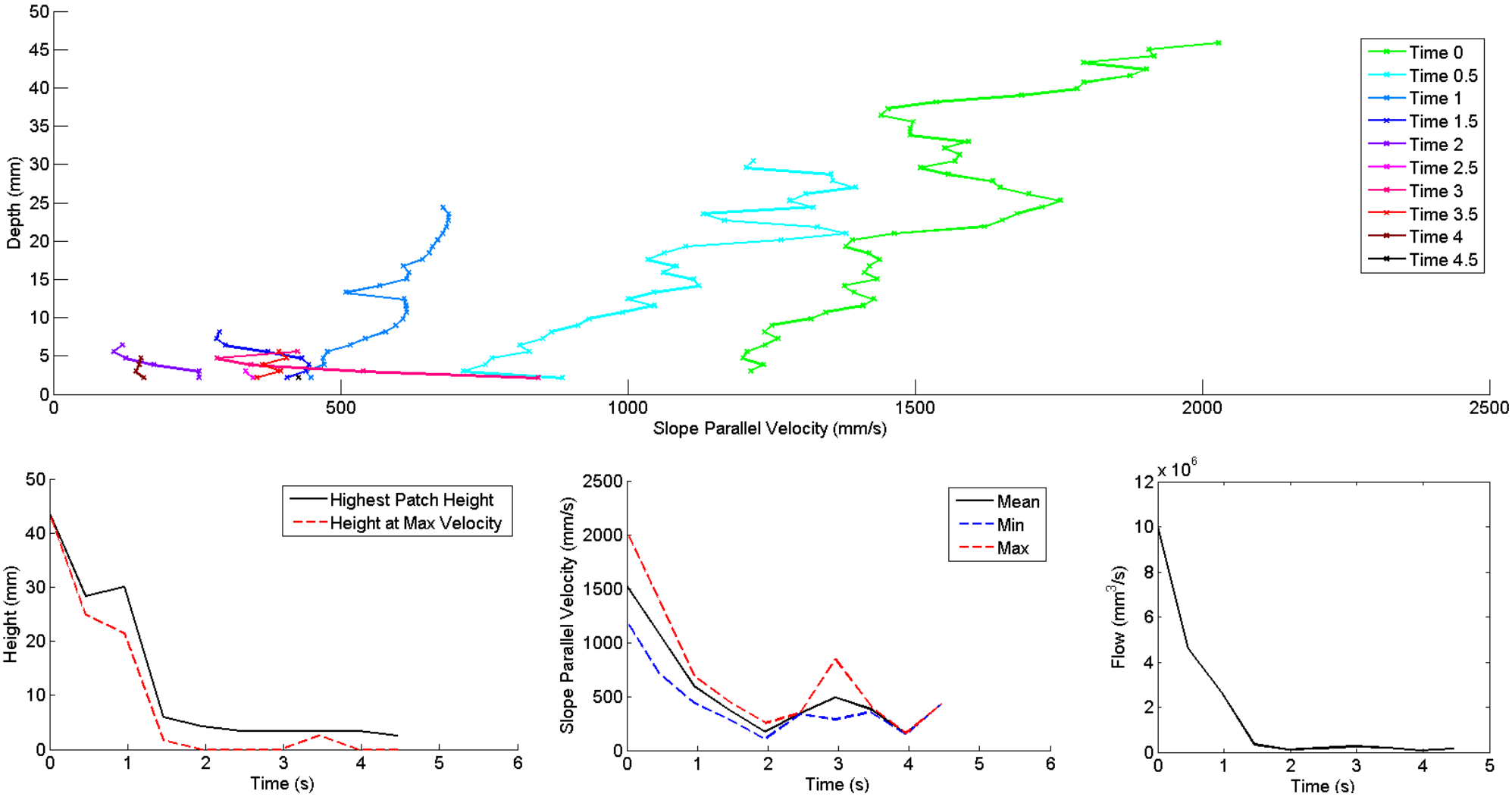

Figure G-2: Velocity profiles, height over time used in analysis, averaged velocity over time and approximated flow of S18W28IN1. Poor image quality leading to some irregularities in PIV results. Vertical spacing at 8 pixels gives rougher profile.

G.1.2.2. S18W28IN4

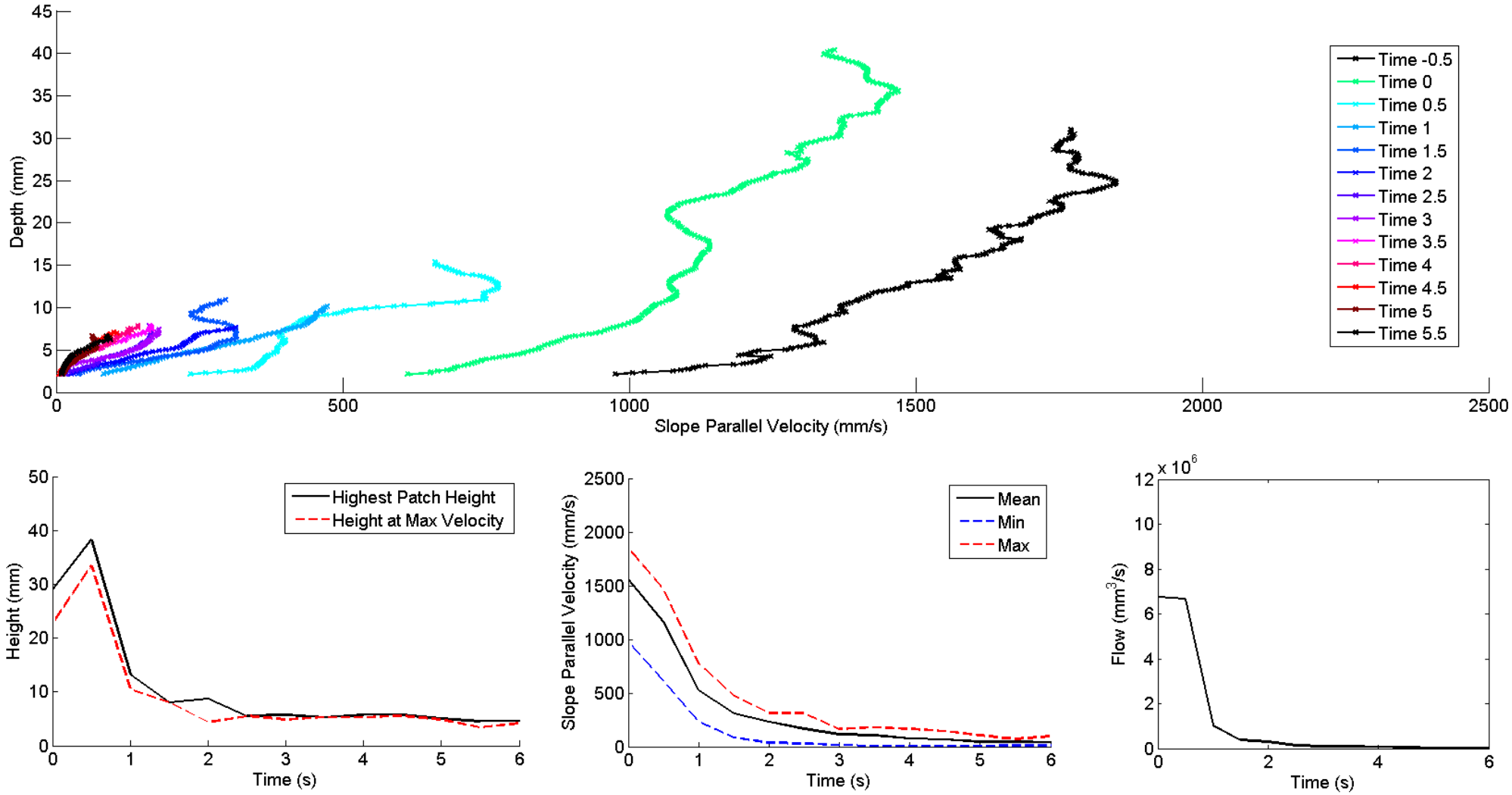

Figure G-3: Velocity profiles, height over time used in analysis, averaged velocity over time and approximated flow of S18W28IN4. First profile occurred before peak saturation level. Second profile is at peak saturation level.

G.1.2.3. S18W28EX1

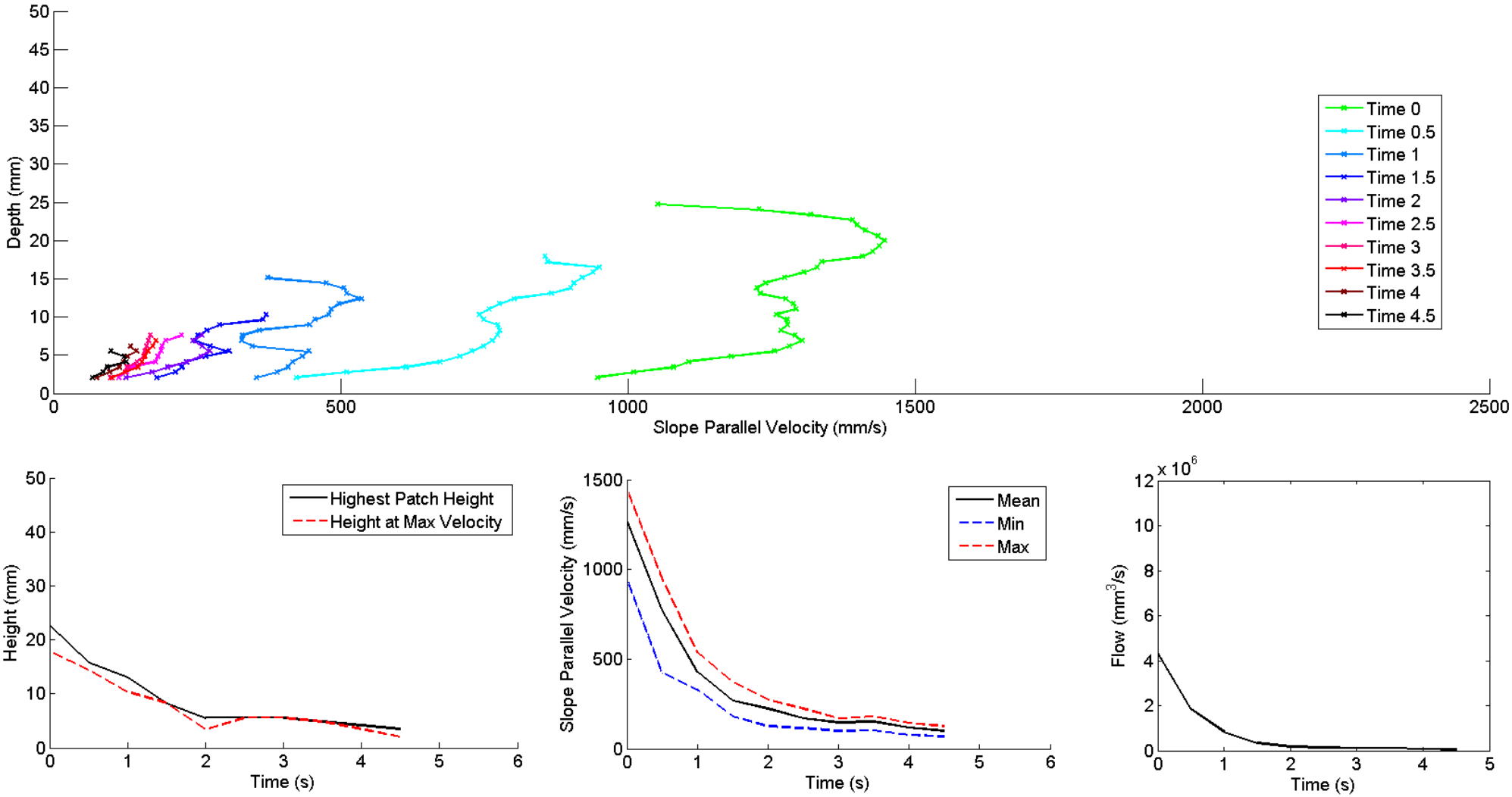

Figure G-4: Velocity profiles, height over time used in analysis, averaged velocity over time and approximated flow of S18W28EX1. Vertical spacing at 8 pixels gives rougher profile

G.1.3. S18 - W32

G.1.3.1. S18W32IN2

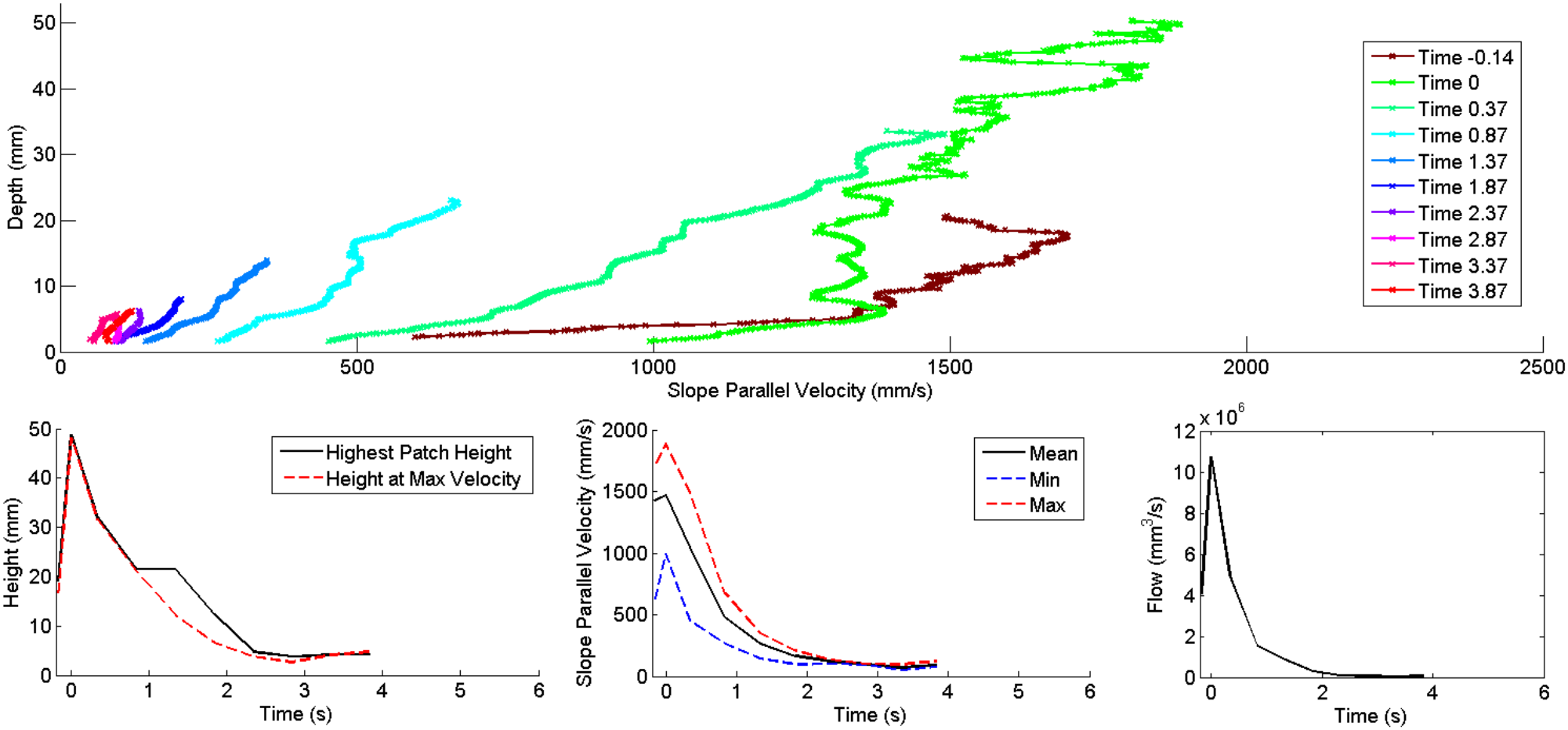

Figure G-5: Velocity profiles, height over time used in analysis, averaged velocity over time and approximated flow of S18W32IN2. First profile occurred before peak saturation level. Second profile is at peak saturation level.

G.1.3.2. S18W32IN6

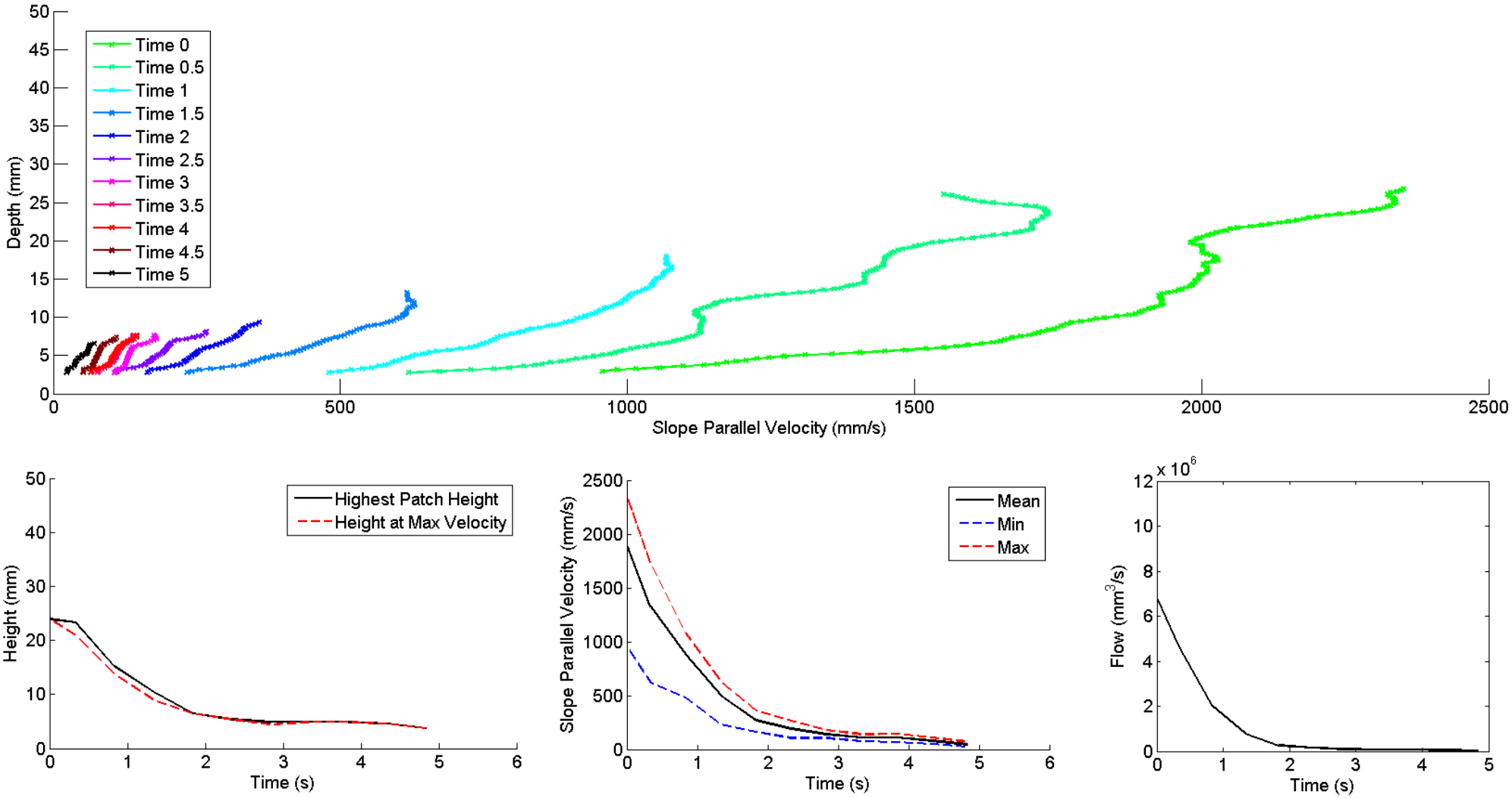

Figure G-6: Velocity profiles, height over time used in analysis, averaged velocity over time and approximated flow of S18W32IN6.

G.1.3.3. S18W32EX2

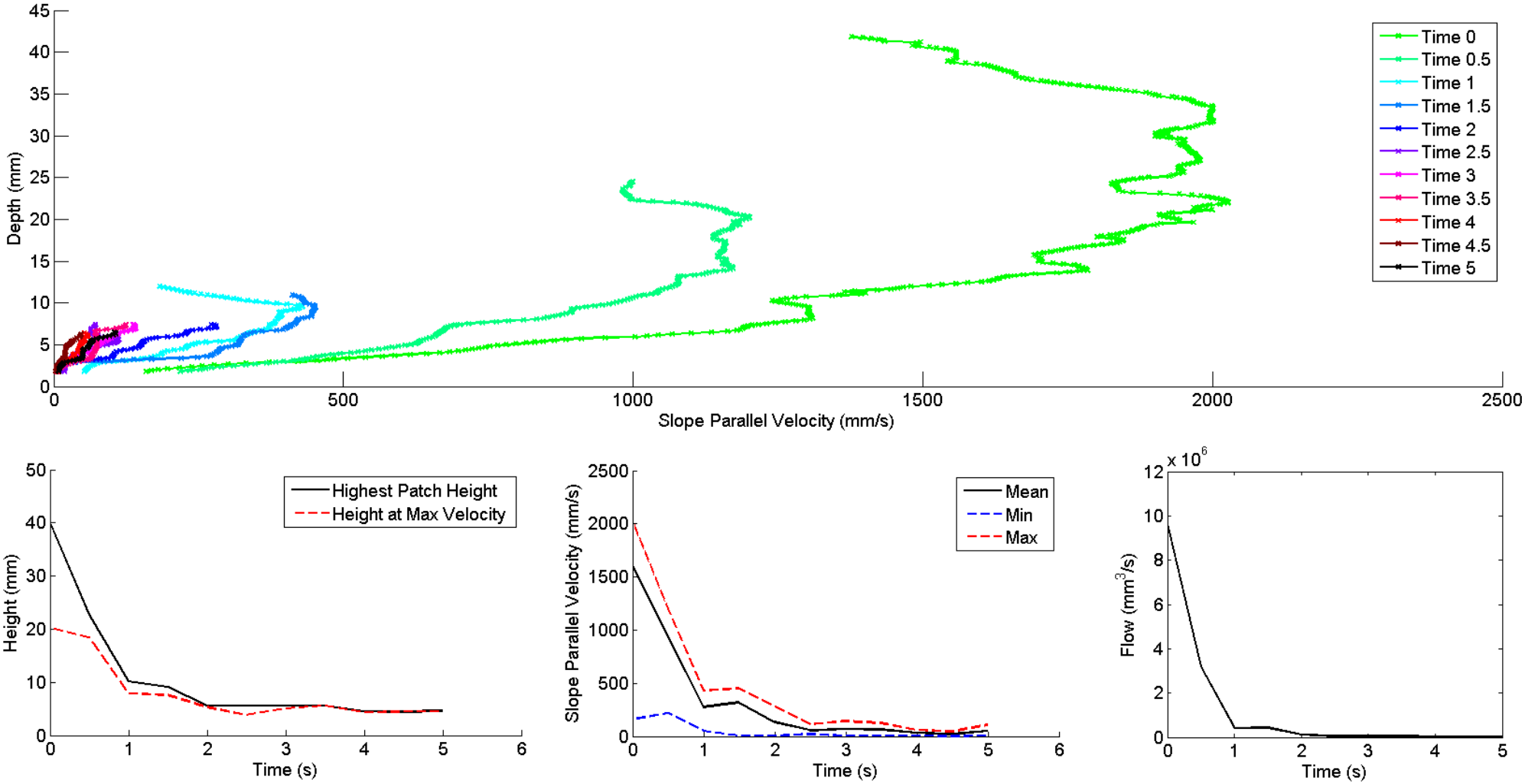

Figure G-7: Velocity profiles, height over time used in analysis, averaged velocity over time and approximated flow of S18W32EX2.

G.1.3.4. S18W32EX4

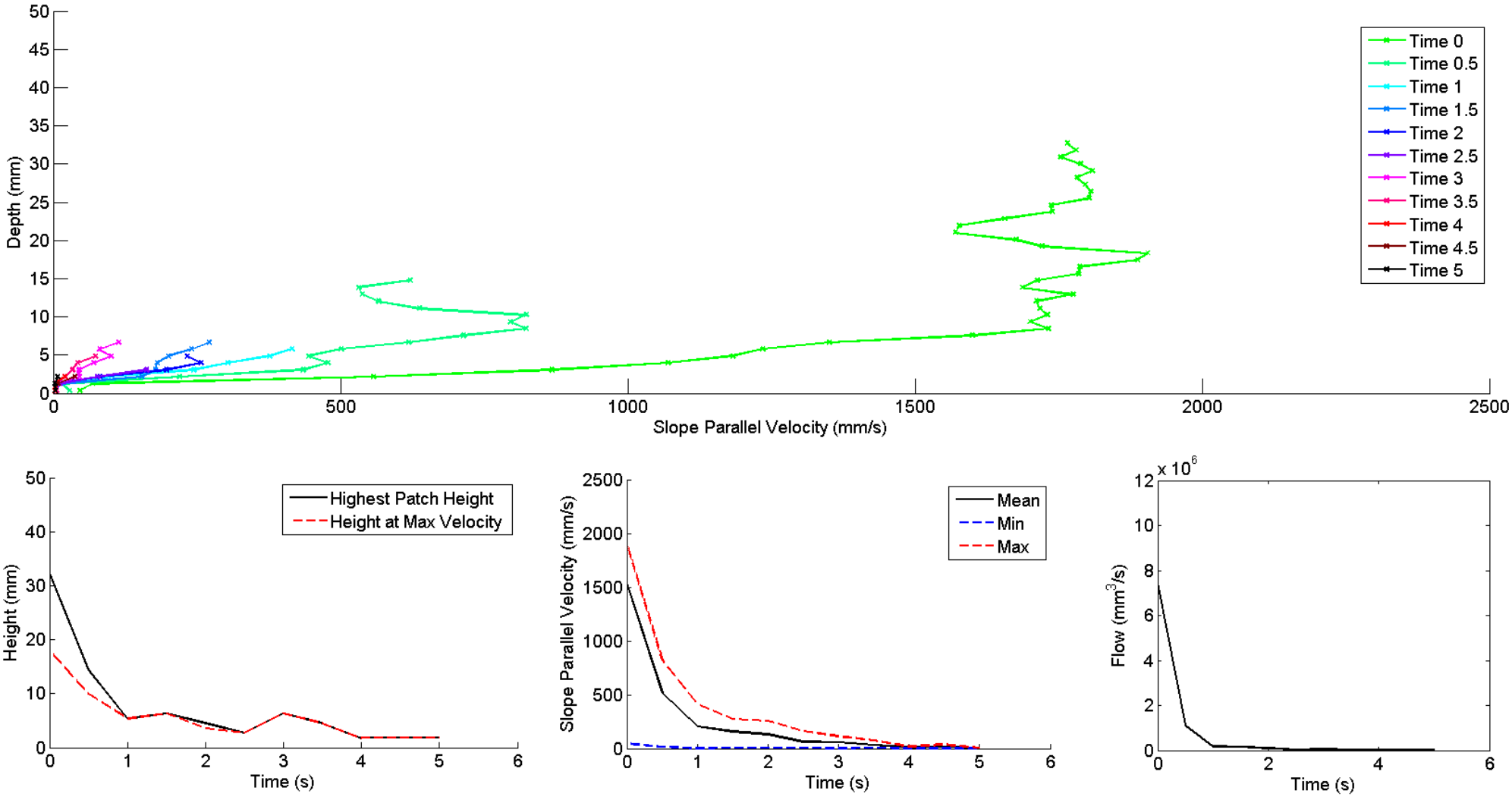

Figure G-8: Velocity profiles, height over time used in analysis, averaged velocity over time and approximated flow of S18W32EX4. Vertical spacing at 8 pixels gives rougher profile.

G.1.4. S18 - W36

G.1.4.1. S18W36IN3

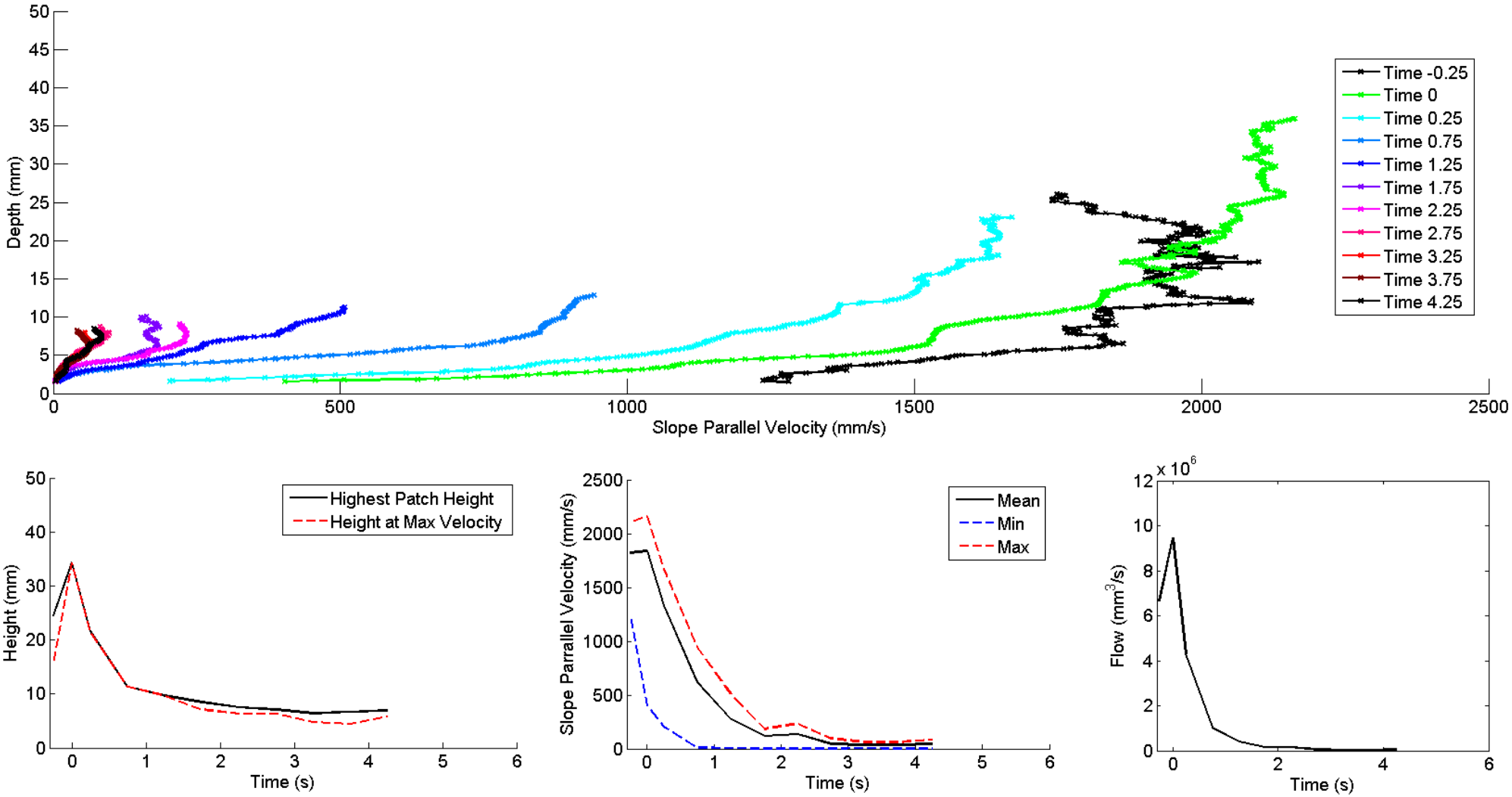

Figure G-9: Velocity profiles, height over time used in analysis, averaged velocity over time and approximated flow of S18W36IN3. First profile occurred before peak saturation level. Second profile is at peak saturation level.

G.1.4.2. S18W36EX3

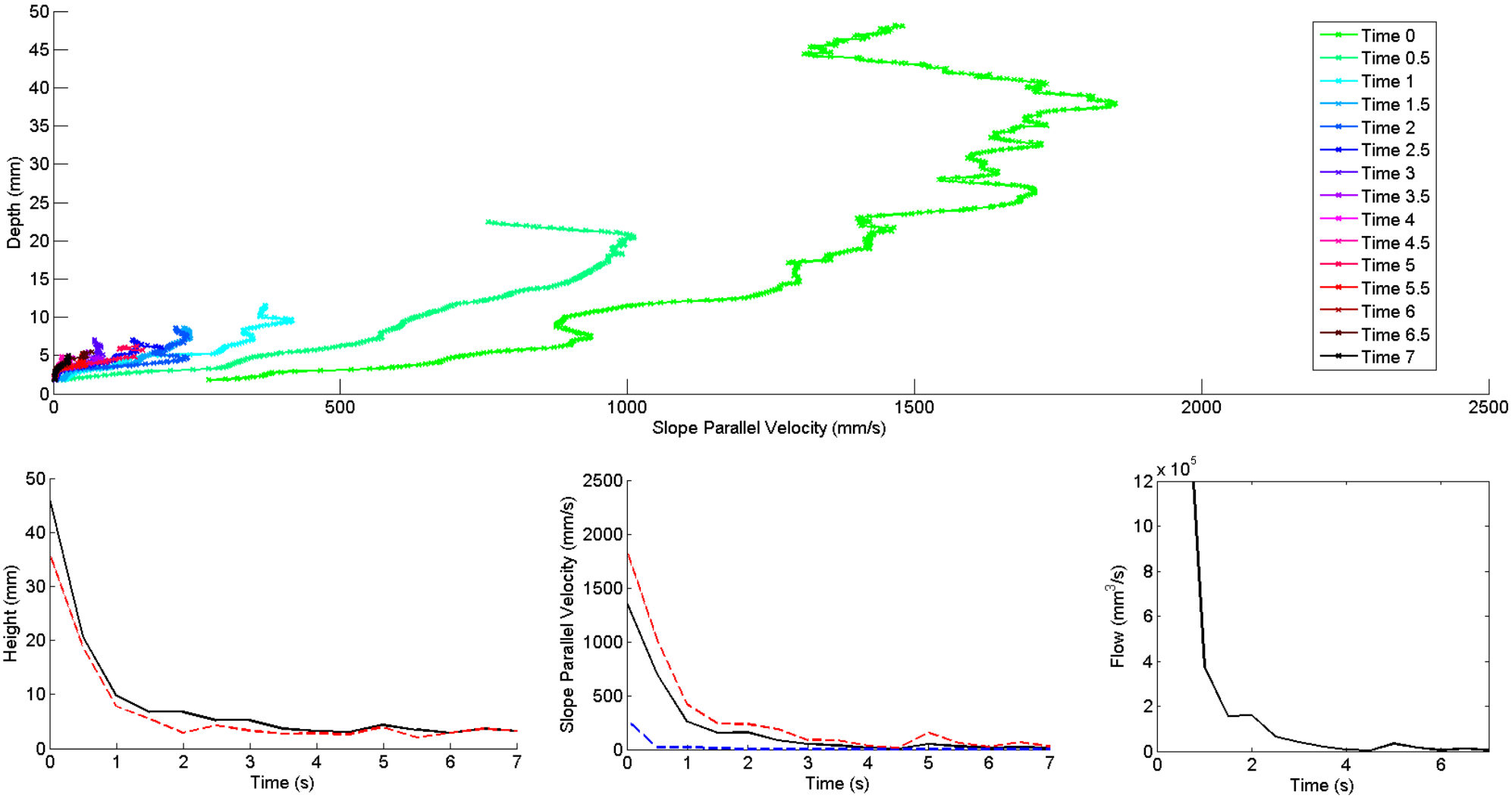

Figure G-10: Velocity profiles, height over time used in analysis, averaged velocity over time and approximated flow of S18W36EX3.

G.1.4.3. S18W36EX5

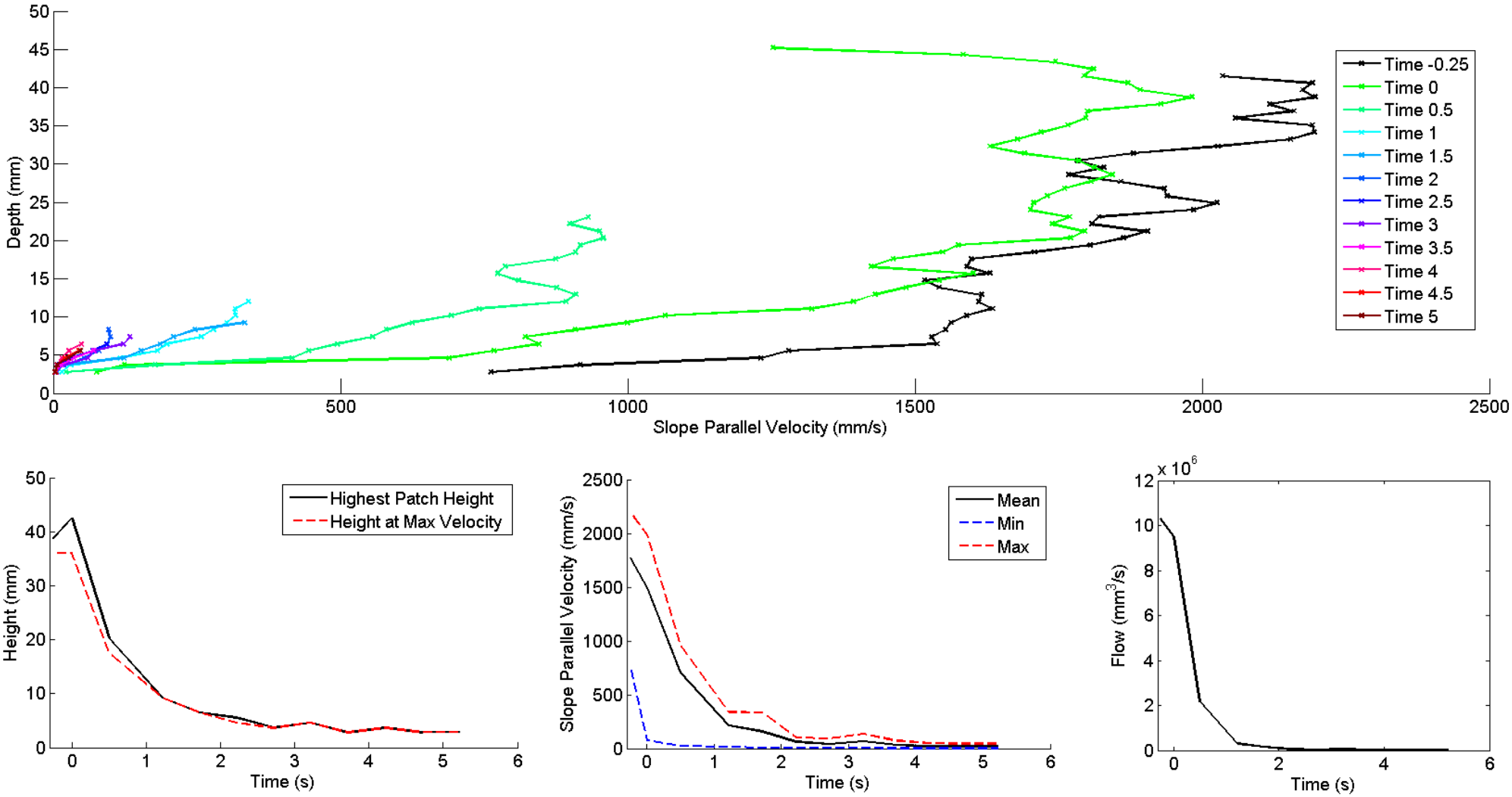

Figure G-11: Velocity profiles, height over time used in analysis, averaged velocity over time and approximated flow of S18W36EX5. First profile occurred before peak saturation level. Second profile is at peak saturation level. Vertical spacing at 8 pixels gives rougher profile.

G.1.5. S24 – W28

G.1.5.1. S24W32EX8

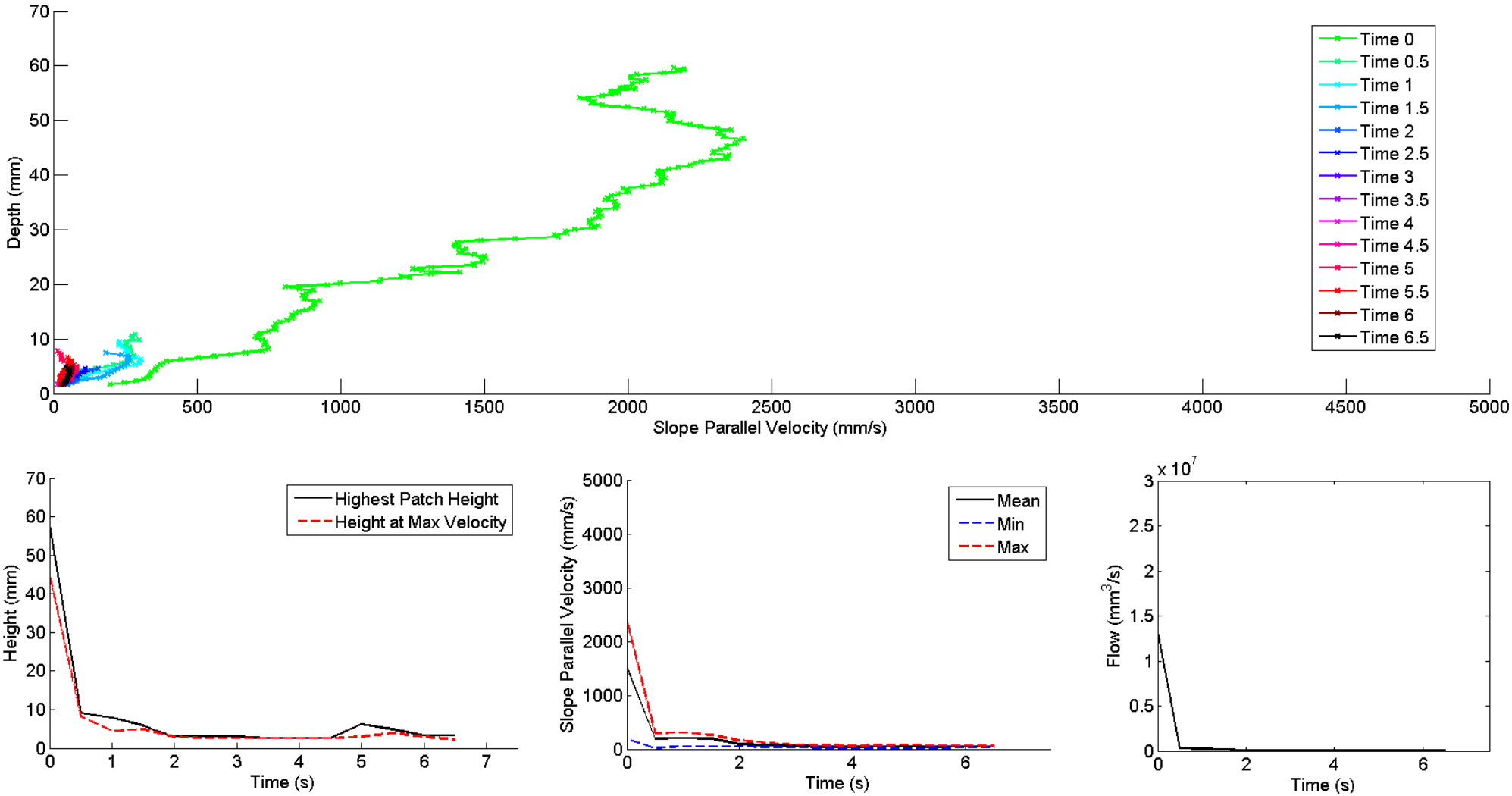

Figure G-12: Velocity profiles, height over time used in analysis, averaged velocity over time and approximated flow of S24W28EX8.

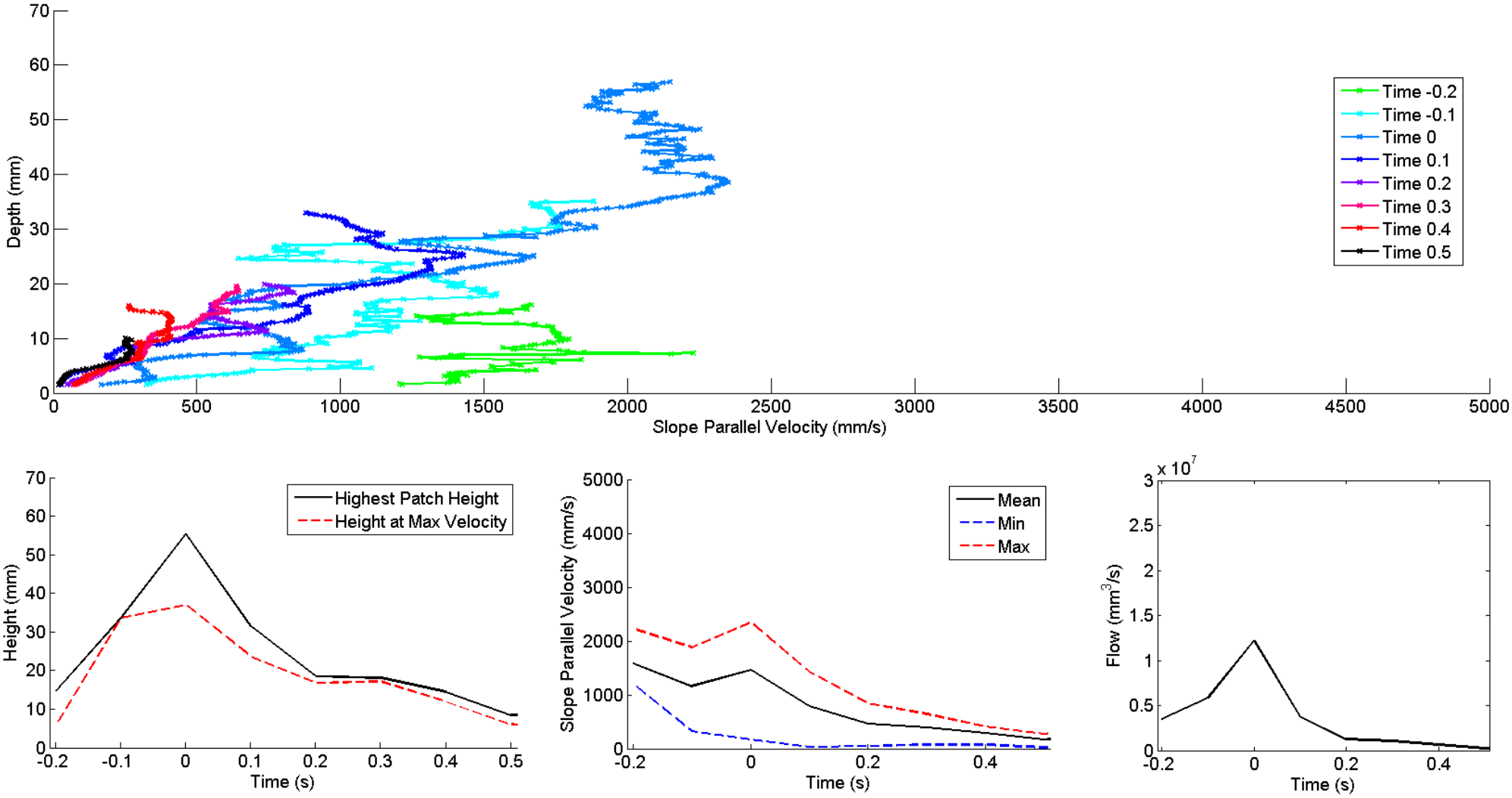

Figure G-13: Velocity profiles, height over time used in analysis, averaged velocity over time and approximated flow of body of S24W28EX8.

G.1.6. S24 – W32

G.1.6.1. S24W32IN7

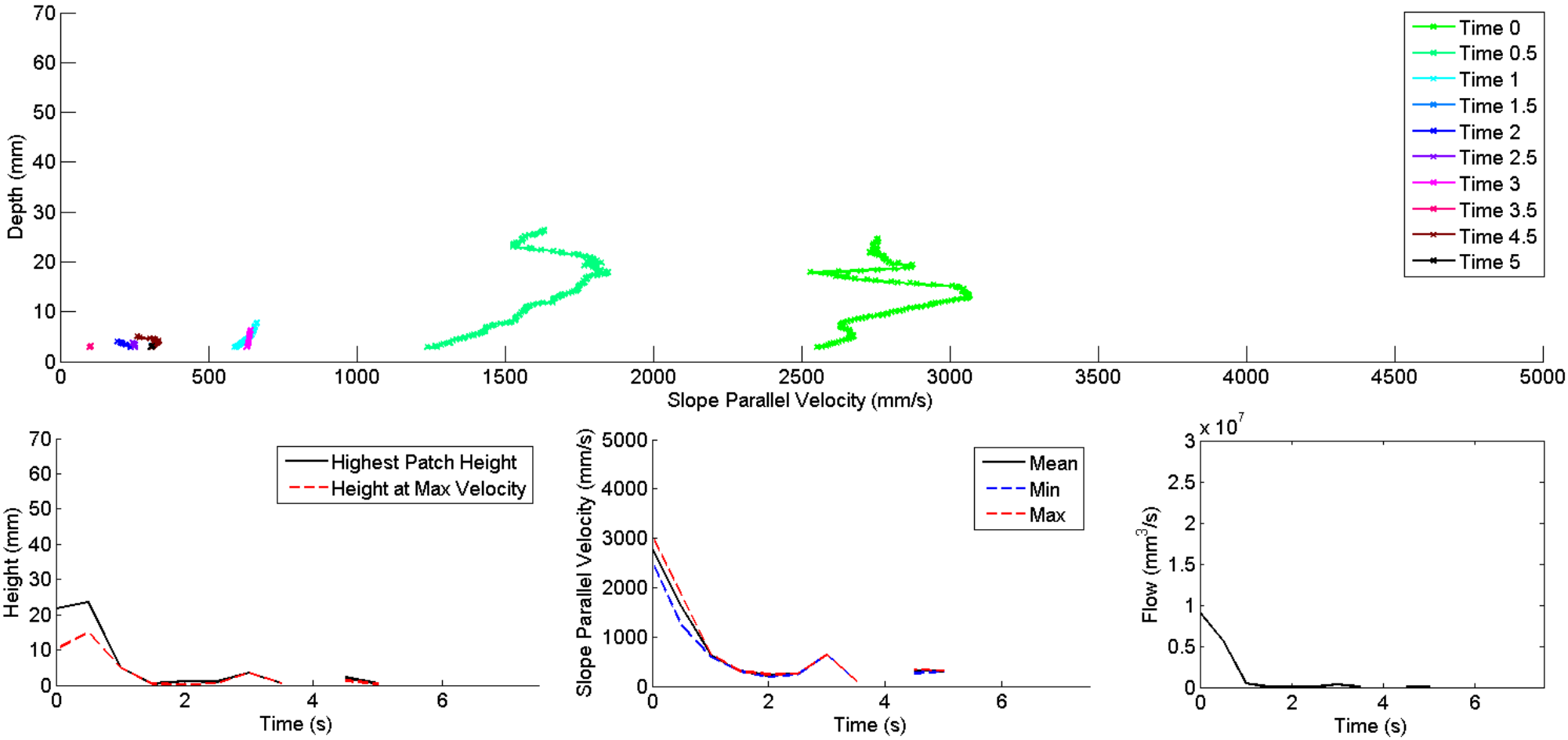

Figure G-14: Velocity profiles, height over time used in analysis, averaged velocity over time and approximated flow of S24W32IN. Poor image quality reduce accuracy and depth of PIV analysis.

G.1.6.2. S24W32IN8

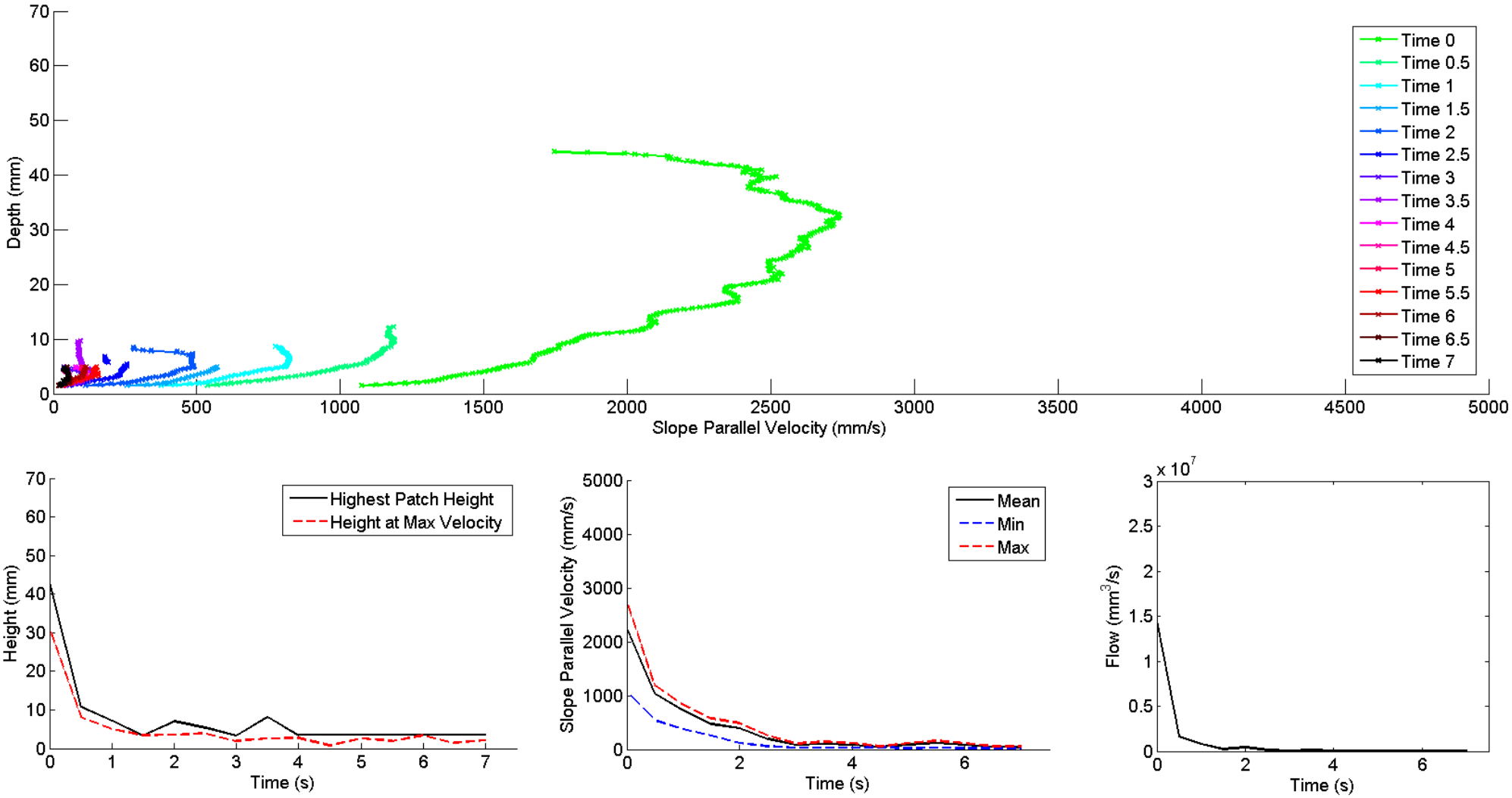

Figure G-15: Velocity profiles, height over time used in analysis; averaged velocity over time and approximated flow of S24W32IN8.

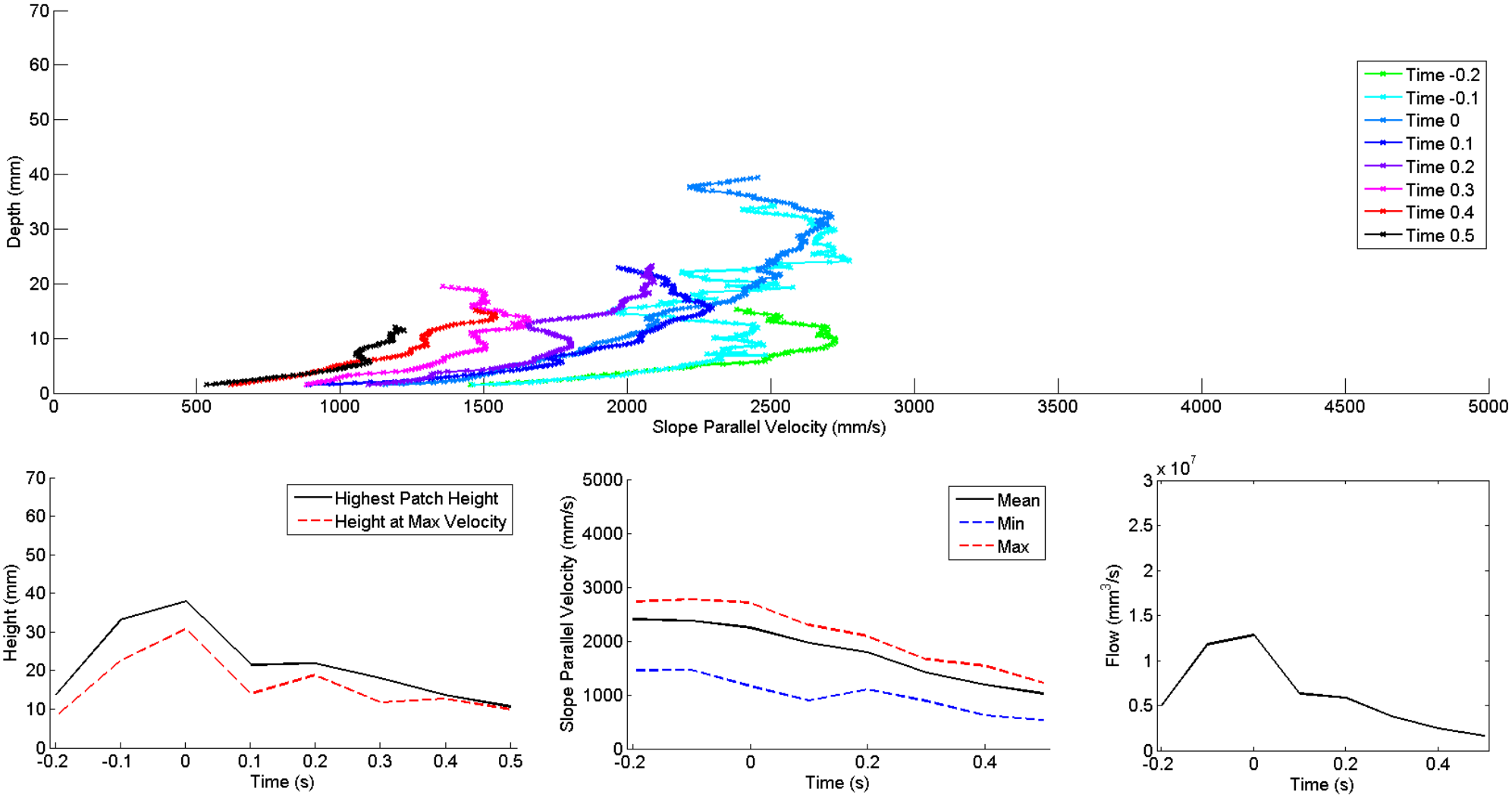

Figure G-16: Velocity profiles, height over time used in analysis, averaged velocity over time and approximated flow of body of S24W32IN8.

G.1.6.3. S24W36EX7

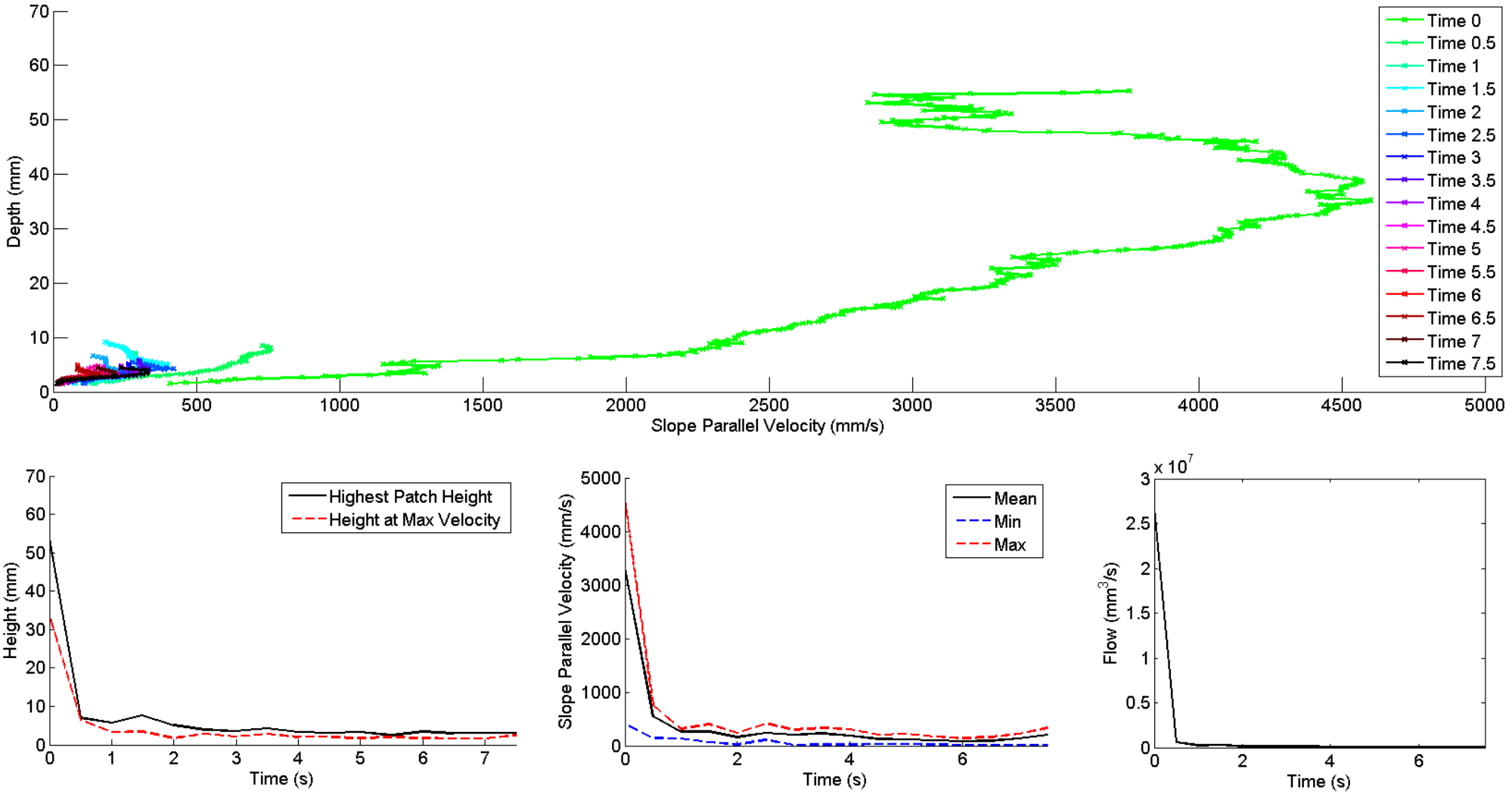

Figure G-17: Velocity profiles, height over time used in analysis, averaged velocity over time and approximated flow of S24W32EX7.

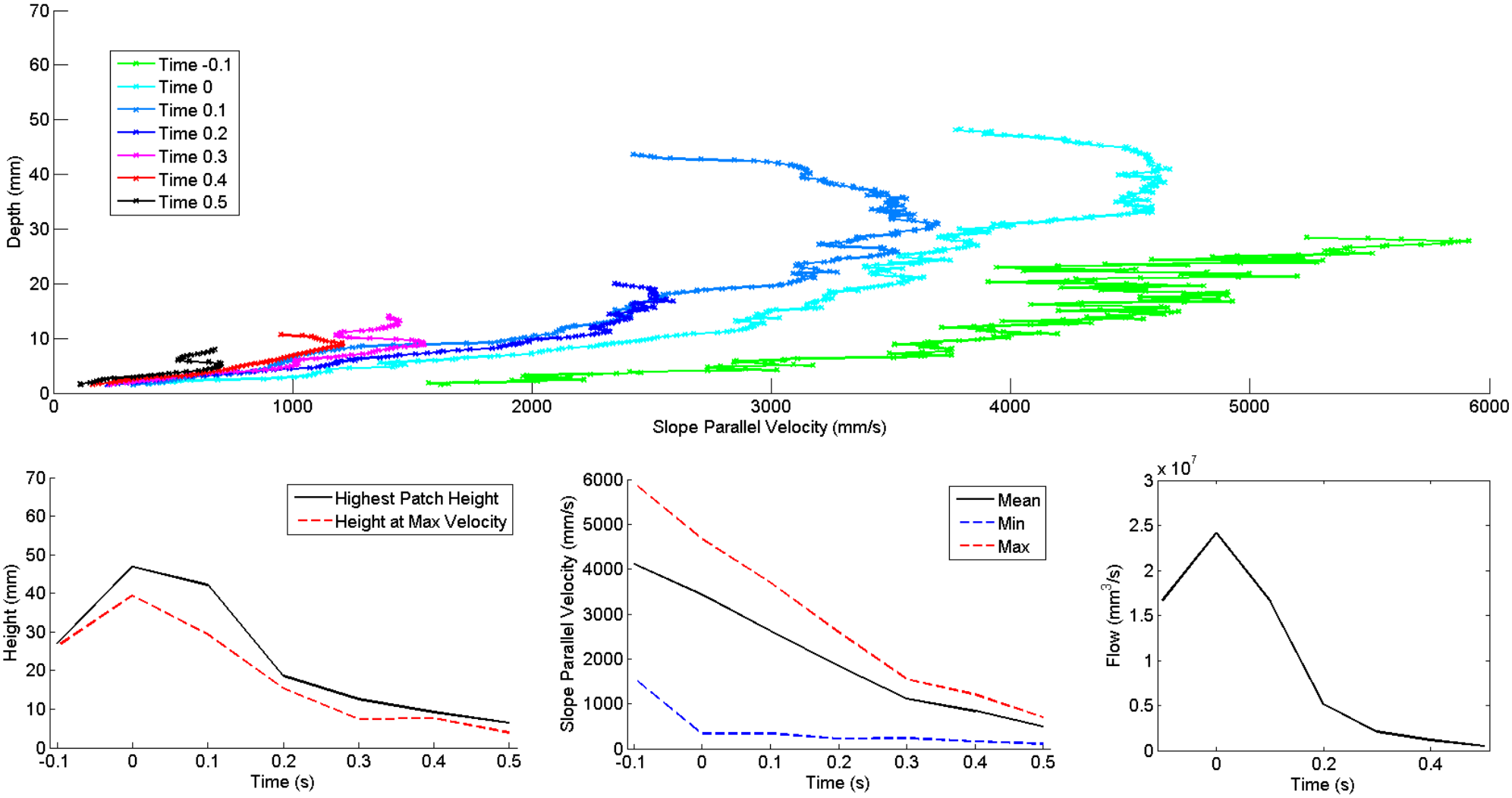

Figure G-18: Velocity profiles, height over time used in analysis, averaged velocity over time and approximated flow of body of S24W32EX7.

G.1.6.4. S24W36EX9

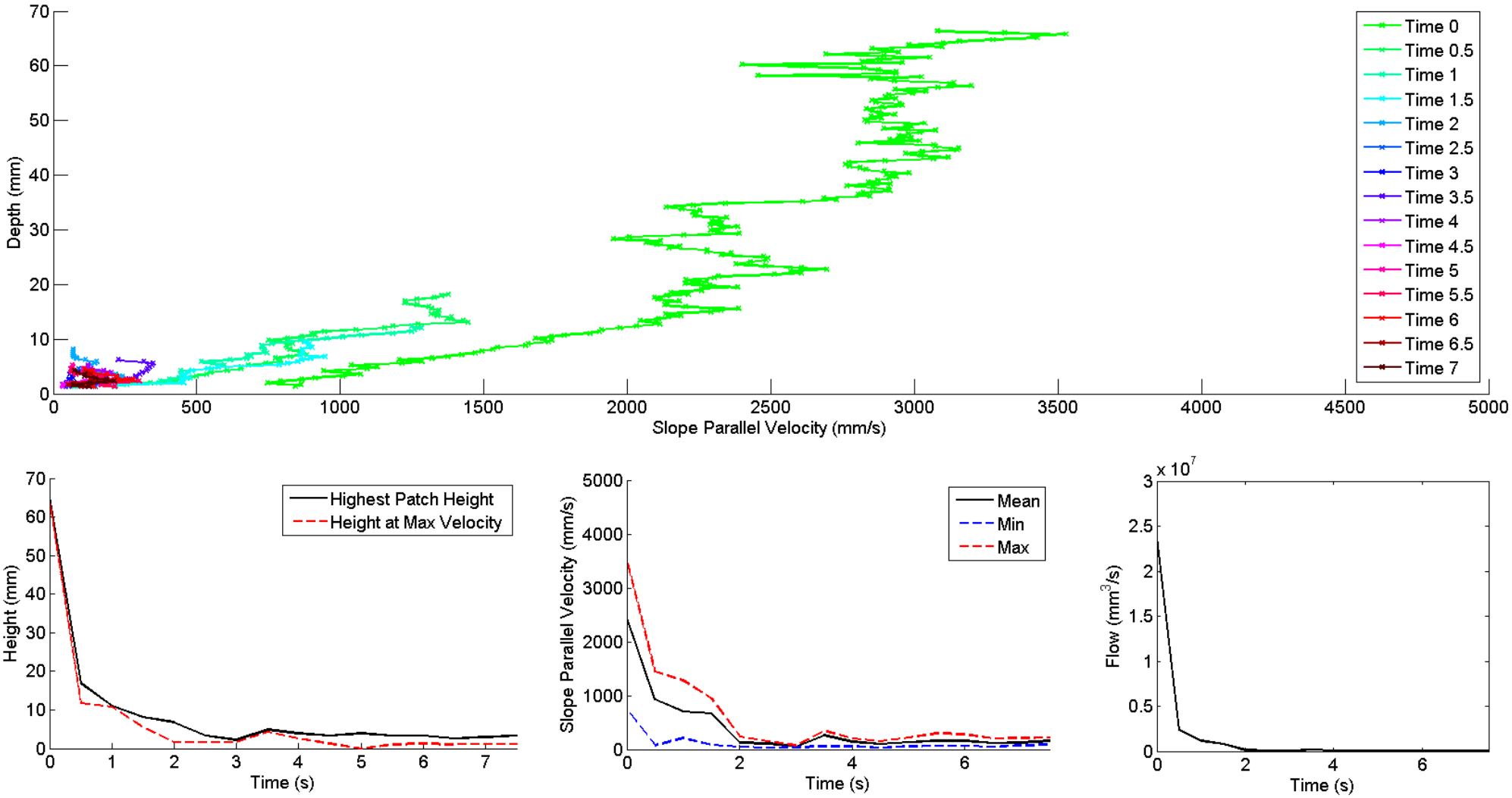

Figure G-19: Velocity profiles, height over time used in analysis, averaged velocity over time and approximated flow of S24W32EX9.

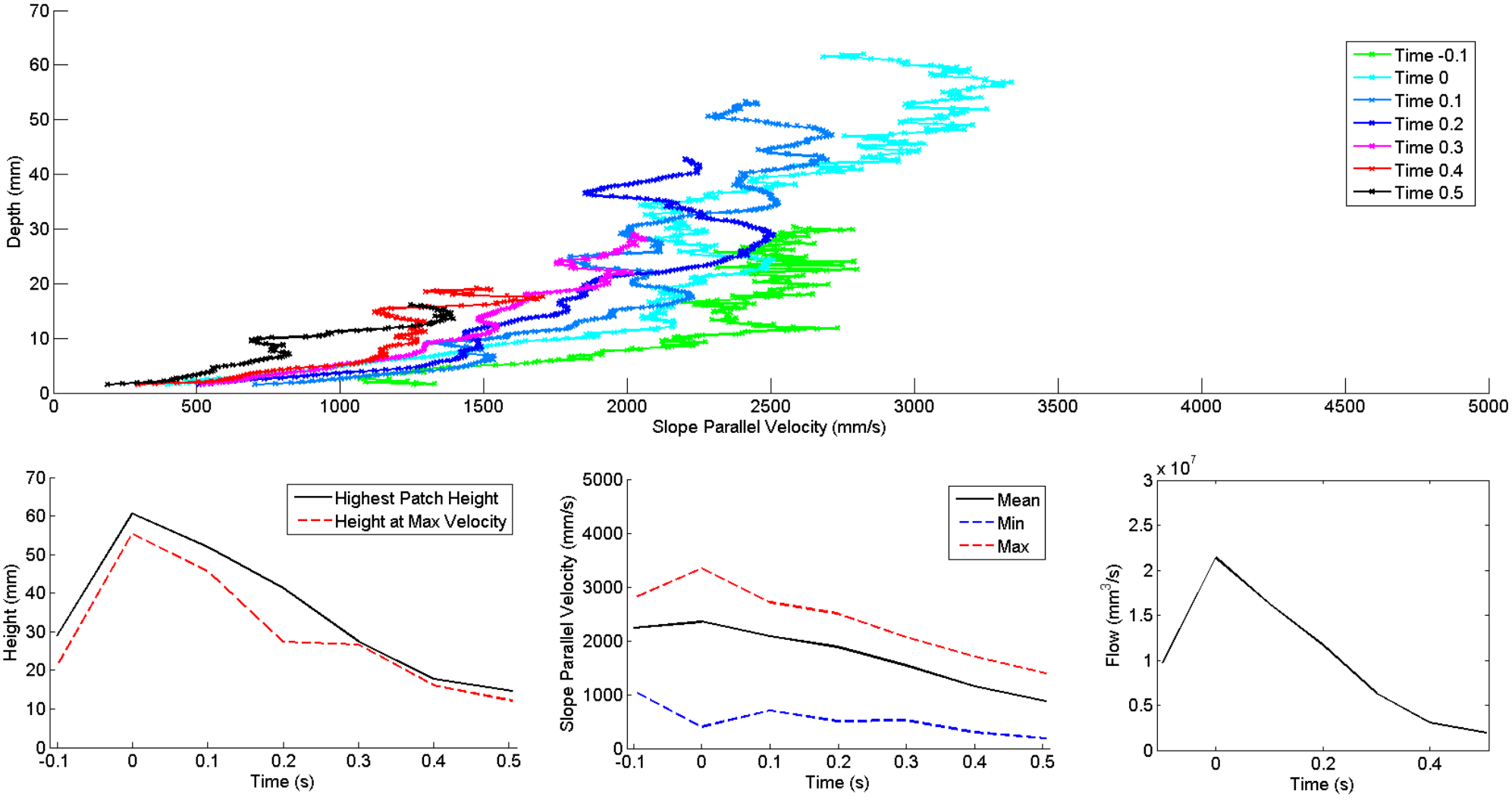

Figure G-20: Velocity profiles, height over time used in analysis, averaged velocity over time and approximated flow of body of S24W32EX9.

G.2. Normalised Velocity Profiles

G.2.1. S18 – W24

G.2.1.1. S18W24IN5

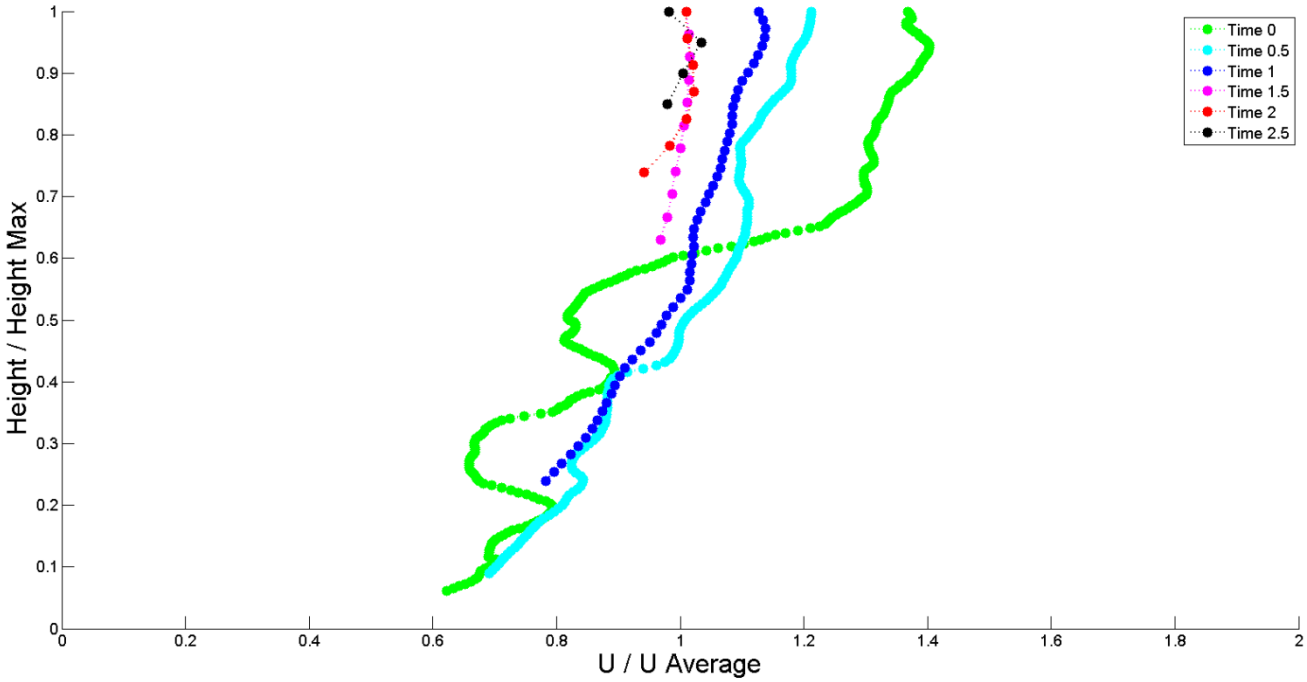

Figure G-1: Normalised velocity profiles of S18W24IN5. The height is normalised by the maximum saturation height. Velocity is normalised by the depth-averaged velocity of the profile. Profiles of tail omitted for this test as the depth was less than patch size.

G.2.2. S18 – W28

G.2.2.1. S18W28IN1

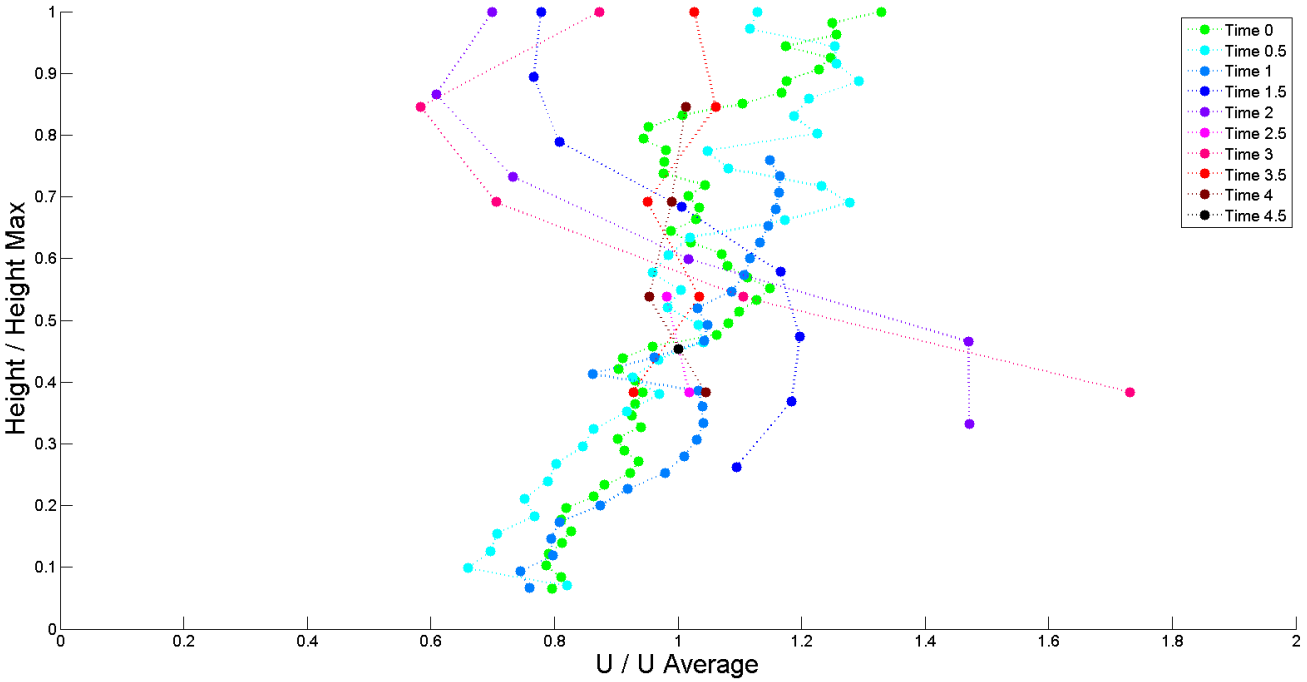

Figure G-2: Normalised velocity profiles of S18W28IN1. The height is normalised by the maximum saturation height. Velocity is normalised by the depth-averaged velocity of the profile. Poor image quality leading to some irregularities in PIV results. Vertical spacing at 8 pixels gives rougher profile.

G.2.2.2. S18W28IN4

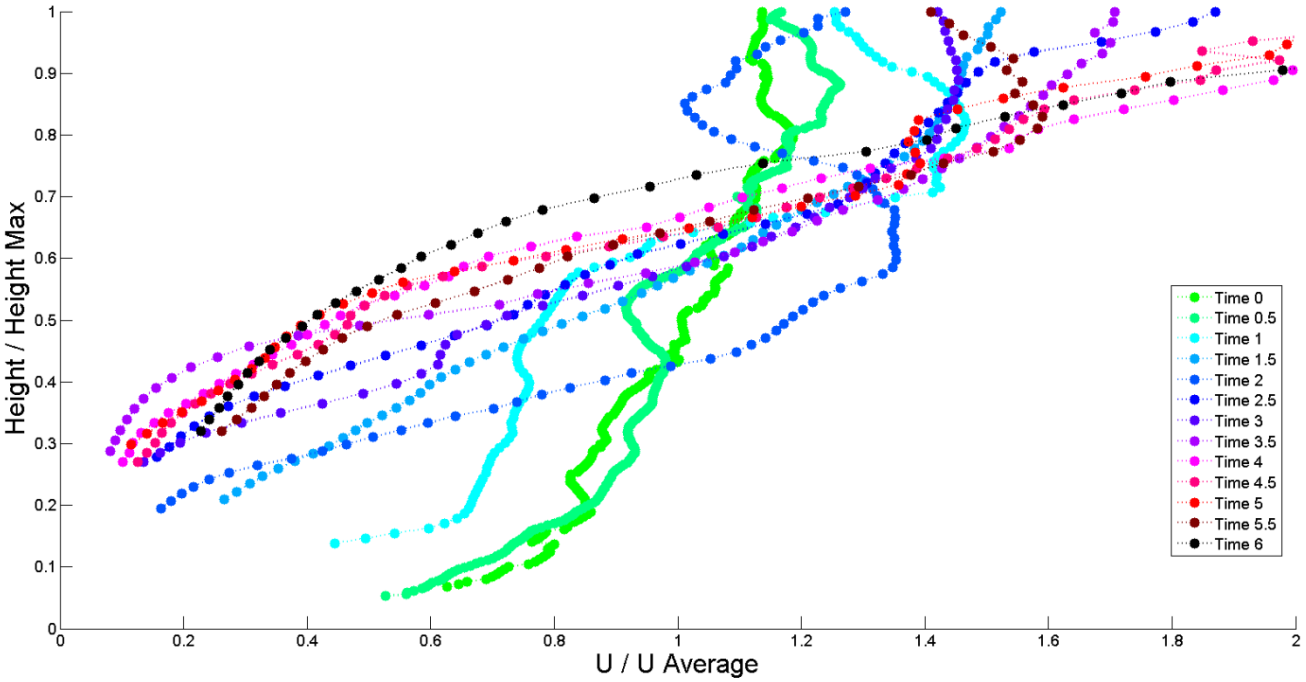

Figure G-21: Normalised velocity profiles of S18W28IN4. The height is normalised by the maximum saturation height. Velocity is normalised by the depth-averaged velocity of the profile.

G.2.2.3. S18W28EX1

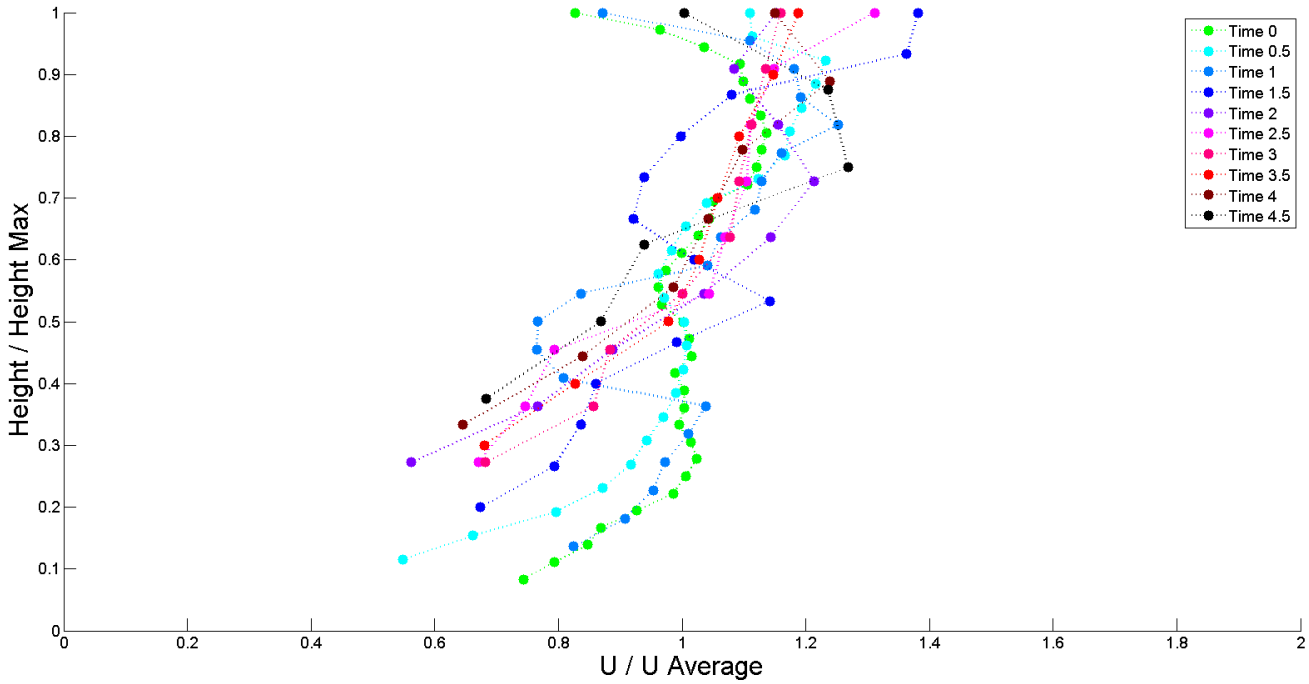

Figure G-22: Normalised velocity profiles of S18W28EX1. The height is normalised by the maximum saturation height. Velocity is normalised by the depth-averaged velocity of the profile. Vertical spacing at 8 pixels gives rougher profile.

G.2.3. S18 - W32

G.2.3.1. S18W32IN2

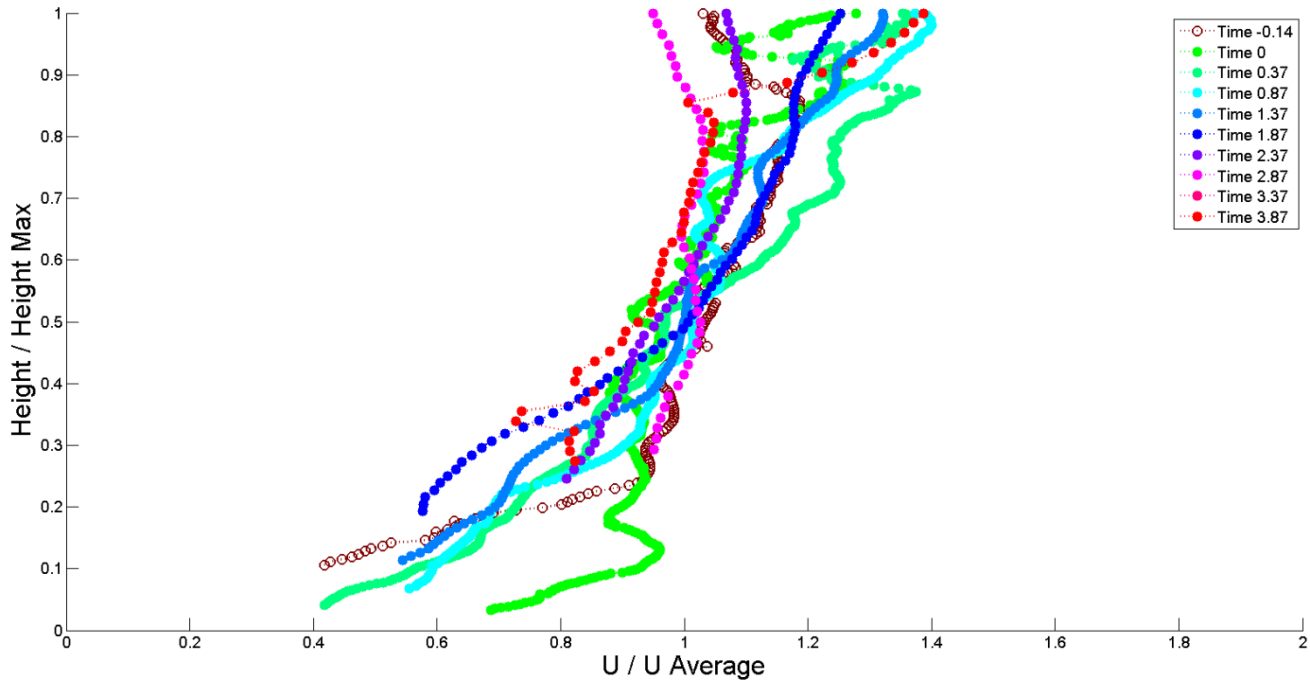

Figure G-23: Normalised velocity profiles of S18W32IN2. The height is normalised by the maximum saturation height. Velocity is normalised by the depth-averaged velocity of the profile.

G.2.3.2. S18W32IN6

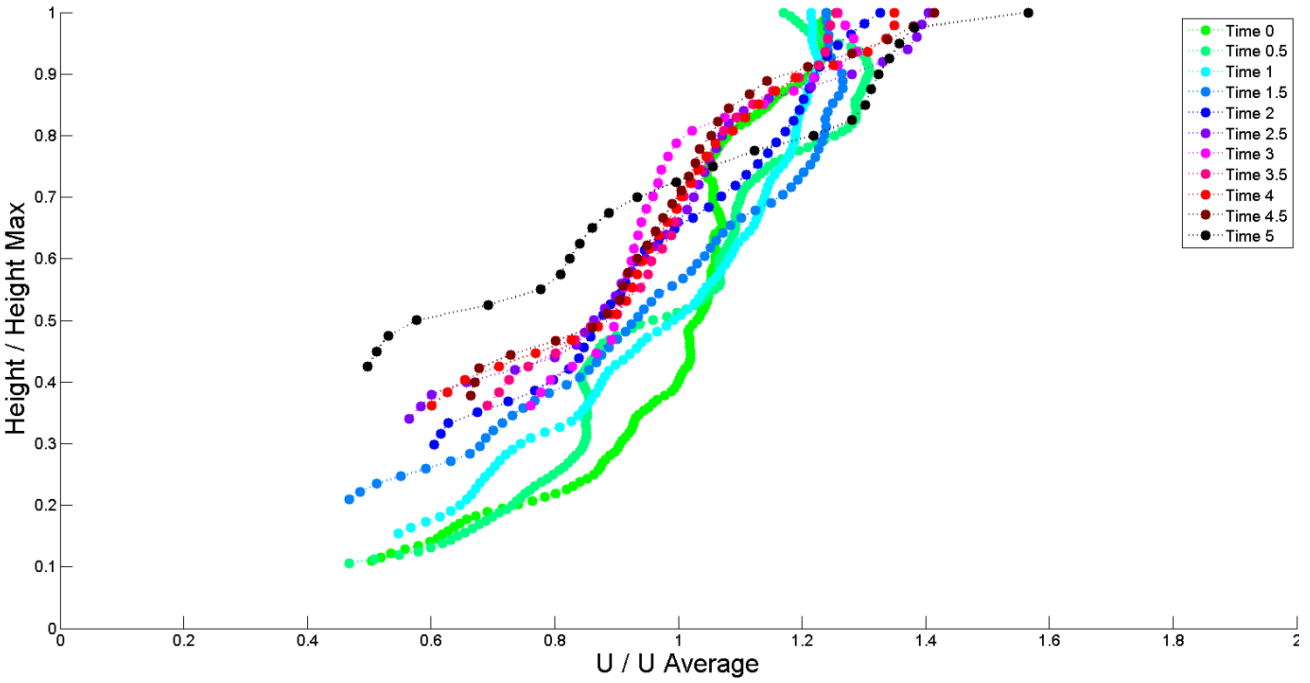

Figure G-24: Normalised velocity profiles of S18W32IN6. The height is normalised by the maximum saturation height. Velocity is normalised by the depth-averaged velocity of the profile.

G.2.3.3. S18W32EX2

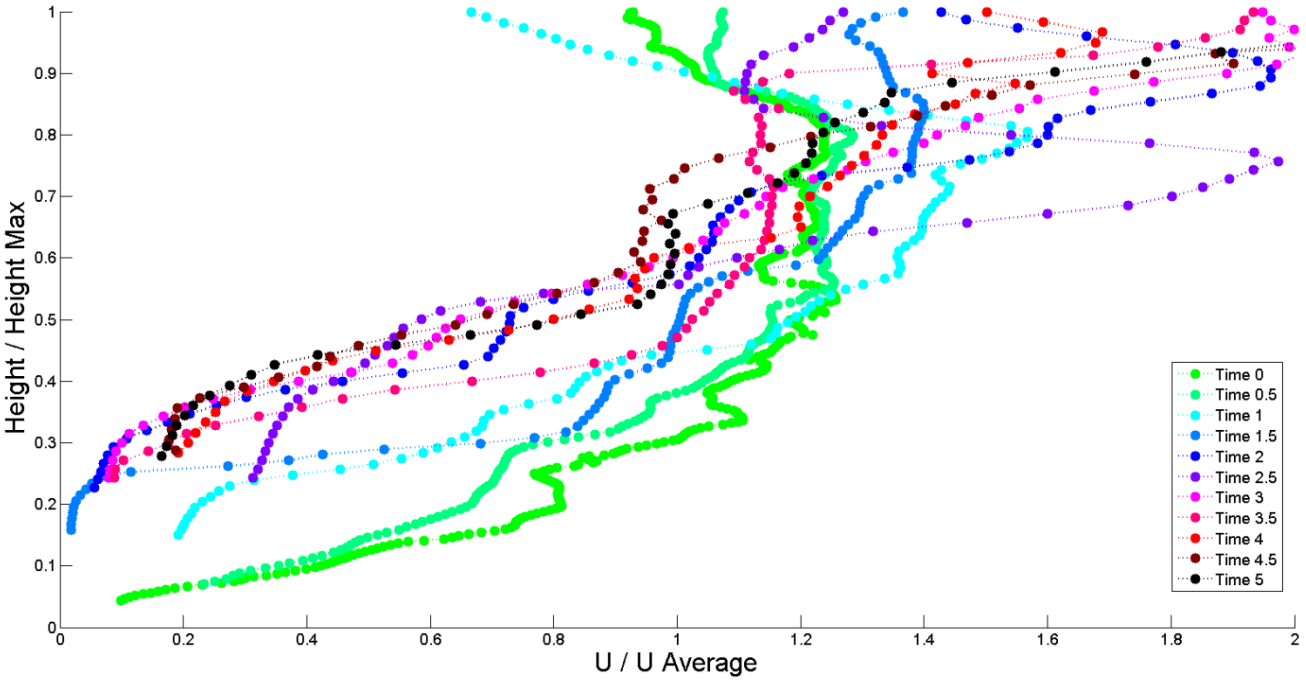

Figure G-25: Normalised velocity profiles of S18W32EX2. The height is normalised by the maximum saturation height. Velocity is normalised by the depth-averaged velocity of the profile.

G.2.3.4. S18W32EX4

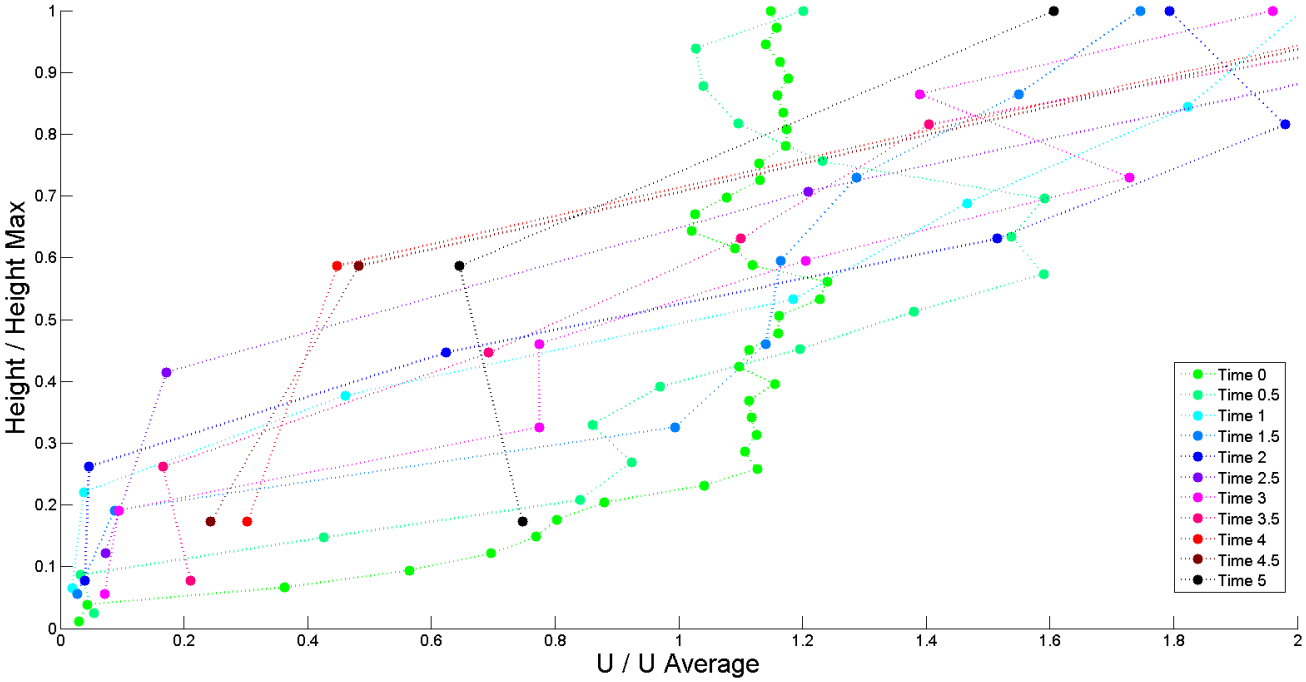

Figure G-26: Normalised velocity profiles of S18W32EX4. The height is normalised by the maximum saturation height. Velocity is normalised by the depth-averaged velocity of the profile. Vertical spacing at 8 pixels gives rougher profile.

G.2.4. S18 - W36

G.2.4.1. S18W36IN3

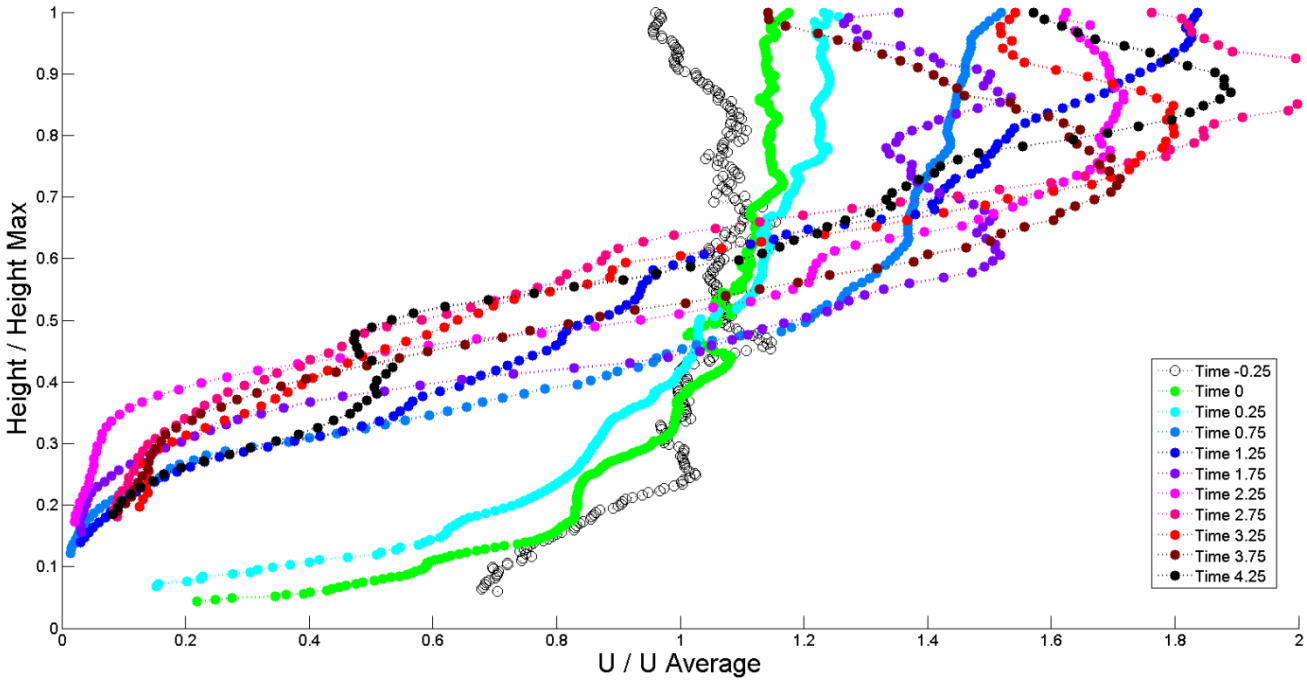

Figure G-27: Normalised velocity profiles of S18W36IN3. The height is normalised by the maximum saturation height. Velocity is normalised by the depth-averaged velocity of the profile.

G.2.4.2. S18W36EX3

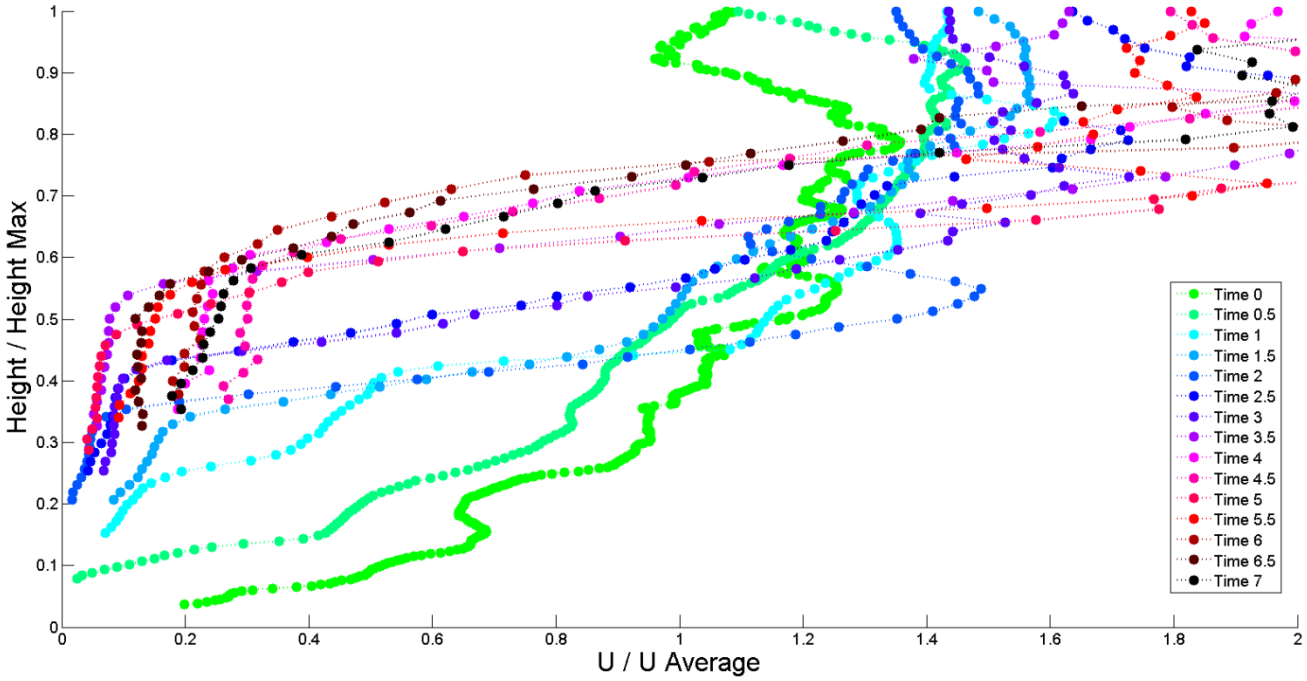

Figure G-28: Normalised velocity profiles of S18W36EX3. The height is normalised by the maximum saturation height. Velocity is normalised by the depth-averaged velocity of the profile.

G.2.4.3. S18W36EX5

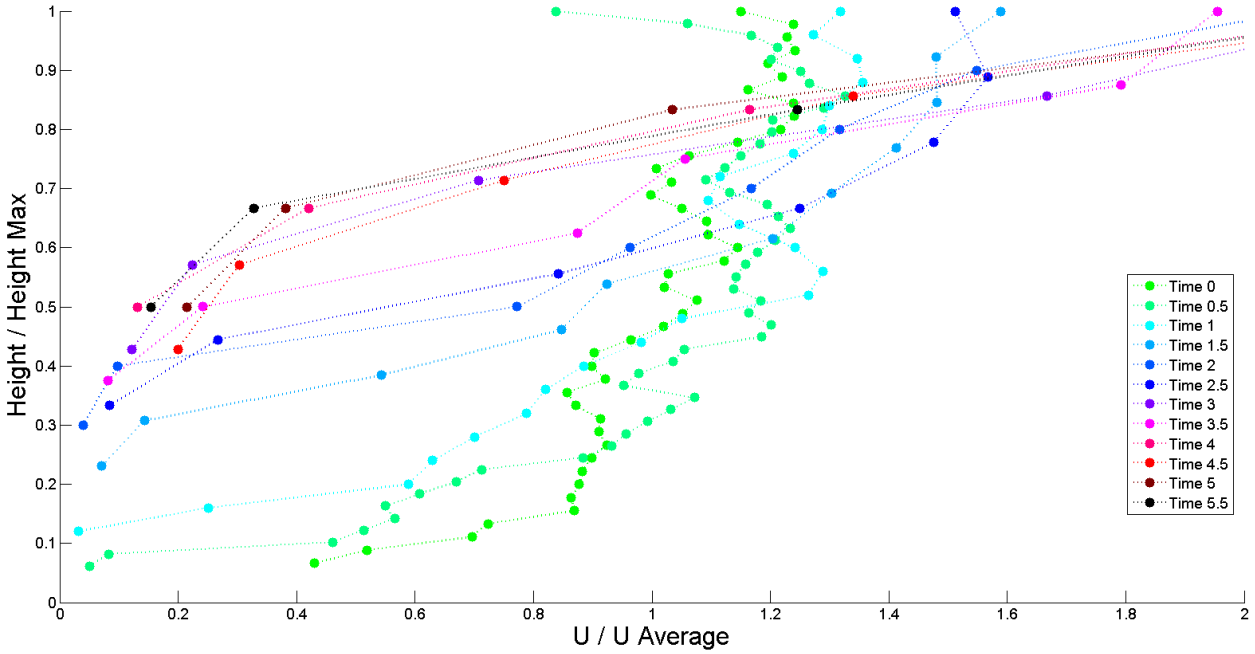

Figure G-29: Normalised velocity profiles of S18W36EX5. The height is normalised by the maximum saturation height. Velocity is normalised by the depth-averaged velocity of the profile. Vertical spacing at 8 pixels gives rougher profile.

G.2.5. S24 – W28

G.2.5.1. S24W32EX8

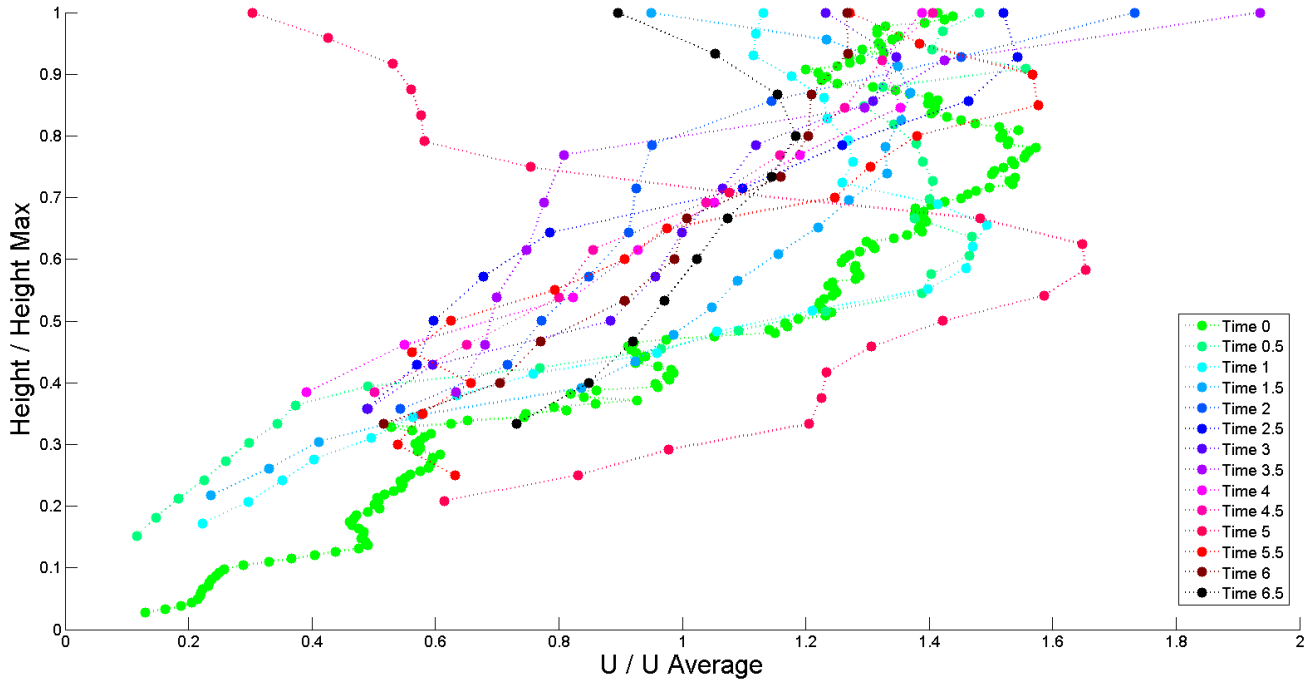

Figure G-30: Normalised velocity profiles of S24W28EX8. The height is normalised by the maximum saturation height. Velocity is normalised by the depth-averaged velocity of the profile.

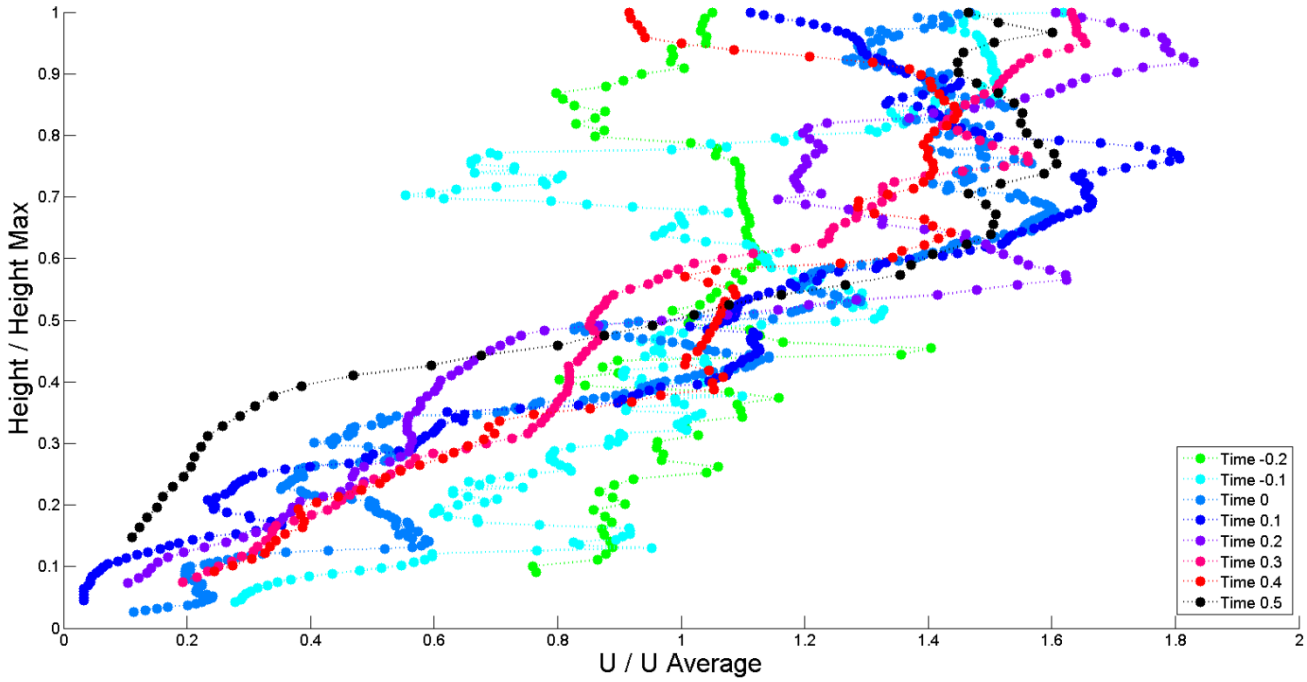

Figure G-31: Normalised velocity profiles of body of S24W28EX8. The height is normalised by the maximum saturation height. Velocity is normalised by the depth-averaged velocity of the profile

G.2.6. 24 – W32

G.2.6.1. S24W32IN7

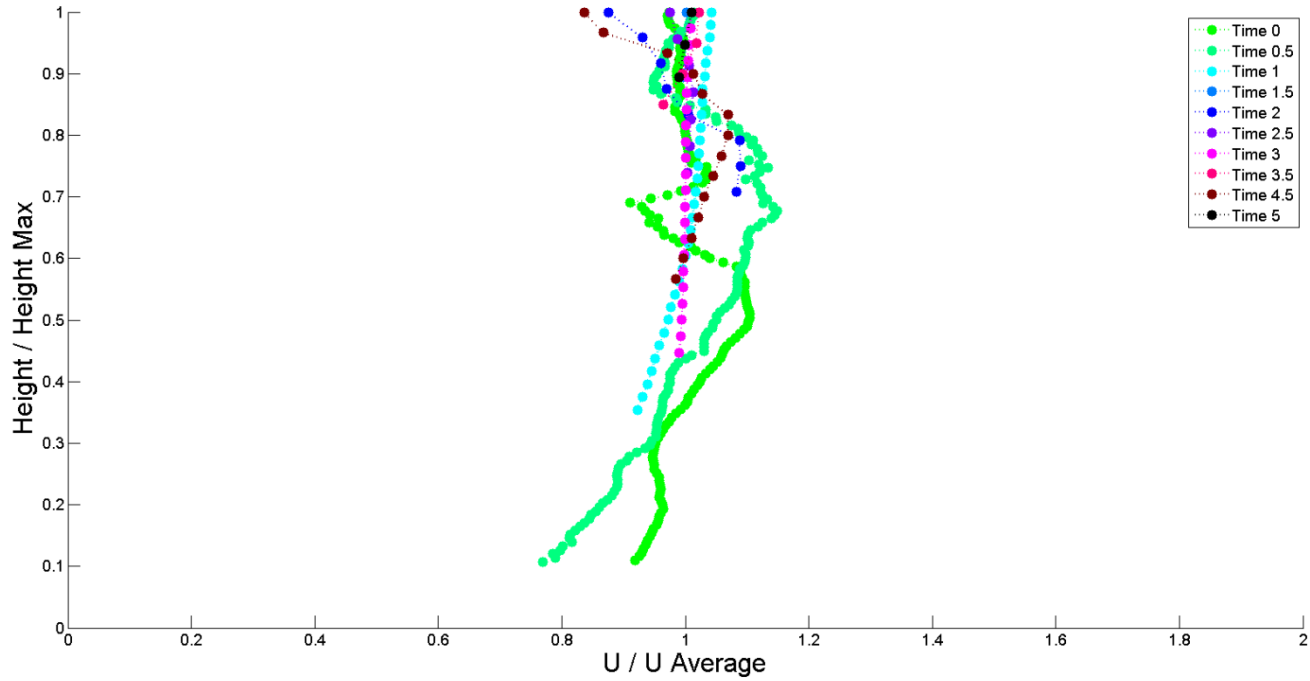

Figure G-32: Normalised velocity profiles of S24W32IN7. The height is normalised by the maximum saturation height. Velocity is normalised by the depth-averaged velocity of the profile. Poor image quality reduces accuracy and depth of PIV analysis.

G.2.6.2. S24W32IN8

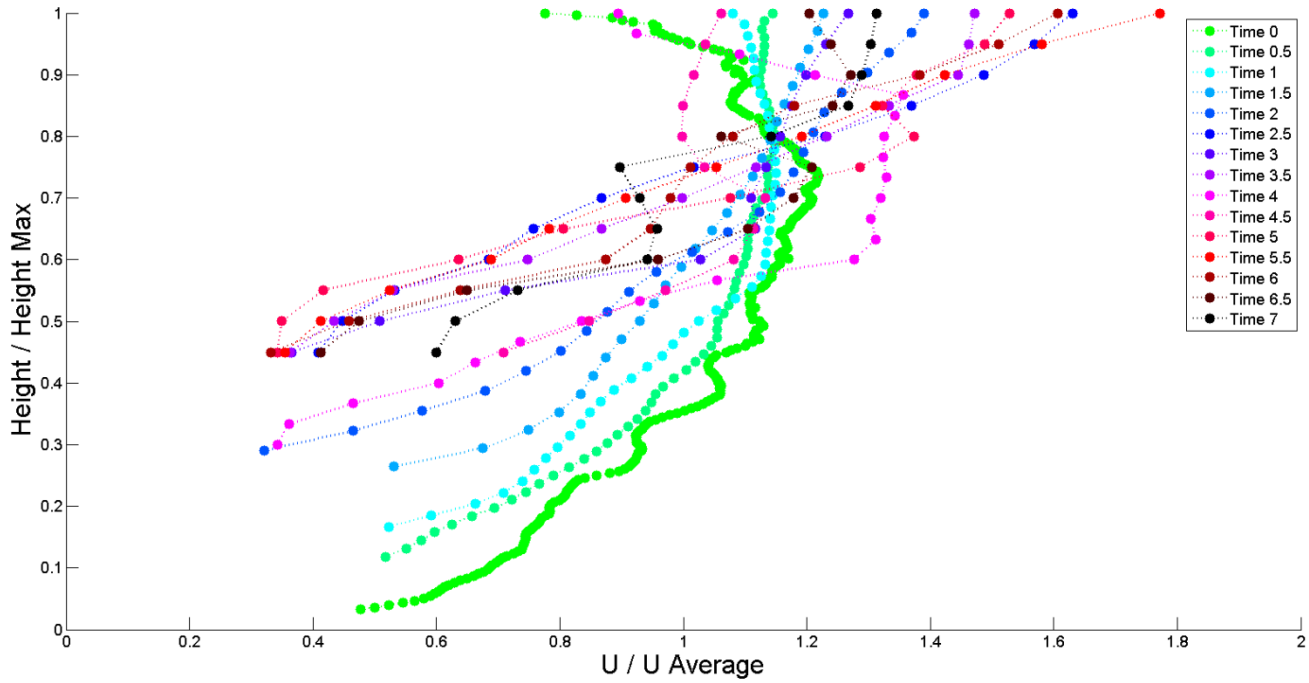

Figure G-33: Normalised velocity profiles of S24W32IN8. The height is normalised by the maximum saturation height. Velocity is normalised by the depth-averaged velocity of the profile.

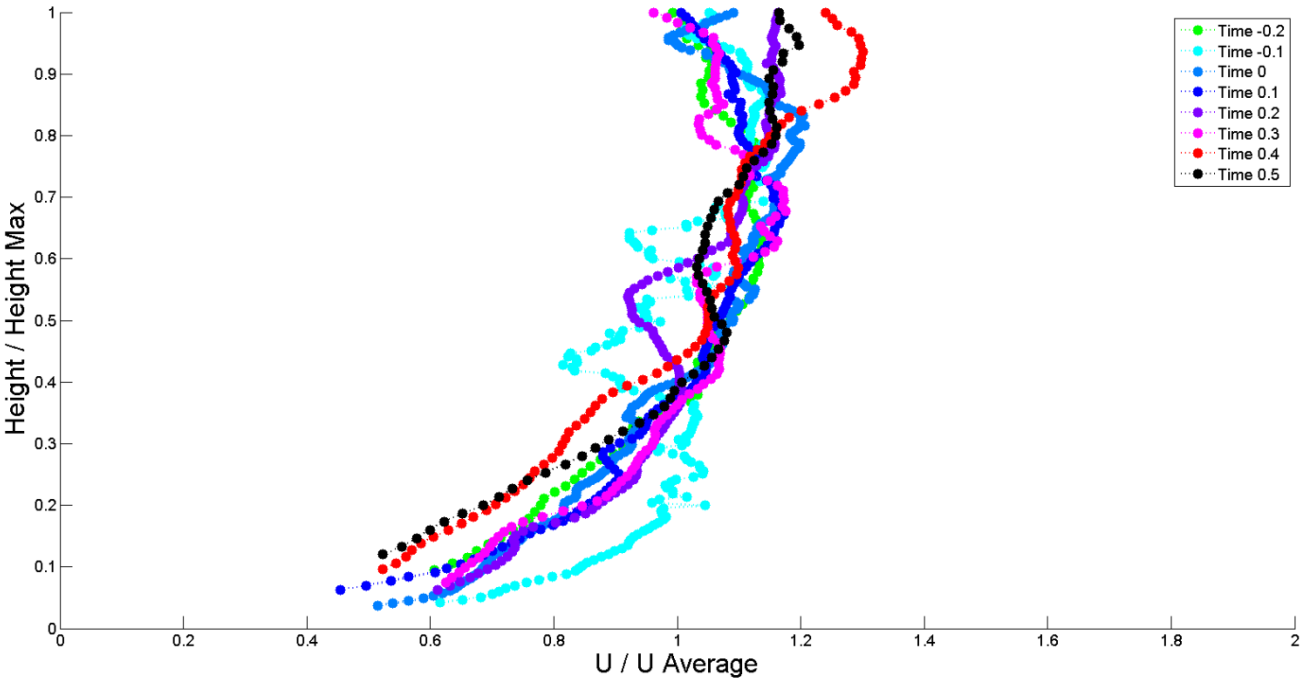

Figure G-34: Normalised velocity profiles of body of S24W32IN8. The height is normalised by the maximum saturation height. Velocity is normalised by the depth-averaged velocity of the profile.

G.2.6.1. S24W32EX7

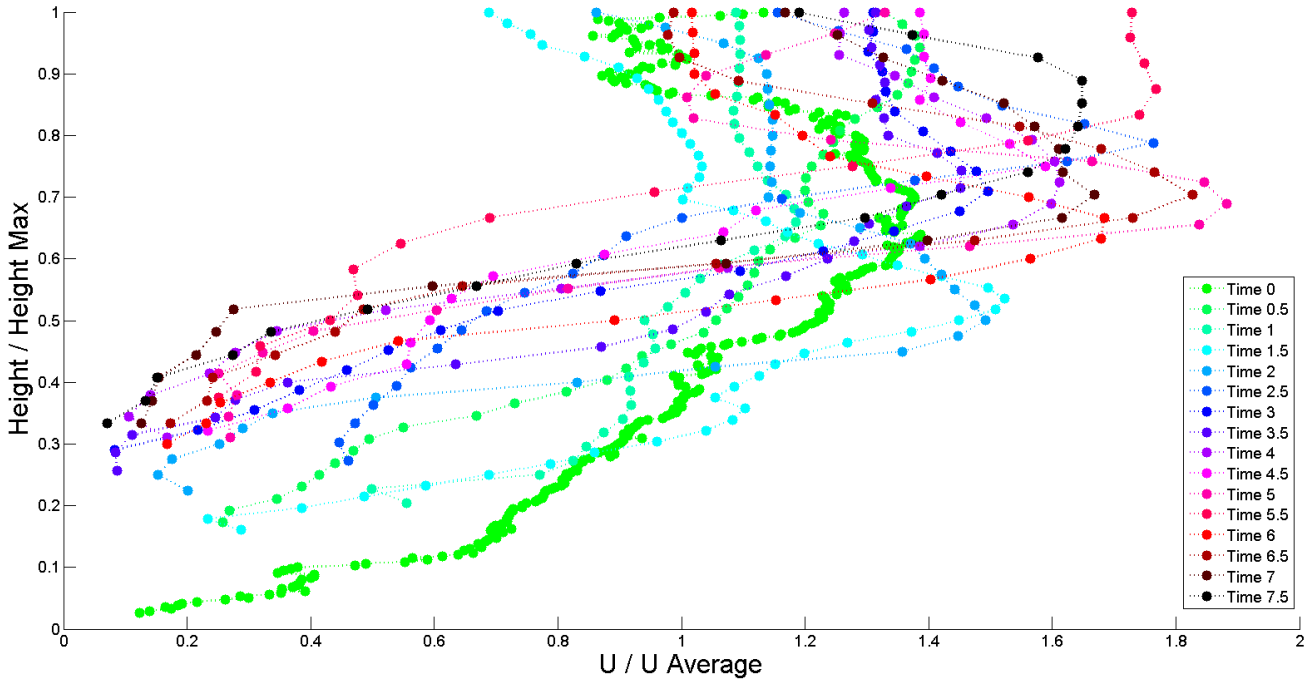

Figure G-35: Normalised velocity profiles of S24W32EX7. The height is normalised by the maximum saturation height. Velocity is normalised by the depth-averaged velocity of the profile.

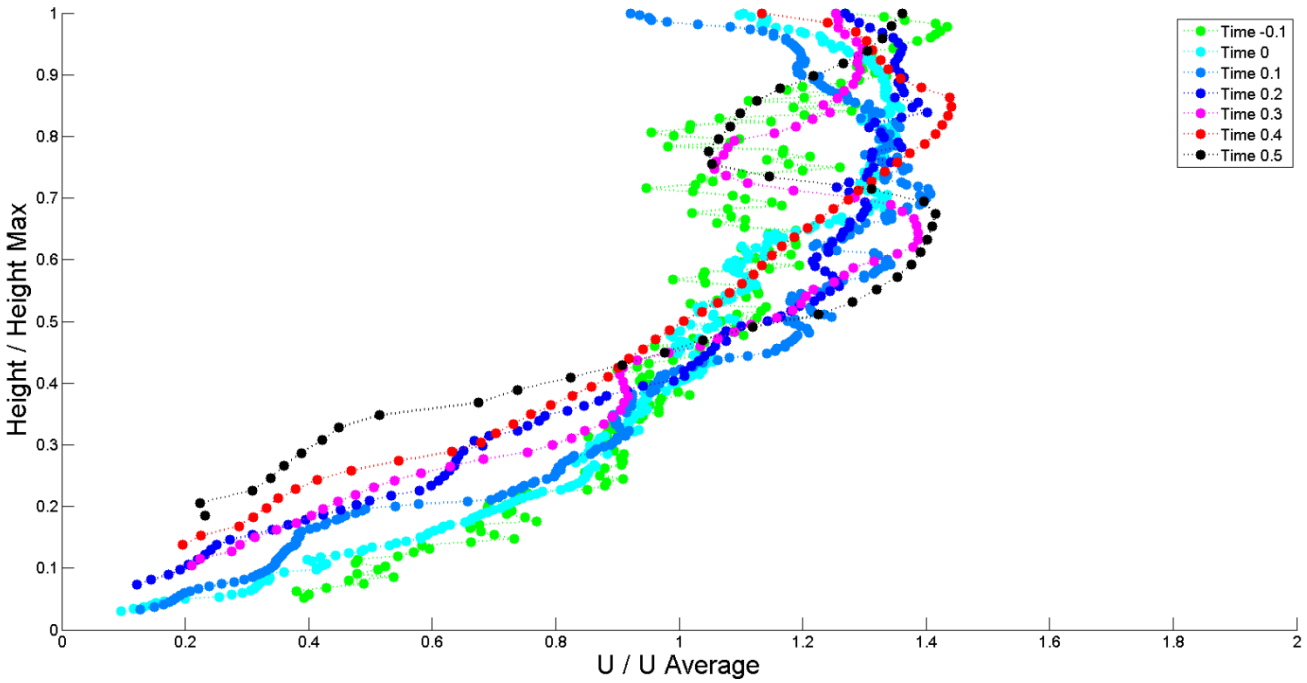

Figure G-36: Normalised velocity profiles of body of S24W32EX7. The height is normalised by the maximum saturation height. Velocity is normalised by the depth-averaged velocity of the profile.

G.2.6.2. S24W36EX9

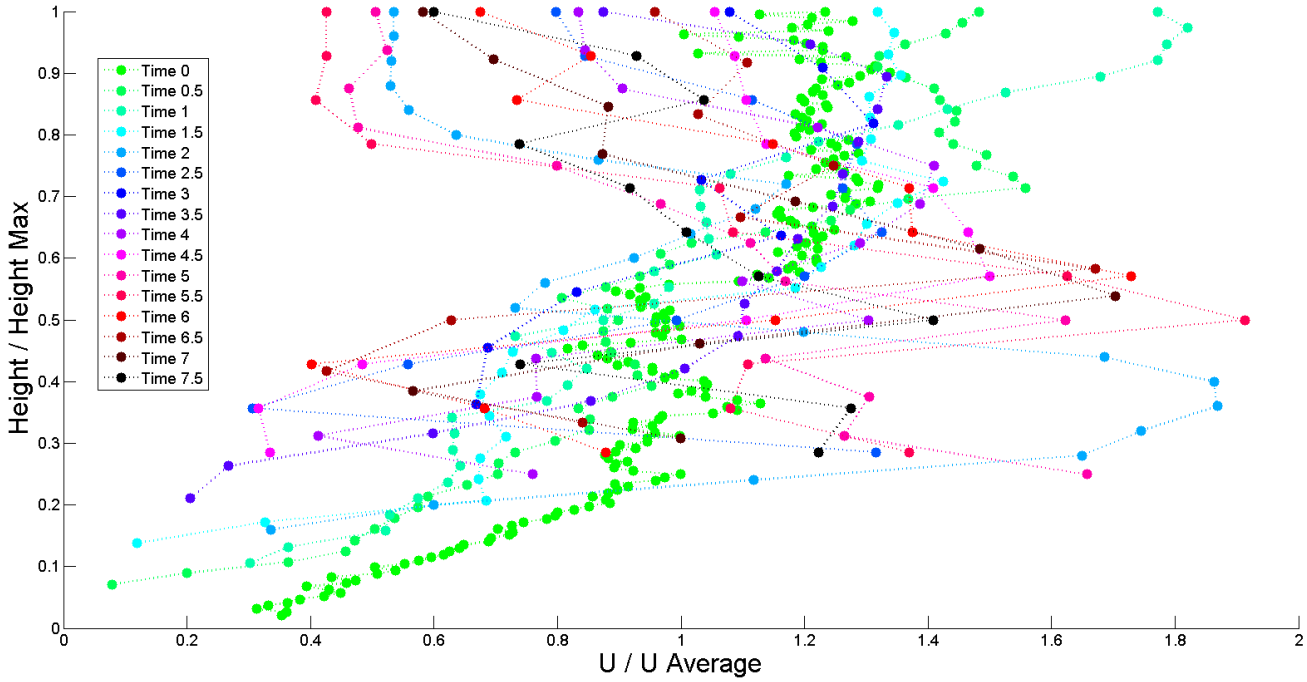

Figure G-37: Normalised velocity profiles of S24W32EX9. The height is normalised by the maximum saturation height. Velocity is normalised by the depth-averaged velocity of the profile.

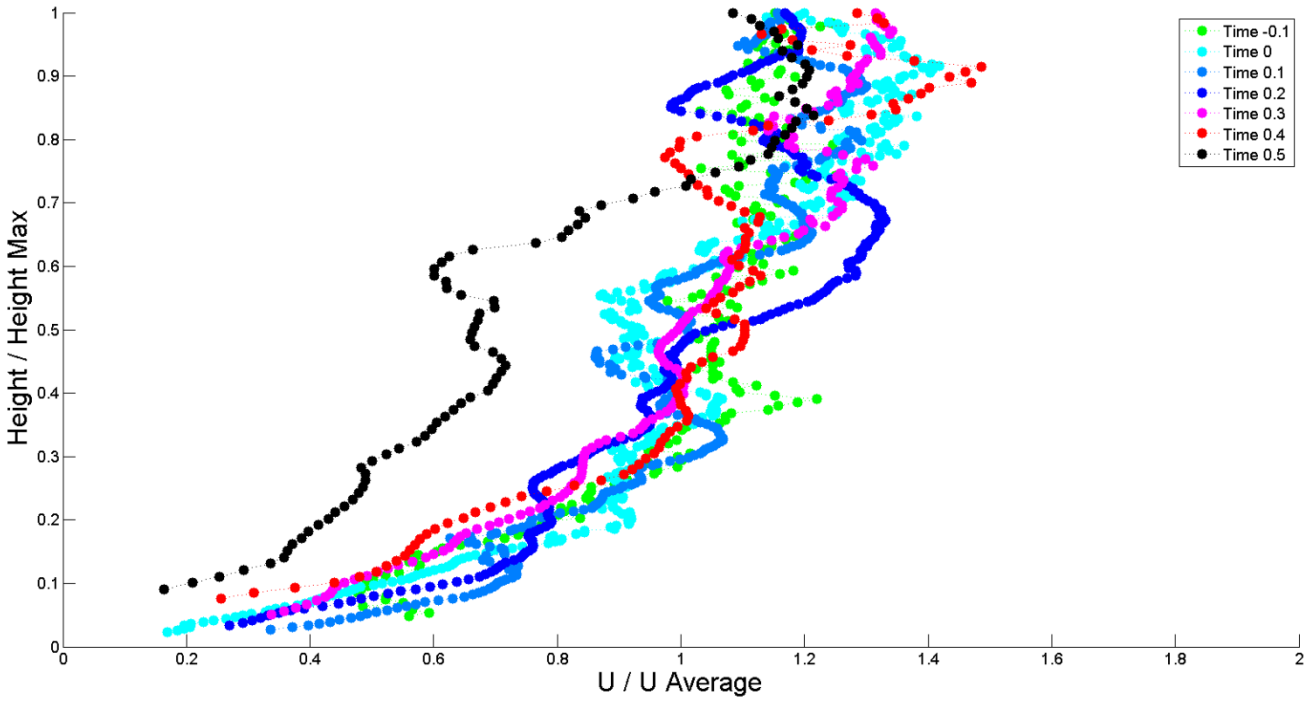

Figure G-38: Normalised velocity profiles of body of S24W32EX9. The height is normalised by the maximum saturation height. Velocity is normalised by the depth-averaged velocity of the profile.